Methods in Cell Biology • Volume 90

Methods in Nano Cell Biology

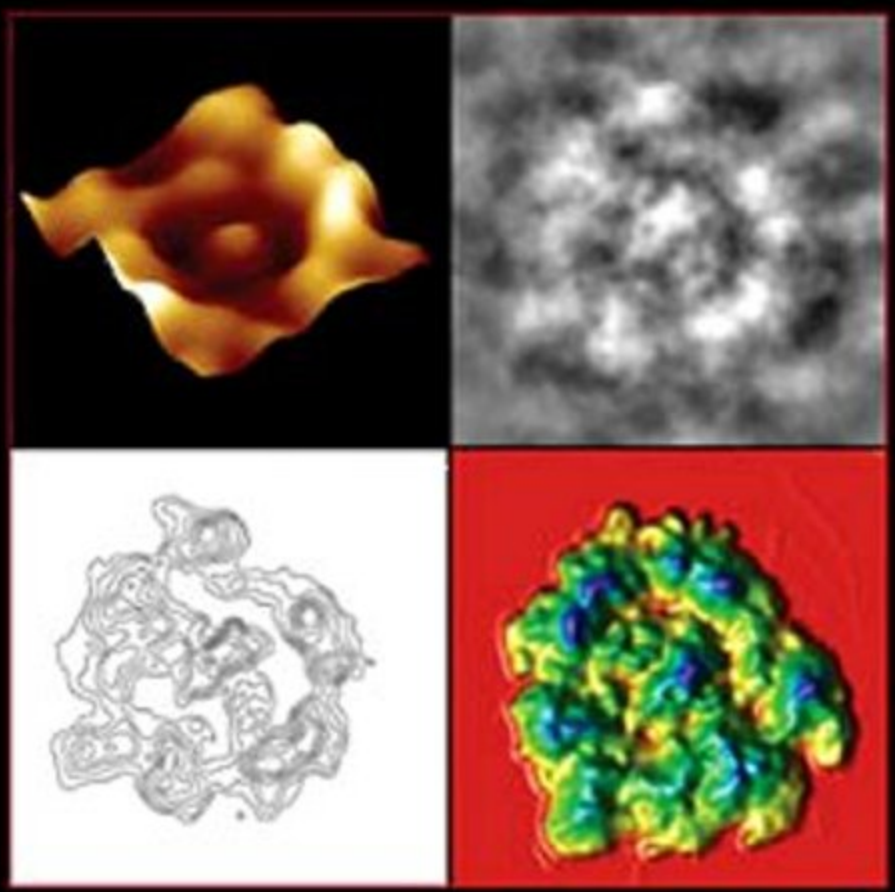

Edited by

Bhanu P. Jena

Series Editors

Leslie Wilson
Department of Molecular, Cellular and Developmental Biology
University of California
Santa Barbara, California

Paul Matsudaira
Whitehead Institute for Biomedical Research
Department of Biology
Division of Biological Engineering
Massachusetts Institute of Technology
Cambridge, Massachusetts

Academic Press is an imprint of Elsevier
30 Corporate Drive, Suite 400, Burlington, MA 01803, USA
525 B Street, Suite 1900, San Diego, CA 92101-4495, USA

First edition 2008

ISBN: 978-1-59749-270-6
ISSN: 0091-679X

For information on all Academic Press publications visit our website at elsevierdirect.com

Printed and bound in USA

08 09 10 11 12 10 9 8 7 6 5 4 3 2 1

CONTRIBUTORS

Numbers in parentheses indicate the pages on which the authors' contributions begin.

David P. Allison (59), Department of Biochemistry and Cellular and Molecular Biology, University of Tennessee, Knoxville, Tennessee 37996-0840

Barry D. Bruce (361), Graduate School of Genome Science and Technology, Department of Biochemistry, Cellular and Molecular Biology, and Department of Microbiology, University of Tennessee at Knoxville, Knoxville, Tennessee 37996

James J. Chambers (213), Department of Chemistry, 602 LGRT, University of Massachusetts, Amherst, Massachusetts 01003-9336

Bin Chen (323), Department of Biochemistry and Molecular Biology, Wayne State University, School of Medicine, Detroit, Michigan 48021

Jianglei Chen (283), Department of Biochemistry and Molecular Biology, Wayne State University, School of Medicine, Detroit, Michigan 48021

Won-Jin Cho (263), Department of Physiology, Wayne State University School of Medicine, Detroit, Michigan 48201

Prakitchai Chotewutmontri (361), Graduate School of Genome Science and Technology, University of Tennessee at Knoxville, Knoxville, Tennessee 37996

Jeremy D. Cook (195), Department of Biochemistry and Molecular Biology, Wayne State University, School of Medicine, Detroit, Michigan

Will Crenshaw (361), Department of Biochemistry, Cellular and Molecular Biology, University of Tennessee at Knoxville, Knoxville, Tennessee 37996

Ashita Dave (361), Department of Biochemistry, Cellular and Molecular Biology, University of Tennessee at Knoxville, Knoxville, Tennessee 37996

Mitchel J. Doktycz (59), Biological & Nanoscale Systems Group, Biosciences Division, Oak Ridge National Laboratory, Oak Ridge, Tennessee 37831-6445

Kevin O. Douglas (413), Biophysics Group, Physics Lab, National Institute of Standards and Technology, Gaithersburg, Maryland 20899-8443

Yves F. Dufrêne (59), Unité de chimie des interfaces, Université Catholique de Louvain, Croix du Sud 2/18, B-1348 Louvain-la-Neuve, Belgium

Philip Fowler (229), Department of Biochemistry, University of Oxford, Oxford, OX1 3QU, United Kingdom

Maria Gaczynska (37), Department of Molecular Medicine, Institute of Biotechnology, University of Texas Health Science Center at San Antonio, 15355 Lambda Drive, San Antonio, Texas 78245

Susan K. Gregurick (413), Department of Chemistry and Biochemistry, University of Maryland, Baltimore County, Baltimore, Maryland 21250.

Mark Hildebrand (59), Scripps Institution of Ocenography, University of California-San Diego, LaJolla, California 92093-0202

Yuefei Huang (283), Department of Biochemistry and Molecular Biology, Wayne State University, School of Medicine, Detroit, Michigan 48021

Bhanu P. Jena (1, 19, 153, 179, 263), Department of Physiology, Wayne State University School of Medicine, Detroit, Michigan 48201

Aleksandar M. Jeremic (263), Department of Biological Sciences, The George Washington University, Washington, District of Columbia 20052

Richard H. Kramer (213), Department of Molecular and Cell Biology, University of California, Berkeley, California 94720-3200

Qianqian Li (283, 323), Department of Biochemistry and Molecular Biology, Wayne State University, School of Medicine, Detroit, Michigan 48021

Geoffrey A. Lott (113), Department of Chemistry, Oregon Center for Optics, University of Oregon, Eugene, Oregon 970403

H. Peter Lu (431), Department of Chemistry, Bowling Green State University, Center for Photochemical Sciences, Bowling Green, Ohio 43403

Andrew H. Marcus (113), Department of Chemistry, Oregon Center for Optics, University of Oregon, Eugene, Oregon 970403

Christopher McCullough (323), Department of Biochemistry and Molecular Biology, Wayne State University, School of Medicine, Detroit, Michigan 48021

Younes Mokrab (229), Department of Biochemistry, University of Oxford, Oxford, OX1 3QU, United Kingdom

Victoria Murray (283, 323), Department of Biochemistry and Molecular Biology, Wayne State University, School of Medicine, Detroit, Michigan 48021

Pawel A. Osmulski (37), Department of Molecular Medicine, Institute of Biotechnology, University of Texas Health Science Center at San Antonio, 15355 Lambda Drive, San Antonio, Texas 78245

James E. Penner-Hahn (195), Department of Chemistry, The University of Michigan, Ann Arbor, Michigan

David F. Plusquellic (413), Biophysics Group, Physics Lab, National Institute of Standards and Technology, Gaithersburg, Maryland 20899-8443

Gabriel Popescu (85), Quantitative Light Imaging Laboratory, Department of Electrical and Computer Engineering, Beckman Institute for Advanced Science and Technology, University of Illinois at Urbana-Champaign, Urbana, Illinois 61801

L. Evan Reddick (361), Department of Biochemistry, Cellular and Molecular Biology, University of Tennessee at Knoxville, Knoxville, Tennessee 37996

Xuefeng Ren (323), Department of Biochemistry and Molecular Biology, Wayne State University, School of Medicine, Detroit, Michigan 48021

Mark S. P. Sansom (229), Department of Biochemistry, University of Oxford, Oxford, OX1 3QU, United Kingdom

Eric N. Senning (113), Department of Chemistry, Oregon Center for Optics, University of Oregon, Eugene, Oregon 970403

Karen Siegrist (413), Electro-optical and Infrared Systems and Technologies Group, Johns Hopkins Applied Physics Laboratory, Laurel, Maryland 20723

Arun Sivashanmugam (323), Department of Biochemistry and Molecular Biology, Wayne State University, School of Medicine, Detroit, Michigan 48021

Phillip Stansfeld (229), Department of Biochemistry, University of Oxford, Oxford, OX1 3QU, United Kingdom

Timothy L. Stemmler (195), Department of Biochemistry and Molecular Biology, Wayne State University, School of Medicine, Detroit, Michigan

Kaihsu Tai (229), Department of Biochemistry, University of Oxford, Oxford, OX1 3QU, United Kingdom

Michael Vaughn (361), Department of Biochemistry, Cellular and Molecular Biology, University of Tennessee at Knoxville, Knoxville, Tennessee 37996

Julio Vera (395), Systems Biology and Bioinformatics Group, Department of Computer Science, University of Rostock, 18051 Rostock, Germany

Jianjun Wang (283, 323), Department of Biochemistry and Molecular Biology, Wayne State University, School of Medicine, Detroit, Michigan 48021

Denys N. Wheatley (135), BioMedES, Leggat House, Keithhall, Inverurie, Aberdeen AB51 0LX, United Kingdom

Olaf Wolkenhauer (395), Systems Biology and Bioinformatics Group, Department of Computer Science, University of Rostock, 18051 Rostock, Germany

Nan Xiao (283), Department of Biochemistry and Molecular Biology, Wayne State University, School of Medicine, Detroit, Michigan 48021

Yunhuang Yang (323), Department of Biochemistry and Molecular Biology, Wayne State University, School of Medicine, Detroit, Michigan 48021

Hailiang Zhang (413), Department of Chemistry and Biochemistry, University of Maryland, Baltimore County, Baltimore, Maryland 21250.

PREFACE

Throughout history of human civilization, our quest to understand *Nature* has fueled our imagination to make the necessary inventions that further our perception of *Nature*, perceptions beyond the natural limits of our senses. Our constant desire to improving our understanding of time and space has been a powerful driving force. For example, the invention of various telescopes for observing distant objects, and microscopes for studying the very small, has enabled discoveries of distant galaxies and planets light years away, and of the micrometer-size unit of life—the ''Cell'', and its nanometer-size subcellular organelles. The ultimate goal, however, is the understanding of cellular structure–function at atomic resolution and in real time in live cells. In the past decade, major advances in technology and approach, has come close to realizing this objective. In this book, examples of the various advancements made in recent years, to realizing the ultimate goal of understanding cellular structure–function at atomic resolution and in real time in live cells, are presented.

Throughout history, the development of new imaging tools has provided new insights into our perceptions of the living world and profoundly impacted human health. The invention of the light microscope more than 300 years ago, was the first catalyst, propelling us into the era of modern cell biology and medicine. Using the light microscope, a giant step into the gates of modern cell biology and medicine was made with the discovery of the ''Cell''. The structure and morphology of normal and diseased cells, and of disease-causing microorganisms, were observed for the first time using the light microscope. Then in the 1930s, with the birth of the electron microscope (EM), dawned a new era. Through the mid 1940s and 1950s, a number of subcellular organelles were discovered and their functions determined using the EM. Viruses, the new life forms, were discovered and studied for the first time, and implicated in diseases ranging from the common cold to autoimmune disease (AIDS). Despite the capability of the EM to image biological samples at near nanometer resolution, sample processing resulting in morphological alterations remained a major concern. Then in the mid 1980s, scanning probe microscopy was invented, further extending our perception of the living world to the near atomic realm. One such scanning probe microscope, the atomic force microscope (AFM), has helped overcome both limitations of light and electron microscopy, enabling determination of the structure and dynamics of live cells and biomolecules in 3D, at near angstrom resolution. The resolving power of the light microscope is dependent on the wavelength of the light used and hence, 250–300 nm in lateral and much less in depth resolution can at best be achieved using light for imaging. As a result, cellular structures measuring less then 250–300 nm in lateral

or depth dimension, had evaded visual detection until invention of the AFM. In this book, the utilization of the AFM in the discovery of a new cellular structure, the "porosome" and its structure and dynamics at nanometer resolution in real time in live cells (Chapter 1), the structure and dynamics of subcellular organelles at nanometer resolution and in real time (Chapters 2 and 3), and in Chapter 4, the examination of the intricate biomineralization in diatoms, is presented. Similarly, the AFM has been utilized to understand the molecular mechanism of membrane fusion in cells (Chapter 8), and the assembly and disassembly of membrane-associated proteins (Chapters 8 and 9). Target membrane proteins, SNAP-25 and syntaxin (t-SNARE) and secretory vesicle-associated membrane protein (VAMP or v-SNARE), are part of the conserved protein complex involved in fusion of opposing bilayers. VAMP and syntaxin are both integral membrane proteins, with the soluble SNAP-25 associating with syntaxin. Therefore, understanding of SNARE-induced membrane fusion required determination of the arrangement and interaction between membrane-associated v- and t-SNARE proteins. Ideally, the atomic coordinates of membrane-associated SNARE complex using X-ray crystallography would provide atomic details of the t-/v-SNARE complex. Such atomic details of membrane-associated t-/v-SNARE complex has not been possible, primarily due to solubility problems of membrane SNAREs, compounded with the fact that v-SNARE and t-SNAREs need to reside in opposing membranes when they meet, to form the appropriate physiologically relevant SNARE complex. The remaining option has been the use of nuclear magnetic resonance spectroscopy (NMR); however, the NMR approach too has not been successful, primarily due to the molecular size limitation of NMR application. Regardless of these set backs and limitations, AFM force spectroscopy has provided for the first time at nm resolution, an understanding of the structure, assembly, and disassembly of the membrane-associated t-/v-SNARE complex in physiological buffer solution (Chapter 8).

The above examples demonstrate the power and scope of the AFM in providing an increased understanding of the cell. Similarly in the book, examples of a number of new and novel approaches in the study of cellular structure-function, is also discussed. In chapter 10 for example, the structure and dynamics of metalloproteins in live cells, has bee investigated using X-ray absorption spectroscopy (XAS). In recent years, XAS has emerged as a new and powerful tool in investigating the structure and dynamics of metals in cells and in metal containing cellular biomolecules. Utilizing the high flux and broad energy range of X-rays supplied by synchrotron light sources, the selective excitation of core electronic transitions in each metal within cells, can be achieved. Spectroscopic signals from these electronic transitions can therefore be used to determine the chemical architecture of metals in cells, in cellular components, and in biomolecules, at varying degrees of structural resolution. Real time investigation of protein folding, structure and dynamics at high resolution in living cells, is the next major step in nano cell biology. In Chapter 14, using a QQ-reagent based protein transduction technology, investigation of protein folding, structure and dynamics, at atomic resolution *in vivo* can be investigated. Today, nano manipulation and tagging using light-activated ion channels, has made

it possible to precisely and remotely regulate activity in neurons (Chapter 11). Quantitative phase imaging (Chapter 5), and Fourier imaging correlation spectroscopy (Chapter 6), now provide novel insights into our understanding of cellular structure–function. Similarly, THz investigation of condensed phase studies, provide further understanding into the structure–function of biomolecules. Lately, a plethora of novel approaches, combined with conventional tools and techniques, provide a better understanding of cellular structure–function (Chapters 6, 8, 11, 15, and 16). Using new and improved computational resources; AFM, XAS, NMR, proteomics, genomics, and molecular dynamic simulation, have become leading and powerful tools and approaches in the study of the cell, and investigation into the new field of "*Nano Cell Biology*".

Bhanu P. Jena, Ph.D., D.Sc.

CHAPTER 1

Extracellular Dynamics at nm Resolution in Live Cells

Bhanu P. Jena

Department of Physiology
Wayne State University School of Medicine
Detroit, Michigan 48201

Abstract

We are all voyagers in time and space, and throughout history of human civilization, our quest to understand Nature has fueled our imagination to make the necessary inventions that further our perception of Nature, perceptions beyond the natural limits of our senses. For example, the invention of various telescopes

METHODS IN CELL BIOLOGY, VOL. 90

0091-679X/08 $35.00
DOI: 10.1016/S0091-679X(08)00801-7

for observing distant objects, and microscopes for perceiving the very small, has enabled discoveries of distant galaxies and planets light years away, and of the micrometer-size unit of life—the "Cell," and of its nanometer-size subcellular organelles. The story of cell secretion, a fundamental process as old as life itself, occurs in all organisms—from the simple yeast to cells in humans. In the last 15 years, primarily using the atomic force microscope—a force spectroscope, a detailed understanding of the molecular machinery and mechanism of secretion in cells has come to light. This has led to a paradigm shift in our understanding of the underlying mechanism of cell secretion. The journey leading to the discovery of the "porosome," a nanometer-size structure at the cell plasma membrane—the universal secretory machinery, and its structure and dynamics in live cells, is briefly discussed in this chapter.

I. Introduction

Secretion is a fundamental cellular process responsible for numerous physiological functions in living organisms, such as neurotransmission and the secretion of hormones and digestive enzymes. Secretory defects in cells are responsible for a host of debilitating diseases, and hence this field has been the subject of intense research for over half a century. Only in the past decade with the discovery of the "porosome" using atomic force microscopy (AFM), and its determination as the universal secretory machinery in cells, finally provides a molecular understanding of cell secretion. In cells, secretory products packaged and stored in membranous sacs or vesicles, dock and establish continuity with the base of the plasma membrane (PM)-associated porosome complexes, to release their contents. The discovery of the porosome as the universal secretory machinery, its isolation, its structure, and dynamics at nanometer resolution and in real-time, its biochemical composition and functional reconstitution into artificial lipid membrane, have been determined (Cho *et al*., 2002a,b, 2004, 2007; Jena, 2005, 2007; Jena *et al*., 2003; Jeremic *et al*., 2003; Schneider *et al*., 1997), greatly advancing our understanding of the secretory process in cells.

The resolving power of the light microscope is dependent on the wavelength of used light and hence 250–300 nm in lateral and much less in depth resolution can at best be achieved using light for imaging. The porosome or fusion pore in live secretory cells are cup-shaped supramolecular structures, measuring 100–180 nm at the opening and 25–45 nm in relative depth in the exocrine pancreas and in neuroendocrine cells. At the nerve terminal or in astrocytes, the porosome is an order of magnitude smaller, measuring just 10–12 nm at the opening to the outside. Due to the nanometer size of the porosome complex, it had evaded visual detection until its discovery using ultrahigh resolution AFM (Alexander *et al*., 1989; Binnig *et al*., 1986; Hörber and Miles *et al*., 2003). The development of the AFM (Binnig *et al*., 1986) has enabled the imaging of live cell structure and dynamics in physiological buffer solutions, at nanometer to near angstrom resolution and in

real-time. In AFM, a probe tip microfabricated from silicon or silicon nitride and mounted on a cantilever spring is used to scan the surface of the sample at a constant force. Either the probe or the sample can be precisely moved in a raster pattern using a xyz piezo to scan the surface of the sample. The deflection of the cantilever measured optically is used to generate an isoforce relief of the sample (Alexander *et al*., 1989). Force is thus used by the AFM to image surface profiles of objects such as live cells (Cho *et al*., 2002a,b, 2004, 2007; Jena *et al*., 2003; Jeremic *et al*., 2003; Schneider *et al*., 1997), subcellular structures (Cho *et al*., 2002c; Jena *et al*., 1997; Kelly *et al*., 2004), and biomolecules (Cho and Jena, 2007; Cho *et al*., 2002d, 2005a; Jeremic *et al*., 2006), submerged in physiological buffer solutions, at ultra high-resolution and in real-time.

II. Materials and Methods

A. Isolation of Pancreatic Acinar Cells

Pancreatic acinar cells and hemi-acini were isolated. For each experiment, a male Sprague Dawley rat weighing 80–100 g was euthanized by ether inhalation. The pancreas was then dissected out and chopped into 0.5-mm^3 pieces, which were then mildly agitated for 15 min at 37 °C in a siliconized glass tube with 5 ml of oxygenated buffer A (98 mM NaCl, 4.8 mM KCl, 2 mM $CaCl_2$, 1.2 mM $MgCl_2$, 0.1% bovine serum albumin, 0.01% soybean trypsin inhibitor, 25 mM Hepes, pH 7.4) containing 1000 units of collagenase. The suspension of acini was filtered through a 224-mm Spectra-Mesh (Spectrum Laboratory Products) polyethylene filter to remove large clumps of acini and undissociated tissue. The acini were washed six times, 50 ml per wash, with ice-cold buffer A. Isolated rat pancreatic acini and acinar cells were plated on Cell-Tak coated glass coverslips. Two to three hours after plating, cells were imaged using the AFM before and during stimulation of secretion. Isolated pancreatic acinar cells and small acinar preparations were used in the study since fusions of regulated secretory vesicles at the plasma membrane (PM) in pancreatic acini are confined to the apical region which faces the acinus lumen, preventing imaging by the AFM in whole acinar preparations. Furthermore, in isolated acinar cells or hemi-acinar preparations, the secretagogue Mas7 has immediate and uniform access to the cells.

B. Isolation of Synaptosomes, Synaptosomal Membrane, and Synaptic Vesicles

Rat brain synaptosomes, synaptosomal membrane, and synaptic vesicles (SVs), were prepared whole brain tissue from Sprague-Dawley rats. Brains from Sprague-Dawley rats weighing 100–150 g were isolated and placed in an ice-cold buffered sucrose solution (5 mM Hepes pH 7.4, 0.32 M sucrose) supplemented with protease inhibitor cocktail (Sigma, St. Louis, Missouri) and homogenized using teflon-glass homogenizer (8e10 strokes). The total homogenate was centrifuged for 3 min

at $2500 \times g$. The supernatant fraction was further centrifuged for 15 min at $14{,}500 \times g$, and the resultant pellet was resuspended in buffered sucrose solution, which was loaded onto 3–10–23% Percoll gradients. After centrifugation at $28{,}000 \times g$ for 6 min, the enriched synaptosomal fraction was collected at the 10–23% percoll gradient interface. To isolate SVs and synaptosomal membrane, isolated synaptosomes were diluted with nine volumes of ice-cold H_2O (hypotonic lysis of synaptosomes to release SVs) and immediately homogenized with three strokes in Dounce homogenizer, followed by a 30 min incubation on ice. The homogenate was centrifuged for 20 min at $25{,}500 \times g$, and the resultant pellet (enriched synaptosomal membrane preparation) and supernatant (enriched SVs preparation) were used in our studies.

C. Isolation of Porosome

To isolate the neuronal fusion pore or porosome complex, SNAP-25 specific antibody conjugated to protein A-sepharose was used. SNAP-25 is present in neurons. One gram of total rat brain homogenate solubilized in Triton/Lubrol solubilization buffer (0.5% Lubrol; 1 mM benzamidine; 5 mM Mg-ATP; 5 mM EDTA; 0.5% Triton X-100, in PBS) supplemented with protease inhibitor mix (Sigma, St. Louis, Missouri) was used. SNAP-25 antibody conjugated to the protein A-sepharose was incubated with the solubilized homogenate for 1 h at room temperature followed by washing with wash buffer (500 mM NaCl, 10 mM Tris, 2 mM EDTA, pH 7.5). The immunoprecipitated sample attached to the immunosepharose beads was eluted using low pH buffer to obtain the porosome complex.

Similarly, porosome from the acinar cells of the exocrine pancreas were immunoisolated from PM preparations, using a SNAP-23 specific antibody (SNAP-23 is present in pancreatic acinar cells). To isolate the porosome complex for reconstitution experiments, SNAP-23 specific antibody conjugated to protein A-sepharose was used. Isolated pancreatic PM preparations were solubilized in Triton/Lubrol solubilization buffer, supplemented with protease inhibitor mix. SNAP-23 antibody conjugated to the protein A-sepharose was incubated with the solubilized membrane for 1 h at room temperature followed by washing with wash buffer, and eluted using low pH buffer.

D. AFM

Cells attached to a Cell-Tak coated glass coverslip were placed in a thermally controlled fluid chamber that allowed both rapid fluid exchange and the direct visualization of the living cells by an inverted microscope. The newly designed BAFM (Digital Instruments, Santa Barbara, California) was used in conjunction with an inverted optical microscope (Olympus IX70). Images of the PM in these cells were obtained by the BAFM, working in the "contact" mode and using a very low vertical imaging force $<$1–3 nN. Silicon and silicon nitride tips were used with spring constants of 0.25 and 0.06 N m^{-1}, respectively. To determine the effect of

force on the PM topology, control experiments were performed, where a scanning force of several nN over a 60 min period demonstrated no significant changes at the PM.

E. Amylase Measurement

Exocytosis from acinar cells was measured by determining the percentage of total cellular amylase release, following exposure of cells to a secretagogue (Mas7) or cytochalasin B (actin depolymerizing agent). Amylase, one of the major contents of secretory vesicles (zymogen granules, ZGs) in the exocrine pancreas was measured by the procedure of Bernfeld. In a typical amylase assay, rat pancreatic acini dissociated as single cells and groups of 2–6 cells were used. About 50–75 cells in 200 μl of total reaction mixture (buffer A) in the presence or absence of Mas7 or cytochalasin B were incubated at room temperature. Following incubation, the cells were centrifuged at $2000 \times g$ for 2 min in an Eppendorf microcentrifuge. The supernatant containing the secreted amylase was assayed. The cells in the remaining 100 ml of incubation mixture were sonicated, and the sonicate was diluted and assayed for amylase. From the above measurements, the total cellular amylase and percent release from the cells were calculated. Five microliters of the supernatant or lysed cell fractions was added to 95 μl of ice-cold amylase assay buffer (10 mM NaH_2PO_4, 10 mM Na_2HPO_4, 20 mM NaCl) placed in 12×75 mm glass tubes in an ice bath. The reaction was initiated by the addition of 100 ml of a 10 mg/ml potato starch in amylase assay buffer solution. The mixture was vortexed and incubated for 15 min at 37 °C. Following the incubation, the mixture was cooled in an ice bath and 400 ml of a color reagent (44 mM 3,5-dinitrosalicylic acid, 200 mM KOH, and 20 mM sodium potassium tartarate) was added. The mixture in glass tubes was covered and lowered into a boiling water bath for 25 min followed by cooling and the addition of 1.4 ml of distilled water. The mixture was then brought to room temperature and transferred to a plastic cuvette, and absorbance at 530 nm was measured with a spectrophotometer (Beckman DU-64).

F. Transmission Electron Microscopy

Isolated rat pancreatic acini were fixed in 2.5% buffered paraformaldehyde for 30 min, and the pellets embedded in Unicryl resin, followed by sectioning at 40–70 nm. Thin sections were transferred to coated specimen transmission electron microscope (TEM) grids, dried in the presence of uranyl acetate and methyl cellulose, and examined using a TEM. For negative staining electron microscopy, purified protein suspensions in PBS, were adsorbed onto hydrophilic carbon support films that were mounted onto formvar-coated, metal specimen grids (EMS, Ft. Washington, Pennsylvania). The adsorbed protein was washed in double-distilled water and negatively stained using 1% aqueous uranyl acetate. After the grids were dried in the presence of the uranyl acetate solution, they were

examined by TEM. To prevent bleaching by the electron beam, micrographs were obtained on portions of the grid not previously examined.

Similarly for TEM of neuronal tissue, rat brain was perfused with normal saline solution, followed by phosphate buffer (pH 7.4) containing 2.5% glutaraldehyde. After perfusion, the brain was carefully removed and diced into 1 mm^3 pieces. The pieces of brain tissue were postfixed in phosphate buffer containing 1.5% osmium tetroxide, dehydrated in graded ethanol and acetone, and embedded in araldite. Tissue blocks were appropriately trimmed and the 40–50 nm sections obtained were stained with lead citrate, and examined under a JEOL JEM-100C TEM.

G. Photon Correlation Spectroscopy

The size of neuronal porosome was also determined using photon correlation spectroscopy (PCS). PCS measurements were performed using a Zetasizer Nano ZS (Malvern Instruments, United Kingdom). In a typical experiment, the size distribution of isolated porosomes was determined using built-in software provided by Malvern Instruments. Prior to the determination of porosome size, calibration of instrument was performed using latex spheres of known size. In PCS, subtle fluctuations in the sample scattering intensity are correlated across microsecond time scales. The correlation function is calculated, from which the diffusion coefficient is determined by the instrument. Using Stokes–Einstein equation, hydrodynamics radius can be calculated from diffusion coefficient. The intensity size distribution, which is obtained as a plot of the relative intensity of light scattered by particles in various size classes, is calculated from correlation function using the built-in software. The particle scattering intensity is proportional to the molecular weight squared. Volume distribution, which assigns more realistic weights to both small and big particles, is calculated from the intensity distribution using Mie theory. The transforms of the PCS intensity distribution to volume distributions are obtained using the provided software by Malvern Instruments.

H. Porosome Reconstitution into Lipid Bilayer for Electrophysiological Measurements

Lipid bilayers were prepared using brain phosphatidylethanolamine (PE) and phosphatidylcholine (PC), and dioleoylphosphatidylcholine (DOPC), and dioleylphosphatidyl-serine (DOPS), obtained from Avanti lipids (Alabaster, Alabama). A suspension of PE:PC in a ratio of 7:3, and at a concentration of 10 mg/ml was prepared. Lipid suspension (100 μl) was dried under nitrogen gas and resuspended in 50 μl of decane. To prepare membranes reconstituted with the immunoisolated fusion pore complex, the immunoisolate was added to the lipid suspension and brushed onto a 200-μm hole in the bilayer preparation cup until a stable bilayer with a capacitance between 100 and 250 pF was established. Alternately, the immunoisolated pore complex was brushed onto a stable membrane formed at the 200-μm hole in the bilayer preparation cup. Electrical measurements of the artificial lipid membrane were performed using a bilayer setup.

Current versus time traces were recorded using pulse software, an EPC9 amplifier and probe from HEKA (Lambrecht, Germany). Briefly, membranes were formed while holding at 0 mV. Once a bilayer was formed and demonstrated to be in the capacitance limits for a stable bilayer membrane according to the hole diameter, the voltage was switched to −60 mV. A baseline current was established before the addition of isolated ZGs in case of pancreatic porosomes, or SVs for reconstituted porosomes from neurons.

I. Discovery of the "Porosome"—The Universal Secretory Machinery in Cells

Porosomes were first discovered in acinar cells of the exocrine pancreas (Schneider *et al.*, 1997). Exocrine pancreatic acinar cells are polarized secretory cells possessing an apical and a basolateral end. This well characterized cell of the exocrine pancreas, synthesize digestive enzymes, which is stored within 0.2–1.2 μm in diameter apically located membranous sacs or secretory vesicles, called ZG. Following a secretory stimulus, ZG's dock and fuse with the apical PM to release their contents to the outside. Contrary to neurons, where secretion of neurotransmitters occurs in the millisecond time regime, the pancreatic acinar cells secrete digestive enzymes over minutes following a secretory stimulus. Being a slow secretory cell, pancreatic acinar cells are ideal for the determination of the molecular steps involved in cell secretion. In the mid 1990s, AFM studies were therefore undertaken on live pancreatic acinar cells, with the sole intent of evaluating at high resolution, the structure and dynamics of the apical PM in both resting and following stimulation of cell secretion. To our great surprise and excitement, isolated live pancreatic acinar cells in physiological buffer solution, when imaged with the AFM (Schneider *et al.*, 1997), reveal cellular structures never seen before. At the apical PM, a group of circular "pits" measuring 0.4–1.2 μm in diameter, contain smaller "depressions" were observed. Each depression measured between 100 and 180 nm in diameter, and typically 3–4 depressions were found within a pit. The basolateral membrane in acinar cells, were devoid of either pits or depressions. High-resolution AFM images of depressions in live acinar cells further revealed a cone-shaped morphology, and the depth of each cone measure 15–35 nm. Subsequently, depressions were found in all cells examined, including growth hormone (GH) secreting cells of the pituitary gland, chromaffin cells, β−cells of the exocrine pancreas, mast cells, the astroglia, and neurons, suggesting their universal presence in secretory cells (Figs. 1–3).

Exposure of pancreatic acinar cells to a secretagogue (mastoparan) results in a time-dependent increase (25–45%) in depression diameter and relative depth, followed by a return to resting size on completion of cell secretion (Cho *et al.*, 2002a; Schneider *et al.*, 1997). No demonstrable change in pit size is detected following stimulation of secretion (Schneider *et al.*, 1997). Enlargement of depression diameter and an increase in its relative depth after exposure to secretagogue, correlate with secretion (Fig. 4). Conversely, exposure of pancreatic acinar cells to cytochalasin B, a fungal toxin that inhibits actin polymerization and secretion,

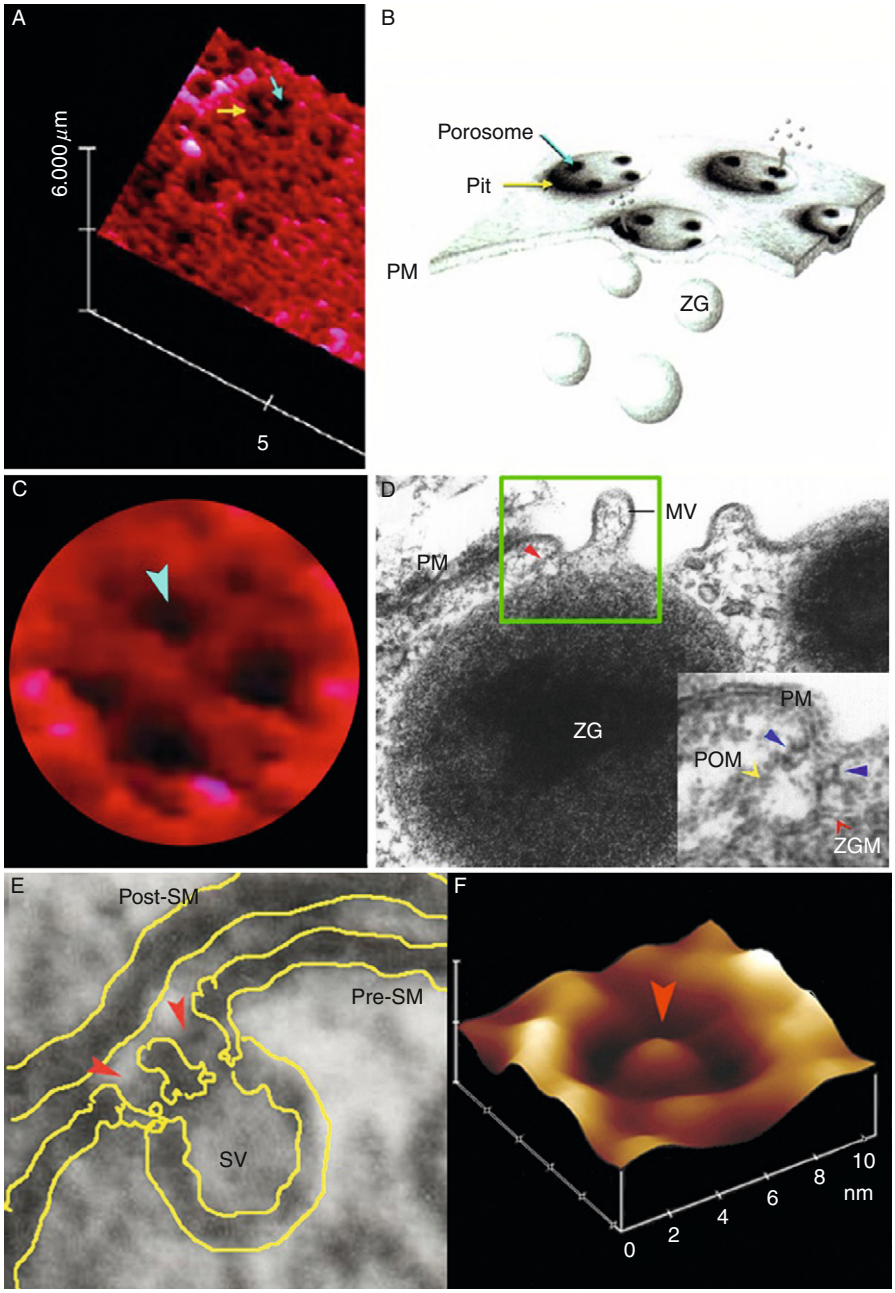

Fig. 1 Porosomes or previously referred to as "depression" at the plasma membrane (PM) in pancreatic acinar cell and at the nerve terminal. (A) AFM micrograph depicting "pits" (yellow arrow) and "porosomes" within (blue arrow), at the apical PM in a live pancreatic acinar cell. (B) To

results in a 15–20% decrease in depression size and a consequent 50–60% loss in secretion (Schneider *et al*., 1997). Results from these studies suggest depressions to be the fusion pores in pancreatic acinar cells. Furthermore, these studies demonstrate the involvement of actin in regulation of both the structure and function of depressions. Analogous to pancreatic acinar cells, examination of resting GH secreting cells of the pituitary (Cho *et al*., 2002b) and chromaffin cells of the adrenal medulla (Cho *et al*., 2002e) also reveal the presence of pits and depressions at the cell PM. The presence of depressions or porosomes in neurons, β-cells of the endocrine pancreas, and in mast cells have also been demonstrated (Cho *et al*., 2004, 2007; Jena, 2004). Porosomes in resting GH cells measure 154 $\pm$ 4.5 nm (mean $\pm$ SE) in diameter, and following exposure to a secretagogue results in a 40% increase in depression diameter (215 $\pm$ 4.6 nm; $p < 0.01$), with no appreciable change in pit size. The enlargement of porosome diameter during cell secretion and its decrease accompanied by loss in secretion following exposure to actin depolymerizing agents (Cho *et al*., 2002b), suggested them to be secretory sites. However, a more direct determination that depressions are the long sought after fusion pores was finally established using immuno-AFM studies. Localization of gold-conjugated antibody to secretory proteins at depressions, demonstrate secretion to occur through the depression opening (Cho *et al*., 2002a,b). ZGs contain the starch digesting enzyme amylase. AFM micrographs demonstrated localization of amylase-specific antibodies tagged with colloidal gold (Fig. 5) at depressions following stimulation of cell secretion (Cho *et al*., 2002a; Jena *et al*., 2003). These studies confirm depressions to be the fusion pores or porosomes in pancreatic acinar cells where membrane-bound secretory vesicles dock and fuse to release their contents. Similarly, in somatotrophs of the pituitary gland, gold-tagged GH-specific antibody was found to selectively localize at depression openings following stimulation of secretion (Cho *et al*., 2002b), again identifying depressions in GH cells as fusion pores. Over the years, the term "fusion pore" has been loosely referred to PM dimples that originate following a secretory stimulus, or to the continuity or channel established between opposing lipid membrane during

the right is a schematic drawing depicting porosomes at the cell PM, where membrane-bound secretory vesicles called zymogen granules (ZG), dock and fuse to release intravesicular contents. (C) A high resolution AFM micrograph shows a single pit with four 100–180 nm porosomes within. (D) An electron micrograph depicting a porosome (red arrowhead) close to a microvilli (MV) at the apical PM of a pancreatic acinar cell. Note association of the porosome membrane (yellow arrowhead), and the zymogen granule membrane (ZGM) (red arrow head) of a docked ZG (inset). Cross section of a circular complex at the mouth of the porosome is seen (blue arrow head). (E) The bottom left panel shows an electron micrograph of a porosome (red arrowhead) at the nerve terminal, in association with a synaptic vesicle (SV) at the presynaptic membrane (Pre-SM). Notice a central plug at the neuronal porosome opening. (F) The bottom right panel is an AFM micrograph of a neuronal porosome in physiological buffer, also showing the central plug (red arrowhead) at its opening. It is believed that the central plug in neuronal porosomes may regulate its rapid close–open conformation during neurotransmitter release. The neuronal porosome is an order of magnitude smaller (10–15 nm) in comparison to porosome in the exocrine pancreas (Cho *et al*., 2005a).

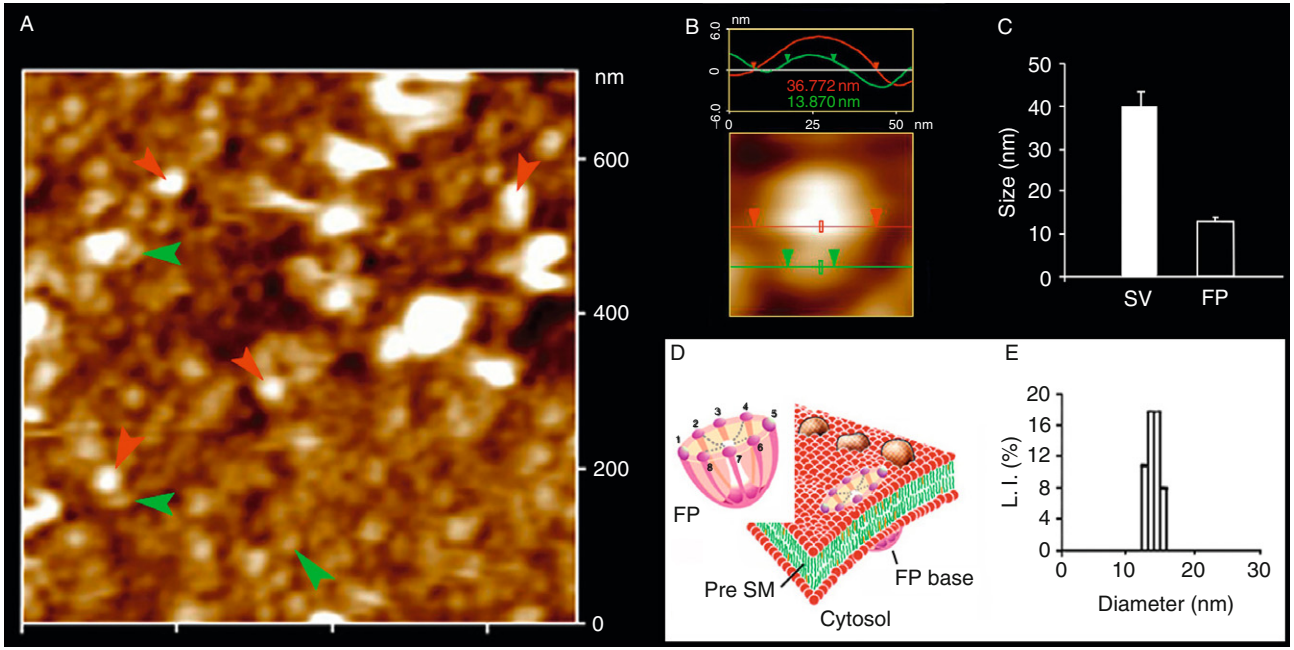

Fig. 2 Neuronal fusion pore distribution, size, and structure. Fig. 2A shows the structure and distribution of fusion pores at the cytosolic compartment of a synaptosome. Inside-out synaptosome preparations when imaged in buffer using AFM, demonstrates inverted 12–16 nm cup-shaped fusion pores, some with docked vesicles. Note one inverted cup-shaped fusion pore (green arrow heads), with a docked SV (red arrow heads), shown at higher magnification in Fig. 2B. (B) Atomic force micrograph shows a 37 nm SV docked to a 14 nm fusion pore at the cytoplasmic compartment in the isolated synaptosomal membrane. (C) AFM measurement of the fusion pores (13.05 ± 0.91) and attached SVs (40.15 ± 3.14) in the cytosolic compartment of synaptosome membrane is demonstrated in Fig. 2C ($n = 15$). (D) Schematic illustration of a neuronal fusion pore, showing the 8 vertical ridges and a central plug. (E) PCS, further, demonstrates fusion pores to measure 12–16 nm (Cho *et al.*, 2007).

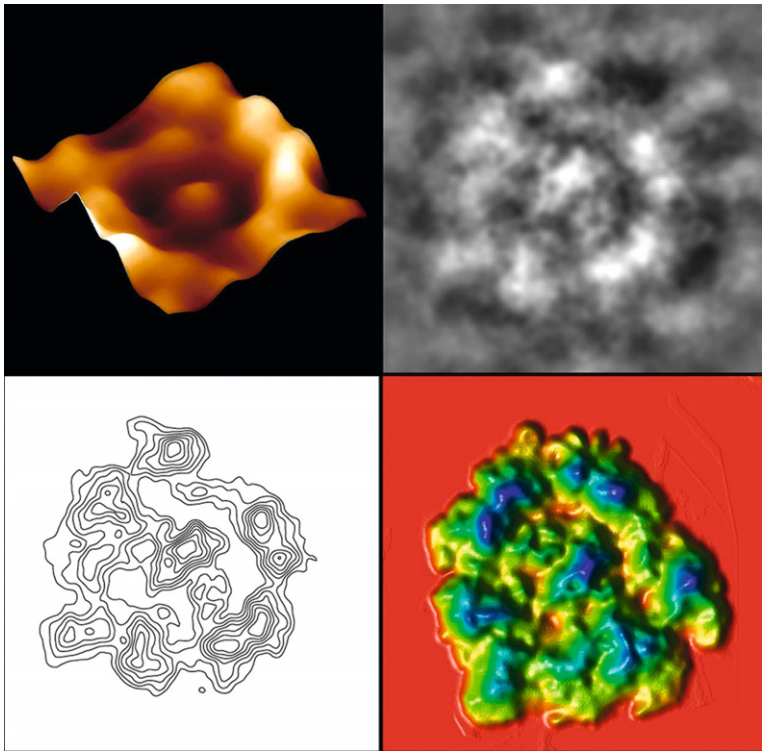

Fig. 3 Nanoscale, three-dimensional contour map of protein assembly within the neuronal porosome complex. Top Left: Atomic force micrograph of an immunoisolated neuronal porosome, reconstituted in lipid membrane. Note the central plug of the porosome complex and the presence of approximately 8 globular units arranged at the lip of the complex. Top Right: Negatively stained electron micrographs of isolated neuronal porosome protein complexes. Note the 10–12 nm complexes exhibiting a circular profile and having a central plug. Approximately 8–10 interconnected protein densities are observed at the rim of the structure, which are connected to a central element via spoke-like structures. Bottom Left: Electron density maps of negatively stained electron micrographs of isolated neuronal porosome protein complexes. Bottom Right: 3D topography of porosomes obtained from their corresponding electron density maps. The colors from yellow, through green to blue, correspond to the protein image density from lowest to the highest. The highest peak in each image represents 27 Å.

membrane fusion. Hence for clarity, the term "porosome" was assigned to this newly discovered structure at the cell PM, where secretory vesicles transiently dock and fuse to release their contents. The porosome at the cytosolic compartment of the PM in the exocrine pancreas (Jena *et al*., 2003), and in neurons (Cho *et al*., 2004), has also been imaged at near nanometer resolution in live tissue.

To determine the morphology of the porosome at the cytosolic compartment of the cell, pancreatic PM preparations were used. Isolated PM in near physiological buffered solution, when placed on freshly cleaved mica, tightly adhered to the mica surface to allow high resolution imaging by the AFM. The PM preparations reveal

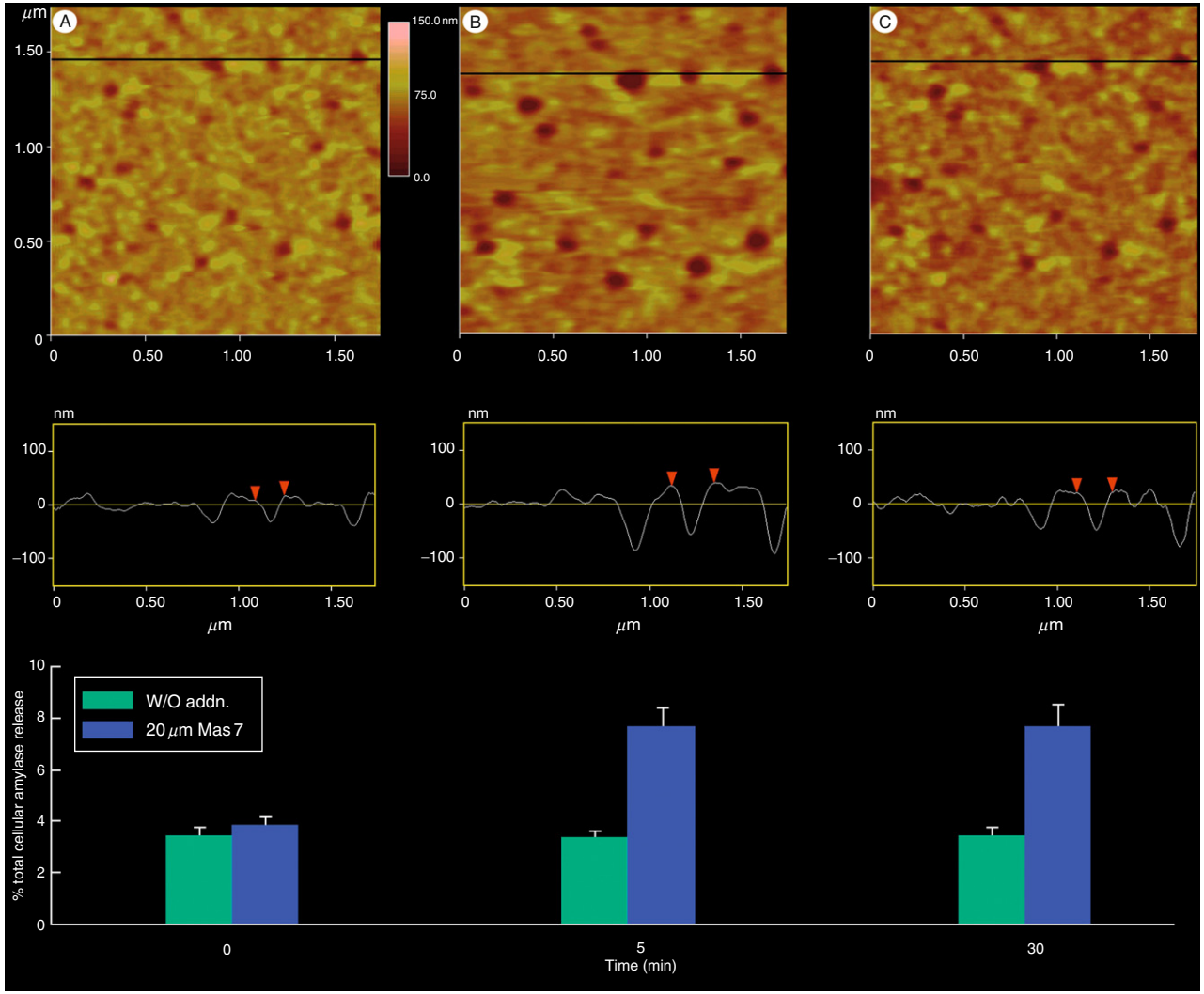
μm
A
B
C
150.0 nm
75.0
0.0
1.50
1.00
0.50
0
0.50
1.00
1.50
nm
100
0
−100
μm
W/O addn.
20 μm Mas 7
% total cellular amylase release
10
8
6
4
2
0
5
30
Time (min)

scattered circular disks measuring 0.5–1 μm in diameter, with inverted cup-shaped structures within (Jena *et al*., 2003). The inverted cups range in height from 10 to 15 nm. On several occasions, ZG's ranging in size from 0.4 to 1 μm in diameter, were observed in association with one or more of the inverted cups. This suggested the circular disks to be pits, and the inverted cups to be porosomes. To further confirm whether the cup-shaped structures were indeed porosomes, immuno-AFM studies were carried out. Target membrane proteins, SNAP-25/-23 (Oyler *et al*., 1989) and syntaxin (Bennett *et al*., 1992) (t-SNARE) and secretory vesicle-associated membrane protein v-SNARE or VAMP (Trimble *et al*., 1988), are part of the conserved protein complex involved in fusion of opposing bilayers in the presence of calcium (Cho and Jena, 2007; Cho *et al*., 2002d, 2005a; Jeremic *et al*., 2006; Malhotra *et al*., 1988; Wilson *et al*., 1992). Since ZGs dock and fuse at the PM to release vesicular contents, it was hypothesized that if porosomes are the secretory sites, then PM-associated t-SNAREs should localize there. The t-SNARE protein SNAP-23 had previously been reported in pancreatic acinar cells (Gaisano *et al*., 1997). A polyclonal monospecific SNAP-23 antibody recognizing a single 23-kDa protein in immunoblots of pancreatic PM fraction, when used in immuno-AFM studies, demonstrated selective localization to the base of the depression structures. These results demonstrate the inverted cup-shaped structures in inside-out isolated pancreatic PM preparations, to be porosomes, the secretory machinery of the cell PM (Jena *et al*., 2003).

The morphology of the pancreatic porosome complex has been further determined using TEM (Jeremic *et al*., 2003). TEM studies confirm the porosome to possess a cup-shaped structure, with similar dimensions as determined from AFM measurement. Additionally, TEM micrographs demonstrate pancreatic porosomes to exhibit a basket-like morphology, with three lateral and a number of vertically arranged ridges. A ring at the base of the complex is also identified (Jeremic *et al*., 2003). Subcellular fractionation and isolation of ZG's following stimulation of secretion, copurifies ZG-associated porosomes complex (Jena *et al*., 2003). Similar to the observations made in electron micrographs of the porosome in intact cells, vertical structures originate from within the porosome complex in the ZG-associated porosomes. Studies using full length recombinant SNARE

Fig. 4 Depression or porosome dynamics in pancreatic acinar cells, following stimulation of secretion. (A) Several porosomes within a pit are shown. The scan line across three porosomes in the top panel is represented graphically in the middle panel and defines the diameter and relative depth of each of the three porosomes. The porosome at the center is represented by red arrowheads. The bottom panel represents percentage total cellular amylase release in the presence and absence of the secretagogue Mas7. (B) Notice an increase in porosome diameter and relative depth, correlating with an increase in total cellular amylase release at 5 min following stimulation of secretion. (C) At 30 min following a secretory stimulus, there is a decrease in diameter and relative depth of porosomes and no further increase in amylase release beyond the 5-min time point. No significant changes in amylase secretion or porosome diameter were observed in control cells in either the presence or absence of the nonstimulatory mastoparan analogue (Mas17), throughout the experiment. High-resolution images of porosomes were obtained before and after stimulation with Mas7, for up to 30 min (Schneider *et al*., 1997).

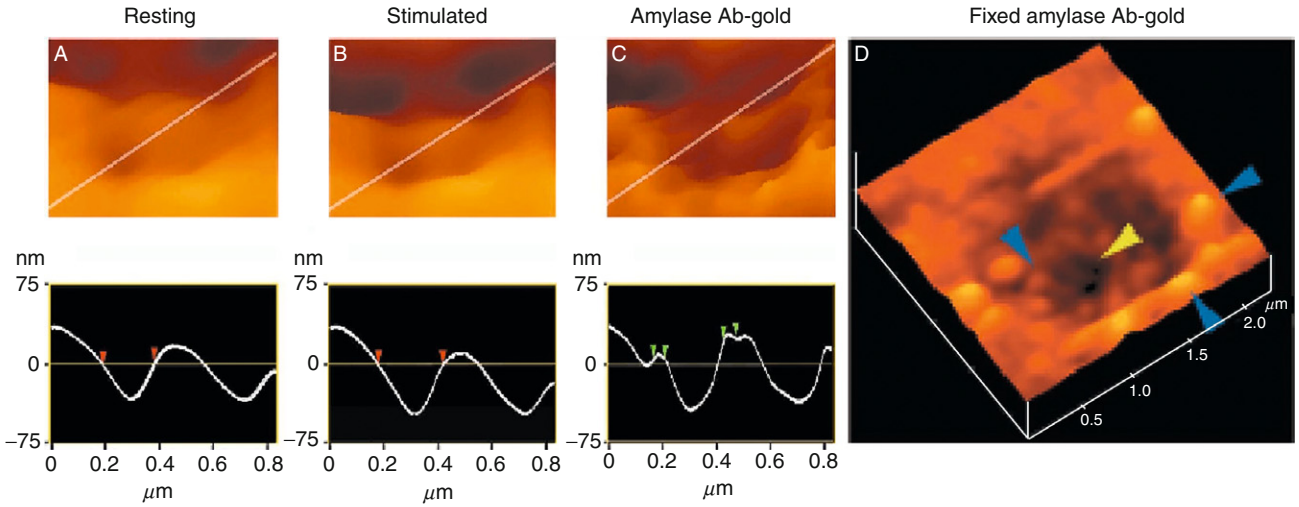

Fig. 5 Porosomes dilate to allow expulsion of vesicular contents. (A and B) AFM micrographs and section analysis of a pit and two out of the four depressions or porosomes, showing enlargement of porosomes following stimulation of secretion. (C) Exposure of live cells to gold conjugated-amylase antibody (Ab) results in specific localization of gold to these secretory sites. Note the localization of amylase-specific immunogold at the edge of porosomes. (D) AFM micrograph of pits and porosomes with immunogold localization is also demonstrated in cells immunolabeled and then fixed. Blue arrowheads point to immunogold clusters and the yellow arrowhead points to a depression or porosome opening.

proteins and artificial lipid membranes demonstrated that t- and v-SNAREs located in opposing bilayers interact in a circular array to form conducting channels (Cho *et al*., 2002d). Since similar circular structures are observed at the base of the pancreatic porosome complex, and SNAP-23 immunoreactivity localized to the same site within the structure, suggests the circular arrangement of proteins at the porosome base to be composed of t-SNAREs. In the past decade, a number of studies demonstrate the involvement of cytoskeletal proteins in cell secretion, some implicating a direct interaction of cytoskeleton protein with SNAREs (Bennett, 1990; Cho *et al*., 2005b; Faigle *et al*., 2000; Goodson *et al*., 1997; Nakano *et al*., 2001; Ohyama *et al*., 2001). Furthermore, actin and microtubule-based cytoskeleton has been implicated in intracellular vesicle traffic. Fodrin, which was previously implicated in exocytosis, has also been shown to directly interact with SNAREs (Nakano *et al*., 2001). Studies demonstrate α-fodrin to regulate exocytosis via its interaction with t-SNARE syntaxin family of proteins. The C-terminal region of syntaxin is known to interact with α-fodrin, a major component of the submembranous cytoskeleton. Similarly, vimentin filaments interact with SNAP23/25 and hence are able to control the availability of free SNAP23/25 for assembly of the t-/v-SNARE complex (Faigle *et al*., 2000). All these findings suggested that vimentin, α-fodrin, actin, and SNAREs may be part of the porosome complex. Additional proteins such as v-SNARE (VAMP or synaptobrevin), synaptophysin, and myosin, may associate when the porosome establishes continuity with the secretory vesicle membrane. The globular tail domain of myosin V contains a binding site for VAMP, which is bound in a calcium independent manner (Ohyama *et al*., 2001). Further interaction of myosin V with syntaxin had been shown to require both calcium and calmodulin. It had also been suggested that VAMP may act as a myosin V receptor on secretory vesicles, and regulate the formation of the SNARE complex (Nakano *et al*., 2001). Interaction of VAMP with synaptophysin and myosin V had also been reported (Ohyama *et al*., 2001). In agreement with these earlier findings, our studies (Cho *et al*., 2004; Jena *et al*., 2003) demonstrate the association of SNAP-23, syntaxin 2, cytoskeletal proteins actin, α-fodrin, and vimentin, and calcium channels $\beta 3$ and α1c, together with the SNARE regulatory protein NSF, in the porosome complex (Cho *et al*., 2004; Jena *et al*., 2003; Jeremic *et al*., 2003). Additionally, chloride ion channels ClC2 and ClC3 were also identified as part of the porosome complex (Cho *et al*., 2004; Jena *et al*., 2003; Jeremic *et al*., 2003). Isoforms of the various proteins identified in the porosome complex have also been demonstrated using 2D-BAC gels electrophoresis (Jeremic *et al*., 2003). Three isoforms each of the calcium ion channel and vimentin were found in porosomes (Jeremic *et al*., 2003). Using yeast two-hybrid analysis, recent studies confirm the presence and interaction of some of these proteins with t-SNAREs within the porosome complex (Cho *et al*., 2005b).

The size and shape of the immunoisolated porosome complex was further determined in greater detail using both negative staining EM and AFM (Jeremic *et al*., 2003). The morphology of immunoisolated porosomes obtained using EM

and AFM, was found to be super imposable (Jeremic *et al.*, 2003). The immunoisolated supramolecular porosome complex has also been reconstituted into liposomes and lipid bilayers (Cho *et al.*, 2004; Jeremic *et al.*, 2003). Transmission electron micrographs of pancreatic porosomes reconstituted into liposomes, reveal a 150–200 nm cup-shaped basket-like structure, similar to what is observed of the complex when coisolated with ZGs. To test the functionality of the reconstituted porosome complex, purified porosomes obtained from the exocrine pancreas or neurons were reconstituted into the lipid membranes of an electrophysiological bilayer setup (EPC9) and exposed to isolated ZGs or SVs. The electrical activity of the reconstituted membrane as well as the transport of vesicular contents from the *cis* to the *trans* compartments of the bilayer chambers was monitored. Results from these experiments demonstrated that the lipid membrane-reconstituted porosomes are functional supramolecular complexes (Cho *et al.*, 2004; Jeremic *et al.*, 2003). ZGs fused with the porosome-reconstituted bilayer as demonstrated by an increase in capacitance and conductance, and a time-dependent transport of the ZG enzyme amylase from *cis* to the *trans* compartment of the bilayer chamber (Jena, 2007; Jeremic *et al.*, 2003). Amylase is detected using immunoblot analysis of the buffer in the *cis* and *trans* chambers, using immunoblot analysis (Jena, 2007; Jeremic *et al.*, 2003). As observed in immunoblot assays of isolated porosomes, chloride channel activity is also present in the reconstituted porosome complex. Furthermore, the chloride channel inhibitor DIDS, was found to inhibit current activity in the porosome-reconstituted bilayer, demonstrating its requirement in intravesicular release via the porosome complex. Similarly, the structure and biochemical composition of the neuronal porosome has also been determined (Figs. 1–3) (Cho *et al.*, 2004, 2007). In summary, these studies demonstrate porosomes to be permanent supramolecular lipoprotein structures at the cell PM, where membrane-bound secretory vesicles dock and fuse to release intravesicular contents to the outside. Porosomes are therefore the universal secretory machinery in cells (Jena, 2004, 2005, 2007).

III. Conclusion

The findings outlined in this chapter, provide the current understanding of the molecular machinery and mechanism of secretion in cells. Porosomes are specialized PM structures universally present in secretory cells, from exocrine and endocrine cells, to neuroendocrine cells and neurons. Since porosomes in exocrine and neuroendocrine cells measure 100–180 nm, and only 20–35% increase in porosome diameter is demonstrated following the docking and fusion of 0.2–1.2 μm in diameter secretory vesicles, it is concluded that secretory vesicles "transiently" dock and fuse at the base of the porosome complex to release their contents to the outside. The discovery of the porosome, and an understanding of its structure and dynamics at nanometer resolution and in real-time in live cells, its composition, and its functional reconstitution in lipid membrane, has greatly

advanced our understanding of cell secretion. It is evident that the secretory process in cells is well coordinated, highly regulated, and a finely tuned biomolecular orchestra. Clearly, these findings could not have advanced without the AFM, and therefore this powerful nano tool, has greatly contributed to a new understanding of the cell. The AFM has enabled the determination of live cellular structure–function at sub nanometer to angstrom resolution, in real-time, contributing to the birth of the new field of *NanoCellBiology*.

Acknowledgments

The author thanks the many students and collaborators who have participated in the various studies discussed in this article. Support from the National Institutes of Health (USA), the National Science Foundation (USA), and Wayne State University, is greatly appreciated.

References

Alexander, S., Hellemans, L., Marti, O., Schneir, J., Elings, V., and Hansma, P. K. (1989). An atomic resolution atomic force microscope implemented using an optical lever. *J. Appl. Phys.* **65,** 164–167.

Bennett, V. (1990). Spectrin-based membrane skeleton: A multipotential adaptor between plasma membrane and cytoplasm. *Physiol. Rev.* **70,** 1029–1065.

Bennett, M. K., Calakos, N., and Schller, R. H. (1992). Syntaxin: A synaptic protein implicated in docking of synaptic vesicles at presynaptic active zones. *Science* **257,** 255–259.

Binnig, G., Quate, C. F., and Gerber, C. (1986). Atomic force microscope. *Phys. Rev. Lett.* **56,** 930–933.

Cho, W. J., and Jena, B. P. (2007). *N*-ethymaleimide sensitive factor is a right-handed molecular motor. *J. Biomed. Nanotech.* **3,** 209–211.

Cho, S.-J., Quinn, A. S., Stromer, M. H., Dash, S., Cho, J., Taatjes, D. J., and Jena, B. P. (2002a). Structure and dynamics of the fusion pore in live cells. *Cell Biol. Int.* **26,** 35–42.

Cho, S.-J., Jeftinija, K., Glavaski, A., Jeftinija, S., Jena, B. P., and Anderson, L. L. (2002b). Structure and dynamics of the fusion pores in live GH-secreting cells revealed using atomic force microscopy. *Endocrinology* **143,** 1144–1148.

Cho, S.-J., Sattar, A. K., Jeong, E. H., Satchi, M., Cho, J., Dash, S., Mayes, M. S., Stromer, M. H., and Jena, B. P. (2002c). Aquaporin 1 regulates GTP-induced rapid gating of water in secretory vesicles. *Proc. Natl. Acad. Sci. USA* **99,** 4720–4724.

Cho, S.-J., Kelly, M., Rognlien, K. T., Cho, J., Hörber, J. K., and Jena, B. P. (2002d). SNAREs in opposing bilayers interact in a circular array to form conducting pores. *Biophys. J.* **83,** 2522–2527.

Cho, S. J., Wakade, A., Pappas, G. D., and Jena, B. P. (2002e). New structure involved in transient membrane fusion and exocytosis. *Ann. New York. Acad. Sci.* **971,** 254–256.

Cho, W. J., Jeremic, A., Rognlien, K. T., Zhvania, M. G., Lazrishvili, I., Tamar, B., and Jena, B. P. (2004). Structure, isolation, composition and reconstitution of the neuronal fusion pore. *Cell Biol. Int.* **28,** 699–708.

Cho, W. J., Jeremic, A., and Jena, B. P. (2005a). Size of supramolecular SNARE complex membrane-directed self-assembly. *J. Am. Chem. Soc.* **127,** 10156–10157.

Cho, W. J., Jeremic, A., and Jena, B. P. (2005b). Direct interaction between SNAP-23 and L-type calcium channel. *J. Cell. Mol. Med.* **9,** 380–386.

Cho, W. J., Jeremic, A., Jin, H., Ren, G, and Jena, B. P. (2007). Neuronal fusion pore assembly requires membrane cholesterol. *Cell Biol. Int.* **31,** 1301–1308.

Faigle, W., Colucci-Guyon, E., Louvard, D., Amigorena, S., and Galli, T. (2000). Vimentin filaments in fibroblasts are a reservoir for SNAP-23, a component of the membrane fusion machinery. *Mol. Biol. Cell* **11,** 3485–3494.

Gaisano, H. Y., Sheu, L., Wong, P. P., Klip, A., and Trimble, W. S. (1997). SNAP-23 is located in the basolateral plasma membrane of rat pancreatic acinar cells. *FEBS Lett.* **414,** 298–302.

Goodson, H. V., Valetti, C., and Kreis, T. E. (1997). Motors and membrane traffic. *Curr. Opin. Cell Biol.* **9,** 18–28.

Hörber, J. K. H., and Miles, M. J. (2003). Scanning probe evolution in biology. *Science* **302,** 1002–1005.

Jena, B. P. (2004). Discovery of the porosome: Revealing the molecular mechanism of secretion and membrane fusion in cells. *J. Cell Mol. Med.* **8,** 1–21.

Jena, B. P. (2005). Molecular machinery and mechanism of cell secretion. *Exp. Biol. Med.* **230,** 307–319.

Jena, B. P. (2007). Secretion machinery at the cell plasma membrane. *Curr. Opin. Struct. Biol.* **17,** 437–443.

Jena, B. P., Schneider, S. W., Geibel, J. P., Webster, P., Oberleithner, H., and Sritharan, K. C. (1997). G_i regulation of secretory vesicle swelling examined by atomic force microscopy. *Proc. Natl. Acad. Sci. USA* **94,** 13317–13322.

Jena, B. P., Cho, S.-J., Jeremic, A., Stromer, M. H., and Abu-Hamdah, R. (2003). Structure and composition of the fusion pore. *Biophys. J.* **84,** 1–7.

Jeremic, A., Kelly, M., Cho, S.-J., Stromer, M. H., and Jena, B. P. (2003). Reconstituted fusion pore. *Biophys. J.* **85,** 2035–2043.

Jeremic, A., Quinn, A. S., Cho, W. J., Taatjes, D. J., and Jena, B. P. (2006). Energy-dependent disassembly of self-assembled SNARE complex: Observation at nanometer resolution using atomic force microscopy. *J. Am. Chem. Soc.* **128,** 26–27.

Kelly, M., Cho, W. J., Jeremic, A., Abu-Hamdah, R., and Jena, B. P. (2004). Vesicle swelling regulates content expulsion during secretion. *Cell Biol. Int.* **28,** 709–716.

Malhotra, V., Orci, L., Glick, B. S., Block, M. R., and Rothman, J. E. (1988). Role of an *N*-ethylmaleimide-sensitive transport component in promoting fusion of transport vesicles with cisternae of the Golgi stack. *Cell* **54,** 221–227.

Nakano, M., Nogami, S., Sato, S., Terano, A., and Shirataki, H. (2001). Interaction of syntaxin with α-fodrin, a major component of the submembranous cytoskeleton. *Biochem. Biophys. Res. Commun.* **288,** 468–475.

Ohyama, A., Komiya, Y., and Igarashi, M. (2001). Globular tail of myosin-V is bound to vamp/synaptobrevin. *Biochem. Biophys. Res. Commun.* **280,** 988–991.

Oyler, G. A., Higgins, G. A., Hart, R. A., Battenberg, E., Billingsley, M., Bloom, F. E., and Wilson, M. C. (1989). The identification of a novel synaptosomal-associated protein, SNAP-25, differentially expressed by neuronal subpopulations. *J. Cell Biol.* **109,** 3039–3052.

Schneider, S. W., Sritharan, K. C., Geibel, J. P., Oberleithner, H., and Jena, B. P. (1997). Surface dynamics in living acinar cells imaged by atomic force microscopy: Identification of plasma membrane structures involved in exocytosis. *Proc. Natl. Acad. Sci. USA* **94,** 316–321.

Trimble, W. S., Cowan, D. W., and Scheller, R. H. (1988). VAMP-1: A synaptic vesicle-associated integral membrane protein. *Proc. Natl. Acad. Sci. USA* **85,** 4538–4542.

Wilson, D. W., Whiteheart, S. W., Wiedmann, M, Brunner, M, and Rothman, J. E. (1992). A multisubunit particle implicated in membrane fusion. *J. Cell Biol.* **117,** 531–538.

CHAPTER 2

Intracellular Organelle Dynamics at nm Resolution

Bhanu P. Jena

Department of Physiology
Wayne State University School of Medicine
Detroit, Michigan, MI 48201

Abstract

In the past 15 years, the dynamics of intracellular membrane-bound secretory vesicles ranging in size from 200 to 1200 nm in pancreatic acinar cells to 30–50 nm in neurons, have been extensively studied, providing for the first time the molecular process involved in vesicular discharge during cell secretion. Live pancreatic acinar cells in near physiological buffer, when imaged using the atomic force microscope (AFM), reveal at nanometer resolution the size of secretory vesicles called

METHODS IN CELL BIOLOGY, VOL. 90

0091-679X/08 $35.00
DOI: 10.1016/S0091-679X(08)00802-9

zymogen granules (ZGs) lying immediately below the surface of the apical plasma membrane. Within 2.5 min of exposure to a secretory stimulus, majority of ZGs within cells swell, followed by a decrease in ZG size, and a concomitant release of secretory products. These studies directly demonstrated intracellular swelling of secretory vesicles following stimulation of cell secretion in live cells, and vesicle deflation following partial discharge of vesicular contents. Furthermore, a direct estimation of vesicle size dynamics at nm resolution under various experimental conditions, have enabled the determination of the molecular mechanism of secretory vesicle swelling. Atomic force microscopy and photon correlation spectroscopy have been major players in these studies.

I. Introduction

Vesicle volume increase following stimulation of secretion had been previously suggested from electrical measurements in mast cells (Curran and Brodwick *et al.*, 1991; Fernandez *et al.*, 1991; Monck *et al.*, 1991; Toledo *et al.*, 1991), and in acinar cells of the exocrine pancreas (Cho *et al.*, 2002a), however a direct visualization of such an increase at nanometer resolution in live cells, and the potential role of vesicle swelling in cell secretion had not been determined until studies by Kelly *et al.* (2004). Although electrophysiological measurements in mast cells suggest granule swelling to follow vesicle fusion at the plasma membrane (Breckenridge and Almers, 1987; Zimmerberg *et al.*, 1987), the potentiating effect of vesicle swelling on its fusion at the cell plasma membrane has also been recognized (Almers, 1990; Finkelstein *et al.*, 1986; Holz, 1986; Sattar *et al.*, 2002). The primary role of secretory vesicle swelling in cell secretion, however remained unclear, until studies were carried our both in a slow secretory cell (pancreatic acinar cell), and a fast secretory cell (neurons), using AFM, photon correlation spectroscopy, and electrophysiological measurements (Kelly *et al.*, 2004). Pancreatic acinar cells are polarized secretory cells, who's apical end possess specialized supramolecular structures called porosomes (Cho *et al.*, 2002b, 2004, 2007; Hörber and Miles *et al.*, 2003; Jena *et al.*, 2003; Jeremic *et al.*, 2003; Schneider *et al.*, 1997) or fusion pores, where zymogen granules (ZGs), the membrane-bound secretory vesicles, dock and fuse to release their contents (Cho *et al* 2002b; Hörber and Miles *et al.*, 2003; Jena *et al.*, 2003; Jeremic *et al.*, 2003; Schneider *et al.*, 1997). The study by Kelly *et al.* (2004), described in this chapter demonstrated that vesicle swelling potentiates its fusion at the cell plasma membrane, and further, is required for the expulsion of intravesicular contents during cell secretion.

II. Materials and Methods

A. Isolation of Pancreatic Acinar Cells

Isolation and preparation of acinar cells for atomic force microscopy (AFM) and electron microscopy (EM), were performed using minor modifications of a published procedure (Jena *et al.*, 1991). For each experiment, a male Sprague

Dawley rat weighing 80–100 g was euthanized by carbon dioxide inhalation. The pancreas was excised and chopped into 0.5-mm^3 pieces, which were mildly agitated for 10 min at 37 °C in a siliconized glass tube with 5 ml of oxygenated buffer A (98 mM NaCl, 4.8 mM KCl, 2 mM $CaCl_2$, 1.2 mM $MgCl_2$, 0.1% bovine serum albumin, 0.01% soybean trypsin inhibitor, 25 mM Hepes, pH 7.4) containing 1000 units of collagenase. The suspension of acini was filtered through a 224 μm Spectra-Mesh (Spectrum Laboratory Products, Saint Paul, MN) polyethylene filter to remove large clumps of acini and undissociated tissue. The acini were washed six times, 50 ml per wash, with ice-cold buffer A. Isolated rat pancreatic acini and acinar cells were plated on Cell-Tak-coated (Collaborative Biomedical Products, Bedford, MA) glass coverslips or mica. Two to three hours after plating, cells were imaged by the AFM before and during stimulation of secretion. Isolated acinar cells and small acinar preparations were used in the study because fusions of regulated secretory vesicles at the cell plasma membrane in pancreatic acini were confined to the apical region and are impossible to image by the AFM in whole tissue or large acinar preparations.

B. Isolation of Zymogen Granules

ZGs were isolated according to a minor modification of a published procedure (Jena *et al.*, 1997). The pancreas from male Sprague–Dawley rats was dissected and diced into 0.5-mm^3 pieces before being suspended in 15% (wt/vol) ice-cold homogenization buffer (0.3 M sucrose, 25 mM Hepes, pH 6.5, 1 mM benzamidine, 0.01% soybean trypsin inhibitor) and homogenized using 3 strokes of a Teflon glass homogenizer. The homogenate was centrifuged for 5 min at 300 $\times g$ at 4 °C. The supernatant fraction was mixed with 2 vol of a Percoll–Sucrose–Hepes buffer (0.3 M sucrose, 25 mM Hepes, pH 6.5, 86% Percoll, 0.01% soybean trypsin inhibitor) and centrifuged for 30 min at 16,400$\times g$ at 4 °C. Pure ZGs were obtained as a loose white pellet at the bottom of the centrifuge tube, and used in the study.

C. Immunoisolation of the Porosome Complex

Fusion pores were immunoisolated from pancreatic plasma membrane preparations using a published procedure (Jena *et al.*, 2003; Jeremic *et al.*, 2003). Porosome from the acinar cells of the exocrine pancreas were immunoisolated from plasma membrane preparations, using a SNAP-23 specific antibody (SNAP-23 is present in pancreatic acinar cells). To isolate the porosome complex for reconstitution experiments, SNAP-23 specific antibody conjugated to protein A-sepharose was used. Isolated pancreatic plasma membrane preparations were solubilized in Triton/Lubrol solubilization buffer (0.5% Lubrol; 1 mM benzamidine; 5 mM Mg-ATP; 5 mM EDTA; 0.5% Triton X-100, in PBS), supplemented with protease inhibitor mix. SNAP-23 antibody conjugated to the protein A-sepharose was incubated with the solubilized membrane for 1 h at room temperature followed by washing with wash buffer (500 mM NaCl, 10 mM Tris, 2 mM EDTA, pH 7.5), and eluted using low pH buffer.

D. Porosome-Reconstituted Bilayer and Bilayer Fusion Assay

Planar lipid bilayers with a capacitance between 100 and 270 pF were formed by brushing 7:3 by weight phosotidylcholine–phosotidylserine from brain (Avanti Polar Lipids) which had been dried and resuspended in decane (20 mg lipid/ml decane) onto the *cis* side of the hole of a bilayer cup inserted into a bilayer chamber (Warner Instruments). Bath solution was symmetric 150 mM KCl, 20 mM 2-N morpholinoethanesulfonic acid (MES), 1 mM $CaCl_2$, pH 6.5. Capacitance, membrane conductance, and bilayer current were recorded for 3–5 min using an EPC9 patch clamp setup and pulse software (HEKA) and ascertained for stability before incorporating porosome into the bilayer membrane using the brush technique (Jeremic *et al*., 2003). ZGs were added to the *cis* side of the bilayer chamber. GTP was added before removal of either the 15 min ($n = 5$) or the 30 min ($n = 5$) time point. For each experiment, 75 μl samples were removed from the *trans* side of the bilayer chamber for α-amylase immunoblot analysis. Following GTP addition, samples were removed at ~0, 5, 10, 15, 30, and 35 min. Capacitance, membrane conductance, and bilayer current were continually monitored and recorded during the experiment using an EPC9 patch clamp system in conjunction with the bilayer setup and pulse software (HEKA).

E. Transmission Electron Microscopy

Isolated rat pancreatic acini ZGs and brain tissue fractions were fixed in 2.5% buffered paraformaldehyde (PFA) for 30 min, and the pellets were embedded in Unicryl resin and were sectioned at 40–70 nm. Thin sections were transferred to coated specimen transmission electron microscopy (TEM) grids, dried in the presence of uranyl acetate and methyl cellulose, and examined in a transmission electron microscope.

F. AFM Volume Measurements of Zymogen Granules

Isolated ZGs in 125 mM KCl–MES buffer, pH 6.5 (25 mM KCl, 100 mM 2-*N* MES) were plated on Cell-Tak-coated glass coverslips or mica. Ten minutes after plating, the coverslips were placed in a fluid chamber and washed with the KCl–MES buffer to remove unattached vesicles, prior to imaging the attached ZGs in KCl–MES buffer, in the presence or absence of 1 mM,, 5 mM, 10 mM, and 20 mM GTP. ZG imaging and dynamics were performed using the Nanoscope IIIa, an atomic force microscope (AFM) from Digital Instruments (Santa Barbara, CA). ZGs were imaged both in the ''contact'' and ''tapping'' mode in fluid (Jena *et al*., 1997, 2003). However, all images presented in this report were obtained in the

"tapping" mode in fluid, using silicon nitride tips with a spring constant of 0.06 Nm^{-1} and an imaging force of less than 200 pN. Images were obtained at line frequencies of 2.523 Hz, with 512 lines per image and constant image gains. GTP dose-dependent, morphological changes in ZG were obtained by using section analysis. Topographical dimensions of ZG were analyzed with the software NANOSCOPE (R) IIIA 4.43r8 supplied by Digital Instruments.

G. Isolation of Synaptosomes, Synaptosomal Membrane, and Synaptic Vesicles

Synaptosomes, synaptosomal membrane, and synaptic vesicles, were prepared from rat brains (Jeong *et al*., 1998; Thoidis *et al*., 1998). Whole rat brain from Sprague-Dawley rats (100–150 g) were isolated and placed in ice-cold buffered sucrose solution (5 mM Hepes pH 7.4, 0.32 M sucrose) supplemented with protease inhibitor cocktail (Sigma, St. Louis, MO) and homogenized using Teflon-glass homogenizer (8–10 strokes). The total homogenate was centrifuged for 3 min at $2500\times g$. The supernatant fraction was further centrifuged for 15 min at $14{,}500\times g$, and the resultant pellet was resuspended in buffered sucrose solution, which was loaded onto 3–10–23% Percoll gradients. After centrifugation at $28{,}000\times g$ for 6 min, the enriched synaptosomal fraction was collected at the 10–23% Percoll gradient interface. To isolate synaptic vesicles and synaptosomal membrane (Thoidis *et al*., 1998), isolated synaptosomes were diluted with 9 vol of ice-cold H_20 (hypotonic lysis of synaptosomes to release synaptic vesicles) and immediately homogenized with three strokes in Dounce homogenizer, followed by 30 min incubation on ice. The homogenate was centrifuged for 20 min at $25{,}500\times g$, and the resultant pellet (enriched synaptosomal membrane preparation) and supernatant (enriched synaptic vesicles preparation) were used in our studies.

H. Light Scattering Measurements of Changes in Synaptic Vesicle Size

Kinetics of rat synaptic vesicle volume changes were monitored by 90° light scattering with excitation and emission wavelength set at 400 nm in a Hitachi F-2000 spectrophotometer. Synaptic vesicle suspension was injected into the thermo-regulated cuvette containing 700 μl of a buffer solution (NaCl 140 mM; KCl 2.5 mM; NaH_2PO_4 0.25 mM; KH_2PO_4 0.25 mM; pH 7.4) at 37 °C. Light scattering was monitored for 1 min following addition of synaptic vesicles to either buffer alone (control) or buffer containing the heterotrimeric Gi-protein agonist, mastoparan (experimental) or its nonagonistic control peptide, Mast-17 (control). Values are expressed as percent increase in light scattered over control values.

III. Discussion

A. Role of Secretory Vesicle Swelling in Cell Secretion

Pancreatic acinar cells (Fig. 1A) were used in the study. Isolated live pancreatic acinar cells in near physiological buffer were imaged using the AFM at high force (200–300 pN), to image ZGs lying immediately under the apical plasma membrane of the cell (Fig. 1B). Within 2.5 min of exposure to a physiological secretory stimulus (1 μM carbamylcholine), the majority of ZGs within cells swell (Fig. 1C), followed by a decrease in ZG size (Fig. 1D) by which time most of the release of secretory products from within ZGs had occurred (Fig. 1E). These studies reveal for the first time in live cells, intracellular swelling of secretory vesicles following stimulation of secretion and their deflation following partial discharge of vesicular contents. Measurements of intracellular ZG size further reveal that different vesicles swell differently, following a secretory stimulus. For example, the ZG marked by the red arrowhead swelled to show a 23–25% increase in diameter, in contrast to the green arrowhead-marked ZG, which increased by only 10–11% (Fig. 1B and C). This differential swelling among ZGs within the same cell, may explain why following stimulation of secretion, some intracellular ZGs demonstrate the presence of less vesicular content than others, and hence have

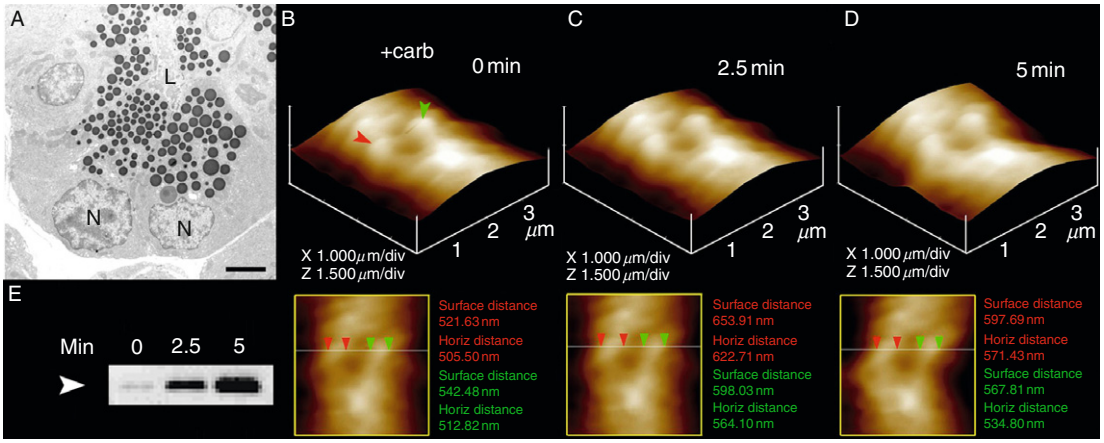

Fig. 1 The swelling dynamics of ZGs in live pancreatic acinar cells. (A) Electron micrograph of pancreatic acinar cells showing the basolaterally located nucleus (N) and the apically located ZGs. The apical end of the cell faces the acinar lumen (L). Bar = 2.5 μm. (B–D) The apical ends of live pancreatic acinar cells were imaged by AFM, showing ZGs (red and green arrowheads) lying just below the apical plasma membrane. Exposure of the cell to a secretory stimulus using 1 μM carbamylcholine, resulted in ZG swelling within 2.5 min, followed by a decrease in ZG size after 5 min. The decrease in size of ZGs after 5 min is due to the release of secretory products such as α-amylase, as demonstrated by the immunoblot assay (E) (Kelly *et al.*, 2004).

discharged more of their contents (Cho *et al.*, 2002a). To determine precisely the role of swelling in vesicle–plasma membrane fusion and in the expulsion of intravesicular contents, an electrophysiological ZG-reconstituted lipid bilayer fusion assay (Jeremic *et al.*, 2003) was employed. The ZGs used in the bilayer fusion assays were characterized for their purity and their ability to respond to a swelling stimulus. ZGs were isolated (Jena *et al.*, 1997) and their purity assessed using EM (Fig. 2A). As previously reported (Abu-Hamdah *et al.*, 2004; Cho *et al.*, 2002c; Jena *et al.*, 1997), exposure of isolated ZGs (Fig. 2B) to GTP resulted in ZG swelling (Fig. 2C). Once again, similar to what is observed in live acinar cells (Fig. 1), each isolated ZG responded differently to the same swelling stimulus. For example, the red arrowhead points to a ZG who's diameter increased by 29% as opposed to the green arrowhead pointing ZG that increased only by a modest 8%. The differential response of isolated ZGs to GTP was further assessed by measuring changes in the volume of isolated ZGs of different size (Fig. 2D). ZGs in the exocrine pancreas range in size from 0.2 to 1.3 μm in diameter (Jena *et al.*, 1997). Not all ZGs were found to swell following a GTP challenge. Most ZGs volume increases were between 5% and 20%. However, larger increases (up to 45%)

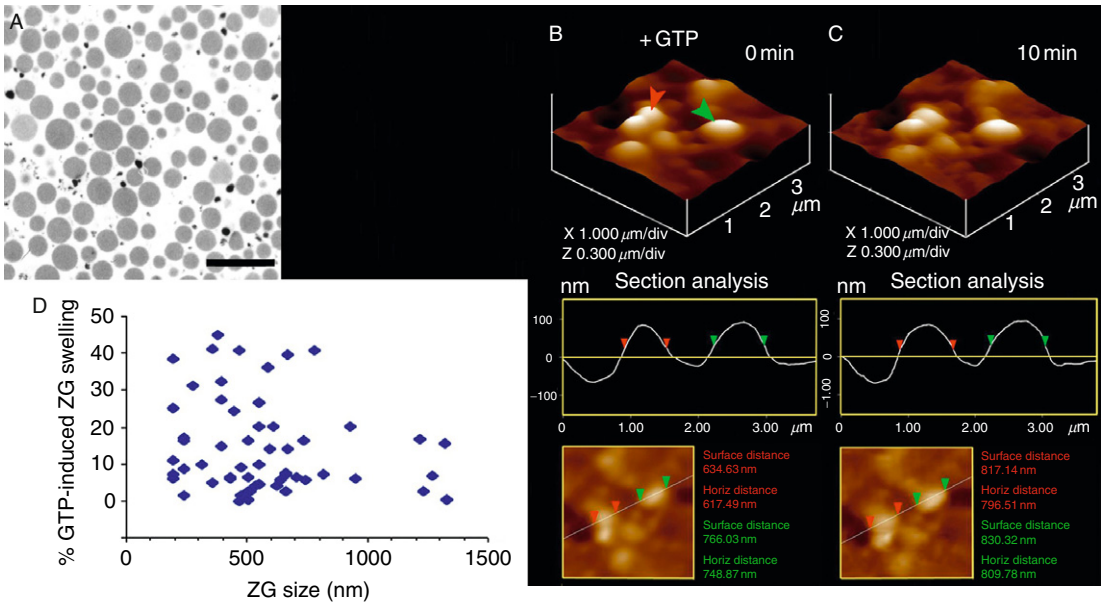

Fig. 2 Swelling of isolated ZGs. (A) Electron micrograph of isolated ZGs demonstrating a homogeneous preparation. Bar = 2.5 μm. (B and C) Isolated ZGs, on exposure to 20 μM GTP, swell rapidly. Note the enlargement of ZGs as determined by AFM section analysis of two vesicles (red and green arrowheads). (D) Percent ZG volume increase in response to 20 μM GTP. Note how different ZGs respond to the GTP-induced swelling differently (Kelly *et al.*, 2004).

were observed only in vesicles ranging from 250 to 750 nm in diameter (Fig. 2D). These studies demonstrate that following stimulation of secretion, ZGs within pancreatic acinar cells swell, followed by a release of intravesicular contents through porosomes (Jeremic *et al*., 2003) at the cell plasma membrane, and a return to resting size on completion of secretion. On the contrary, isolated ZGs stay swollen following exposure to GTP, since there is no release of the intravesicular contents. In acinar cells, little or no secretion was detected 2.5 min following stimulation of secretion, although the ZGs within them were completely swollen (Fig. 1C). However, at 5 min following stimulation, ZGs deflated and the intravesicular α-amylase released from the acinar cell was detected, suggesting the involvement of ZG swelling in secretion.

In the electrophysiological bilayer fusion assay, immunoisolated porosomes from the exocrine pancreas were isolated and functionally reconstituted (Jeremic *et al*., 2003) into the lipid membrane of the bilayer apparatus, where membrane conductance and capacitance were continually monitored (Fig. 3A). Reconstitution of the porosome into the lipid membrane resulted in a small increase in capacitance (Fig. 3B), possibly due to the increase in membrane surface area contributed by incorporation of porosomes, ranging in size from 100 to 150 nm in diameter (Jeremic *et al*., 2003). Isolated ZGs when added to the *cis* compartment of the bilayer chamber, fuse at the porosome-reconstituted lipid membrane (Fig. 3A) and was detected as a step increase in membrane capacitance (Fig. 3B). However, even after 15 min of ZG addition to the *cis* compartment of the bilayer chamber, little or no release of the intravesicular enzyme α-amylase was detected in the *trans* compartment of the chamber (Fig. 3C and D). On the contrary, exposure of ZGs to 20 μM GTP, induced swelling (Abu-Hamdah *et al*., 2004; Cho *et al*., 2002c; Jena *et al*., 1997) and resulted both in the potentiation of fusion as well as a robust expulsion of α-amylase into the *trans* compartment of the bilayer chamber (Fig. 3C and D). These studies demonstrated that during secretion, secretory vesicle swelling is required for the efficient expulsion on intravesicular contents. Within minutes or even seconds following stimulation of secretion, empty and partially empty secretory vesicles accumulate within cells (Cho *et al*., 2002a; Lawson *et al*., 1975; Plattner *et al*., 1997). There may be two possible explanations for such accumulation of partially empty vesicles. Following fusion at the porosome, secretory vesicles may either remain fused for a brief period and therefore time would be the limiting factor for partial expulsion, or inadequately swell and therefore unable to generate the required intravesicular pressure for complete discharge. Data in Fig. 1 suggests that it would be highly unlikely that generation of partially empty vesicles result from brief periods of vesicle fusion at porosomes. After addition of ZGs to the *cis* chamber of the bilayer apparatus, membrane capacitance continued to increase; however, little or no detectable secretion occurred even after 15 min (Fig. 1), suggesting that either variable degrees of vesicle swelling or repetitive cycles of fusion and swelling of the same vesicle or both, may operate during secretion. Under these circumstances, empty and partially empty vesicles could be generated within cells following secretion. To test this

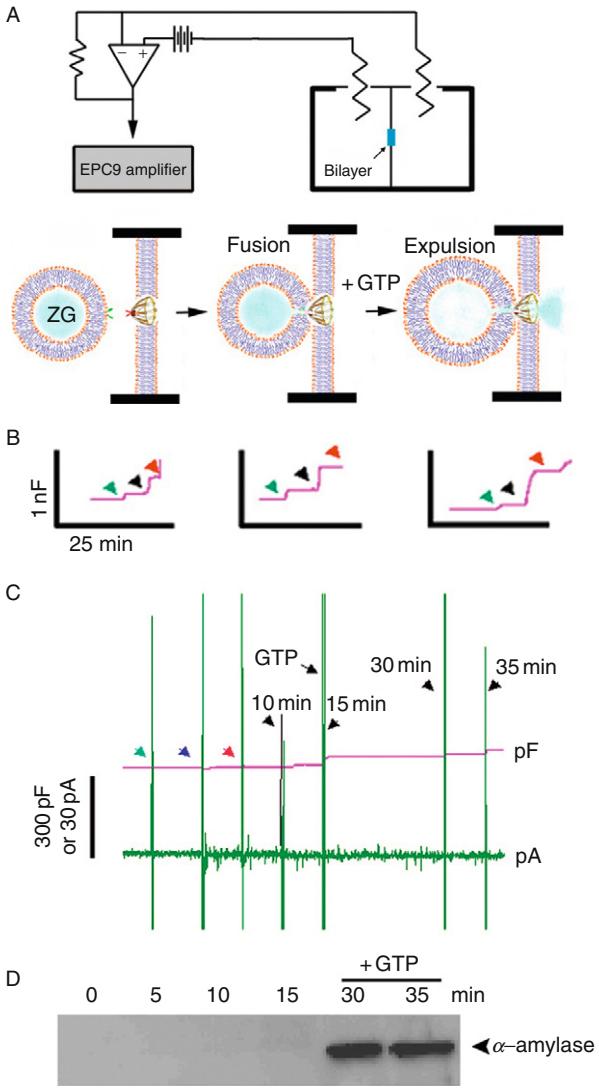

Fig. 3 Fusion of isolated ZGs at porosome-reconstituted bilayer and GTP-induced expulsion of α-amylase. (A) Schematic diagram of the EPC9 bilayer apparatus showing the *cis* and *trans* chambers. Isolated ZGs when added to the *cis* chamber, fuse at the bilayers-reconstituted porosome. Addition of GTP to the *cis* chamber induces ZG swelling and expulsion of its contents such as α-amylase to the *trans* bilayers chamber. (B) Capacitance traces of the lipid bilayer from three separate experiments following reconstitution of porosomes (green arrowhead), addition of ZGs to the *cis* chamber (blue arrowhead), and the red arrowhead represents the 5 min time point after ZG addition. Note the small increase in membrane capacitance following porosome reconstitution, and a greater increase when ZGs fuse at the bilayers. (C) In a separate experiment, 15 min after addition of ZGs to the *cis* chamber, 20 μM GTP was introduced. Note the increase in capacitance, demonstrating potentiation of ZG fusion. Flickers in current trace represent current activity. (D) Immunoblot analysis of α-amylase in the *trans* chamber fluid at different times following exposure to ZGs and GTP. Note the undetectable levels of α-amylase even up to 15 min following ZG fusion at the bilayer. However, following exposure to GTP, significant amounts of α-amylase from within ZGs were expelled into the *trans* bilayers chamber (Kelly *et al.*, 2004).

hypothesis, we examined two key parameters. One, whether the extent of swelling is same for all ZGs exposed to a certain concentration of GTP, and two, whether ZG is capable of swelling to different degrees? And if so, whether there is a correlation between extent of swelling and the quantity of intravesicular contents expelled. The answer to the first question is clear, that different ZGs respond to the same stimulus differently (Fig. 1). Our study revealed that different ZGs within cells or in isolation, undergo different degrees of swelling, even though they are exposed to the same stimuli (carbamylcholine for live pancreatic acinar cells) or GTP for isolated ZGs (Fig. 1B–D, 2B–D). The requirement of ZG swelling for expulsion of vesicular contents was further confirmed, when the GTP dose-dependently increased ZG swelling (Fig. 4A–C) translated into increased secretion of α-amylase (Fig. 4D). Although higher GTP concentrations elicited an increased ZG swelling, the extent of swelling between ZGs once again varied.

To determine if a similar or an alternate mechanism is responsible for the release of secretory products in a fast secretory cell, synaptosomes, and synaptic vesicles from rat brain was used in the study. Since synaptic vesicle membrane is known to possess both Gi and Go proteins, we hypothesized GTP and Gi-agonist (mastoparan) mediated vesicle swelling. To test this hypothesis, isolated synaptosomes (Fig. 5A) were lysed to obtain synaptic vesicles and synaptosomal membrane. Isolated synaptosomal membrane when placed on mica and imaged by the AFM in near physiological buffer, reveal on the cytosolic side the presence of 40–50 nm in diameter synaptic vesicles still docked to the presynaptic membrane. Similar to the ZG's, exposure of synaptic vesicles (Fig. 5B) to 20 μM GTP (Fig. 5C), resulted in an increase in synaptic vesicle swelling. However, exposure to Ca^{2+}, results in the transient fusion of synaptic vesicles at the presynaptic membrane, expulsion of intravesicular contents, and the consequent decrease in size of the synaptic vesicle (Fig. 5D and E). In Fig. 5B–D, the blue arrowhead points to a synaptic vesicle undergoing this process. Additionally, as observed in ZG's of the exocrine pancreas, not all synaptic vesicles swell, and if they do, the swell to different extents even though they had been exposed to the same stimuli. This differential response of synaptic vesicles within the same nerve ending may dictate and regulate the potency and efficacy of neurotransmitter release at the nerve terminal. To further confirm synaptic vesicle swelling and determine the swelling rate, light scattering experiments were performed. Light scattering studies demonstrate a mastoparan-dose dependent increase in synaptic vesicle swelling (Fig. 5F). Mastoparan (20 μM) induces a time-dependent (in seconds) increase if synaptic vesicle swelling (Fig. 5G), as opposed to the control peptide (Mast-17). Results from this study show that following stimulation of secretion, ZGs, the membrane-bound secretory vesicles in exocrine pancreas swell. Different ZGs swell differently, and the extent of their swelling dictates the amount of intravesicular contents to be expelled. ZG swelling is therefore a requirement for the expulsion of vesicular contents in the exocrine pancreas. Similar to ZG's, synaptic vesicles swell enabling the expulsion

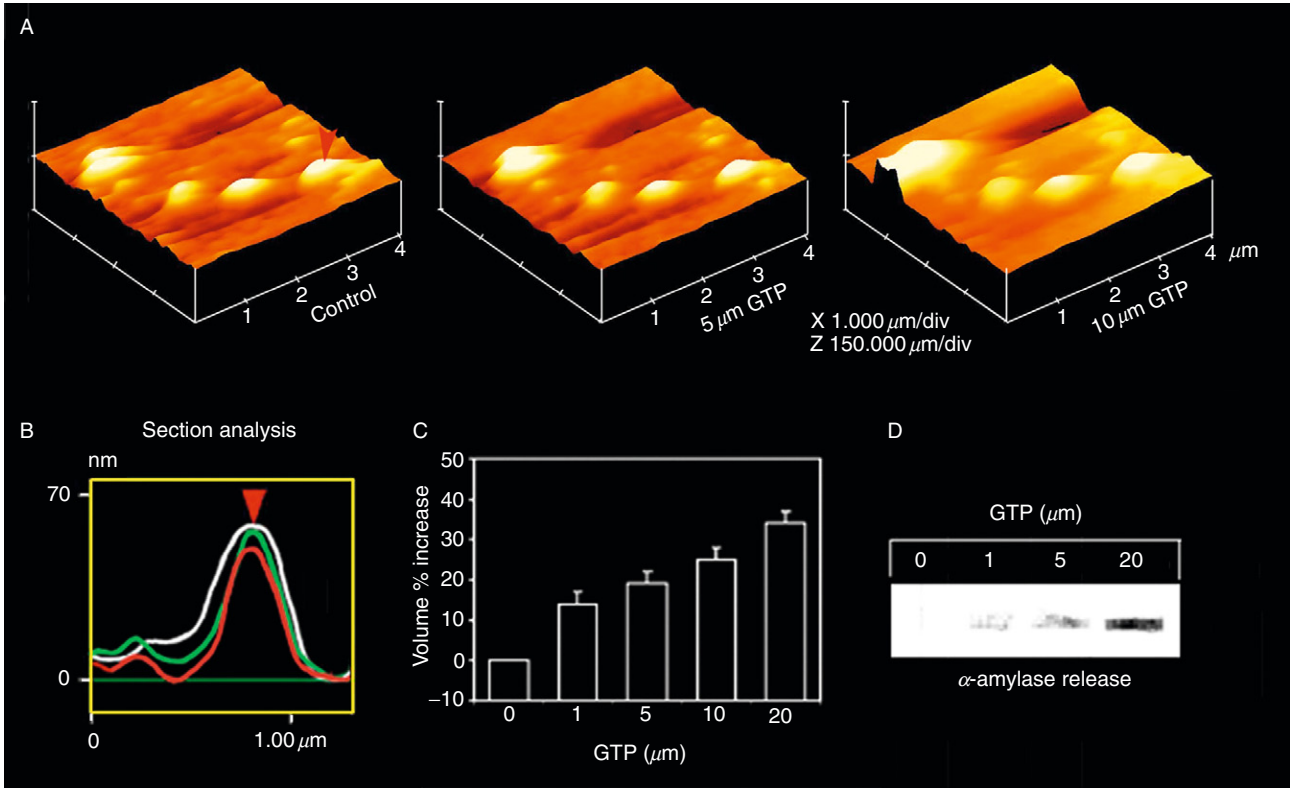

Fig. 4 The extent of ZG swelling is directly proportional to the amount of intravesicular contents released. (A) AFM micrographs showing the GTP dose-dependent increase in swelling of isolated ZGs. (B) Note the AFM section analysis of a single ZG (red arrowhead), showing the height and relative width at resting (control, red outline), following exposure to 5 μM GTP (green outline) and 10 μM GTP (white outline). (C) Graph demonstrating the GTP dose-dependent percent increase in ZG volume. Data are expressed as mean ± SEM. (D) Immunoblot analysis of α-amylase in the *trans* chamber fluid of the bilayers chamber following exposure to different doses of GTP. Note the GTP dose-dependent increase in α-amylase release from within ZGs fused at the *cis* side of the reconstituted bilayer (Kelly *et al.*, 2004).

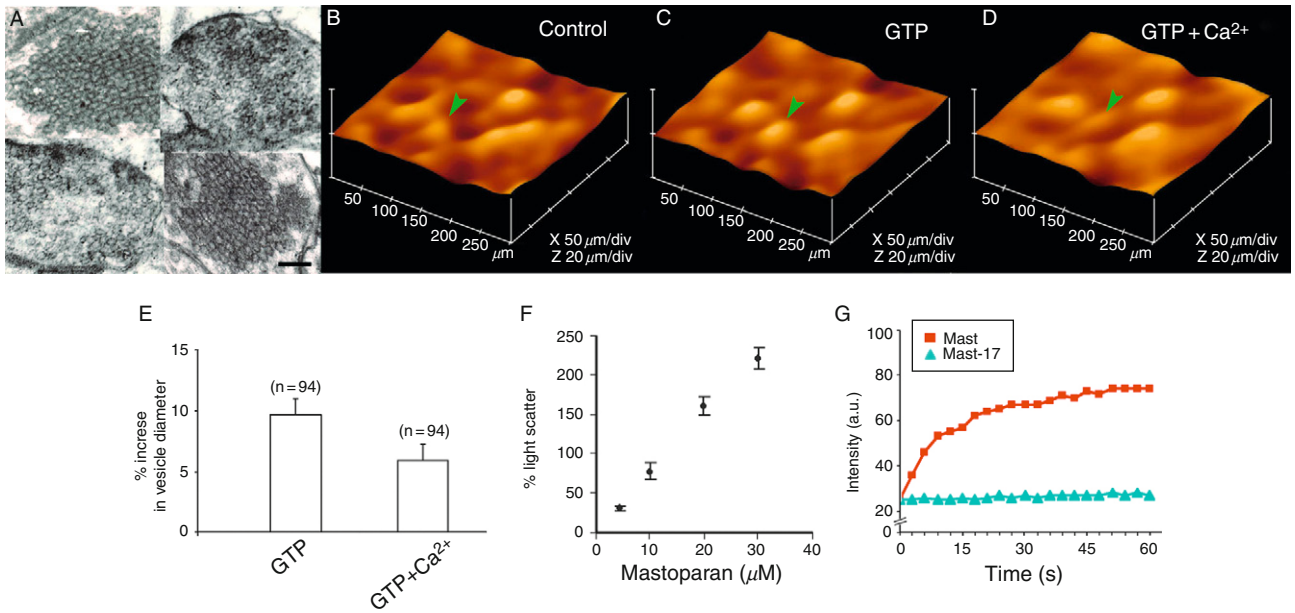

Fig. 5 Synaptic vesicles swell in response to GTP and mastoparan, and vesicle swelling is required for neurotransmitter release. (A) Electron micrographs of brain synaptosomes, demonstrating the presence of 40–50 nm synaptic vesicles within. Bar = 200 nm. (B) AFM micrographs of synaptosomal membrane, demonstrating the presence of 40–50 nm synaptic vesicles docked to the cytosolic face of the presynaptic membrane. (C) Exposure of the synaptic vesicles to 20 mM GTP results in vesicle swelling (blue arrowhead). (D and E) Further, addition of calcium, results in the transient fusion of the synaptic vesicles at porosomes in the presynaptic membrane of the nerve terminal, and expulsion of intravesicular contents. Note the decrease in size of the synaptic vesicle following content expulsion. (F) Light scattering assays on isolated synaptic vesicles demonstrates the mastoparan dose-dependent increase in vesicle swelling (n = 5), and further confirms the AFM results. (G) Exposure of isolated synaptic vesicles to 20 mM mastoparan, demonstrates a time-dependent (in s) increase in their swelling. Note the control peptide mast-17 has little or no effect on synaptic vesicle swelling (Kelly *et al.*, 2004).

of neurotransmitters at the nerve terminal. This mechanism of vesicular expulsion during cell secretion may explain why partially empty vesicles are observed in secretory cells (Cho *et al*., 2002a; Lawson *et al*., 1975; Plattner *et al*., 1997) following secretion. The presence of empty secretory vesicles could result from multiple rounds of fusion–swelling–expulsion, a vesicle may undergo, during the secretory process. These results reflect the precise and regulated nature of cell secretion, both in the exocrine pancreas and in neurons.

B. Molecular Mechanism of Secretory Vesicle Swelling

Our understanding of the molecular mechanism of secretory vesicle swelling has greatly advanced in the last decade. Isolated secretory vesicles and reconstituted swelling-competent proteoliposomes have been utilized (Abu-Hamdah *et al*., 2004; Cho *et al*., 2002c; Jena *et al*., 1997; Jeremic *et al*., 2005; Kelly *et al*., 2004) to determine the mechanism and regulation of vesicle swelling. Isolated ZGs from the exocrine pancreas swell rapidly in response to GTP (Cho *et al*., 2002c; Jena *et al*., 1997; Kelly *et al*., 2004), suggesting rapid water gating into ZGs. Results from studies demonstrate the presence of the water channel aquaporin-1 (AQP1) at the ZG membrane (Cho *et al*., 2002c) and its participation in GTP-mediated water entry and vesicle swelling. Further, the molecular regulation of AQP1 at the ZG membrane has been studied (Cho *et al*., 2002a,c), providing a general mechanism of secretory vesicle swelling. Detergent-solubilized ZGs immunoisolated using monoclonal AQP-1 antibody, coisolates AQP-1, PLA2, $G_{\alpha i3}$, potassium channel IRK-8, and the chloride channel ClC-2 (Abu-Hamdah *et al*., 2004; Figs. 6–10). Exposure of ZGs to either the potassium channel blocker glyburide, or the PLA2 inhibitor ONO-RS-082, blocks GTP-induced ZG swelling. Red blood cells known to possess AQP-1 at the plasma membrane also swell on exposure to the $G_{\alpha I}$ agonist mastoparan, and responds similarly to ONO-RS-082 and glyburide, as do ZGs (Abu-Hamdah *et al*., 2004). Artificial liposomes reconstituted with the AQP-1 immunoisolated complex from solubilized ZGs also swell in response to GTP. Glyburide or ONO-RS-082 is found to abrogate the GTP effect in reconstituted liposomes. AQP-1 immunoisolate-reconstituted planar lipid membrane demonstrate conductance, which is sensitive to glyburide and an AQP-1 specific antibody. These results demonstrate a $G_{\alpha i3}$-PLA2 mediated pathway and potassium channel involvement in AQP-1 regulation at the ZG membrane (Abu-Hamdah *et al*., 2004), contributing to ZG swelling. Similarly, AQP-6 involvement has been demonstrated in GTP-induced and G_o-mediated synaptic vesicle swelling in neurons (Jeremic *et al*., 2005).

In conclusion, *in vivo* and *in vitro* measurements of secretory vesicle dynamics, demonstrate that vesicle swelling is required for the expulsion of intravesicular content from cells during secretion. It is demonstrated that the amount of intravesicular contents expelled, is directly proportional to the extent of secretory vesicle swelling. This unique capability provides cells with the ability to precisely regulate the release of secretory products during cell secretion. The direct

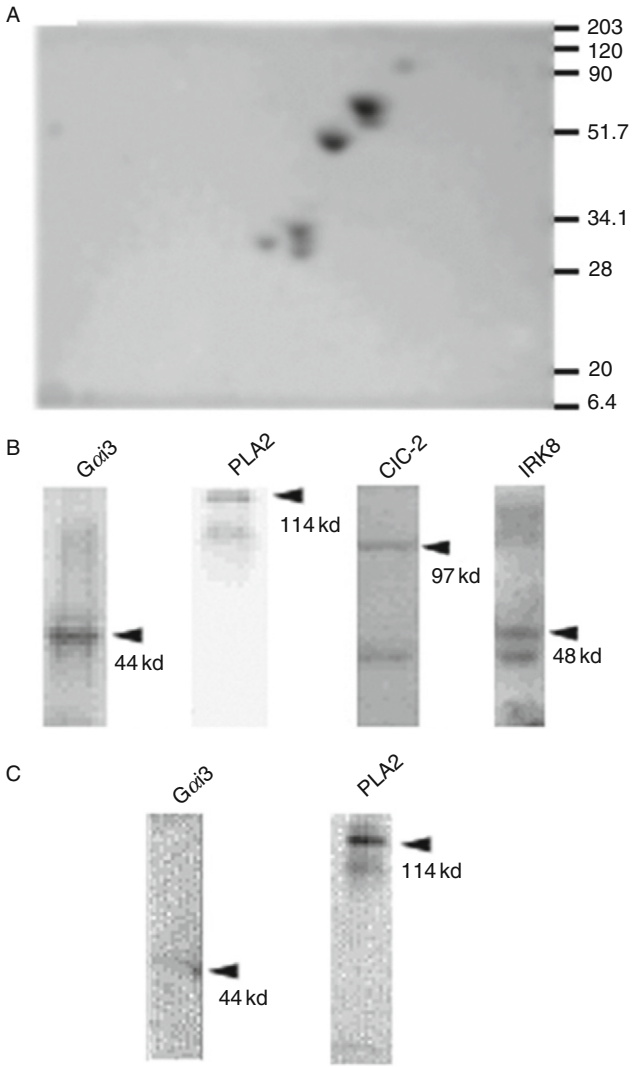

Fig. 6 One (1D) and two dimensionally (2D) resolved, AQP1-immunoisolated proteins from solubilized pancreatic ZG preparations (A and B) and red blood cells (C), using an AQP1-specific antibody. The 2D-resolved proteins were coumassie stained and the 1D resolved proteins transferred to nitrocellulose membranes for immunoblot analysis. Note the identification in the immunoisolates of seven spots in the coumassie-stained 2D-resolved gel (A). Immunoblot analysis of the 1D-resolved immunoisolated proteins demonstrate the presence of PLA_2, $G_{a\ i3}$, the potassium channel IRK-8, and chloride channel ClC-2 (B). Similarly, in red blood cells, PLA_2 and $G_{a\ i3}$ immunoreactive bands are detected (C). Lower molecular weight bands may represent proteolytic cleavage products (Abu-Hamdah *et al.*, 2004).

observation in live cells using the AFM, the requirement of secretory vesicle swelling in cell secretion, also explains the appearance of empty and partially empty vesicles following cell secretion.

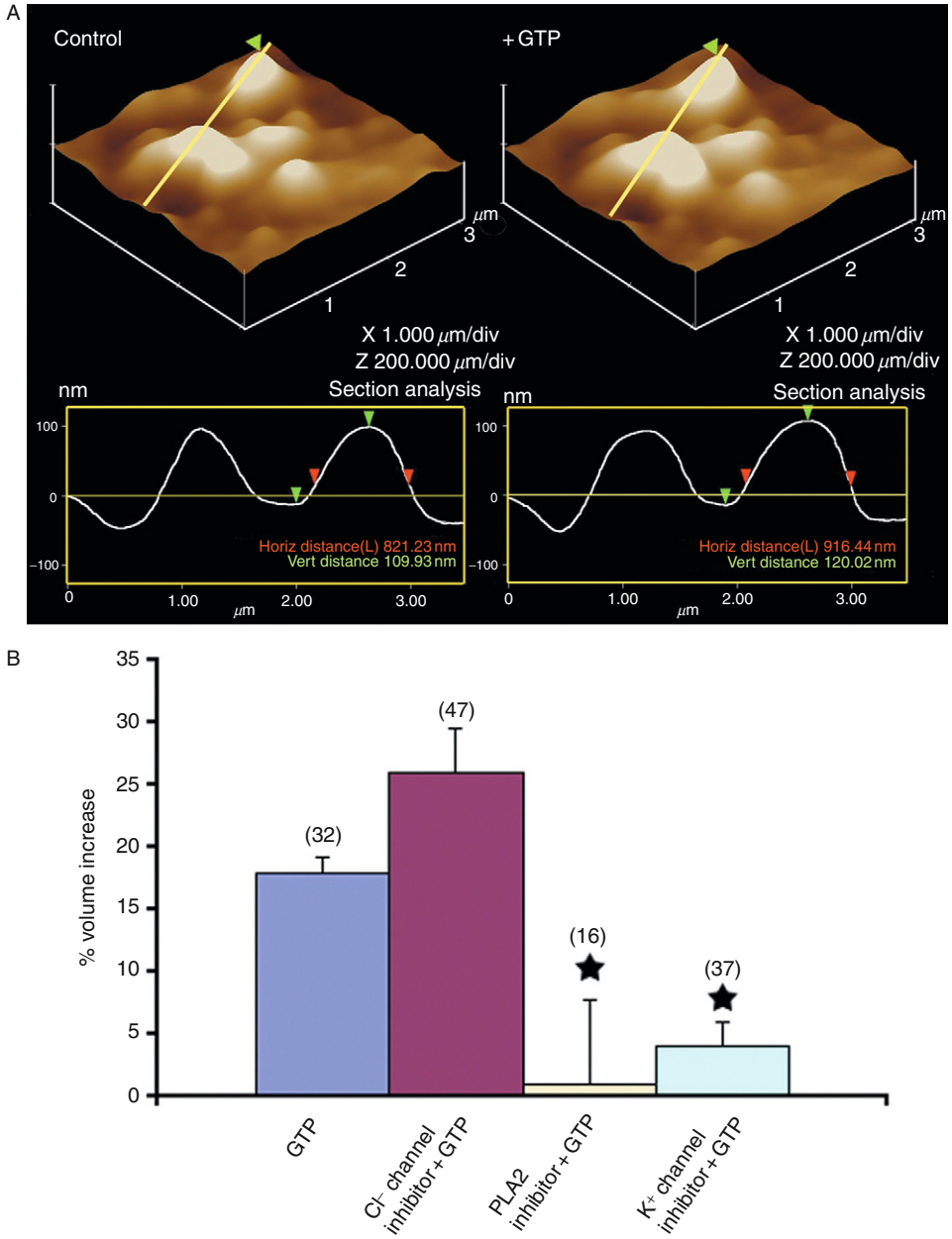

Fig. 7 ZG volume changes measured by AFM. AFM micrographs demonstrating swelling of isolated ZGs in response to 40 mM GTP (A) Histogram showing changes in ZG volume following exposure of isolated ZGs to GTP, and to the inhibitor of the chloride channel DIDS, the inhibitor of the potassium channel, glyburide, or to the inhibitor of PLA_2, ONO-RS-082 (B) Note the significant inhibition of GTP-induced ZG swelling, in the presence of glyburide, or ONO-RS-082. DIDS has little effect on GTP-induced ZG swelling. Values represent mean ± SE of mean of the number of ZGs (in parenthesis), which were randomly selected. A significant ($p < 0.01$) inhibition (*) in the presence of glyburide, or ONO-RS-082 was demonstrated (Abu-Hamdah *et al.*, 2004).

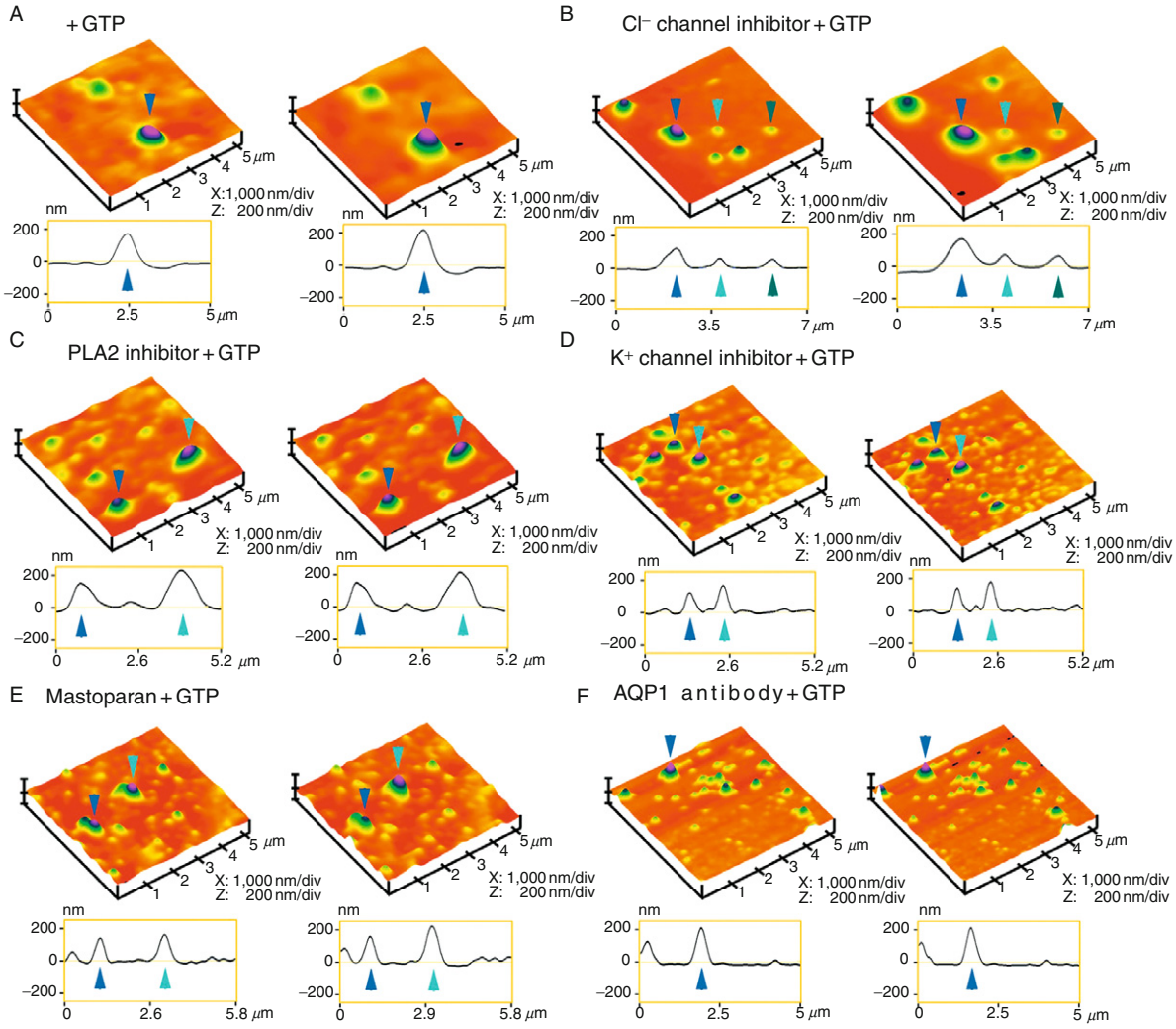
A
+GTP
X:1,000 nm/div
Z: 200 nm/div
nm
200
0
−200
0
2.5
5 μm
B
Cl⁻ channel inhibitor + GTP
X: 1,000 nm/div
Z: 200 nm/div
3.5
7 μm
C
PLA2 inhibitor + GTP
2.6
5.2 μm
D
K⁺ channel inhibitor + GTP
E
Mastoparan + GTP
5.8 μm
F
AQP1 antibody + GTP
2.5

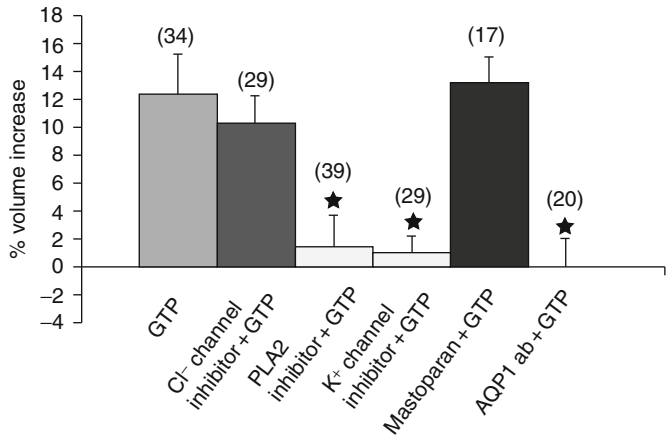

Fig. 9 Percent volume changes in reconstituted liposomes measured by AFM. As observed in the AFM micrographs in Fig. 8, estimation of the changes in liposome volume, demonstrates a 12–15% increase, 5 min following exposure to 40 mM GTP. No significant change in GTP-induced liposome swelling is observed following exposure to the chloride channel inhibitor DIDS or to the $G_{a\ i}$-stimulable peptide mastoparan. Similar to the responses in ZGs, exposure of the reconstituted liposomes to the PLA_2 inhibitor ONO-RS-082, the potassium channel inhibitor glyburide, and the AQP1-specific antibody, significantly inhibits the GTP effect. Values represent mean ± SE of mean of randomly selected liposomes (in parenthesis). A significant ($p < 0.01$) inhibition (*) in the presence of glyburide, ONO-RS-082, and the AQP1-specific antibody, is demonstrated (Abu-Hamdah *et al.*, 2004).

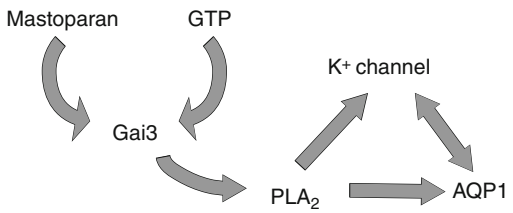

Fig. 10 Schematic outline depicting the regulatory pathway and the main players involved in water channel Aquaporin-1 regulation (Abu-Hamdah *et al.*, 2004).

Fig. 8 AFM micrographs of liposomes demonstrating functional reconstitution of the immunoisolated AQP1-complex. Note swelling of the reconstituted liposomes in response to GTP (A) panel left is control and panel right is 5 min following GTP exposure. Exposure of the chloride channel inhibitor DIDS, did not inhibit GTP-induced swelling (B); however, the PLA_2 inhibitor ONO-RS-082 (C), the potassium channel inhibitor glyburide (D), and the inhibitory AQP1-specific antibody inhibited GTP-induced swelling (F). The $G_{a\ i}$-stimulable peptide mastoparan, demonstrates no additional effect on swelling over GTP (E), hence the GTP effect is mediated through the $G_{a\ i3}$ protein (Abu-Hamdah *et al.*, 2004).

Acknowledgments

The author thanks the many students and collaborators who have participated in the various studies discussed in this article. Support from the National Institutes of Health (USA), the National Science Foundation (USA), and Wayne State University, is greatly appreciated.

References

Abu-Hamdah, R., Cho, W. J., Cho, S.-J., Jeremic, A., Kelly, M., Ilie, A. E., and Jena, B. P. (2004). Regulation of the water channel aquaporin-1: Isolation and reconstitution of the regulatory complex. *Cell Biol. Int*. **28,** 7–17.

Almers, W. (1990). Exocytosis. *Annu. Rev. Physiol.* **52,** 607–624.

Breckenridge, L. J., and Almers, W. (1987). Final steps in exocytosis observed in a cell with giant secretory granules. *Proc. Natl. Acad. Sci. USA* **84,** 1945–1949.

Cho, S.-J., Cho, J., and Jena, B. P. (2002a). The number of secretory vesicles remains unchanged flowing exocytosis. *Cell Biol. Int* **26,** 29–33.

Cho, S.-J., Quinn, A. S., Stromer, M. H., Dash, S., Cho, J., Taatjes, D. J., and Jena, B. P. (2002b). Structure and dynamics of the fusion pore in live cells. *Cell Biol. Int.* **26,** 35–42.

Cho, S.-J., Sattar, A. K., Jeong, E. H., Satchi, M., Cho, J., Dash, S., Mayes, M. S., Stromer, M. H., and Jena, B. P. (2002c). Aquaporin 1 regulates GTP-induced rapid gating of water in secretory vesicles. *Proc. Natl. Acad. Sci. USA* **99,** 4720–4724.

Cho, W. J., Jeremic, A., Rognlien, K. T., Zhvania, M. G., Lazrishvili, I., Tamar, B., and Jena, B. P. (2004). Structure, isolation, composition and reconstitution of the neuronal fusion pore. *Cell Biol. Int.* **28,** 699–708.

Cho, W. J., Jeremic, A., Jin, H., Ren, G., and Jena, B. P. (2007). Neuronal fusion pore assembly requires membrane cholesterol. *Cell Biol. Int.* **31,** 1301–1308.

Curran, M. J., and Brodwick, M. S. (1991). Ionic control of the size of the vesicle matrix of beige mouse mast cells. *J. Gen. Physiol.* **98,** 771–790.

Fernandez, J. M., Villalón, M., and Verdugo, P. (1991). Reversible condensation of mast cell secretory products *in vitro*. *Biophys. J.* **59,** 1022–1027.

Finkelstein, A., Zimmerberg, J., and Cohen, F. S. (1986). Osmotic swelling of vesicles: Its role in the fusion of vesicles with planar phospholipid bilayer membranes and its possible role in exocytosis. *Annu. Rev. Physiol.* **48,** 163–174.

Holz, R. W. (1986). The role of osmotic forces in exocytosis from adrenal chromaffin cells. *Annu. Rev. Physiol.* **48,** 175–189.

Hörber, J. K. H., and Miles, M. J. (2003). Scanning probe evolution in biology. *Science* **302,** 1002–1005.

Jena, B. P., Padfield, P. J., Ingebritsen, T. S., and Jamieson, J. D. (1991). Protein tyrosine phosphatase stimulates Ca(2+)-dependent amylase secretion from pancreatic acini. *J. Biol. Chem.* **266,** 17744–17746.

Jena, B. P., Schneider, S. W., Geibel, J. P., Webster, P., Oberleithner, H., and Sritharan, K. C. (1997). G_i regulation of secretory vesicle swelling examined by atomic force microscopy. *Proc. Natl. Acad. Sci. USA* **94,** 13317–13322.

Jena, B. P., Cho, S.-J., Jeremic, A., Stromer, M. H., and Abu-Hamdah, R. (2003). Structure and composition of the fusion pore. *Biophys. J.* **84,** 1337–1343.

Jeong, E.-H., Webster, P., Khuong, C. Q., Abdus Sattar, A. K., Satchi, M., and Jena, B. P. (1998). The native membrane fusion machinery in cells. *Cell Biol. Int.* **22,** 657–670.

Jeremic, A., Kelly, M., Cho, S.-J., Stromer, M. H., and Jena, B. P. (2003). Reconstituted fusion pore. *Biophys. J.* **85,** 2035–2043.

Jeremic, A., Cho, W. J., and Jena, B. P. (2005). Involvement of water channels in synaptic vesicle swelling. *Exp. Biol. Med.* **230,** 674–680.

Kelly, M., Cho, W. J., Jeremic, A., Abu-Hamdah, R., and Jena, B. P. (2004). Vesicle swelling regulates content expulsion during secretion. *Cell Biol. Int.* **28,** 709–716.

Lawson, D., Fewtrell, C., Gomperts, B., and Raff, M. (1975). Anti-immunoglobulin-induced histamine secretion by rat peritoneal mast cells studied by immunoferritin electron microscopy. *J. Exp. Med.* **142,** 391–401.

Monck, J. R., Oberhauser, A. F., Alvarez de Toledo, G., and Fernandez, J. M. (1991). Is swelling of the secretory granule matrix the force that dilates the exocytotic fusion pore? *Biophys. J.* **59,** 39–47.

Plattner, H., Atalejo, A. R., and Neher, E. (1997). Ultrastructural organization of bovine chromaffin cell cortex-analysis by cryofixation and morphometry of aspects pertinent to exocytosis. *J. Cell Biol.* **139,** 1709–1717.

Sattar, A. K., Boinpally, R., Stromer, M. H., and Jena, B. P. (2002). G-alpha(i3) in pancreatic zymogen granules participates in vesicular fusion. *J. Biochem.* **131,** 815–820.

Schneider, S. W., Sritharan, K. C., Geibel, J. P., Oberleithner, H., and Jena, B. P. (1997). Surface dynamics in living acinar cells imaged by atomic force microscopy: Identification of plasma membrane structures involved in exocytosis. *Proc. Natl. Acad. Sci. USA* **94,** 316–321.

Thoidis, G, Chen, P., Pushkin, A. V., Vallega, G., Leeman, S. E., Fine, R. E., and Kandror, K. V. (1998). Two distinct populations of synaptic-like vesicles from rat brain. *Proc. Natl. Acad. Sci. USA* **95,** 183–188.

Toledo, G., Fernandez, R., and Fernandez, J. M. (1993). Release of secretory products during transient vesicle fusion. *Nature* **363,** 554–558.

Zimmerberg, J., Curran, M., Cohen, F. S., and Brodwick, M. (1987). Simultaneous electrical and optical measurements show that membrane fusion precedes secretory granule swelling during exocytosis of beige mouse mast cells. *Proc. Natl. Acad. Sci. USA* **84,** 1585–1589.

CHAPTER 3

Atomic Force Microscopy as a Tool to Study the Proteasome Assemblies

Maria Gaczynska and Pawel A. Osmulski

Department of Molecular Medicine
Institute of Biotechnology
University of Texas Health Science Center at San Antonio
15355 Lambda Drive, San Antonio, Texas 78245

Abstract

Proteasome is an exceptional enzyme because of its essential physiological role, multiple activities, and structural complexity. It is, in fact, a family of enzymes sharing a common catalytic core and equipped with distinct protein attachments

METHODS IN CELL BIOLOGY, VOL. 90

0091-679X/08 $35.00
DOI: 10.1016/S0091-679X(08)00803-0

regulating the core and adding to its new functional capabilities. As a drug target and a major regulator of cellular processes, proteasome is extensively studied with tools of structural, biochemical, and molecular biology. Atomic force microscopy (AFM) besides X-ray crystallography and electron microscopy is one of the most attractive methods to study proteasome. The noninvasive nature of this method is particularly well suited for investigating the structure–function relationship within the core particle (CP) as well as in higher-order assemblies. Here we review, from the methodological point of view, AFM-based studies on the proteasome. First, we will present the application of height distribution analysis of proteasome complexes to dissect the subunit organization in the base of the regulatory particle (RP). The RP is considered the most physiologically important among all the attachments of the CP; however, its structure remains enigmatic. Then, we will outline the use of AFM imaging to research on structural dynamics of the proteasome, a phenomenon which is starting to gain a broad interest. We will finish with a brief presentation of nanotechnological studies performed using ordered proteasomes and nanolithography carried out with the particles. The presented AFM research offers a unique and often unexpected insight into the structure and function of the proteasome.

I. Introduction

A. Proteasome: An Intracellular Processing Factory and a Challenge for Structural Studies

Proteasome is the major and essential protease performing most of the regulated intracellular protein degradation within the eukaryotic cells. It is a part of multienzyme ubiquitin–proteasome pathway responsible for recognition, tagging, and cleavage of proteins (Varshavsky, 2005). The name ''proteasome'' refers to several protein assemblies sharing a common catalytic core particle (CP) (Groll *et al*., 2005). The 700-kDa CP, also called 20S proteasome in reference to its sedimentation constant, is also a multisubunit assembly. In contrast with numerous structural studies that describe the structure of CP in great detail, makeup of higher-order complexes is poorly established. Core proteasomes from all studied organisms, including the much simpler archaebacterial homolog, follow the same architectural design (Groll *et al*., 1997; Lowe *et al*., 1995; Unno *et al*., 2002). They are fashioned in a shape of a tube or barrel 15–16 nm long and 11–12 nm wide (Fig. 1). The dimensions of CP were established first by electron microscopy (EM) studies and later confirmed by the crystal structures. There are 28 subunits used to construct the CP barrel assembled into four stacked seven-subunit rings. The two outer α rings and inner β rings are identical, so the CP is built from two halves, with a catalytic chamber formed jointly by β rings. In eukaryotes, from yeast to human, each ring is built from seven distinct subunits, either $\alpha 1$–$\alpha 7$ or $\beta 1$–$\beta 7$. In the least advanced archaebacterial particle, the rings are homoheptamers of just two

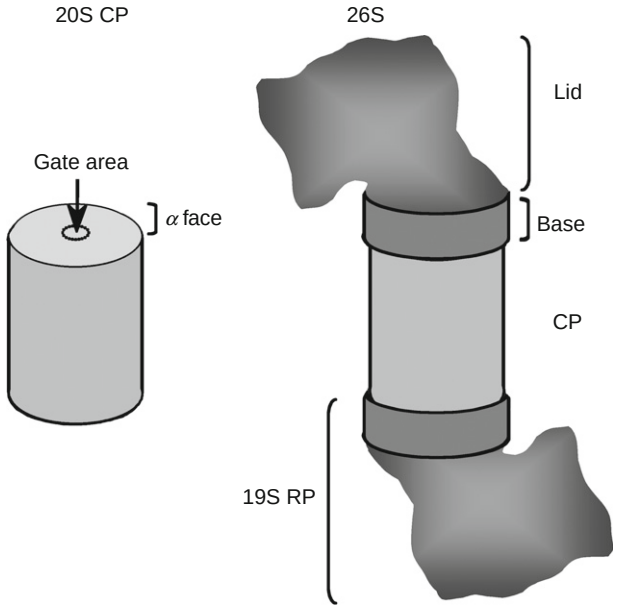

Fig. 1 A cartoon rendering the shape of two major proteasome complexes. The 20S (about 700 kDa) catalytic CP is shown alongside the most complex proteasome assembly, the 26S (about 2500 kDa), which is built from the CP with two 19S (about 900 kDa) RP bound on both sides.

subunits: α and β (Lowe, 1995, p. 26). The external α rings form the α face, a nearly flat outer surface responsible for binding protein complexes that regulate the catalysis. A gate in the center of α rings is woven with short N-terminal sequences (tails) of α subunits, providing the entrance (or exit) to the central channel leading through antechambers to the catalytic chamber. The gate can be open by quite structurally diverse ligands that attach to α face and by poorly understood internal allosteric signals (Bajorek and Glickman, 2004). There are three pairs of active centers of three distinct specificities in the chamber of eukaryotic proteasome (Groll *et al.*, 2005). The centers are equipped with an N-terminal threonine as a catalytic residue. Its hydroxyl and amine groups play the role of a catalytic dyad (Osmulski *et al.*, 2008). The active centers, which differ in the chemical and structural properties of their substrate-binding pockets, cleave polypeptides on the carboxyl site of hydrophobic/branched, basic, and acidic/small neutral amino acids, assuring effective degradation of a variety of substrates. The CP degrades short peptides and unfolded polypeptides. Natively disordered domains of proteins can apparently be cleaved even when rest of the proteins cannot enter the proteasome (Osmulski *et al.*, 2008).

To extend proteolytic capabilities beyond this limited group of substrates, CP secures help from a multisubunit 19S (900 kDa) regulatory particle (RP) that is

affixed to the α face (Groll *et al*., 2005). Crystal structure of 19S has not been solved, notwithstanding the structures of CP–RP or RP–CP–RP higher-order assemblies, the latter known as 26S proteasome (Fig. 1). Therefore, our understanding of the RP structure is primarily based on biochemical, EM, and atomic force microscopy (AFM) studies. The 26S, 2500 kDa particle is the most structurally and functionally advanced among the proteasomes, and the one most physiologically relevant. The apparently low *in vitro* stability of CP–RP complexes and heterogeneity of 19S makes the crystallization very difficult; however, the EM and AFM images show the RP shaped like a dragon's head sitting atop the CP "trunk" (Gaczynska and Osmulski, 2008; Walz *et al*., 1998). Attachment of 19S, beyond postulated gate opening, equips the "greater proteasome" with a capability to recognize, bind, and process proteins tagged for degradation by attachment of chains, at least tetrameric, of a small protein ubiquitin (polyubiquitin). Constitutive and transient subunits of RP take part in remodeling of polyubiquitin tags, removing them (deubiquitination), unfolding the substrates, and feeding them into the central channel of the catalytic core. RP, built from several Rpn (RP nonATPases) and six Rpt (RP ATPases) subunits, can be chromatographically dissected into a base and a lid, connected by a "hinge" subunit Rpn10 (Groll *et al*., 2005; Osmulski *et al*., 2008). There are several other protein modules binding to α face that show lower than the RP structural complication but still impressively diverse array of sizes and shapes. The 11S proteasome activator (PA28/REG) found in higher eukaryotes is a mushroom cap-like heptamer of subunits of molecular weight (MW) close to 30 kDa. PA28 and its homolog PA26 are the only proteasome-binding modules for which the crystal structures have been solved, in the case of PA26—in the complex with the CP. These studies were instrumental in proposing the mechanism used by the activator to open the CP gate (Forster *et al*., 2005).

Other modules include a single-protein, canopy-like activator PA200, extensively studied using EM (about 200 kDa; yeast homolog: Blm10, bleomycin resistance protein 10), and proteasome inhibitor PI31 (31 kDa), imaged using AFM (Gaczynska, Osmulski, Endel, DeMartino, unpublished results) (Ortega *et al*., 2005; Osmulski and Gaczynska, 2005). Besides CP decorated either on one or both sides with single type of regulatory module, there are most likely mixed complexes with two distinct attachments on the two available α faces. The existence of such complexes has been confirmed for 11S and RP but it is also suspected for PI31 and 11S or 19S (Endel, Osmulski, Gaczynska, unpublished data). Such mix-and-match abilities impressively increase the level of structural and functional complication of assemblies under the common name "proteasomes." The hybrid assemblies are waiting for structural and functional analysis. As described later, to achieve a complete understanding of the mechanism of proteasome functioning, the static pictures describing structure of the complexes have to be supplemented with data addressing the structural dynamics. AFM comes as the most convenient and straightforward solution for many problems in structural biology of the giant protease.

B. AFM and the Proteasome

The core proteasome, free or decorated with additional modules, is large enough and stable enough to be a perfect subject for AFM studies. Among all scanning probe microscopies, AFM is the one most used in structural biology (Gaczynska and Osmulski, 2008). It allows for a fast assessment of the shape of objects in a nanometer and micrometer scale (contact and oscillating modes of AFM) and a force of interactions between objects (force mode). The imaging by AFM, especially in oscillating mode, is very well suited for large protein assemblies like the proteasome. The method is noninvasive and allows studying of native, unfixed particles submerged in a water-based, exchangeable liquid ("wet mode"), under physiologically relevant and controllable temperature (Muller *et al.*, 2002; Osmulski and Gaczynska, 2005). Moreover, the method is suitable for single-particle approach: the same molecule can be repeatedly scanned and imaged under distinct conditions, for example, treated with ligands of choice. The only condition is that particles need to be stably attached to a flat surface; however, for oscillating mode even electrostatic interactions between a protein molecule and a naturally charged mineral surface (mica) would suffice (Gaczynska and Osmulski, 2008; Osmulski and Gaczynska, 2005).

In short, at the heart of AFM both in the contact and oscillating modes lays raster scanning of an object with the AFM probe consisting of a very small and sharp tip mounted on a cantilever. In the oscillating mode, the probe vibrates vertically while scanning, with vibrations activated magnetically or acoustically in the hearable range of several kilohertz ("tapping mode"). The tip scans the object in a very close proximity, allowing for van der Waals and electrostatic interactions between the probe and surface atoms of the object. Variations in the distance between the tip and the scanned object perturb the interactions, which in turn induce changes in the amplitude of oscillations. In the contact mode, the tip and the object are in direct contact, leading to cantilever deflection. The changes in deflection or amplitude of oscillations are translated into a topography image of the outer surface of the object, thanks to the constant corrections of the object–probe distance. The precise corrections come as a result of a feedback loop between a sample/tip positioning system and a computer-controlled piezoelement. The z (vertical direction) correction signal from the feedback loop together with the corresponding x and y planes is then used to plot the image of surface topography of the scanned object ("height mode"). The accuracy of vertical signal readout for biological samples is very impressive reaching the angstrom-level. Since electromagnetic waves do not participate in the image creation, the practical lateral resolution is not limited by wavelength but instead by properties of the probe, fidelity of the computer system translating the spatial scanning data into the image, and the dynamic behavior of the scanned objects (Gaczynska and Osmulski, 2008; Osmulski and Gaczynska, 2005). The digital resolution, or pixel size for lateral dimensions in a 500 nm $\times$ 500 nm field scanned with frequency of 512 $\times$ 512 lines is about 1 nm, and nanometer-sized features are usually accessible for identification in AFM images. The actual lateral dimensions are burdened with tip dilation artifact ("tip broadening") depending on the actual dimensions of the scanning tip. The "broadening" problem can be successfully addressed using the

image correction after the determination of tip metrics. These are derived from imaging of a stable object of known dimensions. Summarizing, the achievable vertical and lateral accuracy is more than enough to determine the assembly status of the proteasome. As described later, it is also sufficient to get insight into conformational transitions of this exceptional enzyme.

II. Rationale

AFM has a prominent place in structural studies on the proteasome family, besides EM, cryo-EM, X-ray diffraction, and recently nuclear magnetic resonance (NMR) (Borissenko and Groll, 2007; da Fonseca and Morris, 2008; Osmulski and Gaczynska, 2005; Sprangers and Kay, 2007; Walz *et al.*, 1998). The current applications of AFM in the proteasome research are centered on three major topics. The first is devoted to dissection of the topography of higher-order assemblies like 19S RP and its interactions with the CP. Analysis of conformational transitions of the giant protein complex is pursued in the second. Finally, the use of proteasome as a tool in micropatterning and nanolithography is pursued in the third topic. It is worth to stress that the application of AFM to these structural studies offers specific and unique opportunity and often the only available means to investigate proteasomes. Therefore, the AFM techniques do not aim at repeating achievements of other structural methods. They do not offer simplified versions of studies preferably conducted by other feasible means, either. Instead, the three research blocks take advantage of the exceptional features AFM has to offer, and of the exclusive properties of the proteasome. Namely, AFM provides noninvasive structural analysis of native biomacromolecules in real-time, with a reasonably high practical resolution. On the other hand, proteasome is a large molecule of the easily recognizable shape, distinctive catalytic properties, and ligand-binding capabilities. Moreover, it is stable to imaging conditions with AFM.

As an illustration of the power of AFM applied in the first topic, we will describe the discovery of an unexpected arrangement of RP subunits on the CP α face, complete with both identification of native complexes and their AFM-assisted *in vitro* reconstruction (Rosenzweig *et al.*, 2008). As it was outlined in Section I, although the 19S RP is the most physiologically important, it is also the least structurally elucidated among higher-order proteasome assemblies. We will present a method useful to analyze height of particles. It allows distinguishing populations of a free CP and particles with small protein ligands bound to α face. Such ligands are too small to significantly change the particle volume, a parameter commonly used to compare monomeric and oligomeric molecules imaged by AFM. To the contrary, even small changes of a particle height due to protruding ligands can be reliably registered. In addition to the classification of liganded and unliganded core proteasomes, analysis of AFM images allowed to determine position of ligands on α face and their ability to bind additional proteins. Interplay of AFM and biochemical methods was pivotal for the success of the study (Rosenzweig *et al.*, 2008).

In the second part, we will offer a review of up to date research on the conformational instability and allosteric regulation of the CP. The conformational instability, or diversity, is defined as an ability of proteins to fluctuate between several stable conformational states (Bahar *et al.*, 2007). Only selected states promote ligand binding, a phenomenon known as conformational selectivity. Ligands, on the other hand, may shift the conformational equilibrium and thus act as allosteric regulators. We define allostery here in the broadest sense, as a ligand-induced long-distance transfer of structural signals resulting in modification of a protein's function. The natural conformational transitions have been proved to be essential for catalytic activity (Hammes-Schiffer and Benkovic, 2006). So far, studies on conformational instability, selectivity, and their role in catalysis have been conducted with proteins much less complex than proteasome and with NMR as a method of choice. NMR has recently been added to the array of methods to study the proteasome; however, its application is, so far, limited to the archaebacterial complexes with homooligomeric rings, and the data obtained were concerned mostly with local, not global mobility (Sprangers and Kay, 2007). Here, morphological and morphometrical analysis of CP images lead to detection of global changes in conformation and to linking of these changes with catalytic functions. AFM combined with mutational studies allowed to pinpointing the allosteric effector residue in the proteasome catalytic center (Osmulski and Gaczynska, 2002, 2005).

Finally, we will review the study performed with the archaebacterial proteasome, which was used as a convenient, large, and stable pattern-making molecule easily displaced and recognized by AFM tip working in a novel contact oscillating mode (Tinazli *et al.*, 2007). We will also mention older studies on membrane-immobilized and 2D crystallized CPs, since preparing ordered arrays of particles may prove useful for future proteasome-based diagnostic screens (Thess *et al.*, 2002). Then, on the note of nanotechnology-relevant research, we will outline the method of nanolithography where human 26S proteasome assembly cleaned up the surface covered with polyubiquitinated protein substrate. Since 26S assembly is the only protease able to process and degrade proteins tagged by polyubiquitination, it was likely the most complex and exclusive set of enzyme–substrate ever used in nanolithography (Osmulski and Gaczynska, unpublished data). This diverse collection of proteasome and AFM-related studies demonstrates the power of the method and the splendor of the proteasome.

III. Methods

A. The Height Analysis as a Tool to Detect Ligand-Bound Proteasome Particles

To image proteasomes in the most noninvasive way, we used the oscillation mode AFM in liquid (Osmulski and Gaczynska, 2005). The pure 20S particles were electrostatically attached to the substrate, by depositing a few microliters of a diluted solution of the protein in a neutral pH "imaging buffer" (e.g., Tris–HCl,

pH 7.0, in the range of concentrations 5–50 mM) on the freshly cleaved muscovite mica. After a few minutes, the substrate was covered with 30 μl of the imaging buffer, mounted in the Nanoscope IIIa (Veeco Instruments, Inc.) equipped with a glass cell. Oxide sharpened silicon probes (NP-ST or NP-STT) with a nominal spring constant 0.32 N/m (Veeco Instruments, Inc.) were used, tuned to a resonant frequency 9–10 kHz, with amplitude ranging from 200 to 500 mV and set point from 1.5 to 2 V, assuring low force of tip-sample interaction. Fields from 0.25 to 1 μm^2 were scanned at rates of 2–3 Hz and with resolution of 512 × 512 pixels. By adjusting protein concentration, generally in the nanomolar range, it was possible to obtain a layer of densely packed particles or a sparsely populated field, with particles not touching each other. Both top-view (''standing'') and side-view (''lying'') cylinders were imaged, easily distinguishable by their shape. Interestingly, under the same conditions of binding to the mica substrate, proteasomes from distinct species behaved slightly differently, with *Saccharomyces cerevisiae* (bakers yeast) molecules settling predominantly in top-view position, and human or *Schizosaccharomyces pombe* (fission yeast) molecules presenting a significant (up to 30%) population in side-view orientation (Gaczynska *et al*., 2003; Osmulski and Gaczynska, 2000). The identical buffer and scanning conditions, sometimes with addition of stability-promoting 10% glycerol and $MgCl_2$ (up to 5 mM), were used to image 26S particles. Their distinctive shape was easily recognizable since all the particles were present exclusively in side-view position (Osmulski and Gaczynska, 2005). The mica-bound particles, both core and higher-order assemblies, withstood more than an hour-long repeated scanning without detachment, proving the strength of electrostatic binding (Osmulski and Gaczynska, 2000). This useful property was essential in studies of molecular dynamics, described later. In the current study, the analysis of maximal height of the imaged particles followed by separation of height data into classes allowed for precise distinguishing between free core proteasomes and those extended by attached ligands.

Our aim was to dissect the arrangement and topography of subunits within the 19S RP bound to the CP. The multisubunit ''dragon's head'' 19S cap was found in the past to be composed from two parts: a base (lower ''jaw'' of the dragon) interacting directly with the α face of the core and the lid, capping the base while leaving the ''mouth'' of the dragon open, with a presumably unobstructed access to the gate on α face (Fig. 1). The base consists of a heterohexameric ring of Rpt subunits docking to a heteroheptameric α ring of the CP (Groll *et al*., 2005). Separation and purification of the base revealed that two large proteins, Rpn1 and Rpn2 of unknown position in the complex and a small hinge Rpn10 are copurifying with the ATPases. It was hypothesized that Rpn1 and Rpn2, which primary structures are consistent with α-helical repeats with a natural ''curling'' propensity, may form toroids of about 5 nm in diameter and 3 nm in height (Kajava, 2002). Indeed, AFM imaging of both the proteins revealed donut-shaped structures and confirmed the predicted dimensions (Fig. 2). The Rpn1 and Rpn2 toroids were imaged almost exclusively as monomers. However, when Rpn1 and Rpn2 were mixed in an equimolar ratio, a population of twice-the-height rings was

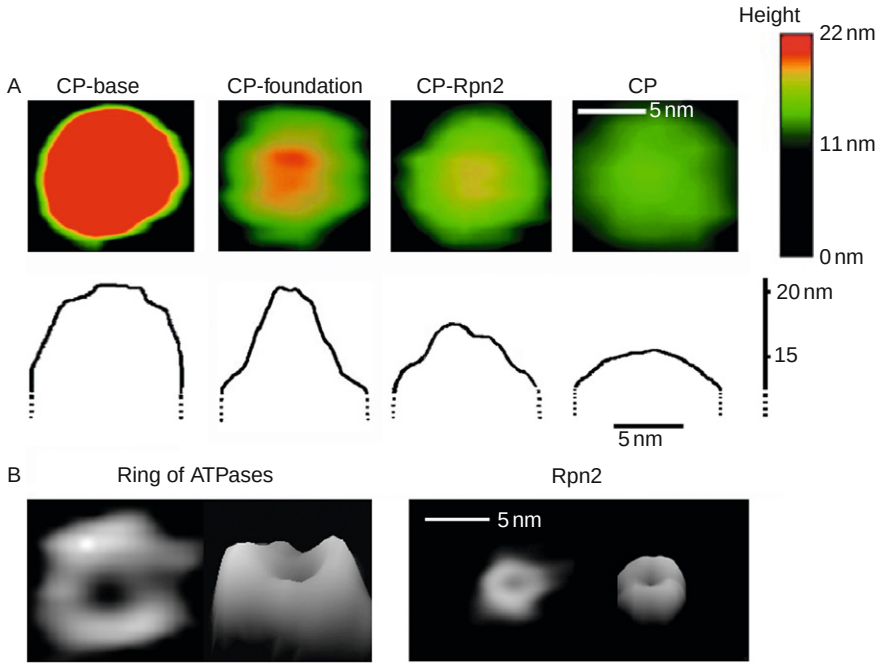

Fig. 2 Atomic force microscopy (AFM) assisted dissection of the subunit arrangement in yeast CP–RP complex. (A) Top-view images of distinct assemblies (see Fig. 1). From the left: CP-Base, CP-foundation (CP–Rpn2–Rpn1), CP–Rpn2, CP. A respective median section is shown below each image. Note the height differences between the assemblies. (B) Images of individual building blocks of the base. A top-view image and a corresponding side plot (3D rendering) are presented for each particle. Left panel: the ring of Rpt subunits; right panel, Rpn2 molecule. According to the proposed model, Rpn2 fits inside the Rpt ring. The presented raw images, not corrected for tip dilation, suggest that such arrangement is plausible.

found, strongly suggesting a formation of stacked heterodimers (Rosenzweig *et al.*, 2008). Mixing heterodimers with the core proteasomes resulted in appearance of a new class of particles: cylinders extended by a stent or chimney protruding from the middle of the α ring (Figs. 2–4). The dimensions of the stent were in good agreement with the dimensions of the Rpn1/2 heterodimer, and the diameters of CPs (11–13 nm after a correction for the tip broadening) and Rpn toroids (5–6 nm after correction) were easily distinguishable (Fig. 2). Collected images of either mixtures of Rpn1 or Rpn2 with the 20S core allowed establishing that only the Rpn2 toroid interacts directly with the α face, and the Rpn1 is always the topmost part of such extended CP (Fig. 4). The presence and size of stent, and therefore, its presumed protein composition was concluded based on the heights of the complexes analyzed with a grain analysis function (SPIP v. 4.3.2.0, Image Metrology, Denmark). First, the images were subjected to the line wise plane correction method, using the LMS third-order fit function of the SPIP software. This method

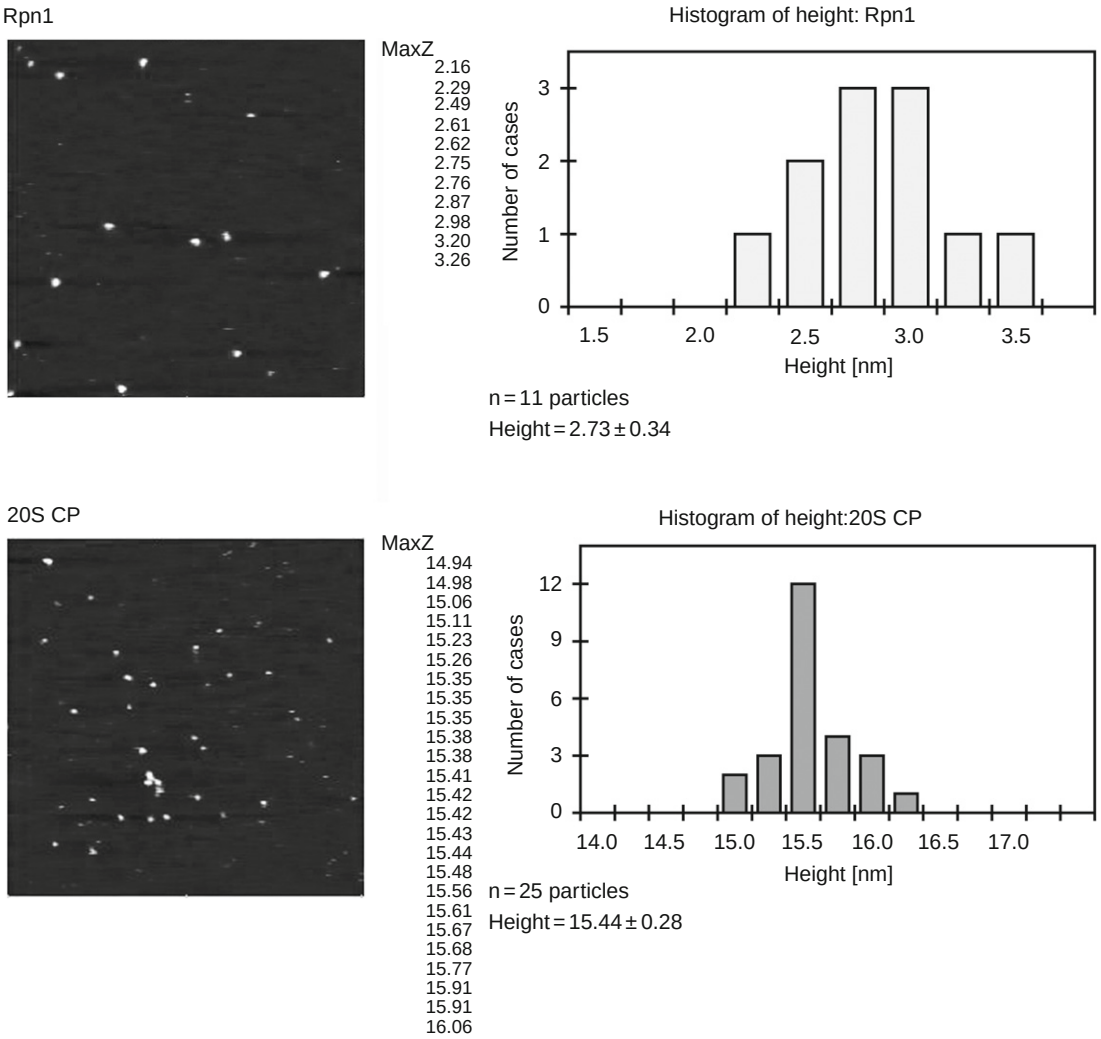

Fig. 3 The height analysis of protein particles. Left: raw fields (600 nm × 600 nm) of yeast Rpn1 and 20S CP. Middle: a list of maximal heights of particles in the field as calculated with a grain analysis function of the SPIP software. Right: the heights from middle column are summarized as histograms of height distribution.

subtracts a fitted polynomial from each scan line and removes most of the baseline noise. Then, the height of molecules was measured from the LMS corrected baseline to the maximum height determined by the software. Histograms of empirical height distribution were prepared using 0.25-nm-wide bins (Fig. 3). To fit the experimental frequency data, particle height distribution was assumed to

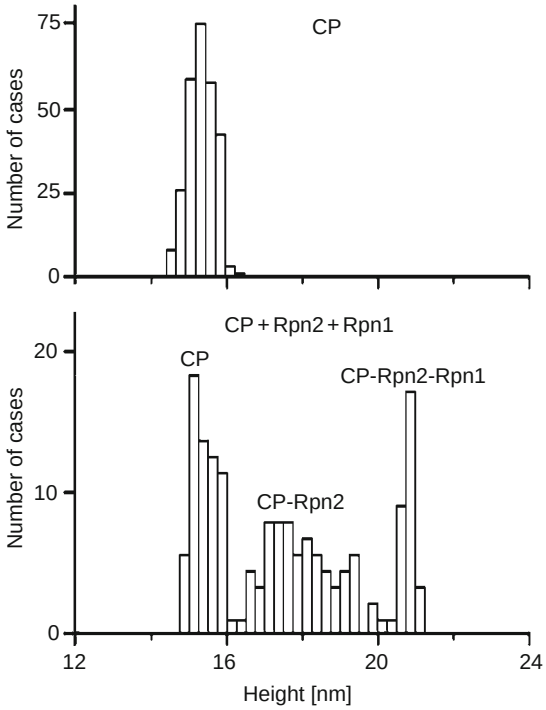

Fig. 4 Histograms of height distribution of the particles in AFM images of 20S CP and a mixture of CP, Rpn2, and Rpn1. The procedure outlined in Fig. 3 was applied to multiple fields containing hundreds of particles. Top: the height of CPs follows the normal distribution, showing the average height of 15.4 nm, consistent with crystal structure and EM data. Bottom: the mixture of particles contains free CP as well as new species of the height consistent with CP extended by single or double Rpn molecules. The average height of new complexes was 17.8 and 20.8 nm, respectively. CP mixed with Rpn1 alone did not produce any new species detectable in a height distribution histogram, prompting the hypothesis that the middle-peak represents CP–Rpn2 complexes. Only this middle-peak did not follow the normal distribution, likely due to unstable nature of the CP–Rpn2 complexes.

follow the normal distribution curve for each type of particles. After such processing, CPs were represented in height distribution histograms by a peak with a maximum at about 15–16 nm. An addition of Rpn2 resulted in detection of a new population of particles with the height around 18 nm, and the presumed attachment of Rpn1/2 heterodimer resulted in a yet another sharp peak around 21 nm (Fig. 4). Only the core proteasomes standing on their bottom α ring and with Rpn toroids attached to the top α ring were detectable. Apparently, the CP extended on both sides by the "chimneys" was not able to stably bind to the mica in a top-view position and were too rare to be identified in images of heterogenous mixtures of Rpns and proteasomes. Interestingly, the side-view proteasomes extended on both ends were detected when Rpn1/2 heterodimers were cross-linked to CP. It is

reasonable to assume that the cross-linking markedly increased the number of double-extended particles over single-extended ones, the former stable only in side-view position, and the latter most stable in the top-view position. The cross-linking was a part of biochemical studies conducted in parallel to the AFM imaging. Importantly, the imaging results were in perfect agreement with biochemical data. For example, Rpn1 and Rpn2 were cross-linked into heterodimers, but not homodimers. Additionally, only Rpn2 was cross-linked to the CP and the α ring subunits were exclusively identified by mass spectroscopy as the proteins bound to Rpn2 (Rosenzweig *et al.*, 2008). The "building-up" of proteasome assemblies was continued with an addition of Rad23 to the stent-extended complexes. This factor is an adaptor protein important for function of the 26S proteasome and known to interact with Rpn1. The AFM imaging showed 20S with chimneys decorated with the Rad23 bead. The bead was present in a fixed position on the side of the top-half of the chimney, consistently with its expected binding to a specific (yet unknown) domain of Rpn1. With the biochemical and imaging data complementing each other, we created the model of proteasome CP with a central channel extended by a molecular stent, or "foundation," capable to bind adaptor proteins, and likely directing substrates to the catalytic chamber (Rosenzweig *et al.*, 2008).

Subsequent AFM studies showed that the CP extended by the stent not only could be reconstructed from individual components but also "excavated" from the complete 26S complex. It is assumed that the base Rpt subunits form a hexameric ring bound to the core α face and assisting in substrate translocation to the catalytic chamber (Rosenzweig *et al.*, 2008). We hypothesized that the Rpt ring likely surrounds the newly discovered Rpn1/2 stent. To confirm such predicted arrangement, 26S assemblies purified from yeast cells were gradually dissected by hydroxyapatite chromatography in a gradient of the increasing ionic strength. The fractions containing proteasomal complexes on distinct stages of dissection were analyzed by biochemical methods and by AFM imaging. Again, the AFM and biochemical data complemented each other in these "tearing-down" experiments. Images of the fraction of the intact 26S assemblies showed a high content of side-view particles with dragon's heads capping the core cylinder. Images of the proteins from a fraction where 20S subunits, Rpn1 and Rpn2 were detectable by Western blotting indeed revealed CPs with the stent, undistinguishable from reconstructed species (Fig. 2A). Importantly, images of the fraction containing the base subunits: Rpt1–6 and Rpn1–2, showed the predicted new architecture: the stent surrounded by a large ring. The ring, presumably formed by the Rpt1–6 proteins, was imaged as a free complex as well, detached from the CP. There seems to be enough space inside the presumed Rpt ring to accommodate the Rpn1/2 stent (Fig. 2B). The images of these complex mixtures were analyzed as earlier, with an important modification. Namely, we applied a diameter of top-view particles on distinct height thresholds as an additional parameter sorting the particles. For example, a particle of 21 nm in height may have about 5 nm in diameter measured at 19 nm threshold (2 nm from the top) or 13 nm. In the first case, the particle was classified as the core-stent assembly, in the second—as the core-base (Rosenzweig

et al., 2008). The next call for interplay of biochemical and AFM studies would be to dissect the role of the stent and surrounding subunits in the uptake and processing of substrates.

B. The Use of Morphologic and Morphometric Analysis to Study Conformational Diversity

The large size and complexity of the proteasome seriously hampers NMR studies and molecular modeling; however, it fits well the capabilities of AFM. The CP isolated from such distinct organisms as yeast and human were imaged by a gentle tapping mode in liquid, under native conditions, as described earlier (Osmulski and Gaczynska, 2005). At the scanning rate of 2–3 Hz and field sizes up to 1 μm^2, the passage of a tip across a single particle takes a few milliseconds. Since a milliseconds-to-seconds scale is a hallmark of global, allostery-driven conformational transitions, we considered such a time frame sufficient to detect potential changes in the shape of molecules. Indeed, a simple visual examination of the images of multiple top-view proteasomes dispersed on a field revealed the presence of two populations: with a smooth and gently convex surface of the α face or with a crater-like dip in the middle (Fig. 5A). Analysis of median cross-sections of the particles confirmed the observation that there were two major conformations of the α face (Osmulski and Gaczynska, 2000). We dubbed them "closed" and "open," respectively for those without and with the middle "hole" (Fig. 5). The median sections in four directions have to demonstrate concave, not convex shape for the particle to be considered open, and more than 95% of all particles were unequivocally classified as open or closed. In any given field of loosely dispersed particles, a three-fourth of CPs was in a closed conformation during a given scan, and the remaining one-fourth was open. Because of the size of the AFM tip, it was impossible to approximate the true depth of the crater since a through-hole would be imaged the same way as a shallow dip. However, since the center of the α ring is the area where the gate and the entrance to central channel are located, it was reasonable to hypothesize that the closed conformation represents the closed gate, whereas the open variant demonstrates the open gate. Such hypothesis seems even more plausible after we found that the proteasomes with the gate severely damaged by deletion of its critical part are exclusively open in AFM images (Osmulski *et al.*, submitted for publication). The opening was confirmed by the X-ray crystallography of the mutated particles (Groll *et al.*, 2000). Proteasomes in the top-view position were not the only ones to show distinct conformations. We analyzed images of side-view particles and noticed that they come in variable shapes as well (Osmulski and Gaczynska, 2002). To quantitate the morphological changes, we analyzed the sections of the side-view particles. We measured the lengths and diameters of the tube-shaped molecules and calculated the length-to-diameter (l/d) ratio. The dimensions were measured at half-height, on frontal (length) and transverse (diameter) sections, without correction for tip dilation. A histogram analysis of the l/d data revealed the presence of two populations, each

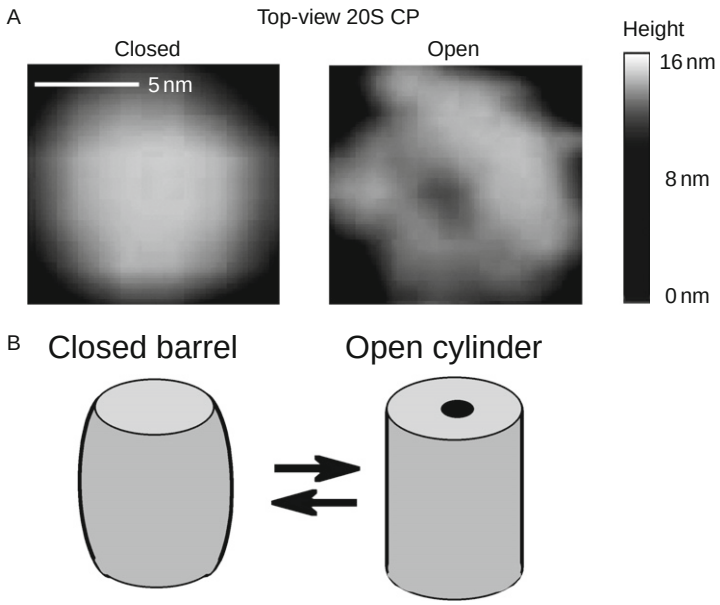

Fig. 5 Conformational diversity of CP molecules. (A) AFM image of typical closed (left) and open (right) top-view CP. The open molecules are distinguished from closed particles by the presence of the characteristic central depression in the gate area. (B) A model integrating the structural diversity detected among top-view (open–closed) molecules and side-view particles (barrels–cylinders). Distribution of the conformers apparently depends on the status of active centers.

bearing normal distribution: with average $l/d = 1.4$ or 1.8. Particles with low l/d were barrel-shaped, whereas the ones with high l/d were cylinder-shaped. Barrels accounted for three-fourth of the total particle population, leaving remaining one-fourth to cylinders. The center of a ring is obviously not accessible for imaging in side-view particles; however, this distribution suggested that "barrels" may be "closed" and "cylinders" may be "open" (Fig. 5B). This notion was confirmed by additional circumstantial evidence when distribution of distinct conformations of ligand-treated proteasomes was studied (Osmulski and Gaczynska, 2002).

Interestingly, repeated scanning and imaging of the same group of particles showed that each molecule was able to assume both the closed and the open, or barrel and cylinder conformations at a seemingly random pace. Long stretches of observations of single particles showed that they always conformed to the distributions established for analysis of multiple particles in a scanned field. Namely, at about three-fourth of the cases, every single particle was closed or barrel-shaped. Both in the case of top-view and side-view particles, images of particles defying

classification, which likely represented intermediates scanned exactly during a transition between the major conformations, were very rare, below 5% of total particle count (Osmulski and Gaczynska, 2000, 2002). These observations established core proteasomes as dynamic proteins, capable to switch between at least two stable conformations (Fig. 5).

The straightforward identification and counting of the two conformers was instrumental in establishing the link between catalysis and conformational equilibrium. Unexpectedly, an addition of protein or peptide substrates to the particles already settled on the mica resulted in a dramatic increase in the occurrence of the open cylinder conformation and reversal of the close to open partition. Now, three-fourth of the particles were open and cylinder-shaped. Proteasomes with active sites blocked by specific inhibitors or disabled by mutations did not switch to the predominantly open conformation. Moreover, peptides not degraded by the enzyme did not prompt the conformational switch (Osmulski and Gaczynska, 2000, 2002). When a very low, below steady state, concentration of substrate was added, the excess of open particles quickly receded and the equilibrium returned to the ''free'' pattern, an expected outcome for an enzyme, which used up all supply of a substrate (Osmulski *et al.*, submitted for publication). Accordingly, we concluded that a catalytic act in any of the active sites correlated with the change of equilibrium. Exploring even deeper the structure–function relationship in the core proteasome, we tested response of CP toward a panel of competitive inhibitors and modifications targeting selected residues in the active center and distinct steps of the catalytic process. We restricted the analysis to easy to classify open and closed conformers focusing on their distribution when CP was treated with inhibitors blocking the hydroxyl group of the catalytic Thr1, the α-amino group, or both of them. Additionally, we tested effects of inhibitors that are the transition state analogues and therefore induce ionization of the catalytic amine while binding to the catalytic hydroxyl (Osmulski *et al.*, 2008). Beyond the inhibitors, we analyzed the proteasomes with acetylated Thr1 catalytic amine. The results showed that inhibitor binding to the hydroxyl alone did not cause detectable shift in the conformational equilibrium. To the contrary, the blocked or charged amine was correlated with a shift toward the open conformation. The shift closely followed the predicted degree of blocking or charging of the amine group. When the excess of irreversible inhibitor abolished 100% of activity in the affected catalytic site, 100% of particles were open. When about a half of the activity in a given site was lost due to one of Thr1 α-amine acetylation, about a half of particles remained open. We hypothesized that a transition state stage of the proteasome catalytic cycle is prompting the gate opening (Osmulski *et al.*, submitted for publication). Moreover, we speculate that the Thr1 α-amine is the major allosteric effector, sending long-distance structural signals from the active site to the gate, several nanometers apart. The functional significance of the observation is profound: the substrate may enter the central channel and catalytic chamber during short periods of gate opening in native, ligand-free core proteasomes. Degradation of the substrates stimulates a more frequent gate opening, thus allowing substrate molecules

to enter the proteasome tube more often than it would be permitted under the "free" conditions. In our subsequent studies, we are postulating that rearrangement of a network of hydrogen bonds involving the catalytic amine is a starter of allosteric signals traveling to the gate and prompting its opening (Osmulski *et al.*, submitted for publication).

C. Application of Immobilized Proteasomes in Micropatterning

The use of AFM in creating and quality testing of arrayed nanostructures is widespread; however, biological macromolecules are by no means a major subject of such attempts. Still, proteasomes were used to prepare ordered layers of the particles and ultimately to conduct micropatterning. The electrostatic attachment is too weak for most of such applications and usually the CP proteasomes were immobilized on lipid supports. For example, particles from archaeon *Thermoplasma acidophilum* with histidine tags introduced at the C terminus of α subunit were specifically attached to a mica-supported, ultra-flat chelator lipid membrane in the first ever AFM studies on proteasome imaging (Dorn *et al.*, 1999). The bilayer membrane was composed from 1-stearoyl-2-oleyl-*sn*-glycero-3-phosphatidylcholine (SOPC) and a chelator lipid *N*-nitrilotriacetic acid–dioctadecylamine (NTA–DODA) loaded with nickel ions. As a result, images were obtained of a dense layer of the 20S particles oriented in a side-view position, forced by the orientation of a His-tag. The best resolution of such immobilized and oriented particles was obtained when scanning was performed in 10 mM Hepes buffer, pH = 7.5 in the presence of 150 mM NaCl (Dorn *et al.*, 1999). A fluid lipid film of SOPC and Ni-NTA–DODA was also used as a support for 2D crystals of archaebacterial 20S proteasomes in a top-view position (Thess *et al.*, 2002). The 2D crystals are often used in EM and in AFM of membrane proteins, since they are easier to form and more stable than 3D crystals. The 20S proteasomes His_6-tagged at the N-termini of α subunits readily crystallized on a nickel-chelating lipid bilayer prepared on mica. Small patches of the self-organized 20S particles were detectable after a 1-h incubation of proteasomes with the lipid-coated mica, and large areas covered with 2D crystals were imaged after an overnight incubation. Analysis of the images revealed that the proteasomes were nested in a top-view position and optimized their packing in a crystal by interlocking both laterally and vertically, ring-to-waist. Apparently, the His-tag linker was elastic enough to support the 2 nm difference in vertical positioning, perhaps thanks to properties of the disordered N-terminal residues of the α subunits, to which the tag was attached. In this case the contact mode AFM, rather than the much more gentle oscillating mode, was used to successfully image the shear-resistant 2D crystals. Proteasomes His-tagged at the β rings formed dense layers of the side-view particles but did not form ordered 2D crystals (Thess *et al.*, 2002).

Interactions of the CPs with different supported lipid bilayers were explored with bovine proteasomes (Furuike *et al.*, 2003). The 20S core specifically bound in

the top-view position to lipid membranes containing phosphatidylinositol. In contrast, lipid bilayers containing phosphatidylcholine, phosphatidic acid, or dioleotrimethylammonium propane did not support proteasome binding. A relatively low practical resolution of imaging prevented obtaining more detailed information about the structure of membrane-bound particles. It remains to be established if the phosphatidylinositol-specific interactions of the proteasome are physiologically relevant for putative binding to the endoplasmic reticulum (ER) membrane.

The above studies did not extend beyond the topography imaging of immobilized CPs. The actual manipulations on the molecules were described recently as an example of native protein nanolithography (Tinazli *et al.*, 2007). His-tagged archaebacterial 20S proteasome particles were first arranged into a uniformly oriented array on a self-assembled monolayer (SAM) of nickel-nitrilotriacetic acid (Ni-NTA) on gold glass coverslips. The array of proteasomes was then imaged by a conventional tapping mode, which was easily switched to micropatterning by lowering the setpoint of the amplitude of tip oscillations. Then, the tip was operating in a novel contact oscillation mode (COM), maintaining a constant contact with the objects and displacing them (''erasing'' the pattern) at forces from 15 to 50 nN. Adding a His-tagged protein of choice resulted in filling (''rewriting'') the ''erased'' areas. If the rewritten passages were formed by proteins of height significantly different from the proteasome, the differences were registered by the AFM tip (''reading''). All the procedures of ''writing, erasing, rewriting, and reading'' were carried out under liquid, with native proteins, suitable for interaction screens of diagnostic value (Tinazli *et al.*, 2007).

Another kind of nanolithography was using native complexes under liquid as well; however, here the proteasomes were used as a cleaning tool for immobilized substrate (Osmulski and Gaczynska, unpublished data). In short, unordered patches of a monolayer of lysozyme were adsorbed on mica by electrostatic forces. Before the adsorption, lysozyme was *in vitro* modified by polyubiquitination, which rendered the protein a suitable substrate for the human 26S proteasome. Tapping mode AFM in liquid was used to scan the layer of a polyubiquitinated lysozyme (Fig. 6). When the purified 26S proteasomes were injected into the AFM wet chamber, after several minutes numerous randomly positioned proteasome particles, easily identified by their shape, settled on the layer of the substrate, finally forming overlaying patches. Most of the mica surface was covered by the substrate overlaid by the proteasome, as indicated by the height of patches. After about an hour of continuous scanning most of proteasomes disappeared leaving large areas of bare mica, again identified by their height (Fig. 6). A subsequent addition of fresh proteasomes did not result in significant adsorption of the enzyme to the mica patches. We interpret these real-time observations as indications of: (1) specific binding of 26S proteasome to a substrate protein adsorbed on mica, and (2) nanolithography-type ''cleaning'' of mica surface from adsorbed substrate, all monitored with the AFM imaging (Gaczynska and Osmulski, unpublished data).

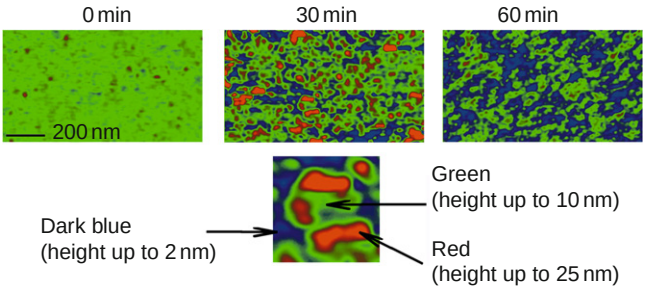

Fig. 6 Nanolitography with human 26S proteasome. Three examples of median filtered for display purposes successive images of the same field. Top left: dense layer of polyubiquitinated lysozyme was electrostatically attached to mica. Right after collecting the image shown, the solution of 26S proteasomes was injected into the AFM wet chamber. Top middle: 30 min later, large particles, presumably 26S proteasomes (see bottom image), were identified atop the substrate layer. Low-lying patches, free of the layer of substrate, are visible. Top right: 60 min later the large particles are not detectable and large areas of the field are low-lying, with a height consistent with background mica. Bottom: an enlarged area of the middle field (150 nm × 150 nm) to explain the color scheme encoding the height. Note the general shape of tall particles consistent with side-view 26S proteasomes (Fig. 1).

IV. Discussion

A. Elucidation of Subunit Organization in a Protein Assembly

Our study dissecting the new subcomplex of the proteasome 19S particle took advantage of a convenient property of CPs to settle on mica preferentially in a top-view position. Such orientation exposes the α face, which is the binding area for regulatory modules, and renders it accessible for AFM analysis. Since height of objects is registered with the great accuracy in AFM images collected in the height mode, we choose this parameter to follow the ligand binding. Analysis of the maximum height applied in our studies helped us to positively detect the decoration of a large 20S proteasome with a single protein, which has seven-times lower MW and more than five-times lower average height. Employing a volume analysis to distinguish between liganded and unliganded proteins gave inconsistent results. The comparison of volumes was reported to work very well for ligands of similar size; however, in our case the difference in volumes between the ligand and the acceptor molecule was too large. The height analysis had even more advantages. Since attachment of an additional ligand of a similar size was followed by the proportional extension of the maximal height, we concluded that the two ligands subunits are stacked on the α face. Combining analysis of the height and diameter in the top most areas of the particles allowed identification of even more subcomplexes of core proteasome with elements of 19S complex. Since these distinct subcomplexes were imaged on the same field, with the same tip, the tip dilation was not posing a problem for the diameter comparison. We recently noticed that an extension of the CP height with a ligand even smaller than the Rpn1 or Rpn2

(about 100 kDa each) could be successfully detected with this approach (Rosenzweig *et al*., 2008). Our preliminary height measurements of CP decorated with PI31, a 31 kDa protein (1/20 of the mass of CP) that binds to α· face showed approximately a 2-nm extension of the 20S core (Gaczynska *et al.*, unpublished results). The maximal height or height and diameter analysis can be obviously used beyond the proteasome, for mapping ligand-acceptor topography in any case where one object is immobilized and another one stably settles on its top.

Interestingly, the latest high-resolution averaged cryo-EM images of 26S proteasomes failed to show the presence of the stent inside the Rpt ring. An alternative positioning of at least one of Rpn subunits was proposed, with a gently curled α-repeat protein wrapping the ring on the outside (da Fonseca and Morris, 2008). There is a possibility that the 19S RP exists in several versions of subunit composition. If the variant with a stent is not a prevailing one under the conditions of EM experiments, its structure may be lost in the process of averaging. The degree of curling of the α-helical repeat proteins like Rpn1 and Rpn2 may depend on the experimental conditions as well. The power of analysis of the height of AFM images stems from the separation of particles into classes, even if the classes are not populous (Fig. 4). By any means, the controversy and discrepancy between AFM and cryo-EM data may prove very useful for revealing the intricacies of the 26S proteasome structure in the near future.

B. Conformational Diversity of Large Protein Assemblies

The core proteasome provides a very convenient subject for AFM-based studies of conformational instability and its role in catalysis. The lifetime of conformational stages is apparently long enough to collect nonblurred AFM images. In a separate pilot study, we approximated the lifetime of conformers in a ''ligand free'' state as about 2 (open) and 6 ms (closed), consistent with the observed 1:3 partition of open and closed molecules (Gaczynska and Osmulski, unpublished data). The simple analysis of the conformational equilibria under the distinct ligand conditions brought an impressive insight into the dynamics of catalysis and linked the conformational instability to efficient catalysis. The discovery of spontaneous and ligand-induced gate opening in the native core proteasome is especially daring taking into account that crystal structure modeling of the molecule showed an exclusively closed-gate conformation (Groll *et al*., 1997; Osmulski and Gaczynska, 2000). This prompted speculations, about alternative routes of substrate uptake or about ''external'' ways of gate opening in catalytic core without gate-opening regulatory modules attached. According to the latter hypothesis, certain substrates putatively interact with the gate, causing its opening (Osmulski *et al*., 2008). While the external gate opening cannot be excluded, the concept of conformational diversity and shifts of conformational equilibrium grossly simplifies the general model of proteolysis by the 20S particle. There is one discrepancy, however, which needs addressing. The crystal structure of ligand-free yeast and bovine CPs showed exclusively closed gate (Groll *et al*., 1997). This may be understandable taking into

account that the modeling based on X-ray crystallography utilizes the most stable conformations. Less trivial to explain is the apparent discrepancy between AFM and crystal structure data showing that proteasomes treated with the transition state analogue inhibitor or with the acetylated active center N-terminus are in exclusively open conformation in AFM images but closed in the crystal structure (Groll *et al.*, 1997, 2006). Fortunately, an AFM experiment suggests a plausible elucidation. Apparently, when a dense layer of 20S proteasomes was analyzed instead of loosely dispersed molecules, we noted a profound decrease (to a few percent) in a number of the open particles, even if the particles were mostly open when loosely dispersed (Osmulski *et al.*, submitted for publication). This observation is consistent with recently detected by cryo-EM dilation of the α ring in proteasomes in the presumably-open conformation (da Fonseca and Morris, 2008). Such dilation was observed also in AFM images (Gaczynska and Osmulski, unpublished data). Spatial constrains in a crystal or in a dense layer of standing particles may prevent the free conformational transitions. Molecular crowding was in fact reported to suppress breathing motions in proteins (Makowski *et al.*, 2008). By any means, a straightforward AFM-based analysis of the shape and dimensions of protein assemblies imaged under native conditions is perfectly complementing the X-ray crystallography and EM when it comes to structural dynamics.

C. Microarrayed Molecular Factories

Micropatterning with proteasomes is in early stages of the development, however, we expect its much broader future applications in nanotechnology (Gaczynska *et al.*, 2006). Immobilization of at least CP does not pose a problem, with tagging strategically placed in a desired position and binding in a highly controlled orientation (Dorn *et al.*, 1999; Thess *et al.*, 2002). Exploring interactions of proteasomes with lipid membranes may help in revealing the postulated role of the protease in degradation of proteins ejected from the ER, for example, during unfolded protein response (UPR). The postulated *in vivo* interactions of proteasome assemblies with the outside of ER membrane are still enigmatic and mastering methods of lipid-based, tag-less immobilization of the enzymes may shed a light on their hydrophobic interactions capabilities (Furuike *et al.*, 2003). Using proteasomes as ''ink particles'' moved around by the ''pen'' formed by AFM tip shows the power of micropatterning with large proteins (Tinazli *et al.*, 2007); however, the proteasome can do more. It can work as ''specific lawn mover'' cleaning protein patches suitable as substrates (Osmulski and Gaczynska, unpublished data). When moved by a tip during micropatterning, it can at the same time hold a cargo in its inside chamber and release it in desired destination by controlling the opening and closing of the gate. Patches of immobilized proteasomes may be involved in production of desired peptides, both by degradation of substrates and by recently described peptide ligation. The ''breathing'' movements of the particles organized in a loose array may be utilized as well, perhaps, as sensors of crowding conditions and nanoturbines or nanopumps to stir or transfer the molecules

(Gaczynska *et al.*, 2006). Experimenting with higher-order proteasomal assemblies like 26S will add even more capabilities to potential microarrays, for example, energy release by the Rpt ring or polypeptide holding and unfolding. The multiple catalytic capabilities of the proteasome will definitely be useful for the future nanotechnology applications.

V. Summary

In this chapter, we outlined the application of AFM to study proteasome, the multisubunit, multifunctional essential protease. We focused on methods used to dissect subunit organization in a protein complex regulating the activities of the proteasome, to reveal structural dynamics of the enzyme and its role in catalysis, and to use the protein assembly in micropatterning and nanolithography. We briefly discussed future directions of the AFM-based proteasome studies and the potential uses of the methods for investigation of other nanoobjects.

Acknowledgment

The work was supported by NIH/NIGMS R01 grant (M.G.).

References

Bahar, I., Chennubhotla, C., and Tobi, D. (2007). Intrinsic dynamics of enzymes in the unbound state and relation to allosteric regulation. *Curr. Opinion Struct. Biol.* **17,** 633–640.

Bajorek, M., and Glickman, M. H. (2004). Keepers at the final gates: regulatory complexes and gating of the proteasome channel. *Cell. Mol. Life Sci.* **61,** 1579–1588.

Borissenko, L., and Groll, M. (2007). 20S proteasome and its inhibitors: Crystallographic knowledge for drug development. *Chem. Rev.* **107,** 687–717.

da Fonseca, P. C. A., and Morris, E. P. (2008). Structure of the human 26S proteasome: Subunit radial displacements open the gate into the proteolytic core. *J. Biol. Chem.* **283,** 23305–23314.

Dorn, I. T., Eschrich, R., Seemuller, E., Guckenberger, R., and Tampe, R. (1999). High-resolution AFM-imaging and mechanistic analysis of the 20 S proteasome. *J. Mol. Biol.* **288,** 1027–1036.

Forster, A., Masters, E. I., Whitby, F. G., Robinson, H., and Hill, C. P. (2005). The 1.9 A structure of a proteasome-11S activator complex and implications for proteasome-PAN/PA700 interactions. *Mol. Cell* **18,** 589–599.

Furuike, S., Hirokawa, J., Yamada, S., and Yamazaki, M. (2003). Atomic force microscopy studies of interaction of the 20S proteasome with supported lipid bilayers. *Biochim. Biophys. Acta (BBA) - Biomembranes* **1615,** 1–6.

Gaczynska, M., and Osmulski, P. A. (2008). AFM of biological complexes: what can we learn? *Curr. Opinion Colloid Interface Sci.* **13,** 351–367.

Gaczynska, M., Osmulski, P. A., Gao, Y., Post, M. J., and Simons, M. (2003). Proline- and arginine-rich peptides constitute a novel class of allosteric inhibitors of proteasome activity. *Biochemistry* **42,** 8663–8670.

Gaczynska, M., Rodriguez, K., Madabhushi, S., and Osmulski, P. A. (2006). Highbrow proteasome in high-throughput technology. *Expert Rev. Proteomics* **3,** 115–127.

Groll, M., Bajorek, M., Kohler, A., Moroder, L., Rubin, D. M., Huber, R., Glickman, M. H., and Finley, D. (2000). A gated channel into the proteasome core particle. *Nature Struct. Biol.* **7,** 1062–1067.

Groll, M., Berkers, C. R., Ploegh, H. L., and Ovaa, H. (2006). Crystal structure of the boronic acid-based proteasome inhibitor bortezomib in complex with the yeast 20S proteasome. *Structure* **14,** 451–456.

Groll, M., Bochtler, M., Brandstetter, H., Clausen, T., and Huber, R. (2005). Molecular machines for protein degradation. *Chembiochem* **6,** 222–256.

Groll, M., Ditzel, L., Lowe, J., Stock, D., Bochtler, M., Bartunik, H. D., and Huber, R. (1997). Structure of 20S proteasome from yeast at 2.4 A resolution. *Nature* **386,** 463–471.

Hammes-Schiffer, S., and Benkovic, S. J. (2006). Relating protein motion to catalysis. *Annu. Rev. Biochem.* **75,** 519–541.

Kajava, A. V. (2002). What curves alpha-solenoids? Evidence for an alpha-helical toroid structure of Rpn1 and Rpn2 proteins of the 26 S proteasome. *J. Biol. Chem.* **277,** 49791–49798.

Lowe, J., Stock, D., Jap, B., Zwickl, P., Baumeister, W., and Huber, R. (1995). Crystal structure of the 20S proteasome from the archaeon T. acidophilum at 3.4 A resolution. *Science* **268,** 533–539.

Makowski, L., Rodi, D. J., Mandava, S., Minh, D. D. L., Gore, D. B., and Fischetti, R. F. (2008). Molecular Crowding Inhibits Intramolecular Breathing Motions in Proteins. *J. Mol. Biol.* **375,** 529–546.

Muller, D. J., Janovjak, H., Lehto, T., Kuerschner, L., and Anderson, K. (2002). Observing structure, function and assembly of single proteins by AFM. *Progress Bioph. Mol. Biol.* **79,** 1–43.

Ortega, J., Heymann, J. B., Kajava, A. V., Ustrell, V., Rechsteiner, M., and Steven, A. C. (2005). The axial channel of the 20S proteasome opens upon binding of the PA200 activator. *J. Mol. Biol.* **346,** 1221–1227.

Osmulski, P. A., and Gaczynska, M. (2000). Atomic force microscopy reveals two conformations of the 20 S proteasome from fission yeast. *J. Biol. Chem.* **275,** 13171–13174.

Osmulski, P. A., and Gaczynska, M. (2002). Nanoenzymology of the 20S proteasome: Proteasomal actions are controlled by the allosteric transition. *Biochemistry* **41,** 7047–7053.

Osmulski, P. A., and Gaczynska, M. (2005). Atomic force microscopy of the proteasome. *In* Ubiquitin and Protein Degradation, (R. J. Deshaies, Ed.), Part A, Vol. 398, pp. 414–425. Elsevier, Amsterdam.

Osmulski, P. A., Tokmina-Lukaszewska, M., Endel, L., Sosnowska, R., and Gaczynska, M. (2008). Chemistry of proteasome. Wiley Encyclopedia of Chemical Biology. *John Wiley and Sons, Inc.* in press.

Rosenzweig, R., Osmulski, P. A., Gaczynska, M., and Glickman, M. (2008). The central unit within the 19S regulatory particle of the proteasome. *Nature Struct. Mol. Biol.* **15,** 573–580.

Sprangers, R., and Kay, L. E. (2007). Quantitative dynamics and binding studies of the 20S proteasome by NMR. *Nature* **445,** 618.

Thess, A., Hutschenreiter, S., Hofmann, M., Tampe, R., Baumeister, W., and Guckenberger, R. (2002). Specific orientation and two-dimensional crystallization of the proteasome at metal-chelating lipid interfaces. *J. Biol. Chem.* **277,** 36321–36328.

Tinazli, A., Piehler, J., Beuttler, M., Guckenberger, R., and Tampe, R. (2007). Native protein nanolithography that can write, read and erase. *Nature Nanotechnol.* **2,** 220–225.

Unno, M., Mizushima, T., Morimoto, Y., Tomisugi, Y., Tanaka, K., Yasuoka, N., and Tsukihara, T. (2002). Structure determination of the constitutive 20S proteasome from bovine liver at 2.75 A resolution. *J. Biochem.* **131,** 171–173.

Varshavsky, A. (2005). Regulated protein degradation. *Trends Biochem. Sci.* **30,** 283–286.

Walz, J., Erdmann, A., Kania, M., Typke, D., Koster, A. J., and Baumeister, W. (1998). 26S proteasome structure revealed by three-dimensional electron microscopy. *J. Struct. Biol.* **121,** 19–29.

CHAPTER 4

Biomineralization at the Nanoscale: Learning from Diatoms

David P. Allison,[*] Yves F. Dufrêne,[†] Mitchel J. Doktycz,[‡] and Mark Hildebrand[§]

[*]Department of Biochemistry and Cellular and Molecular Biology
University of Tennessee
Knoxville, Tennessee 37996-0840

[†]Unité de chimie des interfaces
Université Catholique de Louvain
Croix du Sud 2/18
B-1348 Louvain-la-Neuve, Belgium

[‡]Biological & Nanoscale Systems Group
Biosciences Division
Oak Ridge National Laboratory
Oak Ridge, Tennessee 37831-6445

[§]Scripps Institution of Ocenography
University of California-San Diego
LaJolla, California 92093-0202

METHODS IN CELL BIOLOGY, VOL. 90

0091-679X/08 $35.00
DOI: 10.1016/S0091-679X(08)00804-2

I. Introduction to Nanotechnology

Humans have been fabricating useful devices for several thousand years beginning with primitive tools used for hunting, protection, and building shelters to our present manufacturing capabilities. This evolution of useful manufactured devices has been impressive, driven by technical capability, need, and economic incentives, which have allowed civilized man to enjoy a better quality of life. In almost every aspect of our living experience, we have seen unparalleled progress in device manufacturing in a very short period of time. Just about 60 years ago, computers occupied roughly two hundred square meters of floor space and weighed 30 tons. Today, we remove a computer, orders of magnitude superior to the original computers, from our briefcase as we pass through security to get on an airplane capable of taking us to any location on earth in less than 24 h. Medical devices from the hypodermic syringe to magnetic resonance imaging have contributed toward more than doubling the average human life expectancy. The internet, cell phone, Blackberry, and high-definition television are all relative newcomers in the realm of man made devices that have made possible daily global interaction between human populations.

Although our large scale manufacturing accomplishments of two and three dimensional devices down to the single micron scale has been noteworthy and impressive, fabrication of devices at the nanoscale has remained elusive (Muller, 2001; Sarikaya *et al.*, 2003). Inevitably, the need for nanoscale devices, driven by the demand for increasingly smaller optical, electronic, medical devices, and even nanorobots, has propelled us into the era of nanotechnology that will require nanoscale based fabrication techniques. This demand has also been fueled by observations that materials have unique properties at the nanoscale, not present in the bulk material, which could be developed into useful applications. Electronic properties of semiconductors, properties of nanostructured composites, magnetic properties of particles, and colloidal suspensions all depend on nanoscale dimensions. Examples would include quantum dots whose luminescence scales from the blue to red wavelength depending on nanoparticle size and which have great potential for biomolecular tracking and medical diagnostics (Chan and Nie, 1998). Properties of nanoparticles related to size have also found applications as catalysts where, for example, platinum in bulk is not catalytic but as nanoparticles has found applications in automobile catalytic converters (Bell, 2003; Hvolbæk *et al.*, 2007).

Essentially, two general approaches toward device fabrication at the nanoscale have been followed. One approach involves the adaptation of conventional methods that have already been developed and have been effectively used to manufacture devices with nanoscale features. Most notably, this would include photolithography, the process employed to manufacture most of the microelectronics used today that is capable of patterning features of less than 50 nm (Itani *et al.*, 2003). Photolithography is a parallel process that is scalable, although

expensive, involving ultraviolet exposure of a photo-activated film to resist through a mask and using reduction optics to create a structure. Generally, the finished product requires many steps that have to be precisely orchestrated to be successful, and technical difficulties including extending the process to wavelengths below 157 nm may limit further extension of this technique into the nanoscale (Gates *et al.*, 2004). A similar lithographic technique that has been developed to pattern nanoscale structures on resist surfaces involves scanning a focused beam of electrons (electron beam lithography) or ions (focused ion beam lithography) (Gates *et al.*, 2004). This fabrication technique is serial and slower than photolithography since the pattern is created line-by-line.

These and other conventional techniques are presently commercially available, but nanofabrication also depends on the evolutionary development of new tools in the manufacturing pipeline. For example, both atomic force (AFM) and scanning tunneling (STM) microscopes, developed primarily as high-resolution imaging tools, have demonstrated their utility for creating structure on surfaces at the nanoscale (Garcia *et al.*, 2006). Examples would include dip pen lithography where the AFM tip, coated with molecules designed to interact with a surface, is used to create nanoscale patterns of these molecules on the surface (Jaschke and Butt, 1995; Piner *et al.*, 1999). Local oxidation nanolithography (LON) has been successfully demonstrated using both STM (Dagata *et al.*, 1990) and AFM (Day, 1993) by applying a potential difference between the tip and surface forming a water meniscus, effectively creating a nanometer sized electrochemical cell. By applying voltage pulses, oxide structures as small as 10 nm can be patterned on the surface of silicon, some semiconductors, and on metals such as titanium, aluminum, and nickel (Garcia *et al.*, 2006). Currently, these scanning probe fabrication techniques are serial, but future development using multiple tips may allow fabrication of multiple patterns with a diversity of structures. Improvements in both existing technology and the continued evolution of new technology into our manufacturing base should insure continued progress in synthetic efforts to fabricate devices at the nanoscale.

A second approach to develop fabrication techniques, spanning the nano to the macroscale, is a biomimetic approach that seeks to identify designs and features found in nature that could be developed into useful applications and products. This is not a new approach, since early man quickly realized that fur could be used to keep warm and bone or stone tools that mimicked the claws and teeth of animals could be used for hunting and protection (Vincent *et al.*, 2005). Perhaps, the earliest tool conceived by early man that did not appear to have a natural origin was the wheel, although some creatures do curl up into a ball to roll away from danger (Hesselberg, 2007). For example, Russian thistle, also known as tumbleweed, inhabits dry regions of the western United States. As the plant matures, it becomes spherical so that upon drying and breaking free of its root, the wind causes the plant to roll over a great area releasing its seeds (Carnes *et al.*, 2003).

Ultimately, biomimetics involves gaining an understanding of a particular element in a natural system and applying this knowledge to our manufacturing

base. If we contrast man-made approaches, whose history of a few thousand years and has evolved primarily to satisfy a need, with natural systems that have evolved over many millions of years with survival as the driving force, we find that natural systems generally exhibit superior properties. Very simply, nature does it better and in many cases, cannot be duplicated using the technology we have today.

Man-made approaches are energy inefficient, usually requires heat and pressure, generally results in low yields, and perhaps with toxic byproducts. Conversely, natural synthesis is energy efficient, occurs in a liquid environment at ambient temperature, and without waste (Sanchez *et al.*, 2005; Sarikaya *et al.*, 2003; Tamerler and Sarikaya, 2007). At the macroscale, a biomimetic approach was employed, for example, to the design of boat and ship hulls by duplicating features found in fish and aquatic mammals. Bird wings have served as inspiration and as models for airplane wings. The spider's web was likely the natural design that resulted in fishing nets and screening devices that allow separation of materials according to size. The flippers of seals and the webbed feet of frogs and birds, such as swans, ducks, and gulls, have served as models for swim fins used by swimmers and divers (Bar-Cohen, 2006). An early approach at the microscale, translating natural design to a product, resulted in the invention of Velcro when a Swiss engineer, George de Mestral, found that upon microscopic examination, tiny hooks on the spines of burs he removed from his dogs were responsible for the burs sticking tightly to the fur (Mueller, 2008). Today, with the tool sets we have in hand, we are capable of investigating natural systems from the molecular to the macroscale. How is the gecko able to run up walls at great speed? High-resolution microscopy has identified nanoscale filaments on its toes that through dry adhesion of van der Waals forces allow the gecko to scale vertical walls (Autumn *et al.*, 2002). Efforts to better understand and mimic the gecko's adhesion capabilities is the subject of ongoing research at several universities and at Stanford University, a robot called "stickybot" has already demonstrated the ability to scale a vertical surface (Autumn, 2003; Lanzetta and Cutkosky, 2008; Mueller, 2008). The discovery of the "lotus effect" on lotus leaves, where moisture beads up on the surface and subsequently runs off cleaning the surface, has led to research to understand the mechanism that subsequently resulted in marketing "Lotusan" a paint that allows self-cleaning of surfaces (Barthlott *et al.*, 1997). Antireflective surfaces have been identified on some insect eyes that allow for improved vision in low-light conditions (Parker and Townley, 2007; Parker *et al.*, 1998), and on some insect wings that reduce reflections and thus serve as a means for camouflage (Stoddardt *et al.*, 2006). This structure has been incorporated onto polyethylene sheets that are affixed to glass solar panels resulting in a 10% increase in efficiency (Vincent *et al.*, 2006).

There are a plethora of research initiatives inspired by natural systems, spanning length scales from the nano to the macroscale, that we could identify and include in this communication but this is not our purpose. In general, pattern formation in biology is associated with multicellular organisms where differentiation of different cell types is involved in the process. Here, our interests are in unicellular organisms where individual cells form highly diverse patterns that result from molecular-level

interactions. In particular, we are interested in patterns formed by biomineralization, frozen in time and space, from mineral products organized at the organic/inorganic interface within the cell. The objective through our efforts and the efforts of others is to understand biomineralization in diatoms, organisms which offer a near limitless number of design features in their silica skeletons, with the ultimate goal of understanding and implementing biodesign into our manufacturing base (Fig. 1).

II. Introduction to Diatoms

Diatoms are unicellular, photosynthetic algae that make a composite cell wall out of silica, carbohydrates, and protein. They are found in the oceans, seas, fresh water, and even in moist soil. Early fossil records date diatoms back to the early

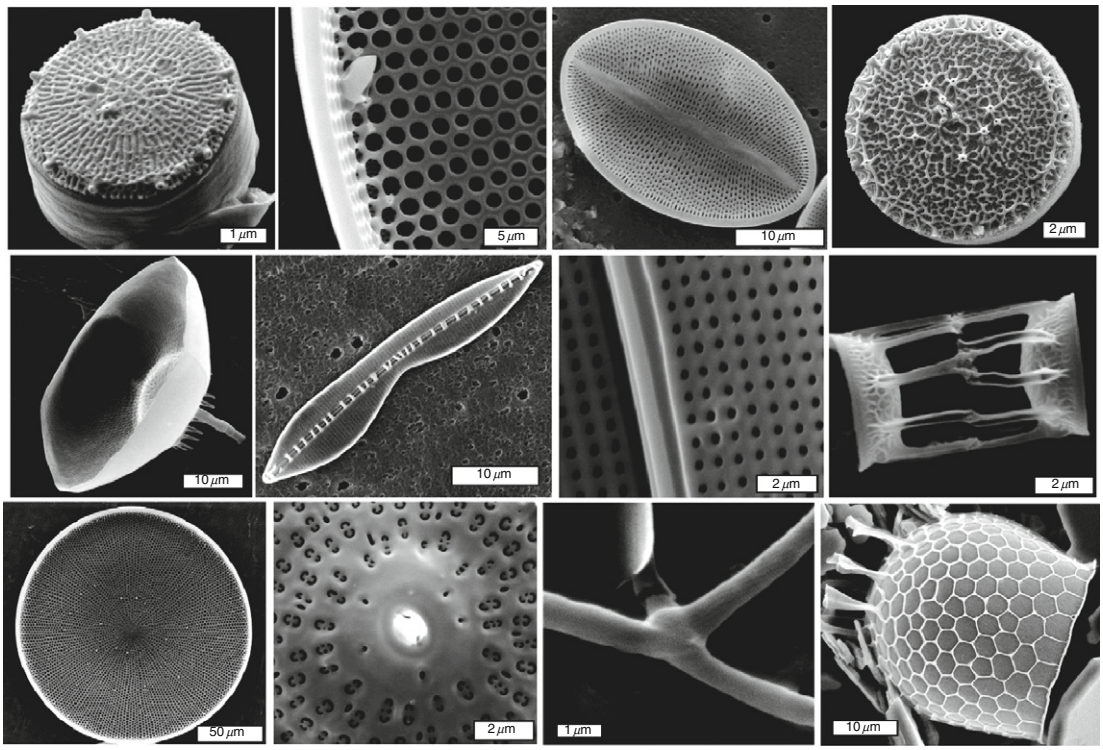

Fig. 1 SEM images of a variety of acid-cleaned diatom silica structures. Upper panel, from left to right, *Thalassiosira pseudonana*, structural detail from, *Coscinodiscus wailesii*, *Cocconeis* sp., and *Thalassiosira weissflogii*. Center panel, left to right, *Ditylum brightwellii*, *Bacillaria paxillifer*, *Gyrosigma balticum*, and *Skeletonema costatum.* Bottom panel, left to right, *Coscinodiscus wailesii*, structural detail of *Ditylum brightwellii*, setae detail in *Chaetoceros laciniosis* and *Stephanopyxis turris*.

Jurassic period some 200 million years ago, although some evidence suggests that their appearance may have coincided with the mass extinction that occurred earlier during the Permian period (Kooistra and Medlin, 1996; Raven and Waite, 2004). From an ecological perspective, diatoms produce 40% of the ocean's yearly production of organic carbon (Nelson *et al.*, 1995). Diatoms also play a key role in the global carbon cycle where it is estimated that they produce approximately 20% of the oxygen that we breathe, an amount slightly exceeding the total produced by all of the terrestrial rain forests (Field *et al.*, 1998; Mann, 1999). Diatoms are generally divided into two orders: centric diatoms that are radially symmetrical, and pennate diatoms that exhibit bilateral symmetry. Several thousand species of diatoms have been classified according to variations in the structure of their silica skeletons, and the total number of diatom species has been estimated to exceed 100,000 (Round *et al.*, 1990). The entire diatom silica cell wall structure is called the frustule; it is divided into two overlapping halves called thecae, similar to a pill box or Petri dish. The upper half is called the epitheca while the lower half is called the hypotheca. Capping the two thecae are the valves (Fig. 2), which are the morphologically specific structures that serve to differentiate diatom species. Overlapping siliceous strips, called girdle bands, form the sides of the diatom silica structure and provide overlap between the two thecae. In many species, the girdle bands are not completely circular, but instead, are broken and taper at the ends near the break. In these cases, adjacent girdle bands have a bell shaped structure called the ligula, which follows the taper filling in the gapped space (Fig. 2). In living diatoms, an organic envelope composed of polysaccharides and proteins covers the diatom silica skeleton (Hecky *et al.*, 1973).

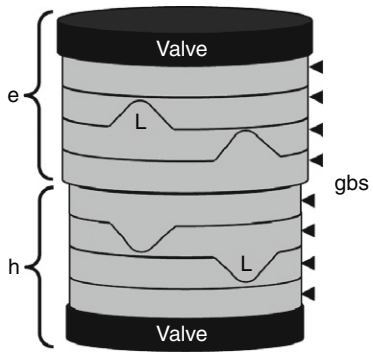

Fig. 2 Schematic, of a diatom cell wall structure. The overall cell wall structure is called a frustule, configured like a Petri dish with the upper half called the epitheca (e) that overlaps the lower half that is called the hypotheca (h). Valves cap the the thecae as shown in the schematic. The thecae sides are comprised of a series of overlapping girdle bands (gbs, arrows). The bell-shaped structure in a girdle band is called the ligula (L identifies two of the four) In *T. pseudonana*, girdle bands are not complete rings, but have a break which tapers to fit the ligula in the adjacent girdle band.

The diatom silica skeleton is fabricated from silicic acid that is actively transported (Hildebrand *et al*., 1997, 1998) into the cell from the environment into a specialized membrane bound vesicle, called the silica deposition vesicle (SDV) (Crawford *et al*., 2001; Drum and Pankratz, 1964; Reimann *et al*., 1966; Schmid *et al*., 1981). Within the SDV, the silicic acid is polymerized into silica. After the valve or girdle band is formed, it is exocytosed across the cell plasma membrane, where it becomes the exoskeleton of the cell. Silica structure formation in diatoms can be divided into three separate scales progressing from the nano to the meso and finally to the microscale (Davis and Hildebrand, 2007; Hildebrand *et al*., 2006). Formation of the micro and nanoscale structure is partially characterized, but little is known about formation of the mesoscale structure. The microscale is the overall shaping of the valve and girdle bands within the SDV through active and passive molding (Round *et al*., 1990). This involves the cytoskeleton, actin, and microtubules which influence the shape and expansion of the SDV (Blank, 1983; Cohn *et al*., 1989; Schmid *et al*., 1990; van de Meene, 2002).

There is still a great deal that we don't know about the interaction of the cytoskeleton with the SDV membrane and how the shape of the SDV is defined by elements of the cytoskeleton. The nanoscale silica structure results from the polymerization of silicic acid and results in both beaded silica and smooth textured silica. The organic components associated with the polymerization of diatom silica (Kröger *et al*., 2000a) are long chain polyamines (LCPAs) and polypeptides called silaffins that have a regulatory role in the polymerization process by organizing LCPAs by electrostatic interactions (Kröger *et al*., 1999, 2002; Poulsen and Kröger, 2004). The polymerization of silica has also been accomplished *in vitro* to produce beaded and smooth silica using LCPAs and silaffins isolated from diatoms (Kröger *et al*., 1999, 2000, 2002; Poulsen and Kröger, 2004), but these experiments do not produce highly organized structure as seen in the frustules of diatoms. In diatoms, higher order structure appears at the mesoscale when organized nanoscale polymerization products are assembled with unique features within the SDV into diatom valves, girdle bands, and other components of the diatom skeleton. Since the organization of exoskeleton components at the mesoscale is poorly understood, and since this is where species-specific structures appear, further understanding of these processes are necessary. Although diatoms are not high on the list of organisms that we equate with research initiatives, the unique features exhibited by the many species of diatoms and the potential for incorporating these features into device fabrication may change this in the near future.

III. Investigating Diatom Mesoscale Silica Formation

Several mechanisms have been proposed to explain how diatom mesoscale structure might be composed within the SDS. Templating of organic materials, carbohydrates, or proteins internal to the SDV (Davis and Hildebrand, 2007; Pickett-Heaps *et al*., 1990; Robinson and Sullivan, 1987), through the association

of LCPAs with silaffins (Kröger and Sumper, 2004; Poulsen and Kröger, 2004; Sumper and Kroger, 2004), perhaps by phase separation that involves LCPAs (Sumper, 2002), or by a chemical process that involves simple diffusion (Gordon and Drum, 1994) have all been suggested. However, the variety, intricacy, and reproducible nature of the three-dimensional structures made by diatoms (Schmid and Schulz, 1979; Schmid and Volcani, 1983) would seem to rule out processes that are solely due to self-association, diffusion, or phase separation. Certainly, there is evidence that these processes do play some role in fabrication of the diatom skeleton; for example, the self-association of silaffins with LCPAs in the presence of silicic acid *in vitro* (Kröger *et al*., 2002; Sumper and Kroger, 2004) has shown that textured silica can be formed, and there is reason to believe that this occurs *in vivo* within the SDV lumen where the pH is low (Vrieling, 1999) and can support silica polymerization (Iler, 1979). The observation that LCPAs can self-associate prompted the idea that perhaps the sequential formation of droplets of LCPAs followed by their incorporation into silica could, by phase separation, result in smaller circular structures as seen in the valve structure of *Coscinodiscus* (Sumper, 2002). Although this is an intriguing possibility, a sequential examination of structural intermediates in *Coscinodiscus* valve formation (Schmid and Volcani, 1983) indicates that other factors are involved. Initially, in *Coscinodiscus,* linear silica structures are deposited to form the base layer of the valve which is inconsistent with the notion of circular droplet formation. Also, the phase separation model does not account for the formation of three dimensional structures, clearly apparent in *Coscinodiscus wailesii* and *Thalassiosira eccentrica*, where distinctly different structures are formed on different internal surfaces of the SDV (Schmid and Schulz, 1979; Schmid and Volcani, 1983). This was recently observed in our own work when we examined structural intermediates of valve formation in *T. pseudonana* (Hildebrand *et al*., 2006). The circular valve in this species was observed to initially form a base layer from flat ribs of silica with spaces between the ribs radiating out from the center of the valve, followed by fusion of the ribs thereby forming the flat thin base layer of the valve (Fig. 3A and B). After the base layer forms in the *x*/*y* axis plane, the rim and center of the valve is built up by addition of silica. We refer to this process as ''spatial cementing'' to describe the expansion of the valve in the *z*-axis dimension (Hildebrand *et al*., 2006). In previous studies on *C. wailesii* and *T. eccentrica* and in our work on *T. pseudonana,* silica deposition and *z*-axis expansion occur only in one dimension, that being toward the outer or distal valve face (Hildebrand *et al*., 2006; Schmid and Schulz, 1979; Schmid and Volcani, 1983). *Z*-axis expansion has been documented in other diatom species and a model suggests anchoring components, possibly from the cytoskeleton, on the outside proximal surface of the SDV that organizes polymerization components, within the SDV lumen, via membrane-spanning proteins (Davis and Hildebrand, 2007; Robinson and Sullivan, 1987). This model is compatible with the deposition of a valve base layer to initiate the valve mesoscale structure. However, it is also likely that other factors including phase separation, chemical effects, and assembly of organics play a role in *z*-axis expansion.

Understanding mesoscale formation in diatoms has benefited greatly from high-resolution microscopies. Both SEM and TEM have served as the primary techniques used to examine the formation of diatom silica structure. Recently, AFM has been employed to complement SEM and TEM studies primarily because it is better at resolving small differences in surface topography. The small differences in surface height revealed by AFM may indicate the presence of underlying organic templates and can be equated to various stages in diatom silica maturation. In conjunction with imaging, the sensitivity of the AFM cantilever has been used to provide information on the micromechanical properties on the diatom surface (Gebeshuber *et al.*, 2003). This technique of measuring surface compliance could, for example, determine what diatom silica structures require ripening after they have been formed. Just as multicellular organisms are composed of tissue and bones, single-celled diatoms are composed of mucilage covering a silica skeleton. Understanding the relationship between structural elements in multicellular organisms is paramount to understanding function. This should also be obvious when studying single-celled organisms and should contribute to our understanding of biomineralization in diatoms. To this end, our goal is to highlight the use of AFM to investigate both surface components in the living diatom and the nano to macroscale development in the diatom skeleton including valves, girdle bands, and setae along with other unique features that define species. In doing so, we hope to illustrate specific points that we have identified in our studies of diatoms that serves as only a beginning toward understanding these marvelous natural creations.

IV. Nanoscale Imaging of Living Diatoms

Currently, AFM is the only technique that can image live microbial cells in real-time and with nanometer resolution (Dufrêne, 2004, 2008). A crucial prerequisite for a reliable experiment is to immobilize the cells using gentle, nondestructive protocols (Dufrêne, 2008). Strong attachment may be achieved by pretreating the substrate with polycations (Schaer-Zammaretti and Ubbink, 2003) or gelatin (Doktycz *et al.*, 2003), or immobilizing the cells mechanically in porous membranes (Kasas, 1995).

Recently, the power of AFM imaging was used to resolve the fine surface structure of *Phaeodactylum* (Francius *et al.*, 2008), a pennate diatom described in three different morphotypes, that is, the fusiform, the triradiate, and the ovoid forms. As opposed to other diatoms, *Phaeodactylum* is very poor in silica. In fact, the ovoid form is the only morphotype which is able to synthesize true silica valves. By contrast, the fusiform and triradiate cell walls possess almost exclusively organic components, mainly polysaccharides and proteins.

AFM images of the fusiforms (Fig. 3A–C) revealed elongated cell shapes, with a length of 20–30 μm and a diameter of 1–3 μm. The girdle region resulting from the valve overlapping could be resolved (Fig. 3B). High resolution images (Fig. 3C)

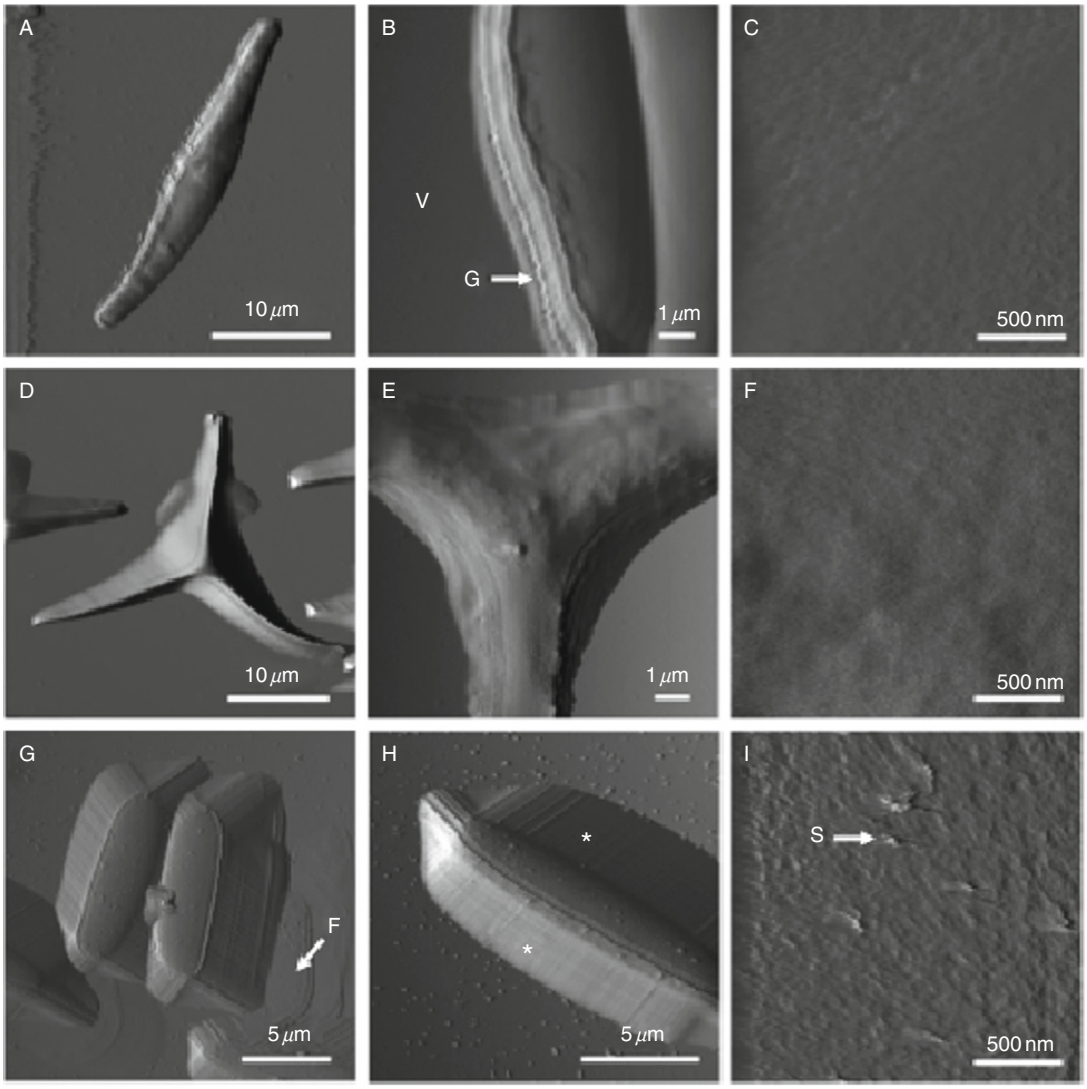

Fig. 3 AFM deflection images recorded in aqueous solution for the fusiform (A–C), triradiate (D–F) and ovoid (G–I) morphotypes of *Phaeodactylum tricornutum*. Labels V, G, F, S correspond to the following features: valve, girdle region, footprint, and streaks. The features highlighted by the asterisks in (H) reflect tip convolution artifacts. Reproduced with permission from ''Francius, G., Tesson, B., Dague, E., Martin-Jézéquel, V., Dufrêne, Y. F. (2008). Nanostructure and nanomechnaics of live *Phaeodactylum tricornutum* morphotypes. *Environ. Microbiol.* **10,** 1344–1356.

revealed that the valve surface was nonstructured and very smooth. Triradiate cells were composed of three arms (15–20 μm) emerging from a central core and forming a star (Fig. 3D–F). High resolution AFM images of this morphotype

(Fig. 3F) were very similar to those of the fusiform, that is, they showed a very smooth, nonstructured morphology. By contrast, ovoid cells were 2–3 times smaller (10–12 μm in length) than the two other morphotypes (Fig. 3G–I), and showed a rougher surface with streaks in the scanning direction, presumably reflecting the presence of excreted polymers involved in adhesion and gliding motility (Chiovitti *et al.*, 2003; Dugdale *et al.*, 2006; Iwasa *et al.*, 1971). Consistent with this notion, polymer footprints about 200 nm thick were seen in the vicinity of some ovoid diatoms (Fig. 3G). These data indicates that AFM is a promising technique to gain insight into the mechanisms leading to the various *Phaeodactylum* morphotypes.

V. Nanoscale Elasticity Measurements

Besides being used as a microscope, AFM can also measure interaction forces, a mode known as force spectroscopy (Butt *et al.*, 2005; Gaboriaud and Dufrêne, 2007). Here, the cantilever deflection is recorded as a function of the vertical displacement of the piezoelectric scanner, that is, as the sample is pushed towards the tip and retracted. Raw curves consist of a voltage measured on the photodetector as a function of the vertical piezo displacement at a given x, y location. Using the slope of the retraction force curve in the region where probe and sample are in contact, the photodiode voltage can be converted into a cantilever deflection (d). The cantilever deflection is then converted into a force (F) using Hooke's law: $F = -kd$, where k is the cantilever spring constant. The zero separation distance corresponding to the contact point between the tip and the sample is positioned at the snap-on attractive instability of the cantilever, that is, the onset of the vertical linear parts. In the case of a stiff surface as discussed so far, the photodetector sensitivity and the contact point are easily defined onto the raw curves.

The resulting force versus displacement curves, as illustrated in Fig. 4, provide a wealth of information on surface forces, mechanical properties, and adhesion properties resulting from the interactions between the AFM tip and the surface. When the tip is lowered towards the surface of the sample (label "A"), a negative deformation of the cantilever (cantilever bends downwards) is produced due to attractive van der Waals interactions (B). Upon contact between the tip and the sample, a deformation of the cantilever is observed (C), which may provide direct information on the mechanical properties of the sample. When the tip is withdrawn from the sample (D), the curve often shows a hysteresis referred to as the adhesion "pull-off" force, which depends on the area, time of contact, and on the surface energy between the tip and the sample (E). Force curves can be recorded either at single, well-defined locations of the (x, y) plane or at multiple locations to yield a so-called "force–volume image." In doing so, spatially resolved maps of sample properties and molecular interactions forces can be produced.

Most microbiological cells are fairly soft and can be significantly deformed by the tip. By subtracting the approach curves obtained for a soft sample (Fig. 4C) and for a rigid reference material (Fig. 4B), it is possible to generate a so-called

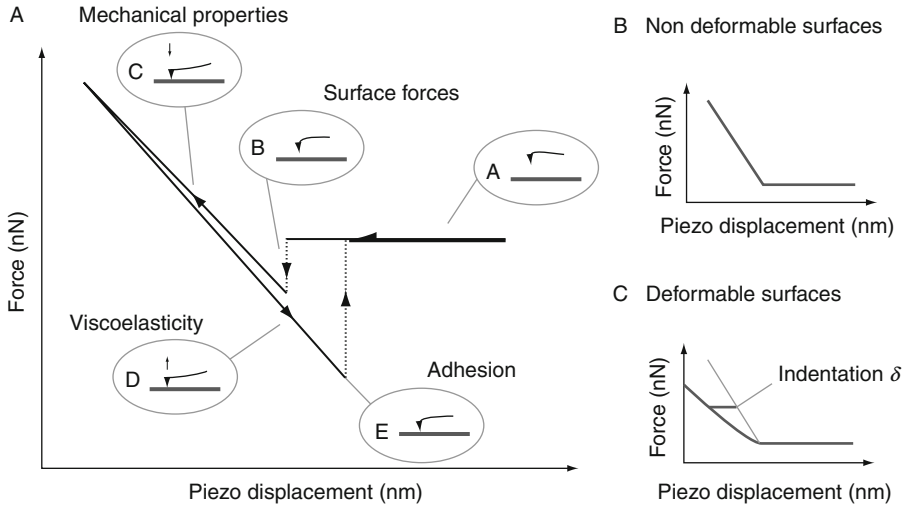

Fig. 4 Principle of elasticity measurements. (A) Typical force curve with attractive forces between the AFM tip and the sample. (B, C) Typical approach force curves for non deformable (B) and deformable (C) samples in the absence of surface forces. Reproduced with permission from "Gaboriaud, F., and Dufrêne, Y. F. (2007). Atomic force microscopy of microbial cells: Application to nanomechanical properties, surface forces and molecular recognition forces. *Colloids and Surfaces B: Biointerfaces* **54,** 10–19.

"force-indentation" curve, the shape of which provides direct information on the sample elastic properties (Burnham and Colton, 1989; Weisenhorn *et al.*, 1993). A widely used model for quantifying such properties is the Hertz model, which for a paraboloid tip versus flat-cell geometry, is given by:

$$F = \frac{4E\sqrt{a}}{3(1-\mu^2)}\delta^{3/2} \quad (1)$$

where μ being the Poisson's ratio, E the Young's modulus and, δ the indentation depth.

During the past years, this method has been widely used to assess the local elasticity of live cells, including animal cells (Matzke *et al.*, 2001), bacteria (Gaboriaud *et al.*, 2005), yeast (Touhami *et al.*, 2003), and diatoms (Francius *et al.*, 2008; Higgins *et al.*, 2003a,b; Losic *et al.*, 2007). By way of an example, the elasticity of the siliceous cell walls of *Navicula pelliculosa* were found to be similar to those of known silicas, the elastic modulus varying from a few to hundreds GPa depending on the location (Almqvist *et al.*, 2001). Similar data were collected for *Coscinodiscus Granii* and *Coscinodiscus sp.* diatoms, and attributed to variations in the biomineralization and porosity of the cell wall (Almqvist *et al.*, 2001; Losic *et al.*, 2007). The elastic modulus of soft extracellular polymeric substances (mucilage layers) has also been measured and found to vary from 250 to

750 kPa, depending on the diatom species and on the region investigated, and was thus much lower than the siliceous cell walls (Higgins *et al.*, 2003a,b).

AFM-based nano-indentation measurements were recently applied to the *P. tricornutum* morphotypes (Francius *et al.*, 2008), with the aim to answer the following questions: does the cell wall elasticity of the morphotypes compare with those of classical siliceous diatoms; does it vary from morphotype to morphotype, and from one morphotype location to another? Force–volume images consisting of arrays of 32 by 32 force curves were recorded across the three morphotypes (Fig. 5). The curves were converted into force-indentation curves and then analyzed using the Hertz theory to generate elasticity maps (Fig. 5A, C, and E) and elasticity histograms (Fig. 5B, D, and F). The marked elasticity contrast in the maps demonstrates that the cells are substantially softer (darker, Young's modulus 80–500 kPa) than the supporting polymer membrane (brighter, Young's modulus ~1 MPa). Force-indentation curves recorded on the fusiform valve surface were well-fitted with the Hertz model, yielding an average Young's modulus of 81 ± 8 kPa that was homogeneously distributed across the surface. These values, much smaller than the GPa values reported for the walls of siliceous diatoms (Almqvist *et al.*, 2001; Losic *et al.*, 2007), indicate that cell walls of *Phaeodactylum* fusiform specimens are poor in silica. Similar conclusions were drawn for triradiate cells, whose average Young's modulus was 102 ± 40 kPa. By contrast, the Young's modulus of the ovoid valve was 501 ± 122 kPa, which is about five times larger that of the fusiform and triradiate values. This larger stiffness is likely to reflect stronger silicification of the cell wall.

Notably, AFM can resolve nanoscale variations of elasticity across single cells. For instance, the valve/girdle interface of the fusiform cells showed heterogeneous elasticity contrast (Fig. 6), the average Young's modulus being 78 ± 14 kPa and 32 ± 13 kPa on the valve and girdle region, respectively. This finding indicates that the girdle region is substantially softer than the valve, a behavior which may reflect the existence of soft organic zones separating the silica bands (Borowitzka *et al.*, 1978). Also, triradiate arms were softer (46.5 ± 5.0 kPa) than the core region (102 ± 40 kPa), a finding that may reflect differences in cell wall thickness since arms are newly formed upon transformation from the ovoïd to the fusiform morphotype. Another possible explanation could be that cell organelles are essentially localized in this central part of the cell, distal ends being occupied by large vacuoles (Borowitzka *et al.*, 1978). For ovoid cells, the girdle region was softer (79 ± 20 kPa) than the valve (316 ± 104 kPa), suggesting that the girdle is poorer in silica. Moreover, Young's modulus values of 100 ± 21 kPa were obtained for the polymer footprints (Fig. 3G), which are much smaller than the valve values. Such mucilaginous footprints, observed only for the ovoid form, are likely to reflect the secretion of extracellular polymers involved adhesion and motility.

In summary, the fusiform, triradiate, and ovoid morphotypes of *P. tricornutum* showed major differences in surface ultrastructure and mechanical properties. While fusiform and triradiate forms were smooth and nonstructured, the ovoid surface was coated with extracellular polymers possibly involved in adhesion and gliding motility. The cell wall of the silicified ovoid form was about five times stiffer

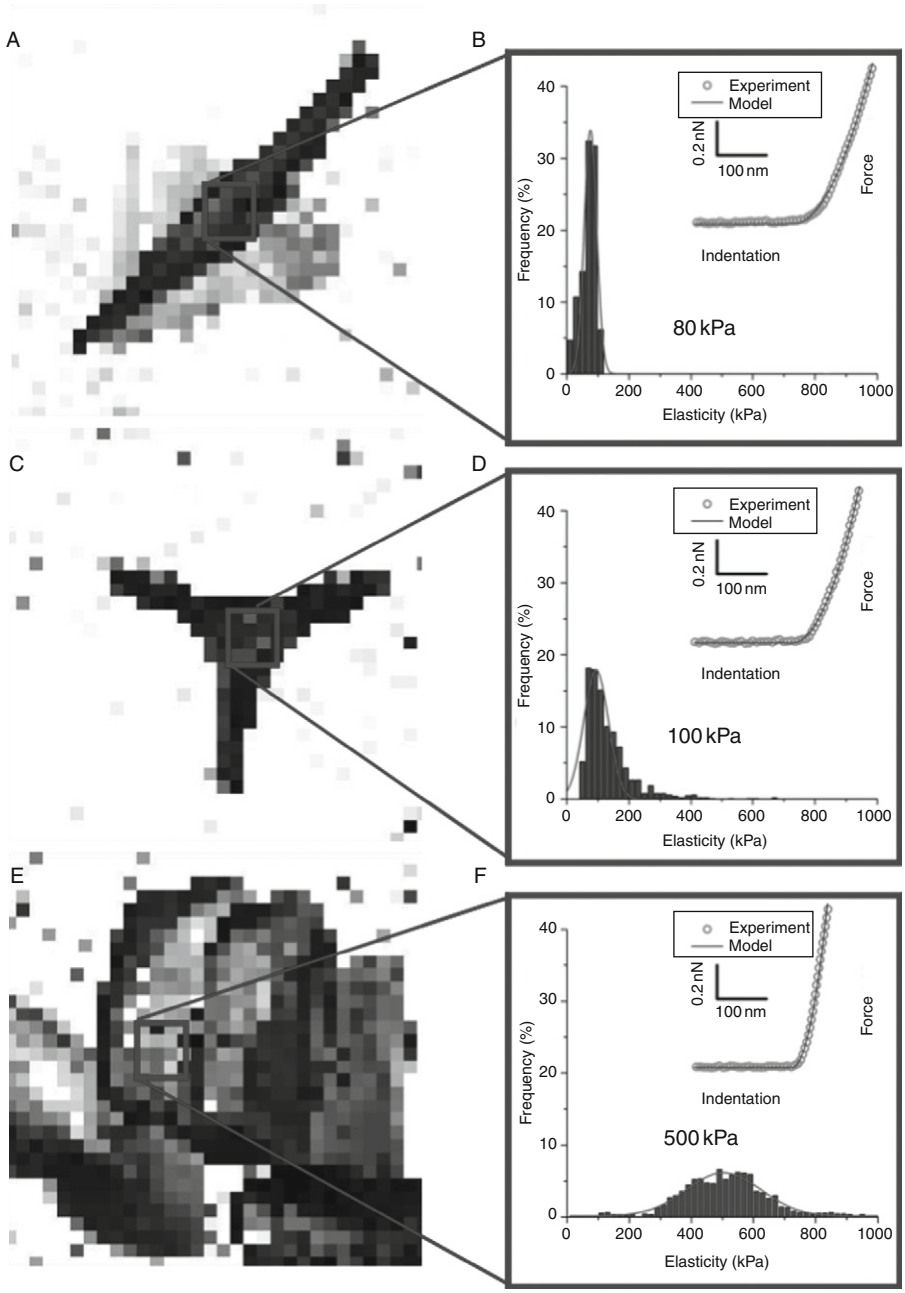

Fig. 5 Elasticity of the *Phaeodactylum tricornutum* morphotypes (A, C, E) Elasticity maps (A and C *z*-range = 700 kPa; E, *z*-range = 1000 kPa) and (B, D, F) distribution of elasticity values ($n = 1024$ force curves) together with representative force-indentation curves recorded on the fusiform (A, B), triradiate (C, D) and ovoid (E, F) morphotypes. Reproduced with permission from ''Francius, G., Tesson, B., Dague, E., Martin-Jézéquel, V., and Dufrêne, Y. F. (2008). Nanostructure and nanomechnaics of live *Phaeodactylum tricornutum* morphotypes. *Environ. Microbiol.* **10,** 1344–1356.

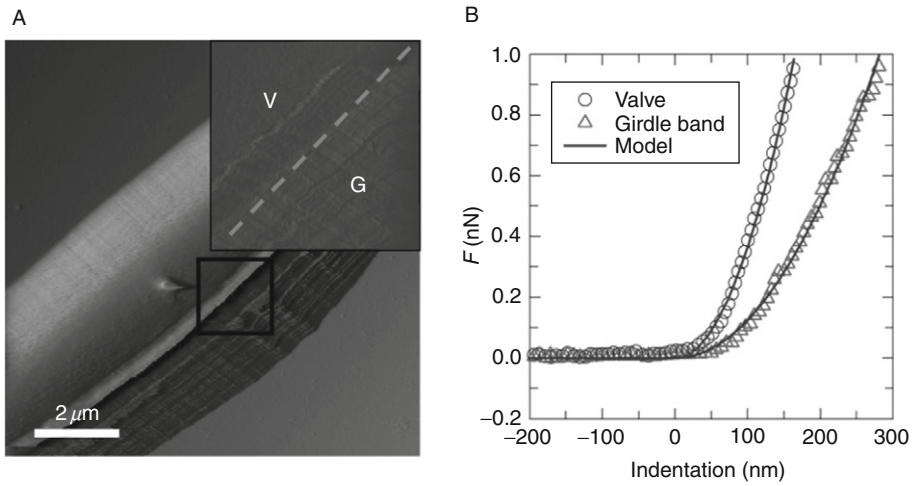

Fig. 6 Resolving nanoscale variations of elasticity. (A) deflection image of the fusiform girdle (G)/vale (V) interface (red line indicates the interface). (B) typical force-indentation curves for the two regions (representative from a total of 1024 force curves). Reproduced with permission from "Francius, G., Tesson, B., Dague, E., Martin-Jézéquel, V., and Dufrêne, Y. F. (2008). Nanostructure and nanomechnaics of live *Phaeodactylum tricornutum* morphotypes. *Environ. Microbiol.* **10,** 1344–1356.

than that of the two nonsilicified forms. The cell wall elasticity showed major variations depending on the location: the girdle region of both fusiform and ovoid forms was five times softer than the valve, the arms of the triradiate form was softer than the core region, and the mucilaginous footprints of the ovoid form showed only moderate stiffness, compared to the valve. Accordingly, these data demonstrate the power of AFM to resolve nanoscale variations of elasticity on intact diatoms. In future, these nanoscale analyses should help understanding the structure–function relationships of the diatom cell walls, particularly the mechanisms of silicification under various environmental conditions (light intensity, nutrient availability).

VI. Examination of Diatom Valves

Earlier, we described the initial stages in formation of the valve in *T. pseudonana* that involved branching ribs that originate from a central point and fuse to form the basal layer that will be the proximal (inner) valve surface. This is followed by *z*-axis growth in the center and periphery of the valve that eventually forms the distal (outer) valve surface. When imaged by SEM, the proximal valve surface appeared to be smooth (Fig. 7A) while the distal valve surface was covered with ridged filaments that appear to radiate outward from the center and interconnected by cross members (Fig. 7B). AFM images confirmed that the proximal valve

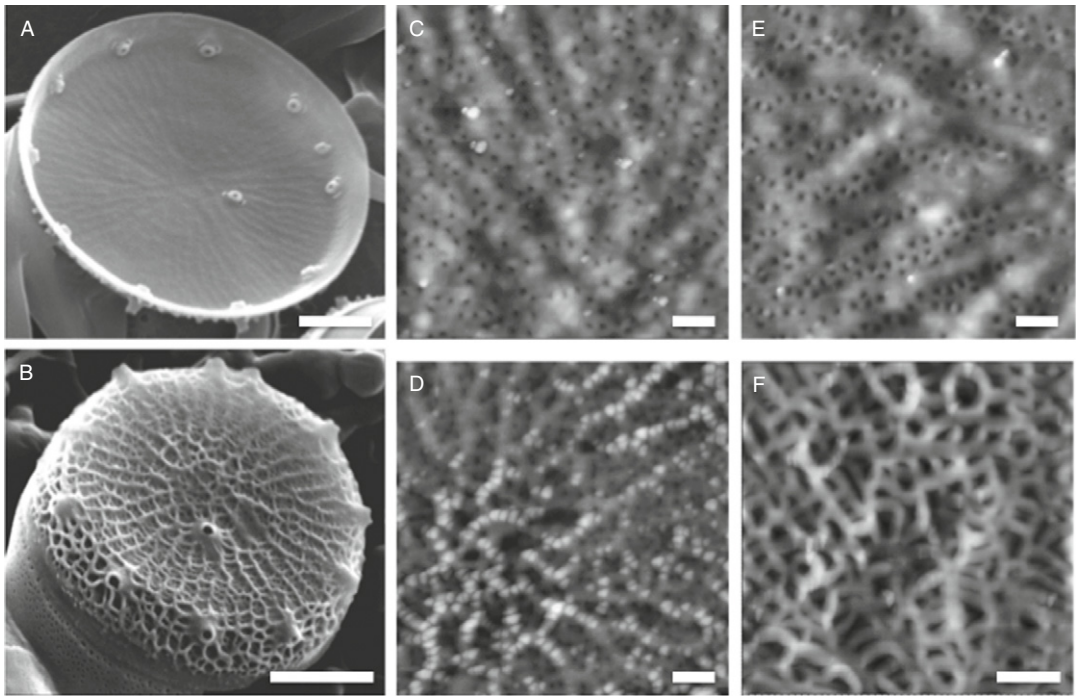

Fig. 7 The AFM reveals nanoscale features on different valve faces of *Thalassiosira pseudonana*. (A) SEM image showing the branched rib structure of the proximal (inner) valve surface (scale bar 1 μm). (B) SEM image of the developing ribs on the *T. pseudonana* distal (outer) valve surface showing their flattened nature (scale bar 1μm). (C) AFM image of the smooth proximal valve surface in *T. pseudonana*, note the pits or holes that are 30 nm in diameter (Scale bar 200 nm). (D) AFM image of the *T. pseudonana* distal valve surface showing 50 nm spherical silica nodules topping the ridged structure (scale bar 200 nm). (E–F) AFM images of the proximal and distal valve surfaces of *T. weissflogii*. The proximal valve surface (E) is smooth, similar to *T. pseudonana* with pits or holes of 30–50 nm in diameter (scale bar 200 nm). The AFM image of the distal valve surface (F) of *T. weissflogii*. shows intricate smooth tubular structure (scale bar 500 nm).

surface was relatively smooth but there was a discernable height difference between the top of a rib and the valley between the adjacent ribs of less than 10 nm (Fig. 7C). AFM images of the distal valve surface revealed that the ridges, observed by SEM that appeared to be solid, were in reality composed of 50 nm silica spheres that were partly fused to compose a ridged structure (Fig. 7D). We also found examples where the particles were absent or sparse perhaps indicating that the "spatial cementing" process is either not always reliable, is a lengthy process, or we were finding examples of immature structures indicating that variables exist in the *z*-axis expansion process, which is perhaps suggestive of a lack of highly organized organic component. AFM examination of another *Thalassiosira* species, *T. weissflogii* also showed a conserved proximal valve surface (Fig. 7E), but with

ribs 47% wider than those observed in *T. pseudonana* but with an identical center to center rib spacing and comparable rib height. If we assume that rib spacing in these two diatom species is mediated by an organic template then the differences observed in the width of the ribs might be explained either by width differences in the two templates or by a different chemical environment in the two species that influences silica polymerization. Nevertheless, the patterning of the ribs, rib heights, and spacing between the ribs would indicate a similar conserved mesoscale formation of the basal valve surface in these two *Thalassiosira* species. However, the distal valve surface in *T. weissflogii* reveals a very different surface than what we observed in *T. pseudonana.* Instead of having a ridged structure of fused spherical silica nodules, as was found in *pseudonana,* a latticework of interconnected tubular silica structure was found to define *weissflogii* distal valve structure (Fig. 7F). The observed differences in the distal valve surface observed between *T. pseudonana* and *T. weissflogii* suggest that a divergent mechanism is involved in *z*-axis expansion between the two species.

In centric diatoms, initial valve formation is commonly initiated by the deposition of linear ribs that radiate out from the center (Pickett-Heaps *et al*., 1990; Round *et al*., 1990). This is also true in bilateral symmetric pennate diatoms where initial deposition of linear structures is present in valve formation (Chiappino ML *et al*., 1977; Pickett-Heaps *et al*., 1990; Round *et al*., 1990). Although the basic ribbed structure of centric diatoms appears to be conserved, that being a reasonably flat ribbed structure radiating out from the center, there are differences in the nanoscale structure. In the diatom *Ditylum brightwellii*, there is much less fusion between ribs (Fig. 8A) and along the long axis of individual ribs. High-resolution AFM images (Fig. 8B arrows) show what appears to be a fusion of silica particles that create a sequential series of bumps along the surface of the ribs. This is in

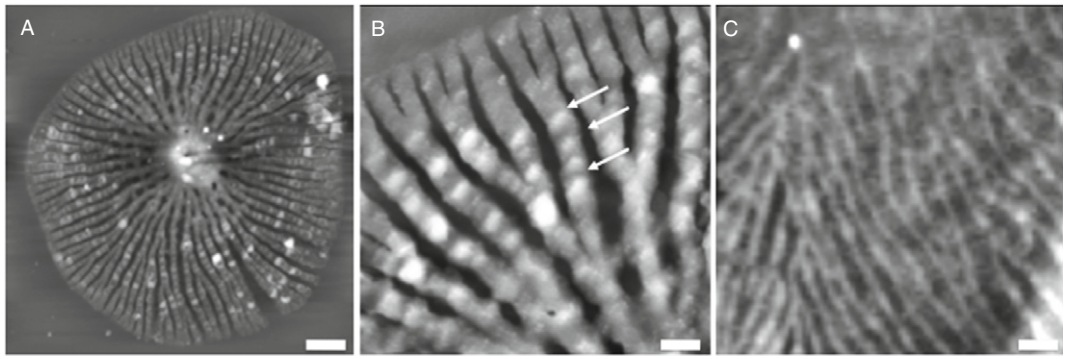

Fig. 8 AFM image of the radial branched silica ribs in *Ditylum brightwellii*. (A) In the forming valve of *D. brightwellii* the ribs appear to be branched with no particular pattern (scale bar 2 μm). (B) A high-resolution AFM image of the ribs shows repeating nanoscale nodules of silica (arrows) along the long axis of the ribs (500 nm). (C) The AFM image of the branched rib structure in the *Chaetoceros laciniosis* shows an absence of particulate nanoscale structure (scale bar 500 nm).

marked contrast to what we observed in *T. pseudonana* and *T. weissflogii*, where the ribs were smooth, similar to what we found in *D. brightwellii*, another centric diatom (Fig. 8C) that we imaged. Our work with centric diatom valves suggests a similar mesoscale rib structure forms in the basal layer but there are different nanoscale polymerization factors that contribute to differences that we observed in the diatom species we examined.

VII. Examination of Diatom Girdle Bands

As we have already described, girdle bands are continuous or overlapping siliceous strips that encircle the two thecae forming the sides of the diatom (Fig. 2). Most commonly, girdle bands are split rings but there are also girdle bands that are continuous and encircle the cell and some that are scale-like structures (Round *et al.*, 1990). Girdle bands also overlap each other starting with the band that is overlapped by the valve and continuing to overlap successive girdle bands away from the valve. Although the girdle bands are less ornate than valves they still have structure that appears to be species dependent and perhaps can offer useful information regarding their fabrication within the SDV. It is known that the girdle bands like valves are synthesized within a SDV (Kröger and Wetherbee, 2000b; Pickett-Heaps *et al.*, 1990). However, little is known about how they are formed or about differences between valve and girdle band SDVs. Because girdle bands are thin, they are relatively transparent to electrons and are difficult to image with the electron microscope. Fortunately, imaging with AFM is not a problem and high-resolution imaging with this instrument is a good place to start in our efforts to understand the mechanisms behind the formation of girdle bands.

The scale-like girdle bands of *D. brightwellii* show features spanning the nano, meso, and microscale (Fig. 9A). A filamentous outline that defines the ligula, clearly seen in the AFM image, must be due to some property(s) that define the SDV circumference. Mesoscale features seen in the image are the regular striated structures and the holes between the striated structures. These holes, or pores, seem to be regular but upon close examination they are not exactly placed at a defined distance from one another. The opposite side of the *D. brightwelli* girdle band (Fig. 9B) appears to be composed of nanoscale silica nodules that appear ordered in an alignment with the striated structures on the opposite side. From previous SEM examination of the girdle band morphology in *T. pseudonana* (Hildebrand *et al.*, 2006, 2008), that has similar features to *D. brightwellii*, we assume the proximal surface of the girdle band exhibits the striated structure while the distal surface is composed of the nanoscale silica nodules. Based on the formation of an initial linearly arranged base layer in valves, followed by diverse structures during *z*-axis (including nodules of silica) in various diatom species, we assume that the striated surface of *D. brightwellii* girdle bands is the proximal surface, while the distal surface is composed of the nanoscale silica nodules. Currently, we are designing an experiment using both AFM and field emission STM to answer this question.

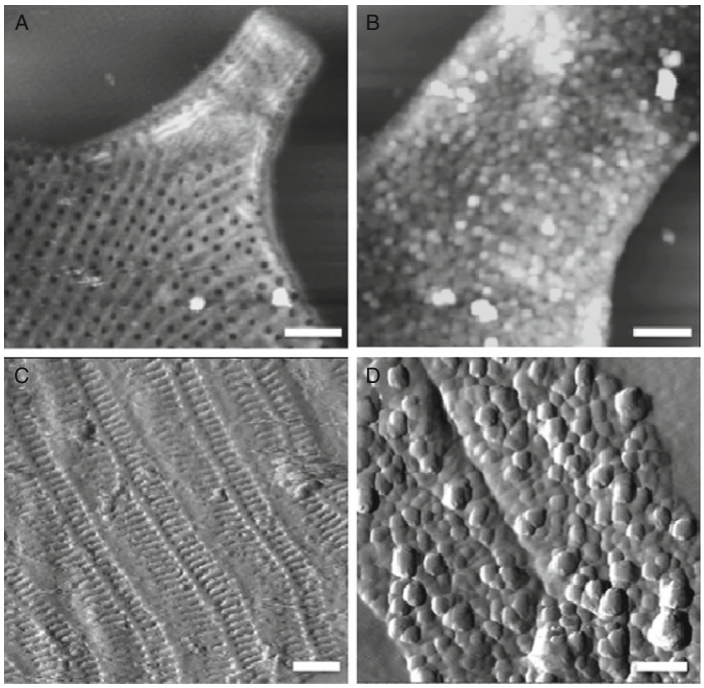

Fig. 9 AFM images of *Ditylum brightwellii* resolve micro-, meso-, and nanoscal structure. (A) The proximal surface of *D. brightwellii* girdle band exhibits microscale molding around the ligula, bordered by filamentous silica, with mesoscale striations in girdle band body (scale bar 1 μm). (B) AFM imaging of the distal girdle band surface shows the presence of particulate nanoscale silica morphology (scale bar 1 μm). (C) A series of overlapping girdle bands with striated structure define the proximal surface of the girdle band (scale bar 500 nm). The AFM image of the *S. costatum* distal girdle band surface indicates a disordered particulate nanoscale silica structure.

In the AFM image of girdle bands in the diatom *Skeletonema costatum* (Fig. 9C), on what we assume to be the proximal surface, a series of striated structure is evident. Where the girdle bands overlap, the material flattens becoming smooth silica without striations. There is also a filament or ridge of silica, perpendicular to the striations that run the length of the girdle band. In a previous study on *T. pseudonana,* we also observed areas of smooth silica between adjacent girdle bands (Hildebrand *et al.*, 2006) and in other studies this feature has also been reported suggesting that inhibition of the SDV may be involved in their formation (Davis and Hildebrand, 2007; Hildebrand, 2003). On the presumed distal face of the *S. costatum* girdle band (Fig. 9D), the nanoparticles of silica do not appear to have a defined size or to be arranged in any particular order. More AFM studies of girdle bands should prove fruitful toward understanding their formation. Comparisons of similarities and differences in mesoscale formation between valves and girdle bands should further contribute to our understanding of the biomineralization process.

VIII. Examination of Diatom Setae

Some diatom species fabricate hollow tubular structures that radiate out from the body of the valve and in the genus *Chaetoceros* they serve as a diagnostic feature of the species (Evensen and Hasle, 1975; Fryxell, 1978; Rogerson *et al.*, 1986). Compared to the dimensions of the cell, the setae can be quite long. For example, the *C. gracilis* frustule is roughly 4 × 6 μm, but at the four corners of the frustule there is a setae that can be as long as 40 μm (Rogerson *et al.*, 1986). In cross section, depending on the species, the setae can be square, triangular, circular, or even polygonal (Evensen and Hasle, 1975). Quite often along the length of the setae are small spines that protrude from the surface and may have a regular arrangement.

AFM examination of the setae of *C. gracilis* reveals a circular tubular structure that is approximately 300 nm in diameter. Along the length of the setae, the spines are arranged in a right-handed helical repeat moving toward the tip that (Fig. 10A) appears to have a periodicity of about 32°. Toward the end of the tip, setae are flattened and consist of several components including longitudinal ribs that terminate in what we believe will eventually be spines (Fig. 10A). The distal end of the setae is quite obviously immature and has not yet rotated in the right-handed twist to form a tubular structure. When the structure on the tip is imaged at high-resolution, it can be clearly seen that the longitudinal ribs are composed of nanoscale silica nodules of uniform size (Fig. 10B) suggesting that a regulatory template is involved within the SDV that forms the setae. Images of *C. diversum* and *C. laciniosis* clearly show species-specific differences that appear in the right handed helical twist. In Fig. 10C, the twist in *C. diversum* is only slightly greater than in *C. gracilis* but the spines are different and the repeating subunit structure is more complex. In *C. laciniosis* (Fig. 10D), the twist is at 33.5° and the surface structure is also distinct when compared to the other two species. AFM images showing the nanoscale complexity of the growing ends of *C. diversum* (Fig. 10E) and *C. laciniosis* (Fig. 10F) clearly can be used to differentiate between the two species and also are markedly different then the high-resolution image of the distal end of *C. gracilis* (Fig. 10B).

Our observations on the three *Chaetoceros* species indicate that the setae are formed from nanoscale nodules of silica that are incorporated into longitudinal ribs that are further assembled into a tubular unit through a species-specific helical twist. Very likely, the uniform size of the nanoscale nodules incorporated into the longitudinal ribs along with the helical twist contributes to the species-specific differences that we observed. Previous TEM investigations of setae formation in *C. peruvianis* revealed that "finger like" projections of silica first formed followed by lateral connections (Pickett-Heaps *et al.*, 1994). This is similar to what we observed by AFM where the longitudinal ribs formed followed by lateral connection between the ribs (Fig. 10B). The TEM study also revealed that an organic material was involved in connecting ribs (Pickett-Heaps *et al.*, 1994). If we assume

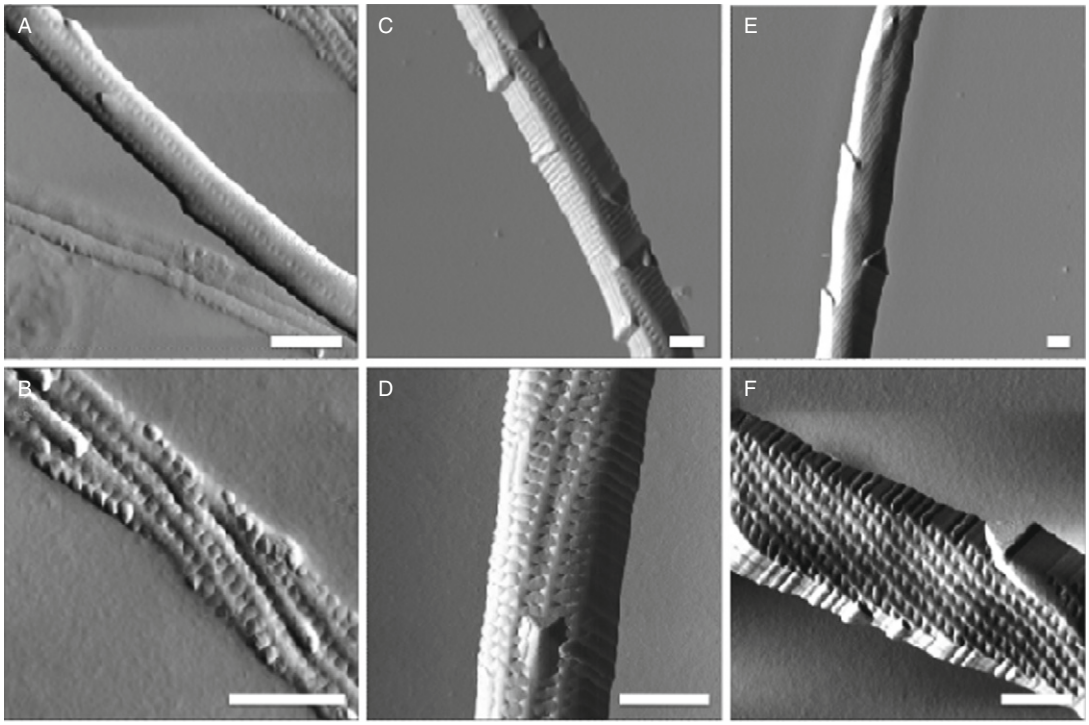

Fig. 10 AFM images of the setae of (A–B) of *Chaetoceros gracilis*, (C–D) *C. diversum*, (E–F) *C. laciniosis*. The lower resolution images of the three species all show somewhat different morphology in the spines radiating off the surface of the setae and a hint of differences in morphology along the long axis of the setae. At higher resolution nanoscale silica structures show clear morphological differences between the three species (scale bar 500 nm).

that this is also the process that occurs in the formation of *C. gracilis* setae, then the acid cleaning of our preparations might remove some of the organic material that would explain gaps between the ribs in our AFM images (Fig. 10B).

IX. Future Directions

What we hope to have demonstrated in this effort is that high-resolution imaging techniques can establish a baseline for investigating biomineralization in diatoms that ultimately may impact our device manufacturing capabilities. Diatoms are an optimal candidate organism for this purpose, chosen because they create an almost limitless number of ornate skeletal structures, have features that span length scales from nano-microscale, and they are easily grown in the laboratory. AFM is the primary tool that we have elected to use in this study since its ability to identify surface topography exceeds SEM and TEM. This is evidenced by the distinct

morphologies that have been identified on the distal and proximal valve surface of *T. pseudonana.* On the distal surface, nanoscale nodules of silica constitute the rib structure and on the proximal valve surface ridges in the base layer were clearly seen, while not evident when imaged by high-resolution SEM due to lack of height information. We have also pointed out in this study that the sensitivity of the AFM cantilever can be used to identify surface compliance in intact diatoms and that this could also be used in like fashion on developing silica features. In this study, just a few diatom species were imaged to gain the information that we have presented and we recognized that more should be done before firm conclusions can be drawn.

Great advances have been made in all areas of science that can facilitate our understanding of biomineralization in diatoms. The genome sequences of two diatom species, *T. pseudonana* (Armbrust *et al.*, 2004) and *P. tricornutum* (http://genome.igi-psf.org/Phatr2/Phatr2.home.html), have been sequenced and others are in the pipeline to be sequenced. Using this information can we, through proteomics, identify the proteins involved in fabrication of diatom skeleton features? Can recognition agents to these proteins involved in the fabrication process, attached to AFM cantilever tips, be used to identify their expression spatially that will eventually allow our building platforms for duplicating structures? Molecular engineering has given us the ability to insert genes from one organism to another; can we customize diatoms to directly produce objects for our use? Magnetotactic bacteria synthesize magnetite and *Pseudomonas stutzeri* has been shown to synthesize silver-based particles (Sarikaya, 1999). Although our current understanding of protein binding chemistries is not yet sufficient to design proteins (Schonbrun and Sarikaya, 2002), using phage display and cell-surface display technology, peptides can be identified for their ability to bind inorganic materials including the noble metals, many metal oxides, and semiconductors (Sarikaya *et al.*, 2003; Tamerler *et al.*, 2007). Can we apply this knowledge to create platforms for synthetic fabrication? In the future can this knowledge be translated to program diatoms, through genetic engineering, to directly produce components from materials other than silica? The answers to these two questions may significantly change future approaches to manufacturing materials and devices that shape the next 1000 years.

Acknowledgments

DPA and MJD acknowledge the support from the Office of Biological and Environmental Research, US Department of Energy. Oak Ridge National Laboratory is managed by UT-Battelle, LLC, for the US Department of Energy under Contract No. DE-AC05-00OR22725.

YFD: This work was supported by the National Foundation for Scientific Research (FNRS), the Université catholique de Louvain (Fonds Spéciaux de Recherche), the Région wallonne, the Federal Office for Scientific, Technical and Cultural Affairs (Interuniversity Poles of Attraction Programme), and the Research Department of the Communauté française de Belgique (Concerted Research Action). YFD is a Research Associate of the FNRS.

MH: This work was supported by the Air Force Office of Scientific Research Multidisciplinary University Research Initiative Grant RF00965521.

References

Almqvist, N., Delamo, Y., Smith, B. L., Thomson, N. H., Bartholdson, A., Lal, R., Brzezinski, M., and Hansma, P. K. (2001). Micromechanical and structural properties of a pennate diatom investigated by atomic force microscopy. *J. Microsc.* **202,** 518–532.

Armbrust, E., *et al*. (2004). The genome of the diatom *Thalassiosira pseudonana*: Ecology, evolution, and metabolism. *Science* **306,** 79–86.

Autumn, K., and Peattie, A. M. (2003). Mechanisms of adhesion in geckos. *J. Integr. Comp. Biol.* **42,** 1081–1090.

Autumn, K., Sitti, M., Liang, Y. A., Peqattie, A. M., Hanen, W. R., Sponberg, S., Kenny, T. W., Fearing, R., Israelachvili, J. N., and Full, R. J. (2002). Evidence for van der Waals attachment by gecko foot-hairs inspires design of synthetic adhesive. *Proc. Natl. Acad. Sci. USA* **99,** 12252–12256.

Bar-Cohen, Y. (2006). Biomimetics-using nature to inspire human innovation. *Bioinspir. Biomim.* **1,** 1–12.

Bell, A. T. (2003). The impact of nanoscience on heterogeneous catalysis. *Science* **299,** 1688–1691.

Blank, G. S., and Sullivan, C. W. (1983). Diatom mineralization of silicic acid VI. The effects of microtubule inhibitors on silicic acid metabolism in Navicula saprophila. *J. Phycol.* **19,** 39–44.

Borowitzka, M. A., and Volcani, B. E. (1978). The polymeric diatom *Phaeodactylum tricornutum*: Ultrastructure of its morphotypes. *J. Phycol.* **14,** 10–21.

Burnham, N. A., and Colton, R. J. (1989). Measuring the nanomechanical properties and surfaces forces of materials using an atomic force microscope. *J. Vac. Sci. Technol. A* **7,** 2906.

Butt, H. J., Cappella, B., and Kappl, M. (2005). Force measurements with the atomic force microscope: Technique, interpretation and applications. *Surf. Sci.* **59,** 1–152.

Carnes, J., Fernandez-Caldas, E., Marina, A., Alonso, C., Lahoz, C., Colas, C., and Lezaun, A. (2003). Immunochemical characterisation of Russian thistle (*Salsola kali*) pollen extracts. Purification of the allergen Sal k 1. *Allergy* **58,** 1152–1156.

Chan, W. C. W., and Nie, S. (1998). Quantum dot bioconjugates for ultrasensitive nonisotopic detection. *Science* **281,** 2016–2018.

Chiappino, M. L., and Volcani, B. E. (1977). Studies on the biochemistry and fine structure of silica shell formation in diatoms VII Sequential cell wall development in the pennate *Navicula pelliculosa*. *Protoplasma* **93,** 205–221.

Chiovitti, A., Basic, A., Burke, J., and Wetherbee, R. (2003). Heterogenous xylose rich glycans are associated with extracellular glycoproteins from the biofouling diatom *Craspedostauros australis* (Bacillariophyceae). *Eur. J. Phycol.* **38,** 351–360.

Cohn, S. A., Nash, J., and Pickett-Heaps, J. D. (1989). The effect of drugs on diatom valve morphogenesis. *Protoplasma* **149,** 130–143.

Crawford, S. A., Higgins, M. J., Mulvaney, P., and Wetherbee, R. (2001). Nanostructure of the diatom frustule as revealed by atomic force and scanning electron microscopy. *J. Phycol.* **37,** 543–554.

Dagata, J., Schneir, J., Harary, H. H., Evans, C. J., Postek, M. T., and Bennett, J. (1990). Modification of hydrogen-passivated silicon by a scanning tunneling microscope operating in air. *Appl. Phys. Lett.* **56,** 2001–2003.

Davis, A. K., and Hildebrand, M. (2007). Molecular Processes of Biosilicification in Diatoms. *In* "Metal Ions in Life Sciences, Volume 4 Biomineralization, From Nature to Application," (H. Sigel and A. Sigel, eds.), Wiley, London, pp. 255–294.

Day, H. C., and Allee, D. R. (1993). Selective area oxidation of silicon with a scanning force microscope. *Appl. Phys. Lett.* **62,** 2691–2693.

Doktycz, M. J., Sullivan, C. J., Hoyt, P. R., Pelletier, D. A., Wu, S., and Allison, D. P. (2003). AFM imaging of bacteria in liquid media immobilized on gelatin coated mica surfaces. *Ultramicroscopy* **97,** 209–216.

Drum, R. W., and Pankratz, H. S. (1964). Post mitotic fine structure of *Gomphonema parvulum*. *J. Ultrastruct. Res.* **10,** 217–223.

Dugdale, T. M., Willis, A., and Wetherbee, R. (2006). Adhesive modular proteins occur in the extracellular mucilage of the motile, pennate diatom *Phaeodactylum tricornutum*. *Biophys. J.* **90,** L58–L60.

Dufrêne, Y. F. (2004). Using nanotechniques to explore microbial surfaces. *Nat. Rev. Microbiol.* **2,** 451–460.

Dufrêne, Y. F. (2008a). Towards nanomicrobiology using atomic force microscopy. *Nat. Rev. Microbiol.* **6**(9), 674–680.

Dufrêne, Y. F. (2008b). Atomic force microscopy and chemical force microscopy of microbial cells. *Nat. Protoc.* **3**(7), 1132–1138.

Evensen, D. L., and Hasle, G. R. (1975). The morphology of some *Chaetoceros* species as seen in the electron microscopes. *Nova Hedw Beihefte* **53,** 153–184.

Field, C. B., Behrenfeld, M. J., Randerson, J. T., and Falkowski, P. (1998). Primary production of the biosphere: Integrating terrestrial and oceanic components. *Science* **28,** 237–240.

Francius, G., Tesson, B., Dague, E., Martin-Jézéquel, V., and Dufrêne, Y. F. (2008). Nanostructure and nanomechnaics of live *Phaeodactylum tricornutum* morphotypes. *Environ. Microbiol.* **10,** 1344–1356.

Fryxell, G. A. (1978). Chain-forming diatoms: Three species of *Chaetoceros*. *J. Phycol.* **14,** 62–71.

Gaboriaud, F., Bailet, S., Dague, E., and Jorand, F. (2005). Surface structure and nanomechanical properties of *Shewanella putrefaciens* bacteria at two pH values (4 and 10) determined by atomic force microscopy. *J. Bacteriol.* **187,** 3864–3868.

Gaboriaud, F., and Dufrêne, Y. F. (2007). Atomic force microscopy of microbial cells: Application to nanomechanical properties, surface forces and molecular recognition forces, colloids and surfaces B. *Biointerfaces* **54,** 10–19.

Garcia, R., Martinez, R. V., and Martinez, J. (2006). Nano-chemistry and scanning probe nanolithographies. *Chem. Soc. Rev.* **35,** 29–38.

Gates, B. D., Xu, Q., Love, J. C., Wolfe, D. B., and Whitesides, G. M. (2004). Unconventional nanofabrication. *Ann. Rev. Mater. Res.* **34,** 339–372.

Gebeshuber, I. C., Kindt, J. H., Thompson, J. B., Delamo, Y., Stachelberger, H., Brzezinski, M. A., Stucky, G. D., Morse, D. E., and Hansma, P. K. (2003). Atomic force microscopy of living diatoms in ambient conditions. *J. Microsc.* **212,** 292–299.

Gordon, R., and Drum, R. W. (1994). The chemical basis of diatom morphogenesis. *Int. Rev. Cytol.* **150,** 243–372.

Hecky, R. E., Mopper, K., Kilham, P., and Degens, E. T. (1973). The amino acid and sugar composition of diatom cell walls. *Mar. Biol.* **19,** 323–331.

Hesselberg, T. (2007). Biomimetics and the case of the remarkable ragworm. *Natursissenschaften* **94,** 613–621.

Higgins, M. J., Molino, P., Mulvaney, P., and Wetherbee, R. (2003a). The structure and nanomechanical properties of the adhesive mucilage that mediates diatom-substratum adhesion and motility. *J. Phycol.* **39,** 1181–1193.

Higgins, M. J., Sader, J. E., Mulvaney, P., and Wetherbee, R. (2003b). Probing the surface of living diatoms with atomic force microscopy: The nanostructure and nanomechanical properties of the mucilage layer. *J. Phycol.* **39,** 722–734.

Hildebrand, M., Dahlin, K., and Volcani, B. E. (1998). Characterization of a silicon transporter gene family in *Cylindrotheca fusiformis*: Sequences, expression analysis, and identification of homologs in other diatoms. *Mol. Gen. Genet.* **260,** 480–486.

Hildebrand, M., Doktycz, M. J., and Allison, D. P. (2008). Application of AFM in understanding biomineral formation in diatoms Pflugers Arch-Eur. *J. Physiol.* **456,** 127–137.

Hildebrand, M., Volcani, B. E., Gassmann, W., and Schroeder, J. I. (1997). A gene family of silicon transporters. *Nature* **385,** 688–689.

Hildebrand, M., and Wetherbee, R. (2003). Components and control of silicification in diatoms. *In* ''Progress in Molecular and Subcellular Biology, Silicon Biomineralization'' (W. E. G. Muller, ed.), pp. 11–57. Springer-Verlag, Heidelberg.

Hildebrand, M., York, E., Kelz, J. I., Davis, A. K., Frigeri, L. G., Allison, D. P., and Doktycz, M. J. (2006). Nano-scale control of silica morphology and three-dimensional structure during diatom cell wall formation. *J. Mater. Res.* **21,** 2689–2698.

Hvolbæk, B., Janssens, T. V. W., Clausen, B. S., Falsig, H., Christensen, C. H., and Nørskov, J. K. (2007). Catalytic activity of Au nanoparticles. *Nanotoday* **2,** 14–18.

Iler, R. K. (1979). "The Chemistry of Silica: Solubility, Polymerization, Colloid and Surface Properties, and Biochemistry." Wiley-Interscience, New York.

Itani, T., Wakamiya, W., Cashmore, J., and Gower, M. (2003). Lithography with high numerical aperature lens for sub-70 nm mode. *Microelectron. Eng.* **67–68,** 39–46.

Iwasa, K., Murakami, S., Shimizu, A., and Imahori, K. (1971). Mechanism of dimorphism and motility of the diatom, *Phaeodactylum tricornutum* Bohlin. *Proc. Int. Seaweed Symp.* **7,** 319–322.

Jaschke, M., and Butt, H. J. (1995). Deposition of organic material by the tip of a scanning force microscope. *Langmuir* **11**(4), 1061–1064.

Kasas, S., and Ikai, A. (1995). A method for anchoring round shaped cells for atomic force microscope imaging. *Biophys. J.* **68,** 1678–1680.

Kooistra, W. H. C. F., and Medlin, L. K. (1996). Evolution of the diatoms (Bacillariophyta): IV. A reconstruction of their age from small subunit rRNA coding regions and the fossil record. *Mol. Phylogenet. Evol.* **6,** 391–407.

Kröger, N., Deutzmann, R., Bergsdorf, C., and Sumper, M. (2000a). Species-specific polyamines from diatoms control silica morphology. *Proc. Natl. Acad. Sci. USA* **97,** 14133–14138.

Kröger, N., Deutzmann, R., and Sumper, M. (1999). Polycationic peptides from diatom biosilica that direct silica nanosphere formation. *Science* **286,** 1129–1132.

Kröger, N., Lorenz, S., Brunner, E., and Sumper, M. (2002b). Self-assembly of highly phosphorylated silaffins and their function in biosilica morphogenesis. *Science* **298,** 584–586.

Kröger, N., and Sumper, M. (2004). The molecular basis of diatom biosilica formation. *In* "Biomineralization: Progress in Biology, Molecular Biology, and Application" (E. Baeuerlein, ed.), pp. 137–158. Wiley-VCH, Weinheim.

Kröger, N., and Wetherbee, R. (2000b). Pleuralins are involved in theca differentiation in the diatom *Cylindrotheca fusiformis*. *Protist* **151,** 263–273.

Lanzetta, M., and Cutkosky, M. R. (2008). Shape deposition manufacturing of biologically inspired hierarchical microstructures. *CIRP Ann. Manuf. Technol.* **57,** 231–234.

Losic, D., Short, K., Mitchell, J. G., Lar, R., and Voelcker, N. H. (2007). AFM nanoindentation of diatom biosilica surfaces. *Langmuir* **23,** 5014–5021.

Mann, D. G. (1999). The species concept in diatoms. *Phycologia* **38,** 437–495.

Matzke, R., Jacobson, K., and Radmacher, M. (2001). Direct, high-resolution measurement of furrow stiffening during division of adherent cells. *Nat. Cell Biol.* **3,** 607.

Muller, B. (2001). Natural formation of nanostructures from fundamentals in metal heteroepitaxy to applications in optics and biomaterials science. *Surf. Rev. Lett.* **8,** 169–228.

Mueller, T. (2008). Biomimetics design by nature. *Natl. Geogr.* **213**(4), 68–91.

Nelson, D. M., Treguer, P., Brzezinski, M. A., and Leynaert, A. (1995). Production and dissolution of biogenic silica in the ocean: Revised global estimates, comparison with regional data and relationship to biogenic sedimentation. *Global Biogeochem. Cycles* **9**(3), 359–372.

Parker, A. R., Hegedus, Z., and Watts, R. A. (1998). Solar-absorber type antireflective in the eye of the Eocene fly. *Proc. R. Soc. B* **265,** 811–815.

Parker, A. R., and Townley, H. E. (2007). Biomimetics of photonic nanostructures. *Nat. Nanotech.* **2,** 353–357.

Pickett-Heaps, J. D., Carpenter, J., and Koutoulis, A. (1994). Valve and seta (spine) morphogenesis in the centric diatom *Chaetoceros-peruvianus brightwell*. *Protoplasma* **181,** 269–282.

Pickett-Heaps, J., Schmid, A. M. M., and Edgar, L. A. (1990). The cell biology of diatom valve formation. *In* "Progress in Phycological Research" (F. E. Round, and D. J. Chapman, eds.), pp. 1–168. Biopress, Bristol.

Piner, R. D., Zhu, J., Xu, F., Hong, S. H., and Mirkin, C. A. (1999). "Dip pen". *Nanolithogr. Sci.* **283,** 661–663.

Poulsen, N., and Kröger, N. (2004). Silica morphogenesis by alternative processing of silaffins in the diatom *Thalassiosira pseudonana*. *J. Biol. Chem.* **279,** 42993–42999.

Raven, J. A., and Waite, A. M. (2004). The evolution of silicification in diatoms: Inescapable sinking and sinking as escape? *New Phytol.* **162,** 45–61.

Reimann, B. E. F., Lewin, J. C., and Volcani, B. E. (1966). Studies on the biochemistry and fine structure of silica shell formation in diatoms. II. The structure of the cell wall of *Navicula pelliculosa* (Breb.). *Hilse. J. Phycol.* **2,** 74–84.

Robinson, D. H., and Sullivan, C. W. (1987). How do diatoms make silicon biominerals? *Tibs* **12,** 151–154.

Rogerson, A., De Freitas, A. S. W., and McInnes, A. G. (1986). Growth rates and ultrastructure of siliceous setae of *Chaetoceros gracilis* (Bacillariophycea). *J. Phycol.* **22,** 56–62.

Round, F. E., Crawford, R. M., and Mann, D. G. (1990). "The Diatoms. Biology and Morphology of the Genera." Cambridge University Press, United Kingdom.

Sanchez, C., Arribart, H., and Guille, M. M. G. (2005). Biomimetism and bioinspiration as tools for the design of innovative materials and systems. *Nat. Mater.* **4,** 277–288.

Sarikaya, M. (1999). Biomimetics: Materials fabrication through biology. *Proc. Natl. Acad. Sci. USA* **96** (25), 14183–14185.

Sarikaya, M., Tamerler, C., Jen, A. K. Y., Schulten, K., and Baneyx, F. (2003). Molecular biomimetics: Nanotechnology through biology. *Nat. Mater.* **2,** 577–585.

Schaer-Zammaretti, P., and Ubbink, J. (2003). The cell wall of lactic acid bacteria: Surface constituents and macromolecular conformations. *Biophys. J.* **85,** 4076–4092.

Schmid, A. M. M. (1990). Valve morphogenesis in diatoms: A pattern-related filamentous system in pennates and the effect of APM, colchicine, and osmotic pressure. *Nova Hedwiga* **33,** 811–847.

Schmid, A. M., Borowitzka, M. A., and Volcani, B. E. (1981). Morphogenesis and biochemistry of diatom cell walls. *In* "Cytomorphogenesis in Plants," (O. Kiermayer, ed.), pp. 63–97. Springer, New York.

Schmid, A. M., and Schulz, D. (1979). Wall morphogenesis in diatoms: Deposition of silica by cytoplasmic vesicles. *Protoplasma* **100,** 267–288.

Schmid, A. M. M., and Volcani, B. E. (1983). Wall morphogenesis in *Coscinodiscus wailesii*. I. Valve morphology and development of its architecture. *J. Phycol.* **19,** 387–402.

Schonbrun, J., Wedemeyer, W. J., and Baker, D. (2002). Protein structure prediction. *Curr. Opin. Struct. Biol.* **12,** 348–354.

Stoddardt, P. R., Cadusch, P. J., Boyce, T. M., Erasmus, R. M., and Comins, J. D. (2006). Optical properties of chitin: Surface-enhanced Raman scattering substrates based on antireflection structures on cicada wings. *Nanotechnology* **17,** 680–686.

Sumper, M. (2002). A phase separation model for the nanopatterning of diatom biosilica. *Science* **295,** 2430–2433.

Sumper, M., and Kroger, N. (2004). Silica formation in diatoms: The function of long-chain polyamines and silaffins. *J. Mater. Chem.* **14,** 2059–2065.

Tamerler, C., and Sarikaya, C. (2007). Molecular biomimetics: Utilizing nature's molecular ways in practical engineering. *Acta Biomater.* **3,** 289–299.

Touhami, A., Nysten, B., and Dufrêne, Y. F. (2003). Nanoscale mapping of the elasticity of microbial cells by atomic force microscopy. *Langmuir* **19,** 4539.

van de Meene, A. M. L., and Pickett-Heaps, J. D. (2002). Valve morphogenesis in the centric diatom *Proboscia alata* Sundstrom. *J. Phycol.* **38,** 351–363.

Vincent, J. F. V. (2005). Selected natural materials in history. *J. Bionic Eng.* **2,** 161–176.

Vincent, J. F. V., Bogatyreva, O. A., Bogatyrev, N. R., Bowyer, A., and Pahl, A. K. (2006). Biomimetics: Its practice and theory. *J. R. Soc. Interface* **3,** 471–482.

Vrieling, E. G., Gieskes, W. W. C., and Beelen, T. P. M. (1999). Silicon deposition in diatoms: Control by the ph inside the silicon deposition vesicle. *J. Phycol.* **35,** 548–559.

Weisenhorn, A., Khorsandi, M., Kasas, S., Gotzos, V., and Butt, H. J. (1993). Deformation and height anomaly of soft surfaces studied with an AFM. *Nanotechnology* **4,** 106.

CHAPTER 5

Quantitative Phase Imaging of Nanoscale Cell Structure and Dynamics

Gabriel Popescu

Quantitative Light Imaging Laboratory
Department of Electrical and Computer Engineering
Beckman Institute for Advanced Science and Technology
University of Illinois at Urbana-Champaign
Urbana, Illinois 61801

Abstract

Quantitative phase imaging (QPI) of live cells has received significant scientific interest over the past decade or so, mainly because it offers structure and dynamics information at the nanometer scale in a completely noninvasive manner. We present recent developments of QPI technology both for full-field and point measurements. Their applications are classified into *static* and *dynamic* according to their temporal selectivity. Several promising prospects are discussed in the summary section.

METHODS IN CELL BIOLOGY, VOL. 90

0091-679X/08 $35.00
DOI: 10.1016/S0091-679X(08)00805-4

I. Introduction and Rationale

Phase contrast (PC) and differential interference contrast (DIC) microscopy have been used extensively to infer morphometric features of live cells without the need for exogenous contrast agents (Stephens and Allan, 2003). These techniques transfer the information encoded in the phase of the imaging field into the intensity distribution of the final image. Thus, the optical phase shift through a given sample can be regarded as a powerful endogenous contrast agent, as it contains information about both the thickness and refractive index of the sample. However, both PC and DIC are *qualitative* in terms of optical path-length measurement, that is, the relationship between the irradiance and phase of the image field is generally nonlinear (Smith, 1955; Zernike, 1955).

Quantifying the optical phase shifts associated with cells gives access to information about morphology and dynamics at the *nanometer scale*. Over the past decade, the development of quantitative phase imaging techniques has received increased scientific interest. The technology can be divided into *single-point* and *full-field* measurements, according to the experimental geometry employed. Several point-measurement techniques have been applied for investigating the structure and dynamics of live cells (Akkin *et al*., 2004; Choma *et al*., 2005; Fang-Yen *et al*., 2004; Joo *et al*., 2005; Rylander *et al*., 2004; Yang *et al*., 2000, 2001). This type of measurement allows for fiber-optic implementation and also high-speed punctual phase measurement by using a single, fast photodetector. Full-field phase measurement techniques, on the other hand, provide simultaneous information from a large number of points on the sample, which has the benefit of studying both the temporal and spatial behavior of the biological system under investigation (Allman *et al*., 2000; Bajt *et al*., 2000; Dunn *et al*., 1997; Ikeda *et al*., 2005; Iwai *et al*., 2004; Mann *et al*., 2005a; Marquet *et al*., 2005; Paganin and Nugent, 1998; Popescu *et al*., 2004, 2005, 2006b; Zicha and Dunn, 1995; Zicha *et al*., 1999). With the recent advances in two-dimensional array detectors, full-field phase images can now be acquired at high speeds (i.e., thousands of frames per second).

In this chapter, we review the main quantitative phase imaging techniques reported in the literature and their applications to studying cell structure and dynamics.

II. Methods

A. Punctual QPI Measurements

Various point-measurement techniques have been developed over the years for quantifying phase shifts at a given point through biological samples. This class of techniques can be described as an extension of optical coherence tomography (Huang *et al*., 1991) to provide measurements of phase, phase dispersion, and birefringence associated with biological structures. DeBoer *et al*. demonstrated

depth-resolved birefringence measurements with a polarization sensitive OCT system (deBoer *et al.*, 1997). Differential phase-contrast OCT images have also been generated with a polarization-sensitive OCT instrument (Hitzenberger and Fercher, 1999). Recently, polarization-sensitive OCT was used to quantify phase retardation in the retinal nerve fiber (Park *et al.*, 2003). An instantaneous quadrature technique was proposed based on using a $1 \times N$ fiber coupler and the inherent phase shift between different output fibers (Choma *et al.*, 2003). Electrokinetic (Youn *et al.*, 2003) and thermorefractive (Kim *et al.*, 2004) properties of tissue and tissue phantoms have been measured by differential phase OCT. Phase sensitive OCT-type measurements have also been performed for studying static cells (Rylander *et al.*, 2004), for monitoring electric activity in nerves (Akkin *et al.*, 2004; Fang-Yen *et al.*, 2004), and spontaneous beating in cardiomyocytes (Choma *et al.*, 2005). However, these methods rely on single point measurements, which, for imaging purposes, require raster scanning. This procedure is often time consuming, reducing the applicability range of the techniques.

B. Full-Field QPI

Recently, new full-field phase imaging techniques, which are suitable for spatially resolved investigation of biological structures, have been recently developed to overcome these limitations. Combining phase shifting interferometry with Horn microscopy, DRIMAPS (digitally recorded interference microscopy with automatic phase-shifting) has been proposed as a new technique for quantitative biology (Dunn and Zicha, 1997; Zicha and Dunn, 1995). This *quantitative phase imaging* technique has been successfully used for measuring cell spreading (Dunn *et al.*, 1997), cell motility (Zicha *et al.*, 1999), cell growth, and dry mass (Dunn and Zicha, 1995). A full-field quantitative phase microscopy method was developed also by using the transport-of-irradiance equation (Gureyev *et al.*, 1995a,b). The technique is inherently stable against phase noise because it does not require using two separate beams as in typical interferometry experiments. This approach requires however recording images of the sample displaced through the focus and subsequently solving numerically partial differential equations.

Digital holography has been developed a few decades ago (Goodman and Lawrence, 1967) as a technique that combines digital recording with traditional holography (Gabor, 1948). Typically, the phase and amplitude of the imaging field are measured at an out-of-focus plane. By solving numerically the Fresnel propagation equation, one can determine the field distribution at various planes. For optically thin objects, this method allows for reconstructing the in-focus field and, thus, retrieving the phase map characterizing the sample under investigation. This method has been implemented in combination with phase shifting interferometry (Yamaguchi and Zhang, 1997). More recently, digital holography has been adapted for quantitative phase imaging of cells (Carl *et al.*, 2004; Mann *et al.*, 2005b; Marquet *et al.*, 2005).

In recent years, new full-field quantitative phase imaging techniques have been developed for studying live cells. The advance of Fourier phase microscopy (FPM) (Lue *et al*., 2007b; Popescu *et al*., 2004), Hilbert phase microscopy (HPM) (Ikeda *et al*., 2005; Popescu *et al*., 2005), and diffraction phase microscopy (DPM) (Park *et al*., 2006; Popescu *et al*., 2006b) came in response to the need for high phase stability over broad temporal scales. The principles of operation of these techniques and their applications for cell biology are described below.

1. Fourier Phase Microscopy (FPM)

FPM combines the principles of phase contrast microscopy (PC) and phase shifting interferometry, such that the scattered and unscattered light from a sample are used as the object and reference fields of an interferometer. The experiment is presented in more detail elsewhere (Popescu *et al*., 2004). Here we present a brief description of the experimental setup depicted in Fig. 1. The collimated low coherence field from a superluminescent diode (SLD, center wavelength 809 nm, and bandwidth 20 nm) is used as the illumination source for a typical inverted microscope. Through the video port, the microscope produces a magnified image positioned at the image plane IP. The lens L_1 is positioned at the same plane IP and has a focal length such that it collimates the zero-spatial frequency field. The Fourier transform of the image field is projected by the lens L_2 (50 cm focal distance) onto the surface of a programmable phase modulator (PPM, Hamamatsu KK photonics, model X8267). This PPM consists of an optically addressed, two-dimensional liquid crystal array with 768 × 768 active pixels. The polarizer P adjusts the field polarization in a direction parallel to the axis of the liquid crystal. In this configuration, the PPM produces precise control over the phase of the light reflected by its surface. The PPM pixel size is 26 × 26 μm^2, whereas the dynamic range of the phase control is 8 bits over 2π. In the absence of PPM modulation, an exact phase and amplitude replica of the image field is formed at the CCD plane, via the beam splitter BS_1. For alignment purposes, a camera is used to image the surface of the PPM via the beam splitter BS_2. The PPM is used to controllably shift the phase of the scattered field component U_1 (dotted line) in four successive increments of $\pi/2$ with respect to the average field U_0 (solid line), as in typical phase shifting interferometry measurements (Creath, 1988). The phase difference between U_1 and U_0 is obtained by combining four recorded interferograms as follows

$$\Delta\varphi(x,y) = \tan^{-1}\left[\frac{I(x,y;3\pi/2) - I(x,y;\pi/2)}{I(x,y;0) - I(x,y;\pi)}\right], \tag{1}$$

where $I(x, y; \alpha)$ represents the irradiance distribution of the interferogram corresponding to the phase shift α. If we define $\beta(x,y) = |U_1(x,y)|/|U_0|$, then the phase associated with the image field $U(x,y)$can be determined

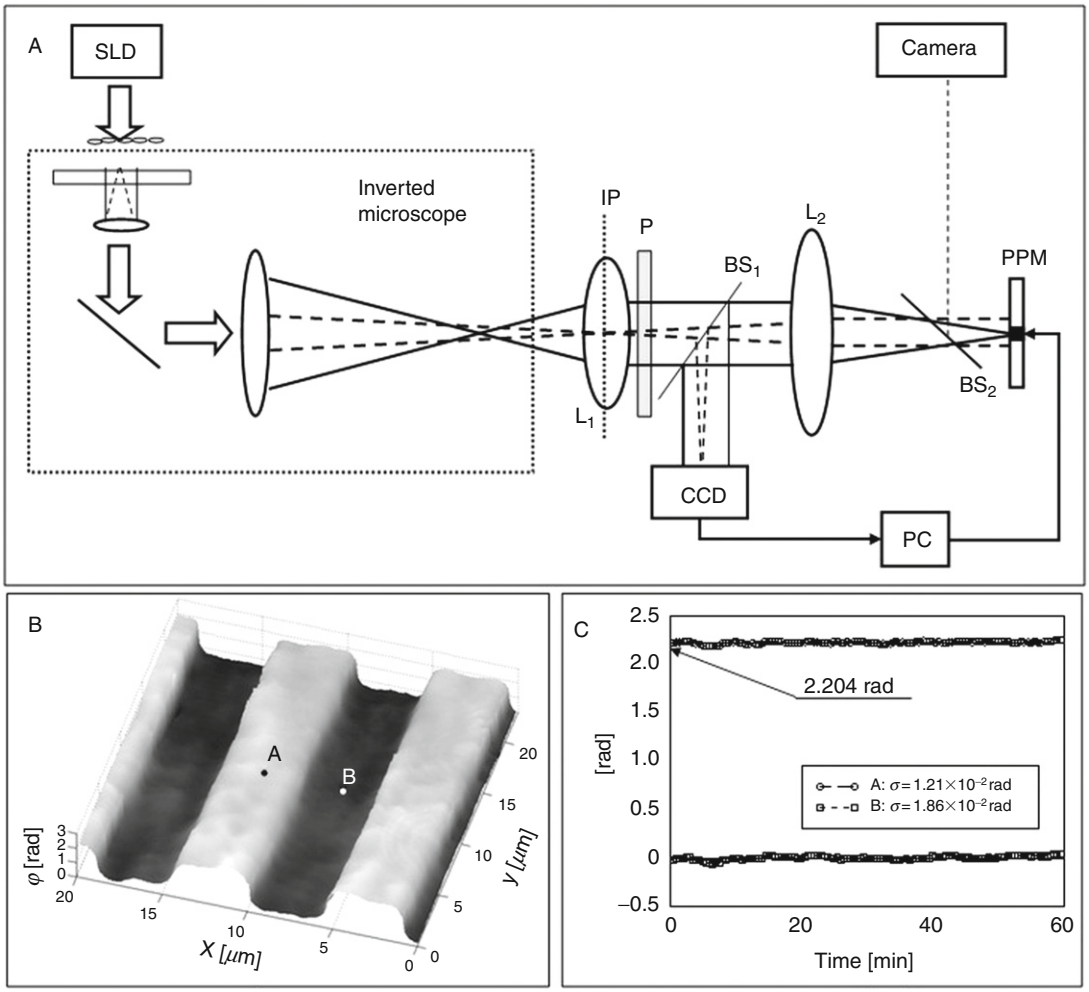

Fig. 1 (A) FPM experimental setup. (B) Quantitative phase image of a phase grating. (C) Temporal fluctuations of the path lengths associated with points A and B on the grating in b).

$$\varphi(x,y) = \tan^{-1}\left[\frac{\beta(x,y)\sin(\Delta\varphi(x,y))}{1+\beta(x,y)\cos(\Delta\varphi(x,y))}\right]. \tag{2}$$

The amplitude ratio β contained in Eq. (2) can be obtained from the 4 frames, taking into account that $\beta_{\varphi\to 0} = 0$ (Popescu *et al.*). The phase image retrieval rate is limited by the refresh rate of the liquid crystal PPM, which in our case is 8 Hz. However, this acquisition rate is not limited in principle and can be further improved using a faster phase shifter. In fact, we recently improved the data acquisition by ~2 orders of magnitude (Lue *et al.*, 2007b).

We employed the procedure presented here to experimentally determine the spatial phase modifications of a field propagating through various transparent media. Figure 1B shows an example of such measurement, obtained for a transmission phase grating. Using a 40× (NA = 0.65) microscope objective, we retrieved the spatially varying phase delay induced by this grating, which is made of glass with the refractive index $n = 1.51$. The profile of the grating was measured by stylus profilometry and the height was found to be 570 ± 10 nm while its pitch had a value of 4 μm. This corresponds to a phase profile of height $\varphi = 2.217 \pm 0.039$ rad. As can be seen in Fig. 1B, the measurement correctly recovers the expected phase distribution. Figure 1C shows the values of the reconstructed phase associated with the point A and B indicated in Fig. 1C, as a function of time. The phase values are averaged over an area that corresponds to 0.6×0.6 μm^2 in the sample plane, which is approximately the diffraction limit of the microscope. The values of the standard deviation associated with the two points are 18 and 12 mrad, respectively, which demonstrate the significant stability of the technique in the absence of active stabilization. Interestingly, the phase stability of the measurement is actually better when wet samples are studied (Popescu *et al.*, 2006a).

2. Hilbert Phase Microscopy

HPM extends the concept of complex analytic signals to the spatial domain and measures quantitative phase images from only one spatial interferogram recording (Ikeda *et al.*, 2005; Popescu *et al.*, 2005). Due to its single-shot nature, the HPM acquisition time is limited only by the recording device and thus can be used to accurately quantify nanometer level path-lengths shifts at the millisecond time scales or less, where many relevant biological phenomena develop. The experimental setup is shown in Fig. 2A. A HeNe laser ($\lambda = 632$ nm) is coupled into a 1×2 single mode fiber-optic coupler and collimated on each of the two outputs. One output field acts as the illumination field for an inverted microscope equipped with a 100× objective. All the optical fibers are fixed to minimize phase noise. The tube lens is such that the image of the sample is formed at the CCD plane via the beam splitter cube. The second fiber coupler output is collimated and expanded by a telescopic system consisting of another microscope objective and the tube lens. This reference beam can be approximated by a plane wave, which interferes with the image field. The reference field is tilted with respect to the sample field such that uniform fringes are created at an angle of 45° with respect to x and y axes. The CCD used (C7770, Hamamatsu Photonics) has an acquisition rate of 291 frames/s at the full resolution of 640×480 pixels, at 1–1.5 ms exposure time. The fringes are sampled by 6 pixels per period. The spatial irradiance associated with the interferogram across one direction is given by

$$I(x) = I_R + I_S(x) + 2\sqrt{I_R I_S(x)} \cos[qx + \phi(x)], \tag{3}$$

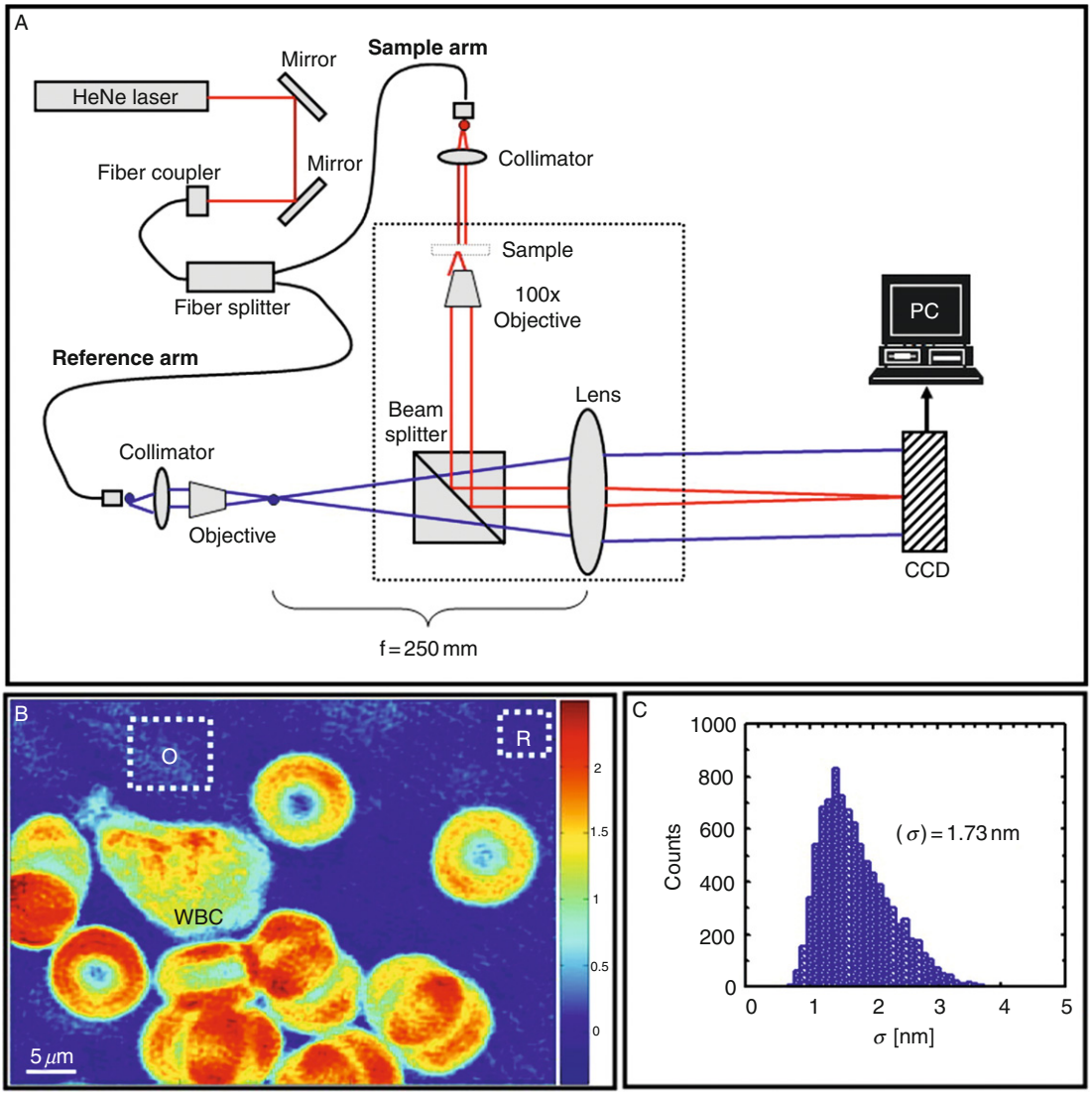

Fig. 2 (A) HPM experimental setup. (B) HPM image of a droplet of blood. (C) The histogram of standard deviations associated with a region in the field of view containing no cells.

where I_R and I_S are, respectively, the reference and sample irradiance distributions, q is the spatial frequency of the fringes, and ϕ is the spatially varying phase associated with the object, the quantity of interest in our experiments. Using high-pass spatial filtering and Hilbert transformation, the quantity ϕ is retrieved in each point of the single-exposure image (Ikeda *et al.*, 2005).

To exemplify the ability of the new instrument to perform live cell dynamic morphometry at the millisecond and nanometer scales, we obtained time-resolved HPM images of red blood cells (RBCs). Droplets of whole blood were simply sandwiched between cover slips, with no additional preparation. Figure 2B shows a quantitative phase image of live blood cells; both isolated and agglomerated erythrocytes are easily identifiable. A white blood cell (WBC) is also present in the field of view. Using the refractive index of the cell and surrounding plasma of 1.40 and 1.34, respectively (Hammer *et al*., 1998), the phase information associated with the RBCs is translated into nanometer scale image of the cell topography. The assumption of optical homogeneity of RBC is commonly used (Brochard and Lennon, 1975; Zilker *et al*., 1987) and justified by the knowledge that cellular content consists mainly of hemoglobin solution. In order to eliminate the longitudinal noise between successive frames, each phase image was referenced to the average value across an area in the field of view containing no cells (denoted in Fig. 2B by R). To quantify the residual noise of the instrument in a spatially relevant way, we recorded sets of 1000 images, acquired at 10.3 ms each and analyzed the path-length fluctuations of individual points within a 100×100 pixel area (denoted in Fig. 2A by O). The path-length associated with each point in O was averaged over 5×5 pixels, which approximately corresponds to the dimensions of the diffraction limit spot. The histogram of the standard deviations associated with all the spots within region O is shown in Fig. 2C. The average value of this histogram is indicated. This noise assessment demonstrates that our HPM instrument is capable of providing quantitative information about structure and dynamics of biological systems, such as RBCs, at the nanometer scale. Recently, an active feedback loop has been added to the HPM system, which further improved the stability of the instrument (Popescu *et al*., 2006c).

3. Diffraction Phase Microscopy

DPM is a novel quantitative phase imaging technique that combines the single shot feature of HPM with the common path geometry associated with FPM. As a result, DPM is characterized by the significant stability of the common path interferometers, while operating at high acquisition speeds, limited only by the detector. The experimental setup is shown in Fig. 3A. The second harmonic radiation of a Nd:YAG laser ($\lambda = 532$nm) was used as illumination for an inverted microscope (Axiovert 35, Carl Zeiss Inc.), which produces the magnified image of the sample at the output port. The microscope image appears to be illuminated by a virtual source point VPS. A relay lens RL was used to collimate the light originating at VPS and replicate the microscope image at the plane IP. A phase grating G is placed at this image plane, which generates multiple diffraction orders containing full spatial information about the image. The goal is to select two diffraction orders (zeroth and first) that can be further used as reference and sample fields, as in Mach–Zender interferometer geometries. In order to accomplish this, a standard spatial filtering lens system L_1–L_2 is used to select the two

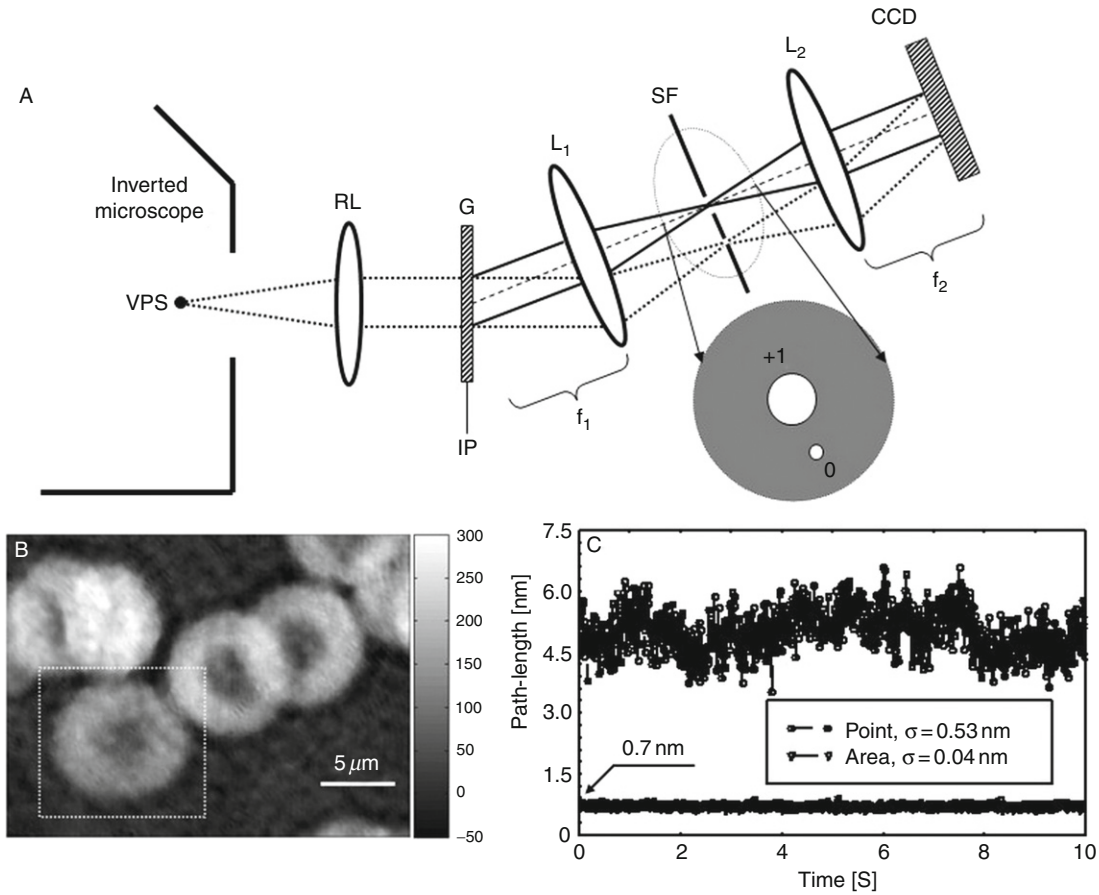

Fig. 3 (A) DPM experimental setup. (B) DPM image of a blood droplet. (C) Temporal path-length fluctuations associated with a point and area.

diffraction orders and generate the final interferogram at the CCD plane. The zeroth-order beam is low-pass filtered using the spatial filter SF positioned in the Fourier plane of L_1, such that at the CCD plane it approaches a uniform field. The spatial filter allows passing the entire frequency content of the first diffraction order beam and blocks all the other orders. The first order is thus the imaging field and the zeroth order plays the role of the reference field. The two beams traverse the same optical components, that is, they propagate along a common optical path, thus significantly reducing the longitudinal phase noise. The direction of the spatial modulation was chosen at an angle of 45° with respect to the x and y axes of the CCD, such that the total field at the CCD plane has the form

$$E(x,y) = |E_0|\exp(\mathrm{i}[\phi_0 + \beta(x+y)]) + |E_1(x,y)|\exp(\mathrm{i}\phi(x,y)). \tag{4}$$

In Eq. (1), $|E_{0,1}|$and $\phi_{0,1}$are the amplitudes and the phase of, respectively, the orders of diffraction 0, 1, while β represents the spatial frequency shift induced by the grating to the zeroth order. Note that, as a consequence of the central ordinate theorem, the reference field is proportional to the spatial average of the microscope image field,

$$|E_0|e^{i\phi_0} \propto \frac{1}{A}\int |E(x,y)|e^{i\phi(x,y)}dxdy, \tag{5}$$

where A is the total image area. The spatial average of an image field has been successfully used before as a stable reference for extracting spatially resolved phase information (Popescu *et al*., 2004).

The CCD (C7770, Hamamatsu Photonics) has an acquisition rate of 291 frames/s at the full resolution of 640 × 480 pixels. To preserve the transverse resolution of the microscope, the spatial frequency β is chosen to match or exceed the maximum frequency allowed by the numerical aperture of the instrument. Throughout our experiments, the microscope was equipped with a 40× (0.65 NA) objective, which is characterized by a diffraction-limited resolution of 0.4 μm. The microscope-relay lens combination produces a magnification of about 100, thus the diffraction spot at the grating plane has a size of approximately 40 μm. The grating pitch is 20 μm, which allows taking advantage of the full resolution given by the microscope objective. The L_1–L_2 lens system has an additional magnification of $f_2/f_1 = 3$, such that the sinusoidal modulation of the image is sampled by 6 CCD pixels per period. The spatially resolved quantitative phase image associated with the sample is retrieved from a single CCD recording via a spatial Hilbert transform, as described in Section 3.2. and in Ikeda *et al*. (2005).

To demonstrate the inherent stability of the system and ability to image live cells, we imaged droplets of whole blood sandwiched between cover slips, with no additional preparation. Figure 3B shows a quantitative phase image of live blood cells, where the normal, discocyte shape can be observed. To quantify the stability of the DPM instrument and thus the sensitivity of cell topography to dynamical changes, we recorded sets of 1000 *no-sample* images, acquired at 10.3 ms each and performed noise analysis on both single points and entire field of view. The *spatial* standard deviation of the path-length associated with the full field of view had a *temporal* average of 0.7 nm and a *temporal* standard deviation of 0.04 nm, as shown in Fig. 3C. Also shown in Fig. 3C is the temporal path-length trace of an arbitrary point (3 × 3 pixel average), characterized by a standard deviation of 0.53 nm. Thus, DPM provides quantitative phase images which are inherently stable to the level of subnanometer optical path-length and at an acquisition speed limited only by the detector. Recently, DPM has been combined with epifluorescence microscopy to simultaneously image, for the first time, both the nanoscale structure and dynamics, as well as specific functional information in live cells (Park *et al*., 2006).

III. Applications of QPI

The full-field quantitative phase imaging techniques presented here are suitable for all cell visualization and morphometric applications associated with traditional microscopy techniques, for example, bright field, dark field, PC, Nomarski/DIC, etc. In the following, we present several cell biology applications that are specific to quantitative phase imaging methods. The classification is with respect to the time scale of cell imaging.

A. Static QPI

1. Red Blood Cell Volumetry

PC (Brochard and Lennon, 1975) and reflection interference contrast microscopy (RICM) (Zilker *et al.*, 1987) have been used previously to measure dynamic changes in RBC shape. Such nanoscale topographic information offers insight into the biophysical properties and health state of the cell. However, these methods are inherently *qualitative*. Thus, three-dimensional quantitative erythrocyte shape measurements have been limited to atomic force and scanning electron microscopy. Nevertheless, due to the heavy sample preparation required by these methods prior to imaging, their applicability to studying cells in physiological conditions has been limited. (Matarrese *et al.*, 2005; Nowakowski *et al.*, 2001).

Mature erythrocytes represent a very particular type of structure; they lack nuclei and organelles and thus can be modeled as optically homogeneous objects, that is, they produce local optical phase shifts that are proportional to their thickness. Therefore, measuring quantitative phase images of RBCs provides cell thickness profiles with an accuracy that corresponds to a very small fraction of the optical wavelength. Using the refractive index of the cell and surrounding plasma of 1.40 and 1.34, respectively (Hammer *et al.*, 1998), the phase information associated with the RBCs can be easily translated into nanometer scale image of the cell topography. An example of nanometer scale topography of RBC quantified by HPM is shown in Fig. 4A. The thickness profile of the cell, $h(x, y)$, relates to the measured phase, $\phi(x, y)$, as $h(x, y) = (\lambda/2\pi\Delta n)\phi(x, y)$, where Δn is the refractive index contrast between the hemoglobin contained in the cell and the surrounding fluid (plasma). The cell thickness profile obtained by this method is shown in Fig. 4B. The volume of individual cells can be measured from the HPM data as $V = \int h(x, y)\mathrm{d}x\mathrm{d}y$. Figure 4C depicts the volume of RBC measured by HPM during spontaneous hemolysis, that is, after the membrane ruptured and the cell started to lose hemoglobin. This result demonstrates the ability of quantitative phase imaging to provide RBC volumetry without the need for preparation. This represents a significant advance with respect to current techniques that require the cells to be prepared such that they assume spherical shapes (Best, 2005). The errors in the volume measurement due to changes in refractive index are not likely to be significant. Spatial inhomogeneities of the imaging fields may affect the accuracy of

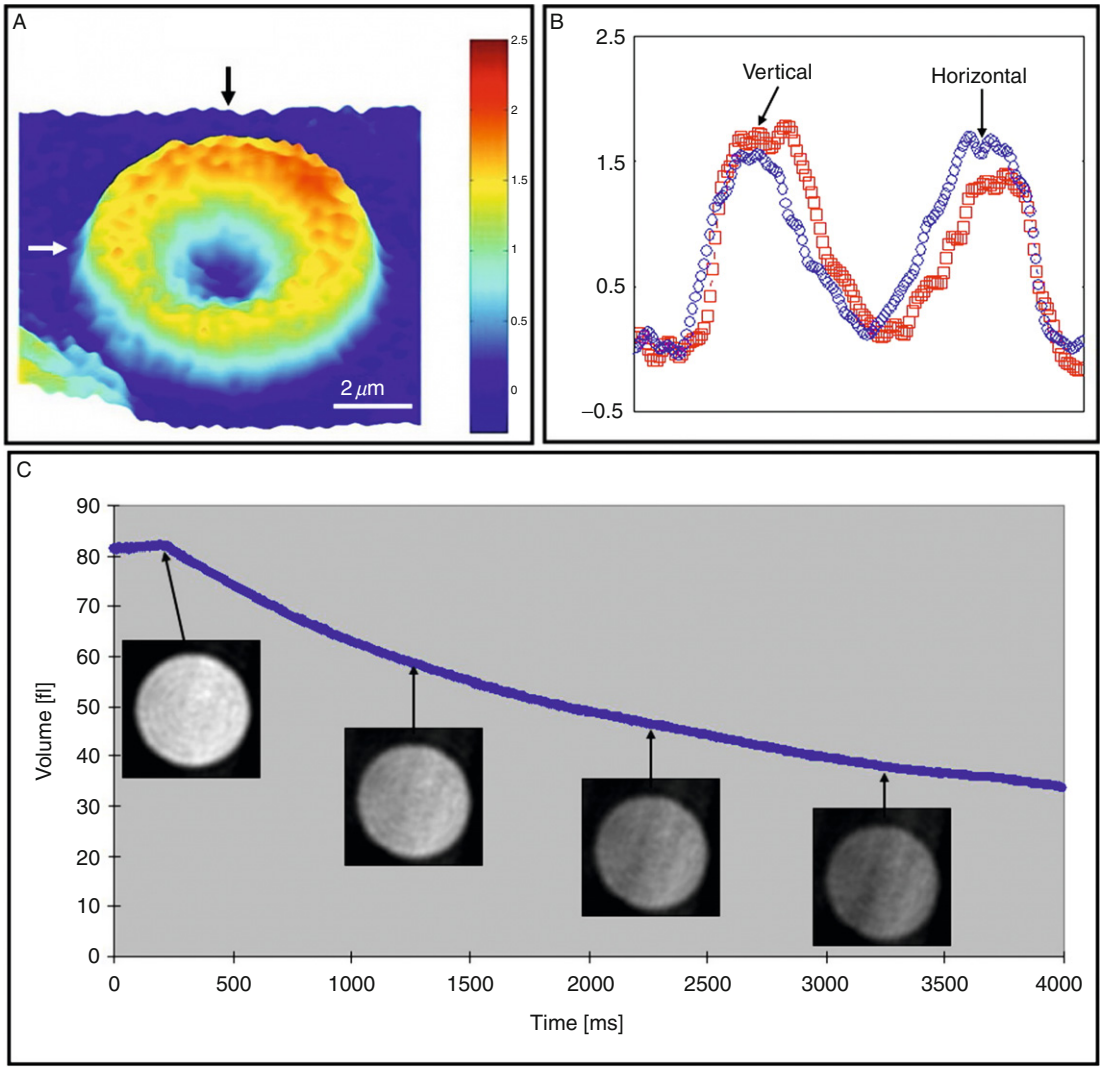

Fig. 4 (A) HPM image of a normal red blood cell. (B) Cell profile across two directions. (C) Cell volume as a function of time during hemolysis that starts at approximately $t = 300$ ms.

the volume measurement and this influence was minimized by accurately spatially filtering and collimating the beams.

2. Cell Dry Mass

Several decades ago, it has been shown that the optical phase shift through the cells is a measure of the cellular *dry mass* content (Baber, 1952; Davies and Wilkins, 1952). Optical interferometry provides access to the phase information of a given

transparent sample; the main challenge is to suppress the environmental noise, which hinders the ability to measure optical path-length shifts quantitatively.

DRIMAPS (digitally recorded interference microscopy with automatic phase shifting) employs Horn microscopy and phase-shifting interferometry to measure phase images from biological samples. The potential of DRIMAPS for studying cell growth has been demonstrated (Zicha *et al.*, 1999). This technique, however, is not inherently stable against phase noise, which limits its applicability to studying cell dynamics. Although other quantitative phase imaging techniques have been reported (Cuche *et al.*, 1999; Paganin and Nugent, 1998), their potential for analysis of cellular dry mass has not been evaluated, to our knowledge.

In order to quantify cell dry mass, we employed FPM described in Section 3.1. It was shown that FPM provides quantitative phase images of live cells with high transverse resolution and low noise over extended periods of time. The general expression for the spatially-resolved quantitative phase images obtained from a cell sample is given by

$$\varphi(x,y) = \frac{2\pi}{\lambda} \int_0^{h(x,y)} \left[n_c^z(x,y,z) - n_0 \right] \mathrm{d}z. \tag{6}$$

In Eq. (6), λ is the wavelength of light, h is the local thickness of the cell, and n_0 is the refractive index of the surrounding liquid. The quantity $n_c^z$is the refractive index of cellular material, which is generally an inhomogeneous function in all three dimensions. Without loss of generality, Eq. (6) can be re-written in terms of an axially-averaged refractive index n_c, as

$$\varphi(x,y) = \frac{2\pi}{\lambda} \left[n_c(x,y) - n_0 \right] h(x,y). \tag{7}$$

However, it has been shown that the refractive properties of a cell composed mainly of protein has, to a good approximation, a simple dependence on protein concentration (Baber, 1952; Davies and Wilkins, 1952),

$$n_c(x,y) = n_0 + \alpha C(x,y). \tag{8}$$

In Eq. (8), α is referred to as the refraction increment (units of ml/g) and C is the concentration of dry protein in the solution (in g/ml). Using this relationship, the dry mass surface density σ of the cellular matter is obtained from the measured phase map as

$$\sigma(x,y) = \frac{\lambda}{2\pi\alpha} \varphi(x,y). \tag{9}$$

To illustrate the potential of FPM for measuring the dry mass distribution of live cells, we used the FPM instrument for imaging confluent monolayers of HeLa cells. Figure 5 shows an example of the dry mass density distribution σ (units of pg/μm^2) obtained from nearly confluent HeLa cells. In applying Eq. (9), we used

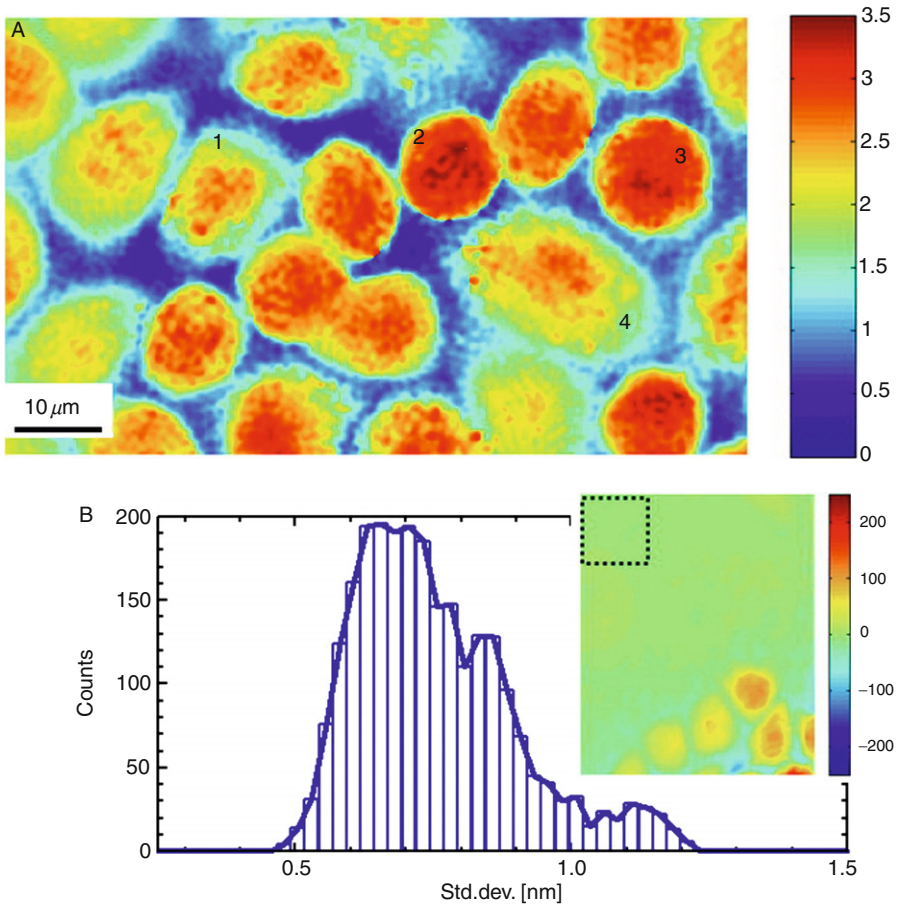

Fig. 5 (A) Dry mass density distribution $\sigma(x,y)$ obtained using FPM. The colorbar has units of picograms_per square micrometer. (B) Histogram of the path-length standard deviation corresponding to the pixels within the 15×15 μm^2 selected area shown in inset. The colorbar of the inset indicates optical path-length in units of nanometers, which sets the ultimate sensitivity to dry mass changes to 4 fg/μm^2.

$\alpha = 0.2$ ml/g for the refraction increment, which corresponds to an average of reported values (Baber, 1952). Quantitative information about the dry mass of the cells thus allows investigation of cell movement, growth or shape change in a totally noninvasive manner. To quantify the phase stability of the instrument, we recorded 240 phase images over 2 h from a cell sample that contained regions with no cells. We measured the path-length standard deviation of each pixel within a 15×15 μm^2 region. The average of these standard deviations had a value of 0.75 nm, which indicates that the sensitivity to changes in dry mass surface density has a value of 3.75 fg/μm^2.

3. Cell Refractometry

Interaction of optical fields with tissues is largely determined by the three-dimensional refractive index distribution associated with the biological structure (Backman *et al.*, 2000; Drezek *et al.*, 1999; Mourant *et al.*, 2000; Tuchin, 2000). All scattering models use the refractive index contrast between the scattering particles and surroundings to make predictions about the interaction of the optical field with biological media (Born and Wolf, 1999; Ishimaru, 1978; van de Hulst, 1981). Highly scattering tissue has been characterized in terms of an average refractive index by optical coherence tomography (Tearney *et al.*, 1995) and, more recently, total internal reflection (Lai *et al.*, 2005).

Live cells, on the other hand, are essentially transparent under visible light, and, thus, can be described as weak scatterers, with subtle refractive index variations in space. The information about the cell structure and, hence, refractive index, is encoded in the wavefront modification of the illuminating field. By quantifying the optical path-length shift associated with the cell can potentially provide noninvasive information about structural changes associated with cell cycling or disease progression. However, this optical phase change produced by the cells is due to the combined effect of both refractive index and thickness variations across the sample. Recently, digital holography has been used to decouple the contributions of these two variables (Rappaz *et al.*, 2005). Nevertheless, this approach requires exposing the same cells to two different surrounding media, which adds constraints to the cell preparation procedure and prevents high-throughput investigation.

In order to extract the refractive index information independently from the cell thickness, we placed live HeLa cells (a human epithelial carcinoma cell line) in microchannels of fixed dimension that confine the cell in vertical direction (Lue *et al.*, 2006). Single input and single output microchannels of rectangular cross sections were prepared by molding elastomer on microstructures fabricated on a silicon wafer (for details see Whitesides *et al.*, 2001). First, the refractive index of the culture medium (CM) was determined by acquiring successive phase images of microchannels filled both with CM and water. Thus, we measured $n_{CM} = 1.337$ with a standard deviation of 0.0015.

HeLa cells suspended in CM were then introduced into the microchannels, which deformed the cells and confined them in the vertical direction. Figure 6A shows an example of a quantitative phase image of such a sample. Because the microchannel thickness exhibits some variability due to the fabrication process, we quantified the phase shift of both the cell and CM with respect to the microchannel, which eliminated the need for *a priori* knowledge of the microchannel height. This procedure was applied for measuring the refractive index of 17 cells and the results summarized in Fig. 6B. This histogram shows that the measured refractive index values are characterized by a small standard deviation, $n_{cell} = 1.384 \pm 0.0018$. This value for the average refractive index is comparable to other results published in the literature (Beuthan *et al.*, 1996; Liu *et al.*, 1996; Maier *et al.*, 1994). We performed also independent measurements of refractive index on cells in suspension.

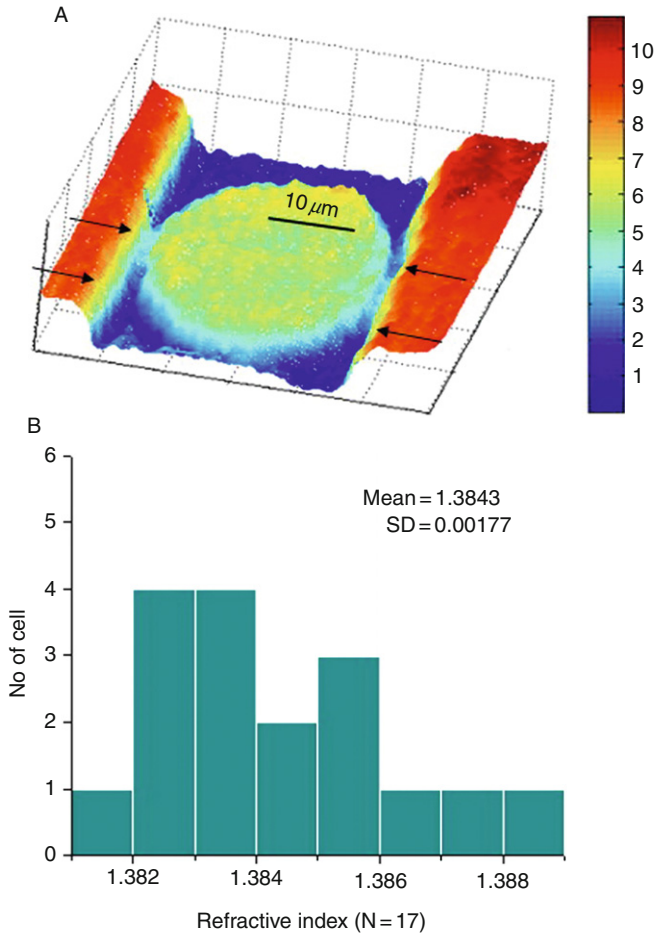

Fig. 6 (A) HeLa cell confined in microchannel. Colorbar indicates path-length in rad. (B) Histogram of cell refractive index.

In this case, we used the fact that cells in suspension assume a spherical shape, which enables extraction of the refractive index from the quantitative phase image. The value obtained, $n_{\text{cell}} = 1.3846 \pm 0.0049$, agrees very well with the result obtained from the microchannel experiments.

B. Dynamic QPI

4. Cell Growth

Quantitative knowledge about this phenomenon can provide information about cell cycling, functioning, and disease (Conlon *et al.*, 2001; Ingber, 1990). We employed FPM to quantify the changes in dry mass of HeLa cells in culture.

Data containing time-resolved FPM images were acquired at a rate of 4 frames a minute over periods of up to 12 h and the dry mass surface density information was extracted as presented above. Each cell fully contained in the field of view was segmented using a MATLAB program based on iterative image thresholding and binary dilation, which was developed in our laboratory. Figure 7A shows the segmented images of the four cells shown in Fig. 5. We monitored the total dry mass of each cell over a period of 2 h. The results are summarized in Fig. 7B. Cell 4 exhibits linear growth, as does cell 1, although it is reduced by a factor of almost 5. In contrast, cell 2 shows virtually no change in mass, while cell 3 appears to exhibit a slight oscillatory behavior, the origin of which is not clearly understood. These results demonstrate the capability of FPM to quantify small changes in cell mass and therefore monitor in detail the evolution of cell cycle and its relationship with function.

5. Cell Motility

The necessity for quantitative, model-based studies of cell motility and migration was recognized decades ago (Weiss and Garber, 1952) and continues to evolve with new experimental and analytical tools (Maini *et al.*, 2004; Zaman *et al.*, 2005).

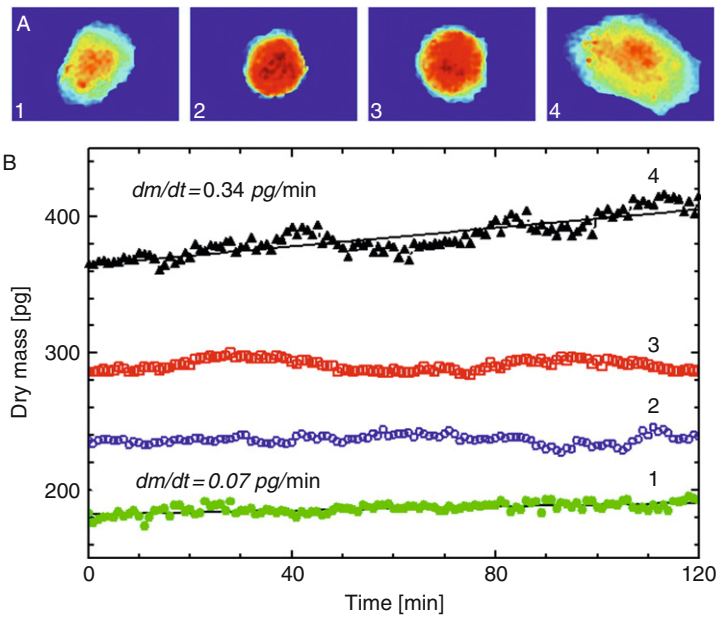

Fig. 7 (A) Images of the cells segmented from Fig. 1, as indicated. (B) Temporal evolution of the total dry mass content for each cell. The solid lines for cells 1 and 4 indicate fits with a linear function. The values of the slope obtained from the fit are indicated.

Understanding the motion of live cells requires tracking their mass-weighted centroid displacements and performing averages over time and ensembles of cell populations. However, historically, optical techniques such as bright field microscopy (Mombach and Glazier, 1996), PC (Czirok *et al*., 1998; Gail and Boone, 1970), and Nomarski/DIC (Grueler, 1984) have been used for tracking the centroid of live cells. For a review and timeline see Ref. (Dunn and Jones, 2004). More recently, confocal microscopy has been used to investigate motility of hydra cells (Upadhyaya *et al*., 2001), and two-photon fluorescence microscopy to study the motion of lymphocytes *in vivo* (Miller *et al*., 2002). However, information provided by these techniques is qualitative in terms of the mass distribution within the individual cells. Therefore, the intensity-weighted centroid of a cell does not necessarily overlap with its true center of mass, and the assessment of cellular motion based on the trajectory of this point may introduce errors, especially for cell displacements that are smaller than the cell diameter.

In addition to the unprecedented sensitivity to cell growth, FPM provides a precise localization of the center of mass, which is instrumental for studying cell motility with high accuracy. Figure 8A shows the mean squared displacement dependence for cells that, during the investigation, appeared to be in a resting state, that is, their total dry mass value did not vary considerably over the period of observation. We will refer to these cells as being in the G0/G1 phase of the cell

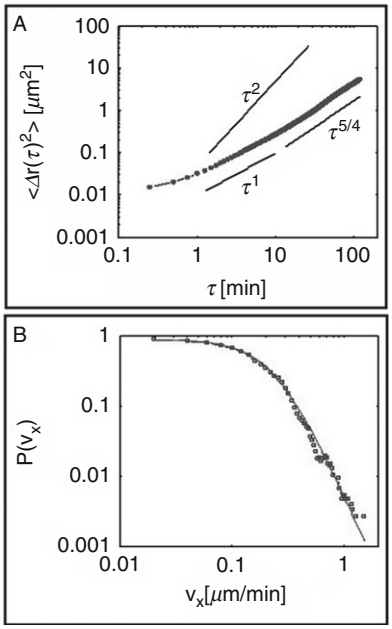

Fig. 8 (A) Mean squared displacement of resting cells. The solid line indicates power laws with various exponents, as reference.

cycle. Remarkably, the long time behavior ($\tau > 10$ min.) shows a power law trend with an exponent $\alpha = 5/4$, which indicates *super-diffusion*. Similar power law dependence was obtained on hydra cell aggregates by Upadhyaya *et al.*, and the underlying thermodynamics of the motion was studied using Tsallis statistics (Upadhyaya *et al.*, 2001). This generalized thermodynamic theory relies on the nonextensive entropy defined as (Tsallis, 1988)

$$S_q = \frac{1 - \int [p(x)]^q \mathrm{d}x}{q - 1}, \tag{10}$$

with p a probability distribution function and q the nonextensiveness parameter, which for $q \to 1$ yields the Gibbs formalism, that is, $S = -\int p(x) \ln [p(x)] \mathrm{d}x$. We calculated the cell velocity distribution for periods of 1 min and found a clear non-Gaussian behavior. Figure 8B shows the probability density of the velocity projected onto the x-axis, which was fitted with the function (Upadhyaya *et al.*, 2001)

$$P(v_x) = C_q \left[1 - (1 - q)\frac{\gamma v_x^2}{2}\right]^{(1/1-q)}. \tag{11}$$

The parameter γ in Eq. (11) is a parameter that contains information about both the apparent mass and equivalent Boltzmann coefficient. However, the cell motion is not thermally driven, and the Boltzmann factor relates to the energetics of cytoskeletal activity. As can be seen in Fig. 8B, Eq. (11) provides a very good description of the data, which demonstrates that the Tsalis formalism can be successfully applied to study this super-diffusive motion. The coefficient q obtained from the fit has an average value of $q = 1.56 \pm 0.04$, which agrees very well with the value of 1.5 previously reported on Hydra cells (Upadhyaya *et al.*, 2001).

However, at times $\tau < 10$ min, the mean squared displacement shown in Fig. 8A exhibits a more complicated behavior, which cannot be modeled by a simple power-law function. Specifically, the center of mass motion appears subdiffusive at $0 < \tau < 2$ min and transitions towards a Brownian regime for $2 < \tau < 10$ min. We hypothesized that the internal mass dynamics such as organelle transport and cytoskeletal remodeling are responsible for the short time behavior of the center of mass. We validated this hypothesis by performing further experiments on cells in the G2/M phase. These cells have a homogeneous distribution of internal structure and, thus, do not exhibit the short time sub-diffusive motion. These findings open the door for a new class of applications, where cell organelles can potentially be used as intrinsic reporters on the viscoelastic properties of intracellular matter.

6. Cell Membrane Fluctuations

Because RBCs have a relatively simple structure (Boal, 2002; Hochmuth and Waugh, 1987), they represent a convenient model for studying cell membranes, which have broad applications in both science and technology (Lipowsky, 1991; Sackmann, 1996). The lipid bilayer is 4–5 nm thick, and exhibits fluid-like

behavior, characterized by a finite bending modulus κ and a vanishing shear modulus, $\mu \approx 0$. The resistance to shear, crucial for RBC function, is provided by the spectrin network, which has a mesh size of ~80 nm. Spontaneous membrane fluctuations, or "flickering," have been modeled theoretically under both static and dynamic conditions in an attempt to connect the statistical properties of the membrane displacements to relevant mechanical properties of the cell (Brochard and Lennon, 1975; Gov, 2004; Gov and Safran, 2005; Gov *et al*., 2003b; Lipowski and Girardet, 1990). These thermally-induced membrane motions exhibit 100 nm scale amplitudes at frequencies of tens of Hertzs. In past studies, measurements of the membrane mean squared displacement versus spatial wave vector, $\Delta u^2(q)$, revealed a q^{-4} dependence predicted by the equipartition theorem, which is indicative of fluidlike behavior (Brochard and Lennon, 1975; Strey *et al*., 1995; Zeman *et al*., 1990; Zilker *et al*., 1987, 1992). These results conflict with the static deformation measurements provided by micropipette aspiration (Discher *et al*., 1994a; Hochmuth *et al*., 1979), high-frequency electric fields (Engelhardt and Sackmann, 1988; Engelhardt *et al*., 1984b), and, more recently, optical tweezers (Suresh *et al*., 2005), which indicate an average value for the shear elasticity of the order of $\mu \sim 10^6$ J/m^2. Gov *et al*. predicted that the cytoskeleton pinning of the membrane has an overall effect of confining the fluctuations and, thus, gives rise to superficial tension much larger than in the case of free bilayers (Gov *et al*., 2003b). This confinement model may offer new insight into the cytoskeleton-bilayer interaction that determines the morphology and physiology of the cell (Lim *et al*., 2002).

Existing optical methods for studying RBC dynamics, including PC (Brochard and Lennon, 1975), RICM (Zilker *et al*., 1987), and fluorescence interference contrast (FLIC) (Kaizuka and Groves, 2006) are limited in their ability to measure cell membrane displacements. It is well known that PCM provides phase shifts quantitatively only for samples that are optically much thinner than the wavelength of light, which is a condition hardly satisfied by any cell type. Similarly, a single RICM measurement cannot provide the absolute cell thickness unless additional measurements or approximations are made (Zidovska and Sackmann, 2006). FLIC relies on inferring the absolute position of fluorescent dye molecules attached to the membrane from the absolute fluorescence intensity, which may limit both the sensitivity and acquisition rate of the technique (Kaizuka and Groves, 2006). Thus, none of these techniques is suitable for making spatially-resolved measurements of the dynamics of cell membrane fluctuations, and testing the hypothesis of Gov *et al*.

We performed highly sensitive experimental measurements of thermal fluctuations associated with RBCs under different morphological conditions. The results reveal the effect of the cytoskeleton on the RBC fluctuations and support the model proposed by Gov *et al*. To quantify membrane fluctuations at the nanometer and millisecond scales with high transverse resolution, we developed a new quantitative phase imaging technique. The method combines HPM (Ikeda *et al*., 2005; Popescu *et al*., 2005) with an electronic stabilization feedback loop and is referred to as the stabilized Hilbert phase microscopy (sHPM) (Popescu *et al*., 2006c).

Our samples were primarily composed of RBCs with typical discocytic shapes, but also contained cells with abnormal morphology which formed spontaneously in the suspension, such as echinocytes, with a spiculated shape, and spherocytes, approaching a spherical shape. By taking into account the free energy contributions of both the bilayer and cytoskeleton, these morphological changes have been successfully modeled (Lim *et al.*, 2002). Figures 9A–C show typical sHPM images of cells in these three groups. For comparison, we also analyzed the motions of RBCs fixed with 40 μM gluteraldehyde, using a standard procedure (Best *et al.*, 2003). The resultant mean squared displacements, $\Delta u^2(q)$, for each group of 4–5 cells are summarized in Fig. 9D. The fixed cells show significantly diminished fluctuations, as expected. The curves associated with the three untreated RBC groups exhibit a power law behavior with an exponent $\alpha = 2$. As in the case of vesicles, this dependence is an indication of tension; however, the RBC tension is determined by the confinement of the bilayer by the cytoskeleton (Gov *et al.*, 2003a,b). Based on this model, we fitted the data to extract the tension coefficient for each individual cell. The average values obtained for the discocytes,

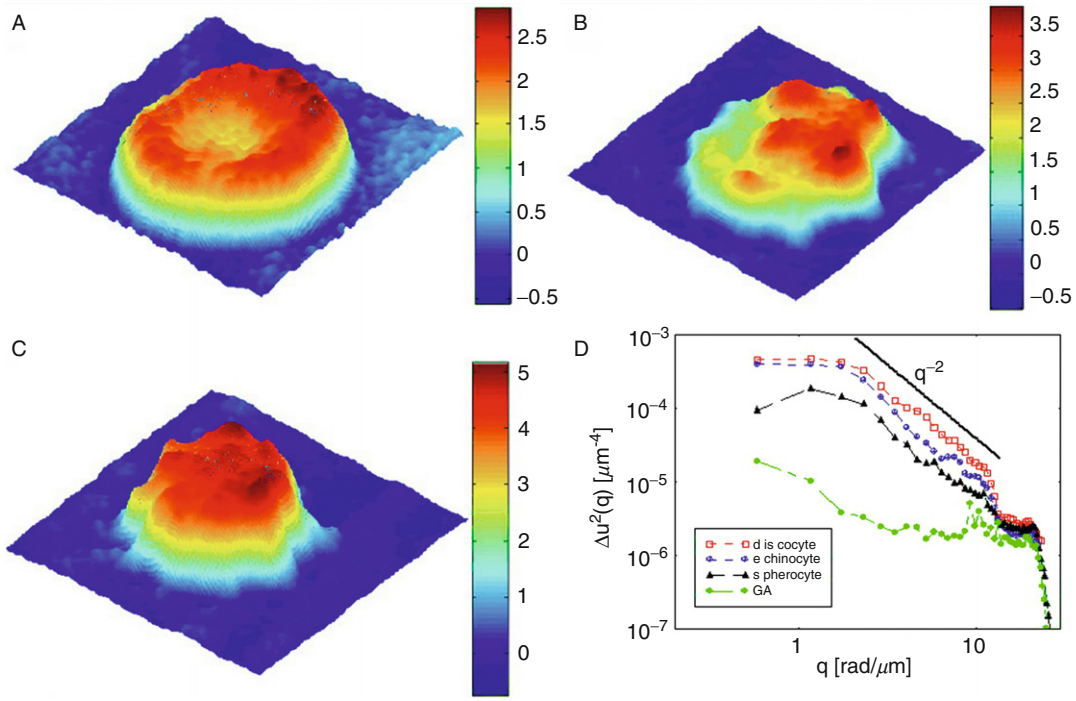

Fig. 9 (A–C) sHPM images of a discocyte (A), echinocyte (B), and spherocyte (C). The color bar shows thickness in microns. (D) Mean squared displacements for the three RBC groups and for the gluteraldehyde (GA) fixed cells.

echinocytes, and spherocytes are, respectively, $\sigma = (1.5 \pm 0.2) \times 10^{-6}$ J/m^2, $\sigma = (4.05 \pm 1.1) \times 10^{-6}$ J/m^2, and $\sigma = (8.25 \pm 1.6) \times 10^{-6}$ J/m^2. The tension coefficient of RBCs is 4–24 times larger than what we measured for vesicles, which suggests that the contribution of the cytoskeleton might be responsible for this enhancement. Further, it is known that the cytoskeleton plays a role in the transitions from a normal RBC shape to abnormal morphology, such as echinocyte and spherocyte (Lim *et al.*, 2002). Therefore, the consistent increase in tension we measured for the discocyte–echinocyte–spherocyte transition can be explained by changes in the cytoskeleton, which pins the bilayer. These findings support the hypothesis that the fluctuations are laterally confined by a characteristic length, $\xi_0 = 2\pi\sqrt{\kappa/\sigma}$, which is much smaller than the cell size (Gov *et al.*, 2003b). Compared to other optical techniques used for studying membrane fluctuations, the sHPM technique used here is quantitative in terms of membrane topography and displacements, highly sensitive to the nanoscale membrane motions, and provides high transverse resolution.

IV. Summary and Outlook

In summary, we reviewed a number of reported techniques for quantitative phase imaging. These methods were divided with respect to their imaging geometry into full-field and point measurements. Further, the full-field QPI capability can be judged by two main parameters: *phase sensitivity*, which defines the smallest phase change that the instrument can capture (i.e., at signal to noise ratio of 1), and *acquisition speed,* which determines the fastest phenomena that can be studied. Thus, we showed that FPM is a highly sensitive technique that is limited in acquisition speed because of the multiple measurements required for each phase image. HPM is a "single-shot" method developed to cover the fast dynamics applications, by trading some phase sensitivity. Finally, DPM combines both the benefits of high-sensitivity associated with FPM and fast acquisition rates of HPM.

Current applications of both static and dynamic QPI were discussed. In the case of RBCs, which have an optically homogeneous structure, cell volumetry, and membrane fluctuations have been demonstrated. In the case of eukaryotic cells, the phase imaging problem is more challenging, as the cell topography and refractive index distribution contribute in a nontrivial manner to the measured path-length map. Thus, decoupling the refractive index contribution from the thickness was discussed. Further, it has been shown that the phase shift map associated with eukaryotic cells can be translated into dry mass density. The sub-nanometer scale accuracy in optical path-length allows for measurements of dry mass at the femtogram scale. With this approach, cell growth and motility can be monitored without the need for contrast agents.

Recent developments in QPI expanded its applicability to new areas. Here we briefly describe several directions that, in author's opinion, promise to make a significant impact in biology and medicine.

A. QPI of Red Blood Cells in Diseased States

Current mechanical measurements of RBCs rely on external loads and are limited to low frequencies (Dao *et al*., 2003; Discher *et al*., 1994b; Engelhardt *et al*., 1984a). RBCs are optically homogeneous, which makes them ideal samples for QPI. Thus, recently, DPM has been applied to quantify the thermal fluctuations of RBC membranes with 3 nm accuracy over a broad range of spatial and temporal frequencies (Park *et al*., submitted for publication-a). The mechanical properties of RBCs were measured during the transition from the normal discoid shape to the abnormal echinocyte and spherical shapes. These measurements indicate that, coincident with this morphological transition, there is a significant increase in the membrane's shear and bending moduli. This mechanical transition can alter cell circulation and impede oxygen delivery.

Extending this principle of investigation to pathology-relevant problems, DPM was used further to quantify membrane fluctuations of human RBCs parasitized by *Plasmodium falciparum* at 37 and 41 °C (Park *et al*., 2008). Alterations of structure cause changes in RBC membrane fluctuations, with stronger effects seen in later stage parasitization and at febrile temperature. These findings offer potential new avenues for identifying, through cell membrane dynamics, pathological states that affect cell function and could result in human diseases (Popescu *et al*., 2008).

B. QPI Imaging of Tissues

Recently, HPM has been applied for the first time to image unstained 5-μm-thick tissue slices of mouse brain, spleen, and liver (Lue *et al*., 2007a). The refractive properties of the tissue are retrieved in terms of the average refractive index and its spatial variation. It was found that the average refractive index varies significantly with tissue type, such that the brain is characterized by the lowest value and the liver by the highest. The spatial power spectra of the phase images reveal power law behavior with different exponents for each tissue type. This approach opens a new possibility for "stain-free" characterization of tissues, where the diagnostic power is provided by the intrinsic refractive properties of the biological structure. Results obtained on liver tissue affected by a lysosomal storage disease showed that QPI can quantify structural changes during this disease development.

C. Three-Dimensional Imaging Using QPI

In 1969, Wolf presented a solution for retrieving the three-dimensional structure of weakly scattering objects using holographic measurements (Wolf, 1969). Since then, this *diffraction tomography* approach, which is analogous to the X-ray computed tomography, has been applied successfully to various inverse problems, such as ultrasonic imaging (Devaney, 1982), geophysics (Devaney, 1984), and microwave imaging (Slaney *et al*., 1984). Experimental implementations in optical imaging have been more limited, most likely due to difficulties imposed by the

requirement of stable phase measurements (Born and Wolf, 1999). Nevertheless, due to new advances in phase retrieval algorithms and experimental techniques, we are witnessing a revival of the field (Carney *et al*., 1999; Chen and Stamnes, 1998; Gbur and Wolf, 2001; Lauer, 2002; Wedberg *et al*., 1995; Zysk *et al*., 2003). Thus, very recently, QPI-based tomographic reconstruction has been applied to live cells (Charriere *et al*., 2006ab; Choi *et al*., 2007).

In a related field of applications, imaging the phase associated with the field scattered by small dielectric particles can reveal the location of the particle with nanoscale accuracy in all three dimensions (Park *et al*., 2007). Using this technique, referred to as Fresnel particle tracking (FPT), tracking probe particles attached to live cells provides insight into their local mechanical properties (i.e., microrheology) at the nanoscale. Recent advances in nanofabrication promise to enable new applications for cell studies, where nanoparticles such as nanotubes, nanowires, and nanorods, can be traced by FPT with unprecedented accuracy.

Acknowledgments

I am grateful to my current and previous coworkers for their contributions to QPI: Huafeng Ding, Zhuo Wang, Ru Wang, and Mustafa Mir (Quantitative Light Imaging Laboratory, Department of Electrical and Computer Engineering, University of Illinois at Urbana-Champaign); YoungKeun Park, Niyom Lue, Shahrooz Amin, Lauren Deflores, Seungeun Oh, Christopher Fang-Yen, Wonshik Choi, Kamran Badizadegan, Ramachandra Dasari, and Michael Feld (Spectroscopy Laboratory, Massachusetts Institute of Technology); Takahiro Ikeda and Hidenao Iwai (Hamamatsu Photonics KK).

I also acknowledge the contributions from collaborators: Martha Gillette (Department of Cell and Developmental Biology, University of Illinois at Urbana-Champaign), Alex Levine, Department of Chemistry and Biochemistry, University of California at Los Angeles. Michael Laposata (Division of Laboratory Medicine and Clinical Laboratories, Vanderbilt University Medical Center), Carlo Brugnara (Department of Laboratory Medicine, Children's Hospital Boston), Catherine Best-Popescu (College of Medicine, University of Illinois at Urbana-Champaign).

References

Akkin, T., Dave, D. P., Milner, T. E., and Rylander, H. G. (2004). Detection of neural activity using phase-sensitive optical low-coherence reflectometry. *Opt. Express* **12,** 2377–2386.

Allman, B. E., McMahon, P. J., Tiller, J. B., Nugent, K. A., Paganin, D., Barty, A., McNulty, I., Frigo, S. P., Wang, Y. X., and Retsch, C. C. (2000). Noninterferometric quantitative phase imaging with soft x rays. *J. Opt. Soc. Am. A-Opt. Image Sci. Vis.* **17,** 1732–1743.

Baber, R. (1952). Interference microscopy and mass determination. *Nature* **169,** 366–367.

Backman, V., Wallace, M. B., Perelman, L. T., Arendt, J. T., Gurjar, R., Muller, M. G., Zhang, Q., Zonios, G., Kline, E., McGilligan, J. A., Shapshay, S., Valdez, T., *et al*. (2000). Detection of preinvasive cancer cells. *Nature* **406,** 35–36.

Bajt, S., Barty, A., Nugent, K. A., McCartney, M., Wall, M., and Paganin, D. (2000). Quantitative phase-sensitive imaging in a transmission electron microscope. *Ultramicroscopy* **83,** 67–73.

Best, C. A. (2005). Fatty acid ethyl esters and erythrocytes: Metabolism and membrane effects, Ph.D. Thesis. Pharmacy and Health Sciences, Northeastern University, Boston.

Best, C. A., Cluette-Brown, J. E., Teruya, M., Teruya, A., and Laposata, M. (2003). Red blood cell fatty acid ethyl esters: A significant component of fatty acid ethyl esters in the blood. *J. Lipid Res.* **44,** 612–620.

Beuthan, J., Minet, O., Helfmann, J., Herrig, M., and Muller, G. (1996). The spatial variation of the refractive index in biological cells. *Phys. Med. Biol.* **41,** 369–382.

Boal, D. (2002). "Mechanics of the cell." Cambridge University Press.

Born, M., and Wolf, E. (1999). "Principles of Optics." Cambridge University Press, Cambridge [England]; New York.

Brochard, F., and Lennon, J. F. (1975). Frequency spectrum of the flicker phenomenon in erythrocytes. *J. Phys.* **36,** 1035–1047.

Carl, D., Kemper, B., Wernicke, G., and von Bally, G. (2004). Parameter-optimized digital holographic microscope for high-resolution living-cell analysis. *Appl. Opt.* **43,** 6536–6544.

Carney, P. S., Wolf, E., and Agarwal, G. S. (1999). Diffraction tomography using power extinction measurements. *JOSA a-Opt. Image Sci. Vision* **16,** 2643–2648.

Charriere, F., Marian, A., Montfort, F., Kuehn, J., Colomb, T., Cuche, E., Marquet, P., and Depeursinge, C. (2006a). Cell refractive index tomography by digital holographic microscopy. *Opt. Lett.* **31,** 178–180.

Charriere, F., Pavillon, N., Colomb, T., Depeursinge, C., Heger, T. J., Mitchell, E. A. D., Marquet, P., and Rappaz, B. (2006b). Living specimen tomography by digital holographic microscopy: Morphometry of testate amoeba. *Opt. Express* **14,** 7005–7013.

Chen, B. Q., and Stamnes, J. J. (1998). Validity of diffraction tomography based on the first Born and the first Rytov approximations. *Appl. Opt.* **37,** 2996–3006.

Choi, W., Fang-Yen, C., Badizadegan, K., Oh, S., Lue, N., Dasari, R. R., and Feld, M. S. (2007). Tomographic phase microscopy. *Nat. Methods* **4,** 717–719.

Choma, M. A., Yang, C. H., and Izatt, J. A. (2003). Instantaneous quadrature low-coherence interferometry with 3×3 fiber-optic couplers. *Opt. Lett.* **28,** 2162–2164.

Choma, M. A., Ellerbee, A. K., Yang, C. H., Creazzo, T. L., and Izatt, J. A. (2005). Spectral-domain phase microscopy. *Opt. Lett.* **30,** 1162–1164.

Conlon, I. J., Dunn, G. A., Mudge, A. W., and Raff, M. C. (2001). Extracellular control of cell size. *Nat. Cell Biol.* **3,** 918–921.

Creath, K. (1988). Phase-measurement interferometry techniques. *Prog. Opt.* **26,** 349–393.

Cuche, E., Bevilacqua, F., and Depeursinge, C. (1999). Digital holography for quantitative phase-contrast imaging. *Opt. Lett.* **24,** 291–293.

Czirok, A., Schlett, K., Madarasz, E., and Vicsek, T. (1998). Exponential distribution of locomotion activity in cell cultures. *Phys. Rev. Lett.* **81,** 3038–3041.

Dao, M., Lim, C. T., and Suresh, S. (2003). Mechanics of the human red blood cell deformed by optical tweezers. *J. Mech. Phys. Solids* **51,** 2259–2280.

Davies, H. G., and Wilkins, M. H. F. (1952). Interference microscopy and mass determination. *Nature* **161,** 541.

deBoer, J. F., Milner, T. E., vanGemert, M. J. C., and Nelson, J. S. (1997). Two-dimensional birefringence imaging in biological tissue by polarization-sensitive optical coherence tomography. *Opt. Lett.* **22,** 934–936.

Devaney, A. J. (1982). A filtered back-propagation algorithm for diffraction tomography. *Ultrason. Imaging* **4,** 336–350.

Devaney, A. J. (1984). Geophysical diffraction tomography. *IEEE Trans. Geosci. Remote Sens.* **22,** 3–13.

Discher, D. E., Mohandas, N., and Evans, E. A. (1994a). Molecular maps of red cell deformation: Hidden elasticity and *in situ* connectivity. *Science* **266,** 1032–1035.

Discher, D. E., Mohandas, N., and Evans, E. A. (1994b). Molecular maps of red cell deformation: Hidden elasticity and *in situ* connectivity. *Science* **266,** 1032–1035.

Drezek, R., Dunn, A., and Richards-Kortum, R. (1999). Light scattering from cells: Finite-difference time-domain simulations and goniometric measurements. *Appl. Opt.* **38,** 3651–3661.

Dunn, G. A., and Zicha, D. (2004). Timeline—Cell motility under the microscope: Vorsprung durch Technik. *Nat. Rev. Mol. Cell Biol.* **5,** 667–672.

Dunn, G. A., and Zicha, D. (1995). Dynamics of Fibroblast Spreading. *J. Cell Sci.* **108,** 1239–1249.

Dunn, G. A., and Zicha, D. (eds.), (1997). Using DRIMAPS system of transmission interference microscopy to study cell behavior. Academic press.

Dunn, G. A., Zicha, D., and Fraylich, P. E. (1997). Rapid, microtubule-dependent fluctuations of the cell margin. *J. Cell Sci.* **110,** 3091–3098.

Engelhardt, H., Gaub, H., and Sackmann, E. (1984a). Viscoelastic properties of erythrocyte membranes in high-frequency electric fields. *Nature* **307,** 378–380.

Engelhardt, H., Gaub, H., and Sackmann, E. (1984b). Viscoelastic properties of erythrocyte membranes in high-frequency electric fields. *Nature* **307,** 378–380.

Engelhardt, H., and Sackmann, E. (1988). On the measurement of shear elastic moduli and viscosities of erythrocyte plasma membranes by transient deformation in high frequency electric fields. *Biophys. J.* **54,** 495–508.

Fang-Yen, C., Chu, M. C., Seung, H. S., Dasari, R. R., and Feld, M. S. (2004). Noncontact measurement of nerve displacement during action potential with a dual-beam low-coherence interferometer. *Opt. Lett.* **29,** 2028–2030.

Gabor, D. (1948). A new microscopic principle. *Nature* **161,** 777.

Gail, M. H., and Boone, C. W. (1970). Locomotion of mouse fibroblasts in tissue culture. *Biophys. J.* **10,** 981–993.

Gbur, G., and Wolf, E. (2001). Relation between computed tomography and diffraction tomography. *J. Opt. Soc. Am. A* **18,** 2132–2137.

Goodman, J. W., and Lawrence, R. W. (1967). Digital image formation from electronically detected holograms. *Appl. Phys. Lett.* **11,** 77.

Gov, N. (2004). Membrane undulations driven by force fluctuations of active proteins. *Phys. Rev. Lett.* **93,** 268104.

Gov, N., Zilman, A. G., and Safran, S. (2003b). Cytoskeleton confinement and tension of red blood cell membranes. *Phys. Rev. Lett.* **90,** 228101.

Gov, N. S., and Safran, S. A. (2005). Red blood cell membrane fluctuations and shape controlled by ATP-induced cytoskeletal defects. *Biophys. J.* **88,** 1859–1874.

Grueler, H. (1984). Analysis of cell movement. *Blood cells* **10,** 61–77.

Gureyev, T. E., Roberts, A., and Nugent, K. A. (1995a). Partially coherent fields, the transport-of-intensity equation, and phase uniqueness. *J. Opt. Soc. Am. A-Opt. Image Sci. Vis.* **12,** 1942–1946.

Gureyev, T. E., Roberts, A., and Nugent, K. A. (1995b). Phase retrieval with the transport-of-intensity equation—Matrix solution with use of zernike polynomials. *J. Opt. Soc. Am. A-Opt. Image Sci. Vis.* **12,** 1932–1941.

Hammer, M., Schweitzer, D., Michel, B., Thamm, E., and Kolb, A. (1998). Single scattering by red blood cells. *Appl. Opt.* **37,** 7410–7418.

Hitzenberger, C. K., and Fercher, A. F. (1999). Differential phase contrast in optical coherence tomography. *Opt. Lett.* **24,** 622–624.

Hochmuth, R. M., and Waugh, R. E. (1987). Erythrocyte membrane elasticity and viscocity. *Ann. Rev. Physiol.* **49,** 209–219.

Hochmuth, R. M., Worthy, P. R., and Evans, E. A. (1979). Red cell extensional recovery and the determination of membrane viscosity. *Biophys. J.* **26,** 101–114.

Huang, D., Swanson, E. A., Lin, C. P., Schuman, J. S., Stinson, W. G., Chang, W., Hee, M. R., Flotte, T., Gregory, K., Puliafito, C. A., and Fujimoto, J. G. (1991). Optical coherence tomography. *Science* **254,** 1178–1181.

Ikeda, T., Popescu, G., Dasari, R. R., and Feld, M. S. (2005). Hilbert phase microscopy for investigating fast dynamics in transparent systems. *Opt. Lett.* **30,** 1165–1168.

Ingber, D. E. (1990). Fibronectin controls capillary endothelial cell growth by modulating cell shape. *Proc. Natl. Acad. Sci. USA* **87,** 3579–3583.

Ishimaru, A. (1978). "Wave Propagation and Scattering in Random Media." Academic Press, New York.

Iwai, H., Fang-Yen, C., Popescu, G., Wax, A., Badizadegan, K., Dasari, R. R., and Feld, M. S. (2004). Quantitative phase imaging using actively stabilized phase-shifting low-coherence interferometry. *Opt. Lett.* **29,** 2399–2401.

Joo, C., Akkin, T., Cense, B., Park, B. H., and de Boer, J. E. (2005). Spectral-domain optical coherence phase microscopy for quantitative phase-contrast imaging. *Opt. Lett.* **30,** 2131–2133.

Kaizuka, Y., and Groves, J. T. (2006). Hydrodynamic damping of membrane thermal fluctuations near surfaces imaged by fluorescence interference microscopy. *Phys. Rev. Lett.* **96,** 118101.

Kim, J., Telenkov, S. A., and Milner, T. E. (2004). Measurement of thermo-refractive and thermo-elastic changes in a tissue phantom using differential phase optical coherence tomography. *Lasers Surg. Med.* 8–8.

Lai, J. C., Li, Z. H., Wang, C. Y., and He, A. Z. (2005). Experimental measurement of the refractive index of biological tissue's by total internal reflection. *Appl. Opt.* **44,** 1845–1849.

Lauer, V. (2002). New approach to optical diffraction tomography yielding a vector equation of diffraction tomography and a novel tomographic microscope. *J. Microsc-Oxford* **205,** 165–176.

Lim, H. W. G., Wortis, M., and Mukhopadhyay, R. (2002). Stomatocyte-discocyte-echinocyte sequence of the human red blood cell: Evidence for the bilayer- couple hypothesis from membrane mechanics. *Proc. Natl. Acad. Sci. USA* **99,** 16766–16769.

Lipowski, R., and Girardet, M. (1990). Shape fluctuations of polymerized or solidlike membranes. *Phys. Rev. Lett.* **65,** 2893–2896.

Lipowsky, R. (1991). The conformation of membranes. *Nature* **349,** 475–481.

Liu, H., Beauvoit, B., Kimura, M., and Chance, B. (1996). Dependence of tissue optical properties on solute-induced changes in refractive index and osmolarity. *J. Biomed. Opt.* **1,** 200–211.

Lue, N., Bewersdorf, J., Lessard, M. D., Badizadegan, K., Dasari, K., Feld, M. S., and Popescu, G. (2007a). Tissue refractometry using Hilbert phase microscopy. *Opt. Lett.* **32,** 3522.

Lue, N., Choi, W., Popescu, G., Dasari, R. R., Badizadegan, K., and Feld, M. S. (2007b). Quantitative phase imaging of live cells using fast Fourier phase microscopy. *Appl. Opt.* **46,** 1836.

Lue, N., Popescu, G., Ikeda, T., Dasari, R. R., Badizadegan, K., and Feld, M. S. (2006). Live cell refractometry using microfluidic devices. *Opt. Lett.* **31,** 2759.

Maier, J. S., Walker, S. A., Fantini, S., Franceschini, M. A., and Gratton, E. (1994). Possible correlation between blood-glucose concentration and the reduced scattering coefficient of tissues in the near-infrared. *Opt. Lett.* **19,** 2062–2064.

Maini, P. K., McElwain, D. L., and Leavesley, D. I. (2004). Traveling wave model to interpret a wound-healing cell migration assay for human peritoneal mesothelial cells. *Tissue Eng.* **10,** 475–482.

Mann, C. J., Yu, L. F., Lo, C. M., and Kim, M. K. (2005a). High-resolution quantitative phase-contrast microscopy by digital holography. *Opt. Express* **13,** 8693–8698.

Mann, C. J., Yu, L. F., Lo, C. M., and Kim, M. K. (2005b). High-resolution quantitative phase-contrast microscopy by digital holography. *Opt. Express* **13,** 8693–8698.

Marquet, P., Rappaz, B., Magistretti, P. J., Cuche, E., Emery, Y., Colomb, T., and Depeursinge, C. (2005). Digital holographic microscopy: A noninvasive contrast imaging technique allowing quantitative visualization of living cells with subwavelength axial accuracy. *Opt. Lett.* **30,** 468–470.

Matarrese, P., Straface, E., Pietraforte, D., Gambardella, L., Vona, R., Maccaglia, A., Minetti, M., and Malorni, W. (2005). Peroxynitrite induces senescence and apoptosis of red blood cells through the activation of aspartyl and cysteinyl proteases. *FASEB J.* **19,** 416–418.

Miller, M. J., Wei, S. H., Parker, I., and Cahalan, M. D. (2002). Two-photon imaging of lymphocyte motility and antigen response in intact lymph node. *Science* **296,** 1869–1873.

Mombach, J. C. M., and Glazier, J. A. (1996). Single cell motion in aggregates of embryonic cells. *Phys. Rev. Lett.* **76,** 3032–3035.

Mourant, J. R., Canpolat, M., Brocker, C., Esponda-Ramos, O., Johnson, T. M., Matanock, A., Stetter, K., and Freyer, J. P. (2000). Light scattering from cells: The contribution of the nucleus and the effects of proliferative status. *J. Biomed. Opt.* **5,** 131–137.

Nowakowski, R., Luckham, P., and Winlove, P. (2001). Imaging erythrocytes under physiological conditions by atomic force microscopy. *Biochim. Biophys. Acta* **1514,** 170–176.

Paganin, D., and Nugent, K. A. (1998). Noninterferometric phase imaging with partially coherent light. *Phys. Rev. Lett.* **80,** 2586–2589.

Park, J., Kemp, N. J., Milner, T. E., and Rylander, H. G. (2003). Analysis of the phase retardation in the retinal nerve fiber layer of cynomolus monkey by polarization sensitive optical coherence tomography. *Lasers Surg. Med.* 55–55.

Park, Y. K., Diez-Silva, M., Popescu, G., Lykotrafitis, G., Choi, W., Feld, M. S., and Suresh, S. Measurement of red blood cell mechanics during morphological changes. *Nat. Mat*. Submitted for Publication.

Park, Y. K., Popescu, G., Badizadegan, K., Dasari, R. R., and Feld, M. S. (2006). "Diffraction phase and fluorescence microscopy". *Opt. Exp.* **14,** 8263.

Park, Y. K., Popescu, G., Dasari, R. R., Badizadegan, K., and Feld, M. S. (2007). Fresnel particle tracking in three dimensions using diffraction phase microscopy. *Opt. Lett.* **32,** 811.

Park, Y. K., Diez-Silva, M., Popescu, G., Lykotrafitis, G., Choi, W., Feld, M. S., and Suresh, S. (2008). Refractive index maps and membrane dynamics of human red blood cells parasitized by Plasmodium falciparum. *Proc. Natl. Acad. Sci. USA* **105,** 13730.

Popescu, G., Badizadegan, K., Dasari, R. R., and Feld, M. S. (2006a). Observation of dynamic subdomains in red blood cells. *J. Biomed. Opt. Lett.* **11,** 040503.

Popescu, G., Deflores, L. P., Vaughan, J. C., Badizadegan, K., Iwai, H., Dasari, R. R., and Feld, M. S. (2004). Fourier phase microscopy for investigation of biological structures and dynamics. *Opt. Lett.* **29,** 2503–2505.

Popescu, G., Ikeda, T., Best, C. A., Badizadegan, K., Dasari, R. R., and Feld, M. S. (2005). Erythrocyte structure and dynamics quantified by Hilbert phase microscopy. *J. Biomed. Opt. Lett.* **10,** 060503.

Popescu, G., Ikeda, T., Dasari, R. R., and Feld, M. S. (2006b). Diffraction phase microscopy for quantifying cell structure and dynamics. *Opt. Lett.* **31,** 775–777.

Popescu, G., Ikeda, T., Goda, K., Best-Popescu, C. A., Laposata, M., Manley, S., Dasari, R. R., Badizadegan, K., and Feld, M. S. (2006c). Optical measurement of cell membrane tension. *Phys. Rev. Lett.* **97,** 218101.

Popescu, G., Park, Y. K., Choi, W., Dasari, R. R., Feld, M. S., and Badizadegan, K. (2008). Imaging red blood cell dynamics by quantitative phase microscopy. *Blood Cells Mol. Dis.*

Rappaz, B., Marquet, P., Cuche, E., Emery, Y., Depeursinge, C., and Magistretti, P. J. (2005). Measurement of the integral refractive index and dynamic cell morphometry of living cells with digital holographic microscopy. *Opt. Exp.* **13,** 9361–9373.

Rylander, C. G., Dave, D. P., Akkin, T., Milner, T. E., Diller, K. R., and Welch, A. J. (2004). Quantitative phase-contrast imaging of cells with phase-sensitive optical coherence microscopy. *Opt. Lett.* **29,** 1509–1511.

Sackmann, E. (1996). Supported membranes: Scientific and practical applications. *Science* **271,** 43–48.

Slaney, M., Kak, A. C., and Larsen, L. E. (1984). Limitations of Imaging with 1st-Order Diffraction Tomography. *IEEE Trans. Microwave Theory Tech.* **32,** 860–874.

Smith, F. H. (1955). Microscopic interferometry. *Res. (Lond.)* **8,** 385.

Stephens, D. J., and Allan, V. J. (2003). Light microscopy techniques for live cell imaging. *Science* **300,** 82–86.

Strey, H., Peterson, M., and Sackmann, E. (1995). Measurement of erythrocyte membrane elasticity by flicker eigenmode decomposition. *Biophys. J.* **69,** 478–488.

Suresh, S., Spatz, J., Mills, J. P., Micoulet, A., Dao, M., Lim, C. T., Beil, M., and Seufferlein, T. (2005). Connections between single-cell biomechanics and human disease states: Gastrointestinal cancer and malaria. *Acta Biomater.* **1,** 15–30.

Tearney, G. J., Brezinski, M. E., Southern, J. F., Bouma, B. E., Hee, M. R., and Fujimoto, J. G. (1995). Determination of the refractive-index of highly scattering human tissue by optical coherence tomography. *Opt. Lett.* **20,** 2258–2260.

Tsallis, C. (1988). Possible generalization of Boltzmann-Gibbs statistics. *J. Statistical Phys.* **52,** 479–487.

Tuchin, V. V. (2000). "Tissue Optics." SPIE- The International Society for Optical Engineering.
Upadhyaya, A., Rieu, J. P., Glazier, J. A., and Sawada, Y. (2001). Anomalous diffusion and non-Gaussian velocity distribution of Hydra cells in cellular aggregates. *Physica A* **549,** 549–558.
van de Hulst, H. C. (1981). "Light Scattering by Small Particles." Dover Publications.
Wedberg, T. C., Stamnes, J. J., and Singer, W. (1995). Comparison of the filtered backpropagation and the filtered backprojection algorithms for quantitative tomography. *Appl. Opt.* **34,** 6575–6581.
Weiss, P., and Garber, B. (1952). Shape and movement of mesenchyme cells as functions of the physical structure of the medium. *Contrib. Quant. Morphol. PNAS* **38,** 264–280.
Whitesides, G. M., Ostuni, E., Takayama, S., Jiang, X., and Ingber, D. E. (2001). Soft lithography in biology and biochemistry. *Annu. Rev. Biomed. Eng.* **3,** 335–373.
Wolf, E. (1969). Three-dimensional structure determination of semi-transparent objects from holographic data. *Opt. Commun.* **1,** 153.
Yamaguchi, I., and Zhang, T. (1997). Phase-shifting digital holography. *Opt. Lett.* **22,** 1268–1270.
Yang, C., Wax, A., Hahn, M. S., Badizadegan, K., Dasari, R. R., and Feld, M. S. (2001). Phase-referenced interferometer with subwavelength and subhertz sensitivity Appl. to the study of cell membrane dynamics. *Opt. Lett.* **26,** 1271–1273.
Yang, C. H., Wax, A., Georgakoudi, I., Hanlon, E. B., Badizadegan, K., Dasari, R. R., and Feld, M. S. (2000). Interferometric phase-dispersion microscopy. *Opt. Lett.* **25,** 1526–1528.
Youn, J. I., Akkin, T., Wong, B. J. F., Peavy, G. M., and Milner, T. E. (2003). Electrokinetic measurements of cartilage measurements of cartilage using differential phase optical coherence tomography. *Lasers Surg. Med.* 56–56.
Zaman, M. H., Kamm, R. D., Matsudaira, P., and Lauffenburger, D. A. (2005). Computational model for cell migration in three-dimensional matrices. *Biophys. J.* **89,** 1389–1397.
Zeman, K., Engelhard, H., and Sackmann, E. (1990). Bending undulations and elasticity of the erythrocyte-membrane-effects of cell-shape and membrane organization. *Eur. Biophys. J.* **18,** 203–219.
Zernike, F. (1955). How I discovered phase contrast. *Science* **121,** 345.
Zicha, D., and Dunn, G. A. (1995). An image-processing system for cell behavior studies in subconfluent cultures. *J. Microsc.* **179,** 11–21.
Zicha, D., Genot, E., Dunn, G. A., and Kramer, I. M. (1999). TGF beta 1 induces a cell-cycle-dependent increase in motility of epithelial cells. *J. Cell Sci.* **112,** 447–454.
Zidovska, A., and Sackmann, E. (2006). Brownian motion of nucleated cell envelopes impedes adhesion. *Phys. Rev. Lett.* **96,** 048103.
Zilker, A., Engelhardt, H., and Sackmann, E. (1987). Dynamic reflection interference contrast (Ric-) microscopy—A new method to study surface excitations of cells and to measure membrane bending elastic-moduli. *J. Phys.* **48,** 2139–2151.
Zilker, A., Ziegler, M., and Sackmann, E. (1992). Spectral-analysis of erythrocyte flickering in the 0.3–4-Mu-M-1 regime by microinterferometry combined with fast image-processing. *Phys. Rev. A* **46,** 7998–8002.
Zysk, A. M., Reynolds, J. J., Marks, D. L., Carney, P. S., and Boppart, S. A. (2003). Projected index computed tomography. *Opt. Lett.* **28,** 701–703.

CHAPTER 6

Fourier Imaging Correlation Spectroscopy for Cellular Structure–Function

Eric N. Senning, Geoffrey A. Lott, and Andrew H. Marcus

Department of Chemistry
Oregon Center for Optics
University of Oregon
Eugene, Oregon 970403

Abstract

Experiments that optically probe the dynamics of intracellular species, including the center-of-mass displacements and internal conformational transitions of biological macromolecules, have the potential to study mechanisms of biochemical processes in living cells. This chapter reviews Fourier imaging correlation spectroscopy (FICS), a novel phase-selective approach to fluorescence fluctuation spectroscopy that measures the collective coordinate fluctuations from a large population of fluorescent species ($N \sim 10^6$). In FICS experiments, a spatially

METHODS IN CELL BIOLOGY, VOL. 90

0091-679X/08 $35.00
DOI: 10.1016/S0091-679X(08)00806-6

modulated optical grating excites a fluorescently labeled sample. Phase-synchronous detection of the fluorescence, with respect to the phase of the exciting optical grating, can be used to monitor the fluctuations of partially averaged spatial coordinates. From these data are constructed two-point space-time correlation functions and probability distributions. FICS achieves a unique balance between signal-to-noise and signal information content. It represents a route to elevate signal levels, while acquiring detailed information about molecular coordinate trajectories.

I. Introduction and Background

In densely crowded macromolecular suspensions, molecular motions are often temporally and spatially correlated. In living cells, molecular motions are further complicated by a dispersion of molecular sizes and shapes, cell compartmental organization, and the influence of cytoskeletal-related proteins. Experiments that optically probe the motions of intracellular species can quantify such motions, and thus, shed light on the underlying mechanisms of intracellular transport. Similarly, experiments that determine center-of-mass motions and internal conformational transitions of biological macromolecules have the potential to examine mechanisms of biochemical activity in living cells.

Single-molecule imaging (SMI) experiments (Weiss, 2000), which observe the fluorescence fluctuations of individual labeled macromolecules and fluorescence correlation spectroscopy (FCS) (Haustein and Schwille, 2004), which measures fluctuations from many molecules in a tightly focused laser spot, are established methods to study the dynamics of intracellular species. Both methods use low intensity fluorescence fluctuations from the illuminated sample to obtain information about equilibrium molecular processes, such as center-of-mass diffusion and molecular conformational transitions. When used to perform studies in ultra-pure solutions and buffers, SMI and FCS can reveal details of molecular processes that are otherwise impossible to observe by conventional methods. Nevertheless, application to *in vivo* studies are hampered by additional limitations: (i) weak fluorescence signals, due to low fluorophore concentrations; (ii) high background scattering, due to the optical dispersion of the heterogeneous intracellular environment; and (iii) rapid sample photo-degradation, due to the use of high laser intensities to overcome the signal-to-noise (S/N) constraints of (i) and (ii). The significance of points (i)–(iii) concerns the practical trade-off between the S/N ratio, and the extent to which the signal is averaged over microscopic molecular coordinates, which results in the course graining of microscopic information. For example, in state-of-the-art SMI, the positions and/or spectral properties of individual molecules are tracked in time, using a microscope. The SMI observables are the nanometer center-of-mass displacements of individual molecules, with temporal and spatial resolution determined by the S/N. In contrast, FCS achieves a high dynamic range by spatially integrating the emission from many molecules, which

are illuminated by a tightly focused laser beam. Although precise information about molecular coordinates is "blurred" by the spatial integration of the measurement, the S/N ratio is enhanced by the factor N, corresponding to the number of molecules within the observation volume. Thus, SMI and FCS exemplify two very different parameterizations to the problem of balancing S/N and the acquisition of detailed molecular coordinate information.

To improve on the capabilities of low signal *in vivo* measurements, it is useful to develop new ways to adjust the balance between S/N and the level of signal averaging over microscopic coordinates. This chapter reviews Fourier imaging correlation spectroscopy (FICS) (Fink and Marcus, 2008; Fink *et al.*, 2006; Grassman, Knowles, *et al.*, 2000; Knowles, Grassman, *et al.*, 2000; Knowles, Guenza, *et al.*, 2002; Knowles *et al.*, 2005; Senning *et al.*, 2008), a phase-selective approach to fluorescence fluctuation spectroscopy that is based on the principle that fluctuations in partially averaged microscopic coordinates can be monitored through variations of an optical signal phase. Unlike SMI and FCS, FICS obtains its signal from a relatively large sample volume, so that it does not share with these methods the advantage of spatial localization. The advantages of FICS are (i) that it boosts its S/N ($\propto \sqrt{\text{signal}}$) well above SMI values by observing a comparatively large number of fluorescent species ($N \sim 10^6$), thus facilitating studies in living cells; and (ii) that its signal represents a partial average over microscopic coordinates that retains significant detail about particle trajectories. In particular, the information provided by FICS is suitable to study temporal and spatial correlations of particle motions, in addition to conformational transitions of biological macromolecules.

II. Theoretical Descriptions of FICS

FICS has been used to study the motions of mitochondrial membranes in living cells (Knowles *et al.*, 2002; Margineantu, Capaldi, *et al.*, 2000). More recently, the FICS method was extended to perform low signal measurements of the diffusion of fluorescent proteins in dilute viscous solutions (Fink *et al.*, 2006). The theoretical principles of these measurements, including their applications to polarization resolved studies of intramolecular conformational transitions (Fink and Marcus, 2008), are described below.

A. FICS for Studies of Intracellular Dynamics of Organelles

As illustrated in Fig. 1A, two laser beams are crossed at the sample plane of a fluorescence microscope to create a spatially modulated intensity grating. The laser resonantly excites chromophore labels in the sample, and the backward emitted fluorescence is separated from the excitation light and focused onto a detector. Figure 1B and C schematically depict the overlap of the intensity grating with a population of biological cells, for which N intracellular compartments are

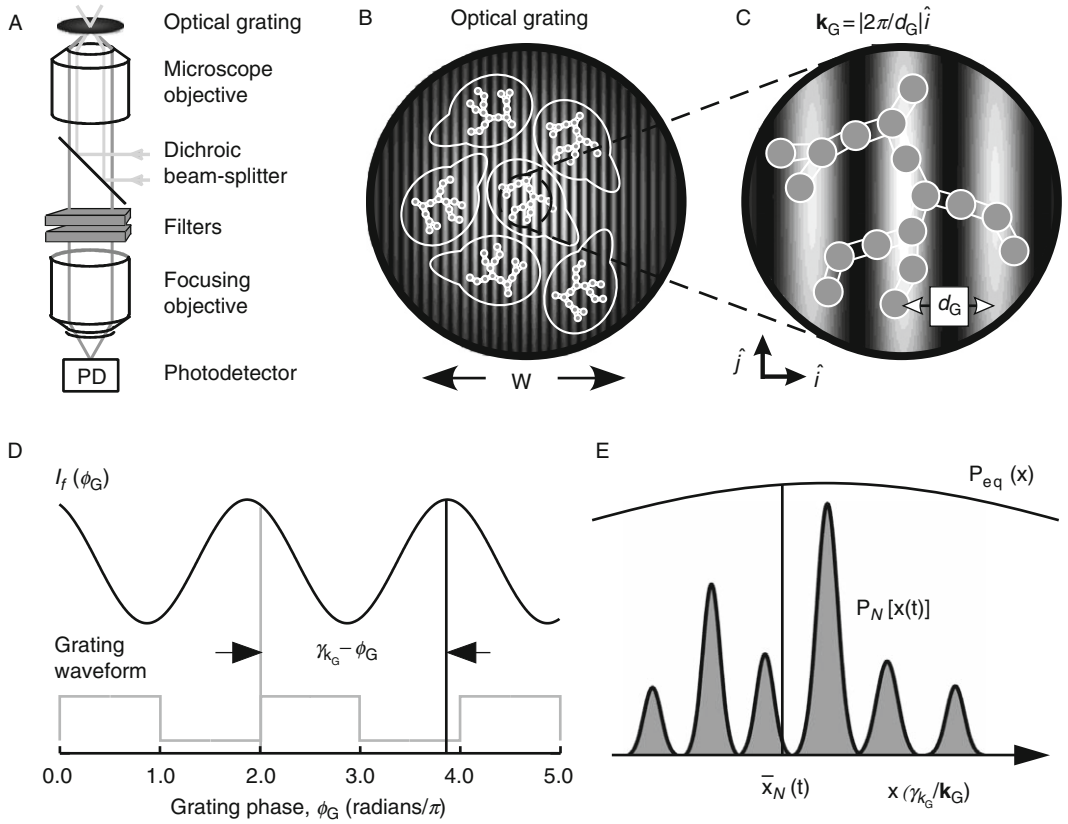

Fig. 1 Schematic diagram of the optical layout for FICS experiments, performed on fluorescently labeled yeast mitochondria. (A) The sample is placed at the focal plane of a fluorescence microscope. The excitation beams (light gray lines) are sent to a focusing objective using a dichroic beam-splitter, and create a spatially modulated intensity grating at the sample. The spatially integrated fluorescence (dark gray lines) is collected by the same objective and focused onto a photo-detector. (B) Condensed view of the focused laser spot with beam waist $\sim 50\ \mu$m. (C) Fluorescently labeled mitochondrial filaments, represented as N interconnected gray disks, are excited by the optical grating with fringe spacing d_G. Signal fluctuations occur as mitochondrial filaments move relative to one another. (D) Schematic of the total fluorescence intensity I_f as a function of the grating phase ϕ_G. The modulated component of the signal has phase $\gamma_{\mathbf{k}_G}$. (E) The signal phase is proportional to the mean position $\bar{x}_N(t)$ of the sampled particle distribution $P_N[x(t)]$. The sampled distribution is a time-dependent subset of the equilibrium distribution $P_{eq}(x)$.

fluorescently labeled (indicated by interconnected gray disks). The average separation between the fluorescent sites must be large enough to roughly match the optical fringe spacing ($d_G \simeq 0.5 - 5\ \mu$m), which can be adjusted by changing the angle between the intersecting laser beams. Typically, the beam waist ($w \simeq 35 - 100\ \mu$m) spans at least ten optical fringes, so that the illuminated sample encompasses a large volume $V \simeq 1500 - 80{,}000$ fL. Since $w \gg d_G$, we approximate the

intensity profile as an infinite plane wave, $I_L(\mathbf{r},\phi_G) = I_0[1 + \cos(\mathbf{k}_G \cdot \mathbf{r} + \phi_G)]$, where I_0 is a constant intensity level, $\mathbf{k}_G$ is the wave vector of the optical grating, and ϕ_G is the grating phase.

The fluorescence intensity I_f is proportional to the spatial overlap of the fluorescent particle sites with the optical grating intensity profile

$$I_f(\phi_G,t) = \int_{-\infty}^{\infty} I_L(r,\phi_G)c(r,t)dr. \quad (1)$$

Equation (1) defines the local particle concentration $c(\mathbf{r},t) = (1/V)\sum_{i=1}^{N} A_i\delta[\mathbf{r} - \mathbf{r}_i(t)]$, where the constants A_i represent the absorption/emission efficiencies of the individual sites and $\delta(x)$ is the Dirac delta function. After carrying out the spatial integration of Eq. (1), the fluorescence intensity takes the form (Fink *et al.*, 2006)

$$I_f(\phi_G,t) = I_0\langle c\rangle + I_0|\hat{c}_{k_G}(t)|\cos[\gamma_{k_G}(t) + \phi_G], \quad (2)$$

where $\langle c\rangle = (1/v)\sum_{i=1}^{N} A_i$ is the mean concentration, and $|\hat{c}_{k_G}(t)|$ and $\gamma_{k_G}(t)$ are, respectively, the amplitude and the phase of the spatial Fourier component of the local particle concentration:

$$\hat{c}_{k_G}(t) = \left(\frac{1}{2\pi}\right)^{3/2} \int_{-\infty}^{\infty} c(\mathbf{r},t)e^{-ik_G\cdot\mathbf{r}}d\mathbf{r} = \sum_{i=1}^{N} A_i\exp[i\mathbf{k}_G\cdot\mathbf{r}_i(t)]. \quad (3)$$

Equation (2) shows that the signal consists of two parts; a stationary (dc) background, proportional to N, and a ϕ_G-dependent (ac) term with amplitude $|\hat{c}_{k_G}(t)| \propto \sqrt{N}$. Figure 1D illustrates how the phase of the modulated fluorescence intensity is shifted by an amount $\gamma_{k_G}(t)$ relative to the phase of the optical grating. The FICS apparatus applies a sweep to the phase $\phi_G(t') = \omega_G t' + \phi_0$ at the carrier frequency $\omega_G/2\pi = 10$ MHz. The period of the modulation is much longer than the fluorescence lifetime, but short in comparison to the center-of-mass coordinate fluctuations. Phase-sensitive detection and low-pass filtering techniques are used to determine the "in-phase" $[X_{k_G}(t) \propto |\hat{c}_{k_G}(t)|\cos\gamma_{k_G}(t)]$ and the "in-quadrature" $[Y_{k_G}(t) \propto |\hat{c}_{k_G}(t)|\sin\gamma_{k_G}(t)]$ signal components. These two quadratures fully characterize the complex signal $X_{k_G}(t) + iY_{k_G}(t) = \hat{c}_{k_G}(t)$, which is equivalently specified by the amplitude $|\hat{c}_{k_G}(t)|$ and the phase $\gamma_{k_G}(t)$. It is important to note that the precision to which the signals are determined depends on the S/N ($\propto \sqrt{N}$) of a particular measurement. Because the signal is spatially integrated over a sample with $N \approx 10^6$, the enhancement of the S/N in comparison to single-particle measurements is about a 1000-fold.

Equation (3) shows that the time-dependence of $\hat{c}_{k_G}(t)$ arises due to particle coordinate fluctuations, which are projected onto the fringes of the optical grating. Since the grating wave vector $\mathbf{k}_G$ points in the $\hat{i}$-direction, only the x-components of the coordinates contribute to the signal. The N coordinates $\{x_1(t), x_2(t), \ldots,$

$x_N(t)\}$ fluctuate continuously about their mean values according to $x_i(t) = \delta x_i(t) + \langle x_i \rangle$. In Fig. 1E, we schematically represent a hypothetical continuous distribution $P_{eq}(x)$ that describes the equilibrium probability of observing a randomly selected particle with coordinate x, mean $\langle x \rangle_{eq} = \int_{-\infty}^{\infty} x P_{eq}(x) dx = 0$ and variance $\sigma_{eq}^2 = \int_{-\infty}^{\infty} x^2 P_{eq}(x) dx$. At a given instant, the FICS signal samples the Fourier transform $\hat{c}_{k_G}(t)$ of a subset $P_N[x(t)] = c(x,t) = (1/N)\sum_{i=1}^{N} A_i \delta[x - x_i(t)]$ of the equilibrium distribution. According to the central limit theorem, the sampled distribution has mean value $\bar{x}_N(t) = \sum_{i=1}^{N} x_i(t) P_N[x_i(t)]$ and variance $\sigma_N^2 = [\delta \bar{x}_N(t)]^2 = \sum_{i=1}^{N} x_i^2(t) P_N[x_i(t)] \propto \sigma_{eq}^2/N$, which is narrowed relative to the equilibrium distribution by the factor N^{-1}. According to Eq. (3), the FICS signal is a characteristic function of $P_N[x(t)] : \hat{c}_{k_G}(t) = \sum_{i=1}^{N} A_i e^{ik_G x_i(t)} = \sum_{i=1}^{N} P_N[x_i(t)] e^{ik_G x_i(t)}$. Using the theory of cumulants (Nitzan, 2006), the FICS signal can be Taylor expanded in terms of the raw moments of $P_N[x(t)]$:

$$\hat{c}_{k_G}(t) = \sum_{m=0}^{\infty} \frac{(ik_G)^m}{m!} \mu'_m, \text{ where } \mu'_m(t) = \int_{-\infty}^{\infty} x^m(t) P_N[x(t)] dx(t). \tag{4}$$

Alternatively, an expansion of the logarithm of $\hat{c}_{k_G}(t)$ defines the cumulants:

$$\ln \hat{c}_{k_G}(t) = \sum_{m=1}^{\infty} \frac{(ik_G)^m}{m!} \kappa_m(t). \tag{5}$$

A term-by-term comparison between Eqs. (4) and (5) leads to $\kappa_1(t) = \mu'_1(t) = \bar{x}_N(t)$ and $\kappa_2 = \mu'_2 - \mu'^2_1 = \langle [x_N(t) - \bar{x}_N(t)]^2 \rangle = [\delta \bar{x}_N(t)]^2$. A good approximation of $\hat{c}_{k_G}(t)$ is given by the cumulant expansion of Eq. (5), truncated at $m = 2$.

$$\hat{c}_{k_G}(t) \simeq \exp\left\{ ik_G \bar{x}_N(t) - \frac{1}{2} k_G^2 [\delta \bar{x}_N(t)]^2 \right\}. \tag{6}$$

Equation (6) shows that the measured phase and the amplitude of $\hat{c}_{k_G}(t)$ can be assigned to physical meanings: $\gamma_{k_G}(t) = k_G \bar{x}_N(t)$ and $|\hat{c}_{k_G}(t)| = \exp\left\{ -\frac{1}{2} k_G^2 [\delta \bar{x}_N(t)]^2 \right\}$, respectively. In this way, the FICS observable determines the size N of the sampled distribution {through the relationship $[\delta \bar{x}_N(t)]^2 \propto N^{-1}$}, and its mean value (illustrated in Fig. 1E).

B. Polarization-Selective FICS for Studies of Biomolecular Dynamics

In the above discussion, the number of fluorescent molecules that decorate each particle site is large ($\geq 10^3$), so that the system is optically isotropic. When the individual sites correspond to isolated fluorescent molecules, then the system has a continuously fluctuating steady-state anisotropy. If the polarizations of the exciting laser and the detected emission are specified, the FICS signal can contain information about molecular anisotropy fluctuations, in addition to center-of-mass motions. As discussed further below, the anisotropy fluctuations can reflect conformational transitions of appropriately labeled macromolecules.

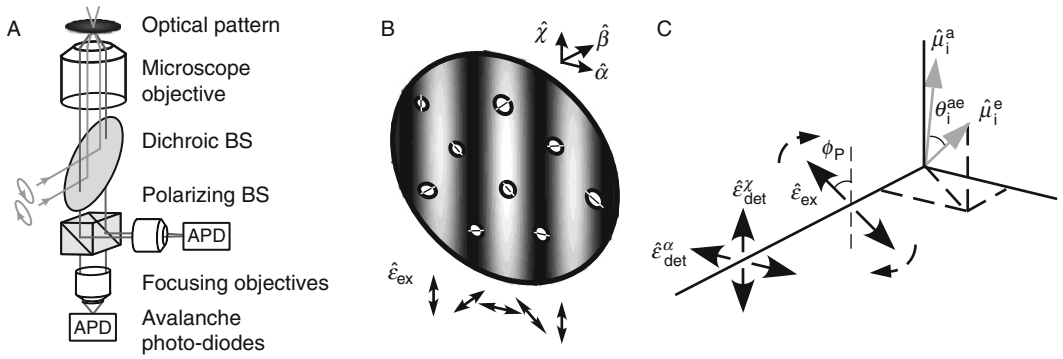

Fig. 2 (A) Schematic diagram of the optical layout for FICS experiments, performed on fluorescent proteins in dilute viscous solution. Two orthogonal, elliptically polarized laser beams are crossed at the sample plane of a fluorescence microscope. The spatially and temporally integrated fluorescence is split using a polarizing beam-splitter (BS), and detected in parallel using two synchronized photon-counting detectors. (B) At the sample, the superposition of the two laser beams creates (simultaneously) a spatially modulated intensity interference pattern and a plane polarization grating. Molecular chromophores are depicted as white circles bisected by line segments, indicating the orientations of transition dipoles. (C) Each optical chromophore is characterized by its absorption and emission dipole moments ($\hat{\mu}_i^a$ and $\hat{\mu}_i^e$, respectively), and its depolarization angle θ_i^{ae}. The two polarized emission signals are each projected onto orthogonal laboratory frame axes (labeled $\hat{\alpha}$ and $\hat{\chi}$).

In polarization-selective FICS, two orthogonal elliptically polarized laser beams are used to create the optical grating (Fig. 2A). The crossed beams simultaneously generate a linear polarization grating and an intensity interference pattern at the sample (Fig. 2B). The signal fluctuations arise from the combined projections of the molecular center-of-mass coordinates onto the intensity grating, and the transition dipole orientational coordinates onto the polarization grating. The polarized fluorescence is separated into laboratory frame orthogonal directions using a polarizing beam splitter, and both signals are phase-synchronously detected.

The plane-polarized fluorescence intensity from the ith molecule $A_i^{\alpha,\chi}(\theta_i^{ae},\phi_G)$ is proportional to $\langle |\,\hat{\varepsilon}_{ex}(\phi_P)\cdot\hat{\mu}_i^a\,|^2\,|\,\hat{\varepsilon}_{det}^{\alpha,\chi}\cdot\hat{\mu}_i^e\,|^2\rangle$, where $\hat{\mu}_i^a$ and $\hat{\mu}_i^e$ are the absorption and emission transition dipole moments, respectively, and the angle brackets $\langle\ldots\rangle$ indicate an orientational average over the distribution of absorption dipoles (Cantor and Schimmel, 1980). As illustrated in Fig. 2C, the laboratory frame detection electric field directions are given by $\hat{\varepsilon}_{det}^{\alpha}$ and $\hat{\varepsilon}_{det}^{\chi}$, and the rotating excitation field direction is given by $\hat{\varepsilon}_{ex}(\phi_P) = \sin\phi_P\hat{\alpha} + \cos\phi_P\hat{\chi}$. Assuming an isotropic distribution of absorption dipole moments, the orientational average leads to the following first-order approximations to the polarized, steady-state intensities (Senning and Marcus, 2008).

$$A_i^x(\theta_i^{ae},\phi_G) \simeq \left|\hat{\mu}_i^a\right|^2\left|\hat{\mu}_i^e\right|^2\left[\frac{17}{36} - \frac{23}{180}\cos(2\theta_i^{ae}) + \frac{2}{9}\cos\left(2\theta_i^{ae} - \frac{\phi_G}{2}\right)\right.$$
$$\left. - \frac{2}{45}\cos\left(2\theta_i^{ae} + \frac{\phi_G}{2}\right) - \frac{1}{36}\cos(\phi_G) + \frac{1}{24}\cos(2\theta_i^{ae} - \phi_G) - \frac{1}{360}\cos(2\theta_i^{ae} + \phi_G)\right], \tag{7}$$

and

$$A_i^{\alpha}(\theta_i^{ae},\phi_G) \simeq |\,\hat{\mu}_i^a\,|^2|\,\hat{\mu}_i^e\,|^2\left[\frac{17}{72}+\frac{23}{360}\cos(2\theta_i^{ae})-\frac{1}{9}\cos\left(2\theta_i^{ae}-\frac{\phi_G}{2}\right)\right.$$
$$\left.+\frac{1}{45}\cos\left(2\theta_i^{ae}+\frac{\phi_G}{2}\right)-\frac{1}{72}\cos(\phi_G)-\frac{1}{48}\cos(2\theta_i^{ae}-\phi_G)+\frac{1}{720}\cos(2\theta_i^{ae}+\phi_G)\right] \tag{8}$$

In Eqs. (7) and (8), θ_i^{ae} is the angle that subtends the absorption and emission dipole moments, and the excitation polarization angle, $\phi_{P,}$ is expressed in terms of the phase of the intensity pattern. Equations (7) and (8) also assume that the time scale of rotational diffusion is much longer than the fluorescence lifetime, which is typically a few nanoseconds.

The total fluorescence from the N molecules is obtained from the spatial integration of Eq. (1). In this case, the local concentration of excited molecules is polarization-dependent, that is, $c^{\alpha,\chi}(\mathbf{r},\theta^{ae}) = \frac{1}{V}\sum_{i=1}^{N} A_i^{\alpha,\chi}(\theta_i^{ae},\phi_G)\delta(\theta^{ae}-\theta_i^{ae})\delta(\mathbf{r}-\mathbf{r}_i)$. The total fluorescence is given by (Fink *et al.*, 2006)

$$I_f^{\alpha,\chi}(k_G,\phi_G,t) = \frac{1_0}{V}\sum_{i=1}^{N} A_i^{\alpha,\chi}[\theta_i^{ae}(t),\phi_G]\{1+\cos[k_G x_i(t)+\phi_G]\}. \tag{9}$$

Substitution of Eqs. (7) and (8) into Eq. (9) and the application of phase-sensitive detection techniques lead to the complex signals $[Z_{k_G}^{\alpha,\chi} = X_{k_G}^{\alpha,\chi} + iY_{k_G}^{\alpha,\chi}]$:

$$Z_{k_G}^{\chi}(t) \simeq \frac{I_0}{V}\sum_{i=1}^{N} |\,\hat{\mu}_i^a\,|^2|\,\hat{\mu}_i^e\,|^2\left\{\frac{1}{3}\exp i[k_G x_i(t)] - \frac{1}{2}\exp i\left[k_G x_i(t) - 2\theta_i^{ae}(t)\right]\right\}, \tag{10}$$

and

$$Z_{k_G}^{\alpha}(t) \simeq \frac{I_0}{V}\sum_{i=1}^{N} |\,\hat{\mu}_i^a\,|^2|\,\hat{\mu}_i^e\,|^2\left\{\frac{1}{6}\exp i[k_G x_i(t)] + \frac{1}{4}\exp i[k_G x_i(t) - 2\theta_i^{ae}(t)]\right\}. \tag{11}$$

Equations (10) and (11) are combined to isolate the local number density fluctuation $Z_{k_G}^{ND}(t) \equiv Z_{k_G}^{\chi}(t) + 2Z_{k_G}^{\alpha}(t) \propto \frac{I_0}{V}\sum_{i=1}^{N}|\,\hat{\mu}_i^a\,|^2|\,\hat{\mu}_i^e\,|^2\exp i[k_G x_i(t)]$, and the anisotropy density fluctuation $Z_{k_G}^{AD}(t) \equiv Z_{k_G}^{\chi}(t) - 2Z_{k_G}^{\alpha}(t) \propto \frac{I_0}{V}\sum_{i=1}^{N}|\,\hat{\mu}_i^a\,|^2|\,\hat{\mu}_i^e\,|^2 \exp i[-k_G x_i(t) - 2\theta_i^{ae}(t)]$. The number density fluctuation is identical to the local concentration defined by Eq. (3), which is well approximated by the truncated cumulant of Eq. (6). A similar treatment of the anisotropy density leads to the approximation

$$Z_{k_G}^{AD}(t) \simeq \exp\left\{i[k_G\bar{x}_N(t) + 2\bar{\theta}_N^{ae}(t)] - \frac{1}{2}[k_G\delta\bar{x}_N(t) + 2\delta\bar{\theta}_N^{ae}(t)]^2\right\}, \tag{12}$$

where the mean depolarization angle of the sampled distribution is given by $\bar{\theta}_N^{ae}(t) = \sum_{i=1}^{N}\theta_i^{ae}(t)P_N[\theta_i^{ae}(t)]$, and the variance is $[\delta\bar{\theta}_N^{ae}(t)]^2 = \sum_{i=1}^{N}[\theta_i^{ae}(t)]^2$

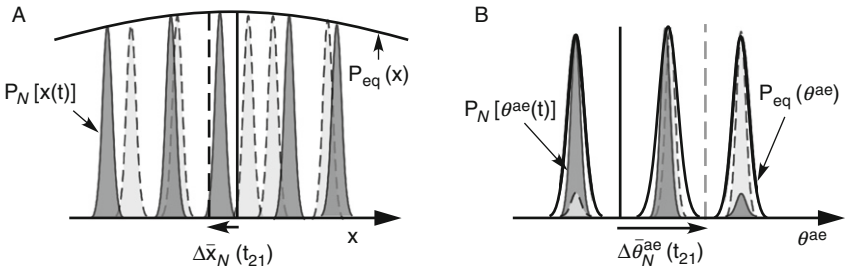

Fig. 3 Schematic illustration of the time-dependent mean coordinate fluctuations sampled using FICS. (A) A hypothetical sampled distribution of molecular center-of-mass coordinates $P_N[x(t)]$ is depicted as a sum of $N = 5$ discreet features. The sampled distributions are shown for two distinct times, which are distinguished by dark and light gray shading. As the molecular center-of-mass coordinates fluctuate, the mean sampled coordinate $\bar{x}_N(t)$ (indicated by solid and dashed vertical lines) explores the continuous equilibrium distribution. (B) A hypothetical sampled distribution of molecular depolarization angle coordinates $P_N[\theta^{ae}(t)]$ is depicted as a sum of $N = 3$ discreet features. As in (A), dark and light gray shaded distributions indicate two distinct times. Transitions between distinct conformational states give rise to time-dependent shifts in the sampled depolarization angle coordinate $\bar{\theta}^{ae}_N(t)$ (indicated by solid and dashed vertical lines).

$P_N[\theta^{ae}_i(t)]$. The argument of Eq. (12) generally contains coupling terms that are proportional to $k_G^2[\delta\bar{x}_N(t)]^2[\delta\bar{\theta}^{ae}_N(t)]^2$. Such terms vanish, if molecular center-of-mass positions are statistically uncorrelated with the depolarization angles. In this case, the anisotropy density fluctuation can be approximated by $Z^{AD}_{k_G}(t) = Z^{ND}_{k_G}(t)Z^A(t)$, where the anisotropy fluctuation is $Z^A(t) \propto \sum_{i=1}^{N} |\hat{\mu}^a_i|^2 |\hat{\mu}^e_i|^2 \exp i[2\theta^{ae}_i(t)]$. While both the number density and the anisotropy density fluctuations are $\mathbf{k}_G$-dependent, the anisotropy fluctuations are independent of the length scale probed.

C. Time-Dependent Coordinate Fluctuations, Measured by FICS

As discussed above, the FICS observables contain information about the mean and variance of the sampled distributions of fluctuating particle coordinates. Figure 3 illustrates schematically the relationships between hypothetical sampled distributions and their mean values, as a function of time. In Fig. 3A, the underlying particle distribution of center-of-mass coordinates $P_N[x(t)]$ is shown as the sum of N discreet features. A sampled distribution at one instant in time (shaded dark gray, solid outline) is compared to a sampled distribution at a later time (shaded light gray, dashed outline). If the particles can diffuse freely, then the equilibrium distribution $P_{eq}(x)$ is smooth and continuous, as shown. As individual particles undergo center-of-mass displacements, the mean sampled coordinate $\bar{x}_N(t)$ (indicated by a solid and dashed vertical line) fluctuates among the possible values specified by the equilibrium distribution. By comparing FICS measurements

performed at distinct times, the mean coordinate displacement $\Delta\bar{x}_N(t_{21}) = \bar{x}_N(t_2) - \bar{x}_N(t_1)$ is determined, where $t_{21} = t_2 - t_1$ is the time interval separating successive measurements. In Fig. 3B, a hypothetical equilibrium distribution of molecular depolarization angles $P_{\text{eq}}(\theta^{ae})$ is shown. For certain biological macromolecules, in which two coupled chromophore labels have well-defined relative orientations, the value of the depolarization angle can reflect the internal conformation of the macromolecule. In such cases, the equilibrium distribution $P_{\text{eq}}(\theta^{ae})$ describes the discreet set of possible conformations. The example of Fig. 3B shows this distribution with three possible conformational states. Underlying sampled distributions $P_N[\theta^{ae}(t)]$ (shaded dark and light gray) and their corresponding mean values $\bar{\theta}^{ae}_N(t)$ (vertical solid and dashed lines) are shown for two distinct times. Comparison between successive FICS measurements allows for the determination of the mean depolarization angle displacement $\Delta\bar{\theta}^{ae}_N(t_{21})$.

D. Two-Point Time-Correlation Functions and Distributions

A convenient characterization of the fluctuations in equilibrium systems is given by the two-point time-correlation function (2P-TCF) $\langle Z^*(0)Z(t_{21})\rangle = \lim -_{\tau\to\infty} \frac{1}{\tau}\int_0^\tau Z^*(t')Z(t_{21}+t')\mathrm{d}t'$, where the angle brackets indicate the integration over time, and $t_{21} = t_2 - t_1 \geq 0$ is the time interval separating two successive measurements. The cumulant approximations of Eqs. (6) and (12) suggest that the number density and anisotropy density 2P-TCFs can be written, respectively,

$$C^{(2)}_{ND}(t_{21}) = \langle Z^{ND^*}_{k_\mathrm{G}}(0)Z^{ND}_{k_\mathrm{G}}(t_{21})\rangle = \langle e^{-\frac{1}{2}k^2_\mathrm{G}\delta\Delta\bar{x}^2_N(t_{21})}\rangle\langle e^{ik_\mathrm{G}\Delta\bar{x}_N(t_{21})}\rangle, \tag{13}$$

and

$$C^{(2)}_{AD}(t_{21}) = \langle Z^{AD^*}_{k_\mathrm{G}}(0)Z^{AD}_{k_\mathrm{G}}(t_{21})\rangle = C^{(2)}_{ND}(t_{21})C^{(2)}_{A}(t_{21}), \tag{14}$$

where the second term on the right side of Eq. (14) is the anisotropy 2P-TCF:

$$C^{(2)}_{A}(t_{21}) = \langle Z^{A*}(0)Z^{A}(t_{21})\rangle = \langle e^{-2\delta\Delta\bar{\theta}^{ae2}_N(t_{21})}\rangle\langle e^{i2\Delta\bar{\theta}^{ae}_N(t_{21})}\rangle. \tag{15}$$

Equation (13) defines the mean center-of-mass displacement $\Delta\bar{x}_N(t_{21}) = \bar{x}_N(t_{21}) - \bar{x}_N(0)$ of the sampled distribution during the time interval t_{21}, and the variance of the displacement distribution $\delta\Delta\bar{x}^2_N(t_{21}) = [\Delta\bar{x}_N(t_{21})]^2$. Similar definitions hold for the mean depolarization displacement and its variance given in Eq. (15). Equations (13)–(15) assume statistical independence between the means and variances of the sampled distributions. The 2P-TCFs are generally complex-valued, with phase factors that depend on the mean coordinate displacements, and amplitudes that depend on the variances. These functions decay, on average, on a time scale for which the magnitude of the phase displacement exceeds $\sim\pi/4$. The number density 2P-TCF described by Eq. (13) is known as the self-part of the intermediate scattering function employed in liquid state theory (Berne and Pecora, 2000). For a system of freely diffusing noninteracting molecules, this

expression can be further simplified using the Gaussian model for single particle motion. Since the observation time scale is large compared to the relaxation time of the velocity autocorrelation function of molecular displacements, we may treat $\Delta\bar{x}_N(t_{21})$ as a Gaussian random variable. Equation (13) is then well approximated by $C^{(2)}_{ND}(t_{21}) \propto \exp[-k_G^2 D_s t_{21}]$, where D_s is the self-diffusion coefficient. Equation (14) suggests that we may isolate the anisotropy 2P-TCF by experimentally determining the ratio $C^{(2)}_{AD}(t_{21})/C^{(2)}_{ND}(t_{21})$. For systems in which particle displacements are highly correlated, deviations of $C^{(2)}_{ND}(t_{21})$ from the Gaussian model behavior is a quantitative measure of the time and length scales over which correlations are important.

While 2P-TCFs convey the average time scales of molecular parameter displacements, more detailed information about the weights and magnitudes of the sampled displacements are contained in two-point distribution functions (2P-DFs). For example, the distribution $P^{(2)}_N[\Delta\bar{x}_N(t_{21})]$ is defined such that $P^{(2)}_N[\Delta\bar{x}_N(t_{21})]\, d\Delta\bar{x}_N$ is the probability of sampling N molecules whose mean center-of-mass has undergone a displacement in the range $\Delta\bar{x}_N$ and $\Delta\bar{x}_N + d\Delta\bar{x}_N$, during the time interval t_{21}. This distribution can be constructed by sampling pair-wise products of the form $Z^{ND*}_{k_G}(0) Z^{ND}_{k_G}(t_{21}) = e^{-\frac{1}{2}k_G^2 \delta\Delta\bar{x}^2_N(t_{21})} e^{ik_G\Delta\bar{x}_N(t_{21})}$. From such two-point products are assembled histograms of the realizations of $\Delta\bar{x}_N(t_{21})$, weighted by the sampled inverse variance ($\propto N$). Referring to the central limit theorem, if $\Delta\bar{x}_N(t)$ behaves as a Gaussian random variable, the distribution $P^{(2)}_N[\Delta\bar{x}_N(t_{21})]$ is expected to be Gaussian and centered at $\langle\Delta\bar{x}_N\rangle = 0$. Furthermore, the variance of the sampled distribution is expected to scale linearly with time according to $\delta\Delta\bar{x}^2_N(t_{21}) = 2D_s t_{21}$, in analogy to the self-part of the van Hove correlation function (Berne and Pecora, 2000).

The joint distribution $P^{(21)}_N[\Delta\bar{x}_N(t_{21}); \Delta\bar{\theta}^{ae}_N(t_{21})]$ is related to the probability of sampling N molecules with mean depolarization angle $\Delta\bar{\theta}^{ae}_N(t_{21})$ and mean displacement $\Delta\bar{x}_N(t_{21})$, during the time interval t_{21}. The joint distribution is constructed by sampling products of the anisotropy density according to $Z^{AD*}_{\mathbf{k}_G}(0) Z^{AD}_{\mathbf{k}_G}(t_{21}) = e^{-\frac{1}{4}k_G^2 \delta\Delta\bar{x}^2_N(t_{21})} e^{-2\delta\Delta\bar{\theta}^{ae2}_N(t_{21})} \times e^{ik_G\Delta\bar{x}_N(t_{21})} e^{i2\Delta\bar{\theta}^{ae}_N(t_{21})} = Z^{ND*}_{k_G}(0) Z^{ND}_{k_G}(t_{21}) Z^{A*}(0)\, Z^{A}(t_{21})$. The factorization between the parameters $\Delta\bar{x}_N(t_{21})$ and $\Delta\bar{\theta}^{ae}_N(t_{21})$ implies that $P^{(2)}_N[\Delta\bar{x}_N(t_{21}); \Delta\bar{\theta}^{ae}_N(t_{21})] = P^{(2)}_N[\Delta\bar{x}_N(t_{21})] P^{(2)}_N[\Delta\bar{\theta}^{ae}_N(t_{21})]$, so that the 2P-DF for the anisotropy fluctuations can be isolated from the ratio $P^{(2)}_N[\Delta\bar{\theta}^{ae}_N(t_{21})] = P^{(2)}_N[\Delta\bar{x}_N(t_{21}); \Delta\bar{\theta}^{ae}_N(t_{21})] / P^{(2)}_N[\Delta\bar{x}_N(t_{21})]$.

III. FICS Optical Layout

Figure 4 shows a schematic diagram of a typical FICS apparatus. Further instrumental details are described by Fink *et al.* (2006). A plane polarized, continuous wave laser beam is split into two beam paths with orthogonal plane polarization components at the entrance of a Mach–Zehnder interferometer (MZI). Within each arm of the MZI are placed an acousto-optic Bragg cell (labeled AO1 and

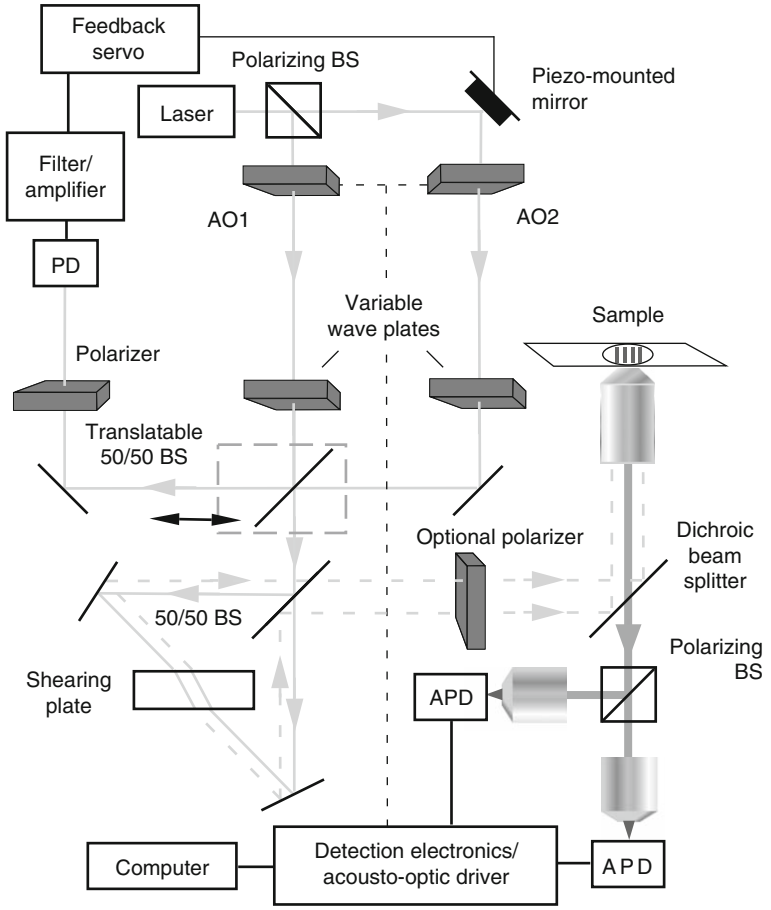

Fig. 4 Schematic diagram of the FICS optical layout (described in text). (Abbreviations have the following meanings: APD, avalanche photo-diode; PD, photo-diode; BS, beam-splitter; AO, acousto-optic Bragg cell.) See (Fink *et al.*, 2006) for further details.

AO2) and a variable wave plate polarization compensator. The AOs impart a time varying phase shift to their respective beams, while the variable wave plates are used to independently adjust the polarization states of each beam. The two beams are brought together at the exit of the MZI, with 50% of the output used to generate the excitation grating at the sample and the remaining light used to generate a reference signal for phase-synchronous detection and mechanical noise reduction. In order to routinely change the fringe spacing produced at the sample, the two input beams are sent through a second Sagnac interferometer. The counter-propagating beams travel through a shear plate, which has the effect of laterally separating the two beams. By manually adjusting the orientation of the shear plate, the incident angle of the beams at the sample can be changed, which determines the fringe spacing.

The precision of FICS measurements is limited by mechanical instabilities of the interferometers, which introduce noise in the interference pattern at the sample. To reduce mechanical noise, an active-feedback system is used to lock the phase of the optical grating in the sample (relative to that of the reference waveform) to within ~1/100 of the fringe spacing. A feedback signal, which is generated by comparing the phase of the modulated excitation intensity to that of the reference waveform, is used (via a Piezomounted optical mirror) to minimize the relative phase error (RPE). When the feedback circuit is engaged, fluctuations of the RPE occur on millisecond time scales with $\langle \mathrm{RPE}^2 \rangle^{1/2} \sim 3.9$ nm. In this case, $(3.9\ \mathrm{nm}/d_G)2\pi$ is the upper boundary to the precision that FICS phase measurements are sensitive.

IV. Examples of FICS Applications

A. Translational Fluctuations of Mitochondria in Living Cells

FICS experiments were conducted to study mitochondrial transport in human osteosarcoma cells (Knowles, Guenza, *et al.*, 2002; Margineantu *et al.*, 2000), and in the budding yeast, *Saccharomyces cerevisiae* (Senning and Marcus, 2008). Presented below is an example for the case of yeast. MATa strains were selected for their sensitivity to α factor, which shifts these cells into the mating phase of the cell cycle. Mitochondria were visualized by transforming cells using the plasmid pRS316, containing DsRed.T1 fused to the COX4 leader sequence. Cells were cultured to log phase in SD media, before treating them with 100 μM α factor for 2 h. Cells were depleted of microfilaments by treatment with Latrunculin-A at 200 μM for a 10-min incubation period. Samples were mounted onto a thin 3% agarose pad using SD media and 10 μM α factor, and sealed using valap to fuse the edges of a coverslip to the glass slide. Microtubules and/or actin microfilments were visualized by antibody staining with rat anti-α-tubulin (YOL 1/2 from clontech) or Alexa-phalloidin-542, followed with a 3.7% paraformaldehyde fixative treatment (Pringle *et al.*, 1991). Studies of the effects of cytoskeletal inhibiting drugs on mitochondrial motility were carried out at 25 °C.

To characterize the dependence of mitochondrial dynamics on cytoskeletal proteins in mating *S. cerevisiae*, cells were cultured to log phase before incubating them in 100 μM α factor for a period of 2 h. In Fig. 5 are shown fluorescence micrographs of typical specimens. For healthy yeast cells, mitochondrial structure is similar to that in higher organisms arrested in G1; a single interconnected network of tubular filaments constituting the reticulum morphology (Knowles, Guenza, *et al.*, 2002; Margineantu *et al.*, 2000) (see Fig. 5A, left inset). The right inset of Fig. 5A shows that the actin cytoskeleton in healthy cells is extensive and concentrated near the cell tip. Prominent features such as actin cables and patches are evident. For cells treated with the actin destabilizing agent Latrunculin-A, the mitochondrial reticulum morphology is disrupted, resulting in a population of intermediate size mitochondrial compartments (Fig. 5B, left inset). No trace of f-actin is detected in Lat-A treated cells (Fig. 5B, right inset).

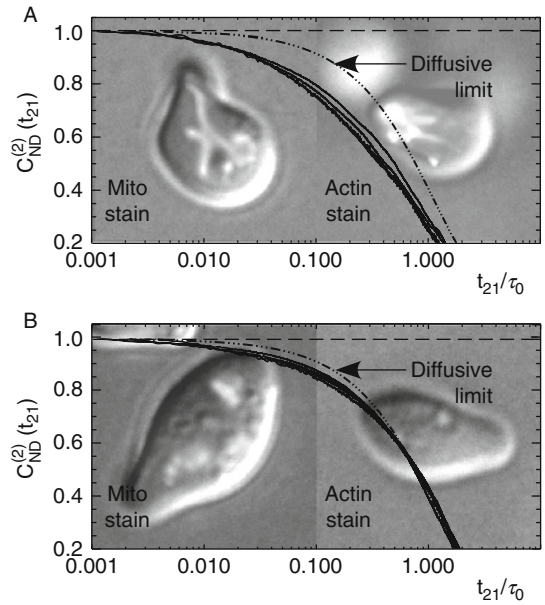

Fig. 5 d_G-dependent two-point time-correlation functions (2P-TCFs), $C^{(2)}_{ND}(t_{21})$, for mitochondria in mating yeast cells under varying cytoskeletal conditions. The time-axes are plotted in reduced time units, t_{21}/τ_0, with $\tau_0 = (k_G^2 D_0)^{-1}$ and $D_0 = 1.8 \times 10^{-4}\ \mu m^2\ s^{-1}$. The insets show fluorescence micrographs of typical specimens on which FICS experiments were conducted. (A) The mitochondria of healthy cells appear in the reticulum morphology with an extensive actin cytotoskeleton. (B) Cells treated with Latrunculin-A appear with mitochondria disrupted into smaller compartments, and the depletion of actin microfilaments. Each panel shows decays of $C^{(2)}_{ND}(t_{21})$ for measurements performed at four different length scales: $d_G = 0.6\ \mu m$, $0.79\ \mu m$, $1.03\ \mu m$, and $1.19\ \mu m$. In panel (A), the 2P-TCFs decay with increasing rate for decreasing values of d_G. In panel (B), the 2P-TCFs appear to decay independent of the value of d_G. In both panels, the dashed-dotted curves show the expected decay of a purely diffusive system with functional form $\exp(-t_{21}/\tau_0)$.

Figure 5 shows the decays of the 2P-TCFs $C^{(2)}_{ND}(t_{21})$ for mitochondrial displacements as a function of the reduced time variable t_{21}/τ_0, with $\tau_0 = (k_G^2 D_0)^{-1}$ and $D_0 = 1.8 \times 10^{-4}\ \mu m^2\ s^{-1}$. By plotting our data in this way, the 2P-TCFs are rescaled to eliminate length scale dependent contributions from random diffusion. For a system of independent Brownian particles, the 2P-TCFs measured at different length scales would all fall upon a single universal curve of the form $\exp(-t_{21}/\tau_0)$. We may thus, compare the length scale dependent differences in mitochondrial mobility due to the influence of cytoskeletal proteins. In panel (A), we plot the 2P-TCFs for healthy cells, and in panel (B), we plot those for cells depleted of microfilaments. From the results shown in panel (A), we see that the TCF's do not lie on a single universal curve, indicating that mitochondria in healthy cells exhibit a length-scale dependent mobility beyond the effects of simple diffusion. The TCF corresponding to $d_G = 1.19\ \mu m$ appears to decay more slowly than for those with $d_G = 0.60\ \mu m$ and $d_G = 0.79\ \mu m$, suggesting a trend of decreasing mobility

with increasing length-scales. For cells depleted of microfilaments, the length scale dependence of the 2P-TCFs vanishes almost completely. These data are compared to the single exponential decay $\exp(-t_{21}/\tau_0)$, corresponding to a simple diffusive limit, with time constant τ_0 approximating the $1/e$ time of the data shown in panel (B). We, further, compare this diffusive limit to data for healthy cells, shown in panel (A). It is noteworthy that the value used for D_0 is the same as that previously obtained in similar experiments conducted on G1 arrested osteosarcoma cells, which were treated with microfilament and microtubule destabilizing agents (Knowles, Guenza, *et al.*, 2002). This suggests that the intracellular environment experienced by mitochondria in the absence of microtubules and microfilaments is quite similar for yeast as for osteosarcoma cells.

B. Translation/Conformation Fluctuations of the Fluorescent Protein DsRed in Solution

FICS has been applied to study center-of-mass diffusion (Fink *et al.*, 2006), and slow polarization fluctuations resulting from the conformational transitions of DsRed, a multicolored fluorescent protein derived from the coral *Discosoma* sp. (Fink and Marcus, 2008; Senning *et al.*, 2008). Fluorescent proteins are widely used in biotechnological applications as reporters of gene expression and other singular events of cell activity (Giepmans *et al.*, 2006). It has been hypothesized that fluorescent proteins from reef-building corals function in an adaptive mechanism to optically interact and to regulate the symbiotic relationship between corals and photosynthetic algae (Field *et al.*, 2006). It is, therefore, interesting to examine in some detail, the conformational transitions that affect the protein's ability to transfer optical excitation energy, and to undergo fluorescence efficiently. DsRed has an exceptionally high extinction coefficient ($\varepsilon = 3 \times 10^5$ cm^{-1} M^{-1}, $\lambda_{ex} \sim 532$ nm), orange-red emission that is easily separated from excitation light, and a high fluorescence quantum yield ($q_f = 0.79$) (Shaner *et al.*, 2004).

In the following are presented FICS measurements of slow (~8 s) anisotropy fluctuations resulting from changes in the incoherent dipolar coupling between the adjacent chromophore sites of DsRed, which is a tetrameric complex of fluorescent protein subunits (Wall *et al.*, 2000). The cylinder-shaped subunits of the complex each contain an optical chromophore, with relative orientation of the transition dipole moments rigidly fixed. The DsRed molecules are free to diffuse in 95% glycerol/water solution. On the time scale of the fluorescence lifetime ($\tau_f \simeq 3.2$ ns) (Heikal *et al.*, 2000), rotational diffusion is very slow ($\tau_R \geq 100$ ns), so that the rate of fluorescence depolarization is not affected by molecular rotation. However, fluorescence depolarization is strongly influenced by intramolecular energy transfer (Heikal *et al.*, 2000). Because the relative distances and orientations between adjacent transition dipoles are small, an excited chromophore site can transfer its energy to one of its unexcited neighbors by a Förster dipole–dipole mechanism. When two sites in the DsRed complex are coupled, the excited state polarization rotates by the angle θ^{ae}, which subtends the absorption dipole moment of the initially excited chromophore and the emission dipole moment of the emitting

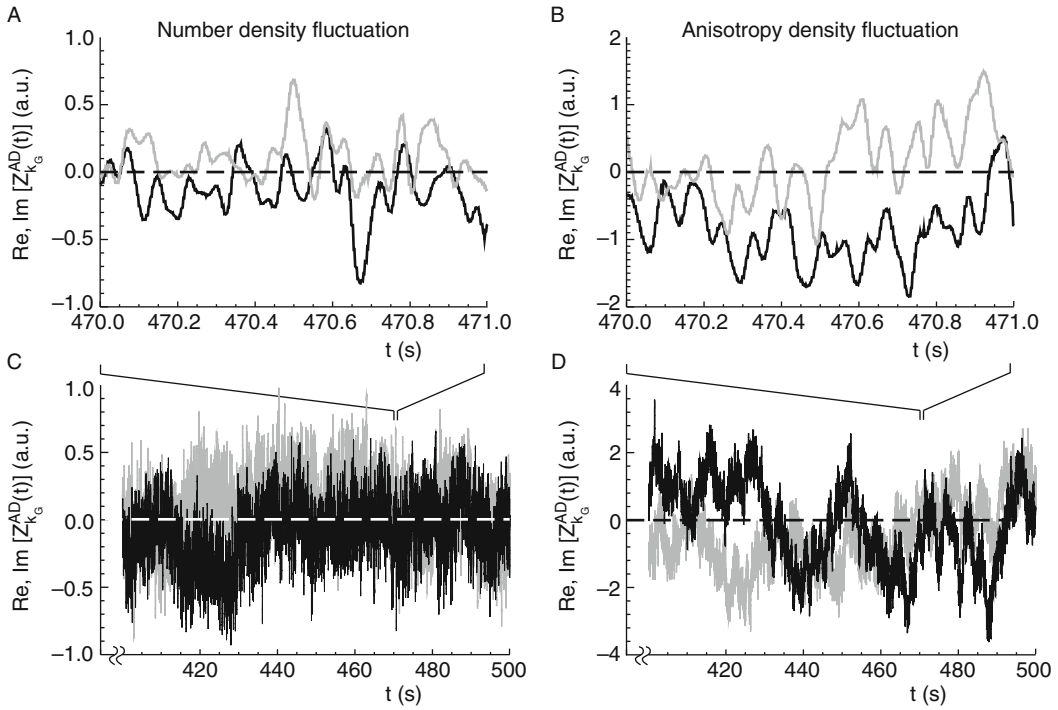

Fig. 6 Experimental trajectories of the number density fluctuation $Z^{ND}_{\mathbf{k}_G}(t)$ and the anisotropy density fluctuation $Z^{AD}_{\mathbf{k}_G}(t)$, constructed from demodulated polarized fluorescence signals, with $d_G = 2.12\ \mu$m. These measurements were recorded from a 10 nM solution of DsRed in 95% glycerol/water, at a frequency of 1 kHz, and over an acquisition period of 512 s. In panels (C) and (D), the final 100 s of the data run are shown. In panels (A) and (B), the time axis is expanded to show the variation over a 1-s time window. In each panel, the two signal quadratures, $\phi_G = 0, \pi/2$, are plotted in black and gray, respectively.

chromophore. Similar to the behavior of the green fluorescent protein (GFP), the individual fluorescent protein subunits of DsRed can undergo so-called "flickering" transitions between "bright" and "dark" states (Malvezzi-Campeggi *et al.*, 2001; Schenk *et al.*, 2004). A locally resonant site (i.e., a "bright" site) can reversibly interconvert to a nonresonant ("dark") site. As local sites flicker between "bright" and "dark" states, the populations of distinct pair-wise coupled conformations are also expected to fluctuate, leading to fluctuations of the polarized fluorescence.

In Fig. 6 are shown experimental trajectories of $Z^{ND}_{k_G}(t)$ and $Z^{AD}_{k_G}(t)$, constructed from the polarized signals, with $d_G = 2.12\ \mu$m. These data represent the final 100 s of an acquisition performed at a sampling rate of 1 kHz, and over a duration of 512 s. In the left column are shown the real and imaginary parts of the number density fluctuation; the top panel shows an expanded time axis, corresponding to a 1 s interval. In the right column are shown the real and imaginary parts of the

anisotropy density fluctuations. Both $Z_{k_G}^{ND}(t)$ and $Z_{k_G}^{AD}(t)$ exhibit rapid subsecond fluctuations, while the anisotropy density contains at least one additional, slow variation on the time scale of a few seconds.

From the experimental trajectories are calculated the normalized 2P-TCFs $C_{ND}^{(2)}(t_{21})$ and $C_{AD}^{(2)}(t_{21})$, defined by Eqs. (13) and (14), respectively. These are shown in Figs. 7A and B, displaced vertically for the five different fringe spacings

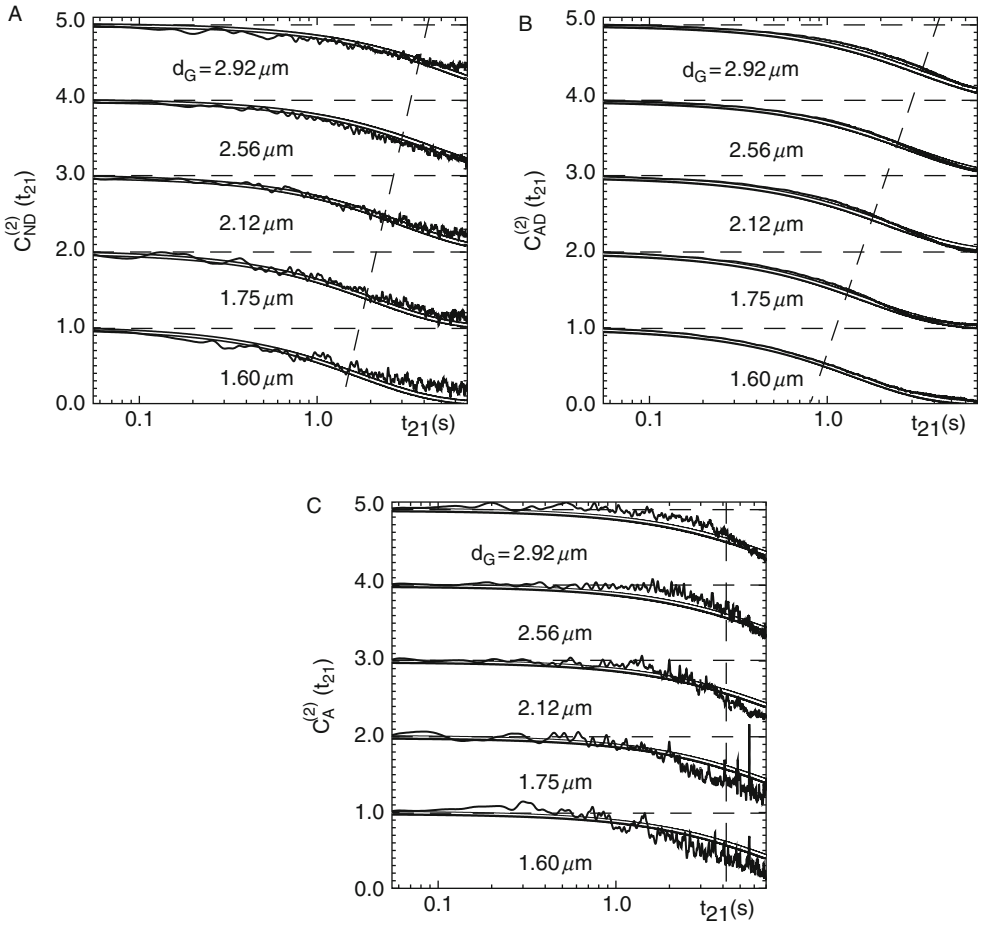

Fig. 7 d_G-dependent two-point time-correlation functions (2P-TCFs) of the number density and the anisotropy density fluctuations, $C_{ND}^{(2)}(t_{21})$ and $C_{AD}^{(2)}(t_{21})$, respectively Decays corresponding to different values of the fringe spacing d_G are vertically displaced. Diagonal and vertical dashed lines are guides to the eye to roughly indicate the decay time scale. In panel (A), we compare $C_{ND}^{(2)}(t_{21})$ to the Gaussian model for Fickian diffusion $\exp(-k_G^2 D_s t_{21})$, where $D_s = 3.7 \times 10^{-10}$ cm^2 s^{-1}. In panel (B), we compare $C_{AD}^{(2)}(t_{21})$ to the function $\exp[-(k_G^2 D_s + 1/\tau_A)t_{21}]$, where $\tau_A = 8$ s is the average time scale of the anisotropy decay, due to intramolecular energy transfer. In panel (C), we compare the ratio of the data shown in panels (A) and (B), $C_A^{(2)}(t_{21}) = C_{AD}^{(2)}(t_{21})/C_{ND}^{(2)}(t_{21})$, to the model decay $\exp(-t_{21}/\tau_A)$.

d_G = 1.6, 1.75, 2.12, 2.56, and 2.92 μm. In Fig. 7A are compared results for $C_{ND}^{(2)}(t_{21})$ (shown in black) to the Gaussian model for single particle diffusion described by $\exp(-k_G^2 D_s t_{21})$ (shown in white). For these calculations are used a value of the self-diffusion coefficient $D_s = 3.7 \times 10^{-10}$ cm^2 s^{-1} that is consistent with previous measurements of DsRed self-diffusion in 95% glycerol/water solution (Fink *et al.*, 2006). For each of the five values of d_G investigated, the time constants of the decays increase with increasing length scale, and the data are well described by the Gaussian model. This is the expected result, since the average separation between DsRed molecules is $\sim$1 μm, and molecular interactions are unlikely to cause deviations from random center-of-mass motion. The assumption of statistical independence between the sampled mean center-of-mass displacement $\Delta\bar{x}_N(t_{21})$ and the mean displacement of the depolarization angle $\Delta\bar{\theta}_N^{ae}(t_{21})$ is tested by comparing the results for $C_{AD}^{(2)}(t_{21})$ to model decays, which account for the factorization described by Eq. (14). For this purpose, a single exponential decay $\exp(-t_{21}/\tau_A)$ is used to represent the average loss of polarization memory described by the anisotropy 2P-TCF $C_A^{(2)}(t_{21})$. Figure 7B compares measurements of $C_{AD}^{(2)}(t_{21})$ to the model decay $\exp\left[-\left(k_G^2 D_s + \frac{1}{\tau_A}\right)t_{21}\right]$, with τ_A = 8 s. Note that the functions $C_{AD}^{(2)}(t_{21})$ decay more rapidly in time than do the functions $C_{ND}^{(2)}(t_{21})$, as the model decays suggest, and that the agreement between the data and the model curves is very good for all values of d_G. Figure 7C shows a comparison between the ratios of the decays shown in Figs. 7A and B, $C_{AD}^{(2)}(t_{21})/C_{ND}^{(2)}(t_{21}) = C_A^{(2)}(t_{21})$, to the model function $\exp(-t_{21}/\tau_A)$. The agreement between the experimental results for $C_A^{(2)}(t_{21})$ and the single-exponential decay, for all values of d_G, demonstrates a clear and unambiguous separation between anisotropy and center-of-mass fluctuations. The value obtained for the relaxation time τ_A = 8 s suggests that this is the slowest time scale for internal conformational fluctuations of DsRed.

Figure 8 shows two-point distribution functions (2P-DFs) of the mean sampled displacement of the center-of-mass $P_N^{(2)}[\Delta\bar{x}_N(t_{21})]$, and the depolarization angle $P_N^{(2)}[\Delta\bar{\theta}_N^{ae}(t_{21})]$. The 2P-DFs are constructed from the FICS measurement trajectories $Z_{\mathbf{k}_G}^{ND}(t)$ and $Z_{\mathbf{k}_G}^{AD}(t)$. In each panel, the distributions are vertically displaced for three different values of the time interval t_{21}. The sampled distributions are symmetric and centered about the origin, and their widths increase as a function of t_{21}. In Fig. 8A, the sampled distribution $P_N^{(2)}[\Delta\bar{x}_N(t_{21})]$ is compared to the self-part of the van Hove correlation function $G_S(\Delta\bar{x}_N, t_{21}) = (4\pi D t_{21})^{-3/2} \exp[-\Delta\bar{x}_N^2/4D_s t_{21}]$ (dashed gray curves), where the value of D_S is the same as that used for the previous comparison between the number density 2P-TCF and the Gaussian model decays. The agreement between the van Hove function and the 2P-DF provides further support that the Gaussian model is an accurate picture of molecular self-diffusion in the DsRed system. It is important to emphasize that the comparison between theory and measurement at the level of the DFs is a more accurate test of

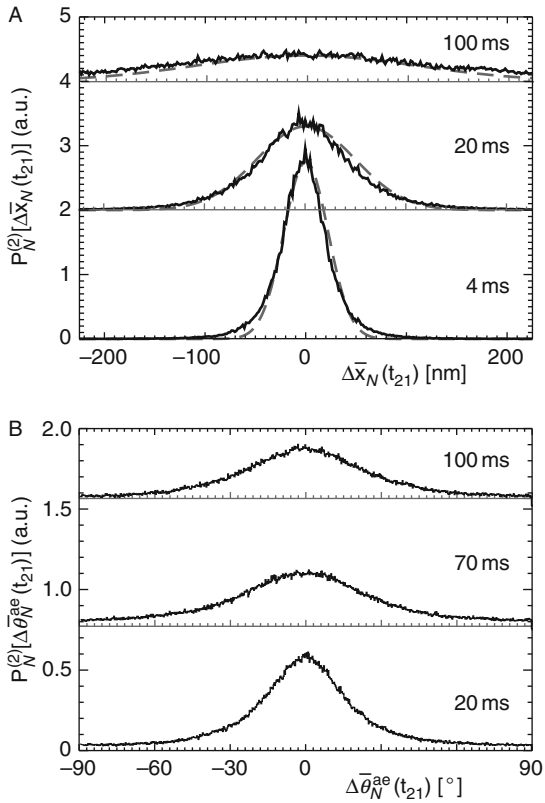

Fig. 8 Two-point distribution functions (2P-DFs) of (A) the mean sampled center-of-mass displacement $P_N^{(2)}[\Delta\bar{x}_N(t_{21})]$, and (B) the mean sampled displacement of the depolarization angle $P_N^{(2)}[\Delta\bar{\theta}_N^{ae}(t_{21})]$. In each panel, we show the distributions vertically displaced for three different time intervals. In panel (A), we compare our measured distribution $P_N^{(2)}[\Delta\bar{x}_N(t_{21})]$ (black) to the self-part of the van Hove correlation function $G_s(\Delta\bar{x}_N,t_{21}) \propto \exp(-\Delta\bar{x}_N^2/4D_s t_{21})$ with $D_s = 3.7 \times 10^{-10}$ cm^2 s^{-1}, which assumes that molecular self-displacements occur by Fickian diffusion (gray dashed curves).

the underlying model than the previous comparison at the level of the 2P-TCFs. This is because the 2P-TCFs represent a statistical average over the distribution of sampled displacements, according to $C_{ND}^{(2)}(t_{21}) = \int_{-\infty}^{\infty} e^{-\frac{1}{2}k_G^2\delta\Delta\bar{x}_N^2(t_{21})} e^{ik_G\Delta\bar{x}_N(t_{21})} \times P_N^{(2)}[\Delta\bar{x}_N(t_{21})]d\Delta\bar{x}_N(t_{21})$. It is, therefore, possible to probe dynamical information that is often obscured in conventional measurements by examining the 2P-DFs directly. In Fig. 8B is shown the 2P-DF of the mean depolarization angle $P_N^{(2)}[\Delta\bar{\theta}_N^{ae}(t_{21})]$. This distribution is isolated from the joint distribution of the anisotropy density $P_N^{(2)}[\Delta\bar{x}_N(t_{21}); \Delta\bar{\theta}_N^{ae}(t_{21})]$ by factoring out translational contribution. This distribution is also roughly Gaussian, and its width broadens on time scales less than 70 ms. On time scales greater than 70 ms, the width remains constant.

V. Conclusions

The movement and redistribution of intracellular species is an essential part of normal cell function. Such processes involve transport and interactions between myriad biochemical species over a broad range of spatial and temporal scales. Measurements that provide information about the microscopic details of intracellular processes can help to resolve mechanisms of biological activity.

Few current methods provide detailed microscopic information about intracellular chemical processes. The low signal limitations of existing methods place constraints on the number of studies that are possible. FICS is a novel fluorescence fluctuation method that achieves enhanced signal levels by spatially integrating over a relatively large sample volume, while retaining microscopic information by imprinting particle center-of-mass coordinates onto an optical signal phase. When employed in a polarization selective optical geometry to suspensions of fluorescent molecules, the FICS approach is suitable to study the internal conformation fluctuations in the presence of molecular diffusion. The phase-selectivity of FICS measurements enables the determination of time correlation functions and probability distributions, which provide detailed information about the time scales and the weighted magnitudes of molecular coordinate displacements, respectively. A straightforward extension of this approach involves analyses based on four-point correlation functions and two-dimensional joint probability distributions (Senning *et al.*, 2008). These two-dimensional analyses will be useful to decompose the dynamics of heterogeneous systems into their various dynamical components, and to provide in-depth information about the microscopic mechanism of biomolecular conformational transitions.

Although the FICS approach has so far been applied only to fluorescent proteins, it has the potential to be valuable for general studies of conformational transitions in fluorescently labeled proteins and nucleic acid systems. The breadth of information provided by such measurements would test fundamental models of biomolecular dynamics, as well as enable new studies of enzymatic function in living cells.

Acknowledgments

We acknowledge support for this research from the National Institutes of Health R01 GM67891 and the National Science Foundation CHE-0303715.

References

Berne, B. J., and Pecora, R. (2000). "Dynamic Light Scattering." Dover, Mineoloa, NY.

Cantor, C. R., and Schimmel, P. R. (1980). "Biophysical Chemistry Part II: Techniques for the Study of Biological Structure and Function." Freeman, New York.

Field, S. F., Bulina, M. Y., Kelmanson, I. V., Bielawski, J. P., and Matz, M. V. (2006). Adaptive evolution of multicolored fluorescent proteins in reef-building corals. *J. Mol. Evol.* **62,** 332–339.

Fink, M. C., Adair, K. V., Guenza, M. G., and Marcus, A. H. (2006). Translational diffusion of fluorescent proteins by molecular Fourier imaging correlation spectroscopy. *Biophys. J.* **91,** 3482–3498.

Fink, M. C., and Marcus, A. H. (2008). Simultaneous measurement of fluorescence anisotropy and translational fluctuations by polarization-modulated MFICS. *Phil. Mag.* in press.

Giepmans, B. N. G., Adams, S. R., Ellisman, M. H., and Tsien, R. Y. (2006). The fluorescent toolbox for assessing protein location and function. *Science* **312,** 217–224.

Grassman, T. J., Knowles, M. K., and Marcus, A. H. (2000). Structure and dynamics of fluorescently labeled complex fluids by Fourier imaging correlation spectroscopy. *Phys. Rev. E* **62**(6), 8245–8257.

Haustein, E., and Schwille, P. (2004). Single-molecule spectroscopic methods. *Curr. Opin. Struct. Biol.* **14,** 531–540.

Heikal, A. A., Hess, S. T., Baird, G. S., Tsien, R. Y., and Webb, W. W. (2000). Molecular spectroscopy and dynamics of intrinsically fluorescent proteins: Coral red (DsRed) and yellow (Citrine). *Proc. Natl. Acad. Sci. USA* **97,** 11996–12001.

Knowles, M. K., Grassman, T. J., *et al.* (2000). Measurement of the dynamic structure function of fluorescently labeled complex fluids by Fourier imaging correlation spectroscopy. *Phys. Rev. Lett.* **85** (13), 2837–2840.

Knowles, M. K., Guenza, M. G., *et al.* (2002). Cytoskeletal-assisted dynamics of the mitochondrial reticulum in living cells. *Proc. Natl. Acad. Sci. USA* **99**(23), 14772–14777.

Knowles, M. K., Honerkamp-Smith, A. R., and Marcus, A. H. (2005). Direct measurement of relative and collective diffusion in a dilute binary colloidal suspension. *J. Chem. Phys.* **122,** 234909-1–13.

Knowles, M. K., Margineantu, D., Capaldi, R. A., and Marcus, A. H. (2002). Translational dynamics of fluorescently labeled species by Fourier imaging correlation spectroscopy. *In* ''Liquid Dynamics: Experiment, Simulation and Theory.'' ACS Symposium Series 820. pp. 58–70. American Chemical Society, Washington, DC.

Malvezzi-Campeggi, F., Jahnz, M., Heinze, K. G., Dittrich, P., and Schwille, P. (2001). Light-induced flickering of DsRed provides evidence for distinct and interconvertible fluorescence states. *Biophys. J.* **81,** 1776–1785.

Margineantu, D., Capaldi, R. A., and Marcus, A. H. (2000). Dynamics of the mitochondrial reticulum in live cells using Fourier imaging correlation spectroscopy and digital video microscopy. *Biophys. J.* **79,** 1833–1849.

Margineantu, D., Capaldi, R. A., *et al.* (2000). Dynamics of the mitochondrial reticulum in live cells using Fourier imaging correlation spectroscopy and digital video microscopy. *Biophys. J.* **79,** 1833–1849.

Nitzan, A. (2006). ''Chemical Dynamics in Condensed Phases.'' Oxford University Press, Oxford.

Pringle, J. R., Adams, A. E. *et al.* (1991). Immunofluorescence methods for yeast. *Methods Enzymol.* **194,** 565–602.

Schenk, A., Ivanchenko, S., Rocker, C., Wiedenmann, J., and Nienhaus, G. U. (2004). Photodynamics of red fluorescent proteins studied by fluorescence correlation spectroscopy. *Biophys. J.* **86,** 384–394.

Senning, E. N., Fink, M. C., Lott, G. A., and Marcus, A. H. (2008). Optical conformational transition pathways in DsRed, elucidated by polarization-modulated MFICS. Manuscript in preparation for submission to *Biophys. J.*

Senning, E. N., and Marcus, A. H. (2008). Actin polymerization driven mitochondrial dynamics in mating *S. cerevisiae*. Manuscript in preparation.

Shaner, N. C., Campbell, R. E., Steinbach, P. A., Giepmans, B. N. G., Palmer, A. E., and Tsien, R. Y. (2004). Improved monomeric red, orange, and yellow fluorescent proteins derived from *Discosoma* sp. red fluorescent protein. *Nat. Biotechnol.* **22,** 1567–1572.

Wall, M. A., Socolich, M., and Ranaganathan, R. (2000). The structural basis for red fluorescence in the tetrameric GFP homolog DsRed. *Nat. Struct. Biol.* **7,** 1133–1138.

Weiss, S. (2000). Measuring conformational dynamics of biomolecules by single molecule fluorescence spectroscopy. *Nat. Struct. Biol.* **7,** 724–729.

CHAPTER 7

Nanobiology of the Primary Cilium—Paradigm of a Multifunctional Nanomachine Complex

Denys N. Wheatley

BioMedES
Leggat House, Keithhall, Inverurie
Aberdeen AB51 0LX
United Kingdom

Abstract

Of all the organelles in the eukaryotic cells, it is argued that the primary cilium is a paradigm in terms of nanomachinery found in the living cell. The components that are brought together in this single structure endow it with an extraordinary range of receptor and signaling functions. This organelle is based on the centriole,

METHODS IN CELL BIOLOGY, VOL. 90

0091-679X/08 $35.00
DOI: 10.1016/S0091-679X(08)00807-8

which is itself a minute compact structure that has been conserved throughout evolution for well over a billion years.

After more than a century of interest in the presence and structural features of the primary cilium, it became clear from the advent of the electron microscope that they were much more ubiquitous and had many more functions in situations other than the most obvious of cases, that is, the retinal rods and cones. However, these other functional activities were considered to be largely speculative by nonspecialists, until more recently. In the last decade, more has been learned about their molecular biology and function than in all the preceding years of research. The impetus came from a better understanding of the process of ciliogenesis at the macromolecular level, the discovery of wide range of receptors localized in the ciliary membrane, and the appropriate signaling mechanisms to relay messages to the cell internum. These are the three central themes of current investigations. The reason for the recent flurry of activity stemmed from work in the mid-1990s emphasizing the fact that the failure of cells to develop primary cilia in certain tissues and organs was directly correlated with some drastic pathological consequences, just as failure to develop the primary cilia that form the basis of retinal cells, observed now over a half a century ago by Sjöstrand, F. S. (Sjöstrand, F. S. (1953). The ultrastructure of the inner segments of the retinal rods of the guinea pig eye as revealed by electron microscopy long ago, so blatantly causes blindness. The medical implications did in due course prove to be of such magnitude that highly intensive work began on primary cilia in the late 1990s and has since shown their involvement in a wide range of both serious and highly prevalent disorders. Since we are referring to an organelle that is made by and comprised of a whole host of nanomachines, it has become an obvious focus of attention in both academic and applied research. These rapid developments have relied on experts from many different disciplines, including engineering and physics, to help solve some of the problems.

This article introduces the primary cilium to scientists from this wide range of disciplines who are interested in nanoscience and to those in particular who see the advantages of looking at biological systems. There is little doubt that our knowledge at the supramolecular (nanoscale) level of the primary cilium will, in turn, help (bio)engineers, (bio)technologists, and others to design and build ever more exquisitely sensitive sensors that will be of immense value in future, especially in fields such as medicine. If any aphorism rings true in these circumstances, it is that ''nature has already been there.'' On this account alone, the primary cilium should command much more of our attention.

I. Introduction

This general introduction to the primary (or 9 + 0) cilium has been written, not with the object of informing you tediously of the full details about its structure and biology, but of enlightening and enthusing you briefly about these extraordinarily

intricate nature of these organelles and their functions. We will also take stock of the general advances in primary ciliatology, and pose relevant questions where gaps in our knowledge exist, particularly where pertinent to problems at the nanoscale. For many who have already turned their attention to the wonders of nature at this level of resolution, we are looking at the basic macromolecular machinery, which maintains the metabolism of the living cell and its responsiveness to its environment. Subcellular structures that constitute the active machines are mostly complex assemblies of macromolecules that cannot readily be observed *in situ,* even at the limit of the highest-powered electron microscope. But structure also goes hand-in-hand with function at this level, that is, the structures you see are indeed the working parts themselves, not being there for support alone. It also has to be kept in mind that a holistic approach is needed when considering the living body, made up of many billions of cells, which must all interact together in a fully coordinated manner. Equally, it must not be forgotten that positive and negative feedbacks, servomechanisms, and many other modern devices came into existence via biology (now called systems biology), where the basis of homeostatic mechanisms was understood.

II. Self-Assembly

Before we explore the complexity of the primary cilium, we ought to consider how such an organelle can be assembled without recourse to huge technical manuals, blueprints, and the like. The process is one of the self-assembly, some of it automatic, such as the polymerization of tubulin dimers to make microtubules (MTs), but much of it in association with nanomachines, of which many more examples will almost certainly be discovered in the next decade. The work-horses of the cell are proteins, most being enzymes, some being structural, and some both. It was estimated 10 years ago that ~200 different types of protein are present in the primary cilium, with many more clearly being involved if we take into account the plethora found in the centriolar-centrosomal domain of the cell from which a primary cilium emanates. A more recent estimate, Christensen *et al.* (2008), placed the figure several fold higher: "in effect, the cilium is comprised of perhaps over 600 proteins in molecular complexes, many of which also function independently as nanomachines."

III. Ciliogenesis

A. One Cilium or More

The primary cilium emanates from a basal body, otherwise known in its unadorned state as a centriole. The origin of the centriole was probably by acquisition via a spirochete ancestor during evolution, according to the endosymbiotic theory of Sagan (1967). In motile cilia found on the surface of the epithelia lining various body tissues (e.g., nasopharynx, oviduct, ventricles of the brain), there is a single

basal body at the foot of each cilium of a whole carpet of them. With primary cilia (generally nonmotile), there are usually two basal bodies at each foot, and the pair often adopt an orthogonal relationship, the mother (older) centriole being the one from which a cilium issues (Fig. 1). In some situations, more than one pair of centrioles may be present in a cell and it will then sometimes express more than one primary cilium. Sorokin (1962, 1967) described the two different patterns of cilium generation in intricate detail, scenarios largely unchanged over the last 40 years. But an exclusion principle operates—if a cell is going to become ciliated, it adopts one of the two patterns, and never indulges in both. This leads to two key questions: (i) what induces a cell to become ciliated? and (ii) what decides whether multiple motile 9 + 2 cilia are generated or a solitary primary cilium is produced? One might easily argue that it depends entirely on where the cell in question is located, but that does not provide an answer in mechanistic terms.

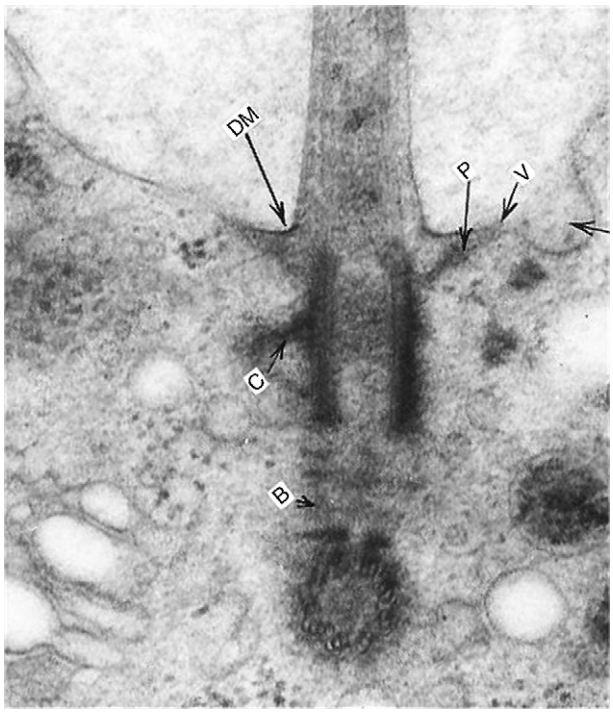

Fig. 1 Electron microscopic image of a primary cilium taken over 40 years ago, but also showing a vast number of the associated features seldom seen in a single 800 Å section (further details shown in Fig. 3). The centrioles are seen as a diplosome (a pair orthogonally disposed to each other). At B, striated rootlets are present, a satellite can be seen at C, and an alar process (P) links the top end of the distal centriole (basal body) to the cell membrane. A dense, thickened cell membrane (DM) surrounds the base of the ciliary shaft. On the right of the alar process is a caveola (arrow). Note the punctuate membrane just to the left of the arrow. On the other side of the shaft, which incidentally stretches out into a large vacuole, the frothy cytoplasm below the cell membrane is material derived from the Golgi apparatus, with the bigger membranes of this organelle seen at the bottom left of the image. Magnification ×45,000.

B. Centrioles and Basal Bodies

The structure of the centriole is highly complex, more so when all its accessory structures are taken into consideration (Fig. 2), many of which are crucial to the full range of activities that can be undertaken by primary cilia, although most of this paraphernalia is likely to be present, when a centriole assumes the role of a basal body.

The centriole was, at one time, thought by many of the earlier researchers to be intimately involved in the division of cells into two daughters, following its own duplication in the cell cycle and subsequent positioning at the astral poles of the spindle (e.g., Brinkley *et al.*, 1967). However, this was shown later to be more by guilt of association than a true function, while now almost everyone accepts that its main function is to act as a template for ciliogenesis, although one should not dismiss the possibility that it may serve other purposes, as discussed below.

Relative to the intense focus on the primary cilium today, attention has been diverted once again from the centriole, yet it remains one of the most enigmatic organelles in eukaryotic cells and its nanobiology deserves much greater attention. It is an extraordinarily durable structure, in which different domains within its framework where many things probably occur, mostly unknown to us. A few of the more bewildering and beguiling problems about the centriole are summarized

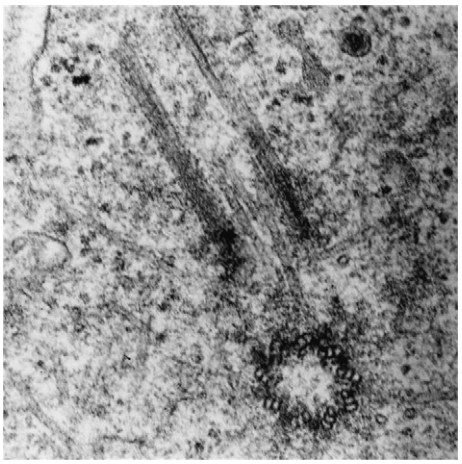

Fig. 2 A diplosome in the typical orthogonal arrangement, where there is a large amount of MTs in its vicinity. Note the lower part of the tubules of the centriole cut in longitudinal section have dense material associated with them, the function of which is unknown. On some occasions during ciliogenesis, the shaft axonemes are elongated before the centriole has docked with the cell membrane, as appears to be the case here. Thus, the sequence of events occurring during ciliogenesis does not always have to be in precisely the same sequence. Magnification ×40,000.

below, although these are mentioned here not because we have answers, but because we need answers:

- Centrioles reproduce, but do so by a most unusual assembly of a "daughter" structure developing orthogonally (i.e., at right angles) to the "parent."
- The pitch of their triplet "vanes" can change, especially noticeable with age.
- A central hub has often been described, but today there is still no firm evidence that it is always present, and even less information about its functional role.
- Material pass up and down the core of a centriole, which is difficult to square with the presence of a central hub; nor do we know what is being transported and whether it is bidirectional.
- In ciliogenesis, where so much depends on the centriole's structure, we have to ask whether there is some essential change in its essential (core) properties associated with it becoming a basal body.
- Finally, with respect to the triplet nature of the centriole tubule sets, *a* and *b* are used as templates for the extension of the axonemal tubules of a cilium, leaving us to consider why the *c* tubule is not included, and what function it otherwise might serve.

Centrioles have certain properties which need to be more thoroughly researched. Once fully duplicated, there will always be an older and a younger centriole in any pair (a diplosome; Fig. 2), which can be distinguished by their different staining properties. In addition, centrioles clearly retain a definite polarity, with one end invariably being the one which docks with a cell membrane in the earliest stages of ciliogenesis, these features being reviewed recently by Dawe *et al.* (2007). Primary cilia cannot exist without a centriole base; while we have learned much more about its extension, the primary cilium, in the last 10 years, our knowledge of the centriole remains very much as it was a quarter of a century ago (Wheatley, 1982). There have been quite a number of ideas, some of them quite extraordinary, regarding the possible function(s) of the centriole other than as a ciliary template—from guidance of the plane of astral divisions in mitosis (reviewed in Wheatley, 1982), to being some kind of inbuilt cellular compass, a rather fanciful notion of a central infra-red sensing nanomachine originally thought to determine the angle ($\sim 40^{\circ}$), through which a cell turned when altering course during its locomotion on a flat substrate (Albrecht-Buehler and Bushnell, 1981). This was followed up by a report in which the design of a pair of orthogonally arranged centrioles was shown to be consistent with their being sensors at the cell centre—"the simplest and smallest device that is compatible with the scrambling influence of thermal fluctuations as are demonstrated by Brownian motion is a pair of cylinders oriented at right angles to each other" (i.e., a diplosome; Albrecht-Buehler, 1981, 1994). The arrangement of the triplet tubules in nine veins as the walls of a cylinder begs for an explanation as to what purpose such a structure might have purely in terms of its physical properties.

C. Ciliary Assembly on the Basal Body Template

The assembly of the primary cilium is somehow initiated when a centriole is positioned near the Golgi, which is often, at this stage, close to the nucleus. Once docked to a vesicular membrane, this subsequently extends to form the ciliary sheath. However, sometimes the centriole moves peripherally in the cell to dock at the cell membrane, whereafter the whole cilium assembly process takes place at the surface. Either way, the cilium can increase considerably in length (e.g., those in kidney epithelial cells can reach 30–50 μm; Roth *et al.*, 1988), in some cells directly emanating from the cell surface (e.g., chrondrocytes; Jensen *et al.*, 2004), and in others from a deep invagination of cell membrane close to the nucleus (e.g., rat pituitary cells; Carpenter, 1971).

Early electron microscopic observation of fibroblasts and smooth muscle cells by Sorokin (1962), recognized three main stages of primary cilium formation. First, a vesicle close to or part of the Golgi apparatus attaches to the distal end of a mother centriole (Fig. 3), and two of its three MTs, extend from the distal centriole into the vesicular to create the *axoneme*, the tubular backbone of the ciliary process, giving it a characteristic $9 + 0$ set of doublet MTs in a circle along its length. The "0" devotes the absence of two single MTs found in motile $(9 + 2)$ cilia. As it becomes a basal body, the centriole seems to acquire a number of accessory structures (Fig. 3A), although "free" centrioles can often be found with different appendages attached to them.

One of these accessories is the *striated rootlet*, a collection of fibers (Fig. 3A and B) that sometimes connect mother and daughter centrioles together, but often go deeper into the local cytoplasm. Striated fibers are almost certainly nanomachines for contraction (i.e., miniature muscles), probably pulling in turn on cytokeratins and other structural elements of the cytoplasm within the near vicinity. *Satellite processes* emanate from midway down the centriole, providing anchorage for cytoplasmic MTs, on which, presumably, they can also pull. The reason for suggesting this is that, although these regular features of a basal body have the semblance of firm anchorage devices, there is clear evidence in many high powered images of them that they are also striated (e.g., Wheatley, 1982, Figures in Chapter 3, especially 3.4 and 3.13; see also Fig. 3A and C). What other nanomachines are hidden in their structure remains to be seen.

A feature of some cilia is the remarkable ability to be withdrawn into a deep sheath of cell membrane within a second or so from a superficial position on the plasma membrane surface. This would require considerable contractile agility and capacity, and undoubtedly, these striated processes must contribute in large measure to this process, although such a scenario has not been formally confirmed.

The attachment of the new basal body through *alar processes* (Wheatley, 1982) to the membrane has in recent years begun to be properly researched (Dawe *et al.*, 2007; Jensen *et al.*, 2004) in nanostructural detail, although this tells us little about what mechanisms operate. There must be at least one for producing these processes at precisely the right place at the distal end of the basal body, and the other

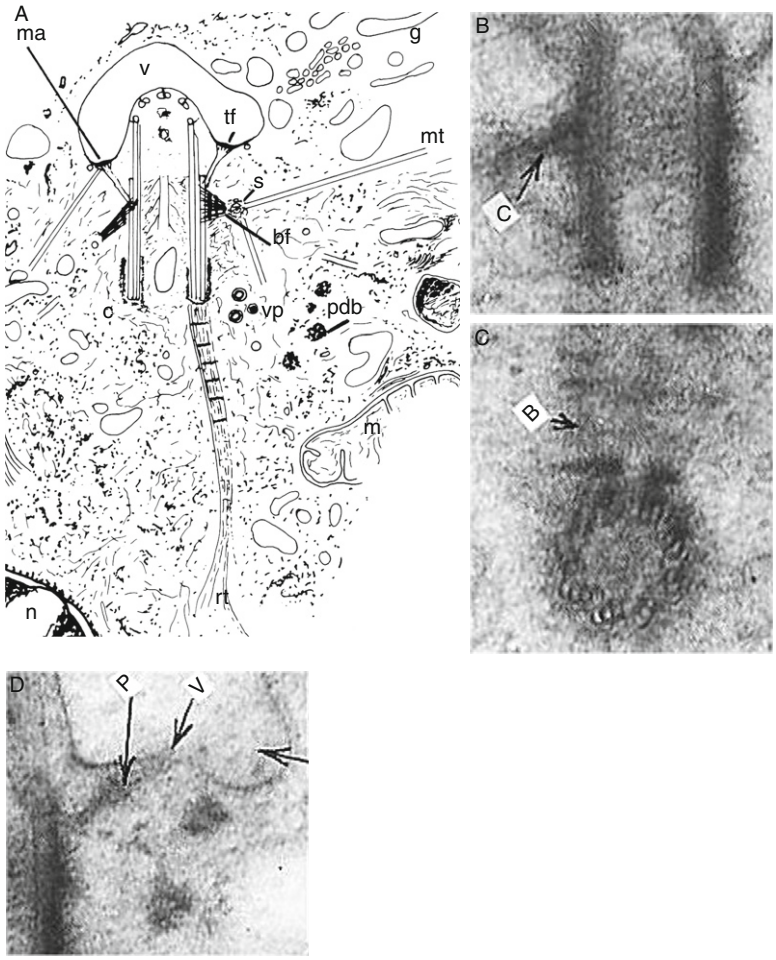

Fig. 3 (**A**) is a schematic representation of the base of a primary cilium during early development recording most of the associated structures, as seen in Fig. 1. **v**: vesicle from the Golgi cisternae into which the shaft emerges. **g**: Golgi apparatus. **s**: satellite, emanates laterally from the centriole and internally in that region, the cylinder is most densely filled with material. In the original description of a satellite, this term was used for the ball like ending to the process, the rest of its attachment to the centriole being referred to as the basal foot (**bf**). Satellites are often more striated than shown in the example of higher magnification from Fig. 1 in Fig 3B. MT profiles can be seen in close proximity, depicted in Fig. 3A in longitudinal rather than transverse section (**mt**). In Fig. 3C, the striated rootlets show freely extending into the cytoplasm (**rt**) seem to link the basal body and the proximal centriole together. Note the density of the material to which this association seems to take place on the lower centriole seen in transverse section. **tf**: transitional fiber, also known as an alar process. Note that it has small vesicles between itself and the cell membrane which might or might not be of microtubular origin. It also has a series of dots just below the region of the membrane. Both these features are depicted at higher magnification from Fig. 1 in Fig. 3D. **ma**: manchette plaque—where the alar process binds firmly to the membrane. In Fig. 3A, caveolae as seen in Fig. 1 are not depicted, but a higher-powered image of the alar process is seen, with small vesicles, previously considered to be MTs in attendance, as well as a

drawing these structures and the cell membrane together. If there is a general mechanism of membrane fusion of vesicles to membranes, as has been recently and most beautifully visualized by Jena and co-workers (Potoff *et al.*, 2008), there is every reason to suppose that a similar mechanism operates in ciliogenesis, only the domain in which this process occurs must be much more cluttered than around a porosome. Of note is that the membrane region close to a docked basal body is of high electron density, but whether this thickening occurs at or after docking is unclear. Very small vesicles on average a little bigger than transverse profiles of a microtubule (>25 nm) can be found interspersed between the membrane and the alar processes (Currie and Wheatley, 1966; "v" in Fig. 1, and see also Fig. 3A and D), but their relevance is unknown. More information might now be gained from focusing our attention on these structures by using such devices as the atomic force microscope, which was not available 40 years ago.

In accounts of ciliogenesis from other sources (e.g., Pedersen *et al.*, 2008), we read of the phase of ciliary development involving many more (smaller) vesicles than the original one from the Golgi fusing with new membrane forming at the ciliary base to create a sheath surrounding the elongating axonemal shaft in which microtubule pairs are quickly assembled. At the ciliary base itself, depressions called caveolae are often present just beyond where the cell membrane is considerably thickened. Interestingly, such depressions were seen in some of the first electron microscopic images of primary cilia (Fig. 1). There are also regularly spaced insertions into the caveola membrane, seen on its left side in Fig. 2C. Such small dots may well represent yet another nanomachine, perhaps of an ion channel, or not so different from the not porosomes of Potoff *et al.* (2008). Also just near the Golgi vesicles and in the "clearer cytoplasm" closer to the many small particles can often be found (Fig. 2C), some undoubtedly comprised of ribonucleoprotein, RNP. Such activity is consistent with the organization and accumulation of precursor materials designated for ciliogenesis, as seen in the early studies of Sorokin (1962).

Within the developing cilium, axonemal MTs are polymerized from tubulin delivered to the site, giving rise to the familiar pattern referred to as the 9 + 0 cilium (*note:* this is contrary to cilia that clothe the surfaces of the cells of the nasopharyngeal mucosa, which beat in synchrony and are of the 9 + 2 variety). For some years, researchers saw cilia in developmental stages and thought them vestigial, which distracted attention of many from investigating situations where the cells

row of dots as the alar process spreads out just below the cell membrane. It is not understood why the cell membrane so adjacent to the dense membrane looks so lacking in integrity. To the right of the alar process in Fig. 3D are two pericentriolar dense bodies (**pdb** in Fig. 3A), presumed to contain material related to ciliogenesis. Several other organelles are depicted in Fig. 3A, including the nucleus (**n**), a mitochondrion (**m**), and virus particles (**vp**). The last have been included because of the propensity of virus particles that sometimes infest cells to be found predominantly in the centrosomal region which surrounds a primary cilium base, as found during ultrastructural examination of cells taken from culture. Magnifications (Fig. 3B, C and D) ca. 70–80,000×.

developed long cilia that clearly carried out some function. Given time, especially when cells move into stationary phase and/or a more fully differentiated state, fewer developing (''rudimentary'') cilia are seen. Admittedly, there are cases in which primary cilia seldom, if ever, develop beyond 1–3 μm, but it has never been shown whether such short or ''poorly developed'' cilia are also devoid of function.

D. The Ciliary Membrane

The membrane-covered short axonemal bud extends as its main MTs array assembles until the top of the vesicular membrane fuses with the plasma membrane. Just above this point of membrane fusion, a specialized region develops at the base of the shaft itself. This is referred to as a *ciliary necklace*, which consists of a many-stranded set of particles spirally embedded in the membrane that connect up internally to the centre of the centriole (Gilula and Satir, 1972). How these particles come to be embedded in this precise position is not known (above the DM region in Fig. 1). The ciliary necklace is involved in Ca^{2+} transfer in and out of the cell, which is highly important in signaling activity. Ca^{2+} transport mechanisms are themselves nanomachines within the ciliary cell membrane. Beyond the ciliary necklace, the membrane of the cilium reverts to normal density, although small bridges are seen attaching it to the closest axonemal MTs, presumably for the sake of rigidity and tension.

E. Transport and the Development of the Ciliary Shaft

The whole process of ciliogenesis is, to all intents and purposes, similar, whether we are talking about 9 + 0 or 9 + 2 types, although the latter may be more complex. How macromolecules from the cell body that are to be integrated reach the developing cilium is the next problem. It is often interesting to watch how a column or a crane is constructed. In some cases, units of the structure are intercalated at the base and jacked up ever higher. In other cases, the units are placed at the top of the developing structure, in the way that a chimney stack is built. The question is, which way does a cilium elongate? While there is evidence that new material is accreted from the top, there is no reason why nature should not employ both routes, that is, some components are intercalated from the bottom up while others are put in place from the top down, but of the two it is probable that the latter predominates for evidence discussed below.

From the centriole (basal body) attached to the cell membrane, MTs start to emerge by a process of polymerization of tubulin dimers, their rigidity being ensured by another set of regularly spaced proteins (MAPs) which lock the spiraled dimer together. At the same time, material begins to pass between these axonemal MTs and the ciliary membrane. The transport mechanism is dependent on nanomachines that have been highly conserved througout all eukaryotic cells, whether they are 9 + 2 motile cilia, 9 + 0 primary cilia or flagella, since their origin hundreds of millions of years ago.

Not only will the complexity of the cilium itself be becoming more apparent to the reader, but the machines required to assemble this structure will increasingly be seen as probably as numerous and diverse. One nanomachine central to this matter provides a major delivery mechanism. Since a cilium of considerable length can be constructed in 20–30 min, devices bringing materials from the cell body must be both numerous and highly active. They were shown to use motor proteins of two kinds, one being kinesin II for anterograde movement, and the other being dynein 2 for retrograde movement. The process is closely akin to the bidirectional movement of cargoes along nerve axons. The key observation that led to the discovery of structures called *intracellular flagella transporters or rafts* (IFTs) moved by these motor proteins came with the finding that disruption of 1 of the 16 specific proteins that make up an IFT resulted in a complete loss of function, and cilium assembly was forestalled. Cole *et al.* (1998) were responsible for showing the gene mutation responsible (Tg737). Since that time, it has become clear that disruption or lack of any of the raft proteins may similarly affect (inhibit) ciliogenesis. The way in which the IFTs carry out their function is to load massive cargoes of precursor materials and haul them up the peripheral axonemes by means of kinesin II in steps of about 2.7–3 Å. An excellent video clip of this movement is depicted on the website of Bolinsky (2008) in "*Life of the Cell*." If these IFTs were to travel as fast as particles carried on neural axons by the same motor proteins, we are talking of speeds of delivery of the order of 2–3 μs^{-1}, but it is probably slower than this in a ciliary shaft. As a raft reaches the top of the assembled cilium, it will shed or have shed its cargo. Whether each raft carries a multitude of different proteins (many of them receptor molecules) or just one or a few, these molecules will more or less simultaneously have to be integrated into the cell membrane either in a focalized nature or more diffusely arranged as the transporter comes by, but we know very little about the regulatory machinery involved, although it is known that at the tip of the forming cilium, one molecule of part B of the IFT (each raft is composed of two subunits, A having 6 proteins, and B having 10) results in the uncoupling from the kinesin motor. Mutants which disturb this uncouples, for example, DYN2CLI, result in a log-jam of IFTs at the ciliary tip. In normal circumstances, however, the raft is set free from kinesin II such that it can now associate with dynein 2. This has the opposite polarity of movement along axonemal MTs, descending on their internal aspects with unwanted cargo or waste products to be returned to the cell body (Fig. 4). Our understanding of this extraordinary assembly process and trafficking increases daily, and while a few dozen biologists were involved in these investigations 10 years ago, today hundreds if not thousands are focused on the nanomachinery associated with ciliogenesis.

Considering the ubiquitous nature of cilia in cells of all kinds of tissues, perhaps, the most remarkable feature is that this complex self-regulating organelle is accurately constructed almost every time. The rare exceptions where things have gone wrong, however, have allowed us a closer insight into the way in which these numerous machines and proteins must interact, because if they do not, dire consequences arise in terms of a range of pathological conditions and syndromes

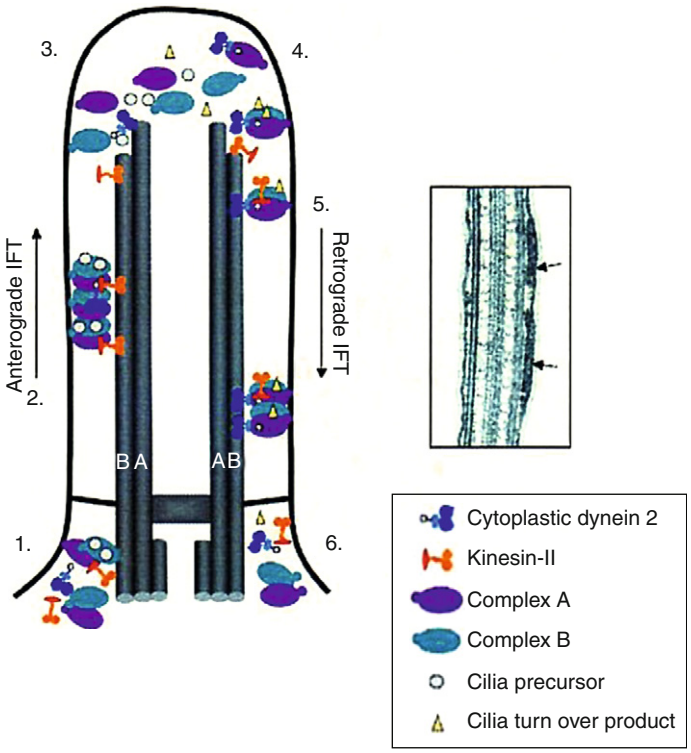

Fig. 4 A cartoon illustrating the loading and trafficking of materials into and out of the primary cilium during assembly, in which anterograde and retrograde movements are directed by intraflagellar transporters or rafts (IFTs) using kinesin II and dynein 2, respectively. The small inset on the right-hand side shows IFTs between the axonemal MTs and the ciliary membrane. Reprinted from Pedersen *et al.* (2008), with the kind permission of the authors and John Wiley and Sons Ltd.

that can be directly attributed to aciliogenesis (see below). For a fuller review of all the genes and their products known to be involved in ciliary morphogenesis and function, the reader is referred to the excellent review of Pedersen *et al.* (2008).

F. Proliferation of Cells and the Variable Incidence of Primary Ciliation

With regard to primary cilium expression in cells proliferating in cultures, early work undoubtedly showed a lower expression rate in the first few days of growth, but as the cells became confluent and reached stationary phase, the incidence was higher. By careful analysis of cells moving into and out of division, Archer and Wheatley (1971) established that cell shed their cilia very shortly before entering into mitosis. Although the daughter cells definitely showed a lower expression of cilia than stationary phase cells, it was nevertheless quite common to see a late

telophase cell already reassembling its cilium. A more statistical and experimental approach to the study of primary cilia began when cell lines became more extensively used for critical analyzes. It was noteworthy that some cell types in culture never seemed to develop cilia (e.g., endothelial cells, HeLa cells, etc.), whereas others did so with high frequency (e.g., PtK2, 3T3, etc.). One of the puzzling things about the expression of cilia is that they can be frequently found in, for example, almost every cell of the basal layer of the epidermis, and yet when cultured *in vitro* and maintaining their typical epithelial characteristics, they seldom if ever express primary cilia (Wheatley *et al.*, 1996). There are other clear models where our understanding of the mechanism of induction of primary cilium expression could progress; for example, endothelial cells in the body possess primary cilia in some vascular sites, whereas in others they are absent.

Analyzes of cilium frequencies, length etc., however, were all very tedious because data originally had to be collected from serially sectioned material examined under the electron microscope. When it was found that primary cilia possessed detyrosinated tubulin, a relatively specific antibody became available (Wehland and Weber, 1987), making the detection and measurement both simpler and quicker (Wheatley and Bowser, 2000), and analysis flourished as never before.

IV. Elucidating the Functional Role of Primary Cilia

The biggest problem with primary cilia was that although they were often almost as highly elaborate and sophisticated as retinal rods, there was no physiology to go with their anatomy even in those found in kidney epithelial cells. The fact that they could act as some form of chemical or mechanical sensor was believed by many ciliatologists, but the lack of no positive evidence meant that such notions were not generally mooted or received with considerable condescension by others. However, Poole *et al.* (1985) were prepared to make such a claim, for which they produced a considerable amount of circumstantial evidence. But research carried out industriously over the next decade clearly kept the notion of the sensory function very much in vogue. Reviewing the situation, Wheatley (1993, 1995) drew clear comparisons between ciliation in normal and pathological tissues, and from it emerged the concept that pathophysiological consequences would probably be inevitable where primary cilia of considerable length and sophistication were not present to carry out some (presumed) sensory role. If elaborate cilia that normally sensed flow in renal epithelia were not present, this would impact on renal function in some way (succinctly reviewed in Ong and Wheatley, 2003). Both these concepts have since been fully vindicated, and currently work has reached fever-pitch because of the medical implications of the absence or malfunctioning of primary cilia in the particular tissues of the human body, from neurons to the serosal cells of the peritoneal cavity.

The primary cilium of the renal proximal tubular epithelium must now be the most studied example, and its length lent it to mechanical investigations into its

role as a putative flow sensor. Schwartz *et al.* (1997) followed ciliary bending under flow conditions. The upper two-thirds of the shaft bent in proportion to the flow rate, while the lower third remained largely rigid. In their own words, they stated that the cilium was close to being "*optimally engineered*." Praetorius and Spring (2001) confirmed that bending of a cilium produced a Ca^{2+} transient in the cell body. The sensor was indeed sending a well known signal to the body of the cell. This was the first clear evidence of the sensory function, in this case to mechanical stress, of a cilium; but we should keep in mind that for a long time, we knew that the primary cilia constituting retinal rods and cones were undoubtedly not only sensors of photons, but were also nature's own photomultiplier tube. A second example might be the long cilia that extend like fingers from the surface of chondrocytes in their lacunae within cartilage. When under pressure, the rotational activity of the cells in their lacunae ceases and the cilium gets bent as it is pressed against the cell surface. As a result, the cell deposits new matrix into the cartilage from the Golgi vesicles adjacent to the primary cilium base, and remarkably, the cartilage is strengthened in the direction of the force of compression (Poole *et al.*, 1997). Pressure is sensed by primary cilia in the flow of dentinal fluid between odontoblasts in teeth (Magloire *et al.*, 2004), and as a final example, Bell (2008) proposes that primary cilia can also found in places where sensors of hydrostatic pressure are needed, with distortion leading to effects on the axonemal MTs that then act like Bowden cables, informing the cell body of the pressure bearing down on them.

But it was also self-evident that primary cilia would also be sensitive to chemicals, and especially biological molecules (e.g., hormones and growth factors), and that they were not just sensors of physical forces and disturbances in the environment. One of the first biomolecules that proved to be intimately involved with the primary cilium was not unexpectedly *inversin*, which helped to identify the gene defects in primary cilia whose dysfunction led to the long recognized condition of *situs inversus* (Morgan *et al.*, 1998). Soon after, cilia were found to be sensitive to somatostatin, the somatostatin receptor 3 being present on neuronal cilia (Händel *et al.*, 1999). Since then, a vast number of other receptors of biological ligands have been reported in the primary cilium membrane which will unfortunately be too long to list and reference here; however, they include the polycystins 1 and 2, PDGFRα, sonic hedgehog (Shh), patched (Ptc), smooth (Smo), taurine transporter, nephrocystins—a list that daily grows (see Pedersen *et al.*, 2008). However, these receptors can usually be found over the rest of the cell membrane, but three important points should be noted: (i) the density of any particular receptor type on the ciliary membrane is usually greater than on any equivalent area of the rest of the cell membrane, and is usually more focalized; (ii) the ciliary membrane extends like a probe into the environment and therefore, its receptors will be the first to encounter the presence of their ligands; and (iii) many primary cilium must combine mechanic-sensory functions with a multitude of chemo-sensory receptors. The multifunctional nature of the primary cilium is a lesson in the efficient use of a single antenna to sense many different properties of its environment, rather than a

plethora of single units sensitive to only one stimulant, and this is why I have referred to it as truly a paradigm of multifunctional nanomachine.

V. The Medical Consequences of Aciliogenesis—A Veritable Pandora's Box

It has already been mentioned that primary cilia contain inversin, and its absence has been known for years to cause situs inversus in man and other animals, but a much bigger story unfolded when it was appreciated that the absence of primary cilia in the renal proximal tubular cells was clearly associated with polycystic kidney disease (PKD). We are talking here about a difference in incidence of a thousand fold or greater in the frequency of these two conditions, situs inversus affecting one in over a million people and PKD one in a thousand. The PKD correlation provided the impetus to look at primary cilium biology in a number of other medical disorders, and soon a whole host of syndromes had been implicated (see, e.g., Badano *et al.*, 2006; Christensen *et al.*, 2007; Yoder, 2002), ranging from Kartagener, Bardet-Biedl, von Hippel-Landau syndromes, to hyperphagia (over-eating) and defective neurogenesis, as well as pathological already discussed in previous sections. It is little wonder that the primary cilium has blazed a trail through medicine and biology like no other organelle before it.

VI. Concluding Remarks

The cilium is a highly sophisticated bio- and mechano-sensory organelle, a veritable paradigm in nanobiology. At the risk of apologizing for including quite a few old images and statements, let it be said that some of the first good images of the centriole–primary cilium complex and ideas have still to be been bettered (e.g., Fig. 1). With ever increasing powers of resolution both in living and preserved cells that come from the introduction of the new technology such as the atomic force microscope, the future is exciting for further revelations on the genesis of primary cilia, but it must be tightly coupled with an understanding of the huge number of receptor-signaling pathways involved. One major objective must be to know exactly what happens in terms of the changes of metabolism of the cells bearing primary cilia when specific signals are sent to the cell body. These must accord with a concerted response to whatever is being reported by way of a change in the environment, be it a mechanical shear force or an encounter with a molecule of vascular endothelial growth factor (VEGF).

Without going into too many specific details, my aim has been to highlight just how dependent the cell and the body is on macromolecular assemblies at the nanoscale level, particularly by one organelle that had been sidelined by the "body of the kirk" in biology for many years as vestigial or of little importance.

At the risk of repeating myself, nothing that a cell does can be taken for granted, "or considered irrelevant and insignificant" (Wheatley, 2005). Also, everything it does has some significance in the grander scale of things, as is the case in all holistic systems such as the living cell. A second lesson is what nature herself with the primary cilium can teach us with regard to design and function of optimally sensitive multiprobe devices yet to be conceived in human technology. Let me finish by drawing your attention to one such sensory device that man has made, but which is trivial in its performance compared with what the primary cilium can do. About the time that the molecular nature of ciliogenesis was beginning to be understood, Guterman (1998) briefly reported in the *New Scientist* a biosensory device developed at the naval research laboratory in Washington, DC. Using a radio-controled aircraft mounted with a probe, this structure sampled bacteria in the air. Inside each probe were antibodies that could detect a small range of different microorganisms. These antibodies were in turn reacted *in situ* with fluorescent secondaries, so that light signals could be detected under UV where bugs were present. By accumulating bacteria in runs of the drogue spaced 5 min apart, the air was monitored and an averaging of the samples made. The main thrust of this project was for this small unmanned aircraft to enter zones where there could be aerial pollution of dangerous bacteria of the type employed in biological warfare. While this was some time ago, the possibilities now exist of developing much more sensitive devices for far greater benefit to mankind in the civilian world. The primary cilium stands as a beacon, a guiding light, taking us into a new era of sensory perception in all fields of science, technology, and especially in the field of biomedicine.

References

Albrecht-Buehler, G. (1981). Does the geometric design of centrioles imply their function? *Cell Motil.* **1,** 237–245.

Albrecht-Buehler, G. (1994). Cellular infrared detector appears to be contained in the centrosome. *Cell Motil. Cytoskeleton* **27,** 262–271.

Albrecht-Buehler, G., and Bushnell, A. (1970). The orientation of centrioles in igrating cells. *Exp. Cell Res.* **120,** 111–118.

Archer, F. L., and Wheatley, D. N. (1971). Cilia in cell-cultured fibroblasts. II. Incidence in mitotic and post-mitotic BHK21 C-13 fibroblasts. *J. Anat.* **109,** 277–292.

Badano, J. L., Mitsuma, N., Beales, P. L., and Katsani, N. (2006). The ciliopathies: An emerging class of human genetic disorders. *Annu. Rev. Genomics Hum. Genet.* **7,** 125–148.

Bell, A. (2008). The pipe and the pinwheel: Is pressure an effective stimulus for the 9 + 0 primary cilium? *Cell Biol. Int.* **32,** 462–468.

Bolinsky, D. (2008).(http://www.stumbleupon.com/demo/#url=http://www.ted.com/).

Brinkley, B. R., and Stubblefield, E. (1970). Ultrastructure and interaction of the kinetochore and centriole in mitosis and meiosis. *Adv. Cell Biol.* **1,** 119–185.

Carpenter, E. (1971). Fine structure of rat pituitary cilia. *Anat. Rec.* **169,** 637–650.

Christensen, S. T., Pedersen, L. B., Schneider, L., and Sait, P. (2007). Sensory cilia and integration of signal transduction in human health and disease. *Traffic* **8,** 97–109.

Christensen, S. J., and Satir, P. (2008). Structure and function of mammalian cilia. *Histochem. Cell Biol.* In press (online).

Cole, D. G., Diener, D. R., Himelblau, A. L., Beech, P. L., Fuster, J. C., and Rosenbaum, J. L. (1998). *Chlamydomonas* kinesin II-dependent intraflagellar transport (IFT): IFT particles contain proteins required for ciliary assembly in *Caenorhabditis elegans*. *J. Cell Biol.* **141,** 993–1008.

Currie, A. R., and Wheatley, D. N. (1966). Cilia of a distinctive structure (9 + 0) in endocrine and other tissues. *Postgrad. Med. J.* **42,** 403–408.

Dawe, H. R., Farr, H., and Gull, K. (2007). Centriole/basal body morphogenesis during ciliogenesis in animal cells. *J. Cell Sci.* **120,** 7–15.

De Harven, E., and Bernhard, W. (1956). Étude au microscope électronique de l'ultrastructure du centriole chez les vertébrés. *Z. Zellforsch. Mik. Anat.* **45,** 378–398.

Gilula, N. B., and Satir, P. (1972). The ciliary necklace. A ciliary membrane specialization. *J. Cell Biol.* **53,** 494–509.

Guterman, L. (1998). Death in the air: Sniffer plane flies into biowarfare danger zones. *New Scientist* 12 September issue.

Händel, M., Schulz, S., Stanarius, A., Schreff, M., Erdtmann-Vourliots, M., Schmidt, H., Wolf, G., and Höllt, V. (1999). Selective targeting of somatostatin receptor 3 to neuronal cilia. *Neuroscience* **89,** 909–926.

Jensen, C. G., Poole, C. A., McGlashan, S. R., Marko, M., Issa, Z. I., Vujich, K. V., and Bowser, S. S. (2004). Ultrastructural, tomographic and confocal imaging of the chonrocyte primary cilium *in situ*. *Cell Biol. Int.* **28,** 101–110.

Magloire, H., Couble, M-L., Romeas, A., and Bleicher, F. (2004). Odontoblast primary cilia: Facts and hypotheses. *Cell Biol. Int.* **28,** 93–99.

Morgan, D., Trunpenny, L., Goodship, J., Dai, W., Majunder, K., Matthews, L., Gardner, A., Schuster, G., Vien, L., Harrison, W., Elder, F. F. B., Penman-Splitt, M., *et al.* (1998). Inversin, a novel gene in the vertebrate left-right axis pathway, is partially deleted in the *inv* mouse. *Nat. Genet.* **20,** 149–156.

Ong, A. C. M., and Wheatley, D. N. (2003). Polycystic kidney disease—the ciliary connection. *Lancet* **361,** 774–776.

Pedersen, L., Veland, I., Schroder, J., and Christensen, S. T. (2008). Assembly of primary cilia. *Dev. Dynam.* (in press).

Poole, C. A., Flint, M. H., and Beaumont, B. W. (1985). Analysis of the morphology and function of primary cilia in connective tissues: A cellular cybernetic probe? *Cell Motil.* **5,** 175–193.

Poole, C. A., Jensen, C. G., Snyder, J. A., Gray, G. C., Hermanutz, V. I., and Wheatley, D. N. (1997). Confocal analysis of primary cilia structure and co-localisation with the Golgi apparatus in chondrocytes and aortic smooth muscle cells. *Cell Biol. Int.* **21,** 483–494.

Potoff, J. J., Issa, Z., Manke, C. W., and Jena, B. P. (2008). Ca^{2+}-dimethylphosphate complex formation: Providing insight into Ca^{2+} mediated local dehydration and membrane fusion in cells. *Cell Biol. Int.* **32,** 359–360.

Praetorius, H. A., and Spring, K. R. (2001). Bending the MDCK cell primary cilium increases intracellular calcium. *J. Membr. Biol.* **184,** 71–79.

Roth, K. E., Rieder, C. L., and Boswer, S. S. (1988). Flexible substratum technique for viewing from the side: Some *in vivo* properties of primary (9 + 0) cilia in cultures of kidney epithelia. *J. Cell Sci.* **89,** 457–466.

Sagan, L. (1967). On the origin of mitosing cells. *J. Theor. Biol.* **14,** 225–274.

Schwartz, E. A., Lenoard, M. L., Bizios, R., and Bowser, S. S. (1997). Analysis and modeling of the primary cilium bending response to fluid shear. *Am. J. Physiol. Renal Physiol.* **41,** F132–138.

Sjöstrand, F. S. (1953). The ultrastructure of the inner segments of the retinal rods of the guinea pig eye as revealed by electron microscopy. *J. Cell. Comp. Physiol.* **42,** 45–56.

Sorokin, S. P. (1962). Centrioles and the formation of rudimentary cilia by fibroblasts and smooth muscle cells. *J. Cell Sci.* **15,** 363–373.

Sorokin, S. P. (1967). Reconstructions of centriole formation and ciliogenesis in mammalian lungs. *Radiat. Res.* **31,** 748–759.

Wehland, J., and Weber, K. (1987). Turnover of the carboxy-terminal tyrosine of α-tubulin and means of reaching elevated levels of detyrosination in living cells. *J. Cell Sci.* **88,** 185–203.

Wheatley, D. N. (1982). "The Centriole: A central Enigma of Cell Biology." Elsevier, Amsterdam.

Wheatley, D. N. (1995). Primary cilia in normal and pathological conditions: A review. *Pathobiology* **63,** 222–238.

Wheatley, D. N. (2004). Primary cilia: New perspectives. *Cell Biol. Int.* **28,** 75–77.

Wheatley, D. N. (2005). Landmarks in the first hundred years of priary (9 + 0) cilium research. *Cell Biol. Int.* **29,** 333–339.

Wheatley, D. N., and Bowser, S. S. (2000). Length control of primary cilia: Analysis of monociluate and multiciliate cells. *Biol. Cell.* **92,** 573–582.

Wheatley, D. N., Wang, A.-M., and Strugnell, G. E. (1996). Expression of primary cilia in mammalian cells. *Cell Biol. Int.* **20,** 73–81.

Yoder, B. K., Hou, X., and Guay-Woodford, L. M. (2002). The polycystic kidney disease proteins, polycytin-1, polycystin-2, polaris, and cystin, are co-localized in renal cilia. *J. Am. Soc. Nephrol.* **13,** 2508–2516.

CHAPTER 8

Assembly and Disassembly of SNAREs in Membrane Fusion

Bhanu P. Jena

Department of Physiology
Wayne State University School of Medicine
Detroit, Michigan 48201

METHODS IN CELL BIOLOGY, VOL. 90

0091-679X/08 $35.00
DOI: 10.1016/S0091-679X(08)00808-X

Abstract

All life processes are governed at the chemical level and therefore knowledge of how single molecules interact provides a fundamental understanding of Nature. An aspect of molecular interactions, is the self-assembly of supramolecular structures. Membrane fusion for example, the very fundamental of life process requires the assembly and disassembly of a supramolecular complex, formed when certain proteins in opposing bilayers meet. Membrane fusion is essential for numerous cellular activities, including hormone secretion, enzyme release, and neurotransmission. In living cells, membrane fusion is mediated via a specialized set of proteins present in opposing bilayers. Target membrane proteins, SNAP-25 and syntaxin (t-SNAREs), and secretory vesicle-associated protein (v-SNARE) are part of the conserved protein complex involved in fusion of opposing lipid membranes. The structure and arrangement of membrane-associated full length SNARE complex, was first examined using atomic force microscopy (AFM). Results from the study demonstrate that t-SNAREs and v-SNARE, when present in opposing bilayers, interact in a circular array to form supramolecular ring complexes each measuring a few nanometers. The size of the ring complex is directly proportional to the curvature of the opposing bilayers. In the presence of calcium, the ring-complex helps in establishing continuity between the opposing bilayers. In contrast, in the absence of membrane, soluble v- and t-SNAREs fail to assemble in such specific and organized pattern, nor form such conducting channels. Once v-SNARE and t-SNAREs residing in opposing bilayers meet, the resulting SNARE complex overcome the repulsive forces between opposing bilayers, bringing them closer to within a distance of 2.8–3 Å, allowing calcium bridging of the opposing phospholipids head groups, leading to local dehydration and membrane fusion.

I. Introduction

Membrane fusion is essential for numerous cellular activities, including hormone secretion, enzyme release, and neurotransmission, to name just a few. In living cells, membrane fusion is mediated via a specialized set of proteins present in opposing bilayers. The first step in our understanding of membrane fusion in cells was made possible following the discovery of an *N*-ethylmaleimide-sensitive factor (NSF; Malhotra *et al.*, 1988) and SNARE proteins (Bennett *et al.*, 1992; Oyler *et al.*, 1989; Trimble *et al.*, 1988), and the determination of their participation in membrane fusion (Cho and Jena, 2007; Cho *et al.*, 2002, 2005; Jeremic *et al.*, 2004a,b, 2006; Weber *et al.*, 1998). VAMP and syntaxin are both integral membrane proteins, with the soluble SNAP-25 associating with syntaxin. Hence, the key to our understanding of SNARE-induced membrane fusion requires determination of the atomic arrangement and interaction between membrane-associated v- and t-SNAREs. Ideally, the atomic coordinates of membrane-associated

SNARE complex using X-ray crystallography would help elucidate the chemistry of SNARE-induced membrane fusion in cells. So far, such structural details at the atomic level of membrane-associated t-/v-SNARE complex have not been realized. This has been primarily due to solubility problems of membrane-associated SNAREs, compounded with the fact that v-SNARE and t-SNAREs need to reside in opposing membranes when they meet, to assemble in a physiologically relevant SNARE complex. The remaining option has been the use of nuclear magnetic resonance spectroscopy (NMR); however, NMR too has been of little help, since the size of t-/v-SNARE ring complexes are beyond the maximum limit for NMR studies. Regardless of these set backs, atomic force microscopy (AFM) spectroscopy has provided for the first time at nanometer to subnanometer resolution, an understanding of the structure, assembly, and disassembly of membrane-associated t-/v-SNARE complexes in physiological buffer solution (Cho and Jena, 2007; Cho *et al.*, 2002, 2005; Jeremic *et al.*, 2004a,b, 2006).

The structure and arrangement of SNAREs associated with lipid bilayers were first determined using AFM (Cho *et al.*, 2002), more than half a decade ago. A bilayer electrophysiological setup allowed measurements of membrane conductance and capacitance during the fusion of v-SNARE-reconstituted liposomes with t-SNARE-reconstituted membrane, and vice versa. Results from these studies demonstrated that t-SNAREs and v-SNARE when present in opposing membrane interact and assemble in a circular array, and in presence of calcium, form conducting channels (Cho *et al.*, 2002). The interaction of t-/v-SNARE proteins to form such a conducting channel is strictly dependent on the presence of t-SNAREs and v-SNARE in opposing bilayers. Addition of purified recombinant v-SNARE to a t-SNARE-reconstituted lipid membrane, results in nonphysiological interactions and without influence on the electrical properties of the membrane (Cho *et al.*, 2002). However, in presence of calcium, when v-SNARE vesicles are added to t-SNARE reconstituted membrane or vice versa, SNAREs assemble in a ring conformation. The resultant increase in membrane capacitance and conductance demonstrate the establishment of continuity between the opposing t-SNARE and v-SNARE reconstituted bilayers. These results confirm that t- and v-SNAREs are required to reside in opposing membrane (as they are in the physiological state in cells) to allow appropriate t-/v-SNARE interactions leading to membrane fusion in the presence of calcium (Cho *et al.*, 2002, 2005). Studies using SNARE-reconstituted liposomes and bilayers (Jeremic *et al.*, 2004a) further demonstrate: (i) a low fusion rate ($\tau = 16$ min) between t- and v-SNARE-reconstituted liposomes in the absence of Ca^{2+}; and (ii) exposure of t-/v-SNARE liposomes to Ca^{2+} drives vesicle fusion on a near physiological relevant time-scale ($\tau \sim 10$ s), demonstrating Ca^{2+} and SNAREs in combination to be the minimal fusion machinery in cells (Jeremic *et al.*, 2004a). Native and synthetic vesicles exhibit a significant negative surface charge primarily due to the polar phosphate head groups, generating a repulsive force that prevent the aggregation and fusion of opposing vesicles. In cells, SNAREs provide direction and specificity, bring opposing bilayers closer

to within a distance of 2–3 Å (Jeremic *et al.*, 2004a), enabling Ca^{2+} bridging and membrane fusion. The bound Ca^{2+} then leads to the expulsion of water between the bilayers at the bridging site, leading to lipid mixing and membrane fusion. Hence SNAREs, besides bringing opposing bilayers closer, dictate the site and size of the fusion area during cell secretion. The size of the t-/v-SNARE complex is dictated by the curvature of the opposing membranes (Cho *et al.*, 2005), hence smaller the vesicle, the smaller the channel formed.

A unique set of chemical and physical properties of the Ca^{2+} ion make it ideal for participating in the membrane fusion reaction. Calcium ion exists in its hydrated state within cells. The properties of hydrated calcium have been extensively studied using X-ray diffraction, neutron scattering, and in combination with molecular dynamics simulations (Bako *et al.*, 2002; Chialvo and Simonson, 2003; McIntosh *et al.*, 2000; Portis *et al.*, 1979). The molecular dynamic simulations include three-body corrections compared with *ab initio* quantum mechanics/molecular mechanics molecular dynamics simulations. First, principle molecular dynamics has also been used to investigate the structural, vibrational, and energetic properties of $[Ca(H_2O)_n]^{2+}$ clusters, and the hydration shell of the calcium ion (Bako *et al.*, 2002). These studies demonstrate that hydrated calcium $[Ca(H_2O)_n]^{2+}$ has more than one shell around the Ca^{2+}, with the first hydration shell having six water molecules in an octahedral arrangement (Bako *et al.*, 2002). In studies using light scattering and X-ray diffraction of SNARE-reconstituted liposomes, it has been demonstrated that fusion proceeds only when Ca^{2+} ions are available between the t- and v-SNARE-apposed proteoliposomes (Jeremic *et al.*, 2004a,b). Mixing of t- and v-SNARE proteoliposomes in the absence of Ca^{2+} leads to a diffuse and asymmetric diffractogram in X-ray diffraction studies, a typical characteristic of short-range ordering in a liquid system (McIntosh, 2000). In contrast, when t-SNARE and v-SNARE proteoliposomes in the presence of Ca^{2+} are mixed, it leads to a more structured diffractogram, with approximately a 12% increase in X-ray scattering intensity, suggesting an increase in the number of contacts between opposing bilayers, established presumably through calcium–phosphate bridges, as previously suggested (Jeremic *et al.*, 2004a,b; Portis *et al.*, 1979). The ordering effect of Ca^{2+} on interbilayer contacts observed in X-ray studies (Jeremic *et al.*, 2004a) is in good agreement with light, AFM, and spectroscopic studies, suggesting close apposition of PO-lipid head groups in the presence of Ca^{2+}, followed by formation of Ca^2–PO bridges between the adjacent bilayers (Jeremic *et al.*, 2004a,b; Laroche *et al.*, 1991). X-ray diffraction studies show that the effect of Ca^{2+} on bilayers orientation and interbilayer contacts is most prominent in the area of 3 Å, with additional appearance of a new peak at position 2.8 Å, both of which are within the ionic radius of Ca^{2+} (Jeremic *et al.*, 2004a). These studies further suggest that the ionic radius of Ca^{2+} may make it an ideal player in the membrane fusion reaction. Hydrated calcium $[Ca(H_2O)_n]^{2+}$, however, with a hydration shell having six water molecules and measuring ~6 Å would be excluded from the t-/v-SNARE apposed interbilayer space, hence calcium has to be present in the buffer solution when t-SNARE vesicles

and v-SNARE vesicles meet. Indeed, studies demonstrate that if t- and v-SNARE vesicles are allowed to mix in a calcium-free buffer, there is no fusion following post addition of calcium (Jeremic *et al.*, 2004b). How does calcium work? Calcium bridging of apposing bilayers may lead to the release of water from the hydrated Ca^{2+} ion, leading to bilayer destabilization and membrane fusion. Additionally, the binding of calcium to the phosphate head groups of the apposing bilayers may also displace the loosely coordinated water at the PO-lipid head groups, resulting in further dehydration, leading to destabilization of the lipid bilayer and membrane fusion. Recent studies in the laboratory (Potoff *et al.*, 2008), using molecular dynamics simulations in the isobaric-isothermal ensemble to determine whether Ca^{2+} was capable of bridging opposing phospholipid head groups in the early stages of the membrane fusion process, demonstrate indeed this to be the case. Furthermore, the distance between the oxygen atoms of the opposing PO-lipid head groups bridged by calcium was in agreement with the 2.8 Å distance previously determined using X-ray diffraction measurements. The hypothesis that there is loss of coordinated water both from the hydrated calcium ion and oxygen of the phospholipid head groups in opposing bilayers, following calcium bridging, is further demonstrated from the study.

In the presence of ATP, the highly stable, membrane-directed, and self-assembled t-/v-SNARE complex, can be disassembled by a soluble ATPase, the NSF. Careful examination of the partially disassembled t-/v-SNARE bundles within the complex using AFM, demonstrates a left-handed super coiling of SNAREs. These results demonstrate that t-/v-SNARE disassembly requires the right-handed uncoiling of each SNARE bundle within the ring complex, demonstrating NSF to behave as a right-handed molecular motor (Cho and Jeena, 2007). Furthermore, recent studies in the laboratory (Cook *et al.*, 2008) using circular dichroism (CD) spectroscopy, report for the first time that both t-SNAREs and v-SNARE and their complexes in buffered suspension, exhibit defined peaks at CD signals of 208 and 222 nm wavelengths, consistent with a higher degree of helical secondary structure. Surprisingly, when incorporated in lipid membrane, both SNAREs and their complexes exhibit reduced folding. NSF, in the presence of ATP, disassembles the SNARE complex as reflected from the CD signals demonstrating elimination of α-helices within the structure. These results further demonstrate that NSF–ATP is sufficient for the disassembly of the t-/v-SNARE complex. These studies have provided a molecular understanding of SNARE-induced membrane fusion in cells. Findings from the studies outlined earlier are described in this chapter.

II. Materials and Methods

A. Preparation of Lipid Bilayer

Lipid bilayers were prepared using brain phosphatidylethanolamine (PE), and phosphatidylcholine (PC); and dioleoylphosphatidylcholine (DOPC), and dioleylphosphatidylserine (DOPS), obtained from Avanti Lipids, Alabaster, AL.

A suspension of PE:PC in a ratio of 7:3, and at a concentration of 10 mg/ml was prepared. Hundred microliters of the lipid suspension was dried under nitrogen gas and resuspended in 50 μl of decane. To prepare membranes reconstituted with VAMP, 625 ng/ml VAMP-2 protein stock was added to the lipid suspension and brushed onto a 200 μm hole in the bilayer preparation cup until a stable bilayer with a capacitance between 100 and 250 pF was formed.

B. Lipid Membrane on Mica Surface

To prepare lipid membrane on mica for AFM studies, freshly cleaved mica disks were placed in a fluid chamber. One hundred and eighty microliters of bilayer bath solution containing 140 mM NaCl, 10 mM HEPES, and 1 mM $CaCl_2$was placed at the center of the cleaved mica disk. Twenty microliters of PC:PS vesicles were added to the above bath solution. The mixture was then allowed to incubate for 60 min at RT, prior to washing (X10), using 100 μl of bath solution/wash. The lipid membrane on mica was then imaged before and following the addition of SNARE proteins and or v-SNARE reconstituted vesicles. Ten microliters of t-SNAREs (10 μg/ml stock) and or v-SNAREs (5 μg/ml stock), was added to the lipid membrane. Similarly, 10 μl of v-SNARE reconstituted vesicles was added to either the lipid membrane alone or lipid membrane containing t-SNAREs.

C. AFM

AFM was performed on mica and on lipid membrane. Lipid membrane alone or in the presence of SNAREs and or v-SNARE reconstituted vesicles on mica, were imaged using the Nanoscope IIIa, an AFM from Digital Instruments, Santa Barbara, CA. Images were obtained both in the ''contact'' and ''tapping'' mode in fluid. However, all images presented in this manuscript were obtained in the ''tapping'' mode in fluid, using silicon nitride tips with a spring constant of 0.38 N/m, and an imaging force of $<$200 pN. Images were obtained at line frequencies of 2 Hz, with 512 lines per image, and constant image gains. Topographical dimensions of SNARE complexes and lipid vesicles were analyzed using the software nanoscopeIIIa4.43r8 supplied by Digital Instruments.

D. EPC9 Electrophysiological Lipid Bilayer Setup

Electrical measurements of the artificial lipid membrane were performed using a bilayer setup (Cohen and Niles, 1993; Kelly and Woodbury, 1996; Woodbury, 1999). Current versus time traces were recorded using pulse software, an EPC9 amplifier and probe from HEKA (Lambrecht, Germany). Briefly, membranes were formed while holding at 0 mV. Once a bilayer was formed and demonstrated to be in the capacitance limits for a stable bilayer membrane according to the hole diameter, the voltage was switched to -60 mV. A baseline current was established before the addition of proteins or vesicles.

E. Preparation of Lipid Vesicles and SNARE Protein Reconstitutions

Purified recombinant SNAREs were reconstituted into lipid vesicles using mild sonication. Three hundred microliters of PC:PS, 100 μl ergosterol, and 15 μl of nystatin (Sigma Chemical Company, St. Louis, Missouri) were dried under nitrogen gas. The lipids were resuspended in 543 μl of 140 mM NaCl, 10 mM HEPES, and 1 mM CaCl2. The suspension was vortexed for 5 min, sonicated for 30 s, and aliquoted into 100 μl samples (AVs). Twenty five microliters of syntaxin 1A-1 and SNAP-25 (t-SNAREs) at a concentration of 25 μg/ml was added to 100 μl of AVs. The t-SNARE vesicles were frozen and thawed three times and sonicated for 5 s before use. Bilayer bath solutions contained 140 mM NaCl and 10 mM HEPES. KCl at a concentration of 300 mM was used as a control for testing vesicle fusion.

F. CD Spectroscopy

Overall, secondary structural content of SNAREs and their complexes, both in suspension and membrane-associated, were determined by CD spectroscopy using an Olis DSM 17 spectrometer. Data were acquired at 25 °C with a 0.01 cm path length quartz cuvette (Helma). Spectra were collected over a wavelength range of 185–260 nm using a 1-nm step spacing. In each experiment, 30 scans were averaged per sample for enhanced signal to noise, and data were acquired on duplicate independent samples to ensure reproducibility. SNAREs and their complexes, both in suspension and membrane-associated, were analyzed for the following samples: v-SNARE, t-SNAREs, v-SNARE + t-SNAREs, v-SNARE + t-SNAREs + NSF and v-SNARE + t-SNAREs + NSF + 2.5 mM ATP. All samples had final protein concentrations of 10 μM in 5 mM sodium phosphate buffer at pH 7.5 and were baseline subtracted to eliminate buffer (or liposome in buffer) signal. Data were analyzed using the GLOBALWORKS software (Olis), which incorporates a smoothing function and fit using the CONTINLL algorithm (Cook *et al.*, 2008).

G. Wide-Angle X-ray Diffraction

Ten microliter of a 10 mM lipid vesicle suspension was placed at the center of an X-ray polycarbonate film mounted on an aluminum sample holder and placed in a Rigaku RU2000 rotating anode X-ray diffractometer equipped with automatic data collection unit (DATASCAN) and processing software (JADE). Similarly, X-ray diffraction studies were also performed using t- and v-SNARE reconstituted liposomes, both in the presence and absence of Ca^{2+}. Samples were scanned with a rotating anode, using the nickel-filtered Cu Kα line ($\lambda = 1.5418$ Å) operating at 40 kV and 150 mA. Diffraction patterns were recorded digitally with scan rate of 3 °/min. using a scintillation counter detector. The scattered X-ray intensities were evaluated as a function of scattering angle 2θ and converted into Angstron units, using the formula d (Å) $= \lambda/2 \sin\theta$.

III. Discussion

A. V-SNARE and t-SNAREs Need to Reside in Opposing Membrane to Appropriately Interact and Establish Continuity Between Those Membranes

Purified recombinant t- and v-SNARE proteins, when applied to a lipid membrane, form globular complexes (Fig. 1A–D) ranging in size from 30 to 100 nm in diameter and 3 to 15 nm in height when examined using AFM. Section analysis of t-SNARE complexes (Fig. 1D) in lipid membrane, prior to (Fig. 1B), and following addition of v-SNARE (Fig. 1C), demonstrate changes only in the size of the complex. A 5% increase in diameter and 40% increase in height were seen following the addition of v-SNARE to the t-SNARE complexes in the lipid membrane. Concomitant studies of conductance changes in the bilayer following reconstitution of SNAREs into phospholipid membranes supported the AFM observations. Addition of t-SNAREs to v-SNARE reconstituted lipid membranes did not alter membrane current (Fig. 1E). Similarly, when t-SNAREs were added to the lipid membrane prior to addition of v-SNARE, no change in the baseline current of the bilayer membrane was demonstrated (Fig. 1F). In contrast, when t-SNAREs and v-SNARE in opposing bilayers were exposed to each other, they interact and arrange in circular pattern, forming channel-like structures (Fig. 2A–D). These channels are conducting, since some vesicles are seen to have discharged their contents and are therefore flattened (Fig. 2 B), measuring only 10–15 nm in height as compared to the 40–60 nm size of filled vesicles (Fig. 2A). Since the t-/v-SNARE complex lies between the opposing bilayers, the discharged vesicles clearly reveal t-/v-SNAREs forming a rosette pattern with a dimple or channel-like opening at the center (Fig. 2B–D). On the contrary, unfused v-SNARE vesicles associated with the t-SNARE reconstituted lipid membrane, exhibit only the vesicle profile (Fig. 2A). These studies demonstrate that the t-/v-SNARE arrangement is in a circular array, having a channel-like opening at the center of the complex.

In order to determine if the channel-like structures were capable of establishing continuity between the opposing bilayers, changes in current across the bilayer were examined. T-SNARE vesicles containing the antifungal agent nystatin, and the cholesterol homologue ergosterol, where added to the *cis* side of the bilayer chamber containing v-SNARE in the bilayer membrane. Nystatin, in the presence of ergosterol, forms a cation-conducting channel in lipid membranes (Cohen and Niles, 1993; Kelly and Woodbury, 1996; Woodbury, 1999; Woodbury and Miller, 1990). When vesicles containing nystatin and ergosterol incorporate into an ergosterol-free membrane, a current spike can be observed since the nystatin channel collapses as ergosterol diffuses into the lipid membrane (Cohen and Niles, 1993; Kelly and Woodbury, 1996; Woodbury, 1999). As a positive control, a KCl gradient was established to test the ability of vesicles to fuse at the lipid membrane (410 mM *cis*:150 mM *trans*). The KCl gradient provided a driving force for vesicle incorporation that was independent of the presence of SNARE proteins (Kelly and Woodbury, 1996). When t-SNARE vesicles were exposed to v-SNARE

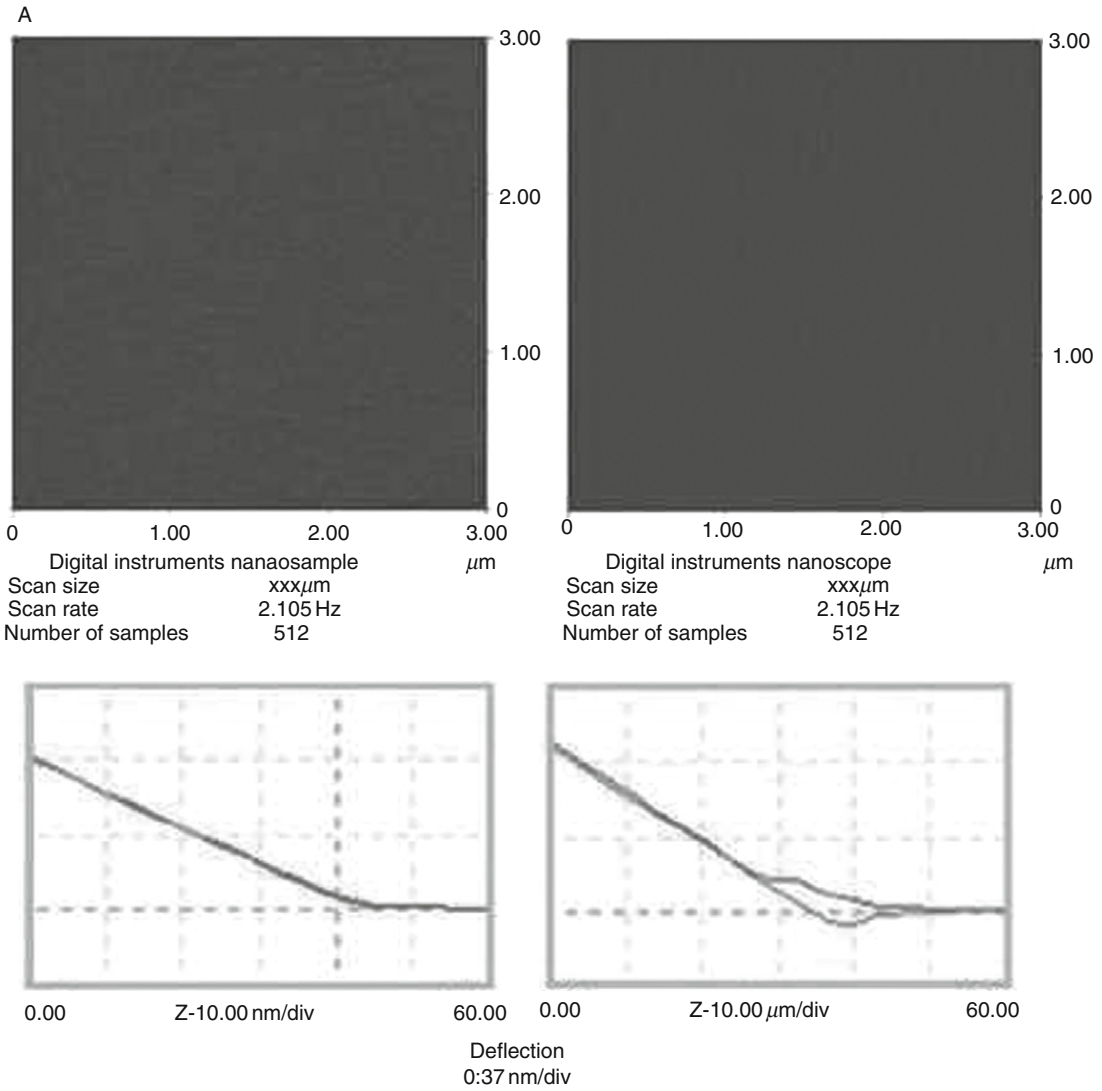

Fig. 1 *(Continued)*

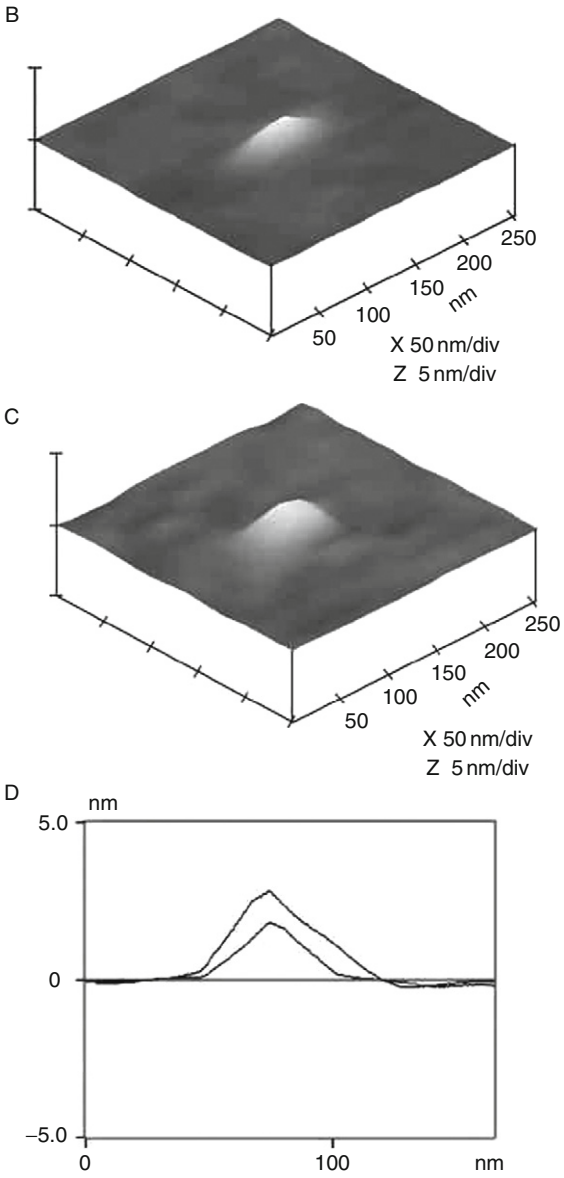

Fig. 1 *(Continued)*

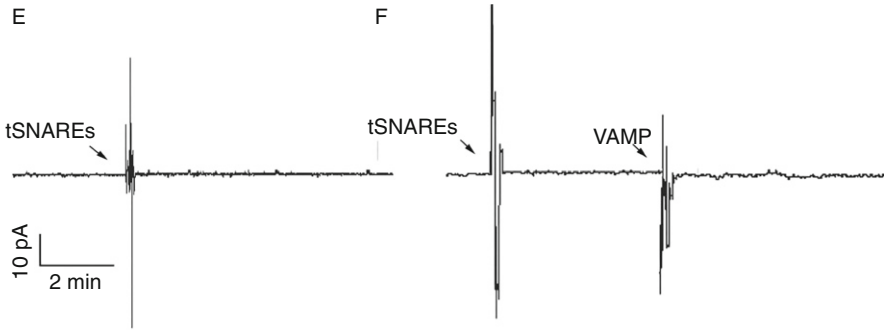

Fig. 1 AFM micrographs and force plots of mica and lipid surface and of SNAREs on lipid membrane. AFM performed on freshly cleaved mica (A, left), and on lipid membrane formed on the same mica surface (A, right), demonstrating differences in the force versus distant curves. Note the curvilinear shape exhibited in the force versus distant curves of the lipid surface in contrast to mica. Three-dimensional AFM micrographs of neuronal t-SNAREs deposited on the lipid membrane (B), and following the addition of v-SNARE (C). Section analysis of the SNARE complex in (B) and (C) is depicted in (D). Note the smaller curve belonging to the t-SNARE complex in (B), is markedly enlarged following addition of v-SNARE. Artificial bilayer lipid membranes are nonconducting either in the presence or absence of SNAREs (E, F). Current versus time traces of bilayer membranes containing proteins involved in docking and fusion of synaptic vesicles while the membranes are held at −60 mV (current/reference voltage). (E) When t-SNAREs are added to the planar lipid bilayer containing the synaptic vesicle protein, VAMP-2, no occurrence of current spike for fusion event at the bilayer membrane is observed ($n = 7$). (F) Similarly, no current spike is observed when t-SNAREs (syntaxin 1A-1 and SNAP25) are added to the *cis* side of a bilayer chamber following with VAMP-2. Increasing the concentration of t-SNAREs and VAMP-2 protein (Cho *et al.*, 2002).

reconstituted bilayers, vesicles fused (Fig. 2E). Fusions of t-SNARE containing vesicles with the membrane were observed as current spikes. To verify if the channel-like structures were continuous across the membrane, capacitance and conductance measurements of the membrane were carried out (Fig. 3A). Phospholipid vesicles that come in contact with the bilayer membrane do not readily fuse with the membrane. When v-SNARE-reconstituted phospholipid vesicles were added to the *cis* compartment of the bilayer chamber, a small increase in capacitance and a simultaneous increase in conductance was observed with little or no further increase over a 5 min period. The increase or no further change in conductance or capacitance is consistent with vesicles making contact with the membrane but not fusing (Fig. 3B). These vesicles were fusogenic because of a salt (KCl) gradient across the bilayer membrane, inducing fusion of vesicles with the lipid membrane. When t-SNARE vesicles containing nystatin and ergosterol are added to the *cis* side of the bilayer chamber, an initial increase in capacitance and conductance occurred followed by a stepwise increase in both membrane capacitance and conductance (Fig. 3C) along with several fusion events, observed as current spikes in separate recordings (Fig. 2E). The stepwise increase in capacitance demonstrates that the docked t-SNARE vesicles are continuous with the

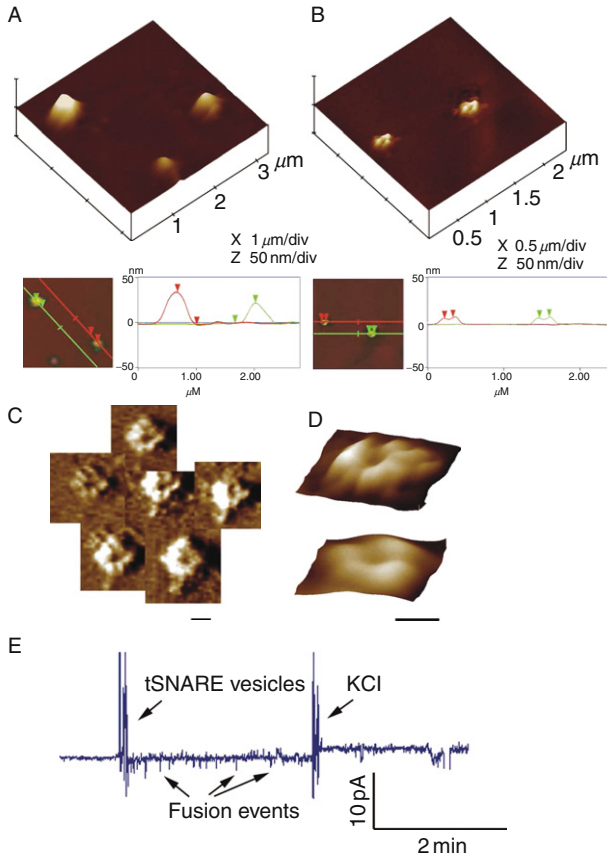

Fig. 2 Pore-like structures are formed when t-SNAREs and v-SNARE in opposing bilayers interact. (A) Unfused v-SNARE vesicles on t-SNARE reconstituted lipid membrane. (B) Dislodgement and/or fusion of v-SNARE-reconstituted vesicles with a t-SNARE-reconstituted lipid membrane, exhibit formation of channel-like structures due to the interaction of v- and t-SNAREs in a circular array. The size of these channels range between 50 and 150 nm (B–D). Several 3D AFM amplitude images of SNAREs arranged in a circular array (C) and some at higher resolution (D), illustrating a channel-like structure at the center is depicted. Scale bar is 100 nm. Recombinant t-SNAREs and v-SNARE in opposing bilayers drive membrane fusion. (E) When t-SNARE vesicles were exposed to v-SNARE reconstituted bilayers, vesicles fused. Vesicles containing nystatin/ergosterol and t-SNAREs were added to the *cis* side of the bilayer chamber. Fusion of t-SNARE containing vesicles with the membrane observed as current spikes that collapse as the nystatin spreads into the bilayer membrane. To determine membrane stability, the transmembrane gradient of KCl was increased, allowing gradient driven fusion of nystatin-associated vesicles (Cho *et al.*, 2002).

bilayer membrane. The simultaneous increase in membrane conductance is a reflection of the vesicle-associated nystatin channels that are conducting through SNARE-induced channels formed, allowing conductance of ions from *cis* to the *trans* compartment of the bilayer membrane. SNARE induced fusion occurs at an

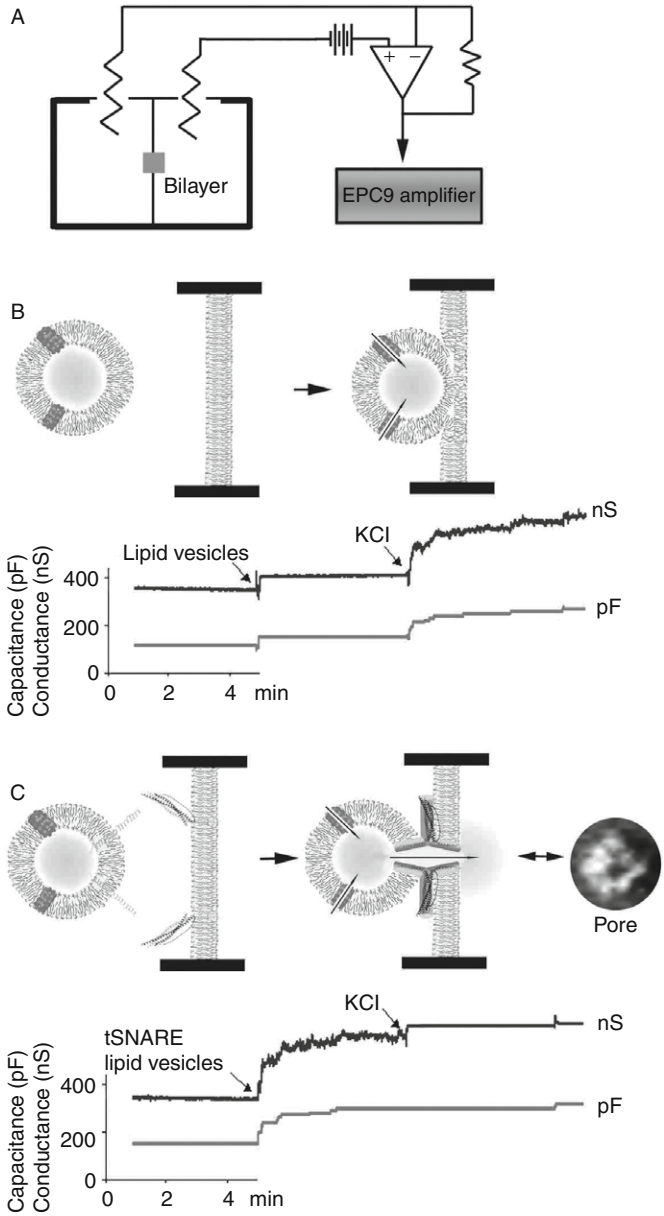

Fig. 3 Opposing bilayers containing t- and v-SNAREs, respectively, interact in a circular array to form conducting pores. (A) Schematic diagram of the bilayer-electrophysiology setup. (B) Lipid vesicle containing nystatin channels (in red) and both vesicles and membrane bilayer without SNAREs, demonstrate no significant changes in capacitance and conductance. Initial increase in conductance and capacitance are due to vesicle-membrane attachment. To demonstrate membrane stability (both bilayer membrane and vesicles), the transmembrane gradient of KCl was increased to allow gradient

average rate of four t-SNARE vesicle incorporations every 5 min into the v-SNARE reconstituted bilayer without osmotic pressure, compared to six vesicles using a KCl gradient ($n = 7$). These studies demonstrate that when opposing bilayers meet, SNAREs arrange in a ring pattern results in the formation of a conducting channel (Cho *et al.*, 2002).

B. Membrane Curvature Dictate the Size of the SNARE Ring Complex

SNARE-ring complexes ranging in size from approximately 15–300 nm in diameter are formed when t-SNARE-reconstituted and v-SNARE-reconstituted lipid vesicles meet. Since vesicle curvature would dictate the contact area between opposing vesicles, this broad spectrum of SNARE complexes observed, may be due to the interaction between SNARE-reconstituted vesicles of different size. To test this hypothesis, t-SNARE- and v-SNARE-reconstituted liposomes (proteoliposomes) of distinct diameters were used (Cho *et al.*, 2005). Lipid vesicles of different sizes used in the study were isolated using published extrusion method (Jeremic *et al.*, 2004a). The size of each vesicle population was further assessed using the AFM (Fig. 4). AFM section analysis demonstrates the presence of small 40–50-nm diameter vesicles isolated using a 50 nm extruder filter (Fig. 4A and B). Similarly, representative samples of large vesicles measuring 150–200 nm and 800–1000 nm were obtained using different size filters in the extruder. Such large vesicles are shown in the AFM micrograph (Fig. 4C and D). Analysis of vesicle size using photon correlation spectroscopy, further confirmed the uniformity in the size of vesicles within each vesicle population. The morphology and size of the SNARE complex formed by the interaction of t-SNARE- and v-SNARE-reconstituted vesicles of different diameter were examined using the AFM (Fig. 5). In each case, the t-SNARE and v-SNARE proteins in opposing proteoliposomes, interact and self-assemble in a circular pattern, forming channel-like structures. The interaction and arrangement of SNAREs in a characteristic ring pattern were observed for all populations of proteoliposomes examined (Fig. 5A–D). However, the size of the SNARE complex was determined to be dictated by the diameter of the proteoliposomes used (Fig. 5; Cho *et al.*, 2005). When small (~50 nm) t-SNARE- and v-SNARE-reconstituted vesicles were allowed to interact, SNARE-ring complexes of ~20 nm in diameter were generated (Fig. 5A and B; Cho *et al.*, 2005). With increase in the diameter of proteoliposomes, larger t-/v-SNARE complexes were

driven fusion and a concomitance increase of conductance and capacitance. (C) When t-SNARE vesicles were added to a v-SNARE membrane support, the SNAREs in opposing bilayers arranged in a ring pattern, forming pores (as seen in the AFM micrograph on the extreme right) and there were seen stepwise increases in capacitance and conductance (−60 mV holding potential). Docking and fusion of the vesicle at the bilayer membrane, opens vesicle-associated nystatin channels and SNARE-induced pore formation, allowing conductance of ions from cis to the *trans* side of the bilayer membrane. Then further addition of KCl to induce gradient driven fusion, resulted in little or no further increase in conductance and capacitance, demonstrating docked vesicles have already fused (Cho *et al.*, 2002).

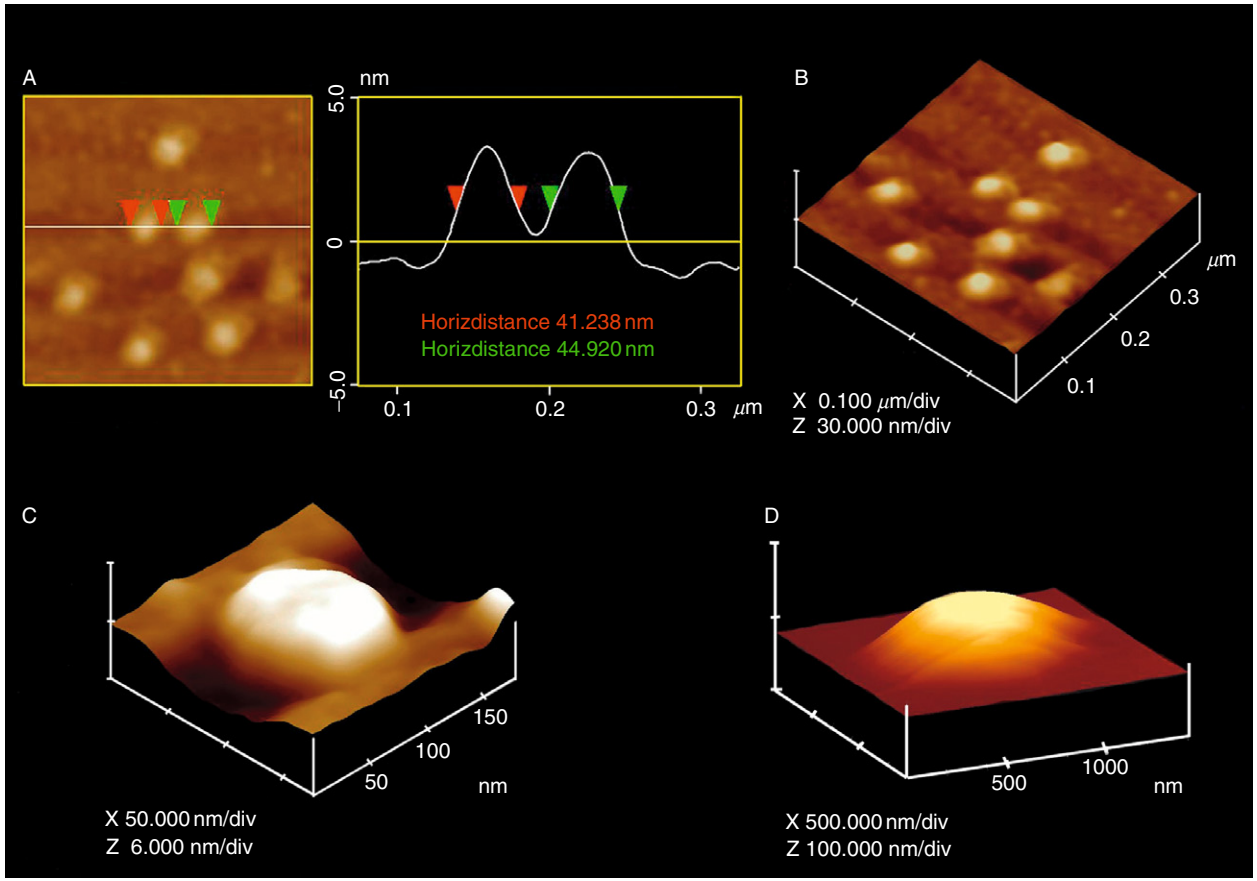

Fig. 4 AFM micrograph of t-SNARE and v-SNARE reconstituted liposomes of different sizes. Note the ~40–50 nm vesicles (A, B), the ~150 nm (C) and ~800 nm vesicle (D) (Cho *et al.*, 2005).

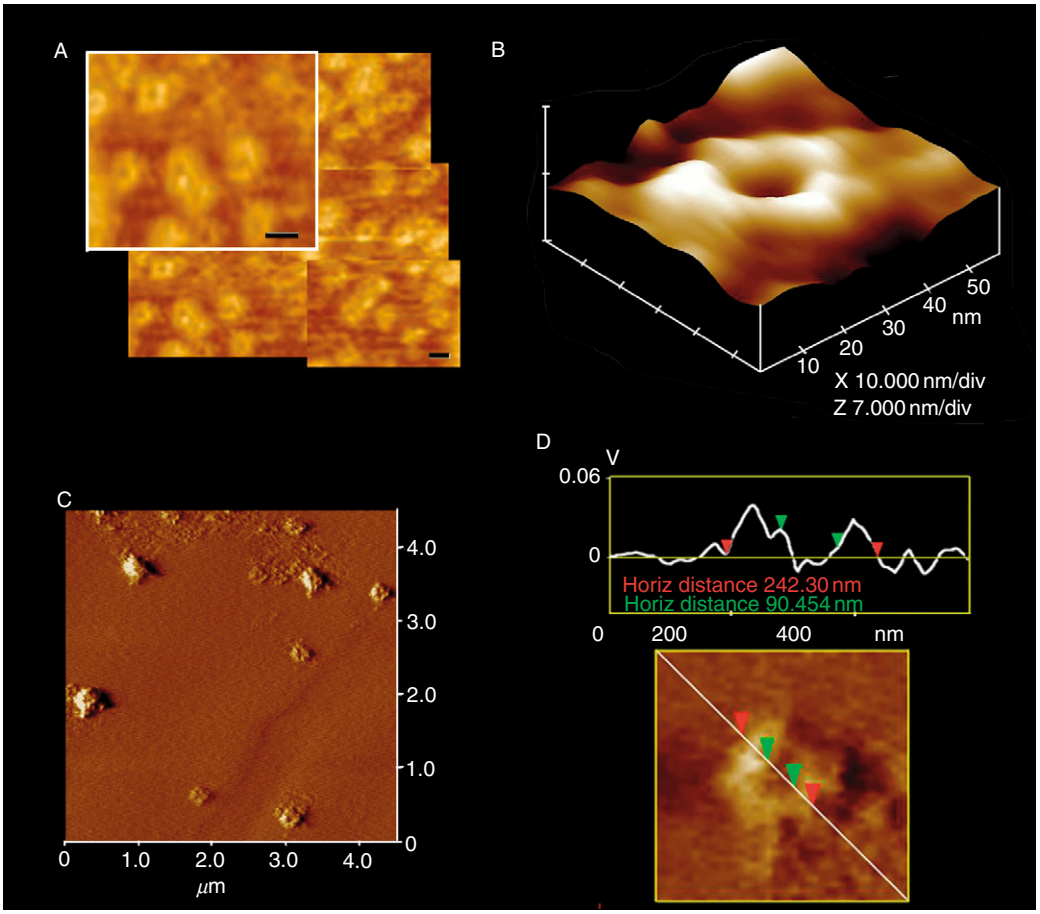

Fig. 5 Representative AFM micrograph of t-/v-SNARE complexes formed when small (A, B) or large (C, D) t-SNARE and v-SNARE reconstituted vesicles interact with each other. Note the formation of different size SNARE complexes, which are arranged in a ring pattern. Bar = 20 nm. AFM section analysis (D) shows the size of a large SNARE complex (Cho *et al.*, 2005).

formed (Fig. 5C and D). A strong linear relationship between size of the SNARE complex and vesicle diameter is demonstrated from these studies (Fig. 6; Cho *et al.*, 2005). The experimental data fit well with the high correlation coefficient, $R^2 = 0.9725$ between vesicle diameter and SNARE-complex size (Fig. 6).

C. Disassembly of the SNARE Complex

Studies demonstrate that the soluble NSF, an ATPase, disassembles the t-/v-SNARE complex in the presence of ATP (Jeremic *et al.*, 2006). This study was also the first conformation by direct physical observation that NSF–ATP alone can

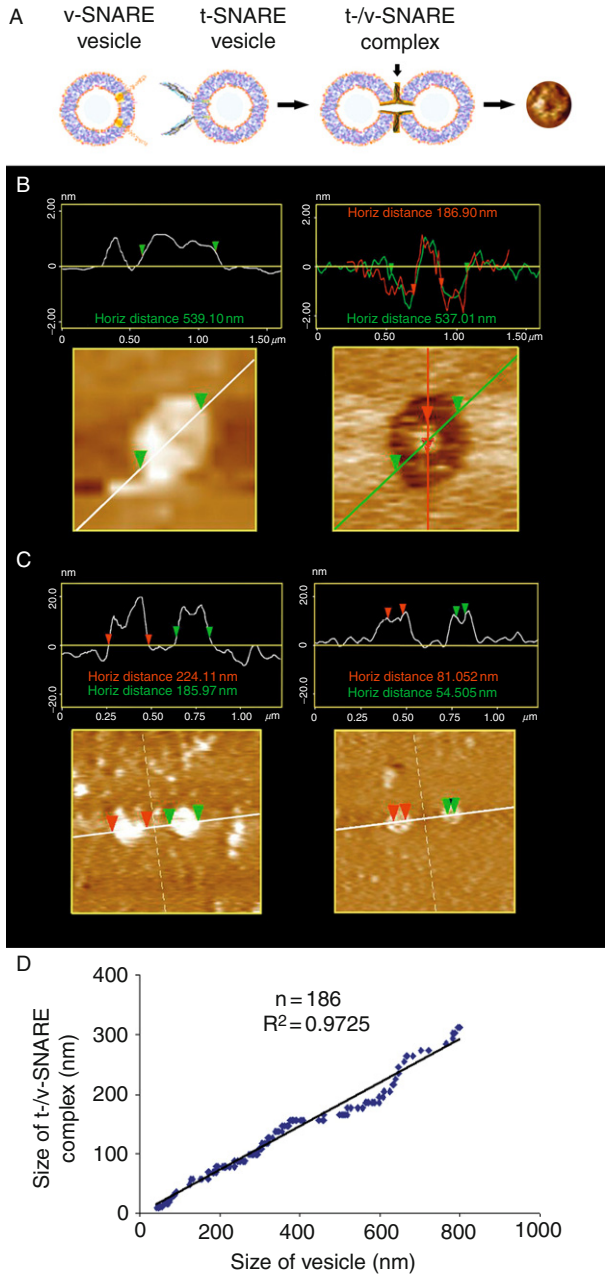

Fig. 6 SNARE complex is directly proportional to vesicle diameter. Schematic diagram depicting the interaction of t-SNARE and v-SNARE reconstituted vesicles. At the extreme right, is a single t-/v-SNARE complex imaged by AFM (A). AFM images of vesicles before and after their removal by the AFM cantilever tip, exposing the t-/v-SNARE complex (B). Interacting t-SNARE- and

lead to SNARE complex disassembly. In this study, using purified recombinant NSF, and t- and v-SNARE-reconstituted liposomes, the disassembly of the t-/v-SNARE complex was examined. Lipid vesicles ranging in size 0.2–2 μm, were reconstituted with either t-SNAREs or v-SNARE. Kinetics of association and dissociation of t-SNARE- and v-SNARE-reconstituted liposomes in solution, in the presence or absence of NSF, ATP, and AMP–PNP (the nonhydrolyzable ATP analog), were monitored by right angle light scattering (Fig. 7A and B). Addition of NSF and ATP to the t-/v-SNARE-vesicle mixture led to a rapid and significant increase in intensity of light scattering (Fig. 7A and B), suggesting rapid disassembly of the SNARE complex and dissociation of vesicles. Dissociation of t-/v-SNARE vesicles occurs on a logarithmic scale that can be expressed by first-order equation, with rate constant $k = 1.1$/s (Fig. 7B). To determine whether NSF-induced dissociation of t- and v-SNARE vesicles is energy driven, experiments were performed in the presence and absence of ATP and AMP–PNP. No significant change with NSF alone, or in presence of NSF–AMP–PNP, was observed (Fig. 7C). These results demonstrate that t-/v-SNARE disassembly is an enzymatic and energy-driven process.

To further confirm the ability of NSF–ATP in the disassembly of the t-/v-SNARE complex, immunochemical studies were performed. It has been demonstrated that v-SNARE and t-SNAREs form a SDS-resistant complex (Jeong *et al.*, 1999). NSF binds to SNAREs and forms a stable complex when locked in the ATP-bound state (ATP–NSF). Thus, in the presence of ATP + EDTA, VAMP antibody has been demonstrated to be able to immunoprecipitate this stable NSF–SNARE complex (Jeong *et al.*, 1999). Therefore, in the present study, when t- and v-SNARE vesicles were mixed in the presence or absence of ATP, NSF, NSF + ATP, or NSF + AMP–PNP, and resolved using SDS-PAGE followed by immunoblots using syntaxin-1 specific antibody, t-/v-SNARE disassembly was found to be complete only in the presence of NSF–ATP (Fig. 7D and E). To further confirm these findings (Fig. 7), direct observation of the t-/v-SNARE complex disassembly was assessed using AFM. When purified recombinant t-SNAREs and v-SNARE in opposing bilayers interact and self-assemble to form supramolecular ring complexes, they disassembled when exposed to recombinant NSF and ATP, as observed at nanometer resolution using AFM (Fig. 8). Since SNARE ring complex requires v-SNARE and t-SNAREs to be membrane-associated, suggested that NSF may require the t-/v-SNARE complex to be arranged in a specific configuration or pattern, for it to bind and disassemble the complex in presence of ATP. To test this hypothesis, t-SNAREs followed by v-SNARE, NSF and ATP were

v-SNARE-vesicles imaged by AFM at low (< 200 pN) and high forces (300–500 pN). Note, at low imaging forces, only the vesicle profile is imaged (left C). However at higher forces, the soft vesicle is flattened, allowing the SNARE complex to be imaged (right C). Plot of vesicle diameter versus size of the SNARE complex. Note the high correlation coefficient ($R^2 = 0.9725$) between vesicle diameter and the size of the SNARE complex (D) (Cho *et al.*, 2005).

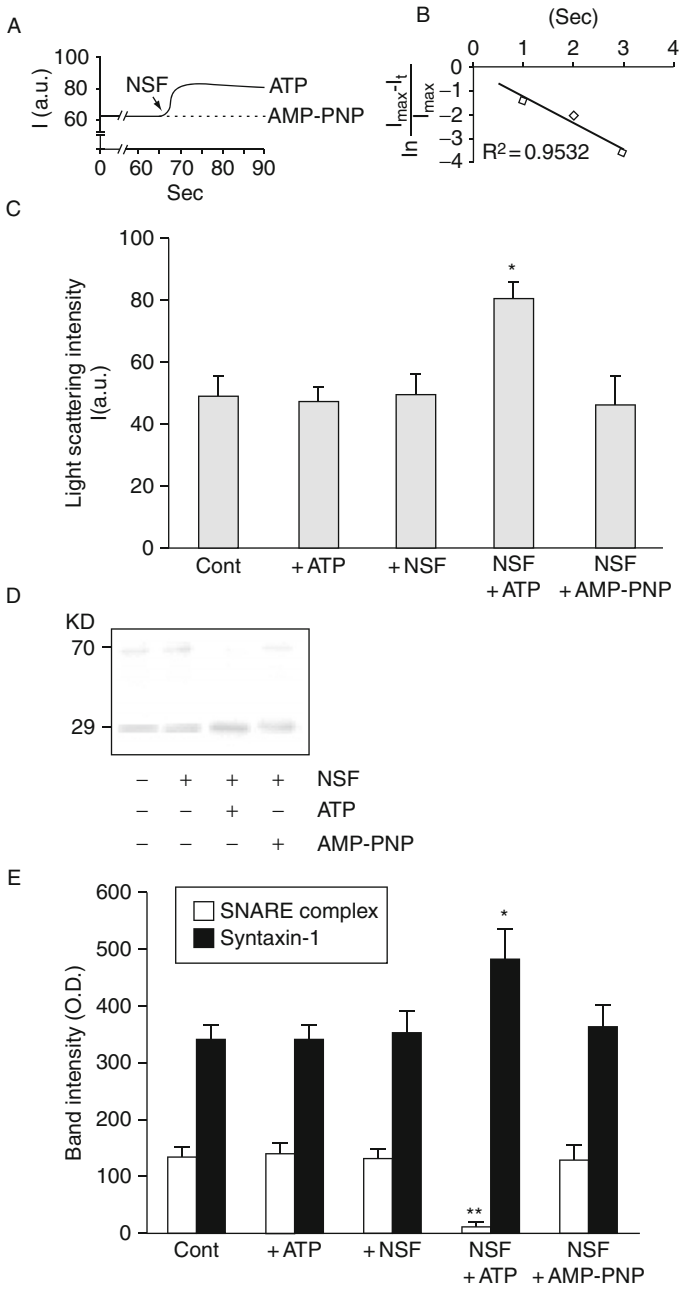

Fig. 7 NSF–ATP induced dissociation of t-SNARE and v-SNARE associated liposomes. (A) Real-time light scattering profiles of interacting t-SNARE and v-SNARE vesicles in solution in the presence and absence of NSF (depicted by arrow). In presence of ATP, NSF rapidly disassembles the SNARE

added to a lipid membrane, and continuously imaged in buffer by AFM (Fig. 9). Results from this study demonstrate that both SNARE complexes either in presence or absence of membrane, disassemble (Jeremic *et al.*, 2006). Furthermore, close examination of the NSF–ATP-induced disassembled SNARE complex by AFM, demonstrates NSF to function as a right-handed molecular motor (Cho and Jena, 2007).

D. CD Spectroscopy Confirm the Requirement of Membrane for Appropriate t-/v-SNARE Complex Assembly, and that NSF–ATP Alone Can Mediate SNARE Disassembly

The overall secondary structural content of full-length neuronal v-SNARE and t-SNAREs, and the t-/v-SNARE complex, both in suspension and membrane-associated, were determined by CD spectroscopy using an Olis DSM 17 spectrometer (Cook *et al.*, 2008). CD spectroscopy reveals that v-SNARE in buffered suspension (Fig. 10 Ai), when incorporated into liposomes (Fig. 10 Bi), exhibit reduced folding (Table I). This loss of secondary structure following incorporation of full-length v-SNARE in membrane may be a result of self-association of the hydrophobic regions of the protein in absence of membrane. When incorporated into liposomes, v-SNARE may freely unfold without the artifactual induction of secondary structure, as reflective of the lack in CD signals at 208 and 222 nm, distinct for α-helical content. The t-SNAREs (Fig. 10 Aii and Bii), shows clearly defined peaks at both these wavelengths, consistent with a higher degree of helical secondary structures formed both in buffered suspension and in membrane, at ca. 66% and 20%, respectively (Table I). Again, the membrane-associated SNARE exhibits less helical content than when in suspension. Similarly, there appears to be a dramatic difference in the CD signal observed in t-/v-SNARE complexes in suspension, and those complexes that are formed when membrane-associated SNAREs interact (Fig. 10 Aiii and Biii). Interestingly, there is no increase of secondary structure upon complex formation. Rather, the CD spectra of the complexes are identical to a combination of individual spectra. Moreover, membrane associated t-/v-SNAREs are less folded than the purified SNARE complex.

---

complex and dissociates SNARE-vesicles represented as a rapid increase in light scattering. No change in light scattering is observed when ATP is replaced with the nonhydrolyzable analog AMP–PNP. (B) Kinetics of NSF-induced dissociation. The graph depicts first-order kinetics of vesicles dissociation elicited by NSF–ATP. (C) NSF requires ATP to dissociate vesicles. NSF in the presence of ATP dissociates vesicles ($p < 0.05$, $n = 4$, Student's t-test). However, NSF alone or NSF in the presense of AMP–PNP had no effect on the light scattering properties of SNARE-associated vesicle ($p > 0.05$, $n = 4$, Student's t-test). (D) When t- and v-SNARE vesicles are mixed in the presence or absence of ATP, NSF, NSF + ATP, or NSF + AMP–PNP, and resolved by SDS-PAGE followed by immunoblots using syntaxin-1 specific antibody, t-/v-SNARE disassembly was found to be complete only in the presence of NSF-ATP (E). Densitometric scan of the bands reveals significant changes in SNARE complex and syntaxin-1 reactivity only when NSF and ATP were included in reaction mixture ($p < 0.05$, $n = 3$; and $p < 0.01$, $n = 3$, Student's t-test).

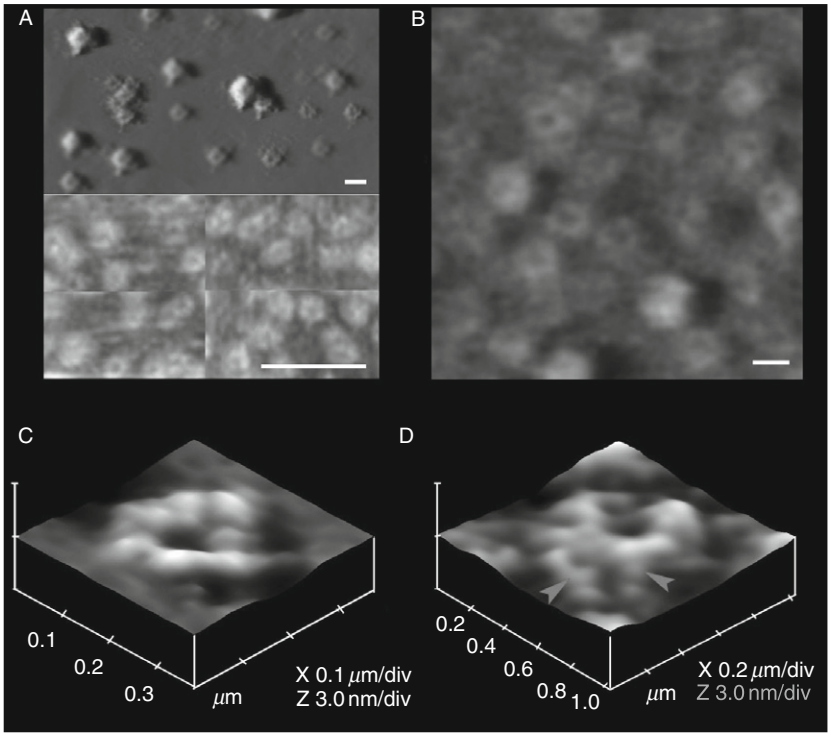

Fig. 8 AFM micrographs of NSF–ATP induced disassembly of the t-/v-SNARE ring complex. Representative AFM micrograph of t-/v-SNARE complexes formed when large (top panel A) or small (bottom panel A) t-/v-SNARE ring complexes are formed due to the interaction of large and small v-SNARE reconstituted vesicles interact with a t-SNARE reconstituted lipid membrane. Bar = 250 nm. (B) Disassembly of large t-/v-SNARE complex. Bar = 250 nm. (C) High resolution of a t-/v-SNARE ring complex, and a disassembled one (D).

This data supports previous AFM results that lipid is required for proper arrangement of the SNARE proteins in membrane fusion. Addition of NSF to the t-/v-SNARE complex results in an increase in the unordered fraction (Fig. 10 Aiv and Biv; Table I), which may be attributed to an overall disordered secondary structure of the NSF, and not necessarily unfolding of the t-/v-SNARE complex. In contrast, activation of NSF by the addition of ATP almost completely abolishes all α-helical content within the multiprotein complex (Fig. 10 Av and Bv). This direct observation of the helical unfolding of the SNARE complex using CD spectroscopy under physiologically relevant conditions (i.e., in membrane-associated SNAREs), confirms earlier AFM reports on NSF–ATP-induced t-/v-SNARE complex disassembly (Jeremic *et al.*, 2006). In further agreement with previously reported studies using the AFM, the consequence of ATP addition to the t-/v-SNARE–NSF complex is disassembly, regardless of whether the t-/v-SNARE + NSF complex is

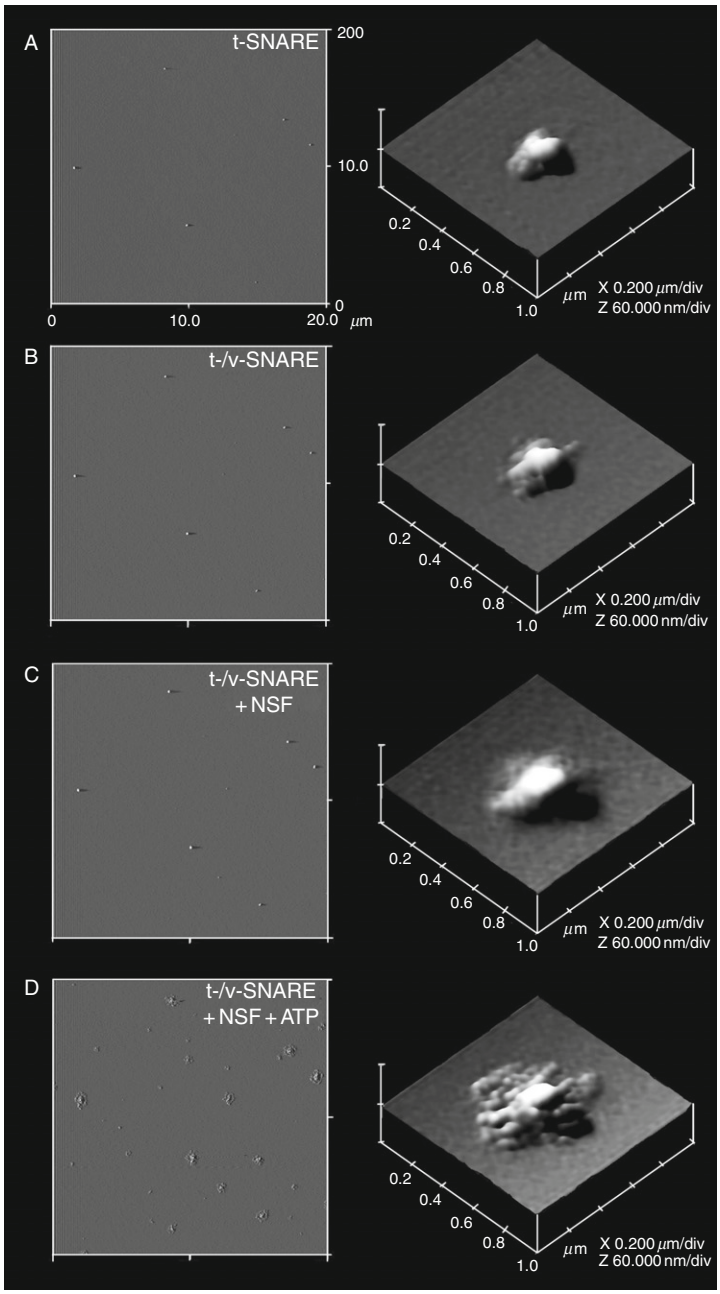

Fig. 9 AFM micrographs of NSF–ATP induced disassembly of the t-/v-SNARE complex formed when v-SNARE is added to a t-SNARE reconstituted lipid membrane. The left panel A–D shows at low resolution, the sequential AFM micrographs of one of ten representative experiments, where v-SNARE is added to a t-SNARE reconstituted lipid membrane, followed by NSF and then ATP. Note the dramatic disassembly of the SNARE complexes in D. The right panel shows at higher resolution, the disassembly of one of such SNARE complexes.

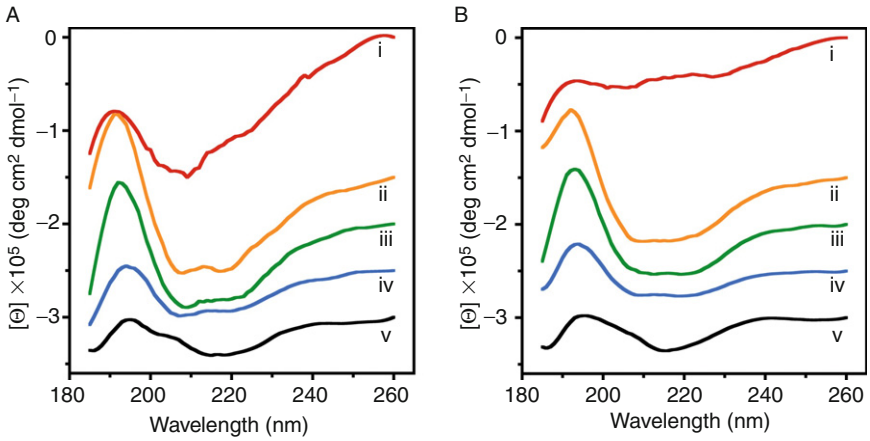

Fig. 10 Circular dichroism (CD) data reflecting structural changes to SNAREs, both in suspension and in association with membrane. Structural changes, following the assembly and disassembly of the t-/v-SNARE complex, are further shown. (A) CD spectra of purified full-length SNARE proteins in suspension and (B) in membrane-associated; their assemblyand (NSF–ATP)-induced disassembly is demonstrated. (i) v-SNARE; (ii) t-SNAREs; (iii) t-/v-SNARE complex; (iv) t-/v-SNARE + NSF; and (v) t-/v-SNARE + NSF + 2.5 mM ATP, is shown. CD spectra were recorded at 25 °C in 5 mM sodium phosphate buffer (pH 7.5), at a protein concentration of 10 μM. In each experiment, 30 scans were averaged per sample for enhanced signal to noise, and data were acquired on duplicate independent samples to ensure reproducibility.

Table I
Secondary structural fit parameters of SNARE complex formation and dissociation

	Suspension (100 × f[a])					Membrane-associated (100 × f)				
Protein[b]	α	β	O	U	Fit[c]	α	β	O	U	Fit
v-SNARE	4	36	18	43	0.19	0	30	32	38	0.21
t-SNAREs	66	34	0	0	0.02	20	15	21	44	0.84
v-/t-SNAREs	48	52	0	0	0.02	20	19	56	5	0.38
v-/t-SNAREs + NSF	20	25	0	55	0.07	18	6	8	68	0.2
v-/t-SNAREs + NSF + ATP	3	39	18	40	0.22	1	27	34	38	0.23

[a]Abbreviations used: *f*, fraction of residues is a given conformational class; α, α-helix; β, β-sheet; *O*, other (sum of turns, distorted helix, distorted sheet); *U*, unordered

[b]Protein constructs: *v-SNARE* (VAMP2); *t-SNAREs* (SNAP-25 + syntaxin 1A); *NSF*, *N*-ethylmaleimide sensitive factor; ATP, adenosine triphosphate

[c]Fit: goodness of fit parameter expressed as normalized spectral fit standard deviation (nm)

membrane-associated or in buffered suspension. In earlier AFM studies, 0.16–0.2 μg/ml of SNARE proteins was used, as opposed to the 800–1000 μg/ml protein concentration required for the current CD studies. To determine if t-SNARE and v-SNARE interact differently at higher protein concentrations, both membrane-associated

and in-suspension v- and t-SNARE complexes used in CD studies, were imaged using the AFM. In confirmation to previously reported AFM studies, results from the CD study demonstrated the formation of t-/v-SNARE ring complexes, only when t-SNARE liposomes are exposed to v-SNARE liposomes. Hence, higher SNARE protein concentrations are without influence on the membrane-directed self-assembly of the SNARE complex (Cook *et al.*, 2008). In summary, the CD results demonstrate that v-SNARE in suspension, when incorporated into liposomes, exhibits reduced folding. Similarly, t-SNAREs which exhibit clearly defined peaks at CD signals of 208- and 222-nm wavelengths, consistent with a higher degree of helical secondary structure in both the soluble and liposome-associated forms, exhibit reduced folding when membrane associated. ATP-induced activation of NSF bound to the t-/v-SNARE complex, results in disassembly of the SNARE complex, eliminating all α-helices within the structure. In addition, these studies are a further confirmation of earlier reports (Jeremic *et al.*, 2006) that NSF–ATP is sufficient for the disassembly of the t-/v-SNARE complex.

E. SNAREs Bring Opposing Bilayers Closer, Enabling Calcium Bridging and Membrane Fusion

Diffraction patterns of nonreconstituted vesicles and t- and v-SNARE-reconstituted vesicles in the absence and presence of 5 mM Ca^{2+} are shown for comparison in Fig. 11. To our knowledge, these are the first recorded wide-angle diffractograms of unilamellar (single bilayer) vesicles in the 2–4 Å diffraction range. They have broad pattern spanning 2θ ranges approximately 23–48 ° or d values of 3.9–1.9 Å with sharp drop off intensity on either sides of the range. Relatively, broad feature of diffractogram indicate multitude of contacts between atoms of one vesicle as well between different vesicles during collision. However,

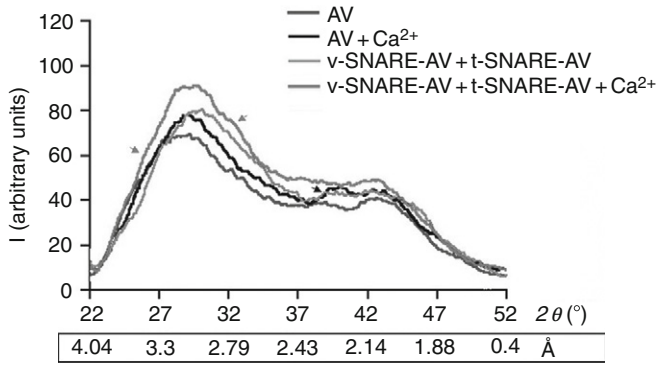

Fig. 11 Wide-angle X-ray diffraction patterns on interacting lipid vesicles. Representative diffraction profiles from one of four separate experiments using plain and t- and v-SNARE-reconstituted lipid vesicles, both in the presence or absence of 5 mM Ca^{2+} is shown. Note the shift in the major peak to the right, when t-SNARE and v-SNARE-reconstituted vesicles interact (Jeremic *et al.*, 2004a).

two broad peaks are visible on the diffractogram, the stronger one at 3.1 Å and a weaker one at 1.9 Å. They indicate that the greatest number of contacts between them have these two distances. Addition of Ca^{2+} or incorporation of SNAREs at the vesicles membrane or both, influence both peaks within the 2.1–3.3 Å intensity range (Fig. 11). However, the influence of Ca^{2+}, SNAREs or both is more visible on peak positioned at 3.1 Å in form of an increased Imax of arbitrary units and 2θ. This increase of Imax at the 3.1 Å can be explained in terms of increased vesicle pairing and/or a decrease in distance between aposed vesicles. Incorporation of t- and v-SNARE proteins at the vesicle membrane allows for tight vesicle–vesicle interaction, demonstrated again as an Imax shifts to 30.5° or 2.9 Å from 3.1 Å. Ca^{2+} and SNAREs work in manner that induces a much higher increase of peak intensity with appearance of shoulders on both sides of the peak at 2.8 and 3.4 Å (Fig. 11). This indicates an increase in number of vesicle contact points at a constant distance between them. Vesicles containing either t- or v-SNAREs have little effect on the X-ray scattering patterns. Only as discussed above, when t-SNARE and v-SNARE reconstituted-vesicles were brought together, we did detect change in the X-ray diffraction patterns. Since exposure of t-SNARE vesicle and v-SNARE vesicle mixture to Ca^{2+} results in maximum increase in a.u. and 2θ using X-ray diffraction, the effect of Ca^{2+} on fusion and aggregation of t-/v-SNARE vesicles were examined using light scattering, light microscopy, AFM, fluorescent dequenching, and electrical measurements of fusion (Jeremic *et al.*, 2004a).

The above mentioned studies and their findings provide a molecular understanding of SNARE-induced membrane fusion in cells.

Acknowledgment

The author thanks the many students and collaborators who have participated in the various studies discussed in this article. Support from the National Institutes of Health (USA), the National Science Foundation (USA), and Wayne State University, is greatly appreciated.

References

Bako, I., Hutter, J., and Palinkas, G. (2002). Car-Parrinello molecular dynamics simulation of the hydrated calcium ion. *J. Chem. Phys.* **117,** 9838–9843.

Bennett, M. K., Calakos, N., and Schller, R. H. (1992). Syntaxin: A synaptic protein implicated in docking of synaptic vesicles at presynaptic active zones. *Science* **257,** 255–259.

Chialvo, A. A., and Simonson, J. M. (2003). The structure of $CaCl_2$ aqueous solutions over a wide range of concentration. Interpretation of diffraction experiments via molecular simulation. *J. Chem. Phys.* **119,** 8052–8061.

Cho, S.-J., Kelly, M., Rognlien, K. T., Cho, J., Hörber, J. K., and Jena, B. P. (2002). SNAREs in opposing bilayers interact in a circular array to form conducting pores. *Biophys. J.* **83,** 2522–2527.

Cho, W. J., and Jena, B. P. (2007). *N*-ethylmaleimide sensitive factor is a right-handed molecular motor. *J. Biomed. Nanotech.* **3,** 209–211.

Cho, W. J., Jeremic, A., and Jena, B. P. (2005). Size of supramolecular SNARE complex: Membrane-directed self-assembly. *J. Am. Chem. Soc.* **127,** 10156–10157.

Cohen, F. S., and Niles, W. D. (1993). Reconstituting channels into planar membranes: A conceptual framework and methods for fusing vesicles to planar bilayer phospholipid membranes. *Methods Enzymol.* **220,** 50–68.

Cook, J. D., Cho, W. J., Stemmler, T. L., and Jena, B. P. (2008). Circular dichroism (CD) spectroscopy of the assembly and disassembly of SNAREs: The proteins involved in membrane fusion in cells. *Chem. Phys. Lett.* **462,** 6–9.

Jeong, E.-H., Webster, P., Khuong, C. Q., Abdus Sattar, A. K., Satchi, M., and Jena, B. P. (1999). The native membrane fusion machinery in cells. *Cell Biol. Int.* **22,** 657–670.

Jeremic, A., Kelly, M., Cho, J., Cho, S.-J., Hörber, J. K., and Jena, B. P. (2004a). Calcium drives fusion of SNARE-apposed bilayers. *Cell Biol. Int.* **28,** 19–31.

Jeremic, A., Cho, W. J., and Jena, B. P. (2004b). Membrane fusion: What may transpire at the atomic level. *J. Biol. Phys. Chem.* **4,** 139–142.

Jeremic, A., Quinn, A. S., Cho, W. J., Taatjes, D. J., and Jena, B. P. (2006). Energy-dependent disassembly of self-assembled SNARE complex: Observation at nanometer resolution using atomic force microscopy. *J. Am. Chem. Soc.* **128,** 26–27.

Kelly, M. L., and Woodbury, D. J. (1996). Ion channels from synaptic vesicle membrane fragments reconstituted into lipid bilayers. *Biophys. J.* **70,** 2593–2599.

Laroche, G., Dufourc, E. J., Dufourcq, J., and Pezolet, M. (1991). Structure and dynamics of dimyristoylphosphatidic acid/calcium complex by 2 H NMR, infrared, spectroscopies and small-angle x-ray diffraction. *Biochemistry* **30,** 3105–3114.

Malhotra, V., Orci, L., Glick, B. S., Block, M. R., and Rothman, J. E. (1988). Role of an *N*-ethylmaleimide-sensitive transport component in promoting fusion of transport vesicles with cisternae of the Golgi stack. *Cell* **54,** 221–227.

McIntosh, T. J. (2000). Short-range interactions between lipid bilayers measured by X-ray diffraction. *Curr. Opin. Struct. Biol.* **10,** 481–485.

Oyler, G. A., Higgins, G. A., Hart, R. A., Battenberg, E., Billingsley, M., Bloom, F. E., and Wilson, M. C. (1989). The identification of a novel synaptosomal-associated protein, SNAP-25, differentially expressed by neuronal subpopulations. *J. Cell Biol.* **109,** 3039–3052.

Portis, A., Newton, C., Pangborn, W., and Papahadjopoulos, D. (1979). Studies on the mechanism of membrane fusion: Evidence for an intermembrane Ca^{2+} phospholipid complex, synergism with Mg^{2+}, and inhibition by spectrin. *Biochemistry* **18,** 780–790.

Potoff, J. J., Issa, Z., Manke, C. W., and Jena, B. P., Jr. (2008). Ca^{2+}-dimethylphosphate complex formation: Providing insight into Ca^{2+} mediated local dehydration and membrane fusion in cells. *Cell Biol. Int.* **32,** 361–366.

Trimble, W. S., Cowan, D. W., and Scheller, R. H. (1988). VAMP-1: A synaptic vesicle-associated integral membrane protein. *Proc. Natl. Acad. Sci. USA* **85,** 4538–4542.

Weber, T., Zemelman, B. V., McNew, J. A., Westermann, B., Gmachi, M., Parlati, F., Söller, T. H., and Rothman, J. E. (1998). SNAREpins: Minimal machinery for membrane fusion. *Cell* **92,** 759–772.

Woodbury, D. J., and Miller, C. (1990). Nystatin-induced liposome fusion. A versatile approach to ion channel reconstitution into planar bilayers. *Biophys. J.* **58,** 833–839.

Woodbury, D. J. (1999). Nystatin/ergosterol method for reconstituting ion channels into planar lipid bilayers. *Methods Enzymol.* **294,** 319–339.

CHAPTER 9

Understanding Membrane F usion: Combining Experimental and Simulation Studies

Bhanu P. Jena

Department of Physiology
Wayne State University School of Medicine
Detroit, Michigan 48201

Abstract

Target membrane proteins, SNAP-25 and syntaxin (t-SNARE), and secretory vesicle-associated membrane protein (v-SNARE), are part of the conserved protein complex involved in fusion of opposing bilayers in biological systems in the presence of calcium. It is known that SNARE interaction allows opposing bilayers to come close within a distance of ~2.8 Å, enabling calcium to drive membrane fusion. X-ray diffraction studies and light scattering measurements performed in SNARE-reconstituted liposomes demonstrate that when reconstituted t-SNARE- and v-SNARE-vesicles are allowed to interact prior to calcium addition, membrane fusion fail to occur. These results suggest that hydrated calcium ions are too

METHODS IN CELL BIOLOGY, VOL. 90

0091-679X/08 $35.00
DOI: 10.1016/S0091-679X(08)00809-1

large (~6 Å) to fit between the SNARE-apposed bilayer space, and as a result, unable to induce membrane fusion. In the presence of calcium, however, t-SNARE vesicles interact with v-SNARE vesicles, allowing formation of calcium–phosphate bridges between the opposing bilayers, resulting in the expulsion of coordinated water at the phosphate of the phospholipid head-groups, and due to disruption of the water shell around the calcium ion, enabling lipid mixing and membrane fusion. This hypothesis when tested using atomistic molecular dynamic simulations in the isobaric–isothermal ensemble using hydrated dimethylphosphate anions (DMP^-) and calcium cations, demonstrate formation of DMP–Ca^{2+} complexes and the consequent removal of water, supporting the hypothesis. As a result of Ca^{2+}–DMP self-assembly, the distance between anionic oxygens between the two DMP molecules is reduced to 2.92 Å, which is in agreement with the 2.8 Å SNARE-induced apposition established between opposing lipid bilayers, reported from X-ray diffraction measurements.

I. Introduction

Calcium ion is essential for life processes and is found in every cell. Ca^{2+} participates in diverse cellular activities, such as metabolism, secretion, proliferation, muscle contraction, cell adhesion, learning, and memory. Although calcium is abundant within the cell, it is well sequestered and is available on demand. Upon certain cellular stimulus for instance, Ca^{2+} concentration at specific nano environment within the cell is elevated by several orders of magnitude within a brief period (<1 ms). This prompt mobilization of Ca^{2+} is essential for a myriad of physiological activities, such as the release of neurotransmitters, hormone release, or cell signaling. A unique set of chemical and physical properties of the Ca^{2+} ion make it ideal for performing these biochemical reactions. Calcium ion [Ca^{2+}] exists in its hydrated state within cells. The properties of hydrated calcium have been extensively studied using X-ray diffraction, neutron scattering, in combination with molecular dynamics simulations (Bako *et al.*, 2002, Chialvo and Simonson, 2003, Licheri *et al.*, 1976, Schwenk *et al.*, 2001). The molecular dynamic simulations include three-body corrections compared with ab initio quantum mechanics/molecular mechanics molecular dynamics simulations. First principles molecular dynamics has also been used to investigate the structural, vibrational, and energetic properties of $[Ca(H_2O)_n]^{2+}$ clusters and the hydration shell of calcium ion. These studies demonstrate that hydrated calcium $[Ca(H_2O)_n]^{2+}$ has more than one shell around it, and the first hydration shell around the Ca^{2+} has six water molecules in an octahedral arrangement (Bako *et al.*, 2002). Calcium drives SNARE-induced fusion of opposing bilayers (Jeremic *et al.*, 2004a,b). SNARE interactions allow opposing bilayers to come close within a distance of approximately 2.8 Å. Using light scattering and X-ray diffraction experiments involving SNARE-reconstituted liposomes, it became clear that fusion proceeds only when Ca^{2+} ions are available between the t- and v-SNARE-apposed bilayers (Jeremic *et al.*, 2004b). Since t-SNAREs and v-SNARE in opposing bilayers interact in a circular array to form

conducting channels in the presence of calcium (Cho *et al.*, 2002), would necessitate Ca^{2+} ions to be present between the SNARE-apposed bilayers, to allow bridging of the opposing membranes. Once calcium forms such a bridge, it can no longer hold its water shells, leading to water expulsion, membrane destabilization, and fusion.

To further test the above results and hypothesis, atomistic molecular dynamic simulations in the isobaric–isothermal ensemble using hydrated dimethylphosphate anions (DMP^-) and calcium cations, were performed (Potoff *et al.*, 2008). DMP^- was chosen for the current study since it represented the smallest molecular fragment of typical membrane phospholipids that retained properties of the phospholipid head-group, while providing a significant reduction in the computational complexity, and hence enhance accuracy of the study. Furthermore, the strategy of using the DMP^-, rather than full phospholipids, in these simulations facilitates the search for spontaneously formed Ca^{2+}–phospholipid structures, which may bridge the head groups of opposing phospholipids bilayers. Simulation results clearly demonstrated that DMP and calcium cations, form DMP–Ca^{2+} complexes and the consequent removal of water, supporting the hypothesis. As a result of Ca^{2+}–DMP self-assembly, the distance between anionic oxygens between the two DMP molecules is reduced to 2.92 Å (Potoff *et al.*, 2008), which is in agreement with the 2.8 Å SNARE-induced apposition established between opposing lipid bilayers, reported from X-ray diffraction measurements (Jeremic *et al.*, 2004a).

II. Materials and Methods

A. Preparation of Liposomes

All lipids were obtained from Avanti Polar Lipids (Alabaster, AL). A 10-mM lipid stock solution was prepared by mixing lipid solution in chloroform–DOPC (1,2-dioleoyl phosphatidylcholine): DOPS (1,2-dioleoyl phosphatidylserine) in 70:30 mol/mol ratios in glass test tubes. The lipid mixture was dried under gentle stream of nitrogen and resuspended in decane. The lipids were suspended in buffer containing 10 mM Hepes–NaOH [pH = 7.5] and 140 mM NaCl by vortexing for 5 min at room temperature. Large unilamellar vesicles (LUV) were formed following sonication for 2 min. Typically, vesicles of 0.2–2 μm in diameter range were obtained as assessed by light and atomic force microscopy. Additionally, two sets of proteoliposomes were prepared by gently mixing t-SNARE complex (Syntaxin-1/SNAP-25; final concentration 5 μg/ml) or VAMP2–His_6 (final concentration 2.5 μg/ml) with the liposomes (Cho *et al.*, 2002), followed by three freeze/thaw cycles to enhance protein reconstitution at the vesicles membrane.

B. Wide-Angle X-ray Diffraction Measurements

Ten microliters of a 10 mM t- and v-SNARE reconstituted liposomes in the presence or absence of Ca^{2+} were placed at the center of an X-ray polycarbonate film, mounted on an aluminum sample holder and placed in a Rigaku RU2000

rotating anode X-ray diffractometer equipped with automatic data collection unit (DATASCAN) and processing software (JADE). Experiments were performed at 25 °C. Samples were scanned with a rotating anode, using the nickel-filtered Cu Kα line ($\lambda = 1.5418$ Å) operating at 40 kV and 150 mA. Diffraction patterns were recorded digitally with scan rate of 3°/min using a scintillation counter detector. The scattered X-ray intensities were evaluated as a function of scattering angle 2θ and converted into Å units, using the formula d (Å) $= \lambda/2 \sin \theta$.

C. Light Scattering Studies

Vesicles aggregation and fusion was monitored using right angle (90°) light scattering with excitation and emission wavelength set at 600 nm in a Hitachi F-2000 spectrophotometer (Wilschut *et al.*, 1980). Seven microliters of t- and v-SNARE vesicles (at a final lipid concentration of 100 μM) were injected into a magnetically stirred cuvette containing 700 μl of assay buffer (in mM: Hepes 10; NaCl 140; pH = 7.4) at 37 °C. In experiments with Ca^{2+}, $CaCl_2$ (5 mM final) was included in assay buffer either prior to the addition of vesicles; or added after 4 min from injection of vesicles. Light scattering intensities are expressed in arbitrary units. When vesicles fuse, there is less scattering of light.

D. Simulation Experiments

NPT molecular dynamics simulations were performed at 298 K and 101.325 kPa on a system containing 2000 water molecules, 11 Ca^{2+} cations and 22 DMP^{-}. Periodic boundary conditions and the minimum image convention were applied in all three dimensions. Electrostatic interactions were calculated using a particle mesh Ewald. Lennard–Jones interactions were truncated after 14 Å. The CHARMM force field version 27 was used to model all interactions between molecules, including water (Foloppe *et al.*, 2000). Simulations were initiated from a random initial configuration created by Packmol (Martínez and Martínez, 2003). NAMD version 2.6 was used for all simulations (Phillips *et al.*, 2005), while visualization of molecular configurations and other data analyses were performed with VMD version 1.8.6 (Humphrey *et al.*, 1996). Simulations were performed for 20 ns (16 ns equilibration, 4 ns production) using a 2 fs time step. The volume of the system reached its average value of 61.4 nm^3 ($r = 1.06$ g/cm^3) within 200 ps. Simulations were run for an additional 10 ns beyond the 20 ns reported in this work and no significant changes were observed in the Ca^{2+}–O(water) radial distribution functions (RDF) after a 16–20 ns period.

III. Discussion

Interactions between Ca^{2+} ion and phosphate at the lipid head group in membrane, has been determined using X-ray diffraction (Jeremic *et al.*, 2004a,b). This experimental approach for monitoring interbilayer contacts, requires the presence

of highly concentrated lipid suspensions (10 mM and above) favoring multiple intervesicular contacts; and the presence of fully hydrated liposomes, where vesicles have complete freedom to interact with each other in solution, thereby establishing confined hydrated areas between adjacent bilayers (Jeremic *et al.*, 2004a). This small fluid space could arise from interbilayer hydrogen bond formation through the water molecules (McIntosh, 2000), and additional bridging forces contributed due to the formation of trans-SNARE complexes (Cho *et al.*, 2002; Jeremic *et al.*, 2004a). Mixing of t- and v-SNARE liposomes in the absence of Ca^{2+} leads to a diffuse and asymmetric diffractogram, as depicted by the gray trace in Fig. 1, typically characteristic of short range ordering in a liquid system. In contrast however, mixing of t-SNARE and v-SNARE liposomes in the presence of Ca^{2+}, leads to a more structured diffractogram as depicted by the black trace in Fig. 1, with ~12% increase in X-ray scattering intensity, reflected by an increase in the number of contacts between apposing bilayers established presumably by calcium–PO bridges (Portis *et al.*, 1979). The ordering effect of Ca^{2+} on interbilayer contacts obtained in these X-ray studies, is in good agreement with the light, atomic force microscopy, and spectroscopic studies, suggesting close apposition of PO lipid head groups in the presence of Ca^{2+} ions followed by the formation of Ca^{2+}–PO bridges between adjacent bilayers (Jeremic *et al.*, 2004a; Laroche *et al.*, 1991). Furthermore, X-ray studies shows that the effect of Ca^{2+} on bilayers orientation and interbilayer contacts, is most prominent in the area of 3 Å, with

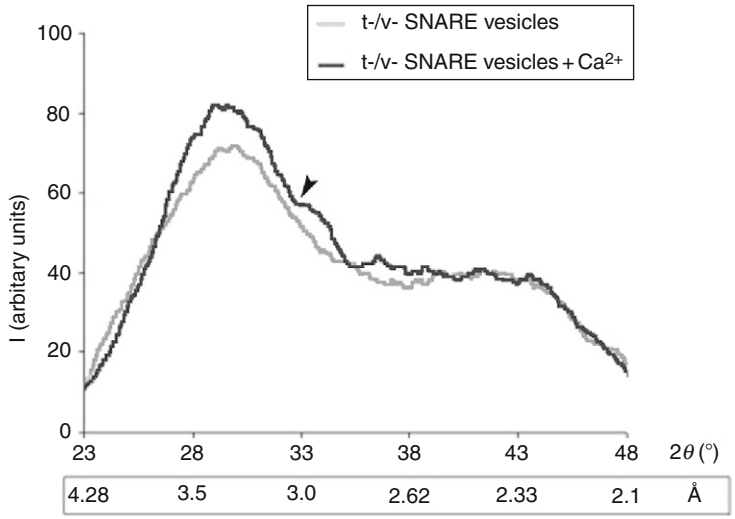

Fig. 1 Wide-angle X-ray diffraction patterns, of interacting v-SNARE- and t-SNARE-associated liposomes. Representative diffraction profiles from one of four separate experiments using t- and v-SNARE-reconstituted lipid vesicles, both in the presence or absence of 5 mM Ca^{2+} is shown. Arrows marks the appearance of a new peak in the X-ray diffractogram, following calcium addition (Jeremic *et al.*, 2004a,b).

the appearance of an additional shoulder peak, positioned at 2.8 Å (arrowhead in Fig. 1), both within the ionic radius of Ca^{2+}. These studies suggest that the ionic radius of Ca^{2+} may play an important role in membrane fusion. However, there is a major spatial problem, that is, hydrated calcium $[Ca(H_2O)_n]^{2+}$ has more than one water shell around it, with the first hydration shell being the strongest and having six water molecules arranged in an octahedral configuration (Bako *et al.*, 2002), measuring ~6 Å (Fig. 2.). Further, in the hydrated Ca^{2+} ion depending on its coordination number, the nearest average neighbor Ca^{2+}–O and Ca^{2+}–H distances are at $r \sim 2.54$ Å and $r \sim 3.2$ Å respectively in the first hydration shell. How then would it be possible for a hydrated calcium ion measuring ~6 Å, to fit between the 2.8 and 3 Å space created between the opposing bilayers by the t-/v-SNARE complex? One possibility would be that calcium has to be present in the buffer solution when t-SNARE vesicles and v-SNARE vesicles meet. In that case, if t- and v-SNARE vesicles are allowed to mix in a calcium-free buffer, no fusion should occur when calcium is later added. This hypothesis was found to be correct when tested in a study (Jeremic *et al.*, 2004a,b).

Light scattering experiments (Fig. 3) performed using t-SNARE- and v-SNARE-reconstituted phospholipids vesicles, in the presence and absence of calcium, and in the presence of NSF+ATP, confirmed the above hypothesis. Light scattering measurements of aggregation and membrane fusion of lipid vesicles was monitored on the second time-scale (Jeremic *et al.*, 2004a; Wilschut *et al.*, 1980). The initial rapid increase in intensity of light scattering was initiated

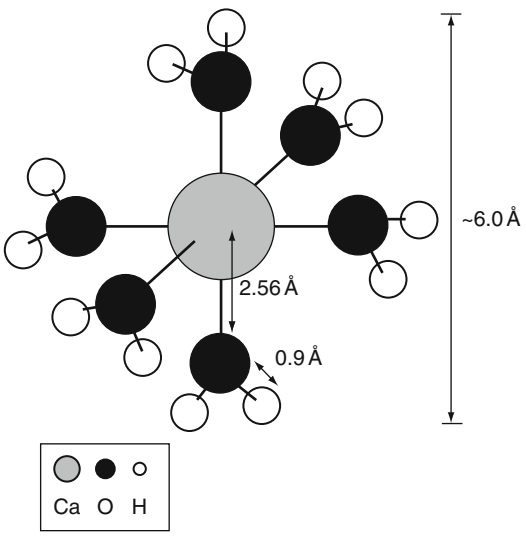

Fig. 2 Schematic diagram of hydrated calcium ion with only the first hydration shell depicted. The hydrated calcium ion containing the six water molecules arranged in an octahedral pattern, and the bond distances are shown (Jeremic *et al.*, 2004b).

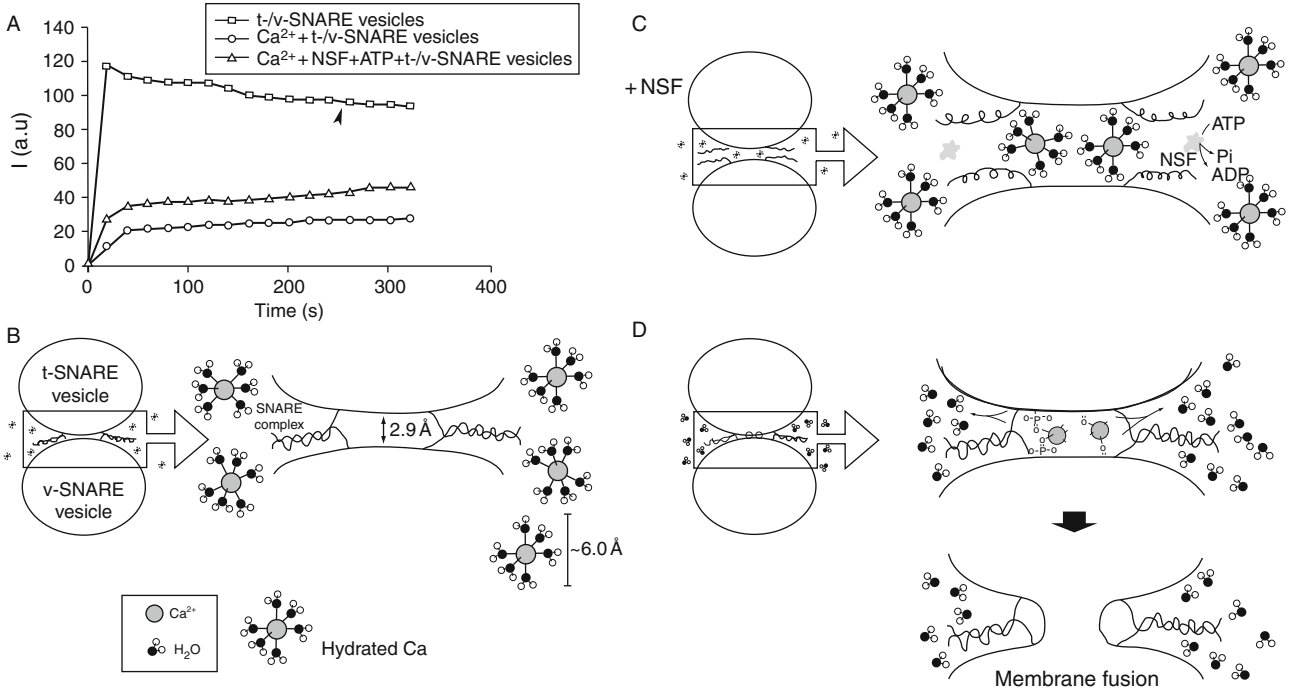

Fig. 3 Light scattering profiles of SNARE-associated vesicle interactions. (A,B) Addition of t-SNARE and v-SNARE vesicles in calcium-free buffer lead to significant increase in light scattering. Subsequent addition of 5mM Ca^{2+} (marked by arrowhead) does not have any significant effect on light scattering (¾). (A, C) In the presence of *NSF*–ATP (1 mg/ml) in assay buffer containing 5 mM Ca^{2+}, significantly inhibited vesicle aggregation and fusion (Δ). (A, D) When the assay buffer was supplemented with 5mM Ca^{2+}, prior to addition of t- and v-SNARE vesicles, it led to a 4-fold decrease in light scattering intensity due to Ca^{2+}-induced aggregation and fusion of t-/v-SNARE apposed vesicles (○). Light scattering profiles shown are representatives of four separate experiments (Jeremic *et al.*, 2004b).

by the addition of t- and v-SNARE vesicles into a calcium-free buffer solution. A slow decay of light scattering (Fig. 3), representing interactions between t-/v-SNARE vesicles was observed. Addition of calcium at a later time (arrowhead in Fig. 3) had little effect on light scattering. These studies demonstrate that if t-SNARE vesicles and v-SNARE vesicles are allowed to interact prior to calcium addition, no significant change in light scattering is observed since there is little or no fusion between the vesicles. On the contrary, when calcium is present in the buffer solution prior to addition of the t-SNARE and v-SNARE vesicles, there is a marked drop in light scattering, as a result of rapid vesicle aggregation and fusion (Fig. 3). In presence of *NSF*–ATP in the assay buffer containing calcium, a significant inhibition in aggregation and fusion of proteoliposomes is demonstrated (Fig. 3), as a result of NSF-induced t-/v-SNARE disassembly. *NSF* in the absence of ATP has no effect on the light scattering properties of the vesicle mixture (data not shown). These results suggest that *NSF*–ATP disassembles the SNARE complex, thereby reducing the number of interacting vesicles in solution. The disassembled trans-SNARE complex leave the apposed vesicles widely separated, out of reach for establishing the Ca^{2+}–PO bridges required for membrane fusion (Fig. 3). Similarly, if restricted areas between adjacent bilayers are created by t-/v-SNARE complexes, bringing opposing vesicle bilayers into close apposation, the subsequent addition of calcium fails to bridge opposing phospholipid headgroups, since the hydrated Ca^{2+} ions measuring ~6 Å, are too large (Fig. 2) to fit between the opposing bilayer space (2.8–3 Å). However, when t-SNARE vesicles interact with v-SNARE vesicles in the presence of $[Ca(H_2O)_n]^{2+}$, the t-/v-SNARE complex formed, allow formation of calcium–phosphate bridges between opposing bilayers, leading to the expulsion of water shells around the Ca^{2+} ion, and the coordinated water at the phospholipid headgroups, leading to local dehydration, membrane destabilization, lipid mixing, and membrane fusion (Fig. 3). The binding of calcium to the phosphate head groups of the apposing bilayers possibly forms a stronger bond then the Ca^{2+}–water complex, resulting in the displacement of the water from the water shell around the Ca^{2+}, as well as the loosely coordinated water at the phospholipid head groups, leading to destabilization of the lipid bilayer. Additionally, the energy gained in Ca^{2+}–PO interaction, may be large enough to overcome repulsive interbilayer forces, further contributing to membrane fusion.

Molecular dynamics simulations in the isobaric–isothermal ensemble at 298 K and 101.325 kPa when used to determine whether Ca^{2+} was capable of bridging opposing phospholipid head groups in membrane fusion, showed indeed this to be the case (Jeremic *et al.*, 2004b). As previously utilized in the study of nucleic acids (Guan *et al.*, 1994, 1995; Schneider *et al.*, 1996), DMP^- was chosen for the study since it represented the smallest molecular fragment of typical membrane phospholipids that retained properties of the phopholipid head-group, while providing a significant reduction in the computational complexity, and therefore enhancing accuracy of the study. Furthermore, the strategy of using the DMP^-, rather than full phospholipids, in these simulations facilitates the search for

spontaneously formed Ca^{2+}–phospholipid structures, which may bridge the head groups of opposing phospholipids bilayers. The DMP^- fragments can undergo free translational and rotational diffusion, as well as rapid internal conformation changes, so that structure formation with Ca^{2+} is explored rapidly and comprehensively, whereas full membrane phospholipids can exist only in self-assembled bilayers that restrain the motion of individual phospholipids molecules and greatly lengthen the time scale for structure formation. For example, in the phospholipids bilayer simulations of Bockmann and Grubmuller (2004), sequential binding of Ca^{2+} to phospholipids carbonyl oxygens within a single bilayer was incomplete even after 150 ns of simulation time, and those simulations did not include mechanisms for Ca^{2+} bridging of opposing bilayers.

The volume fluctuations presented in Fig. 4 for the first 4 ns of simulations, illustrate the rapid equilibration of the system with respect to density. While the volume of the system was stable after 200 ps, significant changes in the microstructure were observed from 0.2 to 8 ns (Fig. 5). Snapshots of molecular configurations observed during the course of the simulations are shown in Fig. 5. Radial distribution functions (RDF) were calculated at various points during the simulation to quantify the local order in the vicinity of Ca^{2+} and the anionic oxygen's of DMP^-. In Fig. 6, the radial distribution function for Ca^{2+} interacting with the oxygen of water is shown as a function of time step. In the early stages of the simulation, all calcium ions are found associated with water. However, as the simulation progresses, preferential association of Ca^{2+} with the anionic oxygen of DMP^- limits the number of water molecules that may associate with Ca^{2+}. The result is a significant reduction in the height of the Ca^{2+}–O(water) peak of the RDF over time. After 8 ns of simulation, the emergence ring structures involving two Ca^{2+} and two DMP^- were observed. In Fig. 7, an example of a ring complex observed after 17 ns of simulation is shown. The average distances between Ca^{2+} and the

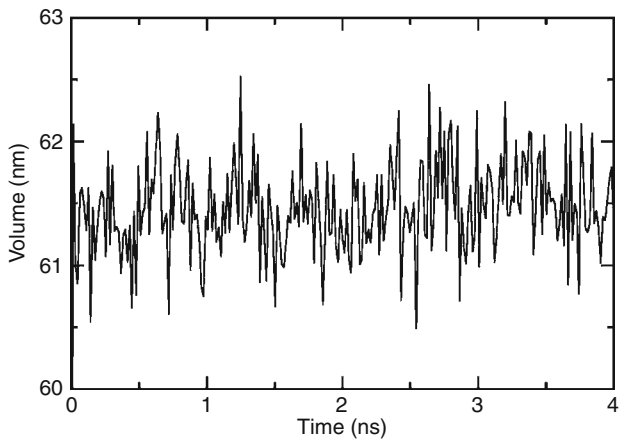

Fig. 4 Volume as a function of time for NPT molecular dynamics simulations at 298 K and 101.3 kPa.

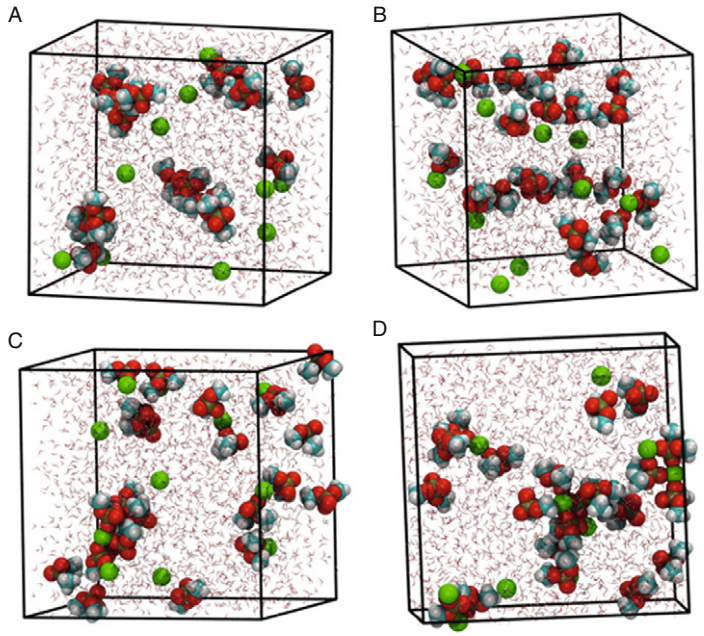

Fig. 5 NPT molecular dynamics simulation at 298 K and 101.3 kPa, demonstrating formation of DMP–Ca^{2+} complex. Initial configuration at time = 0 (A) and after minimization and heating (B) four ns of simulation at 298 K and 101.3 kPa (C), and 8 ns (D) Atoms are color coded as: Carbon (cyan), hydrogen (white), oxygen (red), phosphorous (gold), and Ca^{2+} (green). Water molecules are represented as background red–white V's for clarity.

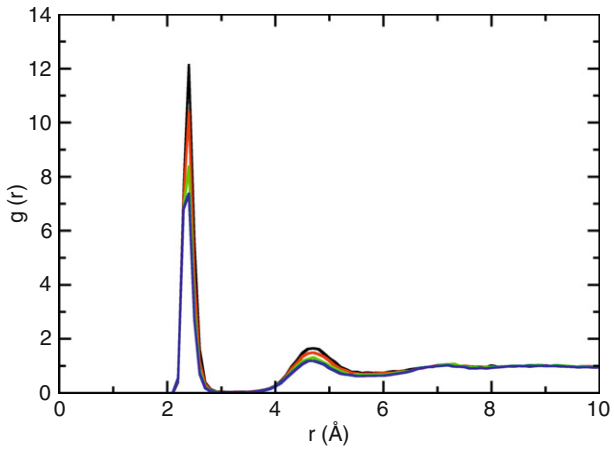

Fig. 6 Radial distribution function for Ca^{2+}–O (water) interactions as a function of timestep. 0–4 ns (black line), 4–8 ns (red line), 8–16 ns (green line), 16–20 ns (blue line).

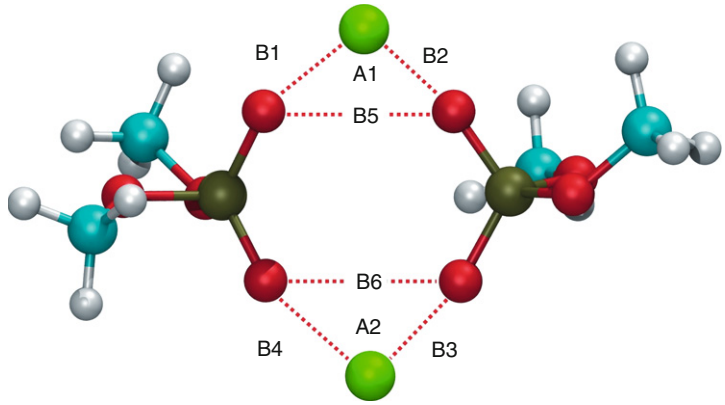

Fig. 7 Ca^{2+}–DMP^{-} ring complex observed during molecular dynamics simulations. Atoms are colored as follows: Carbon (cyan), hydrogen (white), oxygen (red), phosphorous (gold), and Ca^{2+} (green). B1 = 2.146 Å, B2 = 2.145 Å, B3 = 2.140 Å, B4 = 2.145 Å, B5 = 2.92 Å, B6 = 2.92 Å, A1 = 85.79°, A2 = 85.07°.

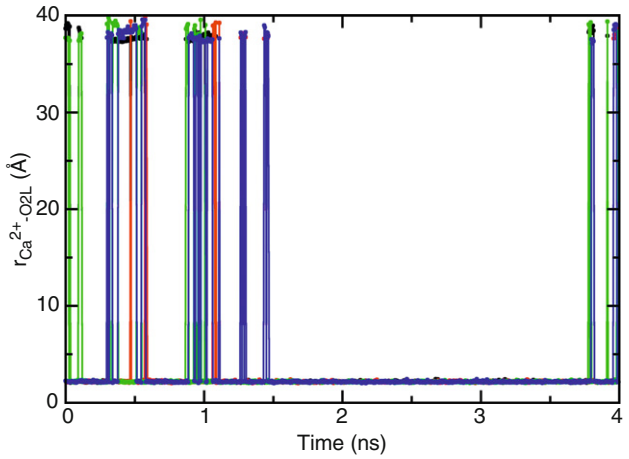

Fig. 8 Ca^{2+}–O(DMP^{-}) interaction distances as a function of time step. Data correspond to the 16–20 ns portion of the NPT molecular dynamics simulations. Distances correspond to labels in Figure S4; B1 (black line), B2 (red line), B3 (blue line), B4 (green line).

anionic oxygen's of DMP^{-} and bond angles formed by O–Ca–O were determined by taking averages during the 2.25 ns when the ring complex was stable. This time period was determined through observation of the Ca^{2+}–O(DMP^{-}) interaction distances as a function of time step for the last 4 ns of the simulation, as shown in Fig. 8. These data show that while the ring complex is quite stable, it does dissociate and reform multiple times over the course of the simulation. These

multiple dissociation and reformation events ensure that the molecular dynamics simulations have adequately sampled phase space and that the ring complex is not simply an artifact of the initial configuration used to start the simulation. Radial distributions were calculated for various interactions of water with DMP- and Ca^{2+}. The RDF for the interacting anionic DMP^{-} oxygens and Ca^{2+} are shown in Fig. 9. In the RDF's, no distinction is made between Ca^{2+} bound to one or two

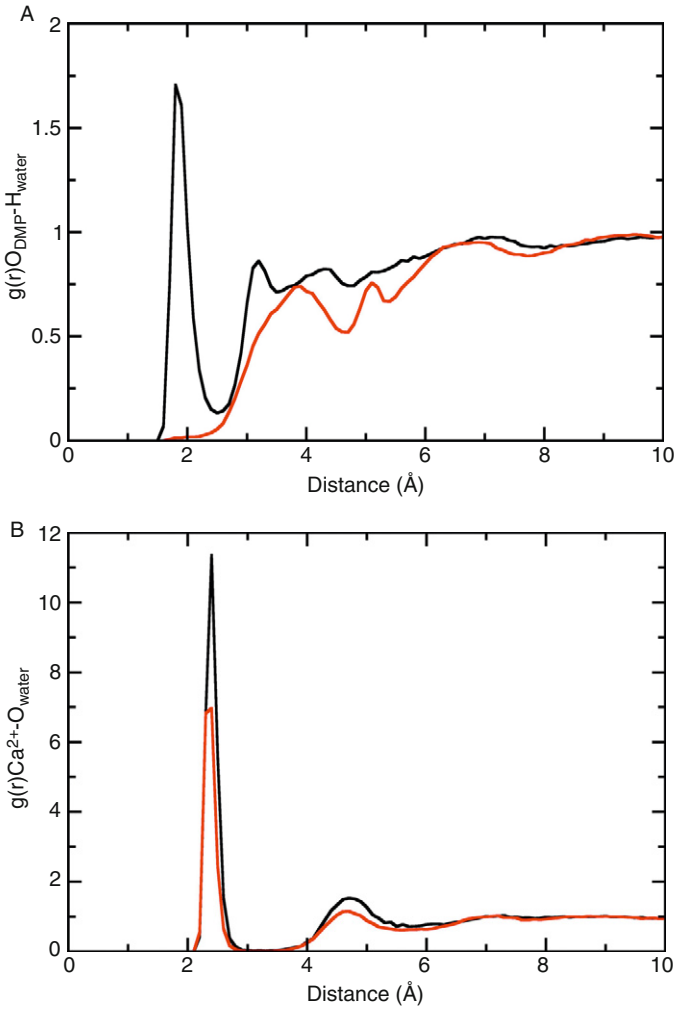

Fig. 9 Radial distribution functions for water interacting with the DMP^{-} and Ca^{2+}. (A) Hydrogen atoms of water interacting with anionic DMP^{-} oxygens. Black curve corresponds to DMP^{-} in free solution; red curve corresponds to DMP^{-} bound to Ca^{2+}. (B) Oxygen of water interacting with Ca^{2+}. Black curve represents Ca^{2+} unbound to DMP^{-}; red curve represents Ca^{2+} bound to DMP^{-}.

DMP^- molecules, nonetheless, the RDF illustrate clearly how the binding of Ca^{2+} to DMP^- alters the local structure of water around the anionic oxygens of DMP^-.

Careful examination of molecular configurations obtained from the molecular dynamics simulations reveals the establishment of self-assembled Ca^{2+}–DMP^- complexes. As shown in Fig. 7, Ca^{2+} can bridge two opposing DMP^- molecules by binding to the anionic oxygens of the DMP molecule, resulting in the formation of a somewhat ring-like structure. In addition to this ring conformation, linear and bent aggregates are also established when a single Ca^{2+} cation bridges two DMP molecules. In Fig. 7, the coordinates of atoms established when such a single Ca^{2+} bridges two DMP molecules, is illustrated. In this illustration, the distance between the interacting atoms and the resulting bond angles formed is shown in angstrom and degrees. It was observed, that without Ca^{2+}, DMP^- molecules fail to associate with each other. Formation of a single O–Ca^{2+}–O bridge was frequently observed during the 16 ns equilibration period, and resulted in an O–Ca^{2+}–O distance of 4.2 Å. However, as shown in Fig. 7, the inclusion of an additional Ca^{2+} results in the formation of a ring-like complex, which provides a means for mitigating the electrostatic repulsion between the two anionic oxygens in the DMP^- molecule. As a result of Ca^{2+}–DMP self-assembly into such a ring complex, the distance between anionic oxygens is reduced to 2.92 Å, which is in close agreement with the 2.8 Å SNARE-induced apposition established between opposing bilayers, reported from X-ray diffraction studies (Jeremic *et al.*, 2004a,b). During the course of the simulation, it was seen that the complex assembled and disassembled a number of times. The bond length and bond angle data presented in Fig. 4 have been averaged over a 2.25 ns period where the ring conformation was stable. The four anionic oxygens participating in the ring complex reside in a planar arrangement, for the full lifespan of the structure, with only minor out-of-plane excursions as the ring structure flexed (Fig. 7). In the Ca^{2+}–DMP^- complex, both Ca^{2+} ions reside above the plane formed by the oxygens, enabling the Ca^{2+} ions to retain interaction with limited water molecules.

A thorough analysis of the structure also revealed that Ca^{2+} binds only to the anionic oxygens. Furthermore, Ca^{2+} was never observed to bridge the anionic oxygens of a single DMP^- molecule. These observations are supported by a number of recent density functional calculations performed on $[Ca(H_2O)_6]^{2+}$ and $[Ca(H_2O_6]^{2+}$–DMP^- clusters (Katz *et al.*, 1996; Pavlov *et al.*, 1998; Petrov *et al.*, 2005; Sundaresan *et al.*, 2006). In case of DFT B3LYP/6–311+G(2d,2p), calculations on $[Ca(H_2O)_n]^{2+}$ clusters and the H_2O–Ca^{2+} binding energies were found to decrease monotonically from −56.9 kcal/mol for one water bound to Ca^{2+} to −24.7 kcal/mol for the sixth water bound to Ca^{2+}. It therefore becomes clear that the enthalpic penalty for removal of a water molecule from the $[Ca(H_2O)_n]^{2+}$ complex progressively increases, with the removal of each additional water molecule. Binding energies for the hexahydrated Ca^{2+} with DMP^- in an implicit water solvent (CPCM) have also been determined by DFT calculations at the B3LYP/6–31g(d,p) level by Petrov *et al.* The net interaction energies for $[Ca(H_2O)_6]^{2+}$ losing a water molecule to become $[Ca(H_2O)_5]^{2+}$ and binding to a single

anionic oxygen (monodentate) for the gg and tg conformers were determined to be −10.17 and −10.74 kcal/mol, respectively. Conversely, net binding energies for $[Ca(H_2O)_6]^{2+}$ losing two water molecules and bridging two anionic oxygens on the same DMP^- molecule (bidentate) for the gg and tg conformers were calculated to be 3.28 and 0.71 kcal/mol, respectively. These results, combined with the results of molecular dynamics simulations presented here, demonstrate the enthalpic loss due to water removal and entropic loss that results from Ca^{2+} bridging anionic oxygens on the same DMP^- molecule, cannot be overcome by the anionic oxygen–Ca^{2+} interaction. However, results from the study show that the loss of a single water molecule from Ca^{2+} is favorably replaced by interactions with anionic oxygen.

Having demonstrated that Ca^{2+} is capable of bridging phospholipid head groups, we then focused on the second aspect of the hypothesis, for example, that binding of Ca^{2+} to oxygens in the phospholipid head group results in an expulsion of water from the head group. Number integrals (Fig. 10) for the interaction of the anionic oxygens with water hydrogen atoms were calculated from our simulations for DMP^- that was unbound, as well as the DMP^- molecules that participated in the formation of Ca^{2+}–DMP^- ring complex (Fig. 7). The number integrals (Fig. 10) show that for unbound DMP^- molecules, there are, on an average, two water molecules associated with each anionic oxygen at a distance of 2.2 Å. On the contrary, when two DMP^- molecules combine with two Ca^{2+} cations to form the ring-like complex, there is a total expulsion of water from the

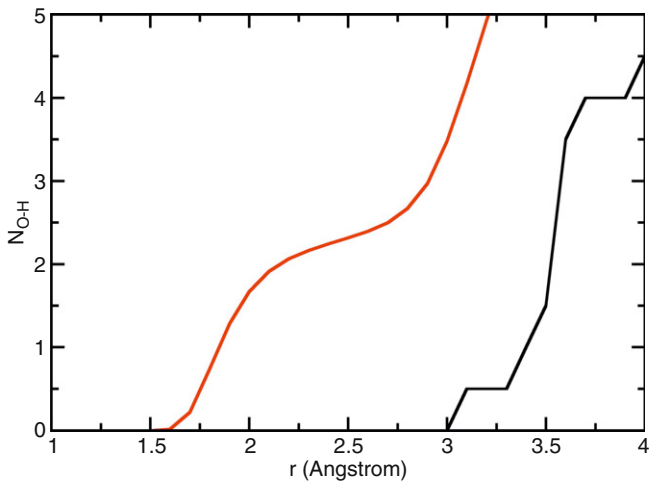

Fig. 10 Number integrals for the anionic oxygens of DMP^- interacting with the hydrogen atoms of water as determined from NPT molecular dynamics simulations at 298 K and 101.3 kPa. Red line corresponds to DMP^- that is not bound to Ca^{2+}, while the black curve represents interactions of water with the same oxygens for the Ca^{2+}–DMP^- ring complex.

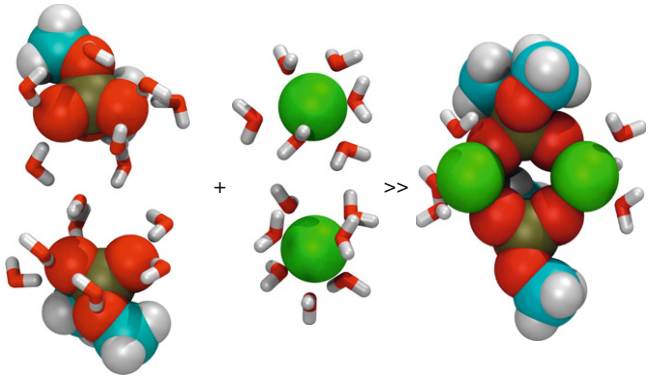

Fig. 11 Ca^{2+}–DMP complex (extreme right) formed in NTP MD simulations at 298 K and 101.3 kPa. Hydrated calcium ions (center), and hydrated DPM molecules (extreme left), interact to form Ca^{2+}–DMP complex (extreme right) having less associated water molecules. Color codes of atoms: Carbon (cyan), Hydrogen (white), Oxygen (red), Phosphorous (gold), Calcium (green), and water (red–white V's).

anionic oxygens of DMP^{-}. Additionally, calculations for DMP^{-} complexed with one Ca^{2+} show that water is completely expelled from the oxygen bound to Ca^{2+}, but 2–3 water molecules remain associated with the oxygen not bound to Ca^{2+}.

These molecular dynamics simulation studies demonstrate that hydrated Ca^{2+} is capable of bridging phospholipid head groups, and that such bridging results in an expulsion of water from both the phospholipid head groups and calcium (Fig. 11). These results are, to our knowledge, the first evidence in support of the principle hypothesis that Ca^{2+} bridging of phospholipid head groups during SNARE-induced membrane fusion results in the release of water from hydrated Ca^{2+} ion and loosely coordinated water at the PO–lipid head groups, leading to bilayer destabilization and membrane fusion in cells (Jeremic *et al.*, 2004b).

Acknowledgments

The author thanks the many students and collaborators who have participated in the various studies discussed in this article. Support from the National Institute of Health (USA), the National Science Foundation (USA), and Wayne State University, is greatly appreciated.

References

Bako, I., Hutter, J., and Palinkas, G. (2002). Car-Parrinello molecular dynamics simulation of the hydrated calcium ion. *J. Chem. Phys.* **117,** 9838–9843.

Bockmann, R. A., and Grubmuller, H. (2004). Multistep binding of divalent cations to phospholipid bilayers: A molecular dynamics study. *Angew. Chem. Int. Ed.* **43,** 1021–1024.

Chialvo, A. A., and Simonson, J. M. (2003). The structure of $CaCl_2$ aqueous solutions over a wide range of concentration. Interpretation of diffraction experiments via molecular simulation. *J. Chem. Phys.* **119,** 8052–8061.

Cho, S.-J., Kelly, M., Rognlien, K. T., Cho, J., Hörber, J. K., and Jena, B. P. (2002). SNAREs in opposing bilayers interact in a circular array to form conducting pores. *Biophys. J.* **83,** 2522–2527.

Foloppe, N., and MacKerell, A. D., Jr. (2000). An improved empirical potential energy function for molecular simulations of phospholipids. *J. Comput. Chem.* **21,** 86–104.

Guan, Y, Wurrey, C. J., and Thomas, G. J., Jr. (1994). Vibrational analysis of nucleic acids. I. The phosphodiester group in dimethyl phosphate model compounds: (CH3O)2PO2-, (CD3O)2PO2-, and (13CH3O)2PO2-. *Biophys. J.* **66,** 225–235.

Guan, Y, Choy, G. S.-C., Glaser, Rainer., and Thomas, G. J. (1995). Vibrational analysis of nucleic acids. 2. Ab initio calculation of the molecular force field and normal modes of dimethyl phosphate. *J. Phys. Chem.* **99,** 12054–12062.

Humphrey, W., Dalke, A., and Schulten, K. (1996). VMD: Visual molecular dynamics. *J. Mol. Grap.* **14,** 33–38.

Jeremic, A., Kelly, M., Cho, J., Cho, S.-J., Hörber, J. K., and Jena, B. P. (2004a). Calcium drives fusion of SNARE-apposed bilayer. *Cell Biol. Int.* **28,** 19–31.

Jeremic, A., Cho, W. J., and Jena, B. P. (2004b). Membrane fusion: What may transpire at the atomic level. *J. Biol. Phys. Chem.* **4,** 139–142.

Katz, A., Glusker, J. P., Beebe, S. A., and Bock, C. W. (1996). Calcium ion coordination: A comparison with that of beryllium, magnesium, and zinc. *J. Am. Chem. Soc.* **118,** 5752–5763.

Laroche, G., Dufourc, E. J., Dufourcq, J., and Pezolet, M. (1991). Structure and dynamics of dimyristoylphosphatidic acid/calcium complex by 2H NMR, infrared, spectroscopies and small-angle x-ray diffraction. *Biochemistry* **30,** 3105–3114.

Licheri, G., Piccaluga, G., and Pinna, G. (1976). X-ray diffraction study of the average solute species in $CaCl_2$ aqueous solutions. *J. Chem. Phys.* **64,** 2437–2446.

Martínez, J. M., and Martínez, L. (2003). Packing optimization for automated generation of complex system's initial configurations for molecular dynamics and docking. *J. Comput. Chem.* **24,** 819–825.

McIntosh, T. J. (2000). Short-range interactions between lipid bilayers measured by X-ray diffraction. *Curr. Opin. Struct. Biol.* **10,** 481–485.

Pavlov, M., Siegbahn, P. E. M., and Sandström, M. (1998). Hydration of beryllium, magnesium, calcium, and zinc ions using density functional theory. *J. Phys. Chem.* **102,** 219–228.

Petrov, A. S., Funseth-Smotzer, J., and Pack, G. R. (2005). Computational study of dimethyl phosphate anion and its complexes with water, magnesium, and calcium. *Int. J. Quantum Chem.* **102,** 645–655.

Phillips, J. C., Braun, R., Wang, W., Gumbart, J., Tajkhorshid, E., Villa, E., Chipot, C., Skeel, R. D., Kale, L., and Schulten, K. (2005). Scalable molecular dynamics with NAMD. *J. Comput. Chem.* **26,** 1781–1802.

Portis, A., Newton, C., Pangborn, W., and Papahadjopoulos, D. (1979). Studies on the mechanism of membrane fusion: Evidence for an intermembrane Ca^{2+} -phospholipid complex, synergism with Mg^{2+}, and inhibition by spectrin. *Biochemistry* **18,** 780–790.

Potoff, J. J., Issa, Z., Manke, C. W., Jr., and Jena, B. P. (2008). Ca^{2+}-Dimethylphosphate complex formation: Providing insight into Ca^{2+} mediated local dehydration and membrane fusion in cells. *Cell Biol. Int.* **32,** 361–366.

Schneider, B., Kabelac, M., and Hobza, P. (1996). Geometry of the phosphate group and its interactions with metal cations in crystals and ab Initio calculations. *J. Am. Chem. Soc.* **118,** 12207–12217.

Schwenk, C. F., Loeffler, H. H., and Rode, B. M. (2001). Molecular dynamics simulations of Ca^{2+} in water: Comparison of a classical simulation including three-body corrections and Born-Oppenheimer ab initio and density functional theory quantum mechanical/molecular mechanics simulations. *J. Chem. Phys.* **115,** 10808–10813.

Sundaresan, N., Pillai, C. K., and Suresh, C. H. (2006). Role of Mg^{2+} and Ca^{2+} in DNA bending: Evidence from an ONIOM-based QM-MM study of a DNA fragment. *J. Phys. Chem.* **110,** 8826–8831.

Wilschut, J., Duzqunes, N., Fraley, R., and Papahadjopoulos, D. (1980). Studies on the mechanism of membrane fusion: Kinetics of calcium ion induced fusion of phosphatidylserine vesicles followed by a new assay for mixing of aqueous vesicle content. *Biochemistry* **19,** 6011–6021.

CHAPTER 10

Structure and Dynamics of Metalloproteins in Live Cells

Jeremy D. Cook,[*] James E. Penner-Hahn,[†] and Timothy L. Stemmler[*]

[*]Department of Biochemistry and Molecular Biology
Wayne State University
School of Medicine
Detroit, Michigan

[†]Department of Chemistry
The University of Michigan
Ann Arbor, Michigan

METHODS IN CELL BIOLOGY, VOL. 90

0091-679X/08 $35.00
DOI: 10.1016/S0091-679X(08)00810-8

Abstract

X-ray absorption spectroscopy (XAS) has emerged as one of the premier tools for investigating the structure and dynamic properties of metals in cells and in metal containing biomolecules. Utilizing the high flux and broad energy range of X-rays supplied by synchrotron light sources, one can selectively excite core electronic transitions in each metal. Spectroscopic signals from these electronic transitions can be used to dissect the chemical architecture of metals in cells, in cellular components, and in biomolecules at varying degrees of structural resolution. With the development of ever-brighter X-ray sources, X-ray methods have grown into applications that can be utilized to provide both a cellular image of the relative distribution of metals throughout the cell as well as a high-resolution picture of the structure of the metal. As these techniques continue to grow in their capabilities and ease of use, so too does the demand for their application by chemists and biochemists interested in studying the structure and dynamics of metals in cells, in cellular organelles, and in metalloproteins.

I. Introduction

Metalloproteins, or proteins that bind metal cofactors, make up a substantial portion of the human proteome and are essential for the viability of both individual cells and of the overall organism. By some estimates, as many as one-third to one-half of all proteins are metalloproteins (Ascone *et al.*, 2003). Both the reactivity and, indeed, even the structure of a protein can change when a metal binds to the organic protein peptide chain. These changes often allow the resulting metalloprotein to accomplish unique chemistry and maintain unique folds that could not be accomplished in the absence of metal. For example, the oxygen binding ability of hemoglobin and the CO_2 hydration activity of carbonic anhydrase have an absolute dependence on the presence of, respectively, heme iron and a divalent cation (typically zinc). Given the versatility in chemistry that each metal can perform, it is no surprise that metalloproteins are selective in the metal they accept, and different metals are utilized to a greater degree in different regions of the cell and in the organism. However, the chemical reactivity provided by metals can be both a blessing and a curse, especially when cellular pathways for metal homeostasis fail. Friedreich's ataxia and Wilson's disease are just two examples of hereditary disorders that are linked to failures in metal homeostasis: iron in the case of Friedreich's ataxia and copper in the case of Wilson's disease. In both diseases, a breakdown in a single component of the complex cellular metal-processing machinery has highly deleterious consequences to the organism.

Cells have, therefore, developed complex and comprehensive protein controlled mechanisms to ensure that metal homeostasis proceeds in an unhindered fashion. At the molecular level, placement of a specific metal, and only the appropriate

metal, in the correct protein binding site is essential. At the same time, the protein-based ligand environment surrounding the metal helps to control the chemical reactivity of the metal (e.g., the porphyrin ring and hydrophobic ligand binding pocket in hemoglobin help promote reversible O_2 binding and release in favor of CO binding and/or formation of μ-oxo bridged hemes, two reactions that are preferred in solution). The individual components of the cellular homeostasis machinery include metal specific pumps to bring the metal into the cell or cellular organelle, metal chaperones that selectively deliver metal to the metalloprotein partner and transcriptional regulation proteins that control the process at the genetic level. To fully understand and appreciate this machinery, it is necessary to understand both the details of the individual protein components, especially at the metal center, and the ways in which these parts interact to form the whole.

II. Rationale

Although genetic studies have proven to be highly effective in helping to determine the global role of metalloproteins within the complex machinery of cellular metal homeostasis, a complete understanding of how this mechanism functions requires knowledge of how the individual components operate. For metals, functional characterization begins with a thorough understanding of the metals themselves, over a range of distance scales from cellular to atomic. At the cellular level, studies of the distribution of each metal within the cell provide a general blueprint of cellular metal homeostasis. Characterization of metal site structure at the cellular organelle level allows one to focus on how metals are compartmentalized and generally utilized within unique regions of the cell. Finally, characterization of metals at the atomic level provides a high-resolution picture of how metalloproteins utilize each metal. While no single technique can answer all of these questions, modern X-ray methods have provided valuable insights at all of these dimensional scales. The goal of this report is to describe two X-ray-based techniques currently employed to characterize metals in cells at different degrees of resolution: X-ray absorption spectroscopy (XAS) and X-ray fluorescence (XRF) imaging.

The extremely high flux of tunable X-rays available at synchrotron radiation laboratories has dramatically expanded the range of applications that can be utilized to characterize metals in cells at different degrees of resolution. XAS is an element-specific probe of the local structural environment of a metal (Scott, 1985). XAS includes both extended X-ray absorption fine structure (EXAFS), which gives information on the bond-lengths, and X-ray absorption near-edge structure (XANES), which gives information on metal geometry and oxidation state. By making measurements on intact whole-cells, these properties can be exploited to characterize the average structural environment for each of the metals in a cell. In those cases where average information is not sufficient, it is necessary to enhance the resolution, either by imaging or by purification. XRF imaging can

provide nanometer scale detail regarding the distribution of metals within cells, but only rarely provides the spectroscopic detail available from XAS. Alternatively, XAS can be used to provide high-resolution details for purified metalloproteins. This provides the highest accuracy structural information, but with the loss of detail regarding spatial distribution within a cell. In the following, we provide a general description of each technique, outline what is required to collect and analyze each type of data and finally provide specific examples of how each technique has been employed to directly address questions regarding metals that are predominately bound to proteins within cells.

III. Methods

A. XAS

XAS can be utilized to determine the high resolution electronic and structural details of metals bound to a single protein sample under a variety of different conditions (substrate vs. inhibitor bound, different metal oxidation states, etc.) or for each metal-bound molecule in a multiprotein complex. Sample constraints for the technique require metal concentrations of at least 0.1–0.3 mM (although higher is better) and solution volumes generally between 50 and 150 μL. Solution samples must be frozen quickly, typically with glassing agents present, in order to avoid ice formation and the absorbing element's atomic number, in most cases, must be bigger than ~19 (i.e., first transition series elements or heavier), although some very nice work has been done on lighter elements, such as sulfur. Questions typically addressed using this technique include: (1) what is the average oxidation state of the metal(s) in the sample, (2) is the metal site affected by the presence of substrates, inhibitors, redox agents, etc., (3) what is the ligand environment around the metal, and (4) is the metal part of a multinuclear cluster in the protein under investigation?

The XAS method utilizes intense monochromatic X-rays from a synchrotron light source to excite the core electrons in the absorbing atom (A) of interest. When the electron is excited to the continuum, the resulting photoelectron wave is scattered by the neighboring atoms (S, the scattering atom). For iron, the electron excitation edge occurs at ca. 7130 eV, as shown in the XANES region of Fig. 1. Information regarding the average oxidation state, ligand coordination geometry, and symmetry of the absorbing atom can be obtained from analysis of the XANES region of the XAS spectrum. In Fig. 1, the EXAFS refers to the modulations in the absorption coefficient on the high energy side of the absorption edge. EXAFS oscillations occur as a consequence of the fact that, depending on the wavelength of the photoelectron wave, the outgoing and backscattering waves can overlap either constructively or destructively to give maxima (E_1) and minima (E_2), respectively, in the absorption coefficient. Simulations of the EXAFS region can be used to determine the average metal–ligand bond distances with good resolution (~0.1 Å), very

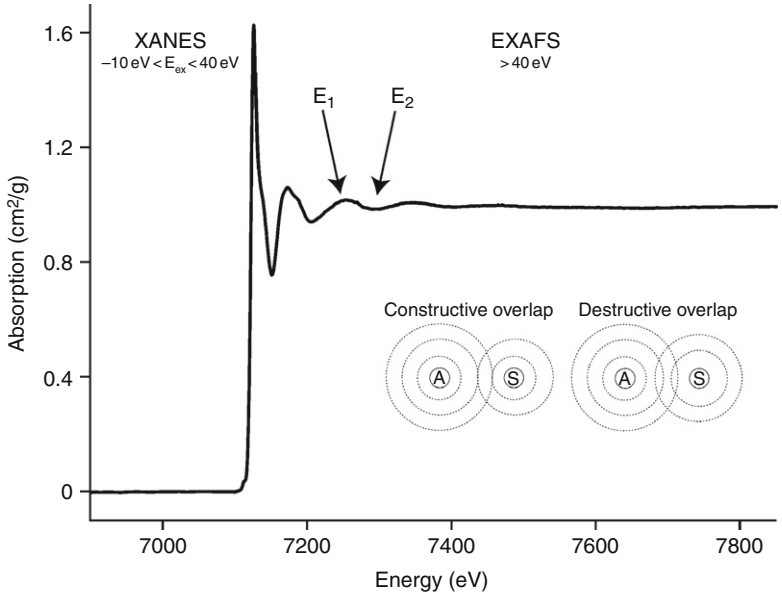

Fig. 1 Iron K-edge XAS spectrum from ferrous ammonium sulphate. Spectra are divided into the XANES region (−10 to +40 eV relative to the large excitation signal) and the EXAFS region (>40 eV above the excitation edge). In the EXAFS region, absorption maxima (E_1) and minima (E_2) are highlighted. Inset: constructive and destructive overlap of photoelectron wave generated from excitation of the iron 1s core electron to the continuum.

good accuracy (~0.02 Å), and outstanding precision (~0.004 Å). Metal–ligand coordination numbers can be determined to ±1 and ligand type can be determined to within a row of the periodic table (i.e., oxygen can be distinguished from sulfur, but not from nitrogen atoms). The information from XAS is thus, similar to that obtained from protein crystallography, but without the need for diffraction quality crystals. The overall information content of protein crystallography is much higher, but even when a crystal structure is available, it is often the case that XAS can nevertheless provide unique information regarding the metal site structure (Tobin *et al.*, 2003).

B. Purified Protein XAS

Historically, almost all biological XAS studies have been performed on purified proteins. This is because XAS is a "bulk" spectroscopy (i.e., it is sensitive to all of the forms of an element that are present in a sample). If the element of interest is present in two different forms, the resulting XAS spectrum will be the weighted average of these two. Thus, a protein that contains one $ZnCys_2His_2$ site and one $ZnCys_4$ site would be indistinguishable from a protein containing two $ZnCys_3His$

sites. A particularly problematic case is protein samples that are heterogeneous, for example, with a mixture of active site metal and adventitious metal.

C. Whole Cell XAS

Despite the limitations inherent in averaging, there has been growing use of XAS to characterize the average coordination structure and electronic properties of heterogeneous samples. Whole cell XAS can be utilized as a direct method for determining the average metal chemistry within the entire cell. The element specificity of X-ray absorption allows one to answer specific questions regarding the form of each metal in the cell. Virtually any form of sample can be used, with examples including whole blood from tunicates, intact biological tissue, isolated bacterial cultures, or even soil samples. Measurements are made in the same way as conventional X-ray absorption. Because the resulting data represents a weighted average of all of the chemical environments of the element of interest, it can be difficult to use with complex mixtures, although there has been some success in modeling the resulting spectra as linear combinations of reference spectra. This is particularly true for elements such as sulfur (Gnida *et al.*, 2007; Pickering *et al.*, 1998), where there is dramatic spectral variation for different chemical species. One common application of whole-cell XAS is for samples where an exogenous metal (perhaps a toxin or a drug) has been added to the sample. In such cases, the absence of an endogenous form of the metal can simplify the analysis since the element of interest may be present in only one predominant form. In this case, whole-cell XAS can be used to determine the chemical state of the added metal, i.e. the form of the metal stored in a tolerant organism.

D. XRF Imaging

With modern, so-called ''third generation'' synchrotron sources, it is possible to focus high-flux, high-energy X-ray beams to very small spot sizes ($\sim$150 nm or smaller). This beam can be raster scanned across a sample in order to obtain spatially resolved data (Paunesku *et al.*, 2006). The simplest experiment is to record the intensity of X-rays emitted from each point in the sample. Since each element emits XRF at a characteristic energy, the resulting emission spectrum permits direct determination of the composition of a sample. By recording XRF spectra at each point in a sample, it is possible to construct a map of the spatial localization of each element heavier than phosphorus. Lighter elements can, in principle, also be imaged; however, this generally requires that samples be mounted in a vacuum chamber. With proper calibration, XRF images can provide absolute elemental concentrations. Most XRF imaging has been performed on thin samples, but it is also possible to extend the technique to three dimensions, using tomographic reconstructions to obtain the complete three-dimensional (3-D) distribution of an element.

E. Combined Spectral and Spatial Resolution

XRF is essentially an atomic phenomenon—that is, the XRF signal is virtually independent of the chemical environment of the atom. Thus, an iron XRF map provides information on the local Fe concentration, but no insight as to whether this is due to a heme protein, a Fe/S protein, or the iron-oxide core of ferritin. To get around this limitation, it is possible to combine XRF imaging with XAS using either microXAS or XANES imaging (Pickering *et al.*, 2000). If one measures the complete XAS spectrum for a spatially resolved portion of the sample (so-called microXAS), it is possible to determine the chemical form (or at least the average chemical form) of a particular element at a distinct point in the sample. Alternatively, one can take advantage of the fact that the excitation profile for each chemical form of an element has a slightly different energy dependence (that is, as noted above, each chemical form has a different XANES spectrum). In simple XRF imaging, samples are illuminated with high-energy X-rays, so that all chemical forms are excited with equal probability. In XANES imaging, an XRF image is excited using several different X-ray energies in the XANES region. Each chemical form of an element will have a slightly different excitation probability at each wavelength. By measuring multiple maps at several different excitation energies, it is possible to tease apart the spatial distributions of each of the chemical forms of an element. Differences in the diverse imaging methods are illustrated schematically in Fig. 2.

IV. Materials

A. Purified Protein XAS

Samples for single molecule XAS metalloprotein studies should be homogeneous with no unbound metal, since the data being collected is the average of protein sites that utilize the excited metal. The technique is buffer and pH independent, so samples can exist under a variety of solution conditions. Samples are generally measured at low temperature as frozen solutions in order to minimize thermal disorder and, more importantly, to limit the extent of X-ray induced radiation damage. As mentioned earlier, agents such as glycerol are generally added at ca. 30% by volume to ensure homogeneous sample glassing and prevent ice formation. Samples can have multiple different elements, as the technique is element specific, however, the same metal at two independent sites in the metalloprotein will appear as the average. Sample cell dimensions are specific for the cryostat being used and cryostats differ at different X-ray facilities. Sample cells are generally constructed from metal free materials, such as Lucite (Bencze *et al.*, 2007). Cells can be a variety of shapes and sizes, although they generally have one long open window that is placed at a 45 degree angle to the incident beam. This exposed window is usually wrapped in metal free Kapton tape to prevent sample loss.

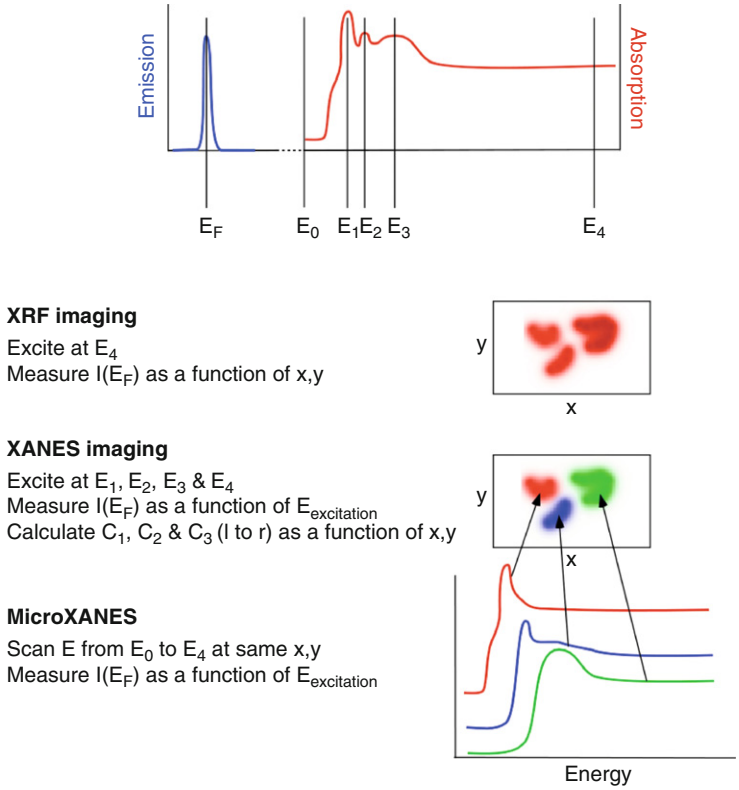

Fig. 2 Schematic illustration of XRF imaging experiments for a sample that has the *average* absorption spectrum shown in the top/right panel. Because all forms of the element emit with nearly the same emission, there is only a single resolved X-ray fluorescence peak, shown in the top/left panel. For XRF imaging, the sample is excited well above the edge (E_4) and the XRF intensity is measured as a function of the location (x,y) that is excited. The resulting pattern gives an elemental map with no chemical information. If the peaks at E_1, E_2, and E_3 are due to different chemical species (**1**–**3**), it is possible to perform XANES imaging by measuring XRF at each energy and calculating the relative concentration of each: C_1, C_2, and C_3 (typically measurements at several additional energies are necessary to obtain a robust solution). In this illustration, each species is well separated spatially (middle image). Finally, by measuring a full XAS spectrum with a microbeam, it is possible to obtain spatially resolved XAS spectra. In this simplified example, spectra measured at the point marked by the three arrows are the spectra for pure **1**–**3**.

Because they are so dilute, biological XAS spectra are almost always measured as fluorescence excitation spectra. In this experiment, the characteristic XRF intensity is monitored as the excitation energy is scanned. In the limit of thin or dilute samples, fluorescence intensity is proportional to X-ray absorption cross-section. Most modern XAS beam lines are equipped with a solid-state energy-resolving XRF detector.

B. Whole Cell XAS

Many strategies have been utilized to prepare whole-cell XAS samples. In order to achieve good signal to noise ratios, the concentration of the metal within the cell must first be considered. In some cases, it may be sufficient to prepare a monolayer of confluent cells or directly use bacterial cells in a cell culture. If metal concentrations within the cells are low (submicromolar range), one may consider harvesting a population of cells into a small volume to increase the amount of sample being exposed to the X-ray beam and hence, increase the signal intensity. This has been done simply by filtration of a bacterial culture using a 0.2 μm filter, sandwiching the filter paper between layers of Kapton tape followed by flash freezing in liquid nitrogen. Others have harvested cells by centrifugation and placed the collected cells directly into a 140 μL Lucite XAS sample cell using a customized setup.

C. XRF Imaging

Perhaps, the most important part of an imaging experiment is the focused X-ray beam. Reflective optics (e.g., Kirkpatrick–Baez mirrors; Kirkpatrick and Baez, 1948) work well for beam sizes down to $\sim$1 μm and are thus well suited for XRF imaging of millimeter scale sample (e.g., intact tissue samples). Better spatial resolution, down to $\sim$100 nm or better, can be achieved with zone-plate optics (Cai *et al.*, 2003; Schroer, 2006). Samples for XRF imaging are typically placed on an X-ray transparent substrate such as ultra thin ($\sim$100 nm) silicon nitride. The mechanical systems that are used to position the sample relative to the X-ray beam need to have precision and stability that is better than the desired spatial resolution. Fortunately, most of the synchrotron laboratories have one or more beam lines dedicated to XRF imaging, including all of the necessary focusing and sample positioning hardware, together with the standard XAS hardware for tunable X-ray excitation and energy-resolved XRF detection.

V. Discussion

Examples of how these X-ray techniques have been applied in order to address specific questions regarding the cellular utilization of metals are provided in the following section. These applications include specific examples that cover excitation of a variety of different elements including both metals and nonmetals.

A. Purified Protein XAS

Numerous laboratories have utilized XAS to answer structural and functional questions regarding many different metalloproteins. We have chosen three specific examples from the long library of protein XAS studies that illustrate how the technique was used to address specific questions regarding metal(s) bound to a protein. These examples are outlined below in detail. In the first example, superoxide

reductase (SOR) from *Pyrococcus furiosus* was used to determine mechanistic issues regarding the enzyme's active site. This in an excellent example where characterization of the structural and electronic properties of the bound metal by XAS helped elucidate the enzyme's reaction mechanism. In the second example, the multimetal/multinuclear sites in particulate methane monooxygenase (pMMO) from Methylococcus capsulatus were characterized by XAS to provide the high resolution details of the metal center that could not be obtained by X-ray crystallography. In the third example, the Zn finger domain of the ubiquitin binding protein Np14 was characterized by XAS; the Zn structural parameters were then utilized in combination with NMR spectroscopy to provide the high-resolution structural details of the protein. In addition to structural insight, XAS can in some cases also provide insight into reaction dynamics. As an example, we discuss the time resolved XAS of the Zn site in alcohol dehydrogenase (ADH), an excellent example of how structural changes during catalysis provide insight into the dynamic nature of an enzyme.

Although the *in vivo* function of this protein is unknown, SOR is believed to provide a mechanism to combat against oxidative stress in anaerobes, which typically lack superoxide dismutase, by reducing superoxide to hydrogen peroxide (Imlay, 2002). To elucidate the role of iron in enzymatic activity, the mononuclear Fe metal center was characterized in both the ferric and ferrous oxidation states by XAS (Clay *et al.*, 2002). Iron in the ferric form is high spin and six-coordinate, with a coordination geometry constructed by four equatorial histidyl ligands, an axial cysteinate, and a monodentate glutamate ligand. Ferric iron EXAFS data were best fit using one Fe-S at 2.36 Å and five Fe-N/O bonds at an average distance of 2.12 Å. In the reduced state, the ferrous site of SOR was shown to have square-pyramidal coordination geometry with four equatorial histidines and one axial cysteine; Fe EXAFS data for this sample were best fit by one Fe-S at 2.37 Å and four Fe-N/O at an average distance of 2.15 Å. A ligand for the iron can be substituted in the oxidized form, and the vacant site can be populated in the ferrous form by cyanide, which acts as a molecular mimic for superoxide. The ability to bind exogenous ligands in both the ferrous and ferric sites of SOR was suggested to be consistent with an inner-sphere catalytic mechanism involving superoxide binding at the ferrous site to yield a ferric-(hydro)peroxo intermediate. Additional mechanistic insight was supplied by characterizing the sulfur K-edge XAS for the cysteine bound to the iron in SOR (Dey *et al.*, 2007). XANES analysis of the sulfur edge indicated that the thiolate is a highly anionic covalent ligand; the anionic character of the thiolate most likely increases the pK_a of the Fe(III)-OOH intermediate, facilitating protonation and eventual release. Combined, these studies paint a structural picture of how the ligand environment facilitates catalytic turnover during enzymatic activity.

pMMO is a multicopper membrane bound enzyme that catalyzes the oxidation of methane to methanol in methantropic bacteria. Prior to complete structural characterization of this multicomponent enzyme, Cu K-edge XAS studies were utilized to determine the average oxidation state and provide structural details regarding copper bound to pMMO. Initial Cu XANES spectra of as isolated Bath pMMO indicated a near equal distribution of Cu(I) and Cu(II) for the ca. four

coppers bound to the protein, based on general edge features and the observation of both 1s→3d and 1s→4p electronic transitions apparent in the edge (Lieberman *et al.*, 2003). Subsequent reports confirmed the protein could be prepared in a homogeneous metal oxidation state (Lieberman *et al.*, 2006). EXAFS analysis of the as isolated protein confirmed the presence of a dinuclear Cu center, with a copper separation of 2.51 Å, and showed that the Cu–Cu distance increases to 2.65 Å when the metal is fully reduced. The remaining ligands were completely oxygen/nitrogen based and located at an average distance of 1.97 and 2.22 Å in the as isolated protein and 1.98 and 2.14 Å in the reduced sample. The high-resolution structural details provided by XAS helped contribute to the correct assignment of the high-resolution crystal structure of pMMO (Lieberman and Rosenzweig, 2005).

Protein ubiquitination plays an important role in a variety of cellular processes. Ubiquitinated proteins are directed into the different cellular pathways through interactions with effector proteins that contain conserved ubiquitin binding motifs. The solution structure of one such motif, NZF, was solved utilizing the metrical parameters of the metal center provided by Zn K-edge XAS studies (Wang *et al.*, 2003). Simulations of the Zn EXAFS showed Zn was bound to four sulfur atoms at an average bond length of 2.33 Å. The Debye–Waller factor, a measure of metal–ligand bond disorder was 0.00454 $Å^2$ indicating the average Zn-ligand environment was most likely distorted. During the solution structure calculations, the Zn bond lengths obtained by XAS were used as constraints while the value for the Debye–Waller factor was utilized to generate limits for these distance constraints. XAS is, therefore, an effective tool that can be used to provide unique structural details not attainable by other techniques, especially in the case of the generally spectroscopically silent metals like Zn.

ADH catalyzes the oxidative conversion between alcohols and aldehydes or ketones. The catalytic active site of *Thermoanaerobacter brockii* ADH contains a Zn ion bound to a single cysteine, histidine, aspartate, and a glutamate. Prior to this study, two catalytic mechanisms were proposed for the protein: the first required a four-coordinate Zn intermediate generated from water displacement at the Zn site, the second mechanism involved a five-coordinate Zn site where the water, rather than being displaced acts as a site for transient proton transfer. In a very interesting application of XAS, Sagi and coworkers utilized time-resolved freeze-quench XAS to trap TbADH during multiple stages within a single catalytic turnover cycle, hence providing snapshots of the Zn site during turnover (Kleifeld *et al.*, 2003). Two distinct intermediates were detected during the mixing time range of 3 and 70 ms, and bound Zn was pentacoordinate at each step. Intermediate 1 (IM1) detected between 3 and 5 ms, and IM2, detected between 15 and 19 ms after mixing, both had 4 O/N and 1 S ligands bound to Zn; however, there was a distinct ca. 0.15 Å expansion in two Zn-O/N bond lengths relative to the starting Zn–ligand complex. Results from this study allowed the authors to select the more appropriate proposed catalytic mechanism in agreement with the structural details regarding the catalytic Zn site in the enzyme.

An additional emerging application of the technique involves the detailed characterization of the near edge XANES data for metal containing systems using the

multiple scattering edge simulation package MXAN. Utilized recently by the Hodgson and Hedman groups, MXAN analysis was applied to characterize the mononuclear copper complex $[Cu(TMPA)(OH_2)](ClO_4)_2$ (Sarangi *et al.*, 2005). When applied to this copper complex, that authors nicely illustrated the utility of the technique for accurately abstracting geometric information of the metal center from an XAS spectrum. When coupled with the highly accurate bond lengths obtained from EXAFS analysis, MXAN can be incorporated to provide an accurate metal–ligand geometric picture of homogeneous metal centers in biomolecules.

B. Whole Cell XAS

Numerous published reports utilized whole-cell XAS to determine the overall metal speciation within different cell types. The following section highlights three examples of how the technique was applied at the cellular level and in the process, nicely illustrate the range of applications for this method towards addressing diverse biological and environmental questions. In the first report, whole-cell studies were used to investigate the high concentration of vanadium in the blood of subtidal marine organisms. In the second report, whole-cell XAS studies were utilized to determine metal chelation strategies for five different Zn tolerant microbes found in a highly Zn-contaminated lake. In the final report, whole-cell XAS was used to quantitate the generally spectroscopically silent sulfur contained within equine blood.

Tunicates are fascinating subtidal marine organisms in that some species, such as *Ascidia nigra* and *Ascidia ceratodes*, have the ability to accumulate and concentrate vanadium to levels over a million fold higher than found in seawater. Although the reason for this unusual storage ability remains unknown, much work has been done to determine the method of uptake and storage of metal in each system. Vanadium resides in multiple cell types within the blood of these organisms and interestingly the V-containing cells and the chemical speciation of metal differ even between closely related organisms. In the report by Frank and coworkers, whole-cell XAS of blood cell samples from *A. nigra* and *A. ceratodes* were used to investigate species dependent differences for V distribution, which may have possible taxonomical implications (Frank *et al.*, 1998). Subtle differences between XANES spectra for each sample were identified, confirming a unique global V environment in each cell type. A shoulder in the XANES region of intact *A. ceratodes* blood cells occurred at 5476 eV, closely matching the feature found for V(III) in *aquo*-VSO_4^+. In contrast, the large 1s→3d pre-edge transition of *A. nigra* indicated ~25% of the V in this species closely matches the vanadyl ion ($[V(IV) = O]^{2+}$), which has a characteristic feature at 5468.6 eV. The edge energies for these two species differ by approximately 1 eV (5480.5 eV for *A. ceratodes* vs. 5479.5 eV for *A. nigra* samples), suggesting the remaining V(III) found in *A. nigra* has a different ligation environment from that in *A. ceratodes*. These differences suggest

unique vanadium storage distributions between species, despite the fact that the biochemical mechanisms responsible for V uptake and storage appear to be very similar.

The rise in industrialization over the past few centuries has led to environmental contamination of areas surrounding large manufacturing facilities. Operations, such as smelting, introduce high levels of Zn into local water supplies. Decontamination of these areas requires an understanding of metal mobility, toxicity, and reactivity beginning with an understanding of the Zn speciation in metal-contaminated areas. In one such study, Webb and coworkers identified five bacterial anaerobes that were able to thrive in the Zn contaminated waters of lake DePue (IL) (Webb *et al.*, 2001). These microbes were collected and grown in a laboratory setting using high Zn media. Whole cell XAS was used to determine the peptide coordination of the metal. Fitting analysis revealed unique global Zn coordination in all five species. One isolate showed Zn ligation solely by sulfur (4 S at an average bond distance of 2.34 Å), two had mixed sulfur and oxygen/nitrogen coordination (3 S at average bond distances of 2.34 Å and 1 O/N at 1.97 Å, or 2 S at 2.34 Å and 2 O/N at 1.96 Å), while the final two showed all oxygen/nitrogen ligation (4 O/N at 1.96 or 5 O/N at 1.97 Å). The data were consistent with the low-Z (i.e., "O") ligands coming from phosphoryl groups. Given the number of phosphate groups located outside the cell (i.e., at the level of the cell membrane), these results may suggest that O/N dominated microbes may bind/store Zn on their outer cell surface while the S ligand dominated microbes may store Zn within the cell.

Although not a metal, sulfur is one of the essential elements most easily studied by XAS, since there are dramatic spectral variations between different chemical forms of the element. Relatively little is known about the chemical reactivity of sulfur *in vivo* due to the limited number of direct methods that can be used to study it. Its ability to cycle between different redox states makes it useful in numerous life processes towards regulating oxidation chemistry, as well as for serving as a soft base for metals themselves. Its high abundance in the cell make it perfectly suited for XAS studies, as this technique is extremely sensitive for detecting structural and redox state changes. As a proof of concept, Pickering and coworkers were able to quantitate sulfur speciation in intact equine blood cells without chemical manipulations of the sample using K-edge XAS (Pickering *et al.*, 1998). By fitting empirical data with linear combinations of spectra from a model library, they were able to determine the relative quantities of different sulfur species within samples. The authors observed sulfur within red blood cells to be 21.4% disulfide, 54.4% thiol, 21.3% thioether, 2.1% sulfoxide, and 0.8% sulfate. In contrast to the intact erythrocytes, the sulfur present in the plasma had drastically different speciation: 76.5% disulfide, 20.6% thiol, 0% thioether, 0% sulfoxide, and 2.9% sulfate. These results provide confirmation of the conventional wisdom regarding the chemical form of intra and extracellular sulfur in blood, namely that extracellular cysteine is predominately in a disulfide bond while intracellular sulfur is much more likely to be present as the reduced cysteine.

C. XRF Imaging

As noted above, XRF imaging is conveniently divided into macroscopic (micrometer scale imaging using mirrors) and microscopic (nanometer scale imaging using zone plates). Macroscopic studies have examined a variety of tissues. Given the available resolution, these studies generally do not provide cellular detail, but can be used to correlate metal concentrations with histologically identifiable regions of tissue. There have been several recent reviews of XRF imaging (e.g., Lankosz *et al.*, 2007; Paunesku *et al.*, 2006), including a careful analysis of the relative benefits of particle beam versus X-ray excitation (Petibois and Cestelli Guidi, 2008), and consequently, only the key points will be summarized here. Much of the interest in macroscopic-scale XRF imaging derives from attempts to correlate metal levels with disease states. One of the more interesting tissues to study is brain tissue. For example, there is substantial evidence that metals are associated, in some way, with Alzheimer's disease. Recent work combining XRF imaging with IR microscopy succeeded in showing that Cu and Zn colocalize specifically with the β-sheet form (i.e., the "misfolded" form) of the amyloid β protein that is the principle component of senile plaques in Alzheimer's disease (Miller *et al.*, 2006). A key to this study, and to all such studies, is the development of appropriate methods (IR imaging in this case) that allow the investigator to correlate the metal levels, as seen by XRF, with specific features in the tissue.

A second area that has received significant attention is cancer, where there have been numerous attempts to correlate changes in metal levels (either essential metals such as Fe, Cu, and Zn, or toxic metals such as Cd, Cr, and As) with disease state. Although this work remains largely phenomenological at this point, it is clear that there exist many tantalizing differences in metal status between diseased and healthy tissue. The challenge, and also the promise, of such studies will lie in sorting out cause and effect. That is, is a low or high level of a particular metal a cause or a symptom of the disease?

One approach to disentangling cause and effect is to treat samples with different concentrations of the element of interest (e.g., a toxic element) and follow the distribution of this element through the sample in both space and time (Isaure *et al.*, 2006; Mesjasz-Przybylowicz *et al.*, 2007). Much of this sort of work has been done on plants because of their ease of manipulation. One of the first such examples was an elegant study by Pickering *et al.* (2000) that used XANES imaging to study the distribution and speciation of selenium in plants that had been exposed to 5 mM selenate. By measuring the absorbance, the X-ray scatter, and the XRF at two different excitation energies, they were able to determine that Se is present predominantly as selenate in the mature leaf tissue while young leaves and roots contain almost exclusively organoselenium. This observation may be helpful in understanding the biological basis of selenium hyperaccumulation in some plants.

XRF imaging can, in principle, be used for elements as light as phosphorus (or even lighter with the use of vacuum sample chambers). For heavy elements (e.g., first transition series metals and higher), X-ray absorption by the sample is

relatively unimportant, at least for samples that are no more than a few hundred μm thick. However, attenuation by the sample can be quite important for thick samples, leading to apparent heterogeneities in composition (i.e., light elements appear to be depleted from the far side of the sample because the fluorescence is absorbed by the intervening sample (Mesjasz-Przybylowicz *et al.*, 2007). A second difficulty with XRF studies of light elements is that, even if the sample is thin and dilute on an average, the local concentration of the element of interest may still be large enough to significantly distort the spectrum. This is important, for example, in studies of sulfur metabolism by bacteria where sulfur is present as globules of essentially pure sulfur, which can significantly distort the resulting XANES spectrum (Pickering *et al.*, 2001).

Most XRF imaging studies have used thin, flat samples and have thus obtained only two-dimensional (2-D) data. For 3-D samples, one can measure data at several different angles and use the resulting data to infer localization (Young *et al.*, 2007), and complete 3-D information is available if full tomographic measurements are done. A beautiful demonstration of the ability of the latter to provide biologically relevant information was a study by Kim *et al.* (2006) showing that iron is specifically accumulated in the provascular system of *Arabidopsis* seeds. Many studies have been carried out on chemically fixed samples, but recent work on cryogenically fixed samples suggest that this may be a viable approach (Kanngiesser *et al.*, 2007) for preparing samples that are closer to biologically-relevant wet conditions.

The discussion above focused on macroscopic XRF imaging. Increasingly, however, additional studies have focused on nanometer scale imaging. With this resolution, it is possible to determine directly the intracellular variations in metal concentration. Once again, there are a variety of possible biological applications (Fahrni, 2007; Paunesku *et al.*, 2006). A representative example is the study by Finney and co-workers of the role of copper in angiogenesis (Finney *et al.*, 2007). It has long been known that copper is important in angiogenesis, and there have been suggestions that by modifying Cu metabolism (e.g., with Cu specific chelators), it may be possible to inhibit angiogenesis and thus interfere with tumor growth. X-ray nanoprobe images of individual cells showed that during angiogenesis, the bulk of the intracellular Cu is relocalized to the tips of nascent endothelial cell filopodia and across the cell membrane, providing direct evidence for the role Cu plays. Interestingly, Cu chelation, while disrupting angiogenesis, had little effect on the observed Cu relocalization. The ability to determine metal concentrations with subcellular resolution was critical to this work. A variety of other groups have used analogous studies to explore the effect of metals (both toxins and metallodrugs) on cells, exploring both the localization of the added compound and the effect that it has on cellular metal metabolism. Although the available X-ray resolution is $\sim$100 nm, and even better resolution should still be possible, it can nevertheless be challenging to determine the precise localization of a particular element. The reason is cell thickness is typically much more than 100 nm, and therefore, 2-D metal distributions are, in reality, the average of the spatial

distribution across the cell. In practice, this means that it is often only possible to distinguish between cytoplasm and nucleus, but not to identify finer scale structures, unless one looks at thin sections cut from a cell (Dillon *et al.*, 2002).

The lower flux and smaller sample volumes in nanoprobe studies mean it is difficult to perform full XANES imaging studies analogous to those discussed above for microprobe imaging. However, even here some spectra resolution is possible, demonstrating, for example, that most of the copper in NIH 3T3 fibroblasts is present as Cu(I) (Yang *et al.*, 2005).

VI. Summary

As synchrotron capabilities have developed, the applications of XAS to biology have grown to the point that this is now a mature field. For most purified proteins, it is now (relatively) straightforward to obtain direct structural information for the metal site using XAS. This information is complementary to that available from crystallography, and is often critical to understanding the structural and chemical properties of the protein. It is possible, but more challenging, to extend these studies to more complex samples, for example, heterogeneous whole-cell samples or time-dependent samples, but even these studies are becoming more common. Focused X-ray beams can also be used for elemental imaging, providing information similar to that available from particle beam microscopy, but with greater sensitivity to heavy elements, and much greater tolerance for "wet" samples. While far from routine, X-ray microprobe studies of macroscopic samples (e.g., biological tissues) and X-ray nanoprobe studies of microscopic samples (e.g., single cells) are increasingly being used to interrogate subcellular distributions of elements. Much remains to be learned about the normal variability of metal concentrations within healthy cells before it will be possible to interpret the effect of drugs and disease on metal distributions. Nevertheless, it is clear that XRF imaging has the potential to revolutionize the study of metal ions in biology.

Acknowledgments

This work was supported in part by grants from the National Institutes of Health (DK068139 to TLS, GM38047 and GM70545 to JEPH). Representative spectra shown in this report were collected at the Standford Synchrotron Radiation Laboratory (SSRL). SSRL is a national user facility operated by Standford University on behalf of the U.S. Department of Energy, Office of Basic Energy Sciences.

References

Ascone, I., Fourme, R., and Hasnain, S. S. (2003). Introductory overview: X-ray absorption spectroscopy and structural genomics. *J. Synchrotron Radiat.* **10,** 1–2.

Bencze, K. Z., Kondapalli, K. C., and Stemmler, T. L. (2007). X-Ray absorption spectroscopy. *In* "Applications of Physical Methods in Inorganic and Bioinorganic Chemistry: Handbook,

Encyclopedia of Inorganic Chemistry'' (R. A. Scott, and C. M. Lukehart, eds.), 2nd edn. pp. 513–528. Wiley, Chichester, UK.

Cai, L. Z., Liu, Q., and Yang, X. L. (2003). Phase-shift extraction and wave-front reconstruction in phase-shifting interferometry with arbitrary phase steps. *Opt. Lett.* **28,** 1808–1810.

Clay, M. D., Jenney, F. E., Jr., Hagedoorn, P. L., George, G. N., Adams, M. W., and Johnson, M. K. (2002). Spectroscopic studies of *Pyrococcus furiosus* superoxide reductase: Implications for active-site structures and the catalytic mechanism. *J. Am. Chem. Soc.* **124,** 788–805.

Dey, A., Jenney, F. E., Jr., Adams, M. W., Johnson, M. K., Hodgson, K. O., Hedman, B., and Solomon, E. I. (2007). Sulfur K-edge X-ray absorption spectroscopy and density functional theory calculations on superoxide reductase: Role of the axial thiolate in reactivity. *J. Am. Chem. Soc.* **129,** 12418–12431.

Dillon, C. T., Lay, P. A., Kennedy, B. J., Stampfl, A. P. J., Cai, Z., Ilinski, P., Rodrigues, W., Legnini, D. G. B. L., and Maser, J. (2002). Hard X-ray microprobe studies of chromium(VI)-treated V79 Chinese hamster lung cells: Intracellular mapping of the biotransformation products of a chromium carcinogen. *J. Biol. Inorg. Chem.* **7,** 640–645.

Fahrni, C. J. (2007). Biological applications of X-ray fluorescence microscopy: Exploring the subcellular topography and speciation of transition metals. *Curr. Opin. Chem. Biol.* **11,** 121–127.

Finney, L., Mandava, S., Ursos, L., Zhang, W., Rodi, D., Vogt, S., Legnini, D., Maser, J., Ikpatt, F., Olopade, O. I., and Glesne, D. (2007). X-ray fluorescence microscopy reveals large-scale relocalization and extracellular translocation of cellular copper during angiogenesis. *Proc. Natl. Acad. Sci. USA* **104,** 2247–2252.

Frank, P., Hodgson, K. O., Kustin, K., and Robinson, W. E. (1998). Vanadium K-edge X-ray absorption spectroscopy reveals species differences within the same ascidian genera. A comparison of whole blood from *Ascidia nigra* and *Ascidia ceratodes*. *J. Biol. Chem.* **273,** 24498–24503.

Gnida, M., Sneeden, E. Y., Whitin, J. C., Prince, R. C., Pickering, I. J., Korbas, M., and George, G. N. (2007). Sulfur X-ray absorption spectroscopy of living mammalian cells: An enabling tool for sulfur metabolomics. *In situ* observation of uptake of taurine into MDCK cells. *Biochemistry* **46,** 14735–14741.

Imlay, J. A. (2002). What biological purpose is served by superoxide reductase? *J. Biol. Inorg. Chem.* **7,** 659–663.

Isaure, M. P., Fraysse, A., Deves, G., Le Lay, P., Fayard, B., Susini, J., Bourguignon, J., and Ortega, R. (2006). Micro-chemical imaging of cesium distribution in *Arabidopsis thaliana* plant and its interaction with potassium and essential trace elements. *Biochimie* **88,** 1583–1590.

Kanngiesser, B., Malzer, W., Pagels, M., Luhl, L., and Weseloh, G. (2007). Three-dimensional micro-XRF under cryogenic conditions: A pilot experiment for spatially resolved trace analysis in biological specimens. *Anal. Bioanal. Chem.* **389,** 1171–1176.

Kim, S. A., Punshon, T., Lanzirotti, A., Li, L., Alonso, J. M., Ecker, J. R., Kaplan, J., and Guerinot, M. L. (2006). Localization of iron in Arabidopsis seed requires the vacuolar membrane transporter VIT1. *Science* **314,** 1295–1298.

Kirkpatrick, P., and Baez, A. V. (1948). Formation of optical images by X-rays. *J. Opt. Soc. Am.* **38,** 766–777.

Kleifeld, O., Frenkel, A., Martin, J. M., and Sagi, I. (2003). Active site electronic structure and dynamics during metalloenzyme catalysis. *Nat. Struct. Biol.* **10,** 98–103.

Lankosz, M., Szczerbowska-Boruchowska, M., Chwiej, J., Wójcik, S., and Adamek, D. (2007). Elemental imaging of human brain glioma tissue with the use of synchrotron radiation. *Acta. Neuropathol.* **114,** 317–318.

Lieberman, R. L., Kondapalli, K. C., Shreshta, D. B., Hakemian, A. S., Smith, S. M., Telser, J., Kuzelka, J., Gupta, R., Borovik, A. S., Lippard, S. J., Hoffman, B. M., Rosenzweig, A. C., *et al.* (2006). Characterization of the Particulate Methane Monooxygenase Metal Centers in Multiple Redox States by X-ray Absorption Spectroscopy. *Inorg Chem* **45,** 8372–8381.

Lieberman, R. L., and Rosenweig, A. C. (2005). Crystal structure of a membrane-bound metalloenzyme that catalyses the biological oxidation of methane. *Nature* **434,** 177–182.

Lieberman, R. L., Shrestha, D. B., Doan, P. E., Hoffman, B. M., Stemmler, T. L., and Rosenzweig, A. C. (2003). Purified particulate methane monooxygenase from Methylococcus capsulatus (Bath) is a dimer with both mononuclear copper and a copper-containing cluster. *Proc. Natl. Acad. Sci. USA* **100,** 3820–3825.

Mesjasz-Przybylowicz, J., Barnabas, A., and Przybylowicz, W. (2007). Comparison of cytology and distribution of nickel in roots of Ni-hyperaccumulating and non-hyperaccumulating genotypes of *Senecio coronatus*. *Plant Soil.* **293,** 61–78.

Miller, L. M., Wang, Q., Telivala, T. P., Smith, R. J., Lanzirotti, A., and Miklossy, J. (2006). Synchrotron-based infrared and X-ray imaging shows focalized accumulation of Cu and Zn co-localized with beta-amyloid deposits in Alzheimer's disease. *J. Struct. Biol.* **155,** 30–37.

Paunesku, T., Vogt, S., Maser, J., Lai, B., and Woloschak, G. (2006a). X-ray fluorescence microprobe imaging in biology and medicine. *J. Cell. Biochem.* **99,** 1489–1502.

Petibois, C., and Cestelli Guidi, M. (2008). Bioimaging of cells and tissues using accelerator-based sources. *Anal. Bioanal. Chem.* **391,** 1599–1608.

Pickering, I. J., George, G. N., Yu, E. Y., Brune, D. C., Tuschak, C., Overmann, J., Beatty, J. T., and Prince, R. C. (2001). Analysis of sulfur biochemistry of sulfur bacteria using X-ray absorption spectroscopy. *Biochemistry* **40,** 8138–8145.

Pickering, I. J., Prince, R. C., Divers, T., and George, G. N. (1998). Sulfur K-edge X-ray absorption spectroscopy for determining the chemical speciation of sulfur in biological systems. *FEBS Lett.* **441,** 11–14.

Pickering, I. J., Prince, R. C., Salt, D. E., and George, G. N. (2000). Quantitative, chemically specific imaging of selenium transformation in plants. *Proc. Natl. Acad. Sci. USA* **97,** 10717–10722.

Sarangi, R., Benfatto, M., Hayakawa, K., Bubacco, L., Solomon, E. I., Hodgson, K. O., and Hedman, B. (2005). MXAN analysis of the XANES energy region of a mononuclear copper complex: Applications to bioinorganic systems. *Inorg. Chem.* **44,** 9652–9659.

Schroer, C. G. (2006). Focusing hard X-rays to nanometer dimensions using Fresnel zone plates. *Phys. Rev. B* **74,** 0334051–0334054.

Scott, R. A. (1985). Measurement of Metal-Ligand Distances by EXAFS. *Methods in Enzymology*. **117,** 414–459.

Tobin, D. A., Pickett, J. S., Hartman, H. L., Fierke, C. A., and Penner-Hahn, J. E. (2003). Structural characterization of the zinc site in protein farnesyltransferase. *J. Am. Chem. Soc.* **125,** 9962–9969.

Wang, B., Alam, S. L., Meyer, H. H., Payne, M., Stemmler, T. L., Davis, D. R., and Sundquist, W. I. (2003). Structure and ubiquitin interactions of the conserved zinc finger domain of Npl4. *J. Biol. Chem*. **278,** 20225–20234.

Webb, S. M., Gaillard, J. F., Jackson, B. E., and Stahl, D. A. (2001). An EXAFS study of zinc coordination in microbial cells. *J. Synchrotron. Radiat.*. **8,** 943–945.

Yang, L., McRae, R., Henary, M. M., Patel, R., Lai, B., Vogt, S., and Fahrni, C. J. (2005). Imaging of the intracellular topography of copper with a fluorescent sensor and by synchrotron X-ray fluorescence microscopy. *Proc. Natl. Acad. Sci. USA* **102,** 11179–11184.

Young, L., Westcott, N., Christensen, C., Terry, J., Lydiate, D., and Reaney, M. (2007). Inferring the geometry of fourth-period metallic elements in *Arabidopsis thaliana* seeds using synchrotron-based multi-angle X-ray fluorescence mapping. *Ann. Bot.* **100,** 1357–1365.

CHAPTER 11

Light-Activated Ion Channels for Remote Control of Neural Activity

James J. Chambers[*] and Richard H. Kramer[†]

[*]Department of Chemistry
602 LGRT, University of Massachusetts
Amherst, Massachusetts 01003-9336

[†]Department of Molecular and Cell Biology
University of California
Berkeley, California 94720-3200

Abstract

Light-activated ion channels provide a new opportunity to precisely and remotely control neuronal activity for experimental applications in neurobiology. In the past few years, several strategies have arisen that allow light to control ion channels and therefore neuronal function. Light-based triggers for ion channel control include caged compounds, which release active neurotransmitters when photolyzed with light, and natural photoreceptive proteins, which can be expressed

METHODS IN CELL BIOLOGY, VOL. 90

0091-679X/08 $35.00
DOI: 10.1016/S0091-679X(08)00811-X

exogenously in neurons. More recently, a third type of light trigger has been introduced: a photoisomerizable tethered ligand that directly controls ion channel activity in a light-dependent manner. Beyond the experimental applications for light-gated ion channels, there may be clinical applications in which these light-sensitive ion channels could prove advantageous over traditional methods. Electrodes for neural stimulation to control disease symptoms are invasive and often difficult to reposition between cells in tissue. Stimulation by chemical agents is difficult to constrain to individual cells and has limited temporal accuracy in tissue due to diffusional limitations. In contrast, ion channels that can be directly activated with light allow control with unparalleled spatial and temporal precision. The goal of this chapter is to describe light-regulated ion channels and how they have been tailored to control different aspects of neural activity, and how to use these channels to manipulate and better understand development, function, and plasticity of neurons and neural circuits.

I. Introduction

Neurons possess ion channels that are opened by changes in membrane voltage, changes in temperature, ligand binding, and mechanical forces, but none are known to be directly sensitive to light. Therefore, when experimentalists want to modulate neuronal activity mediated by ion channels, they typically will apply external electrical or chemical stimuli. This entails either the placement of electrodes or perfusion devices into or onto a neuronal preparation. Light stimulation from afar could in many instances be preferable to stimulation with physically invasive electrodes or inaccurate perfusion devices. Light can be projected onto a tissue preparation with great temporal and spatial precision. It can be focused onto single cells or even subcellular structures and it can also be quickly redirected between different cells in a population. With modern laser scanning technology, patterns of light can be "painted" on large groups of neurons, enabling precise control over neural networks through the light-mediated activation of ion channels allowing for much more advanced experiments than have been previously possible. In addition, three-dimensional two-photon excitation offers the promise of activating structures deep inside tissue; areas that were once inaccessible without physical damage to the tissue.

A. Photorelease of Caged Compounds

The caged neurotransmitter approach utilizes small, drug-like molecules that contain a neurotransmitter (e.g., glutamate (GLU)) that is protected by a photolabile accessory group (the "cage"). Illumination with light of the correct frequency rapidly removes the cage from the molecule, releasing active neurotransmitter. Photo-induced release of caged GLU has been used to accurately mimic the kinetics of synaptic release (Callaway and Yuste, 2002; Katz and Dalva, 1994) with spatial

control that has allowed mapping of neuronal connections (Callaway and Katz, 1993; Matsuzaki *et al*., 2008; Shoham *et al*., 2005). However, the approach does have drawbacks that could hinder some experiments. Uncaged neurotransmitter can diffuse through the extracellular milieu and linger for some time, potentially activating neighboring, untargeted neurons and limiting the frequency of repetitive stimulation. Moreover, other liberated photoproducts (i.e., the free cage) may result in unintended side effects on exposed cells. While the global concentration of caged neurotransmitters is typically rather high (millimolar range), the local concentration of the caged compound may become depleted with even moderately long illumination (>1 s). This approach may be inappropriate for eliciting long-term responses like those thought to underlie long-term potentiation that result from homeostatic regulation of ion channels and receptors.

B. Photoactivation Using Natural Photoproteins

The natural photoprotein approach involves exogenous expression of an opsin-related protein (e.g., rhodopsin). The protein does not itself sense light, but operates through a covalently attached photoisomerizable chromophore (e.g., retinal). Usually, the light-activated protein signals downstream cellular events through a G-protein-coupled mediated cascade and at least some of these accessory proteins must be coexpressed to support a heterologous light response (Zemelman *et al*., 2002). Light responses triggered by photoproteins such as rhodopsin (Zemelman *et al*., 2002) or melanopsin (Melyan *et al*., 2005) are typically slow and variable in type, probably reflecting differences in the downstream targets activated by the signaling cascade (i.e., the specific type of ion channel). However, a rhodopsin homolog with intrinsic ion channel activity has recently been borrowed from green algae (Nagel *et al*., 2003). This protein, called channelopsin-2 (CHOP-2), can be expressed in mammalian neurons, where it covalently attaches to naturally-occurring retinal to form light-sensitive channel rhodopsin which when activated with 460 nm light elicits rapid depolarization in response to brief flashes of light (Boyden *et al*, 2005). Light triggers an "On" response in transfected retinal neurons due to the nonselective cation channel properties of CHOP-2, simulating the normal light response of On-retinal ganglion cells (Bi *et al*., 2006). CHOP-2 is a promising tool for allowing optical activation of neuronal firing and has been adopted by many biologists as a turn-key solution to light activation of cells. More recently, another opsin-related protein has been studied that hyperpolarizes cells in response to 580 nm light. Halorhodopsin is a selective chloride channel found in the archaebacterium *Natronomas pharaonis* (Han and Boyden, 2007; Zhang *et al*., 2007). This protein, in conjunction with CHOP-2 now offers biologists the ability to use light to activate some cells, while inactivating others, allowing much more complicated experiments to be performed.

C. Photoactivation Using Bioconjugated Ion Channels

The photoswitch approach utilizes a combination of synthetic chemistry and molecular biology to reengineer ordinary ion channels, so that they are sensitive to light. To date, two disparate types of ion channels have successfully undergone reengineering: a K^+-selective ion channel (Banghart *et al*., 2004) and an ionotropic GLU receptor (Volgraf *et al*, 2006).

The light-activated K^+ channel, called Synthetic Photoisomerizable Azobenzene Regulated K^+ (SPARK) channel has two parts: a synthetic photoswitchable small molecule and a modified Shaker K^+ channel protein. The photoswitch is a functionalized version of the photoisomerizable molecule azobenzene (AZO) (Fig. 1A). Connected to the AZO on one end is a cysteine-reactive maleimide (MAL) group, which allows attachment to a surface-exposed cysteine residue on the channel, and on the other end a quaternary ammonium (QA) group, which blocks the pore of K^+ channels. The system has been designed so that the QA can reach the pore-blocking

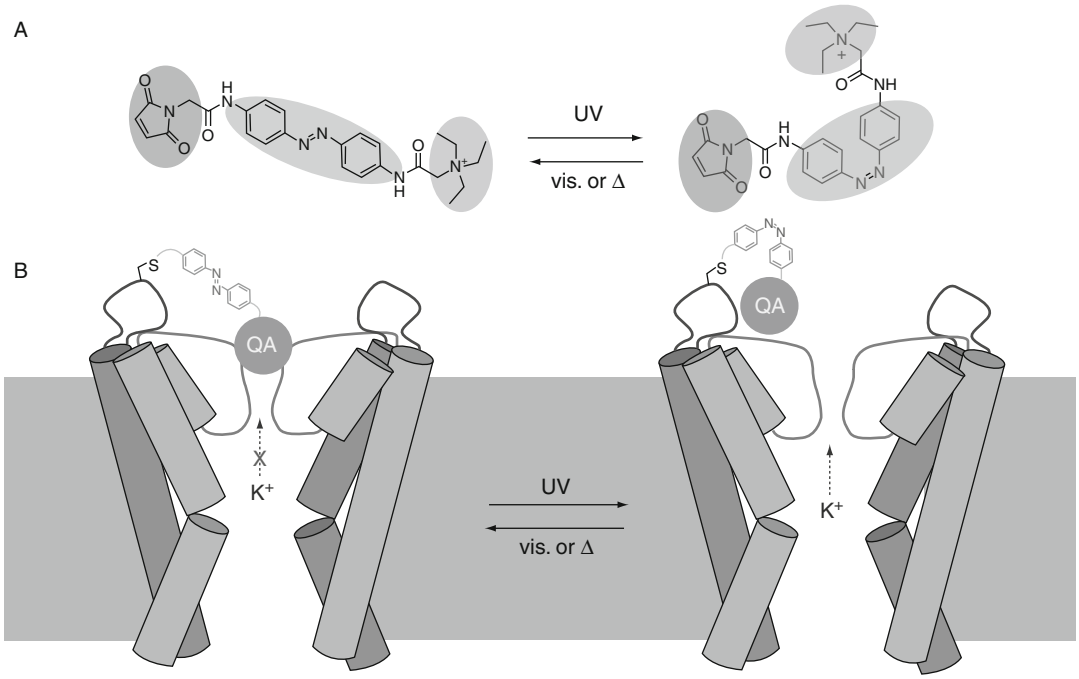

Fig. 1 Light regulation of current flow in SPARK channels. (A) The MAL-AZO-QA photoswitch isomerizes to the *cis* form upon exposure to UV light and returns to the lower energy *trans* form with visible light or through thermal relaxation. (B) Schematic representation of the K^+-selective SPARK channel. The QA group moiety ion conduction when AZO is in its *trans* configuration (left). UV light induces photoisomerization to the higher energy *cis* form, retracting the QA group, thus allowing K^+ to flow out and hyperpolarize the cell.

binding site and arrest ion conduction when the AZO is in its low energy, elongated *trans* form, but not in its higher energy, bent *cis* form (Fig. 1B). As UV light photoisomerizes the AZO from *trans* to *cis*, it retracts the QA group and unblocks the channel, whereas longer wavelength visible light restores the blocked state by accelerating the reverse *cis* to *trans* conversion. The higher energy *cis* form of AZO is less stable than that of the *trans* form, so reblocking of the channel also occurs spontaneously, but slowly, if the system is left in the dark.

The GLU receptor was reengineered to site-specifically attach a tethered analog of GLU that was attached to a photoswitchable AZO to the edge of the ligand-binding domain of the receptor. In one state, the ligand-binding domain could be occupied by the GLU analog allowing activation of the ion channel and in the other, the receptor would be in the unoccupied, native state. Photoisomerization switches between these two states with the low energy, *trans* state disallowing binding and the high energy, *cis* state causing agonism of the receptor and thus opening of the channel and depolarization of the cell.

II. Discussion

A. Inhibition of Neuronal Activity with Light-Activated Ion Channels

1. SPARK Channels

There are several methods in current use for photostimulation of action potential firing in neurons, yet methods for optical inhibition remain limited. To impart reversible optical silencing of neural activity, a system has been designed that consists of an engineered Shaker potassium channels that gates in response to light when functionalized with a covalently attached, photoswitchable pore blocker. SPARK channels consist of a synthetic AZO-containing photoswitch and a genetically modified Shaker K^+ channel protein. When tested in the heterologous *Xenopus* oocyte expression system, after microinjection of mRNA encoding the channel, it was found that the SPARK channels open and close rapidly (within seconds) upon exposure to 380 and 500 nm light, respectively (Fig. 2A). Opened channels also close in the dark, but over the much slower time course of several minutes (Fig. 2B).

In addition to the inside-out patch clamp *Xenopus* oocyte experiements, SPARK channels has been used to regulate action potential firing in cultured rat hippocampal neurons (Fig. 2C). Several mutations have been introduced into the Shaker channel to maximize the dynamic range of light-induced voltage changes. N-type inactivation has been minimized by removal of the Shaker "ball" and voltage-dependence of activation shifted to hyperpolarized potentials, presumably making the channel constitutively open at normal neuronal resting potentials. Neurons that have been transfected with the channel gene and treated with the photoswitch become directly sensitive to light, with short wavelengths opening the channels and silencing activity and longer wavelengths closing the channels and

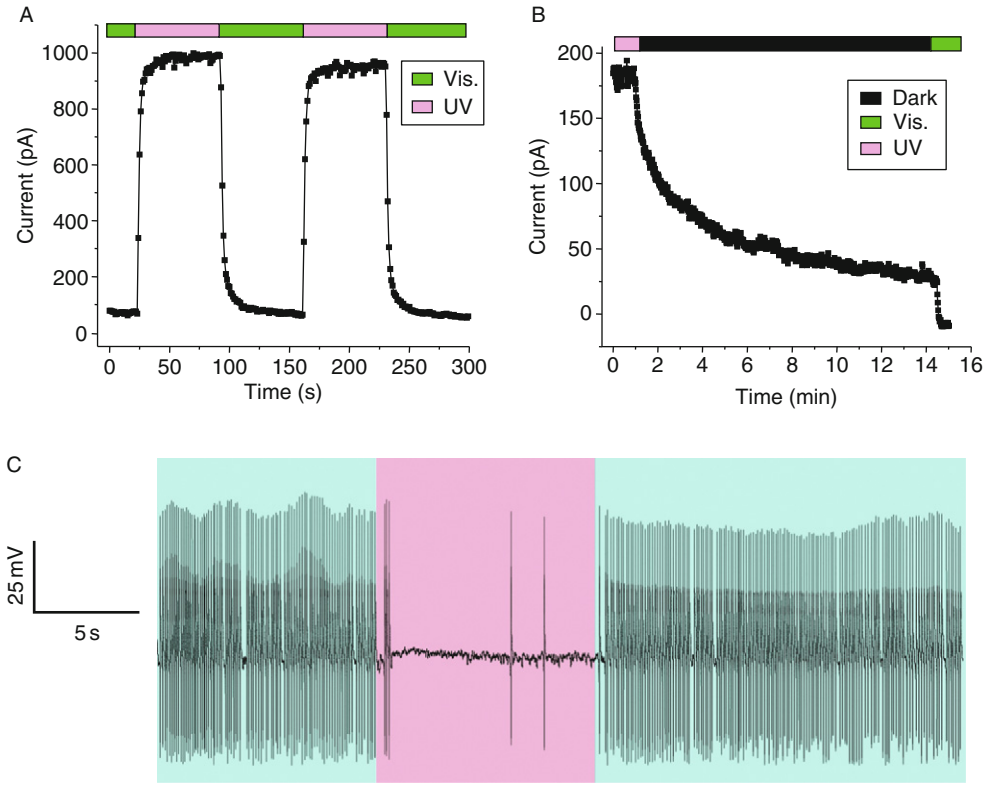

Fig. 2 Photoswitching of SPARK channels. (A) UV light opens channels and visible light closes channels in an inside–out patch taken from a MAL-AZO-QA-treated *Xenopus* oocyte expressing SPARK channels. (B) SPARK channels close slowly in the dark as the photoswitches relaxes back to the *trans* configuration. (C) Suppression of spontaneous action potentials by UV light (380 nm) in a MAL-AZO-QA-treated cultured hippocampal neuron expressing SPARK channels. Exposure to visible light (500 nm) restores spontaneous firing.

allowing spontaneous firing of action potentials to resume. Action potential firing can be switched on and off within seconds and can be controlled repeatedly for tens of minutes or as long as the patched cell-seal remains.

The photoswitch that has been used in most experiments was MAL-AZO-QA and consisted of a cysteine-reactive MAL group, an AZO group, which is photoisomerizable, and a QA group, which is a blocker of the pore of K^+ channels. Remarkably, the MAL-AZO-QA photoswitch appears to be selective for the expressed Shaker channel, having no measurable effect on the many other types of K^+ channels in these neurons that are known to be blocked by QA ions (Fortin *et al.*, 2008). It is hypothesized that the selectivity exhibited by MAL-AZO-QA is a consequence of the close matching of the molecular length in the *trans*, or extended, form with the spacing of the engineered cysteine and the QA-binding

site on the Shaker channel. The covalent attachment of the MAL group to the introduced cysteine in the channel appears to be accelerated by the binding of the QA group to the pore, which is about 17 Å away. If any MAL-AZO-QA does, in fact, attach to another ion channel family on the neuronal surface, it would likely have little physiological effect because the QA group would not be ideally situated in a position where it could block the pore. The specificity of the photoswitch for the exogenously expressed Shaker channel suggests that SPARK channels can be targeted to different types of neurons simply by targeting gene expression, for example, with cell-type-specific promoters or by using virally-mediated transfection.

2. PALS—Photoswitchable Affinity Labels

All of the light-activated channels described in this chapter, require exogenous expression of a gene encoding either a foreign or genetically modified ion channel, followed by covalent bioconjugation of a photoswitchable small molecule (e.g., retinal for CHOP-2 or MAL-AZO-QA for SPARK). Exogenous gene expression can be routinely accomplished using a variety of methods, including chemically facilitated gene transfection (e.g., lipofection or calcium phosphate) or viral-mediated gene transfer, but in all cases exogenous gene expression is slow, requiring hours to weeks depending on multiple variables. Due to the time constraints, tissue culture is often employed, either using dissociated neurons in a dish or organotypic cultures (e.g., brain slice cultures). The level of exogenous gene expression varies widely within a population of transfected neurons and successful introduction of foreign genes is often a low-probability event (e.g., in our hands $\ll 10\%$ for calcium phosphate transfection). Foreign ion channel genes can also be introduced into transgenic animals, but this requires months, is rather expensive, and there may be consequences for the proper development of cells and tissues expressing the genes, thereby confounding interpretation of the results. Additionally, using exogenously-expressed genes is sometimes not suitable for multisubunit receptors, since overexpression of monomers of a particular receptor may bias natural receptor subtype composition (Bredt and Nicoll, 2003). For these reasons, a method for conferring light-sensitivity that does not require exogenous gene expression, but rather can be carried out on freshly obtained, native, neural tissue would be a great improvement.

The MAL-AZO-QA photoswitch for SPARK channels contains a MAL group, which presumably reacts with a cysteine residue that has been introduced at the correct position on the channel protein surface. The PAL compound that has been used recently for imparting light sensitivity to K^+ channels is identical to MAL-AZO-QA, with one difference: instead of a MAL at one end, the new molecule contains a ''promiscuous'' acrylamide group, which can react more readily with several nucleophilic sidechains on the protein surface, including lysine, serine, threonine, in addition to cysteine. Presumably, the bioconjugation occurs through the QA first binding to the pore site, slowing its departure from the vicinity of the

channel thus, increasing the local effective concentration of the acrylamide moiety. This promotes covalent attachment to the channel protein, if it happens to possess a nucleophilic amino acid sidechain at an appropriate distance from the QA binding site (~17 Å away). Hence, the labeling of native channels by the highly reactive portion of the molecule is promoted through ligand-binding interaction, as in classical photoaffinity labeling experiments (Chowdhry and Westheimer, 1979). In contrast to SPARK channels, where two components are required to impart light-sensitivity to cells (i.e., the engineered ion channel gene and the MAL-AZO-QA photoswitch), this is a one-component system, where only the PAL molecule is required. This allows PAL to react with and thus impart light-sensitivity on native K^+ channels in neurons with no need for exogenous gene expression. Like SPARK channels, PAL-treated channels allow precise and reversible control over membrane potential and action potential firing in neurons, but in a different and complementary way. SPARK can be genetically targeted through ion channel expression and PAL can be globally applied to an experimental preparation.

The possibility of using PAL to activate cells with light was tested first using the Shaker K^+ channel as a test system (Fortin *et al*., 2008). Addition of PAL to a Shaker channel that has a cysteine-substitution at position E422 (E422C) imparts light-sensitivity on the channel in a way very similar to MAL-AZO-QA. However, PAL works equally well on a Shaker channel that does not have the cysteine substitution. Hence, it appears that the PAL molecule can locate an alternative attachment site at an appropriate distance from the pore, such that light-elicited changes in photoswitch geometry can reversibly block and unblock the pore of the channel. Steady-state current–voltage curves from a hippocampal neuron in culture that has been treated with PAL have demonstrated that exposure to 380 nm light increases the voltage-gated outward current at membrane potentials positive to about −20 mV, and 500 nm light reverses the effect. In contrast, MAL-AZO-QA failed to impart light sensitivity on untransfected neurons that express only their native ion channels. PAL treatment also confers light-dependent effects on action potential firing. Under current clamp mode, 380 nm light silences spontaneous firing and 500 nm light allows native firing (Fortin *et al*., 2008).

B. Excitation of Neuronal Activity with Light-Activated Ion Channels

1. D-SPARK (Depolarizing SPARK) Channels

Wild-type Shaker channels are highly selective for K^+ conduction through their pore over other cations (Hille, 1992). To convert the hyperpolarizing and thus silencing SPARK channel into a nonselective cation channel and thus depolarizing (D-SPARK), a single point mutation has been introduced into the pore-lining domain, converting valine-443 into glutamine (V443Q). Mutation of this residue, which is part of the conserved signature sequence of voltage-gated K^+ channels, reduces the K^+:Na^+ permeability ratio of Shaker from <0.02 to about 0.70

(Heginbotham *et al.*, 1994). Other than this single pore mutation, the structure of the D-SPARK channel protein is identical to the SPARK protein. The D-SPARK system also consists of the same MAL-AZO-QA molecule bioconjugated to the protein to impart light-induced gating as the SPARK channel (Chambers *et al.*, 2006).

To characterize the biophysical properties of D-SPARK channels steady-state current–voltage curves were recorded and show that exposure to 380 and 500 nm light, increased and decreased the conductance, respectively, and that the reversal potential of the light-regulated conductance was near 0 mV (Fig. 3A), which is indicative of a nonselective ion channel. The light-activation effect was not observed when control cells were tested (Fig. 3B). Light had similar effects on cells expressing hyperpolarizing SPARK, but the reversal potential was closer to −70 mV, as expected for a K^+-selective channel (Fig. 3C). A point mutation (L366A) has been introduced into the voltage-sensing domain of both SPARK and D-SPARK to shift the activation potential to about −70 mV as compared to

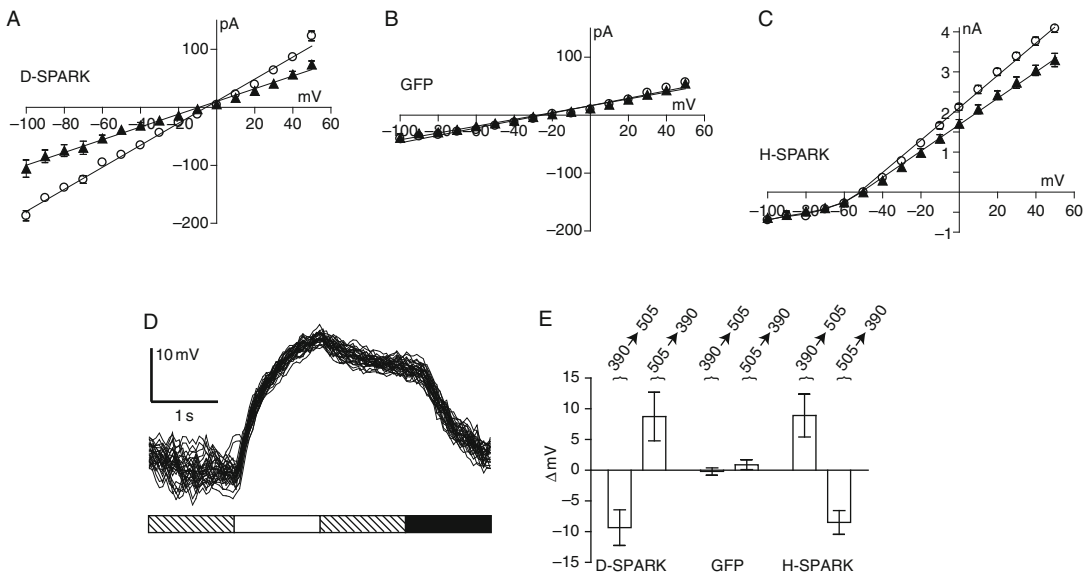

Fig. 3 Properties of SPARK and D-SPARK channels expressed in CHO cells. Steady-state I–V curves showing the effect of photoswitching. (A) Cells transfected with GFP-tagged D-SPARK channels and treated with MAL-AZO-QA elicit more current when stepped to any given voltage when UV light is used for illumination (open circles) when compared to visible light (closed triangles). (B) Control cells transfected with GFP plasmid and similarly treated with MAL-AZO-QA do not respond to light. (C) Cells expressing SPARK channels and treated with MAL-AZO-QA also conduct more current upon exposure to UV light. (D) Current clamp recording from a CHO cell showing repeatable depolarization by exposure to UV light (white bar) and hyperpolarization in visible light (black bar). D-SPARK channels closed slowly in the dark (hashed bar) through thermal relaxation of the photoswitch. (E) Average membrane potential changes elicited by light ($n = 10$ CHO cells for each treatment).

−35 mV for wild-type channels (Lopez *et al.*, 1991). This mutation along with deletion of fast N-type inactivation renders SPARK constitutively active at physiological membrane potentials (>−65 mV), but the channel can be closed at potentials <−65 mV. A surprising difference between the voltage-dependency of gating for SPARK and D-SPARK channels was observed. D-SPARK remained open at membrane potentials down to −100 mV. It appears that the combination of the pore mutation and a voltage-sensor mutation disrupts the normal voltage-control over the permeation pathway, a finding that is not without precedent (Molina *et al.*, 1998).

In experiments, where current-clamp configuration is employed, D-SPARK cells depolarize when illuminated with 380 nm light, and hyperpolarize when illuminated with 500 nm light, reaching steady-state within several seconds (Fig. 3D). Channels that are opened with 380 nm light are observed to close spontaneously in the dark, but the rate of closure is slow (tens of seconds). When cells were current clamped to a membrane potential similar to the resting potential of many cells (−40 mV), opening and closing the channels had opposite effects on cells expressing D-SPARK and SPARK channels (Fig. 3E). Cells expressing D-SPARK depolarized by about 9 mV upon exposure to 380 nm light, whereas cells expressing SPARK hyperpolarized by about 8 mV. Switching to 500 nm light reversed the effect in both cell-types.

D-SPARK channels could also be expressed and photoswitched in mammalian neurons. The gene encoding the D-SPARK channel protein was transfected into hippocampal neurons in culture using a calcium phosphate transfection method (Dudek *et al.*, 2003). It was found that D-SPARK-transfected cells showed an increase in membrane conductance upon exposure to 380 nm light and a decrease upon exposure to 500 nm light under voltage clamp conditions. Under current clamp configuration, 380 nm light depolarized transfected neurons and triggered bursts of action potentials, and 500 nm light reversed the depolarization, halting action potential bursting (Fig. 4).

D-SPARK channels are designed to be constitutively open in neurons before the addition of the bioconjugated photoswitch. To investigate concerns about toxicity of D-SPARK tonic activity prior to photoswitch application, cell viability was measured. A constitutively open cation channel could lead to tonic depolarization, lowered input resistance, continual Ca^{2+} influx, and possibly, cell death. Remarkably, expression of the D-SPARK protein without MAL-AZO-QA application did not reduce the viability of hippocampal neurons in culture when compared to control groups. The percentage of neurons successfully transfected with GFP-tagged D-SPARK or GFP alone were the same (about 0.5% in both cases), and there was no significant difference in the fraction of each that tested positive for DEAD Red nuclear staining. In fact, culturing transfected neurons in the presence of other Shaker channel blockers including 4-aminopyridine, dendrotoxin-K, or charybdotoxin, did not change viability, and therefore was not necessary for future experiments. D-SPARK expression had no significant effect on input resistance or on resting membrane potential. Interestingly, addition of MAL-AZO-QA to

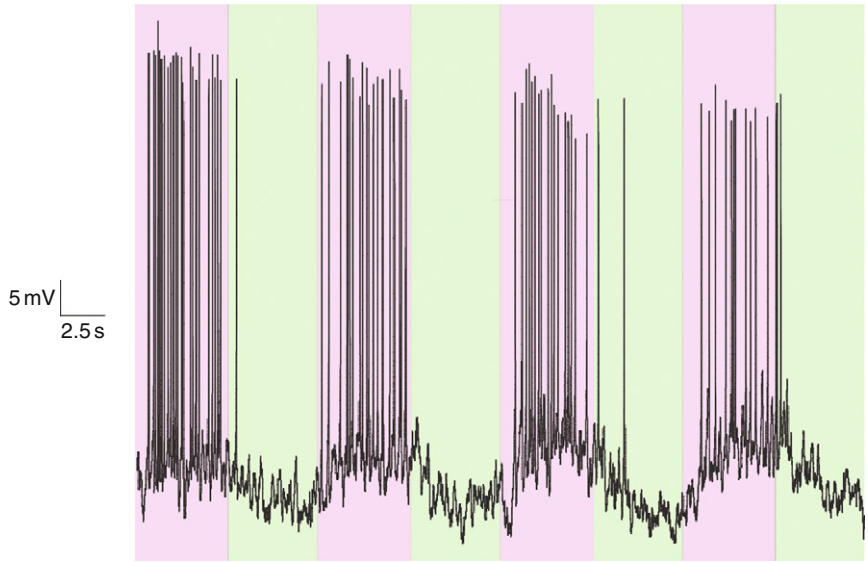

Fig. 4 Opening of D-SPARK channels causes action potential firing in mammalian neurons. Bursts of action potentials are elicited when a D-SPARK transfected and MAL-AZO-QA treated neuron is illuminated with UV light purple background. The action potential bursts are halted when the cell is illuminated with visible light green background.

D-SPARK-expressing neurons also had no significant effect on these measures. There are several possible explanations for these surprising observations. First, hippocampal neurons may compensate for D-SPARK expression by homeostatically altering expression levels of other channels in order to maintain the cell-programmed "set point" (Turrigiano and Nelson, 2004). This could help explain the similar values of resting membrane potential and cell viability between control and D-SPARK expressing cells, but would not explain why input resistance is unaffected by D-SPARK expression. Second, D-SPARK channels may be preferentially expressed in electrotonically distant portions of the neurons, such that blocking and unblocking them with the photoswitch has no measurable effect on input resistance or resting potential measured in the cell body, but it has a very strong influence on action potential initiation. Compartments of the neuron may have a high local input resistance, such that opening or closing a small number of channels may have a large impact on action potential firing frequency. Finally, a likely scenario is that D-SPARK channel subunits may coassemble with native K^+ channel subunits in neurons to produce heteromeric channels whose properties differ from those of homomeric D-SPARK channels expressed in CHO cells including their persistent activity. A heteromeric ion channel consisting of some D-SPARK subunits may display hybrid electrophyiscal properties.

2. LiGluR (Ligand-Gated Ionotropic GLU Receptor)

Recently, a light-gated, agonist-mediated design has been developed for use on the ionotropic GLU receptor. A molecule similar to MAL-AZO-QA but instead MAL-AZO-GLU was covalently attached to the ligand-binding domain of an ionotropic glutamate receptor (iGluR6). This compound consists of a cysteine-reactive MAL, a photoswitchable AZO moiety, and an agonist analog of GLU. In the extended *trans* form of the AZO, the ligand-binding domain cannot bind the tethered agonist and close. Only after photoisomerization to the *cis* form can the photoswitchable tether present the agonist to the binding site, thus causing closure of the domain and opening of the ion channel (Fig. 5). Overall, the reversible switching of an AZO allosterically triggers the opening and closing of the entire ion channel, mediated by the clamshell-like movement of the ligand-binding domain. LiGluR has also been used to trigger action potentials in neuronal culture using 1–5 ms pulses of light to achieve responses very similar to those observed during normal neuronal functioning (Szobota *et al.*, 2007).

C. Possible Future Directions for Light-Gated Ion Channels

1. Thermostable Photoswitches

Since the *trans* configuration of AZO is the low energy state of the MAL-AZO-QA photoswitch, for instance, in the dark and in visible light, covalent attachment of MAL-AZO-QA to ion channels in neurons will result in tonic K^+ channel

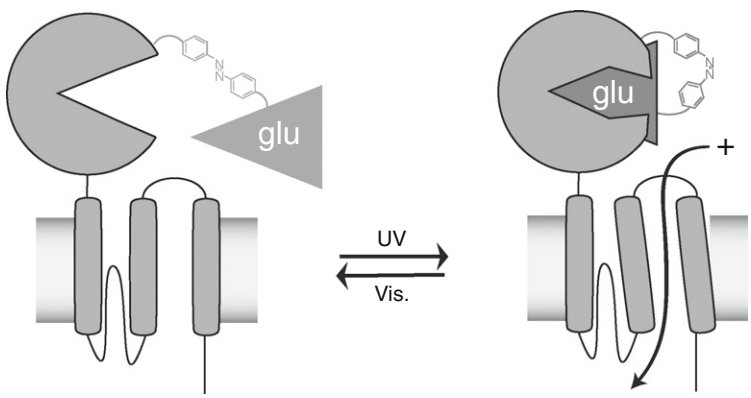

Fig. 5 Illumination of LiGluR channels with UV light allows the tethered glutamate (GLU) analog to bind to the ligand-binding domain. Then a conformational change occurs that allows the ion channel to open and cations to flow through the channel, thus depolarizing the cell.

blockade and neuronal depolarization. This can be overcome by maintained illumination with 380 nm light. However, perhaps a better way to turn off MAL-AZO-QA-treated channels is with a thermostable photoswitch, in which the *cis* form can persist for many hours. With a molecule such as this, a brief flash of UV light would be all that is required to maintain native K^+ channels in their normal, unblocked state, even though a photoswitch was still attached. Then, at any moment, a flash of 500 nm light could be used to block the channels and stimulate the cells. Open SPARK channels revert to their closed state within minutes because the *cis* configuration of MAL-AZO-QA spontaneously relaxes to the *trans* configuration. As long as SPARK channels are exposed to 380 nm light they will remain open, but prolonged illumination may not always be desirable.

2. MultiPhoton-Sensitive Photoswitches

With the further development of optical techniques, advances could be used to the advantage of light-gated ion channels. Instead of using AZO as the photoswitchable unit, other multiphoton sensitive chromophores will surely be explored that will allow more robust and deeper tissue activation.

3. Applications of Light-Activated Ion Channels

One potential application for light-activated ion channels of particular interest is the retina. Light-activated ion channels provide an alternative approach to building a retinal prosthetic. In the case of light-activated ion channels, the prosthetic device would be downstream from the neuron itself (e.g., a retinal ganglion cell), which is induced to become directly sensitive to light. Expression of silencing channels in retinal ganglion cells could produce "virtual Off-cells," which are inhibited by illumination. Expression of stimulating channels should produce "virtual On-cells" that are stimulated with light. Since the SPARK and D-SPARK channels use the same photoswitch, the spectral sensitivity of channel opening and closing is the same. This greatly simplifies the task of regulating the activity of retinal ganglion cells, assuming the appropriate channel type could be expressed selectively in the appropriate cell type. The identification of proteins that are expressed differentially in On-versus Off-retinal ganglion cells (Yamagata *et al.*, 2002) could lead to identification of gene regulatory elements for allowing selective expression of light-activated channels in their appropriate neuronal populations. This would greatly simplify the task of regulating the activity of retinal ganglion cells, assuming the appropriate channel type could be expressed selectively in the appropriate cell type.

Light-activated ion channels may be useful for allowing selective and noninvasive activation with light of individual neurons in a neural circuit. With a high enough photon flux to fully open or close all the channels instantaneously, the temporal resolution of activation with D-SPARK may be similar to that achieved with either GLU uncaging or channelrhodposin-2 stimulation (Boyden *et al.*, 2005;

Ishizuka *et al.*, 2006; Nagel *et al.*, 2003). However, unlike neurotransmitter uncaging, SPARK activation is specific to targeted cells and does not produce diffusible products that can have unintended effects on neighboring cells. Unlike the use of natural photoproteins, the photoswitch approach is versatile because it is easy to modify either the ion channel protein or the photoswitch.

III. Methods

CHO cells were cultured on glass coverslips in 10% FBS/F12 media to ~70% confluency. Primary dissociated hippocampal cultures were prepared from embryonic day E18–19 Sprague-Dawley rat embryos and were cultured on polylysine-coated glass coverslips in serum-containing medium. Both mammalian cell types were grown in 7% CO_2 in air at 37 °C. All animal care and experimental protocols were approved by the Animal Care and Use Committee at UC, Berkeley.

For experiments, involving expression of exogenous ion channels, both cell line and primary cell culture were typically transfected with 0.8 mg DNA per 12 mm coverslip encoding either eGFP or eGFP-tagged Shaker H4 channels, with the following mutations: Δ6–46, L366A, E422C, V443Q (for D-SPARK only), and T449 V. The eGPF was tagged to the N-terminal of the Shaker gene using standard PCR and molecular cloning techniques. Transfections with $CaPO_4$ were carried out for 10–13 days *in vitro* for the primary culture; and electrophysiological recording was performed ~48 h later (Dudek *et al.*, 2003). Coverslips containing cells were typically treated for 15 min with 300 mM of photoswitch at 37 °C in an extracellular recording solution containing 138 mM NaCl, 1.5 mM KCl, 1.2 mM $MgCl_2$, 5 mM HEPES, 2.5 mM $CaCl_2$, and 10 mM glucose at pH 7.4. The concentration of DMSO in the treatment bath did not exceed 0.1%. Patch pipettes (4–8 MΩ) were filled with 10 mM NaCl, 135 mM K-gluconate, 10 mM HEPES, 2 mM $MgCl_2$, 2 mM Mg-ATP, and 1 mM EGTA at pH 7.4. After washout of unbound photoswitch with extracellular solution, whole-cell patch was established. Voltage-clamp configuration was used to generate I–V data and then the configuration was changed to current-clamp and the membrane potential was recorded. Initial recordings were made at the resting potential to evaluate the effects of light on spontaneous activity in neurons. Pulse protocols and measurements were carried out with pCLAMP 8.0 software, a DigiData 1200 series interface, and an Axo-Patch 200A amplifier (Axon Instruments). Samples were taken at 10 kHz, and the data were filtered at 1 kHz. Seals with a leak current of >200 pA were not included in analyses. Cells were irradiated using a Lambda-LS illuminator containing a 125-W xenon arc lamp (Sutter Instruments Company) equipped with narrow-bandpass (±10 nm) filters through a Fluor 20X, 0.5 n.a. objective lens (Nikon). Cell viability assays were performed according to the protocol provided by the vendor of the Live/Dead Kit (Invitrogen). Variability among data is expressed as Mean ± SD.

IV. Conclusion

The photoswitch approach, the caged neurotransmitter approach, and the natural photoprotein approach each provide new opportunities to precisely and remotely control neuronal activity for experimental and potentially medical applications. Each approach has strengths and weaknesses and is best used in specific contexts. The probable outcome of the current state of research in this field is that all of these methods will continue to find important uses in cell biology in general, and neurobiology in particular. These techniques may eventually be used as medical tools for the noninvasive and precise input of information into the nervous system, downstream of sites of degeneration or injury. It is worth noting that the remarkable advances in this field are driven not only by new discoveries in chemical and molecular biology, but also by new and supremely accurate and powerful optical technology. Together, these tools constitute a new optical interface for controlling the function of cells, tissues, and perhaps entire organisms.

Acknowledgments

We thank S. Ahituv for technical support, M. Banghart, K. Borges, D. Fortin, I. Hafez, E. Isacoff, D. Trauner for critical experiments, discussion, and advice. This work was supported by grants to RHK from the NIH (EY016249) and Fight-for-Sight. JJC was supported by a NIH NRSA fellowship.

References

Banghart, M., Borges, K., Isacoff, E., Trauner, D., and Kramer, R. H. (2004). Light-activated ion channels for remote control of neuronal firing. *Nat. Neurosci.* **7,** 1381–1386.

Bi, A., Cui, J., Ma, Y. P., Olshevskaya, E., Pu, M., Dizhoor, A. M., and Pan, Z. H. (2006). Ectopic expression of a microbial-type rhodopsin restores visual responses in mice with photoreceptor degeneration. *Neuron* **50**(1), 23–33.

Boyden, E. S., Zhang, F., Bamberg, E., Nagel, G., and Deisseroth, K. (2005). Millisecond-timescale, genetically targeted optical control of neural activity. *Nat. Neurosci.* **8,** 1263–1268.

Bredt, D. S., and Nicoll, R. A. (2003). AMPA receptor trafficking at excitatory synapses. *Neuron* **40**(2), 361–379.

Callaway, E. M., and Katz, L. C. (1993). Photostimulation using caged glutamate reveals functional circuitry in living brain slices. *Proc. Natl. Acad. Sci. USA* **90,** 7661–7665.

Callaway, E. M., and Yuste, R. (2002). Stimulating neurons with light. *Curr. Opin. Neurobiol.* **12,** 587–592.

Chambers, J. J., Banghart, M. R., Trauner, D., and Kramer, R. H. (2006). Light-induced depolarization of neurons using a modified shaker K^+ channel and a molecular photoswitch. *J. Neurophysiol.* **96,** 2792–2796.

Chowdhry, V., and Westheimer, F. H. (1979). Photoaffinity labeling of biological systems. *Annu. Rev. Biochem.* **48,** 293–325.

Dudek, H., Ghosh, A., and Greenberg, M. E. (2003). Calcium phosphate transfection of DNA into neurons in primary culture. *In* "Current Protocols in Neuroscience" (J. N. Crawley, C. R. Gerfen, M. A. Rogawski, D. R. Sibley, P. Skolnick, and S. J. Wray, eds.), Wiley, Chichester.

Fortin, D. L., Banghart, M. R., Dunn, T. W., Borges, K., Wagenaar, D. A., Gaudry, Q., Karakossian, M. V., Otis, T. S., Kristan, W. B., Trauner, D., and Kramer, R. H. (2008). Photochemical control of endogenous ion channels and cellular excitability. *Nat. Methods* **5,** 331–338.

Han, X., and Boyden, E. S. (2007). Multiple-color optical activation, silencing, and desynchronization of neural activity, with single-spike temporal resolution. *PLoS ONE* **2**(3), e299 DOI:10.1371/journal.pone.0000299.

Heginbotham, L., Lu, Z., Abramson, T., and MacKinnon, R. (1994). Mutations in the K^+ channel signature sequence. *Biophys. J.* **66,** 1061–1067.

Hille, B. (1992). "Ionic Channels of Excitable Membranes." Sinauer Associates, Sunderland, MA.

Ishizuka, T., Kakuda, M., Araki, R., and Yawo, H. (2006). Kinetic evaluation of photosensitivity in genetically engineered neurons expressing green algae light-gated channels. *Neurosci. Res.* **54,** 85–94.

Katz, L. C., and Dalva, M. B. (1994). Scanning laser photostimulation: A new approach for analyzing brain circuits. *J. Neurosci. Methods* **54,** 205–218.

Lopez, G. A., Jan, Y. N., and Jan, L. Y. (1991). Hydrophobic substitution mutations in the S4 sequence alter voltage-dependent gating in Shaker K + channels. *Neuron* **7,** 327–336.

Matsuzaki, M., Ellis-Davies, G. C., and Kasai, H. (2008). Three-dimensional mapping of unitary synaptic connections by two-photon macro photolysis of caged glutamate. *J. Neurophysiol.* **99**(3), 1535–1544.

Melyan, Z., Tarttelin, E. E., Bellingham, J., Lucas, R. J., and Hankins, M. W. (2005). Addition of human melanopsin renders mammalian cells photoresponsive. *Nature* **433,** 741–745.

Molina, A., Ortega-Saenz, P., and Lopez-Barneo, J. (1998). Pore mutations alter closing and opening kinetics in Shaker K + channels. *J. Physiol.* **509**(Pt. 2), 327–337.

Nagel, G., Szellas, T., Huhn, W., Kateriya, S., Adeishvili, N., Berthold, P., Ollig, D., Hegemann, P., and Bamberg, E. (2003). Channelrhodopsin-2, a directly light-gated cation-selective membrane channel. *Proc. Natl. Acad. Sci. USA* **100,** 13940–13945.

Shoham, S., O'Connor, D. H., Sarkisov, D. V., and Wang, S. S. (2005). Rapid neurotransmitter uncaging in spatially defined patterns. *Nat. Methods* **2**(11), 837–843.

Szobota, S., Gorostiza, P., Del Bene, F., Wyart, C., Fortin, D. L., Kolstad, K. D., Tulyathan, O., Volgraf, M., Numano, R., Aaron, H. L., Scott, E. K., Kramer, R. H., *et al*. (2007). Remote control of neuronal activity with a light-gated glutamate receptor. *Neuron* **54**(4), 535–545.

Turrigiano, G. G., and Nelson, S. B. (2004). Homeostatic plasticity in the developing nervous system. *Nat. Rev. Neurosci.* **5**(2), 97–107.

Volgraf, M., Gorostiza, P., Numano, R., Kramer, R. H., Isacoff, E. Y., and Trauner, D. (2006). Allosteric control of an ionotropic glutamate receptor with an optical switch. *Nat. Chem. Biol.* **2,** 47–52.

Yamagata, M., Weiner, J. A., and Sanes, J. R. (2002). Sidekicks: Synaptic adhesion molecules that promote lamina-specific connectivity in the retina. *Cell* **110**(5), 649–660.

Zemelman, B. V., Lee, G. A., Ng, M., and Miesenbock, G. (2002). Selective photostimulation of genetically chARGed neurons. *Neuron* **33,** 15–22.

Zhang, F., Wang, L. P., Brauner, M., Liewald, J. F., Kay, K., Watzke, N., Wood, P. G., Bamberg, E., Nagel, G., Gottschalk, A., and Deisseroth, K. (2007). Multimodal fast optical interrogation of neural circuitry. *Nature* **446,** 633–639.

CHAPTER 12

Molecular Modeling and Simulation Studies of Ion Channel Structures, Dynamics and Mechanisms

Kaihsu Tai, Philip Fowler, Younes Mokrab, Phillip Stansfeld, and Mark S.P. Sansom

Department of Biochemistry
University of Oxford
Oxford, OX1 3QU, United Kingdom

METHODS IN CELL BIOLOGY, VOL. 90

0091-679X/08 $35.00
DOI: 10.1016/S0091-679X(08)00812-1

Abstract

Ion channels are integral membrane proteins that enable selected ions to flow passively across membranes. Channel proteins have been the focus of computational approaches to relate their three-dimensional (3D) structure to their physiological function. We describe a number of computational tools to model ion channels. Homology modeling may be used to construct structural models of channels based on available X-ray structures. Electrostatics calculations enable an approximate evaluation of the energy profile of an ion passing through a channel. Molecular dynamics simulations and free-energy calculations provide information on the thermodynamics and kinetics of channel function.

I. Introduction

Ion channels are integral membrane proteins that allow ionic currents to flow across membranes. Channels allow selected ions to flow across membranes down their electrochemical gradients through nanoscopic pores through the centre of the channel protein molecule (Hille, 2001). Channels play key roles in the physiology of a wide range of cells, especially those with excitable membranes, and are important drug targets. They have also been the focus of a wide range of computational approaches in an attempt to relate their 3D structure to their physiological function. In this context, we review a range of computational tools which can be used to reveal the workings of ion channels. Firstly, we discuss homology modeling which may be used to construct models which complement available crystallographic structures. Secondly, electrostatics calculations based on the Poisson–Boltzmann (PB) equation provide a computationally inexpensive way to evaluate the energy profile of an ion going through the pore of a channel. Finally, molecular dynamics (MD) simulations, and especially free-energy calculations, can provide information on the thermodynamics and kinetics of channel function. Together, these tools can reveal the inner workings of ion channels and their interactions with the membrane environment.

II. Homology-Based Structure Prediction of Transmembrane Proteins

Transmembrane (TM) proteins comprise roughly 30% of all proteins (Wallin and von Heijne, 1998) and play key roles in many cellular processes. In addition, nearly two-thirds of all current drug targets are TM receptors and ion channels (Terstappen and Reggiani, 2001). Being difficult to express and purify, to date, few distinct TM protein structures have been solved by high-resolution methods such as X-ray crystallography and nuclear magnetic resonance (NMR), accounting for less than 1% of the total number of structures deposited to the Protein Data Bank (PDB) (Berman

et al., 2000). Direct structural determination, especially for many eukaryotic TM proteins, may remain difficult for years to come. In an attempt to overcome this problem, approaches for modeling 3D structures computationally have been developed (Petrey and Honig, 2005), which have aided not only experimental studies but also theoretical calculations, such as MD and molecular docking. In this section, we discuss the basics of some methods used to model 3D structures of TM proteins and provide an illustrative case study of modeling an ion channel protein.

A. Homology Modeling: A Biological Approach to Protein Structure Prediction

Despite a qualitative understanding of the forces that shape the protein folding process, current knowledge is not sufficient to predict protein structure from first principles on a reasonable timescale. However, the accumulation of a large number of sequenced genomes and protein structures has led to the development of knowledge-based methods for predicting the 3D structure of a protein from its amino acid sequence.

Over the years, three main approaches of structure prediction have developed: *ab initio* prediction, homology-based modeling, and threading (Petrey and Honig, 2005). These are distinguished by how much information from amino acid sequence and protein structural databases is used in building the model. In principle, *ab initio* prediction makes no use of information from databases; the goal being to predict the structure based entirely on laws of physics and chemistry. In practice, the terms "*ab initio*" or "*de novo*" are often used to describe methods, which predict the structure for a protein with no similar structures, but still use information from predicted secondary structure or local sequence and structural relationships to short protein fragments (Bradley *et al.*, 2005). Homology-based modeling (or simply, homology modeling), which currently gives the most accurate and reliable models, is based on the general observation that evolutionarily related (homologous) proteins are likely to have similar structures (Chothia and Lesk, 1986). Consequently, a structure model can be built for a protein of interest (target) based on the known structure of a close homologue (template). Threading refers to the case in which the structures of one or more distant homologues exist but can not be easily recognized because of the low sequence similarity. Here, the biggest challenge is to find and use such template(s) to build the model, which is often a difficult task.

Therefore, with the exception of pure physics-based approaches, most protein prediction methods make use of templates that range from relatively small fragments as in the *ab initio* methods to entire proteins as in homology modeling. For a given target, there are often several potential templates with various levels of similarity, including those which cover only certain regions of the protein. This led to the raising of questions about the nature of the evolutionary relationships between proteins and protein domains. Methods were developed for the superposition of 3D structures (Kolodny *et al.*, 2005), helping to recognize homology that was not evident from sequence. Subsequently, databases such as SCOP (Murzin *et al.*, 1995) and CATH (Orengo *et al.*, 1997) were constructed, in which protein

structures were divided into domains and organized hierarchically. The domains were grouped into families based on simple sequence relationships, into superfamilies based on structural and functional relationships and less obvious sequence relationships, and into folds based entirely on structure.

However, protein classification can be difficult especially at the fold level. There is a great deal of ambiguity in the definition of a fold, and some argue that fold space should be viewed as continuous, whereby available structures can be divided into substructures that may fall under a number of different known folds (Berman *et al.*, 2000). Therefore, a main challenge in structure prediction is to recognize sequence and structure relationships between proteins that might not be expected to be related, at least based on existing classification schemes. A significant improvement to homology recognition is expected to come from the ongoing structural genomics initiatives. These aim at solving 3D structures for the representatives of as many protein families as possible so that homology models can be built for, or at least overall topology can be assigned to, other family members (Brenner and Levitt, 2000).

B. Process of Homology Modeling

As illustrated in Fig. 1, a typical homology modeling exercise consists of six steps repeated iteratively until a satisfactory model is obtained: (1) finding one or more suitable template proteins related to the target (homology recognition), (2) aligning the target and template sequences, (3) building a preliminary model for the target based on the 3D structure of the template, (4) *ab initio* modeling of sidechains and loops in the target that are different from the template, (5) refining the model, which often involves changing its conformation slightly, and finally (6) evaluating the model. These steps are explained in details in the next subsections.

1. Template Identification

A sequence alignment method is used to identify a statistically significant relationship between the target and one or more possible templates. Methods of increasing sophistication have been developed for this task, in which the target and template sequences are represented in various ways. The current state-of-the-art alignment methods represent templates and/or targets as position-specific substitution matrices (also known as profiles), such as PSI-BLAST (Altschul *et al.*, 1997) or as hidden Markov models (HMMs) (Eddy, 1998). In a profile or HMM, each position represents not a single amino acid as in standard sequence alignments, but a group of features which are obtained form a multiple sequence alignment involving homologous proteins. In this way, profiles and HMMs take into account the variability at individual position in a protein sequence, leading to more sensitive homology detection (Marti-Renom *et al.*, 2004). Recently, better profiles and HMMs methods were built by accounting for common features in protein structures, leading to the identification of more remote homologues compared to

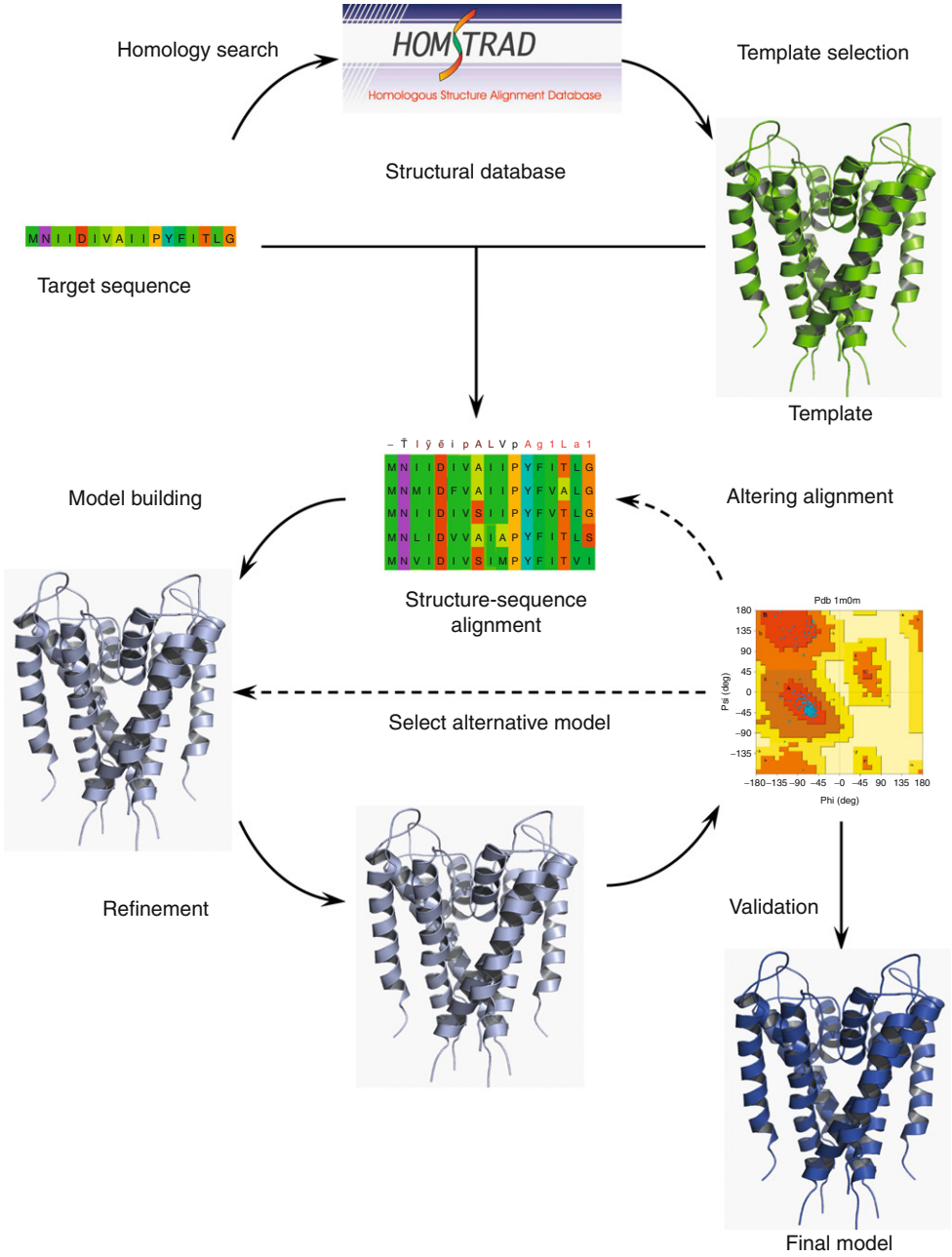

Fig. 1 The various steps in homology modeling. First, starting from a target sequence, suitable template(s) are obtained through a homology search. An alignment is then generated between the target and template, identifying regions that are structurally conserved and those which are variable such as insertions and missing N and C termini. A model is then built for the target Cα backbone and sidechains are modeled. The resulting model is refined and evaluated iteratively by altering the alignment and selecting alternative models (discontinuous lines).

conventional methods. For example, environment-specific substitution tables (ESSTs) are used in the construction of template profiles in FUGUE (Allen *et al.*, 2001). Other methods have been developed notably by Honig (Tang *et al.*, 2003), Russell (Shah *et al.*, 2005), and Orengo and their co-workers (Sillitoe *et al.*, 2005).

2. Sequence–Structure Alignment

Often, alignment methods are successful in identifying distant homologues but lead to "suboptimal" target-template alignments which are not completely correct. The correct alignment is considered to be the one that leads to the best model, that is, most accurately identifies residues in the target sequence that are equivalent to residues in the template sequence. Potential alignment errors can arise from real differences between the target and the template structures, and regions in the alignment where sequence similarity is not high enough to unambiguously identify structurally equivalent residues.

To solve these problems, many methods use different parameters to generate the final target-template alignment, mainly affecting gap penalties and substitution matrices. For example, FUGUE uses different parameters for either homology recognition or target-template alignment. Recently, such parameters have been optimized for TM protein alignments, leading to a significant improvement in performance (Mokrab *et al.*, submitted to J. Mol. Biol.). On a large scale, this approach was adopted by "metaservers," which combine alignment results obtained from different sources, in search for the set of parameters or methods that produce the correct alignment (Chivian *et al.*, 2005; Fischer, 2003). For instance, 3D-Shotgun builds multiple models and creates a final model based on fragments obtained from the initial models using a consensus approach, that is, the fragments which are assembled into the final model are the most often observed in the initial models (Fischer, 2003). Although metaserver strategies greatly improve the probability of generating the correct alignment, the problem of suboptimal alignments in homology recognition remains unsolved. Ideally, parameters should be optimized by building models for each possible alignment and evaluating the set of models using some scoring function that reflects the stability of a given conformation.

3. Model Building and Refinement

Several methods have been developed for producing a 3D model based on a target-template alignment. These methods fall into three categories: rigid-body assembly, segment matching, and modeling by satisfaction of spatial restraints. The first modeling programs were based on rigid-body assembly methods in which the model is assembled from a small number of rigid bodies obtained from the core of the aligned regions. This is implemented in COMPOSER, the earliest of this kind (Sutcliffe *et al.*, 1987), SWISS-MODEL (Schwede *et al.*, 2003)

and 3D-JIGSAW (Bates *et al.*, 2001). The segment-matching approach uses a subset of atomic positions derived from the alignment as a guide to find matching segments in a representative database of known structures. This is implemented in SegMod/ENCAD (Levitt, 1992). Modeling by satisfaction of spatial restraints uses a set of restraints derived from the alignment, and the model is then, obtained by minimizing the violations of these restraints. The popular modeling program MODELLER uses this approach (Sali and Blundell, 1993).

Although all these programs aim to produce models which are as similar as possible to the templates, there are cases where structural features in the model are genuinely distinct from the template. These often involve sidechains and loops connecting secondary structure elements. For the calculation of sidechain conformations, common methods use the relationship between sidechain conformation and backbone conformation as observed from known structures, and knowledge-based rotamer libraries (Dunbrack, 2002). Currently, prediction of the conformations of buried sidechains is close to experimental accuracy (Xiang and Honig, 2001). Prediction is less good for surface sidechains, but this may be due to the constraints imposed by the crystallization media on X-ray structures (Jacobson *et al.*, 2002).

Loop modeling usually involves the building of the loop in ''open'' conformation (where one end of the loop is not connected to the protein) and then closing the loop using various algorithms (Jacobson *et al.*, 2004). This procedure is repeated with different starting conformations, evaluating each resulting conformation using a particular energy function. Currently, reasonably accurate predictions (<1 Å RMSD) can be made for loops with up to nine residues, although achieving such level of accuracy is computationally demanding (Jacobson *et al.*, 2004).

Even in the simplest cases of homology modeling, a fundamental problem is the existence of genuine differences between the target and the template, reducing the accuracy of the model. These differences include different number and orientation of secondary structure elements, insertions, and deletions. The refinement problem of starting from an inaccurate model (2–4 Å RMSD difference between the model and the real target structure) and improving its accuracy is still a big challenge in modeling. The encouraging successes in loop and sidechain modeling—although being much easier problems—indicate that refinement may be feasible for entire proteins, yet likely to come at a high computational cost. Indeed, some of the best results, so far, were obtained with 150 days of computer time for small proteins (Bradley *et al.*, 2005).

4. Model Evaluation

There is no single rule on how to assess the quality of homology models. Existing methods mainly measure whether a model satisfies standard steric and geometric criteria (Morris *et al.*, 1992). Although each step in the construction of the model (template selection, alignment, model building, and refinement) consists of internal measures of quality, the ultimate quality measure of a model is its conformational energy. Therefore, a scoring function which reflects this energy is needed to decide between various models.

Simplified functions have been used to classify all models generated in a prediction, allowing a subset to be selected for a more detailed and often computationally demanding evaluation. A common scoring function is that of Verify 3D, which evaluates parts of a model based on the consistency of residue environments with observed propensities (Chen *et al.*, 1997). Other methods, such as ProSA use a statistics-based scoring function, measuring the stability of a polypeptide based on the frequency of appearance of the model's atom–atom and residue–residue interactions in databases of known structures (Sippl, 1993).

Other measures of conformational stability use MD force fields (Lazaridis and Karplus, 2000), which proved to be successful in applications to the "decoy" problem: the ability to identify the X-ray structure from amongst a set of models of the same protein (Bigelow *et al.*, 2004). Therefore, these all-atom measures are likely to identify the most native-like model, if it is present in a set of models. However, the major challenge for this is sampling and evaluating enough conformations (Bigelow *et al.*, 2004). One might expect that MD methods that can fold protein fragments from unfolded states could be applied to an incorrect model that is relatively close to the native structure and refine it to a conformation that is close to the native state. However, this has not been achieved yet. Meanwhile, the ultimate way for improving model quality is likely to require a combination of better scoring functions and sampling procedures and improved alignment and homology recognition methods.

C. Accuracy of Homology Models

Once a satisfactory homology model is produced, it can be used to identify residues involved in catalysis, examine protein–protein interactions, correlate genotypic and phenotypic data, and guide experiments. However, the soundness of a homology model for a particular application depends on its quality, which decreases as the target and templates become more divergent (Ginalski, 2006). According to statistics from the CASP blind assessment exercises of structure prediction (Kryshtafovych *et al.*, 2005), models based on templates more than 50% sequence identity (PID) are generally highly accurate ($\sim$1 Å Cα RMSD from the experimental structure). Proteins with 30–50% PID share at least 80% of their structures; CASP models within this range of PID are typically 2–3 Å RMSD from the experimental structure, errors being mainly in loop regions. Structural conservation can be as low as 55% for proteins showing 20–30% PID or even lower, when PID drops below 20%. In addition to the extent of structural conservation between the target and the template, the accuracy of homology models also depends on the accuracy of the alignments. While alignments are often near optimal for targets with more than 30% PID to the template structures (easy targets), alignment quality sharply decreases when sequence identity is less than 20%. However, with the increased availability of sequences and structures for the homologues of the protein of interest, alignments can be improved, as discussed earlier.

D. Case Study of the Application of Homology Modeling

Homology models may be used to inform our understanding of the mechanisms of ion channels, for which a rich amount of physiological and pharmacological data is available. For example, $GABA_A$ receptor, a member of the cys-loop ligand-gated ion channel receptors is the target of many clinically important drugs, yet its structure has not yet been determined.

To explore its structure and interactions with agonists, homology models were built (Mokrab *et al.*, 2007) for the human $GABA_A$ receptor $(\alpha1)_2(\beta2)_2\delta2$, (Fig. 2) using the homologous structures of the nicotinic acetylcholine receptor (nAChR) (Miyazawa *et al.*, 2003; Unwin, 2005) and a number of acetylcholine binding proteins (AChBP) in either ligand-bound or ligand-unbound states (e.g., Brejc *et al.*, 2001). One model was generated based entirely on the nAChR structure, while a second model was produced based on the nAChR for the TM region and the AChBP structures for the extracellular domain. The first model was used for the docking of GABA and the widely prescribed anaesthetics muscimol, flunitrazipam, and halothane (Fig. 2B and C). Ligand positions and orientations were found to be largely consistent with experimental mutagenesis data. A comparison between the two models suggests that the first model may represent the *apo* form of the receptor, while model 2 may be an agonist-bound receptor complex that favors channel opening. Despite the relatively low resolution (4 Å) of the nAChR template structure used to model the TM region, the models have shown strong correlation with mutagenesis data, therefore, allowing the design of new experiments and the refinement of the existing models. In particular, such models may be used to explore the energetics of ion permeation, as described in the following sections.

III. PB Profiles for the Energetics of an Ion in a Channel

The renaissance of classical eletrostatics in biology and chemistry was heralded more than a decade ago (Honig and Nicholls, 1995), with the PB equation being the comprehensive and readily applicable theory (Fogolari *et al.*, 2002). Soon after, attempts were made to apply this to simple models of ion channels (Moy *et al.*, 2000; Weetman *et al.*, 1997). Critical appraisals and skepticism followed (Allen *et al.*, 2004b; Kuyucak and Bastug, 2004).

A better understanding of the usefulness of PB theory, in the context of ion channels, was provided by Beckstein *et al.* (2004). They compared PB methods with molecular-mechanics sampling methods, which is more accurate. These comparisons were done on a variety of systems from model nanopores to channel structures. They showed that knowing the electrostatic energy profile along an ion channel pore gives a first indication, at a relatively low computational cost, of the level of ion permeation. The relationship between the pore radius and the barrier height in this profile has also been explored (Tai *et al.*, 2008).

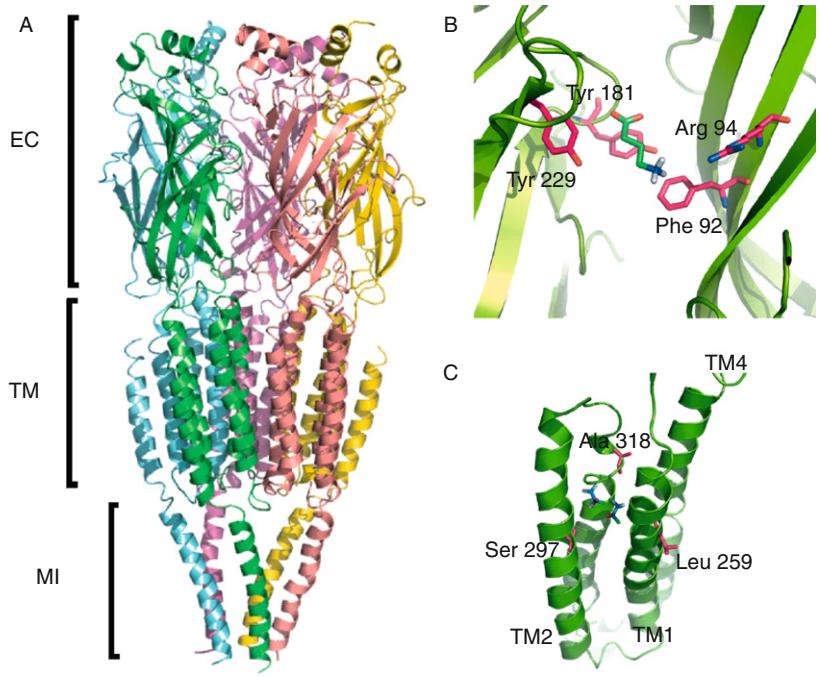

Fig. 2 A homology model for the structure and ligand-binding for the human $GABA_A$ receptor. (A) Side view (perpendicular to the pore axis) of the model. The five subunits are shown in different colors. EC, extracellular; TM, transmembrane; MI, intracellular. (B) View of the GABA docked into the binding site of the model. Six configurations were found to be docked in this position, with the GABA COOH group facing Tyr 181 and Tyr 229. Implicated residues are labeled and highlighted in magenta. (C) Halothane (blue) docked into its putative binding site of model 1, in the $\alpha 1$ subunit. Figures adopted from (Mokrab *et al.*, 2007).

Here, we describe the protocol to apply the PB method to an ion channel pore. The example system is the TM domain of the nAChR. We use the PB equation to calculate the electrostatic energy profile along the nAChR pore, to see what electrostatic environment a cation encounters when it passes through the pore (Amiri *et al.*, 2005).

A. Theory

The PB equation deals with electrostatic forces. These are long-range forces, as described by Coulomb's law, but can be screened by solvent (or other polarizable medium). The extent of such screening is accounted for by the inclusion of the dielectric coefficient of the polarizable medium in a revised form of Coulomb's law. The larger the value of this coefficient, the more effective the screening. In vacuum, the dielectric coefficient $\varepsilon = 1$; water has $\varepsilon = 78.5$ at 300 K; ε for proteins is usually considered to be about 2–4.

From this revised Coulomb's law, one can derive the work (energy) to move an ion of a certain radius from vacuum to water; that is, the solvation energy. This simple generalization is called the Born equation. The "Born energy" can be calculated analytically. The Poisson equation further generalizes the Born equation to describe heterogeneous systems, such as the solvation of a protein. Solving the Poisson equation gives the electrostatic potential for a set of fixed charges (e.g., those in a protein) as a function of space. This potential integrated in space gives the solvation energy.

Electrostatics can be further screened by mobile ions due to the ambient salt in the solution. Mobile counterions (whose concentration is described by the ionic strength of the solution) congregate around fixed charges. This, we describe using a Boltzmann distribution under the influence of the potential obtained above. This is solved until convergence (self-consistent). This, finally, is called solving the PB equation.

To calculate the PB profile of an ion upon encountering the protein channel pore, we select a series of sample points along the pore. For each of these points, we calculate the electrostatic energies for the three systems: $E_{\text{ion}}(z)$, that for the ion by itself (at the sample point along the pore axis z); E_{protein}, that for the protein channel alone; and $E_{\text{complex}}(z)$, that for the protein–ion complex (with the ion at z). The PB energy at this point z is then $\Delta E_{\text{PB}}(z) = E_{\text{complex}}(z) - E_{\text{ion}}(z) - E_{\text{protein}}$. Moving to the next sample point, we calculate $\Delta E_{\text{PB}}(z)$ for a different z values along the pore axis. By sampling enough points, we construct the PB energy profile (Fig. 3).

Note that this method has its limitations. In particular, only the long-range electrostatic forces are considered here, on a static protein structure. Therefore, the nonelectrostatic (steric van der Waals) effects (Beckstein and Sansom, 2006) and those due to movements of the pore-lining residues (Mamonov *et al.*, 2003) are not considered in a PB energy profile. Full energy profiles including these effects can be obtained by potential of mean force (PMF) calculations (see below) based on molecular mechanics, which are at the same time more expensive.

B. Calculations

For the PB calculations, the easy-to-use Adaptive PB Solver (APBS) (Baker *et al.*, 2001) can be obtained from http://apbs.sourceforge.net/. For molecular visualization, VMD (Humphrey *et al.*, 1996) is often used, but several good alternatives exist. To annotate the PDB format structure files (Berman *et al.*, 2003) with charge and radius information, one may use one of the PDB2PQR web servers (Dolinsky *et al.*, 2004) linked from http://pdb2pqr.sourceforge.net/ or install the stand-alone PDB2PQR program locally. A program, such as HOLE (Smart *et al.*, 1997), can be used to identify the pore axis (and radius profile) and to define the sample points along the pore (z) axis along which the PB electrostatic energy profile is evaluated.

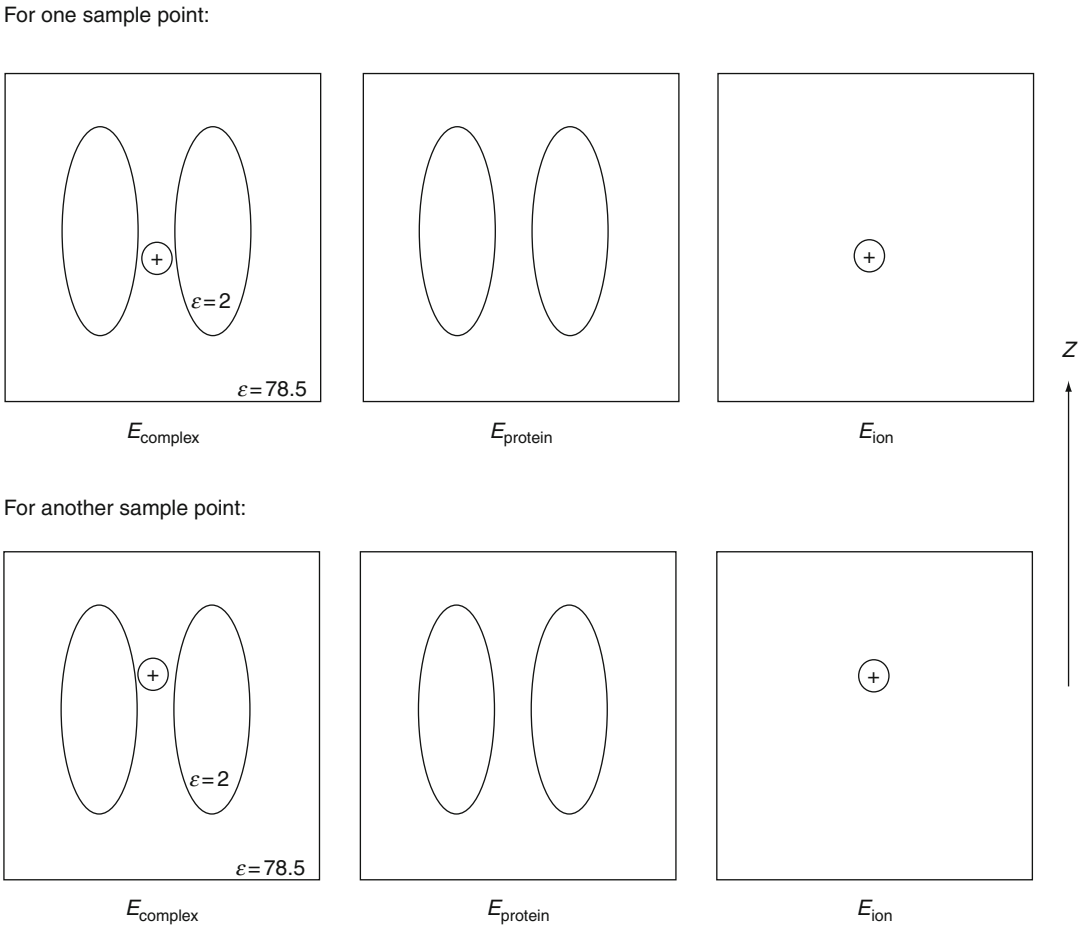

Fig. 3 A précis of the theory behind calculating the PB profile for an ion channel. The dielectric coefficients for protein and water (ε) are indicated. The PB energy at this point z is $\Delta E_{\mathrm{PB}}(z) = E_{\mathrm{complex}}(z) - E_{\mathrm{ion}}(z) - E_{\mathrm{protein}}$.

A plot of PB profiles is shown in Fig. 4 for a cation (sodium) encountering the nAChR pore in the TM domain under different ionic strengths (that is, various ambient salt concentrations); and for comparison, a profile for an anion (chloride) through the same pore. Focusing on the cation traces, one can imagine a sodium ion approaching the channel from the extracellular domain (right). This ion first encounters the favorable attraction which is a continuation of the extracellular vestibule. Then it encounters an energy barrier at the channel gate at $z \sim 70$ Å; this barrier is more moderate as more screening is provided by higher ambient ion concentrations. The anion does not have a favorable vestibule attraction, and encounters a lower, but still significant, barrier at the gate region.

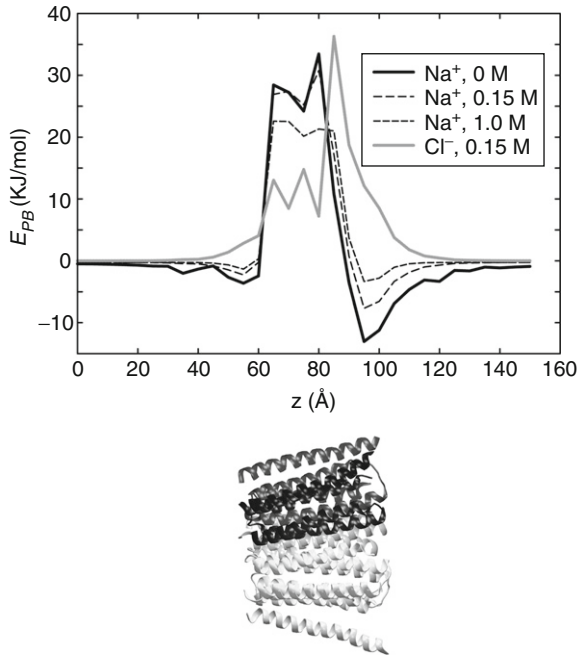

Fig. 4 The resulting PB energy profiles for a sodium ion (black lines, under various ionic strengths) and a chloride ion (grey line) upon encountering the nAChR pore, sampling every 5 Å. The structure of the TM domain of nAChR, rendered by Raster3D (Merritt and Bacon, 1997), is aligned to show the region of calculation. To the left is the cytoplasmic domain; right, extracellular (neither shown).

IV. MD Simulations

Although there are currently ~20 unique ion channel TM domain structures in the PDB (for an updated list, see http://blanco.biomol.uci.edu/Membrane_Proteins_xtal.html), these structures have been captured by X-ray crystallography as a time- and space- averaged snapshot, in frozen crystals far removed from their native environment. MD simulations provide a means for animating these static structures by replicating the normal motions of the protein of interest. The information afforded by MD is such that the motions of individual atoms can be tracked, enabling the understanding of structure and dynamics in precise detail. In the context of this chapter, simulation studies can be used to investigate the structural stability of an ion channel within a lipid membrane, indicate mechanisms for channel gating and propose pathways for the conduction of ions. These examples are by no means the limit of MD, but serve to illustrate the potential of this method. In this section, we will introduce the underlying theory to MD

simulation before describing the typical protocol for preparing and running an ion channel simulation.

A. Theory

For less complex systems, computational chemistry methods, such as quantum mechanics, are able to provide accurate insights into the physics of the system involved. However, to model larger or more complex systems, a compromise needs to be made and empirically based approaches, such as MD, are generally used. MD simulations provide a means to observe local conformational dynamics and transitions in proteins, for timescales in the nanosecond range. Empirical approximations, known as force fields, allow the interactions and potential energy of the system to be calculated from the coordinates of atoms described as point particles.

A force field, classically, consists of a potential function and a set of parameters for different atom types. The potential function can be further broken down into bonded and nonbonded interactions within the system. In this instance, each particle (typically an atom) is treated as a point mass, with a partial point charge, which is bonded to other atoms by harmonic forces; classified as the "balls and springs" model. Bonded interactions are calculated through the summation of bond, angle, and dihedral energies, which include bond stretching, angle bending, and torsion rotations. The vibrations of bonds are constrained in most simulations by using algorithms such as SHAKE (Ryckaert *et al.*, 1977) or LINCS (Hess *et al.*, 1997), permitting extended timesteps. Nonbonded interactions may be broken down into a summation of Coulomb electrostatics, optimally through particle mesh Ewald (PME) (Darden *et al.*, 1993) and van der Waals interactions, determined by the Lennard-Jones repulsion and dispersion of particles, governed by cutoffs. These parameters are typically computed every 5–10 steps within the simulation.

MD simulations are set in a mathematical framework governed by Newton's laws of motion; with Newton's second law relating to the force F_i exerted on a particle i to its mass m_i, and acceleration a_i:

$$F_i = ma_i \tag{1}$$

This equation describes the exertion of forces between all atoms and results in the rate and direction of motion of the system; as a result all atoms are assigned initial velocities prior to commencing the MD simulations. These velocities are also governed by the constant temperature of the system, with the system warmed until the desired temperature is reached and the energy has equilibrated over all the atoms. Simplistically, MD simulations calculate the force on each atom, and from that information, the position of each atom throughout a specified period of time.

Periodic boundary conditions (PBC) are usually imposed to prevent surface artifacts; as a result, if a molecule exits the left-hand side of the box, it will automatically reenter the box on the right-hand side. Ideally the box should be

suitably large so that a molecule will not impact on its periodic copy. Each system is generally coupled to a thermostat (e.g., Berendsen *et al.*, 1984) and barostat (e.g., Paranello and Rahman, 1981) to maintain constant temperature and pressure—the latter of which results in the scaling of the box surrounding the system.

B. MD Software

There are currently a number of packages to choose from when performing MD simulations. Packages currently at the forefront of MD simulations include NAMD (Phillips *et al.*, 2005), GROMACS (van der Spoel *et al.*, 2005), and the recently developed Desmond. These packages are able to run a number of different force fields, including CHARMM (Brooks *et al.*, 1983), GROMOS96 (Scott *et al.*, 1999), AMBER (Pearlman *et al.*, 1995; Weiner and Kollman, 1981), and OPLS-AA (Kaminski *et al.*, 2001).

The major deficiency of most of the existing force fields is that they do not account for electronic polarization of the environment, an effect that can significantly reduce electrostatic interactions of partial atomic charges. This problem has been addressed by the development of polarizable force fields (e.g., AMOEBA (Piquemal *et al.*, 2006)) or using a macroscopic dielectric constant; however, the application of a single value of dielectric constant is problematic in the highly diverse environments of proteins or biological membranes. In addition, van der Waals forces are also strongly driven by their environment as these forces originate from interactions of induced and instantaneous dipoles. The deficiencies of the force fields remain a major problem in modeling protein dynamics and this has only been highlighted further by improvements to the MD software and parallel computing that facilitate simulations approaching the millisecond timescale. For this reason, alternative empirical scoring functions have been developed specifically for ligand docking, protein folding, computational protein design, and modeling of proteins in membranes, and are continuously being improved to enhance the accuracy of MD (Moult, 2005).

C. Setting up the System

1. Preparing the Initial Protein Structure

Having retrieved an ion channel structure of interest from the PDB or created a homology model, it is important to verify that the structure is appropriate for simulations. Most importantly, any atoms that are missing from the structure may need to be added prior to starting the simulations. Missing amino acids sidechains can be added, either manually using PyMOL (DeLano, 2002), or automatically using Swiss-PDBviewer (Guex and Peitsch, 1997).

Next, it is essential to consider whether an all- or united-atom force field will be used. In the latter, only polar hydrogens are explicitly included. The protonation

states of residues should also be considered and as a result, it is worth using a pK_a prediction program (such as PROPKA (Bas *et al.*, 2008)) to indicate whether a residue is likely to be protonated in an atypical manner. The five residues that are usually considered are Histidine (neutral or positive), Aspartate (negative or neutral), Glutamate (negative or neutral), Lysine (positive or neutral), and Arginine (positive or neutral). (The default state at pH = 7 is underlined). Furthermore, the polar proton on a neutral histidine sidechain may be found on either nitrogen atom and thus, it is worth considering the network of hydrogen bond surrounding the sidechain. Ideally, all hydrogen atoms should be removed from the protein with the hydrogen atoms added by the simulation package. An example of the importance of the protonation state in ion channels is found behind the selectivity filter of the KcsA channel, where Asp80 forms a hydrogen bond with a protonated (neutral) Glu71 (Ranatunga *et al.*, 2001). The strength of this interaction is believed to alter the structure of the selectivity filter of the channel and as a result alter ionic conduction (Cordero-Morales *et al.*, 2006, 2007).

2. Protein Insertion into the Lipid Membrane

Ion channels are integral membrane proteins and therefore, simulations should be performed in a lipid bilayer. It is possible to perform simulations of membrane proteins using an implicit membrane, but in this section, the focus will be on explicit membrane models. The currently preferred method is to insert the protein structure into a preformed bilayer. This is done by aligning the protein structure and bilayer so that the protein is central to the bilayer plane. The position of the protein perpendicular to the membrane can be implied by the locations of the Tyrosine and Tryptophan residues, which act as anchors at the membrane–solvent interface (Amiri *et al.*, 2005). Further guidance can provided by TM helix predictions and the positions of the more polar and charged residues (Jones *et al.*, 1994). A more comprehensive method is to use coarse-grained (CG) MD methods to insert a protein into its bilayer environment by allowing more coarsely defined lipid molecules to assemble around a CG-representation of a protein (this method is discussed in more detail in (Scott *et al.*, 2008)). This can then be converted back to atomistic by aligning a preformed atomistic bilayer over the self-assembled CG membrane and the atomistic protein structure over the CG model of the protein. Once overlaid, the overlapping lipid molecules are removed, leaving a hole in the bilayer, into which the protein can be placed, without lipid–peptide clashes. The remainder of the periodic box either side of the lipid should then be solvated, along with any cavities within the channel pore. Counterions should also be added to neutralize the system. Prior to commencing any MD simulation, the system should be energy minimized to remove or reduce any strains on the system and improve the accuracy of the model.

3. Equilibrating the Lipid Around the Protein

Once the system has been energy minimized, the next step is to equilibrate both the solvent and more importantly, the lipid around the membrane protein. This is generally performed by restraining the motions of all heavy atoms in the protein, to keep it static whilst the lipid settles around. This removes the vacuum between protein and lipids that was formed when the overlapping lipid molecules were removed. The protein restraints can then be lifted in one step or in concurrent steps with the force constant for the restraints gradually reduced. It is also possible to release the sidechain restraints in isolation from those of the backbone. The relaxation of restraints can also be done in association with warming steps with the temperature of the system steadily increased to prevent abnormal velocities and energies. The standard timescale for the equilibration step can be anything between 500 ps and 3 ns. This step is usually performed as an NPT ensemble, with the number of atoms, pressure, and temperature all kept constant.

4. Production Run

Once all restraints are removed and the required temperature is reached, the simulation enters the production stage. If a simulation of a soluble protein was being performed, the pressure of the system may also be turned off at this point, with the volume of the system kept constant rather than the pressure (*NVT* ensemble). However, the presence of the lipid bilayer means that the pressure will be slightly different along the plane of the membrane than perpendicular to it. As a result, it is best to maintain the pressure coupling, with either semiisotropic or anisotropic conditions used rather than isotropic. Simulations currently range from 10 to 50 ns, depending on the size of the system and resources available, with output written roughly every 1000 steps, and between 1 and 10 ps. Depending on the size of your system and length of your simulation, the output frequency may be decreased, to reduce the amount of disk space used.

A number of studies have also attempted to replicate the electrochemical gradient across the membrane. The TM potential can be reproduced by applying an artificial voltage across the bilayer, while a chemical gradient can be applied by adding differing concentrations of ions to either side of the protein containing membrane. To do this, a second bilayer (Sachs *et al.*, 2004), or an artificial "air" boundary (Delemotte *et al.*, 2008) is required to keep the two salt baths separate, due to the nature of the PBC perpendicular to the bilayer.

D. Analysis of the Simulations

1. Assessing the Stability

Once the simulation has completed, it is sensible to check that the structure of the ion channel is not significantly different from the starting structure. Although this can be done by eye, the principal two routines for confirming structural

stability are the root mean standard deviation (RMSD) and root mean standard fluctuation (RMSF). The former calculates the structural drift of the selected atoms (usually Cα) over the course of the simulation. This is usually observed as a sharp rise in drift followed by a plateau that should level out at ~3 Å. RMSF, on the other hand, assesses at the stability of specific residues, with looped regions usually showing the largest changes in structure. These values generally show good agreement with the B-factor values recorded in the associated X-ray crystal structures. A third method for checking structural stability is to monitor the secondary structure of the protein throughout the simulation duration. In this instance, the secondary structure is defined by the DSSP classification (Kabsch and Sander, 1983). If this deviates drastically from the starting structure, it is likely that the stimulation is not overly stable. Nonetheless, structural changes during the simulation are to be expected and some of the instabilities may be related to physiologically relevant conformational changes of the protein. Indeed, changes in backbone conformation within the selectivity filter can be detected by DSSP and may be involved in gating of this region of the potassium channel (Bernèche and Roux, 2005; Domene *et al.*, 2004).

2. More Specific Analysis

Further analysis depends on the original aims of the MD simulations. Analyses specific to membrane proteins often involve quantifying the interactions between the protein and the bilayer over the course of the simulation. This allows protein-induced deformations of the bilayer to be identified along with revealing the lipid-exposed residues. More precisely H-bonding interactions between the lipid headgroups and residues at the bilayer–solvent interface can be detected. All interactions can be colored onto the protein to highlight the residues involved.

Similar methods can be extended to the protein itself, where H-bonding interactions and other distances can be measured between residues and therefore it is possible to assess whether certain interactions are maintained over the course of the simulation or indeed if the simulations drive formation of new contacts. If other cofactors, such as ions and ligands, are also present, it may also be of interest to calculate their interactions; especially, if it is possible to relate their binding to conformational changes that occur in the protein—either by induced fit of the ligand within the binding site or more speculatively through gating of the protein.

Unfortunately, the timescales usually required for gating of ion channels are several orders of magnitude larger than those accessible to MD simulations. Therefore, it is only really possible to glimpse at the early stages and primary motions of the structural changes involved. These dynamics may often be lost in the "noise" of the simulation and therefore, a number of past studies have used Principal Component (PCA) or Normal Modes (NMA) Analyses to filter out the chief movements that are relevant to the gating processes (Grottesi *et al.*, 2005).

These methods have been used to disclose the gating of inner helices of potassium channels over the course of a MD simulation (Grottesi *et al.*, 2005). The

simulations show a kink and swivel about the conserved glycine-hinge that is comparable to the gating proposed by the open state crystal structures, MthK and KvAP (Jiang *et al.*, 2002a, 2003).

Probably, the most fundamental property of an ion channel is its ability to permit passage of ions across the lipid membrane. Even the short timescales afforded by MD simulations permit the flow of ions. In K^+ channels, the ions pass through the channel in single file, driven through the tight canal formed by the selectivity filter (Doyle *et al.*, 1998). This feature contains four ion binding sites, termed S1–S4, with ions shown to occupy either S1:S3 or S2:S4 conformations. Simulations show good agreement with both structural data and free energy (see below) calculations for the binding of ions at these sites (Åqvist and Luzhkov, 2000; Bernèche and Roux, 2001; Zhou *et al.*, 2001).

In summary, MD simulations provide a powerful tool for investigating motions of membrane bound ion channels. The simulations enable evaluation of structural stability in a dynamic and physiologically realistic setting, freed from the constraints imposed by the lattice of a crystal. In addition to assessing the protein in isolation, it is possible to consider dynamic interactions with the surrounding membrane, solvent, ligands, and conducting ions.

V. Free Energy Methods

A primary aim of the computer modeling of ion channels is to link the electrophysiological behavior of an individual ion channel to its structure. Specifically how does current vary with time through a single channel (Fig. 5) as measured by a patch-clamp experiment? An ion channel can be characterized by the following properties: selectivity (which ions are permitted to pass), conductance (how easy it is for a single ion to pass), and gating (the likelihood of the channel being open or closed). A single ion may take tens to hundreds of nanoseconds to pass through an ion channel, yet the different gating states may persist for milliseconds or seconds and therefore these properties span a wide range of timescales. In this section we shall describe how free energy methods can and have been used to investigate the selectivity and conductivity of ion channels. We shall also make some comments about gating, but it has proved far more difficult to study this phenomenon using computer modeling due to the longer timescales involved.

In this section, we shall mainly discuss potassium ion channels since these have been the most widely studied and the first structure of an ion channel was of KcsA, a potassium ion channel, in 1998 (Doyle *et al.*, 1998). All potassium ion channels share the same topology; each is a homotetramer with each monomer comprising of two TM α-helices, called M1 and M2, a pore helix, and the selectivity filter (Clayton *et al.*, 2008; Jiang *et al.*, 2002a, 2003; Kuo *et al.*, 2003; Long *et al.*, 2005, 2007; Nishida *et al.*, 2007; Shi *et al.*, 2006; Zhou *et al.*, 2001). Unfortunately, although several of the structures are more open than others, no single ion channel has been captured in both open and closed states. The selectivity filter contains the

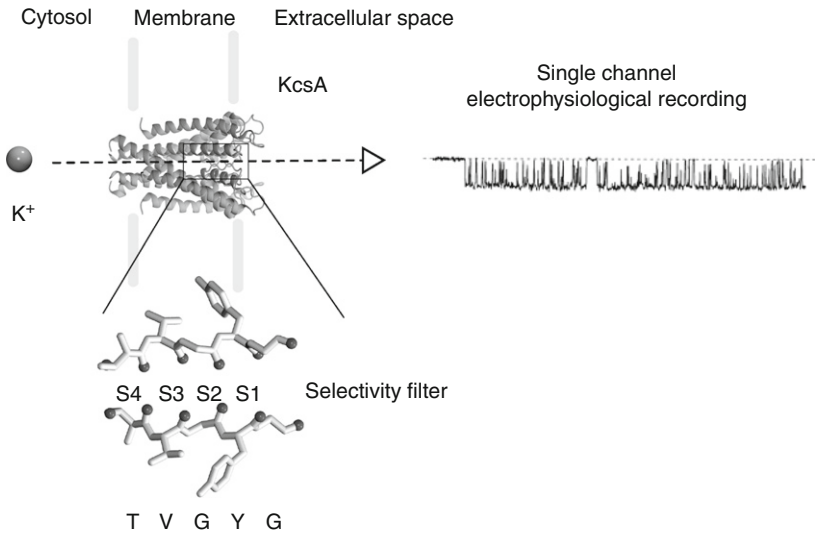

Fig. 5 Ion channels, such as KcsA, permit the passive diffusion of some species of ions across membranes. Single channel recordings (as shown on the right, courtesy of Frances Ashcroft) show how, even under stable conditions, the channel is fluctuating between an open and one or more closed (inactivated) states. Note that the width of a lipid bilayer is ~3–4 nm.

consensus sequence TVGYG and is a highly conserved loop that forms a constriction close to the extracellular side of the channel through which ions must pass. As the name suggests, this region of the protein discriminates between potassium and sodium ions. Within the selectivity filter, there are four sites to which ions can bind; these are called S1–S4 and are labeled in Fig. 5. There are many different potassium ion channels and they can be found in bacterial, eukaryotic, and archeal cells. Perhaps most obviously, potassium ion channels are involved in the creation and transmission of electrical impulses between electrically excitable cells.

If we consider conductivity and selectivity from the perspective of the ion, we can reduce the influence of the protein and its environment to how the free energy of that ion varies along the pore axis (assuming that the protein and its environment relax more quickly than the conduction event). This is shown schematically in Fig. 6. The profile encapsulates both the kinetics and thermodynamics of a conduction event and therefore can be used in principle to estimate the conductivity of a particular ion channel to a certain species of ion. If it is possible to calculate free energy profiles for a range of ions, then the selectivity can also be estimated. The electrostatic methods, discussed earlier in this chapter, are an approximation for these free energy profiles, although it should be noted that whilst they are less accurate, they are significantly cheaper and easier to calculate. Gating, that is closure of an ion channel, would lead to changes in this profile which would prohibit the passage of ions. Describing conduction and selectivity in this way,

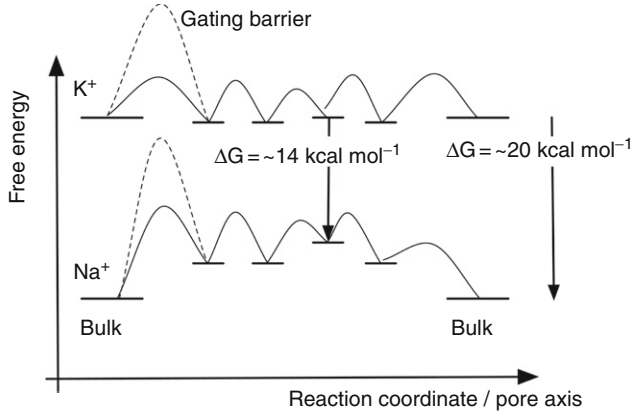

Fig. 6 A schematic illustration of the free energy profile for the conduction of an ion through an ion channel. The profile shows the hypothetical thermodynamics and kinetics of a conduction event. The values for ΔG were estimated by simulation (Noskov and Roux, 2006) and result in a selectivity of 6 kcal/mol for K^+ over Na^+ ions. Note that this is simplistic and, for example, ignores cooperative effects between successive ions, such as the knock-on mechanism. The effect of gating at the helix bundle crossing is illustrated by the dotted line. It has proved difficult to calculate PMFs along the entire pore axis of existing structures of ion channels because many of these are closed, for example KcsA (Zhou *et al.*, 2001) and those that are more open usually have lower resolution, for example MthK (Jiang *et al.*, 2002a,b).

makes it clear that these are nonequilibrium properties and cannot be inferred by solely studying the static structures solved by X-ray crystallography: the dynamics of the protein and the interactions between the ion and the protein must be taken into account.

Computer modeling, specifically classical MD (see above), has proved valuable in furthering our understanding of this important class of proteins. In the remainder of this section, we shall first consider methods that apply biases in chemical space to calculate so-called alchemical free energies before describing methods that apply biases in physical space to calculate potentials of mean force. The former correspond to the differences between the free energy profiles in Fig. 6, whilst the latter are the free energy profiles themselves.

A. Alchemical Methods

These are methods which estimate the change in free energy when one or more atoms are replaced by a set of different atoms. For example, what is the difference in the free energy when two potassium ions at positions S2 and S4 of the selectivity filter of KcsA are replaced by sodium ions? This concept of ''transmuting'' one species into another in order to calculate the free energy has led to these techniques being called alchemical methods. There is a spectrum of methods for estimating alchemical free energies ranging from *ab initio* to empirical methods; however, we

shall limit ourselves here to those that have primarily been applied to ion channels, namely methods derived from classical statistical mechanics.

Åqvist and Luzhkov (2000) first applied these methods to ion channels. They estimated the free energy for all possible combinations of water and potassium ions in the selectivity filter of KcsA and therefore what is the likely sequence of events leading to the conduction of a single ion through the ion channel. The central result is that conduction results from a cycling between two states; one with potassium ions bound at S1 and S3 and another with potassium ions bound at S2 and S4 (with waters bound at the remaining sites).

These free energies were estimated using free energy perturbation (FEP), a well-established technique for calculating alchemical free energies. Such methods enable us to calculate the Gibb's free energy difference (ΔG) between two macrostates X and Y. If, as is usual, the phase spaces of states X and Y do not overlap sufficiently, then an ensemble of structures generated in state X will not accurately sample the phase space of state Y. This problem can be addressed by splitting the transformation into several smaller perturbations, or windows, using a progress parameter, λ. The free energy difference between successive windows is then, summed to give the final free energy difference between X and Y.

To demonstrate the use of this method to estimate the selectivity of an ion channel, let us consider how the free energy changes when a K^+ ion is transmuted into a Na^+ ion at S1 in KcsA. The progress parameter, λ, is defined in Fig. 7. This alchemical ion can be represented using either a single or dual topology (Pearlman and Rao, 1999). We shall only discuss using the single topology approach here. When $\lambda = 0.5$ the nonbonded characteristics of the alchemical ion are intermediate between K^+ and Na^+. In practice, a simulation is started with $\lambda = 0$ and is run until converged. The value of λ is then incremented and the process repeated. In this way, the value of ΔG is calculated as shown in Fig. 7.

There has recently been a flurry of new techniques, along with improvements to existing methods. These are reviewed by Rodinger and Pomès (2005) and we shall not discuss them further. All free energy methods suffer from two main sources of error: (1) incomplete sampling of phase space and (2) an inaccurate description of the atomic interactions. Note that we are implicitly invoking the ergodic hypothesis to allow us to construct a statistical mechanical ensemble from the conformations generated by simulation. Perhaps counter-intuitively, insufficient sampling can lead to an underestimation of the error and so longer simulations often lead to larger (but more accurate) errors (Chipot and Pearlman, 2002). Whichever technique is used, a large number of simulations need to be run making these approaches expensive and slow. This often results in only a few values of ΔG being calculated, although there are technological approaches to improve this (Fowler *et al.*, 2007).

Despite these shortcomings, free energy methods have been used to study the selectivity of potassium ion channels by calculating ΔG when sodium is substituted for potassium at the different ion binding sites within the selectivity filter (Bernèche and Roux, 2001; Luzhkov and Åqvist, 2001; Noskov and Roux, 2006, 2007;

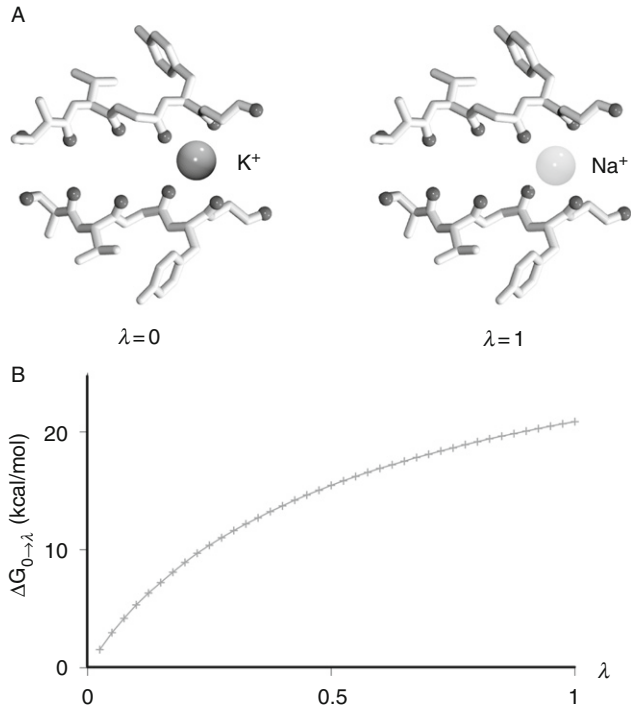

Fig. 7 (A) In this example when $\lambda = 0$ a K^+ ion is bound at S1 and when $\lambda = 1$ a Na^+ ion is bound. Between both these states, the interactions between both K^+ and Na^+ and the remainder of the system are weighted by $1-\lambda$ and λ, respectively. (B) Using FEP, the change in free energy, ΔG, can be calculated as λ is increased in stages during the simulation.

Noskov *et al.*, 2004). Noskov and Roux (2006), for example, show that ΔG ranges between 3.5 and 5.9 kcal/mol for S2 of KcsA, depending on the forcefield used. S2 of KcsA is believed to be responsible for the selectivity of this channel. This degree of selectivity is comparable with estimates derived from electrophysiology experiments (LeMasurier *et al.*, 2001). More recently, theoretical studies of this kind have not only sought to estimate the magnitude of selectivity, but also to explain the molecular basis of selectivity. There are currently several competing theories in the literature: the snug-fit (Doyle *et al.*, 1998), field-strength (Noskov *et al.*, 2004), and the over-coordination hypotheses (Asthagiri *et al.*, 2006; Bostick and Brooks, 2007; Thomas *et al.*, 2007; Varma and Rempe, 2007; Varma *et al.*, 2008). The snug-fit hypothesis originally described the ion channel as providing a rigid scaffold in which cations binds and that this is optimized for potassium, but not sodium, ions. More recently, a weaker version has been described where the protein "conforms more favorably to an ion of a particular size" (Gouaux and MacKinnon, 2005). The field-strength and over-coordination hypotheses are different aspects of the carbonyl-repulsion mechanism, which was first proposed

by Noskov *et al.* (2004). This mechanism states that a sodium ion is relatively less stable within the selectivity filter as the carbonyl oxygens are more tightly packed around the smaller ion, leading to increased repulsion between carbonyl groups. The field strength hypothesis emphasizes the repulsion between the carbonyl ligands, whereas the over-coordination hypothesis states that altering the number of coordinating ligands leads to selectivity.

Many of the recent papers in this field have chosen to use simplified models of the selectivity filter, often only including the carbonyl groups (Bostick and Brooks, 2007; Noskov *et al.*, 2004) or the immediate protein scaffolding (Thomas *et al.*, 2007; Varma and Rempe, 2007; Varma *et al.*, 2008) that binds the potassium ion. These simplified models have allowed more accurate descriptions of the interactions between the protein and the ion, for example, the use of *ab initio* (Varma and Rempe, 2007; Varma *et al.*, 2008) or classical polarizable (Bostick and Brooks, 2007) forcefields. To date, the selectivity filter has been shown to be too flexible for the snug-fit hypothesis to be correct (Fowler *et al.*, 2008; Noskov *et al.*, 2004). Of the remaining two hypotheses, the current view is that the carbonyl repulsion mechanism is correct and fixing the number of ligands (the over-coordination hypothesis) is the dominant factor (Fowler *et al.*, 2008).

B. Potential of Mean Force Methods

As mentioned earlier, if we wish to study the passage of an ion through an ion channel then the free energy profile, or PMF, $\Phi(z)$, is a useful quantity. The PMF is defined along a reaction coordinate, in this case the pore axis, z:

$$\Phi(z) = -kT \ln \langle p(z) \rangle \tag{2}$$

where k is Boltzmann's constant, T is the temperature and $\langle p(z) \rangle$ is the probability of finding the ion at that value of z. We could, of course, run an unbiased classical MD simulation to estimate $\langle p(z) \rangle$; however, in practice this would fail, since the ions would either remain trapped in their initial states or, at best, escape to a neighboring state. The entire reaction coordinate would therefore not be sampled and so our estimate of the PMF would be inaccurate. Instead, it is more efficient to add biasing forces to ensure that the whole reaction coordinate is sampled. We shall discuss three of these methods: umbrella sampling (Roux, 1995; Torrie and Valleau, 1977) (US), Jarzynski's equality (Jarzynski, 1997) (JE), and the adaptive biased forcing method (Davre and Pohorille, 2001; Hénin and Chipot, 2004) (ABF). Of these, the first, US, is the most established and has been applied extensively to ion channels (Allen *et al.*, 2006).

US was first applied by Bernèche and Roux (2001) to KcsA. They were able, by carefully considering the motion of ions and waters in the selectivity filter, to construct 2D PMFs that showed the precise order in which the ions moved in a conduction event. This, along with the earlier work by Åqvist and Luzhkov (2000), proved very insightful and helped mould our current understanding of conduction. US has also been successfully applied to calculate PMFs through gramicidin

A (Allen *et al.*, 2004a, 2006), a canonical ion channel that has been much studied. PMFs obtained in this way have also been used in conjunction with Brownian dynamics simulations to estimate the current–voltage curves for specific ion channels (Berneche and Roux, 2003).

To calculate a 1D PMF using US of, for example, an ion moving through an ion channel, one runs a series of simulations (see Fig. 8). In each, the ion is restrained by a harmonic potential to lie at a certain point along the pore axis. Of course, during the simulation the ion experiences both the restraining potential and potential due to the surrounding protein and therefore the distribution it adopts

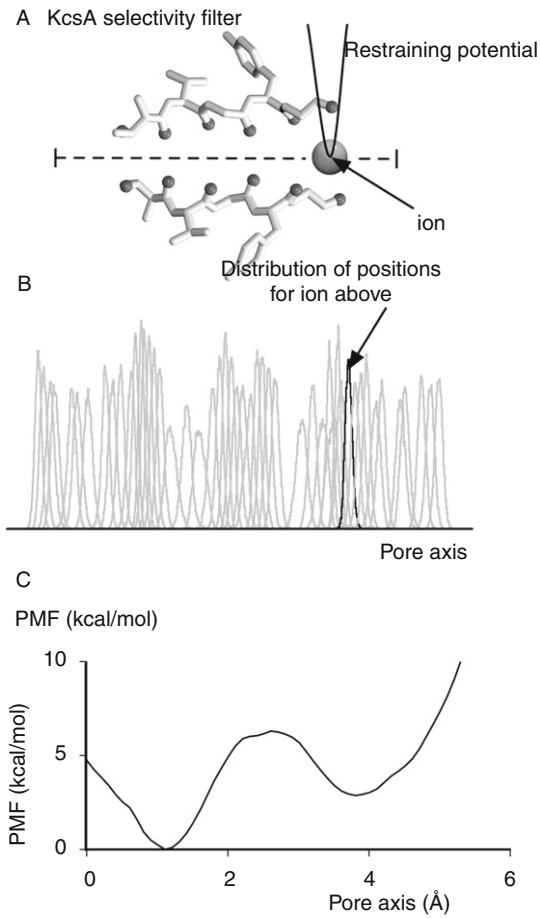

Fig. 8 (A) For an US calculation, the ion is restrained a series of points along the pore axis. (B) The distribution of the ion during each simulation is recorded. It is important to ensure that neighboring distributions overlap with one another. (C) The PMF is then calculated from these distributions using the WHAM method (Kumar *et al.*, 1992).

relative to the position of the restraining potential contains information about the potential due to the protein, that is the PMF. It is necessary to ensure that successive distributions overlap; this is done by careful choice of both the distance between the points and the spring constant of the restraining potential. The PMF can then be recovered from the resulting overlapping distributions using the weighted-histogram analysis method (WHAM) (Kumar *et al.*, 1992).

JE (Jarzynski, 1997) is a nonequilibrium approach and is therefore very different to both US and ABF. The nub of the method is the following equality

$$e^{-\beta\Delta G(z)} = \left\langle e^{-\beta\Delta W(z)} \right\rangle \tag{3}$$

where $\beta = (1/kT)$, $\Delta G(z)$, is the free energy profile or PMF and $\Delta W(z)$ is the work done. In practice, a force is applied to, in our case, an ion to move it through the pore. Each simulation therefore results in a work done profile and the simulations that require a comparatively small of work to move the ion through the channel contribute disproportionately to the result and therefore many simulations have to be performed so that these rare occurrences can be adequately sampled. This approach has been used by Treptow and Tarek (2006a) to calculate the PMF between the up (ions bound at S2 and S4) and down (ions bound at S1 and S3) states of KcsA and Kv1.2 (Long *et al.*, 2005, 2007), a voltage-gated ion channel.

ABF is a comparatively new method (Davre and Pohorille, 2001; Hénin and Chipot, 2004). Like US, it is an equilibrium method but instead of the positions and stiffness of the biasing forces being determined prior to the simulations, the simulation continuously measures the average force along the reaction coordinate and, given sufficient samples have been collected, applies the same force but with the opposite magnitude onto, in our case, the ion or ions that are moving along the reaction coordinate. This procedure gradually flattens the potential that the ion experiences until it undergoes free diffusion through the channel. At this point, the PMF is equated to the applied biasing force. This technique has been applied to both closed and partially open models of the Kv *Shaker* B channel and the open conformation of Kv1.2 to show that Val478 is the constriction point during gating (Treptow and Tarek, 2006b).

Each of the three methods that have been applied to ion channels have advantages and disadvantages: the magnitude of the errors in a PMF calculated using US or JE methods will fluctuate significantly along the reaction coordinate, potentially leading to inefficiency or inaccuracy. The efficiency of the JE method critically depends on how fast the ion is pulled through the channel and the strength of the spring that is attached to the pulling atom. This is less important for ion channels than for many other proteins since ions and water do not have many degrees of freedom and therefore, the time taken for the ion and/or water to relax is faster than the time taken for the surrounding protein to relax. Of course, all three of these methods assume that one can easily define a reaction coordinate: this is usually simple when studying the conduction of potassium ion channels.

We have already briefly mentioned how the ABF method has been used to study the gating of ion channels (Treptow and Tarek, 2006b). As discussed earlier, studying gating is difficult due to the timescales involved and simulations must be carefully designed. PMFs calculated using classical MD, however, are at the forefront of research in this area. The majority of research has been focused on understanding how voltage-gated potassium channels, such as Kv1.2 (Long *et al.*, 2005, 2007), open and close in response to changes in the potential difference across the cell membrane. Unlike simpler channels, such as KcsA, each monomer has an additional domain of four α-helices, called the voltage-sensor, which contains four arginine amino acids and is thought to move up and down in the membrane in response to changes in the applied potential. This motion is then coupled to the gating of the ion channel.

Two types of PMF studies have been used to test and refine this hypothesis. These are computing the PMFs of arginine residues and toxins, respectively, as they move across the hydrophobic environment of a membrane. The goal of the former is to determine if arginine (or a sidechain equivalent) can traverse a bilayer and if so, whether or not it is charged (Li *et al.*, 2008; MacCallum *et al.*, 2008). Although these studies agree that the bilayer deforms, thereby allowing the arginine to interact with water, there remains some disagreement on whether arginine is charged or not and whether the computed PMFs permit a large or require a small movement in the voltage sensor. The second type of PMF study seeks to determine where certain toxins, such as VSTx1, partition in lipid bilayers (Wee *et al.*, 2007, 2008). This is because these toxins interact with the voltage sensor of Kv ion channels and lock the channels open and therefore, finding where the toxin resides places constraints on where the voltage sensor must be located in the lipid bilayer. Finally, the flipping of carbonyl groups in the selectivity filter has been suggested to be the mechanism responsible for C-type (slow) inactivation (Bernèche and Roux, 2005).

VI. Summary

In summary, we have shown how molecular modeling, PB, MD, and free energy methods have proved themselves very useful in furthering our understanding the relationship between structure and function (i.e., selectivity, conduction, and gating) of ion channels. The number of experimentally determined structures of ion channels has increased significantly in the past few years and so there is plenty of opportunity to test if our current understanding of the structural basis for the electrophysiological behavior of ion channels is correct. Historically, for example, free energy calculations (which enable us to relate structure to permeation and selectivity) have been expensive and difficult calculations to perform. However, with the speed of computer processors increasing, existing approaches being improved and new theories being developed, such approaches will become more readily used in both the study of ion channels and related transport proteins.

Acknowledgments

We thank all of our colleagues, and especially, Nathan Baker, Oliver Beckstein, and Philip Biggin for helpful discussions concerning this work. Research in MSPS's group is funded by the BBSRC and the Wellcome Trust.

References

Allen, T. W., Andersen, O. S., and Roux, B. (2004a). Energetics of ion conduction through the gramicidin channel. *Proc. Natl. Acad. Sci. USA* **101,** 117–122.

Allen, T. W., Andersen, O. S., and Roux, B. (2004b). On the importance of atomic fluctuations, protein flexibility, and solvent in ion permeation. *J. Gen. Physiol.* **124,** 679–690.

Allen, T. W., Andersen, O. S., and Roux, B. (2006). Ion permeation through a narrow channel: Using gramicidin to ascertain all-atom molecular dynamics potential of mean force. *Biophys. J.* **90,** 3447–3468.

Allen, S. J., Kim, J. M., Khorana, H. G., Lu, H., and Booth, P. J. (2001). Structure and function in bacteriorhodopsin: The effect of the interhelical loops on the protein folding kinetics. *J. Mol. Biol.* **308,** 423–435.

Altschul, S. F., Madden, T. L., Schaffer, A. A., Zhang, J., Zhang, Z., Miller, W., and Lipman, D. J. (1997). Gapped BLAST and PSI-BLAST: A new generation of protein database search programs. *Nucleic Acids Res.* **25,** 3389–3402.

Amiri, S., Tai, K., Beckstein, O., Biggin, P. C., and Sansom, M. S. P. (2005). The a7 nicotinic acetylcholine receptor: Molecular modelling, electrostatics, and energetics. *Mol. Membr. Biol.* **22,** 151–162.

Åqvist, J., and Luzhkov, V. (2000). Ion permeation mechanism of the potassium channel. *Nature* **404,** 881–884.

Asthagiri, D., Pratt, L. R., and Paulaitis, M. E. (2006). Role of fluctuations in a snug-fit mechanism of KcsA channel selectivity. *J. Chem. Phys.* **125,** 024701.

Baker, N. A., Sept, D., Joseph, S., Holst, M. J., and McCammon, J. A. (2001). Electrostatics of nanosystems: Application to microtubules and the ribosome. *Proc. Natl. Acad. Sci. USA* **98,** 10037–10041.

Bas, D. C., Rogers, D. M., and Jensen, J. H. (2008). Very fast prediction and rationalization of pK_a values for protein–ligand complexes. *Proteins: Struct. Func. Bioinf.* .

Bates, P. A., Kelley, L. A., MacCallum, R. M., and Sternberg, M. J. (2001). Enhancement of protein modeling by human intervention in applying the automatic programs 3D-JIGSAW and 3D-PSSM. *Proteins: Struct. Func. Bioinf.* **45**(Suppl. 5), 39–46.

Beckstein, O., and Sansom, M. S. P. (2006). A hydrophobic gate in an ion channel: The closed state of the nicotinic acetylcholine receptor. *Phys. Biol.* **3,** 147–159.

Beckstein, O., Tai, K., and Sansom, M. S. P. (2004). Not ions alone: Barriers to ion permeation in nanopores and channels. *J. Am. Chem. Soc.* **126,** 14694–14695.

Berendsen, H. J. C., Postma, J. P. M., van Gunsteren, W. F., DiNola, A., and Haak, J. R. (1984). Molecular dynamics with coupling to an external bath. *J. Chem. Phys.* **81,** 3684–3690.

Berman, H., Henrick, K., and Nakamura, H. (2003). Announcing the worldwide protein data bank. *Nat. Struct. Biol.* **10,** 980.

Berman, H. M., Westbrook, J., Feng, Z., Gilliland, G., Bhat, T. N., Weissig, H., Shindyalov, I. N., and Bourne, P. E. (2000). The protein data bank. *Nucleic Acids Res.* **28,** 235–242.

Bernèche, S., and Roux, B. (2001). Energetics of ion conduction through the K^+ channel. *Nature* **414,** 73–77.

Bernèche, S., and Roux, B. (2003). A microscopic view of ion conduction through the K^+ channel. *Proc. Natl. Acad. Sci. USA* **100,** 8644–8648.

Bernèche, S., and Roux, B. (2005). A gate in the selectivity filter of potassium channels. *Structure* **13,** 591–600.

Bigelow, H. R., Petrey, D. S., Liu, J., Przybylski, D., and Rost, B. (2004). Predicting transmembrane beta-barrels in proteomes. *Nucleic Acids Res.* **32,** 2566–2577.

Bostick, D. L., and Brooks, C. L. (2007). Selectivity in K^+ channels is due to topological control of the permanent ion's coordinated state. *Proc. Natl. Acad. Sci. USA* **104,** 9260–9265.

Bradley, P., Misura, K. M., and Baker, D. (2005). Toward high-resolution de novo structure prediction for small proteins. *Science* **309,** 1868–1871.

Brejc, K., van Dijk, W. J., Klaassen, R. V., Schuurmans, M., van der Oost, J., Smit, A. B., and Sixma, T. K. (2001). Crystal structure of an ach-binding protein reveals the ligand-binding domain of nicotinic receptors. *Nature* **411,** 269–276.

Brenner, S. E., and Levitt, M. (2000). Expectations from structural genomics. *Protein Sci.* **9,** 197–200.

Brooks, B. R., Bruccoleri, R. E., Olafson, B. D., States, D. J., Swaminathan, S., and Karplus, M. (1983). CHARMM: A program for macromolecular energy, minimisation, and dynamics calculations. *J. Comp. Chem.* **4,** 187–217.

Chen, D., Lear, J., and Eisenberg, B. (1997). Permeation through an open channel: Poisson-Nernst-Planck theory of a synthetic ionic channel. *Biophys. J.* **72,** 97–116.

Chipot, C., and Pearlman, D. A. (2002). Free energy calculations: The long and winding gilded road. *Mol. Simulat.* **28,** 1–12.

Chivian, D., Kim, D. E., Malmstrom, L., Schonbrun, J., Rohl, C. A., and Baker, D. (2005). Prediction of CASP6 structures using automated Rosetta protocols. *Proteins: Struct. Func. Bioinf.* **61**(Suppl. 7), 157–166.

Chothia, C., and Lesk, A. M. (1986). The relation between the divergence of sequence and structure in proteins. *EMBO J.* **5,** 823–826.

Clayton, G. M., Altieri, S., Heginbotham, L., Unger, V. M., and Morais-Cabral, J. H. (2008). Structure of the transmembrane regions of a bacterial cyclic nucleotide-regulated channel. *Proc. Natl. Acad. Sci. USA* **105,** 1511–1515.

Cordero-Morales, J. F., Cuello, L. G., and Perozo, E. (2006). Voltage-dependent gating at the KcsA selectivity filter. *Nat. Struct. Mol. Biol.* **13,** 319–322.

Cordero-Morales, J. F., Jogini, V., Lewis, A., Vasquez, V., Cortes, D. M., Roux, B., and Perozo, E. (2007). Molecular driving forces determining potassium channel slow inactivation. *Nat. Struct. Mol. Biol.* **14,** 1062–1069.

Darden, T., York, D., and Pedersen, L. (1993). Particle mesh Ewald—An N.log(N) method for Ewald sums in large systems. *J. Chem. Phys.* **98,** 10089–10092.

Davre, E., and Pohorille, A. (2001). Calculating free energies using average force. *J. Chem. Phys.* **115,** 9169–9183.

DeLano, W. L. (2002).The PyMOL Molecular Graphics System. http://www.pymol.org.

Delemotte, L., Dehez, F., Treptow, W., and Tarek, M. (2008). Modeling membranes under a transmembrane potential. *J. Phys. Chem. B* **112,** 5547–5550.

Dolinsky, T. J., Nielsen, J. E., McCammon, J. A., and Baker, N. A. (2004). PDB2PQR: An automated pipeline for the setup, execution, and analysis of Poisson-Boltzmann electrostatics calculations. *Nucleic Acids Res.* **32,** W665–W667.

Domene, C., Grottesi, A., and Sansom, M. S. P. (2004). Filter flexibility and distortion in a bacterial inward rectifier K^+ channel: Simulation studies of KirBac1.1. *Biophys. J.* **87,** 256–267.

Doyle, D. A., Cabral, J. M., Pfuetzner, R. A., Kuo, A., Gulbis, J. M., Cohen, S. L., Cahit, B. T., and MacKinnon, R. (1998). The structure of the potassium channel: Molecular basis of K^+ conduction and selectivity. *Science* **280,** 69–77.

Dunbrack, R. L., Jr. (2002). Rotamer libraries in the 21st century. *Curr. Opin. Struct. Biol.* **12,** 431–440.

Eddy, S. R. (1998). Profile hidden Markov models. *Bioinformatics* **14,** 755–763.

Fischer, D. (2003). 3D-SHOTGUN: A novel, cooperative, fold-recognition meta-predictor. *Proteins: Struct. Func. Bioinf.* **51,** 434–441.

Fogolari, F., Brigo, A., and Molinari, H. (2002). The Poisson-Boltzmann equation for biomolecular electrostatics: A tool for structural biology. *J. Mol. Recogn.* **15,** 377–392.

Fowler, P. W., Geroult, S., Jha, S., Waksman, G., and Coveney, P. V. (2007). Rapid, accurate and precise calculation of relative binding affinities for the SH2 domain using a computational grid. *J. Chem. Theor. Comput.* **3,** 1193–1202.

Fowler, P. W., Tai, K., and Sansom, M. S. P. (2008). The selectivity of K^+ ion channels: Testing the hypotheses. *Biophys. J.* doi:10.1529/biophysj.108.132035.

Ginalski, K. (2006). Comparative modeling for protein structure prediction. *Curr. Opin. Struct. Biol.* **16,** 172–177.

Gouaux, E., and MacKinnon, R. (2005). Principles of selective ion transport in channels and pumps. *Science* **310,** 1461–1465.

Grottesi, A., Domene, C., and Sansom, M. S. P. (2005). Conformational dynamics of M2 helices in kirbac channels: Helix flexibility in relation to gating via molecular dynamics simulations. *Biochemistry* **44,** 14586–14594.

Guex, N., and Peitsch, M. C. (1997). SWISS-MODEL and the Swiss-pdbviewer: An environment for comparative protein modeling. *Electrophoresis* **18,** 2714–2723.

Hénin, J., and Chipot, C. (2004). Overcoming free energy barriers using unconstrained molecular dynamics simulations. *J. Chem. Phys.* **121,** 2904–3004.

Hess, B., Bekker, H., Berendsen, H. J. C., and Fraaije, J. G. E. M. (1997). LINCS: A linear constraint solver for molecular simulations. *J. Comp. Chem.* **18,** 1463–1472.

Hille, B. (2001). "Ionic Channels of Excitable Membranes." 814 p. Sinauer Associates, Sunderland, MA.

Honig, B., and Nicholls, A. (1995). Classical electrostatics in biology and chemistry. *Science* **268,** 1144–1149.

Humphrey, W., Dalke, A., and Schulten, K. (1996). VMD—visual molecular dynamics. *J. Mol. Graph.* **14,** 33–38.

Jacobson, M. P., Friesner, R. A., Xiang, Z., and Honig, B. (2002). On the role of the crystal environment in determining protein side-chain conformations. *J. Mol. Biol.* **320,** 597–608.

Jacobson, M. P., Pincus, D. L., Rapp, C. S., Day, T. J., Honig, B., Shaw, D. E., and Friesner, R. A. (2004). A hierarchical approach to all-atom protein loop prediction. *Proteins: Struct. Func. Bioinf.* **55,** 351–367.

Jarzynski, C. (1997). Equilibrium free-energy differences from nonequilibrium measurements: A master-equation approach. *Phys. Rev. E* **56,** 5018–5035.

Jiang, Y., Lee, A., Chen, J., Cadene, M., Chait, B. T., and MacKinnon, R. (2002a). Crystal structure and mechanism of a calcium-gated potassium channel. *Nature* **417,** 515–522.

Jiang, Y., Lee, A., Chen, J., Cadene, M., Chait, B. T., and MacKinnon, R. (2002b). The open pore conformation of potassium channels. *Nature* **417,** 523–526.

Jiang, Y., Lee, A., Chen, J., Ruta, V., Cadene, M., Chait, B. T., and Mackinnon, R. (2003). X-ray structure of a voltage-dependent K^+ channel. *Nature* **423,** 33–41.

Jones, D. T., Taylor, W. R., and Thornton, J. M. (1994). A model recognition approach to the prediction of all-helical membrane protein structure and topology. *Biochemistry* **33,** 3038–3049.

Kabsch, W., and Sander, C. (1983). Dictionary of protein secondary structure: Pattern-recognition of hydrogen-bonded and geometrical features. *Biopolymers* **22,** 2577–2637.

Kaminski, G. A., Friesner, R. A., Tirado-Rives, J., and Jorgensen, W. L. (2001). Evaluation and reparametrization of the OPLS-AA force field for proteins via comparison with accurate quantum chemical calculations on peptides. *J. Phys. Chem. B* **105,** 6474–6487.

Kolodny, R., Koehl, P., and Levitt, M. (2005). Comprehensive evaluation of protein structure alignment methods: Scoring by geometric measures. *J. Mol. Biol.* **346,** 1173–1188.

Kryshtafovych, A., Venclovas, C., Fidelis, K., and Moult, J. (2005). Progress over the first decade of CASP experiments. *Proteins: Struct. Func. Bioinf.* **61**(Suppl. 7), 225–236.

Kumar, S., Bouzida, D., Swendsen, R. H., Kollman, P. A., and Rosenberg, J. M. (1992). The weighted histogram analysis method for free-energy calculations on biomolecules. I. The method. *J. Comp. Chem.* **13,** 1011–1021.

Kuo, A., Gulbis, J. M., Antcliff, J. F., Rahman, T., Lowe, E. D., Zimmer, J., Cuthbertson, J., Ashcroft, F. M., Ezaki, T., and Doyle, D. A. (2003). Crystal structure of the potassium channel KirBac1.1 in the closed state. *Science* **300,** 1922–1926.

Kuyucak, S., and Bastug, T. (2004). Physics of ion channels. *J. Biol. Phys.* **29,** 429–446.

Lazaridis, T., and Karplus, M. (2000). Effective energy functions for protein structure prediction. *Curr. Opin. Struct. Biol.* **10,** 139–145.

LeMasurier, M., Heginbotham, L., and Miller, C. (2001). KcsA: It's a potassium channel. *J. Gen. Physiol.* **118,** 303–313.

Levitt, M. (1992). Accurate modeling of protein conformation by automatic segment matching. *J. Mol. Biol.* **226,** 507–533.

Li, L., Vorobyov, I., MacKerell, A. D., and Allen, T. W. (2008). Is arginine charged in a membrane? *Biophys. J.* **94,** L11–L13.

Long, S. B., Campbell, E. B., and MacKinnon, R. (2005). Crystal structure of a mammalian voltage-dependent shaker family K^+ channel. *Science* **309,** 897–902.

Long, S. B., Tao, X., Campbell, E. B., and MacKinnon, R. (2007). Atomic structure of a voltage-dependent K^+ channel in a lipid membrane-like environment. *Nature* **450,** 376–382.

Luzhkov, V. B., and Åqvist, J. (2001). Mechanisms of tetraethylammonium ion block in the KcsA potassium channel. *FEBS Lett.* **495,** 191–196.

MacCallum, J. L., Bennett, W. F. D., and Tieleman, D. P. (2008). Distribution of amino acids in a lipid bilayer from computer simulations. *Biophys. J.* **94,** 3393–3404.

Mamonov, A. B., Coalson, R. D., Nitzan, A., and Kurnikova, M. G. (2003). The role of the dielectric barrier in narrow biological channels: A novel composite approach to modeling single-channel currents. *Biophys. J.* **84,** 3646–3661.

Marti-Renom, M. A., Madhusudhan, M. S., and Sali, A. (2004). Alignment of protein sequences by their profiles. *Protein Sci.* **13,** 1071–1087.

Merritt, E. A., and Bacon, D. J. (1997). Raster3D: Photorealistic molecular graphics. *Methods Enzymol.* **277,** 505–524.

Miyazawa, A., Fujiyoshi, Y., and Unwin, N. (2003). Structure and gating mechanism of the acetylcholine receptor pore. *Nature* **423,** 949–955.

Mokrab, Y., Bavro, V. N., Mizuguchi, K., Todorov, N. P., Martin, I. L., Dunn, S. M., Chan, S. L., and Chau, P. L. (2007). Exploring ligand recognition and ion flow in comparative models of the human GABA type A receptor. *J. Mol. Graph. Model.* **26,** 760–774.

Morris, A. L., MacArthur, M. W., Hutchinson, E. G., and Thornton, J. M. (1992). Stereochemical quality of protein structure coordinates. *Proteins: Struct. Func. Genet.* **12,** 345–364.

Moult, J. (2005). A decade of CASP: Progress, bottlenecks and prognosis in protein structure prediction. *Curr. Opin. Struct. Biol.* **15,** 285–289.

Moy, G., Corry, B., Kuyucak, S., and Chung, S. H. (2000). Tests of continuum theories as models of ion channels. I. Poisson-Boltzmann theory versus Brownian dynamics. *Biophys. J.* **78,** 2349–2363.

Murzin, A. G., Brenner, S. E., Hubbard, T., and Chothia, C. (1995). SCOP: A structural classification of proteins database for the investigation of sequences and structures. *J. Mol. Biol.* **247,** 536–540.

Nishida, M., Cadene, M., Chait, B. T., and MacKinnon, R. (2007). Crystal structure of a Kir3.1-prokaryotic Kir channel chimera. *EMBO J.* **26,** 4005–4015.

Noskov, S. Y., Bernèche, S., and Roux, B. (2004). Control of ion selectivity in potassium channels by electrostatic and dynamic properties of carbonyl ligands. *Nature* **431,** 830–834.

Noskov, S. Y., and Roux, B. (2006). Ion selectivity in potassium channels. *Biophys. Chem.* **124,** 279–291.

Noskov, S. Y., and Roux, B. (2007). Importance of hydration and dynamics on the selectivity of the kcsa and nak channels. *J. Gen. Physiol.* **129,** 135–143.

Orengo, C. A., Michie, A. D., Jones, S., Jones, D. T., Swindells, M. B., and Thornton, J. M. (1997). CATH—A hierarchic classification of protein domain structures. *Structure* **5,** 1093–1108.

Parrinello, M., and Rahman, A. (1981). Polymorphic transitions in single-crystals—A new molecular-dynamics method. *J. Appl. Phys.* **52,** 7182–7190.

Pearlman, D. A., Case, D. A., Caldwell, J. W., Ross, W. S., Cheatham, T. E., Debolt, S., Ferguson, D., Seibel, G., and Kollman, P. (1995). Amber, a package of computer-programs for applying molecular mechanics, normal-mode analysis, molecular-dynamics and free-energy calculations to simulate the structural and energetic properties of molecules. *Comp. Phys. Commun.* **91,** 1–41.

Pearlman, D. A., and Rao, B. G. (1999). Free energy calculations: Methods and applications. *In* "Encyclopedia of Computational Chemistry" (P. von Ragué Schleyer, ed.), pp. 1036–1061. Wiley, Chichester.

Petrey, D., and Honig, B. (2005). Protein structure prediction: Inroads to biology. *Mol. Cell* **20,** 811–819.

Phillips, L. R., Milescu, M., Li-Smerin, Y., Midell, J. A., Kim, J. I., and Swartz, K. J. (2005). Voltage-sensor activation with a tarantula-toxin as cargo. *Nature* **436,** 857–860.

Piquemal, J. P., Perera, L., Cisneros, G. A., Ren, P., Pedersen, L. G., and Darden, T. A. (2006). Towards accurate solvation dynamics of divalent cations in water using the polarizable AMOEBA force field: From energetics to structure. *J. Chem. Phys.* **125,** 054511.

Ranatunga, K. M., Shrivastava, I. H., Smith, G. R., and Sansom, M. S. P. (2001). Sidechain ionisation states in a potassium channel. *Biophys. J.* **80,** 1210–1219.

Rodinger, T., and Pomès, R. (2005). Enhancing the accuracy, the efficiency and the scope of free energy simulations. *Curr. Opin. Struct. Biol.* **15,** 164–170.

Roux, B. (1995). The calculation of the potential of mean force using computer simulations. *Comp. Phys. Commun.* **91,** 275–282.

Ryckaert, J. P., Ciccotti, G., and Berendsen, H. J. C. (1977). Numerical integration of the Cartesian equations of motion of a system with constraints: Molecular dynamics of *n*-alkanes. *J. Comput. Phys.* **23,** 327.

Šali, A., and Blundell, T. L. (1993). Comparative protein modeling by satisfaction of spatial restraints. *J. Mol. Biol.* **234,** 779–815.

Sachs, J. N., Crozier, P. S., and Woolf, T. B. (2004). Atomistic simulations of biologically realistic transmembrane potential gradients. *J. Chem. Phys.* **121,** 10847–10851.

Schwede, T., Kopp, J., Guex, N., and Peitsch, M. C. (2003). SWISS-MODEL: An automated protein homology-modeling server. *Nucleic Acids Res.* **31,** 3381–3385.

Scott, K. A., Bond, P. J., Ivetac, A., Chetwynd, A. P., Khalid, S., and Sansom, M. S. P. (2008). Coarse-grained MD simulations of membrane protein-bilayer self-assembly. *Structure* **16,** 621–630.

Scott, W. R. P., Hunenberger, P. H., Tironi, I. G., Mark, A. E., Billeter, S. R., Fennen, J., Torda, A. E., Huber, T., Kruger, P., and van Gunsteren, W. F. (1999). The GROMOS biomolecular simulation program package. *J. Phys. Chem. A* **103,** 3596–3607.

Shah, P. K., Aloy, P., Bork, P., and Russell, R. B. (2005). Structural similarity to bridge sequence space: Finding new families on the bridges. *Protein Sci.* **14,** 1305–1314.

Shi, N., Ye, S., Alam, A., Chen, L., and Jiang, Y. (2006). Atomic structure of a Na^+- and K^+-conducting channel. *Nature* **440,** 570–574.

Sillitoe, I., Dibley, M., Bray, J., Addou, S., and Orengo, C. (2005). Assessing strategies for improved superfamily recognition. *Protein Sci.* **14,** 1800–1810.

Sippl, M. J. (1993). Recognition of errors in three-dimensional structures of proteins. *Proteins: Struct. Func. Genet.* **17,** 355–262.

Smart, O. S., Breed, J., Smith, G. R., and Sansom, M. S. P. (1997). A novel method for structure-based prediction of ion channel conductance properties. *Biophys. J.* **72,** 1109–1126.

Sutcliffe, M. J., Haneef, I., Carney, D., and Blundell, T. L. (1987). Knowledge based modelling of homologous proteins, Part I: Three-dimensional frameworks derived from the simultaneous superposition of multiple structures. *Protein Eng.* **1,** 377–384.

Tai, K., Haider, S., Grottesi, A., and Sansom, M. S. P. (2008). Ion channel gates: Comparative analysis of energy barriers. *Eur. Biophys. J.* doi:10.1007/S00249-008-0377-x.

Tang, C. L., Xie, L., Koh, I. Y., Posy, S., Alexov, E., and Honig, B. (2003). On the role of structural information in remote homology detection and sequence alignment: New methods using hybrid sequence profiles. *J. Mol. Biol.* **334,** 1043–1062.

Terstappen, G. C., and Reggiani, A. (2001). In silico research in drug discovery. *Trends Pharmacol. Sci.* **22,** 23–26.

Thomas, M., Jayatilaka, D., and Corry, B. (2007). The predominant role or coordination number in potassium channel selectivity. *Biophys. J.* **93,** 2635–2643.

Torrie, G. M., and Valleau, J. P. (1977). Nonphysical sampling distributions in Monte-Carlo free energy distributions: Umbrella sampling. *J. Comp. Phys.* **23,** 187–199.

Treptow, W., and Tarek, M. (2006a). K^+ conduction in the selectivity filter of potassium channels is monitored by the charge distribution along their sequence. *Biophys. J.* **91,** L81–L83.

Treptow, W., and Tarek, M. (2006b). Molecular restraints in the permeation pathway of ion channels. *Biophys. J.* **91,** L26–L28.

Unwin, N. (2005). Refined structure of the nicotinic acetylcholine receptor at 4 Å resolution. *J. Mol. Biol.* **346,** 967–989.

van der Spoel, D., Lindahl, E., Hess, B., Groenhof, G., Mark, A. E., and Berendsen, H. J. (2005). GROMACS: Fast, flexible, and free. *J. Comput. Chem.* **26,** 1701–1718.

Varma, S., and Rempe, S. B. (2007). Tuning ion coordination architectures to enable selective partitioning. *Biophys. J.* **93,** 1093–1099.

Varma, S., Sabo, D., and Rempe, S. B. (2008). K^+/Na^+ selectivity in K channels and valinomycin: Over-coordination versus cavity-size constraints. *J. Mol. Biol.* **376,** 13–22.

Wallin, E., and von Heijne, G. (1998). Genome-wide analysis of integral membrane proteins from eubacterial, archean, and eukaryotic organisms. *Protien Sci.* **7,** 1029–1038.

Wee, C. L., Bemporad, D., Sands, Z. A., Gavaghan, D., and Sansom, M. S. P. (2007). SGTx1, a Kv channel gating-modifier toxin, binds to the interfacial region of lipid bilayers. *Biophys. J.* **92,** L07–L09.

Wee, C. L., Gavaghan, D., and Sansom, M. S. P. (2008). Lipid bilayer deformation and the free energy of interaction of a K_v channel gating-modifier toxin. *Biophys. J.* **95,** 3816–3826.

Weetman, P., Goldman, S., and Gray, C. G. (1997). Use of the Poisson-Boltzmann equation to estimate the electrostatic free energy barrier for dielectric models of biological ion channels. *J. Phys. Chem.* **101,** 6073–6078.

Weiner, P. K., and Kollman, P. A. (1981). AMBER–assisted model-building with energy refinement—a general program for modeling molecules and their interactions. *J. Comp. Chem.* **2,** 287–303.

Xiang, Z. X., and Honig, B. (2001). Extending the accuracy limits of prediction for side-chain conformations. *J. Mol. Biol.* **311,** 421–430.

Zhou, Y., Morais-Cabral, J. H., Kaufman, A., and MacKinnon, R. (2001). Chemistry of ion coordination and hydration revealed by a K^+ channel-Fab complex at 2.0 Å resolution. *Nature* **414,** 43–48.

CHAPTER 13

Nano-Scale Imaging and Dynamics of Amylin-Membrane Interactions and Its Implication in Type II Diabetes Mellitus

Won-Jin Cho,[*] Bhanu P. Jena,[*] and Aleksandar M. Jeremic[†]

[*]Department of Physiology
Wayne State University School of Medicine
Detroit, Michigan 48201

[†]Department of Biological Sciences
The George Washington University
Washington, District of Columbia 20052

METHODS IN CELL BIOLOGY, VOL. 90

0091-679X/08 $35.00
DOI: 10.1016/S0091-679X(08)00813-3

Abstract

Amylin, a 37-amino acid peptide hormone produced and secreted by pancreatic β-cells, is the principal constituent of amyloid deposits in Type II Diabetes Mellitus (TTDM). Although much progress has been made in the understanding of amylin aggregation, molecular determinants that contribute to amylin aggregation in the pancreas and TTDM remain largely unknown. In order to better understand amylin aggregation and how membranes contribute to this process, visualization of amylin aggregation and deposition on membrane surface is of utmost importance. Here, we describe a new atomic force microscopy (AFM) approach to visualize amylin aggregation and to asses amylin–surface interactions. Using AFM in contact or tapping mode in fluid, amylin phase transitions on different supports were studied in real time and with high spatial nanometer-resolution. On mica, a two-stage sequential conversion of amylin from soluble monomer to small oligomers and further to mature amyloid fibrils was revealed by the AFM. This amylin conversion was accompanied by peptide conformational transition from random coil to β-sheets assessed by CD spectroscopy. In contrast to mica, amylin formed amorphous amyloid deposits on planar lipid membranes consistent with pathological findings in diabetic subjects. Anionic lipid phosphatidylserine (PS) and membrane cholesterol had opposing effect on the kinetics and the extent of amylin aggregation. PS stimulated amylin aggregation, whereas cholesterol reversed the effect of PS. In addition, cholesterol sequestered amylin aggregates into membrane microdomains that in turn decreased amyloid deposition across the membranes. Hence, this reconstituted AFM approach offers new molecular insights to the etiology of diabetes that could be extended to investigate amylin aggregation in living islet cells at a subcellular resolution.

I. Introduction

Type II Diabetes mellitus (TTDM) is a complex and degenerative metabolic disease that has reached epidemic proportions, with more than 150 million people worldwide affected by the disease. Individuals suffering from diabetes have impaired insulin production ensuing hyperglycemia that if left untreated can cause cardiovascular disease, kidney failure, nerve damage, blindness, and ultimately death. The onset of TTDM is characterized by three determining factors: the insufficient ability of pancreatic β–cells to secrete insulin, decreased insulin sensitivity of peripheral tissues, and the deposition of amylin-derived aggregates or amyloid (Clark and Nilsson, 2004; Kahn, 2001). In spite of well established roles of first two factors in the etiology of diabetes, there is still a critical gap in the knowledge that centers on why amyloid is formed in the pancreas and how it contributes to the disease.

Islet amyloid polypeptide (IAPP) or amylin is 37-aa peptide hormone produced and cosecreted with insulin by islet β-cells in the pancreas. Amylin displays a broad

range of both physiologic and pathologic effects on variety of cells, ranging from the regulation of glucose metabolism to β-cell apoptosis (Lorenzo *et al.*, 1994; Zhang *et al.*, 2003; Haataja *et al.*, 2008). Under normal physiologic conditions human amylin is secreted in soluble form from the pancreatic β-cells despite its high propensity to aggregate *in vitro*. In late-onset of TTDM, however, it comprises the major component of the islet amyloid deposits that are toxic to islet cells (Ritzel *et al.*, 2007). Studies have identified amyloidogenic region (IAPP 20–29 aa) within amylin sequence driving amylin aggregation both *in vitro and in vivo*. Notably, three Pro substitutions within amylin amyloidogenic sequence are thought to be critical for the lack of amyloid formation in rodents (Westermark *et al.*, 1990; Moriarty and Raleigh 1999; Green *et al.*, 2003). A transgenic rat expressing human amylin is prone to amyloid formation that contributes to a decreased β-cell mass in the rodent diabetic model (Butler *et al.*, 2004). Interestingly, small oligomers rather than mature amylin fibrils are shown to confer amylin cytotoxicity in the pancreas (Meier *et al.*, 2006; Ritzel *et al.*, 2007). Pathological studies underscore important role of amylin in progression of the disease as there is a positive relationship between amylin extracellular deposition and the clinical severity of diabetes revealed both in humans (Narita *et al.*, 1992; Rocken *et al.*, 1992) and in animal models (de Koning *et al.*, 1993; Hoppener *et al.*, 1999; Soeller *et al.*, 1998). Studies also suggest that amylin undergoes a nucleation-dependent aggregation *in vitro*, in a process that is both time- and concentration-dependent (Goldsbury *et al.*, 1997; Padrick and Miranker, 2002; Rhoades *et al.*, 2000). While there is a growing body of knowledge that suggests how amylin aggregates in cell-free conditions, it is still entirely unclear what causes amylin to aggregate *in vivo* (in the pancreas).

Plasma membranes (PM) represent natural substrates for the assembly of amylin aggregates and their accumulation at extracellular sites in the islets of Langerhans and have only recently gained more attention as possible regulators of amylin function. Despite a body of literature explaining general molecular mechanisms underlying amylin aggregation and of other amyloidogenic proteins (Jaikaran and Clark, 2001; Ruschak and Miranker, 2007; Sawaya *et al.*, 2007), the role of membranes in amylin aggregation is however sparsely investigated. Molecular studies examining amylin–membrane interactions and their implication to diabetes are particularly lacking. Current biochemical studies identify membranes as a possibly important and missing link in amylin aggregation in pancreas (Jayasinghe and Langen, 2005, 2007; Knight and Miranker, 2004; Knight *et al.*, 2006). Anionic lipids such as phosphatidyl serine (PS) are accelerators of amylin aggregation *in vitro*, dependent on amylin structural transition from soluble random coil to insoluble β-sheets (Jayasinghe and Langen, 2005; Knight *et al.*, 2006; Lopes *et al.*, 2007). To the best of our knowledge, only one attempt has been made prior to this study to visualize process of amylin aggregation and to track its assembly on membranes (Domanov and Kinnunen, 2008). Using Fluorescence Resonance Energy Transfer (FRET) microscopy the Kinnunen group was able to show a tight connection between lipids and amylin aggregates deposited on lipid bilayers. In order to fully investigate

dynamics of amylin–membrane interactions and to visualize amylin structural transitions on membranes a new method is yet to be devised.

The recent development of high-resolution imaging techniques such as atomic force microscope (AFM) is an emerging tool that has allowed visualization of molecular processes on membranes and cells (Jena and Horber, 2006; Jena, 2007). Using this imaging approach and mica as a substrate the mechanism of amylin fibrilogenesis has been investigated by a few groups (Goldsbury *et al.*, 1999; Green *et al.*, 2004; Marek *et al.*, 2007). This approach reveals two distinct phases in amyloid formation on mica: oligomers growth followed by fibril elongation (Green *et al.*, 2004). Here, we describe a new high-resolution AFM imaging method to investigate and to visualize amylin aggregation on membranes in real time and at nanometer level. Amylin aggregation on planar membranes was imaged by time-lapse AFM operated in a tapping or contact mode, and obtained data confirmed using classical spectroscopic methods such as thioflavin-T (Th-T) fluorescent assay and CD spectroscopy. The results highlight the importance of certain lipids and sterols in the regulation of amylin aggregation. Notably, anionic phospholipids and membrane cholesterol emerged as the main catalyst and inhibitor of amylin aggregation, respectively.

II. Materials and Methods

A. Materials

Phosphatidylcholine (PC), phosphatidylserine (PS), and cholesterol were obtained from Avanti Polar Lipids (Alabaster, AL). Human and rat amylin peptides were purchased from Bachem (Torrance, CA) in a lyophilized form. All other reagents were purchased from Sigma (Saint Louis, MO).

B. Preparation of Amylin

Lyophilized synthetic human and rat amylin were used for preparations of amylin stock solutions (500 μM–2 mM) using hexafluoride isopropanol (HFIP) as a solvent. Appropriate amounts of the peptides were weighed and solubilized in HFIP for 1–2 days in order to completely dissolve amylin. This approach efficiently removes any preformed amylin aggregates (Green *et al.*, 2003). In all of our experiments, the final concentrations of amylin and HFIP were the same 5–20 μM and 1–2%, respectively.

C. Preparation of Liposomes and Planar Membranes

Large unilalamellar vesicles (LUV) and supported planar membranes were prepared according to our published procedure (Jeremic *et al.*, 2004, 2006). A 10-mM lipid stock solution was prepared by mixing lipid solution in chloroform:

DOPC (1,2-dioleoyl phosphatidylcholine): DOPS (1,2-dioleoylphosphatidylserine) in 70:30 mol/mol ratios in glass test tubes, or DOPC: DOPS: Cholesterol in 56:24:20 mol/mol/mol ratios. The lipid mixture was dried under gentle stream of nitrogen and resuspended in decane. The lipids were then suspended in buffer containing 10 mM Hepes–NaOH [pH = 7.5] and 140 mM NaCl by vortexing for 5 min at room temperature. Vesicles were prepared following sonication for 2 min, and extrusion using a LiposoFast extruder (Avestin, Ottawa) and polycarbonate membranes of different pore size. LUV were prepared by a published extrusion method (MacDonald *et al.*, 1991), using several passes of the liposomal solution through polycarbonate membranes of 100 nm pore size. Planar bilayers were prepared by liposome fusion method (Jeremic *et al.*, 2006). 20 μM of liposome suspension was placed at the center of a freshly cleaved mica disks and incubated for 45 min on R.T. in the bilayer buffer (140 mM NaCl, 10 mM HEPES, 1 mM $CaCl_2$). Nonfused vesicles were removed by washing (10x), and fused planar membranes imaged by AFM prior to the addition of amylin to check for membrane consistency. AFM revealed that membranes spread uniformly on the mica surface and were free of defects.

D. Atomic Force Microscopy

Samples were analyzed by AFM to characterize size, growth kinetics, and morphology of amylin aggregates. Freshly prepared amylin stock solution (500 μM in HFIP) was added to mica or preformed planar membranes (obtained by fusing liposomes of defined-chemical composition). Changes in size and morphology (polymorphism) of amylin aggregates were monitored in real time by time-lapse AFM. The membranes were imaged by AFM in contact or tapping mode in fluid to capture distinct phases of amylin fibril assembly. There were no significant differences in results using the different imaging modalities. The size of individual fibrils and oligomers (the width, height, and length) were determined for each time point using the single particle analysis software (Veeco, Santa Barbara, CA). Particle dimensions were determined, averaged, and plotted over time to obtain fibril growth curve. The rates of amylin aggregation on mica were determined by analyzing the slope of the growth curve, as previously described (Jeremic *et al.*, 2004). AFM micrographs of amylin aggregation are obtained using Bioscope and the Nanoscope IIIa controller from Digital Instruments (Santa Barbara, CA). All images presented in this study were obtained in the ''tapping'' mode in fluid at room temperature, using silicon nitride tips with a spring constant of 0.06 Nm^{-1} and an imaging force of less than 200 pN. Images were obtained at line frequencies of 2.523 Hz, with 512 lines per image and constant image gains. Topographical dimensions of amylin aggregates were analyzed using the NANOSCOPE (R) IIIA 4.43r8 software, supplied by Digital Instruments. Images presented here are either in height or amplitude ''tapping'' mode.

E. Th-T Fluorescence Assay

The kinetics and extent of amylin aggregation in solution were monitored in real time by Tthioflavin-T (Th-T) fluorescent assay. Freshly prepared stock solutions (500 μM) of the human amylin (hIAPP) or rat amylin (rIAPP) in HFIP were used to ensure absence of proto-fibrils in incubation medium. Amylin was used in the 5–20 μM concentration range depending on the experiment. For the experiments with lipid vesicles, LUV concentration in the reaction buffer was kept constant (100 μM). Changes in Th-T intensity at 482 nm over time was recorded at 10 s interval in Hitachi F-2000 spectrofluorometer using excitation and emission wavelength set to 450 nm and 482 nm, respectively. In addition to fluorescent intensity measurements, fluorescence emission profiles of Th-T for the human and rat amylin were recorded to confirm amylin aggregation. An increase in emission maximum at 482 nm was confirmed for human but not rat amylin, thus confirming that increase in Th-T fluorescence is due to amylin aggregation. Data were collected, plotted, and compared using Excel graphic program. All experiments were performed at room temperature. Determinations of the kinetic constants and the reaction rates are described elsewhere (Jeremic *et al.*, 2004, 2005).

F. CD Spectroscopy

Peptides were dissolved from stock solutions into PBS and immediately transferred into a 1 mm path length quartz quevette for CD measurements. All measurements were performed at room temperature. CD ellipticity (θ, millidegrees) of human and rat amylin were measured either alone or in the LUV presence (1/20 mol/mol peptide–lipid ratio) using a Jasco J-710 spectropolarimeter. CD data were collected every 1 nm between 195 nm and 250 nm at a scan rate of 50 nm/min. Raw CD spectra were corrected by subtracting appropriate backgrounds. To obtain kinetics of amylin conformational transition from random coil to β-sheets ellipticity was continuously measured at 220 nm as a function of time (1 s interval). An ellipticity minimum at 220 nm is indicative of amylin adopting β-sheet conformation (Jayasinghe and Langen, 2007).

III. Results and Discussion

The dynamics of amylin–membrane interactions and amylin structural transitions during aggregation were studied both in the solution and on solid supports by fluorescence/CD spectroscopy, and AFM. In biology, the distinct advantage of this scanning probe microscope over the electron microscope (EM) is its unique ability to directly monitor changes in the conformation or aggregation state of macromolecules, and to study dynamic aspects of molecular interaction in their physiological buffer environment. We therefore studied amylin aggregation on different supports including planar phospholipid/cholesterol membranes and

mica by time-lapse AFM operating either in contact or tapping mode aiming to capture structural intermediates during amylin fibril assembly. There are two principles of imaging with the AFM: contact and tapping mode. By operating AFM in a contact mode (tip is in contact with the surface at all times during scanning), imaging of individual surface atoms is feasible. Tapping mode however is better suited for imaging soft samples in the fluid due to the smaller shear and vertical forces exerted on the surface *via* the tip, which reduces the overall stress of elastic and delicate biological samples such as planar membranes (in this case tip oscillates at its resonant frequency and lightly touches the sample during scanning). Using this AFM imaging mode an investigation of organization, dynamics, and ultrastructure of amylin aggregates on membranes at ~5–10 nm resolution is possible.

A. Structure and Supramolecular Organization of Amylin Aggregates on Solid Supports Revealed by the AFM

We studied the organization of amylin aggregates on mica and on planar lipid membranes bearing different chemical composition and distinct physical properties. AFM was used both in contact and tapping modes. Since the results obtained by the two imaging modes were quite similar, all representative AFM micrographs presented in this article are therefore obtained in the tapping mode for consistency. We imaged and analyzed growth of amylin fibrils on mica in real-time by AFM (Fig. 1). Fibril growth was measured for a total duration of 30–60 min with the

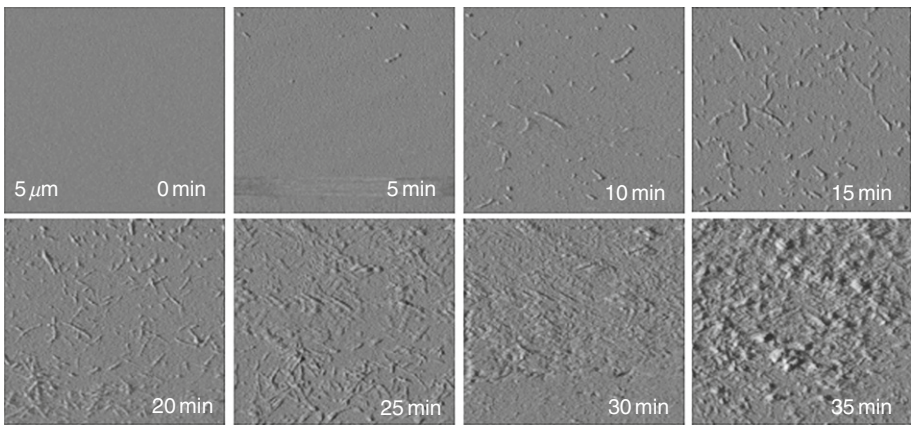

Fig. 1 Time-lapse AFM imaging of amylin aggregation on mica. Structural intermediates, oligomers, and fibrils, are resolved during amylin aggregation on mica by AFM (tapping mode amplitude images). Note a time-dependent transition of human amylin from small round oligomers (0–10 min) into fibrils during early-mid stage of amylin aggregation (10–25 min). Late-stage of amylin aggregation (25–35 min) is characterized by accumulation of massive peptide deposits on the mica surface. All micrographs are 5×5 μm.

speed of acquisition of ~5 min/image. Amplitude AFM micrographs reveal structural transitions of amylin from small spherical oligomers to extended fibrils on mica over a 30-min time period (Fig. 1). After acquiring micrographs the size of individual fibrils and oligomers (i.e., radius, length, and height), deposited on mica or on planar membranes, were determined using the section analysis tool (Veeco, Santa Barbara, CA). Cross-section analysis of amylin aggregates revealed that amylin fibrils, varied by length, and consistently measured 90–110 nm in width and 5–6 nm in height, respectively (Fig. 2, lower panel). In addition to amplitude AFM images (Fig. 1) we also included height-AFM micrographs (Figs. 2–4) to show changes in fibril height during amylin aggregation. Changes in particle height are more visible in the height imaging mode as compared to amplitude images, which are better suited for imaging the fine morphological details of amylin aggregates (Fig. 1). Some fibrils were relatively short (less than 200 nm), whereas some fibrils extended over 500 nm in length (Figs. 2 and 3). Using time-lapse AFM imaging we monitored changes in size of individual fibrils that allowed us to construct amylin fibril growth curves (Fig. 3C). To construct fibril growth curves, the average size of oligomers and fibrils was determined for each time point, and plotted (Fig. 3A–C). Massive amyloid-like amylin deposits generally developed after 30 min of incubation (Fig. 1, 30–35 min) precluding the monitoring of fibril extension for extended period of time. Nevertheless, AFM

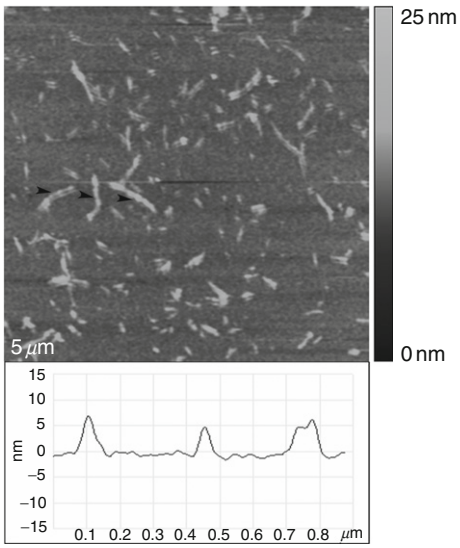

Fig. 2 Structure and size of human amylin aggregates on mica. Height-AFM micrograph (upper panel) depicts fibril formation and their homogeneous distribution across mica surface in PBS buffer. Differences in fibril heights are represented using pseudo-color scale (0–25 nm, right bar). Micrograph is 5×5 μm scale. Cross-section analysis of three mature fibrils (depicted by arrowheads) reveals similarity in fibrils size (height and width only, lower panel).

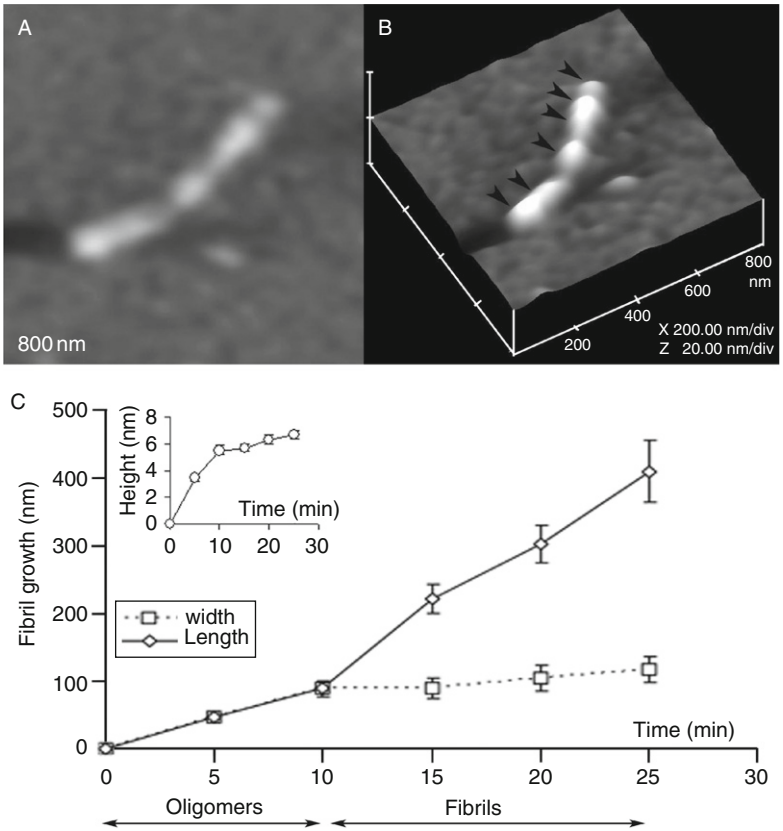

Fig. 3 Amylin phase transitions during aggregation. The 2-D (A) and 3-D (B) AFM images of a single full-grown fibril on mica showing arrangement of several amylin oligomers and their bidirectional extension into a fibril (depicted by arrowheads). Micrographs are 800 × 800 nm scale. (C) Fibril growth curves depicts two phases of amylin aggregation, an early first phase (0–10 min) characterized by oligomers formation, followed by oligomers extension and fibrils formation (10–25 min, second phase or fibril maturation). Note the significant increase in oligomer heights (Fig. 3C, inset) and widths during the first phase of amylin aggregation, and an abrupt increase in fibrils length following formation of full-size oligomers (second phase, Fig. 3C). Data represents mean particle size at each time point (mean ± SEM), obtained from three independent time-lapse AFM experiments.

resolved amylin structural intermediates prior to amyloid accumulation. Formation of fibrils occurred in two distinct phases: initially through the deposition of small spherical oligomers having a diameter (width) and height of 47 ± 7 nm and 3.4 ± 0.3 nm, respectively (Fig. 1, 0–5 min; and Fig. 3C). During the next 5 min oligomers almost doubled in size (diameter: 89 ± 13 nm, height: 5.5 ± 0.4 nm; Fig. 3C) followed by oligomers bidirectional extensions into a fibril at average fibrilization rate of 21 nm/min (Fig. 1, 10–25 min; and Fig. 3C). Growth curves revealed two distinct phases in amylin aggregation: the first phase or oligomer growth is characterized by the large change in oligomers height and width within

the first 10 min of amylin aggregation (reaching ~90% of its maximum values, Fig. 3C, inset), accounting only for ~20% of maximum fibril length during that period; and second phase or fibrils growth, when fibrils rapidly elongated by doubling their extension rate from 9 nm/min (0–10 min interval, Fig. 3C) to 21 nm/min (10–25 min interval, Fig. 3C). Taken together our results suggest that fibrils are formed on mica by longitudinal extension of full-grown oligomers rather than by lateral association of protofibrils as previously suggested (Goldsbury *et al.*, 1999). Hence, amylin fibrilization depends on formation of "building block" oligomers or nuclei measuring ~6 nm in height and ~90 nm in diameter that once formed to align and elongate into a fibril (Figs. 1–3), a scenario originally proposed by Aebi and coworkers (Green *et al.*, 2004). However, which of these two likely scenarios drives amylin aggregation in the pancreas, a lateral association of protofibrils (Goldsbury *et al.*, 1997, 1999) or longitudinal extension of full-width oligomers, observed in our study and also reported by Green *et al.* (2004), remains to be determined.

B. Surface Distribution Patterns of Amylin Aggregates: Role of Membranes

In addition to studying structure and dynamics of amylin aggregates on mica, we also used AFM to investigate how surfaces other than mica such as planar lipid membranes influence aggregation and deposition of amylin aggregates. Planar membranes represent a valuable tool for assessing many protein–lipid interactions, and were used in our study to mimic interactions between amylin and β-cell PM that likely occur during amylin aggregation in the pancreas in patients with TTDM. By carefully choosing phospholipids of different chemical compositions we prepared chemically-distinct planar membranes and liposomes in order to investigate if and how surface charges, hydrophobicity, and other intermolecular forces contribute to amylin aggregation (Figs. 4–7). AFM revealed that amylin aggregates (fibrils) are homogeneously deposited across the mica surface (Figs. 1 and 2). We observed a similar uniform surface distribution of amylin aggregates on other charged supports such as PC and PC:PS membranes (Fig. 4). Interestingly, the structure of amylin aggregates varied according to the physicochemical properties of the support used in the study: we consistently observed accumulation of fibrils on stiff and polar surface like mica, a buildup of short thick aggregates on soft zwitteronic/negatively-charged PC and PC:PS membranes, whereas short and condensed amyloid structures preferentially deposited in microdomains of the membranes containing cholesterol (Fig. 4). Furthermore, while amylin oligomers were initially formed on planar membranes (data not shown), they did not elongate into extended fibrils in stark contrast to amylin aggregation on mica (Fig. 4). Reason(s) for polymorphism of amylin aggregates and their diverse deposition patterns on different supports are vague at this time and require further studies. However, we can infer something from these experiments about the nature of forces driving amylin–mica and amylin–membrane interactions, and hence amylin

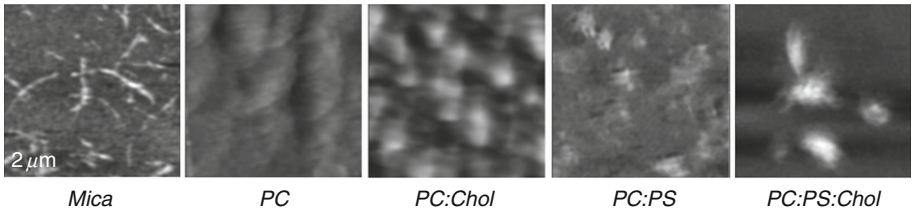

Fig. 4 Cholesterol regulates amylin aggregation and deposition on planar membranes. The AFM micrographs depict distinct organization of amylin aggregates on various surfaces. In the membrane absence, amylin forms elongated fibrils on mica. On planar membranes, however amylin forms short condensed structures, consistent with pathology findings in TTDM subjects. In the cholesterol absence, amylin aggregates are homogeneously distributed across most hydrophilic surfaces (mica, PC, and PC:PS membranes). In the lipid raft membrane model (8:2 lipid/sterol mol/mol) amylin aggregates are restricted in small membrane regions. Note the accumulation of amylin aggregates in the membrane microdomains, and the lack of amylin aggregates in surrounding membrane areas when cholesterol is present (PC:Chol. and PC:PS:Chol.) Also note the absence of elongated fibrils during amylin aggregation on planar membranes. All micrographs are 2×2 μm scale, and are taken at the same time point (20 min) during amylin aggregation.

aggregation. Mica, like most planar membranes, has hydrophilic surface and is overall negatively charged (moderate negative surface charges ~0.1 electron per nm^2 have been reported for mica; Pashley, 1981). Mica also exhibits unusual high attractive van der Waals forces (Nonretarded Hamaker constants of $A = 2 \times 10^{-20}$ J; Israelachvili, 1992). Thus, while the combination of electrostatic and van der Waals forces may drive amylin–mica interactions and amylin aggregation, combination of surface charges, aromatic interactions and to lesser extent hydrophobic forces may account for amylin-membrane interactions and amylin aggregation on planar membranes (Fig. 4; Knight and Miranker, 2004; Porat *et al.*, 2004; Jayasinghe and Langen, 2005; Marek *et al.*, 2007). In addition to contribution of these long-range intermolecular forces to amylin–surface interactions and amylin deposition, other surface properties such as membrane mobility and fluidity (i.e., membrane liquid ordered/disordered domains) and/or membrane elasticity may possibly contribute to amylin aggregation. Studies show an important role of certain lipids and sterols in aggregation of other amyloidogenic proteins such as β-amyloid (Avdulov *et al.*, 1997; Yip *et al.*, 2001; Ashley *et al.*, 2006). It is worth noting here that the structure of amylin aggregates and their deposition patterns on planar membranes obtained in our AFM studies resemble the amorphous amyloid deposits that occur in diabetes (Jaikaran and Clark, 2001), indicating that our reconstituted approach is valid and of pathophysiological relevance. Taken together, these findings postulate an important and possibly regulatory role of pancreatic cell PM in the development of pancreatic amyloidosis and TTDM. Recent *in vitro* study supports this view by showing accelerated aggregation of synthetic human amylin in the presence of membranes isolated from the pancreas of TTDM subjects (Knight and Miranker, 2004).

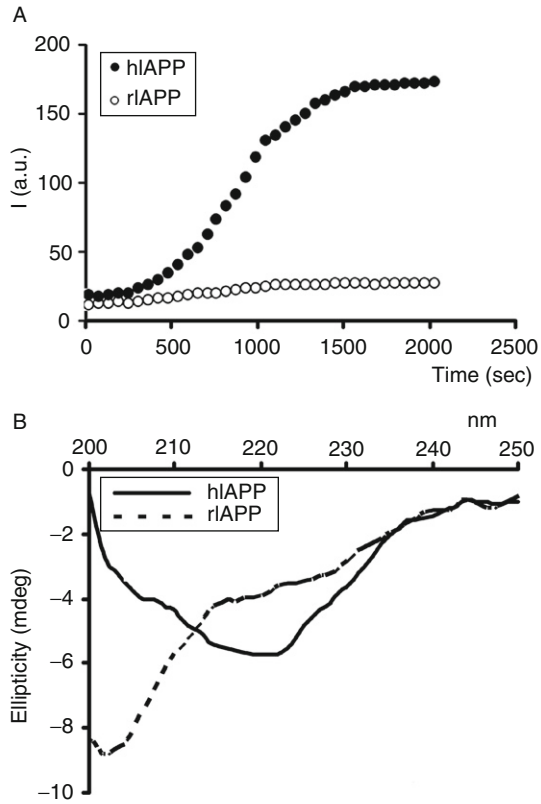

Fig. 5 Aggregation of human amylin coincides with the changes of its secondary structure. (A) Kinetics and extent of aggregation of human amylin (hIAPP) and rat amylin (rIAPP) in PBS as a function of time is shown. Thioflavin-T fluorescent assay reveals fibrilogenesis of 20 μM human amylin in solution (closed circles) and lack of aggregation of nonamyloidogenic rat amylin (20 μM; open circles). Graph depicts changes in Th-T fluorescence intensity (arbitrary units, a.u.) at 482 nm as a function of time. (B) Far-UV CD spectra of human and rat amylin taken after 20 min in PBS solution. Note the absorption minimum at ~220 nm for human but not rat amylin, a typical of peptides and proteins adopting β-sheets conformation.

C. Dynamical and Conformational Aspects of Amylin Aggregation in Solution

The unique feature common to all amyloidogenic proteins is their conformational transitions from soluble random coil or α-helical conformation to non-soluble β-sheets (Sawaya *et al.*, 2007). In this part of the study we used CD spectroscopy and Th-T fluorescence assay to examine amylin conformational transitions and aggregation in real time under different experimental conditions (i.e., in the absence or in the presence of liposomes; or solvents of different ionic strengths). We first measured the extent and kinetics of amylin aggregation in solution by Th-T fluorescence assay. The Th-T binds with high affinity to amylin aggregates but not monomers and is accompanied by the increase in dye's emission

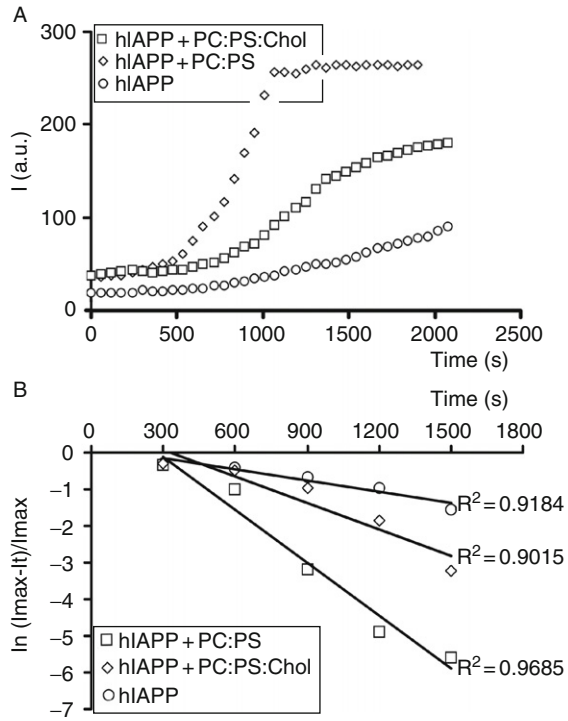

Fig. 6 An inverse effect of membrane cholesterol and anionic phospholipids on the kinetics of amylin aggregation in solution. (A) Thioflavin-T fluorescent assay reveals slow aggregation of 5 μM human amylin in solution (circles). Presence of 100 μM phosphatidylcholine:phosphatidylserine (PC: PS) lipid vesicles (diamonds) in incubating solution (PBS, 1%HFIP) potentiates amylin aggregation that was reversed by inclusion of cholesterol in the lipid vesicles (PC:PS:Chol., squares). (B) Kinetics of amylin aggregation is regulated by membrane cholesterol. Presence of negatively-charged PC:PS vesicles (squares) in the incubation buffer increased the rate of amylin aggregation (circles) by more than four times. The stimulatory effect of anionic PS on amylin aggregation was decreased by ~30% by inclusion of cholesterol in the vesicle membrane (PC:PS:Cholesterol LUV, diamonds). All three curves follow first-order kinetics ($R^2 > 0.9$, Fig. 6B).

maximum at 482 nm (Munishkina and Fink, 2007). As may be expected, nonamyloidiogenic rat amylin (20 μM) did not aggregate in mark contrast to human amylin (20 μM) that readily aggregates in solution (Fig. 5A). Increasing the salt concentrations in the incubation medium (to minimize electrostatic interactions in solution) decreased both the rate and the extent of amylin aggregation (data not shown). Thus, amylin aggregation inversely correlates with ionic strength of its solvent, which suggests that electrostatic interactions drive amylin–amylin interactions and amylin aggregation in solution as they also drive amylin–membrane interactions (Figs. 6 and 7). We further correlated amylin aggregation with amylin conformational transitions in time by CD spectroscopy (Fig. 5B). CD spectra of human and rat amylin (20 μM) taken after 20 min revealed a conformational

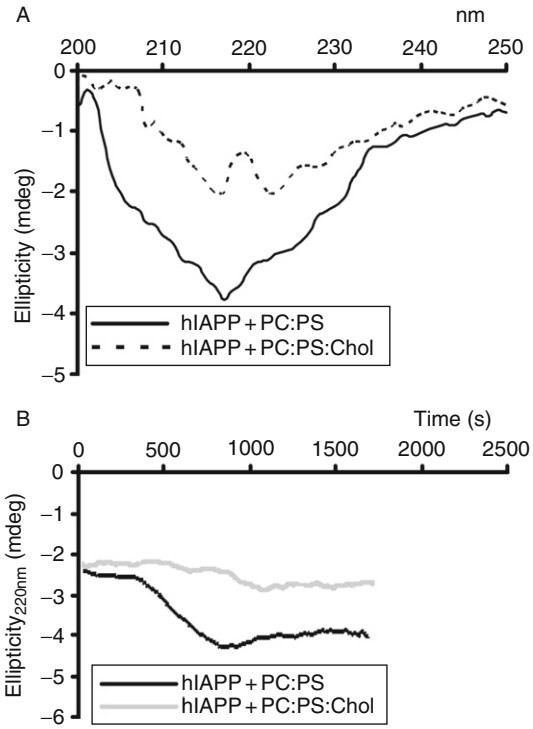

Fig. 7 Dynamics of amylin secondary structural transitions in solution are regulated by membranes. (A) CD spectra of human amylin (5 μM) incubated with 100 μM PC:PS LUV (solid line) or PC:PS: Cholesterol LUV (dashed line) for 20 min. Note the shift in CD spectrum of cholesterol-containing liposomes and the rise of a new minimum at 222 nm indicative of α-helix. (B) Real-time changes of amylin secondary structure in solution assed by CD spectroscopy. Continuous recording of CD spectra of human amylin in solution reveals its swift transition from random coil conformation to β-sheets in the presence of LUV composed of PC:PS (black line) but not PC:PS:Cholesterol (gray line). CD spectra were continuously acquired at 220 nm, which represents a minimum for most peptides and proteins adopting β-sheet conformation. Note that time frames of amylin aggregation and the structural transition from random coil to β-sheets coincide (Figs. 6A and 7B).

transition of human but not rat amylin from random coil to β-sheets. This conformational change of human amylin is revealed by the shift in the peptide's absorption minimum from 208 to ~220 nm, and by the characteristic v-shape curve unique to peptides with β-sheet conformation (Fig. 5B). Thus, as in case of other amyloidogenic proteins, amylin conformational transitions from random coil to β-sheets and amylin aggregation strongly correlated in time (Fig. 5A and B).

D. Role of Charge and Membrane Cholesterol in Amylin Aggregation

Results from Our AFM and spectroscopic studies, together with previous reports (Knight and Miranker, 2004; Jayasinghe and Langen, 2005; Knight *et al.*, 2006), strongly suggest that amylin–amylin and amylin–membrane interactions, along

with amylin aggregation are driven at least in part by electrostatic forces. To confirm this, we further examined the effect of membranes on the dynamics and the extent of amylin aggregation in solution by the Th-T fluorescent assay (Fig. 6A). We used 5 μM concentration of human amylin to better evaluate modulatory effect of lipids on amylin aggregation. Under our experimental conditions (solvent concentration 1% HFIP) and 35 min experiment, 5 μM represents a near-threshold concentration for amylin aggregation (Fig. 6A). In marked contrast to peptide alone, presence of negatively charged liposomes (PC:PS) in the incubation solution potentiated amylin aggregation by increasing both the extent and the rate of amylin aggregation (Fig. 6A and B). Amylin aggregated at a slow rate following first order law with $k = 0.0010\ s^{-1}$, whereas presence of PC:PS liposomes accelerated amylin aggregation by ~450% to $k = 0.0045\ s^{-1}$ (PC:PS, Fig. 6B). Zwitteronic PC liposomes do not significantly affect the rate or the extent of amylin aggregation in solution (data not shown). Incorporation of cholesterol in membranes of the negatively-charged liposomes attenuated stimulatory effect of PS on amylin aggregation in solution by ~30%, $k = 0.0032\ s^{-1}$ (PC:PS:Cholesterol, Fig. 6B), a decrease comparable to the inhibitory effect of cholesterol on amylin deposition across planar membranes (Fig. 4). Applying the calculated rate constants to Arrhenius equation it can be inferred that presence of the negatively charged PC:PS vesicles decreases energy of activation of the aggregation process by $\Delta E_a = -3726$ J/mol as compared to amylin alone, which in turn increases the rate of amylin aggregation by more than four times (Fig. 6A and B). In contrast, inclusion of cholesterol in PC:PS vesicles reverses their stimulatory effect on amylin aggregation by increasing activation energy by $\Delta E_a = 845$ J/mol (Fig. 6B). Both thermodynamic values are calculated for amylin aggregation at room temperature (25 °C). Interestingly, despite marked difference in their aggregation rates all three curves exhibit first-order kinetics ($R^2 > 0.9$; Fig. 6B). These results suggest that membranes modulate amylin aggregation by changing the activation energy of the amylin phase transition from random coil to β-sheets rather than by changing its mechanistic pathway.

Analogous to kinetic studies of amylin aggregation (Fig. 6), we observed similar inverse effect of PS and cholesterol on amylin conformational transitions in our CD spectroscopy studies (Fig. 7). In the absence of liposomes, 5 μM amylin slowly acquired β-sheet conformation over 60-min period (data not shown). Addition of PC:PS liposomes (100 μM) to incubating solution stimulates amylin conformation transition from random coil to β-sheets characterized by absorption minimum at 217 nm (Fig. 7A). Insertion of cholesterol in lipid vesicles shifted equilibrium toward the peptide's soluble α-helical conformation as the spectral shift and two minimums at 217 nm and 222 nm were detected (Fig. 7A), a spectroscopic signature of a mixture of α- and β-conformers in solution (Knight *et al.*, 2006). Furthermore, kinetics of amylin conformational transition from α-helix to β-sheets was considerably delayed in the cholesterol-containing vesicles (PC:PS:Cholesterol) when compared to control PC:PS vesicles (Fig. 7B) that coincided with a decrease in amylin aggregation (Fig. 6A).

How does cholesterol regulate amylin aggregation and deposition on the membrane? It is well established that proteins and peptides can partition between

cholesterol-enriched and cholesterol-free domains in the cell PM depending on their preference for binding to cholesterol (Epand, 2006). Based on this general protein propensity, amylin should then be either included or excluded from the cholesterol-enriched membrane domains depending on its affinity toward cholesterol, which is still unknown. In either case, cholesterol should initiate selective accumulation of amylin aggregates on the membrane, which was indeed observed in our AFM studies (Fig. 4). How cholesterol suppresses stimulatory effect of PS-containing vesicles on amylin aggregation in solution is harder to explain. We, however, propose two plausible scenarios for observed inhibitory cholesterol effect on amylin aggregation: (1) cholesterol, by modulating membrane fluidity, also changes membrane elasticity that outweigh electrostatic attractions between positively charged amylin (+3) and negatively charged PS-containing liposomes, thus acting downstream to amylin–membrane electrostatic interactions; and (2) cholesterol, due to its ability to sequester PS in membrane microdomains (Bakht *et al.*, 2007), also minimizes distribution of negative surface charges across the membrane that in turn decreases the overall number of amylin nucleation sites on the membrane. It is important to note here that because amylin aggregation is always accompanied by its conformational transitions, effect of cholesterol on amylin–membrane interactions and amylin aggregation eventually will be interrelated to its ability to modulate amylin secondary structure (Figs. 6–8).

IV. Summary

In this study using the AFM we were able to physically demonstrate for the first time how distinct membrane components such as lipids and sterols regulate amylin aggregation and deposition on planar membranes, which can be relevant for amyloid formation in the pancreas. Two membrane components, negatively-charged lipids and cholesterol, regulated both the kinetics and the extent of amylin aggregation in mutual inverse manner. PS was found to be stimulatory whereas cholesterol reversed effect of PS on amylin aggregation. In addition, cholesterol was solely responsible for sequestering amylin aggregates in membrane domains, allowing parts of membranes to be free of amylin deposits (Fig. 8). In contrast to mica, amylin aggregated on planar lipid membranes as short thick amyloid deposits showing little evidence of higher order fibril assembly. The reason for the different organization and the distinct transitions of amylin aggregates on different supports is unknown at present, and warrants further studies. It will be interesting to extrapolate findings from this study to the amylin aggregation on native membranes (i.e., cell PM), and to investigate in the future how distinct PM components (i.e., cholesterol, PS, or phosphatidylinositols) influence amylin aggregation in β-cells. We anticipate that new high-resolution imaging study of amylin aggregation in pancreatic cells is particularly needed since extracellular amylin aggregation and amyloid formation in the pancreas is a hallmark and main pathological feature of TTDM. More importantly in many diabetic subjects accumulation of amylin

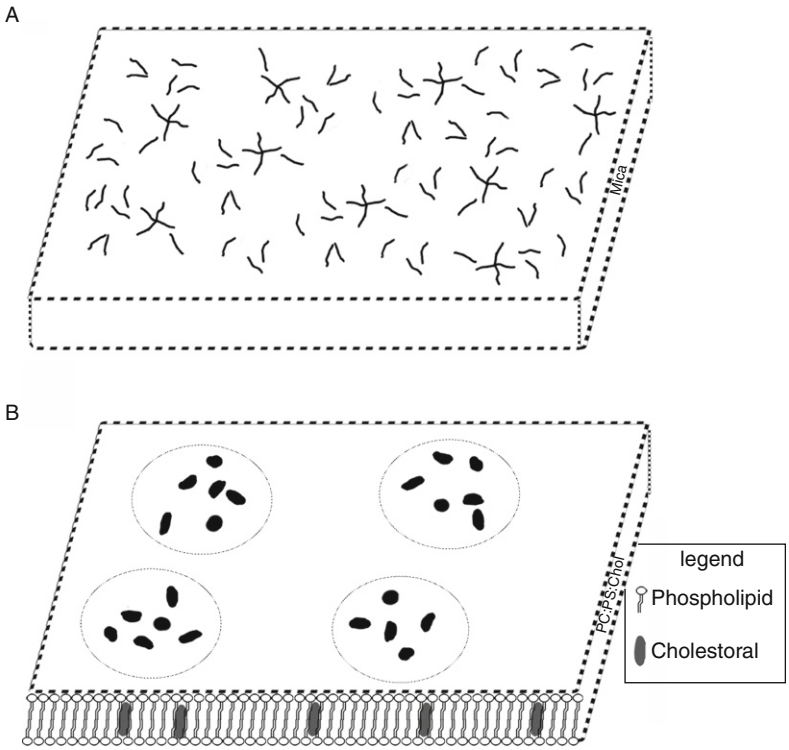

Fig. 8 Our proposed model of human amylin–surface interactions is illustrated. (A) On mica, amylin aggregates in a two-stage sequential process, in which small round oligomers are formed first followed by longitudinal extension of a full-width oligomers into fibrils. Thus formed amylin fibrils distribute evenly across the mica surface. (B) In the case of lipid membranes, electrostatic attractions between positively-charged amylin and negatively-charged anionic lipids drive amylin aggregation and deposition on lipid bilayers characterized by accumulation of a short and thick amylin deposits. Membrane cholesterol sequesters amylin aggregates into membrane micro-domains, which hampers the ability of human amylin to aggregate and to deposit on membranes *via* "nucleation" mechanism.

deposits parallels islet dysfunction. Therefore, identification and understanding of molecular forces and factors regulating amylin aggregation in the pancreas is crucial for designing new approaches and drugs that will ultimately advance our ability to manage diabetes.

Acknowledgments

We are grateful to Anne-Claude Gavin and Vladimir Rybin for their generous support of our project and useful discussions during the preparation of the manuscript. We thank EMBL Structural and Computational Biology Unit for access to their CD spectropolarimeter. This study was supported by the George Washington University Facilitating Research Fund.

References

Ashley, R. H., Harroun, T. A., Hauss, T., Breen, K. C., and Bradshaw, J. P. (2006). Autoinsertion of soluble oligomers of Alzheimer's Abeta(1–42) peptide into cholesterol-containing membranes is accompanied by relocation of the sterol towards the bilayer surface. *BMC Struct. Biol.* **6,** 21.

Avdulov, N. A., Chochina, S. V., Igbavboa, U., Warden, C. S., Vassiliev, A. V., and Wood, W. G. (1997). Lipid binding to amyloid beta-peptide aggregates: Preferential binding of cholesterol as compared with phosphatidylcholine and fatty acids. *J. Neurochem.* **69,** 1746–1752.

Bakht, O., Pathak, P., and London, E. (2007). Effect of the structure of lipids favoring disordered domain formation on the stability of cholesterol-containing ordered domains (lipid rafts): Identification of multiple raft-stabilization mechanisms. *Biophys. J.* **93,** 4307–4318.

Butler, A. E., Jang, J., Gurlo, T., Carty, M. D., Soeller, W. C., and Butler, P. C. (2004). Diabetes due to a progressive defect in beta-cell mass in rats transgenic for human islet amyloid polypeptide (HIP Rat): A new model for type 2 diabetes. *Diabetes* **53,** 1509–1516.

Clark, A., and Nilsson, M. R. (2004). Islet amyloid: A complication of islet dysfunction or an aetiological factor in Type 2 diabetes? *Diabetologia* **47,** 157–169.

de Koning, E. J., Bodkin, N. L., Hansen, B. C., and Clark, A. (1993). Diabetes mellitus in Macaca mulatta monkeys is characterised by islet amyloidosis and reduction in beta-cell population. *Diabetologia* **36,** 378–384.

Domanov, Y. A., and Kinnunen, P. K. (2008). Islet amyloid polypeptide forms rigid lipid-protein amyloid fibrils on supported phospholipid bilayers. *J. Mol. Biol.* **376,** 42–54.

Epand, R. M. (2006). Cholesterol and the interaction of proteins with membrane domains. *Prog. Lipid Res.* **45,** 279–294.

Goldsbury, C. S., Cooper, G. J., Goldie, K. N., Muller, S. A., Saafi, E. L., Gruijters, W. T., Misur, M. P., Engel, A., Aebi, U., and Kistler, J. (1997). Polymorphic fibrillar assembly of human amylin. *J. Struct. Biol.* **119,** 17–27.

Goldsbury, C., Kistler, J., Aebi, U., Arvinte, T., and Cooper, G. J. (1999). Watching amyloid fibrils grow by time-lapse atomic force microscopy. *J. Mol. Biol.* **285,** 33–39.

Green, J. D., Goldsbury, C., Kistler, J., Cooper, G. J., and Aebi, U. (2004). Human amylin oligomer growth and fibril elongation define two distinct phases in amyloid formation. *J. Biol. Chem.* **279,** 12206–12212.

Green, J., Goldsbury, C., Mini, T., Sunderji, S., Frey, P., Kistler, J., Cooper, G., and Aebi, U. (2003). Full-length rat amylin forms fibrils following substitution of single residues from human amylin. *J. Mol. Biol.* **326,** 1147–1156.

Haataja, L., Gurlo, T., Huang, C. J., and Butler, P. C. (2008). Islet amyloid in Type 2 diabetes, and the toxic oligomer hypothesis. *Endocr. Rev.* **29**(3), 303–316.

Hoppener, J. W., Oosterwijk, C., Nieuwenhuis, M. G., Posthuma, G., Thijssen, J. H., Vroom, T. M., Ahren, B., and Lips, C. J. (1999). Extensive islet amyloid formation is induced by development of Type II diabetes mellitus and contributes to its progression: Pathogenesis of diabetes in a mouse model. *Diabetologia* **42,** 427–434.

Israelachvili, J. (1992). "Intermolecular and Surface Forces." Academic Press, London, UK.

Jaikaran, E. T., and Clark, A. (2001). Islet amyloid and type 2 diabetes: From molecular misfolding to islet pathophysiology. *Biochim. Biophys. Acta* **1537,** 179–203.

Jayasinghe, S. A., and Langen, R. (2005). Lipid membranes modulate the structure of islet amyloid polypeptide. *Biochemistry* **44,** 12113–12119.

Jayasinghe, S. A., and Langen, R. (2007). Membrane interaction of islet amyloid polypeptide. *Biochim. Biophys. Acta* **1768,** 2002–2009.

Jena, B. P. (2007). Secretion machinery at the cell plasma membrane. *Curr. Opin. Struct. Biol.* **17,** 437–443.

Jena, B. P., and Horber, H. (2006). "Force Microscopy: Applications in Biology and Medicine." Wiley, Hoboken, New Jersey.

Jeremic, A., Cho, W. J., and Jena, B. P. (2005). Involvement of water channels in synaptic vesicle swelling. *Exp. Biol. Med. (Maywood)* **230,** 674–680.

Jeremic, A., Kelly, M., Cho, J. A., Cho, S. J., Horber, J. K., and Jena, B. P. (2004). Calcium drives fusion of SNARE-apposed bilayers. *Cell Biol. Int.* **28,** 19–31.

Jeremic, A., Quinn, A. S., Cho, W. J., Taatjes, D. J., and Jena, B. P. (2006). Energy-dependent disassembly of self-assembled SNARE complex: Observation at nanometer resolution using atomic force microscopy. *J. Am. Chem. Soc.* **128,** 26–27.

Kahn, S. E. (2001). Clinical review 135: The importance of beta-cell failure in the development and progression of type 2 diabetes. *J. Clin. Endocrinol. Metab.* **86,** 4047–4058.

Knight, J. D., and Miranker, A. D. (2004). Phospholipid catalysis of diabetic amyloid assembly. *J. Mol. Biol.* **341,** 1175–1187.

Knight, J. D., Hebda, J. A., and Miranker, A. D. (2006). Conserved and cooperative assembly of membrane-bound alpha-helical states of islet amyloid polypeptide. *Biochemistry* **45,** 9496–9508.

Lopes, D. H., Meister, A., Gohlke, A., Hauser, A., Blume, A., and Winter, R. (2007). Mechanism of islet amyloid polypeptide fibrillation at lipid interfaces studied by infrared reflection absorption spectroscopy. *Biophys. J.* **93,** 3132–3141.

Lorenzo, A., Razzaboni, B., Weir, G. C., and Yankner, B. A. (1994). Pancreatic islet cell toxicity of amylin associated with type-2 diabetes mellitus. *Nature* **368,** 756–760.

MacDonald, R. C., MacDonald, R. I., Menco, B. P., Takeshita, K., Subbarao, N. K., and Hu, L. R. (1991). Small-volume extrusion apparatus for preparation of large, unilamellar vesicles. *Biochim. Biophys. Acta* **1061,** 297–303.

Marek, P., Abedini, A., Song, B., Kanungo, M., Johnson, M. E., Gupta, R., Zaman, W., Wong, S. S., and Raleigh, D. P. (2007). Aromatic interactions are not required for amyloid fibril formation by islet amyloid polypeptide but do influence the rate of fibril formation and fibril morphology. *Biochemistry* **46,** 3255–3261.

Meier, J. J., Kayed, R., Lin, C. Y., Gurlo, T., Haataja, L., Jayasinghe, S., Langen, R., Glabe, C. G., and Butler, P. C. (2006). Inhibition of human IAPP fibril formation does not prevent beta-cell death: Evidence for distinct actions of oligomers and fibrils of human IAPP. *Am. J. Physiol.* **291,** E1317–E1324.

Moriarty, D. F., and Raleigh, D. P. (1999). Effects of sequential proline substitutions on amyloid formation by human amylin20–29. *Biochemistry* **38,** 1811–1818.

Munishkina, L. A., and Fink, A. L. (2007). Fluorescence as a method to reveal structures and membrane-interactions of amyloidogenic proteins. *Biochim. Biophys. Acta* **1768,** 1862–1885.

Narita, R., Toshimori, H., Nakazato, M., Kuribayashi, T., Toshimori, T., Kawabata, K., Takahashi, K., and Masukura, S. (1992). Islet amyloid polypeptide (IAPP) and pancreatic islet amyloid deposition in diabetic and non-diabetic patients. *Diabetes Res. Clin. Pract.* **15,** 3–14.

Padrick, S. B., and Miranker, A. D. (2002). Islet amyloid: Phase partitioning and secondary nucleation are central to the mechanism of fibrillogenesis. *Biochemistry* **41,** 4694–4703.

Pashley, R. M. (1981). DLVO and hydration forces between mica surfaces in Li+, Na+, K+, and Cs+ electrolyte solutions: A correlation of double-layer and hydration forces with surface cation exchange properties. *J. Colloid Interface Sci.* **2,** 531–546.

Porat, Y., Mazor, Y., Efrat, S., and Gazit, E. (2004). Inhibition of islet amyloid polypeptide fibril formation: A potential role for heteroaromatic interactions. *Biochemistry* **43,** 14454–14462.

Rhoades, E., Agarwal, J., and Gafni, A. (2000). Aggregation of an amyloidogenic fragment of human islet amyloid polypeptide. *Biochim. Biophys. Acta* **1476,** 230–238.

Ritzel, R. A., Meier, J. J., Lin, C. Y., Veldhuis, J. D., and Butler, P. C. (2007). Human islet amyloid polypeptide oligomers disrupt cell coupling, induce apoptosis, and impair insulin secretion in isolated human islets. *Diabetes* **56,** 65–71.

Rocken, C., Linke, R. P., and Saeger, W. (1992). Immunohistology of islet amyloid polypeptide in diabetes mellitus: Semi-quantitative studies in a post-mortem series. *Virchows Arch.* **421,** 339–344.

Ruschak, A. M., and Miranker, A. D. (2007). Fiber-dependent amyloid formation as catalysis of an existing reaction pathway. *Proc. Natl. Acad. Sci. USA* **104,** 12341–12346.

Sawaya, M. R., Sambashivan, S., Nelson, R., Ivanova, M. I., Sievers, S. A., Apostol, M. I., Thompson, M. J., Balbirnie, M., Wiltzius, J. J., McFarlane, H. T., Madsen, A. O., Riekel, C.,, *et al*. (2007). Atomic structures of amyloid cross-beta spines reveal varied steric zippers. *Nature* **447,** 453–457.

Soller, W. C., Janson, J., Hart, S. E., Parker, J. C., Carty, M. D., Stevenson, R. W., Kreutter, D. K., and Butler, P. C. (1998). Islet amyloid-associated diabetes in obese a(vy)la mice expressing human islet amyloid polypeptide. *Diabetes* **47**(5), 743–750.

Westermark, P., Engstrom, U., Johnson, K. H., Westermark, G. T., and Betsholtz, C. (1990). Islet amyloid polypeptide: Pinpointing amino acid residues linked to amyloid fibril formation. *Proc. Natl. Acad. Sci. USA* **87,** 5036–5040.

Yip, C. M., Elton, E. A., Darabie, A. A., Morrison, M. R., and McLaurin, J. (2001). Cholesterol, a modulator of membrane-associated Abeta-fibrillogenesis and neurotoxicity. *J. Mol. Biol.* **311,** 723–734.

Zhang, S., Liu, J., Dragunow, M., and Cooper, G. J. (2003). Fibrillogenic amylin evokes islet beta-cell apoptosis through linked activation of a caspase cascade and JNK1. *J. Biol. Chem.* **278,** 52810–52819.

CHAPTER 14

Real Time Investigation of Protein Folding, Structure, and Dynamics in Living Cells

Qianqian Li,[*] Yuefei Huang,[*] Nan Xiao,[*] Victoria Murray,[*] Jianglei Chen,[*] and Jianjun Wang[*,†]

[*]Department of Biochemistry and Molecular Biology
Wayne State University, School of Medicine
Detroit, Michigan 48021

[†]This work was supported by an RO1 grant from NIH (HL074365 to JW)

0091-679X/08 $35.00
DOI: 10.1016/S0091-679X(08)00814-5

Abstract

Real time investigation of protein folding, structure, and dynamics at high resolution in living cells, is the next major step in nano cell biology. However, there are a number of major hurdles that need to be overcome, such as coupled translation and folding, the intervention of chaperones and folding enzymes, translocation, export, and the targeting machinery, proteasomes and degradation signals, etc. Although some progress has been made in recent years (Royer, 2006), current technology available in the field is limited for an enhanced resolution study, and no major breakthrough has been achieved in this direction. The major challenge is to develop new approaches that permit high-resolution, direct, and accurate structural measurements of protein folding and structure, in specific compartments of living cells. In this chapter, we focus on a review of a QQ-reagent based protein transduction recently developed in our laboratory technology that may allow us to develop a high-resolution *in vivo* investigation of protein folding, structure, and dynamics.

I. Introduction

A. Challenges in Cell Biology

Traditional cell biology studies of living cells, including cell physiological properties, structures, organelle properties, interactions with cell environment, cell life cycle, division, and death (Alberts *et al.*, 2002). It utilizes techniques such as microscopy with immunostaining, gene manipulation/transfection, cell culture with radioactive tracers, PCR, *in situ* hybridization, and microarrays. Although these techniques are quite powerful, they are low-resolution techniques, with the most powerful electron microscopy achieving a resolution of no better than 100 nm (Alberts *et al.*, 2002). Green fluorescence protein (GFP) has become a popular reporter in cell biology (Shaner *et al.*, 2007). GFP technology may also provide rough structural information of protein complexes in living cells using Forster Resonance Energy Transfer (FRET) (Piston and Kremers, 2007). However, GFP is a 27-kDa protein, a size that prohibits any accurate distance measurement, and thus it is still a low-resolution technique. Structural biology, in contrast, studies the architecture/shape/structure of biological micromolecules and what causes them to have their structures (Liljas *et al.*, 2008). This subject is of great

interest to biologists since micromolecules carry out their functions based on their specific three-dimensional (3D) structure. The structural biology methods include: X-ray crystallography, nuclear magnetic resonance (NMR), ultra fast laser spectroscopy, electron cryomicroscopy (cryo-EM), fluorescence spectroscopy, and circular dichroism (Liljas *et al.*, 2008). Among these methods, only X-ray crystallography, NMR, and cryo-EM allow for determination of 3D structure of biomolecules at atomic resolution. Unfortunately, these techniques are *in vitro* methods and use samples of pure micromolecules in a test tube, potentially resulting in a high risk of artifacts and unreliable prediction of biochemical functions. The key problem to date is the separation or noninteraction between cell biology and structural biology. We cannot apply techniques from both disciplines simultaneously and synergistically to the identical sample.

Most proteins function inside cells. The cellular environment is a highly crowded, viscous solution that harbors an intricate network of biological activities simultaneously exerted by a large number of micromolecules (Ellis and Minton, 2006). A pure protein in the test tube does not necessarily represent the true nature of the cellular environment. Although *in vitro* structural analyses of pure proteins have shaped our understandings of many biological processes at atomic resolution, these understandings do not necessarily reflect the true process inside the cell. Indeed, there is no experimental data currently demonstrating that the *in vitro* determined protein structure is identical to the structure of the protein inside the cells. There are many fundamental questions that remain unanswered in cell biology and structural biology: Does an *in vitro* determined protein structure represent its cellular conformation? How do posttranslational modifications affect protein structure? Does a protein exhibit the same fold and undergo the same folding pathway outside/inside cells? Does a protein exhibit the same dynamics outside/inside cells? Do proteins bind to their interacting partners in the same way outside/inside cells? Are the binding-induced conformational changes of proteins the same outside/inside cells? How does a protein respond structurally to cellular processes, such as cell cycle progression, apoptosis, or cell differentiation? Clearly, these are key issues and no current technology can be used to address these important questions.

B. In-Cell Structural Biology

To enhance cell biology to atomic resolution, the major challenge is how to synchronize and integrate cell biology and structural biology techniques, for simultaneous and synergistic application of these techniques to the same samples. Among high-resolution structural biology techniques, X-crystallography, and cryo-EM are intrinsically prohibited from *in vivo* applications using living cells, due to the requirement for single crystals (X-ray) or frozen, vitrified (Cyro-EM) samples (Frank, 2006; Usón and Sheldrick, 1999). NMR spectroscopy, the only other technique for structural determination at atomic resolution, allows for direct observation of labeled proteins within any unlabeled cellular environment and

can be employed to study proteins inside cells (Serber *et al.*, 2006). To perform high-resolution NMR experiments, the bio-micromolecule has to be isotopically labeled with stable isotopes. For example, protein NMR requires proteins to be isotopically labeled with ^{13}C, ^{15}N, and ^{2}H (Tugarinov *et al.*, 2006). Bacteria cells are usually used to isotopically label protein, since bacterial cells can grow in a minimal essential medium that contains ^{13}C-glucose, $^{15}NH_4Cl$, and D_2O as the nitrogen, carbon, and deuteron source (McIntosh and Dahlquist, 1990; Sivashanmugam *et al.*, 2008).

Indeed, NMR spectroscopy has been used to monitor the folding and structures of different proteins in living bacterial cells (Serber *et al.*, 2006). This *in-cell* NMR technique takes advantage of high-level expression and isotope-labeling of a protein of interest in bacteria (Selenko and Wagner, 2007; Serber *et al.*, 2006). Recently, a STINT–NMR technique has been developed to map the structural interactions that underlie protein–protein complex formation (Burz *et al.*, 2006). This method entails sequentially expressing two (or more) proteins within a single bacterial cell in a time-controlled manner and monitoring their interactions using *in-cell* NMR spectroscopy. In 2006, a report from Wagner's laboratory showed *in-cell* NMR studies of a small protein, protein G B1 domain, in intact oocytes (Selenko *et al.*, 2006). This study used a eukaryotic cellular system, the *Xenopus laevis* oocyte, for *in-cell* NMR analyses of biomolecules at high resolution and delineated the experimental reference conditions for successful implementations of *in vivo* NMR measurements in this cell type. Very recently, the same group, used the same cellular system, reported an *in situ* observation of protein phosphorylation, which is the first observation of *de novo* protein phosphorylation in whole live oocyte cells (Selenko *et al.*, 2008). To introduce the isotope-labeled protein needed for NMR experiments, these authors took advantage of the large size of oocytes and micro-injected a high concentration isotope-labeled protein into the oocytes. Although this oocyte system is quite attractive for *in-cell* NMR, it raises a critical question regarding the physiological relevance of these *in-cell* NMR experiments. Does this micro-injected exogenous protein undergo the same secretion pathway as that of the endogenous protein? Since a biochemical reaction of an intracellular protein can only occur in a certain intracellular compartment, the secretion pathway of this micro-injected protein inside cells will be critical to the physiological relevance of *in-cell* NMR experiments. The second major question concerns the high protein concentration that is required for these *in-cell* NMR experiments. NMR technique is not a sensitive technique and generally requires >50 μM protein concentration for data collection (Kelly *et al.*, 2002). The physiological relevance of such high concentrations will be a major concern for biologists, since no protein has such a high concentration inside cells. Finally, the micro-injection method is not a universal protein transduction method that can be utilized to introduce isotopically labeled proteins into any eukaryotic cells.

Fluorescence spectroscopy is another structural technique (Lakowicz, 2006). Although it is generally considered to be a lower resolution technique, the well developed FRET technique is often used *in vitro* to measure the distances between

fluorescence donor and acceptor at atomic resolution and can thus provide important information about protein folding and structure (dos Remedios and Moens, 1995). However, FRET can only provide one distance from one pair of fluorescence donor and acceptor each time. To determine a protein structure at atomic resolution, hundreds to thousands of distances within a protein are necessary. This requires enormous amount of work, including mutagenesis, protein production, fluorescence labeling and, FRET measurement of every pair of fluorescence donor and acceptor. FRET measurement can also be carried out in living cells using the GFP/RFP technique (Piston and Kremers, 2007). The *in vivo* FRET measurement is widely used to study protein–protein interactions and protein domain–domain interactions, however, the distance measurement between GFP and RFP seems to be meaningless, since both GFP and RFP are proteins of 25–28 kDa. Therefore, *in-cell* fluorescence spectroscopy is not considered to be a viable high-resolution structural biology tool. To solve this problem, small molecule fluorophores would have to be introduced into the protein for accurate distance measurement between fluorescence donor and acceptor, which is not possible for *in vivo* labeling. Although tremendous efforts have been made over the past two decades for *in vivo* fluorescence labeling, little progress has been made so far (Giepmans *et al.*, 2006). On the other hand, *in vitro* fluorescence labeling is a mature technique that is routinely used by structural biologists to label micromolecules.

Fluorescence imaging is a technique routinely used to study protein location and trafficking in living cells (Giepmans *et al.*, 2006). Currently, this technique extensively utilizes GFP-fused protein in either the N- or the C-terminal end of a protein. Using a confocal microscope, the GFP-labeled protein can be visualized for their locations and trafficking inside the cells. However, it is unknown whether the GFP fusion changes the location of the protein of interest inside cells (Piston and Kremers, 2007). Thus, extensive control experiments have to be carried out. Even with these control experiments, sometimes the situation inside the cells is complex and no definite conclusion can be made using fluorescence imaging (Piston and Kremers, 2007). Once again, small molecule fluorescence labeling is also preferred for fluorescence imaging to minimize the artifact of these experiments. An alternative method is to fluorescence label protein *in vitro* and to deliver it into the cells. The micro-injection technique has been used to inject the *in vitro* small molecule fluorescence labeled protein inside cells (Heikkila *et al.*, 2006; Korthout *et al.*, 2000). Once again, the same question, regarding the secretion pathway of injected protein, applies to *in-cell* fluorescence imaging.

C. Challenges in Intracellular Protein Therapy

The cell membrane builds a barrier that regulates micromolecular material flow into and out of the cell to maintain cell integrity and block exogenous proteins, peptides, genes, and RNA from freely entering the cell (Foged and Nielsen, 2008). While the cell membrane maintains cell integrity and protects the cells from foreign

material invasion, this protective barrier also blocks micromolecules from entering the cells, thus hindering high-efficient therapeutic applications using these ''information-rich'' micromolecules. Traditional pharmaceutical approaches have therefore largely relied upon the serendipitous discovery of specific small molecule drugs that are ''information-poor,'' often suffering from poor target specificity, adverse side-effects, and toxicity (Shaikh *et al.*, 2007). To solve these problems, the major challenge is to circumvent the cell membrane barrier, so that the therapeutic micromolecule can be readily delivered into the specific target cells/tissues and intracellular compartment for highly efficient therapy. Until recently, transduction of micromolecules was usually achieved by microinjection, electroporation, viral delivery systems, liposomes, and receptor mediated endocytosis (Wu and Wu, 1991). Unfortunately, these methods are often plagued by limited efficiency, complicated manipulation, and cellular toxicity (Trehin and Merkle, 2004). For example, gene therapy usually applies viral delivery systems to deliver gene inside the cells for therapeutic applications (Hu, 2008; Park *et al.*, 2008). This viral delivery system may result in significant complications, causing serious viral infections to the patients (Breyer *et al.*, 2001; Marshall, 2000). Another major problem of the above transduction methods is the lack of targeting capability. These methods cannot specifically deliver micromolecules to certain tissue types and different cellular compartments (Park *et al*, 2008; Schwendener, 2007). This raises a major question about the physiological relevance of these techniques. Indeed, if the micromolecules delivered using the above techniques scramble everywhere inside the cells, they may cause significant cellular toxicity. In contrast, a targeted delivery of micromolecules to the specific tissues and intracellular compartments, where the biochemical reaction occurs for this micromolecule, will efficiently utilize this micromolecule for therapeutic application with minimal intracellular toxicity.

Many human diseases are related to the malfunctioning of particular proteins, either systemically or locally. Therapeutic proteins, including native and engineered proteins, can be used as highly effective medical treatments (protein therapy) for a wide array of diseases in which the proteins are either lacking or deficient, or, alternatively, to inhibit biological processes that cause diseases. For example, insulin is routinely used for muscle injection to treat diabetes patients, since insulin interacts with plasma membrane located insulin receptors. One potential problem of protein therapy, though, is that the therapeutic protein can be metabolized before it even reaches the target tissues and intracellular locations. Additionally, for many diseases, the disease-causing biological processes occur intracellularly. Therefore, intracellular protein therapy may be required to use therapeutic protein to treat these diseases. Intracellular protein therapy requires a special delivery system that not only delivers the therapeutic protein to the diseased tissues, but also to the correct cellular compartment where the disease-causing biochemical reaction occurs. These additional requirements make intracellular protein therapy a much more complicated undertaking, so that currently we do not have such a ''smart'' delivery system available for intracellular protein therapy.

D. Protein Transduction Techniques

A new, noninvasive protein transduction technology is emerging, following the discovery of the protein transduction domain (PTD) or cell-penetrating peptide (CPP) (Trehin and Merkle, 2004; Wadia and Dowdy, 2002). These PTD/CPPs are small peptides of less than 30 amino acids that have the ability of entering cells in an unconventional way. Fusion of PTD/CPP with bioactive cargo, such as protein, DNA, or RNA, allows for the intracellular delivery of this micromolecule (Deshayes *et al.*, 2005; Melikov and Chernomordik, 2005; Wadia and Dowdy, 2005). The protein transduction using PTD/CPP was galvanized by a report on the ability of HIV-1 Tat fusion to deliver β-galactosidase to multiple tissues, including the liver, spleen, lung, heart, and brain, in mice (Schwarze *et al.*, 1999). However, PTD/CPP fused proteins do share common disadvantages, including high cost, metabolic instability, and lack of targeting capability. Efforts are being made to pursue non-peptide reagents that can effectively deliver bioactive cargo into cells. Polyethyleneimine (PEI) has been used as a food additive and is found to have the ability to deliver protein and DNA intracellularly (Futami *et al.*, 2005; Huang *et al.*, 2005). A recent publication reported small molecule mimics (SMoCs) that have a similar protein transduction property (Okuyama *et al.*, 2007), which is considered a breakthrough in protein transduction, especially for its *in vivo* applications.

Despite these notable successes, the use of protein transduction technology has yet to become common place in cell biology and in intracellular protein therapy. Several major challenges lay in front of this new technology and prevent it from being widely used in many fields of biomedical sciences. The first challenge is the fate or secretion pathway of delivered exogenous proteins using protein transduction technology. It is still unknown how the exogenous proteins traffic inside cells after being delivered into cells. The famous Blobel's "Signal Theory" guides the fate of endogenous protein to traffic inside the cells and dictates the intracellular locations of endogenous proteins (Blobel and Sabatini, 1971). Questions have been raised regarding whether the exogenous proteins, after transduction inside cells, follow the same secretion pathway. These questions must be addressed in order to establish the physiological and pathological relevance of protein transduction technology. The second major challenge is the lack of delivery specificity of the current protein transduction agents, in terms of targeting to specific cell types and specific cell compartments. Indeed, the current protein transduction reagents are not "smart" enough to specifically deliver exogenous proteins into a target tissue or to a target cellular compartment. It is particularly critical to target different intracellular compartments for cell biology applications. In addition, lack of targeting capability of the current protein transduction technology also inhibits the application of intracellular protein therapy.

E. A Possible Solution to Address These Challenges

We report here a new protein transduction reagent, the QQ reagents, and their application in cell biology. The QQ reagents were newly developed in our laboratory and they are PEI-based, with several other ingredients. The QQ reagents have the

following features that are unique and novel and distinctly different from the currently available protein transduction reagents (Li and Wang, 2008a; Li *et al.*, 2008a):

1. A high efficiency of protein transduction (near mM protein delivery into the cells).
2. A noninvasive protein transduction method that is applicable to any mammalian cells.
3. A protein transduction method with the capability of specific delivery of exogenous proteins to their target intracellular compartments.
4. The QQ reagents can either noncovalently or covalently associate with protein and dissociate from the protein inside cells. Thus, the protein under investigation is not functionally altered.
5. The QQ reagents are food additives that have been approved by the FDA, and have no or little intracellular toxicity.
6. The QQ reagent protects proteins from protease degradation inside the cells.
7. The application of QQ reagent is very simple and requires only a single step of incubation with cells. No other steps, such as molecular cloning in the case of CPP/PTB, are necessary.
8. The QQ reagent enables multiple proteins to be delivered into cells simultaneously or consecutively.

With these unique and novel features of the QQ reagents, we are able to develop novel techniques to study protein folding, structure, interaction, intracellular trafficking, and location in living mammalian cells. Furthermore, these unique and novel features of the QQ reagents make protein transduction technology physiologically and pathologically relevant. Finally, with the ''targeting capability'' of the QQ reagents, we are also currently exploring intracellular protein therapy to treat human diseases.

II. Rationale

Our rationale is straightforward: To develop smart protein transduction reagents that can efficiently deliver either labeled proteins or therapeutic proteins into specific cellular compartments. Thus, delivery efficiency and target capability are the two key components of these smart protein transduction reagents. Figure 1 summarizes this rationale (Li and Wang, 2008a; Li *et al.*, 2008a). However, several fundamental questions need to be addressed before we can apply this protein transduction technique to cell biology and intracellular protein therapy. The first question is the refolding capability by cellular folding machinery, since bacterial expression often results in misfolded protein with either no defined structure or a misfolded structure. An answer to this question directly determines if the intracellular protein transduction technology is useful. The second question is the

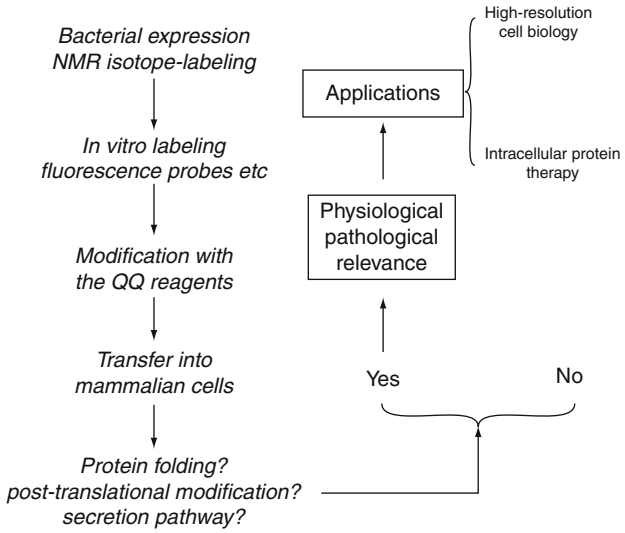

Fig. 1 A schematic diagram of the QQ-reagent based protein transduction technology and its potential applications.

capability of posttranslational modification by cellular machinery, since bacterial cells do not have this capability. The third question is the secretion pathway of the QQ reagent delivered exogenous proteins. We have to determine if the delivered bacterial expressed proteins follow the same secretion pathway as the endogenous proteins, or if they create a different secretion pathway. Obviously, an answer to this third question would also directly determine the physiological and pathological relevance of this protein transduction technology. We designed and carried out experiments, particularly to address these three important questions.

III. Methods and Materials

In this section, we will primarily focus on a review of the QQ reagents, by demonstrating their unique and novel features. In addition, our experimental data demonstrates that the bacterial expressed proteins, once they enter into mammalian cells, can be properly folded and posttranslationally modified by the mammalian cell machinery and carry out the correct biological functions. Most importantly, these exogenous proteins follow the identical secretion pathway as that of the endogenous proteins. Thus, our data establishes the physiological and pathological relevance of QQ-reagent based protein transduction technology. This review contains a large body of unpublished results that we have already submitted to different journals for publications.

A. The QQ Reagents

The QQ reagent is a cocktail of several different reagents that enables proteins to be delivered into mammalian cells (Li and Wang, 2008a; Li *et al.*, 2008a). The QQ reagent includes cation reagents, a lipid and, an enhancer. One example of an appropriate cation reagent is polyethylenimine (M.W.: 600, 2000, and 25,000 Da). The lipids that we used include: DOTAP, DOPE, POPC, and DMPE. The enhancers are MG132, protease inhibitor, $CaCl_2$, DMSO, and Na_2HCO. Table I lists recipes of seven different QQ reagents. Usually, we prepare stock solutions of each reagent as in Table II. The QQ reagents are usually freshly prepared before protein transduction experiments by mixing different cation reagents, lipids, and enhancers according to the recipe shown in Table I. We usually make a final volume of 5 ml of the QQ reagents.

For different experiments, different QQ reagents can be chosen. For example, to observe protein trafficking and location using fluorescence imaging, QQ1 which causes the smallest degree of cellular toxicity, can be used. Our results showed that QQ1 could be incubated with cells in the presence of protein for a few days without causing significant cell death. For production of a large quantity of properly folded and posttranslationally modified protein, which requires maximum loading in a

Table I
Recipes for Different QQ Reagents from the Stock Solution of Cation Reagents, Lipids, and Enhancers

		Cation reagents				Lipids				Enhancers		
QQ	2K	8K	12K	25K	60K	DOTAP	DOPE	POPC	DMPE	DMSO	MG132	Ca^{2+}
Reagent[a]	μl	μl	μl	μl	μl	μl	μl	μl	μl	μl	μl	μl
QQ1	200					50	50			50	5	10
QQ2	200			50	5	50	50			50	5	10
QQ3	100	100		100		50	50			50	5	10
QQ4	100	50	50	50		50	50			50	5	10
QQ5	100	100		50		50	50			50	5	10
QQ6	100	50	50	50				50	50	50	5	10
QQ7	100	50	50	50		25	25	25	25	50	5	10

[a]Total volume is 5 ml when preparing the QQ reagents. We also dissolve the protein at a concentration of 0.2–8.0 mg/ml, depending on protein solubility and the purpose of the studies.

[b]In our hand, 2K produces the least cellular toxicity whereas 60K produces the most cellular toxicity.

Table II
Concentrations of Cation Reagents, Lipids, and Enhancers in the Stock Solutions

	Cation Reagents				Lipids				Enhancers		
2K	8K	12K	25K	60K	DOTAP	DOPE	POPC	DMPE	DMSO	MG132	Ca^{2+}
mg/ml	mg/ml	mg/ml	mg/ml	mg/ml	mg/ml	mg/ml	mg/ml	mg/ml	mM	mM	mM
50	20	20	50	50	1	1	1	1	100	1	1000

short time, QQ2 or QQ7 may be used. Cells survive and remain healthy for a short period of incubation time (8–14 h) with these QQ reagents. For these experiments, cells are washed after loading using regular culture medium several times to remove the excess QQ reagent and then incubated with culture medium.

B. Protein Modifications with the QQ Reagents

Proteins of interest are first dissolved into sodium phosphate buffer (50 mM, pH 7.0, NaCl 50 mM) at concentrations of 0.5–10 mg/ml, depending on the protein solubility. To completely dissolve proteins, an overnight stir of the protein solution at room temperature is performed.

A lipid DOTAP/DOPE (1:1) emulsion is prepared using the following method: 1 mg of DOTAP/DOPE (0.5 mg:0.5 mg = 1:1) mixture is dissolved in chloroform and dried under N_2 gas. The dried lipid film is then dissolved in PBS buffer, pH7.0, and the lipid solution is sonicated for 3 × 30 s using a power of 7–8 W on a sonicator from Fisher Scientific (Model 100) with a micro probe. The lipid solution is further incubated at 37 °C for 2 h until the suspension becomes semi-clear. The prepared emulsion is stored at 4 °C, where it is stable for 1 month.

The QQ reagents (not including the lipid emulsion, Ca^{2+}, and DMSO) are mixed in a tube, according to the recipe described in Table I. The QQ reagent is then titrated into the protein solution very slowly dropwise, while stirring, and then adding lipid emulsion and Ca^{2+}. Once the titration is complete, the protein solution is left at room temperature for 4 h before use. During this period, the solution is gently stirred to allow for completion of the protein modification reaction. If precipitation is observed, the protein solution can be centrifuged to remove the precipitate. A BCA protein assay is carried out on the supernatant to check protein concentration. To ensure the efficiency of protein transduction, the concentration of modified protein has to be at >0.2 mg/ml. If the majority of the protein precipitates, another QQ reagent can be used for protein modification. The QQ series reagents cover a wide range of cationization reagents along with different lipids and enhancers, thus the precipitation problem should be easily solved. The modified proteins are passed through a desalting column or a spin column to separate the modified protein from the remaining free QQ reagents. The purified protein fractions can be concentrated using a spin column and can be stored at 4 °C or −20 °C for a few weeks (Li and Wang, 2008a; Li *et al.*, 2008a).

C. Protein Transduction into Mammalian Cells

The fresh modified protein is mixed with cell culture medium (DMEM) with MG132 (3 ng/ml), protease inhibitor cocktail (2 μg/ml), DMSO (30–50 μl/ml), and growth factor (1 ng/ml) (with or without 2% FBS). The culture medium is kept on a shaking platform for 10 min at room temperature to make sure that the protein is completely dissolved. The mammalian cells are then added, which are seeded for 2–3 days to about 80–90% confluency for monolayer cells or 3–5 day old HeLa cell

suspensions. The FBS concentration used in the experiments does not affect the protein delivery.

Once protein loading is started, the cells are closely monitored using a microscope. Though minor cell morphology changes are observed after protein loading, these cell morphology changes are reversible. Upon removing the loading medium and resuspending the cells into normal DMEM culture medium, cells are able to return to their original morphology. In addition, the cell morphological changes during protein transduction depend on the amount of free QQ reagents in the medium. Initially, much significant cell morphology changes were detected when free QQ-reagent was not removed. This was because of the large ratio of QQ reagent to protein used. Once a purification step was added to remove the free QQ reagents, only minor cell morphology changes were observed. However, generally, a purification step is only necessary when cellular toxicity becomes an issue.

After protein transduction, the cells are washed three times with 15 ml PBS buffer (pH 7.4). This is a very important step for all experiments. The last wash can be using a lower pH PBS buffer (pH 5) to remove any cell surface bound proteins. This wash is for only 1 min and the cells are kept on ice. The low pH PBS wash buffer is quickly removed by spinning down the cells and discarding the supernatant. The cells are then resuspended into DMEM cell culture medium (pH 7.4), and are ready for further experiments (Li and Wang, 2008a; Li *et al.*, 2008a).

D. High Protein Transduction Efficiency Using the QQ Reagents

Using human apolipoprotein AI (apoAI) (Marcel and Kiss, 2003), we tested our QQ reagents with different mammalian cell lines, including: HeLa, HEK-293T, CHO, Raw264.7, MCF7, and BHK-21 cell lines. Figure 2, Right Panel demonstrates the experimental protocol for these experiments. Left Panel A shows the results, clearly demonstrating that apoAI has been delivered into these different mammalian cells. We used an anti-His-tag antibody in these experiments since the apoAI we used contains a short His-tag. Indeed, endogenous proteins in these mammalian cells do not contain a His-tag, thus, a band shown in the western blot indicates the intracellular location of delivered apoAI by the QQ reagent. We also tested different QQ reagents for their protein delivery efficiency into the HeLa cells. Left Panel B shows the results, demonstrating that QQ1 and QQ2 have the best delivery efficiency for human apoAI under the condition we used. Other QQ reagents, such as QQ3 and QQ4 or lipids show poor delivery efficiency. Left Panel C suggests that the ratio of QQ1/apoAI is important for high protein transduction efficiency. For example, at smaller ratios of QQ1/apoAI, such as 5:1, 10:1, and 20:1, protein delivery efficiency was low. As negative controls, HeLa cell lysate does not contain apoAI and apoAI itself without QQ1 (QQ1: apoAI = 0:1) cannot penetrate into HeLa cells. In contrast, ratios of 40:1 and 100:1 gave good protein transduction efficiency. In our experiments, we usually use QQ/protein ratio >40:1, as indicated in the figure legend. In Left Panel D, we did a time course and found that 1 h after incubation, the protein transduction efficiency was

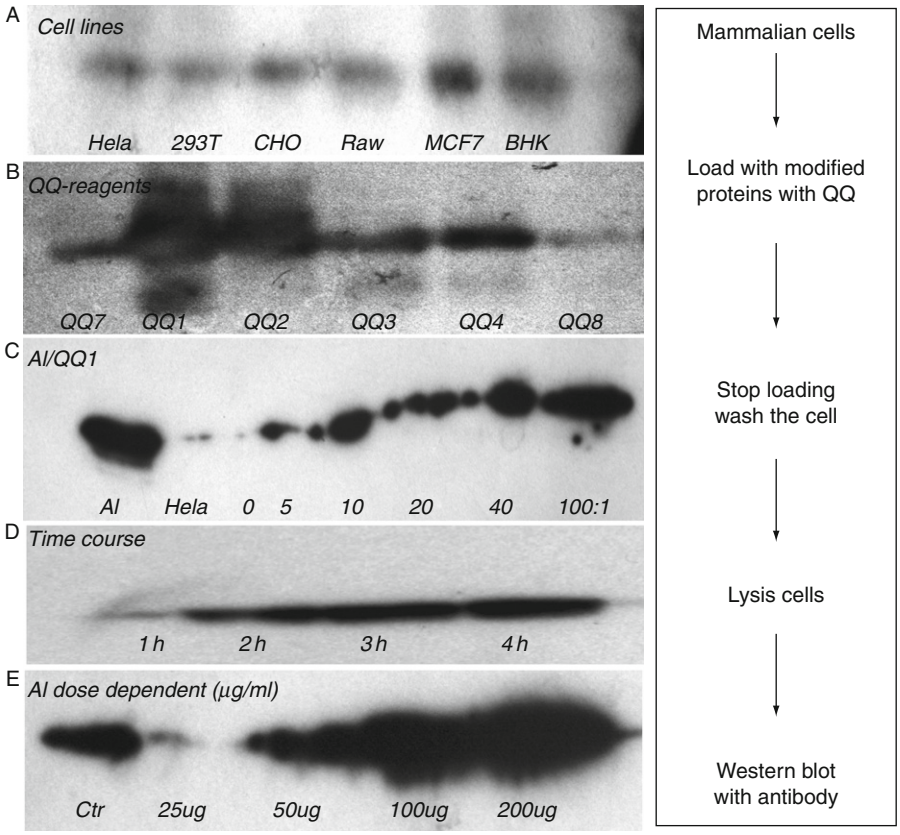

Fig. 2 Right Panel: A schematic diagram of the experimental procedure used in obtaining Left Panel. Left Panel: (A) A western blot of transduced human apoAI in different cell lines as indicated in the bottom. (B) A western blot of transduced apoAI in HeLa cells using different QQ reagents. The cell loading time: 2 h. The protein:reagent ratio kept the same: 1:50. (C) A western blot of transduced apoAI in HeLa cells using different ratio of apoAI/QQ1 reagent, as indicated in the bottom. (D) A western blot of the time course of transduced apoAI using an apoAI/QQ1 ratio of 40. The time points are shown in the bottom. (E) A western blot of apoAI dose dependence at a fixed apoAI/QQ1 ratio of 1:40. ApoAI concentrations are shown in the bottom. The antibody is an anti-His-tag antibody since the apoAI we used contains a short his-tag. ApoAI concentration: 1 mg/ml. Protein loading time: 2 h unless indicated.

low. However, after 2 h, apoAI transduction significantly increased and reached a maximum loading after 3–4 h. No significant increase of apoAI transduction was observed after 4 . Left Panel E demonstrates that the apoAI concentration is critical for the protein transduction efficiency. A low protein transduction was observed at low apoAI concentrations (25 μg/ml and 50 μg/ml). However, a higher apoAI concentration of 100–200 μg/ml produced high transduction efficiency.

Figure 3 lists the other proteins tested, including the ligand-binding domain (LBD) of apolipoprotein E receptor 2 (LBD-apoER2), the first YWTD/EGF

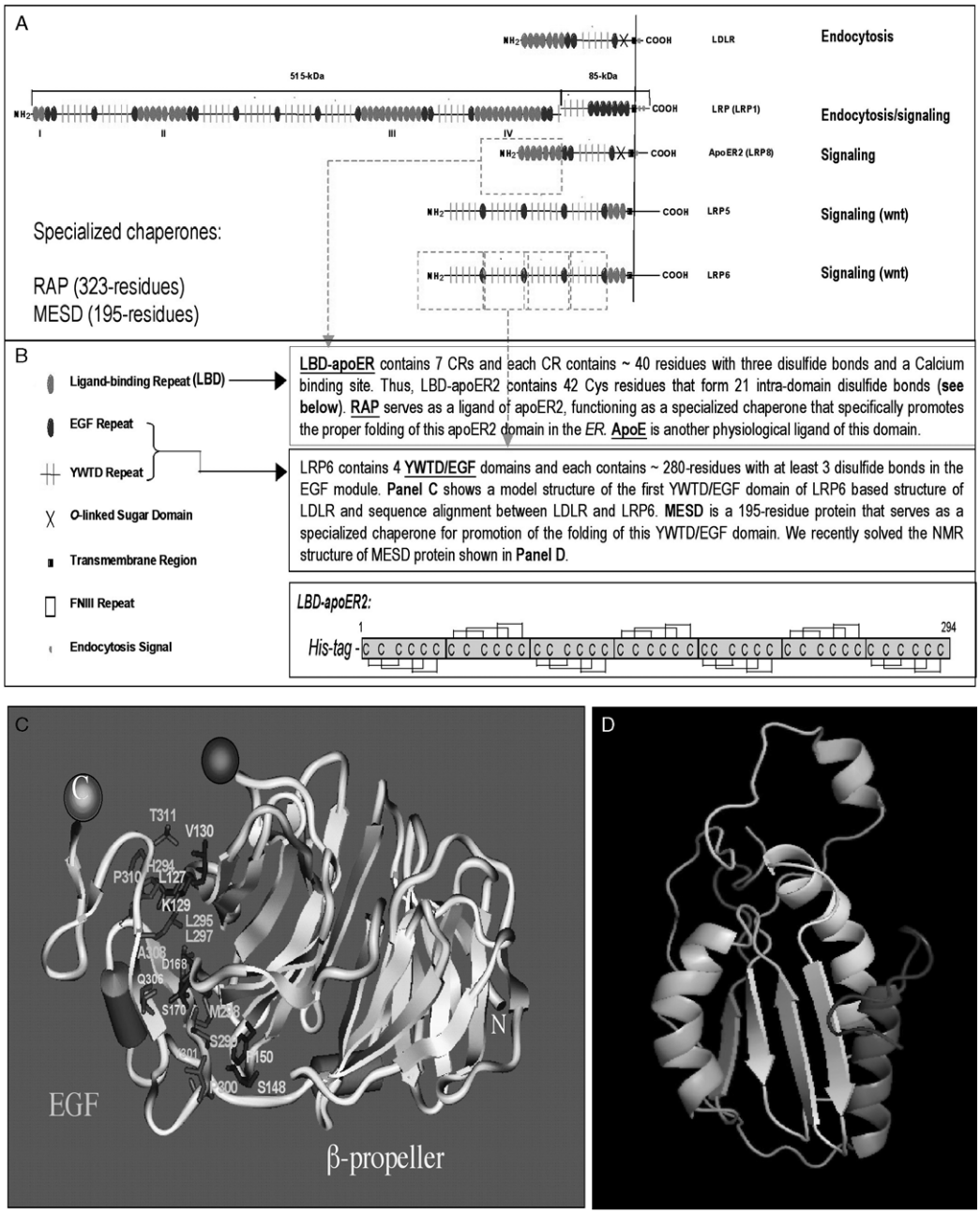

Fig. 3 Panel A: A schematic diagram of the modular structures of the representative members of the LDL receptor family, including: LDLR, LRP1, apoER2, LRP5, and LRP6. Panel B: Left: Different sequence modules within the members of the LDLR family. Right: Explanation of the sequence,

domain of lipoprotein receptor related protein 6 (LRP6), apoE, receptor associated protein (RAP), and mesoderm development protein (MESD). Panel A shows several representative members of the low-density lipoprotein (LDL) receptor family, which contains several different modules, including the ligand-binding repeats, the YWTD/EGF module, O-linked sugar domain, a transmembrane domain, and a cytoplasmic domain (Panel B) (Li *et al.*, 2001; Nykjaer and Willnow, 2002; Strickland *et al.*, 2002). ApoER2 is a member of the LDL receptor family which serves as a Reelin receptor that regulates Reelin signaling, playing a critical role in neuronal migration, synaptic transmission, and male fertility (D'Arcangelo, 2005; May *et al.*, 2005). The ligand-binding repeat contains the seven Complement-type Repeats (CRs). Each CR contains ~40-residues including six Cysteine residues, forming three intraCR disulfide bonds. In addition, each CR also has a Ca^{2+}-binding site. The YWTD/EGF module also contains at least six Cysteine residues in the EGF module. The folding of these two domains is very complex. The X-ray crystal structure of the YWTD/EGF domain of the LDL receptor is solved by Blacklow's laboratory which shows a β-propeller structure (Jeon *et al.*, 2001). Using homology structural modeling, we generated the structure of the first YWTD/EGF domain of LRP6 (Panel C), based on this crystal structure and sequence alignment between low-density lipoprotein receptor (LDLR) and LRP6. RAP is a 323-residue protein, which serves as a ligand of LBD-apoER2. The biological function of RAP serves as a specialized chaperone that specifically promotes the proper folding of LBD (Bu and Schwartz, 1998). ApoE is a physiological ligand of the LBD-apoER2 (Hatters *et al.*, 2006). MESD is a 195-residue protein that serves as a specialized chaperone for proper folding and trafficking of the YWTD/EGF domain (Culi and Mann, 2003; Culi *et al.*, 2004; Hsieh *et al.*, 2003). We recently determined the NMR structures of the most conserved domain of MESD (Chen *et al.*, 2008a) and full-length MESD (Chen *et al.*, 2008b) (Panel D). In this report, we mainly focus on LBD-apoER2, the first YWTD/EGF domain of LRP6, RAP, and MESD.

Figure 4 shows more examples using three different proteins. Panel A is an SDS-PAGE, showing the loading efficiency of human apolipoprotein E (apoE) N-terminal domain, apoE(1–183). Human apoE is a lipid transport protein that plays a critical role in atherosclerosis and Alzheimer's disease (Hatters *et al.*, 2006). In this panel, Lanes 5–8 provide defined concentrations of apoE(1–183) at 50 μM (Lane 5), 100 μM (Lane 6), 200 μM (Lane 7), and 350 μM (Lane 8), serving as controls. Lane 1 is HeLa cell lysate without apoE transduction as a negative

structure, and functional properties of the proteins that are used in this study, including: LBD-apoER2, RAP, apoE, the first YWTD/EGF domain of LRP6 and MESD. Right Bottom: A schematic diagram of sequence property of LBD-apoER2 with 21 intraCR disulfide bonds. Panel C: A homology model structure of the first YWTD/EGF domain of LRP6 based on the X-ray crystal structure and sequence homology of this domain between LDLR and LRP6. Panel D: The NMR structure of MESD(12–155) which is the most conserved domain of this protein. This NMR structure is determined recently in our laboratory.

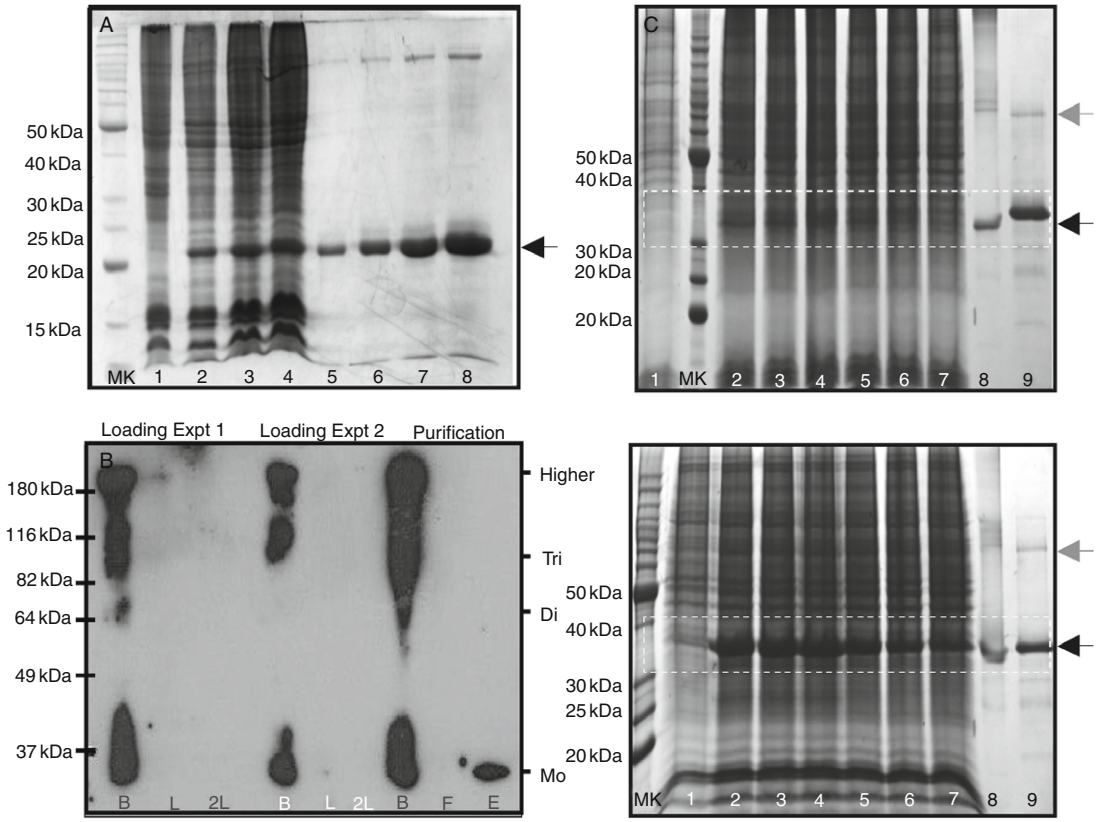

Fig. 4 (A) A SDS-PAGE, showing the loading efficiency of human apoE N-terminal domain. Lane 1: HeLa cell lysate without apoEN transduction (20 μl). Lanes 2–4: HeLa cell lysate with apoEN transduction (Lane 2: 10 μl, Lane 3: 20 μl, and Lane 4: 40 μl lysate loaded in the SDS-PAGE). Lanes 5–8: Defined concentration of apoEN (20 μl loading) as control (ApoEN concentration: Lane 5: 50 μM, Lane 6: 100 μM, Lane 7: 200 μM, and Lane 8: 350 μM). (B) A western blot of cell loading efficiency of QQ reagent modified LBD-apoER2 using an anti-His-tag antibody. The QQ-reagent modified LBD-apoER2 was incubated with HeLa cell for 4 h (Lane L). The cell was spun down and washed several times. New HeLa cells were added to the medium and incubated for another 4 h (Lane 2L). The experiment was repeated twice. The loaded cells were lysed and purified using a His-bind resin column. Lane F: the flow through during purification. Lane E: Elution of purification using 0.5 M immidizole, only showing one single band. Lane B: Bacterial expressed LBD-apoER2, showing different oligomers. C, Upper: A SDS-PAGE, showing the loading efficiency of the first YWTD domain (YWTD1) of human LRP6. Lanes 1–8: sample without DTT. Lane 1: HeLa cell lysate without YWTD1 transduction. Lanes 2–7: HeLa cell lysate with YWTD1 transduction at 3.0, 2.5, 2.0, 1.5, 1.0, and 0.5 h. Lane 8: Bacterial expressed YWTD1 without DTT. Lane 9: Bacterial expressed YWTD1 with DTT. Both Lanes 8–9 serve as control. C, Lower: The same SDS-PAGE as C, Upper, except the samples in lanes 1–8 contained 10 mM DTT.

control, showing no band of apoE(1–183) (Red arrow). In contrast, Lanes 2–4 are HeLa cell lysates with apoE(1–183) transduction (2 h after transduction), indicating a clear band with an increased band intensity. The band intensity is certainly comparable with an apoE(1–183) concentration of $>100\ \mu$M. This result clearly demonstrated a very high efficiency of protein transduction. Panel B shows the second example, LBD-apoER2. It is a western blot of the cell loading of the QQ reagent modified LBD-apoER2 using an anti-His-tag antibody. The bacterial expressed LBD-apoER2 is misfolded, forming different oligomers due to intermolecular disulfide bond formation (Lane B). The QQ reagent modified LBD-apoER2 was incubated with HeLa cell for 4 h. The cells were spun down and the medium was loaded on gel (Lane L). The cells were washed several times and new HeLa cells were added to the medium and incubated for another 4 h and the medium was loaded again on gel (Lane 2L). The experiment was repeated twice. The loaded cell lysate was purified using a His-bind resin column. Lane F was the flow through during purification and Lane E was the elution using 0.5 M immidizole. It is very interesting that the elution band only shows one single band at the monomer level, indicating that the HeLa cell machinery converted oligomeric LBD-apoER2 into a monomer. Our results also demonstrate a high cell loading efficiency of the QQ reagent modified LBD-apoER2. Indeed, after a 4-h incubation, the QQ reagent modified LBD-apoER2 was completely delivered into the HeLa cells, no trace protein was detected in the medium. In addition, our results indicated that LBD-apoER2 might be refolded inside HeLa cells, since only monomeric LBD-apoER2 was observed (Lane E). We suggest that the oligomeric change is due to the correct folding of LBD-apoER2, thus eliminating the intermolecular disulfide bond formation. The third example is the first YWTD/EGF domain of LRP6 (Panel C). LRP6 is a member of LDL receptor superfamily which serves as a coreceptor for wnt signaling (He *et al.*, 2004). It contains four YWTD/EGF domains in its N-terminus. The first YWTD/EGF domain also contains eight Cysteines among which six are in the EGF module, forming three disulfide bonds. Panel C are two SDS-PAGEs of HeLa cell lysates before (Lane 1) and after YWTD/EGF transduction (Lanes 2–7), with (Lower) or without (Upper) DTT. Lanes 2–7 are the HeLa cell lysates of time course, ranging from 0.5 h (Lane 7) to 3.0 h (Lane 2). In addition, bacteria expressed YWTD/EGF domain is also shown in the Figure without (Lane 8) or with (Lane 9) DTT, showing the monomeric YWTD/EGF domain of LRP6 as controls. We noticed that the bacterial expressed YWTD/EGF showed a slightly different mobility with and without DTT. Without DTT, the monomeric YWTD/EGF seems to move slightly faster in the SDS-PAGE. In the upper panel, a band of YWTD/EGF is clearly seen without DTT although this band is much weaker. In contrast, the lower panel shows a strong band of YWTD/EGF with DTT. Interestingly, both lower and upper panels demonstrate that the band intensity of YWTD/EGF is dependent on protein transduction time. The longer time the YWTD/EGF is incubated, the stronger

the monomeric band is in both lower and upper SDS-PAGEs. We suggest that the monomeric band of YWTD/EGF in the upper panel shows the properly folded protein and some oligomers are also formed in this panel due to misfolding (Gray Arrow). Adding DTT in the same sample broke up these oligomers, making the monomeric band much stronger. Thus, Panel C demonstrates a high transduction efficiency of the QQ reagent for YWTD/EGF domain delivery. In addition, by comparison of the monomeric band intensity between the samples with and without DTT, we may estimate the percentage of properly folded YWTD/EGF domain protein by the HeLa cell folding machinery.

Taken together, we conclude that the QQ reagents can be used to efficiently deliver protein into mammalian cells. The delivered proteins can be easily visualized using an SDS-PAGE. In addition, this high protein delivery efficiency seems to be universal for different proteins. Thus, the QQ reagents provide a series of powerful protein transduction reagents for different applications (Li and Wang, 2008a; Li *et al.*, 2008a).

E. QQ-Reagents Protect the Delivered Protein from Intracellular Protease Degradation

Since QQ reagent is used to deliver exogenous proteins into the mammalian cells, one potential problem is that these exogenous proteins may experience degradation by intracellular proteases if they are not folded properly. We found that the QQ reagent modified proteins actually resist these potential intracellular degradations. Figure 5 shows an example. The experimental protocol is highlighted on the Right. We used mouse apoAI protein as the target protein, which is either QQ reagent modified or a ''naked protein'' without QQ reagent modification. We then added either protease cocktail with/without a protease inhibitor or HeLa cell lysate that contains cellular proteases. Upper Panel shows an SDS-PAGE of mApoAI in the presence of protease cocktail. On the left, Lanes 2–7 are mApoAI without QQ reagent modification in the presence of a different amount of protease cocktail, as indicated in the bottom of the Panel, without (Lanes 2–4) and with protease inhibitor (Lanes 5–7). On the right, Lanes 9–14 are the same as Lanes 2–7, except mApoAI is modified with the QQ reagent. Lanes 1 and 8 are mApoAI only. It is clear that in the presence of protease cocktail, ''naked mApoAI'' is completely degraded (Lanes 2–4). Protease inhibitors rescued mApoAI partially (Lanes 5–7). In contrast, apoAI modified with the QQ reagent partially resists protease digestion, as evidenced in Lanes 9–11. Furthermore, addition of protease inhibitors completely rescued mApoAI (Lanes 12–14). Lower Panel shows an SDS-PAGE of mApoAI in the presence of a different amount of HeLa cell lysate, as indicated in the bottom of this panel. Once again, ''naked mApoAI'' is completely degraded by the intracellular proteases in the HeLa cells (Lanes 1–3). However, apoAI modified with the QQ reagent partially resists protease digestion (Lanes 4–6). Based on these results, we conclude that QQ reagent modification protects protein from intracellular protease degradation (Li and Wang, 2008a,b).

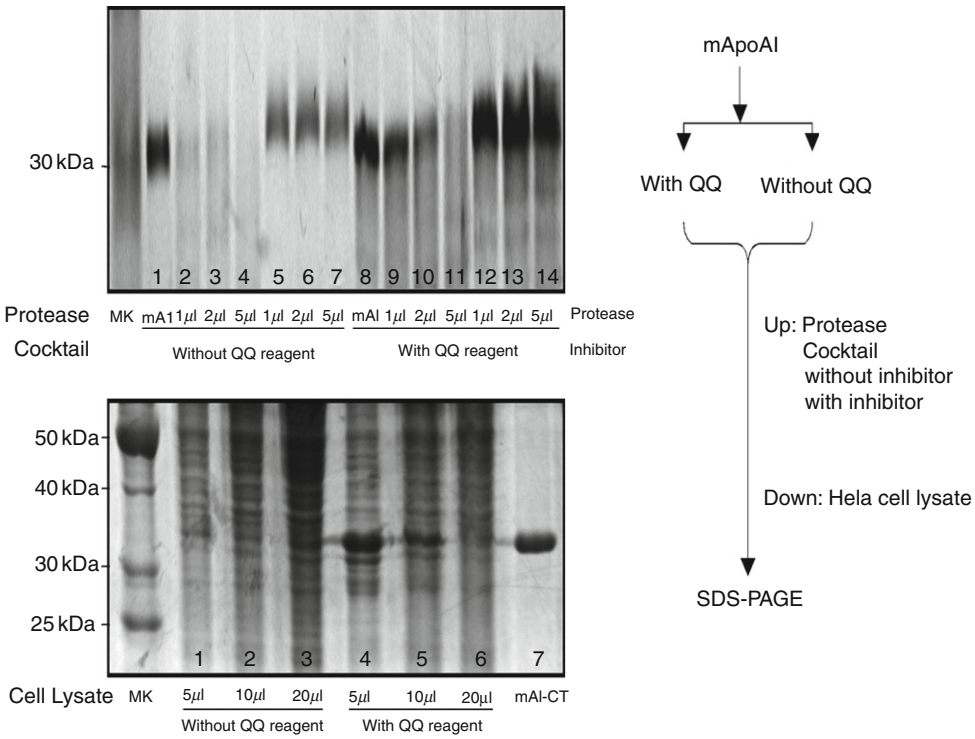

Fig. 5 Left Panel: Upper: A SDS-PAGE of mouse apoAI(1–216) either with QQ reagent modification (With QQ-reagent) or without QQ-reagent modification (Without QQ-reagent) in the presence of protease cocktail without (Lanes 2–4 and 9–11) and with (Lanes 5–7 and 12–14) protease inhibitors. Lanes 1 and 8 are mouse apoAI(1–216) without protease cocktail as a positive control. We loaded an equal amount of mouse apoAI(1–216) in all lanes. Lower: A SDS-PAGE of mouse apoAI(1–216) either without QQ-reagent modification (Lanes 1–3) or with QQ-reagent modification (Lanes 4–6) in the presence of HeLa cell lysate that contains intracellular proteases. Lane 7 is mouse apoAI(1–216) without HeLa cell lysate as a control. Right Panel: Experimental design of QQ-reagent modified mouse apoAI against degradation by proteases.

F. The QQ-Reagent has a Capability of Specific Delivery of Exogenous Proteins into Their Target Intracellular Compartments

To explore whether the QQ reagent has a capability of specific delivery of exogenous proteins to their target intracellular compartments, we used MESD, which is an endoplasmic reticulum (*ER*)-located specific chaperone protein for the proper folding of the YWTD/EGF domain of the LDL receptor family (Culi and Mann, 2003; Culi *et al.*, 2004; Hsieh *et al.*, 2003). MESD contains an RDEL ER retention signal in its C-terminus, we expect this protein to be located in the ER after protein transduction. To monitor the trafficking of this protein, we used fluorescence imaging. We took advantage of the QQ reagent and labeled MESD

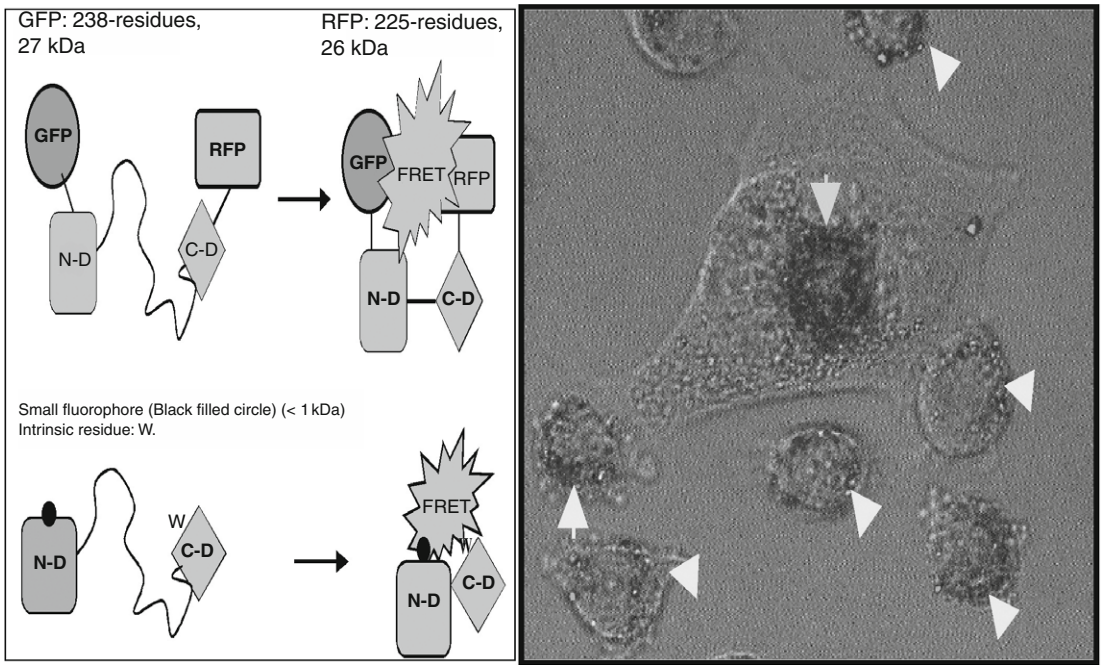

Fig. 6 Left Panel: A schematic diagram that compares GFP-based technology with the QQ-reagent based fluorescence labeling strategy. N–D and C–D indicate N- and C-terminal domain of the target protein. Right Panel: MESD was fluorescence labeled with ArrayIt 640 (Red) and then modified with the QQ1 reagent. The fluorescence labeled, QQ1-modified MESD was incubated with HeLa cells for 2 h and the cells were washed and incubated in regular cell culture medium for another 2 h before subject to fluorescence imaging. The *red color* shows the location of MESD, which is only in the perinuclei or ER/Golgi areas as highlighted by *light blue arrow*. MESD protein contains a RDEL ER retention signal, which directed this protein to be located in the ER/Golgi, as clearly showed in this figure.

in vitro using a small fluorophore, ArrayIt Red640, which has a MW of 799.8 Da. The fluorescence labeled MESD was purified with a spin column to remove the free fluorophore. We then modified labeled MESD with the QQ reagent and added the HeLa cells to incubate for 2 h. The cells were washed with the culture medium three times and then incubated for another 2 h before fluorescence imaging. Figure 6, Right Panel shows a fluorescence image that depicts the locations of the red fluorescence labeled MESD in the HeLa cells, demonstrating that the delivered exogenous MESD is predominantly located in the perinuclear area, which are the ER and *Golgi* locations, as highlighted by the light blue arrows. In this panel, the light microscopy images are superimposed with the fluorescence images, indicating the cell shapes. Interestingly, no fluorescence signals scramble to the other locations of the HeLa cells, such as the nucleus and cytosol. This data provide strong experimental evidence that the QQ reagent modification does not alter the normal intracellular locations of the transduced exogenous proteins inside

cells. This is an important evidence, since it suggests, for the first time, that the exogenous proteins, after transduction inside cells, may follow the same, normal secretion pathway as the endogenous proteins. Although more experimental evidence is required to confirm this suggestion, it shall provide, if proved, the physiological and pathological relevance of the QQ-reagent based protein transduction technology (Li and Wang, 2008a; Li *et al.*, 2008a).

Figure 6, Left Panel shows a schematic diagram that compares GFP-based technology with the fluorescence labeling strategy that we used in the above example. GPF/RFP are proteins with MW of 26–28 kDa. Although they are widely used in cell biology to study protein location, trafficking, and protein–protein interactions, it is always a concern whether the fusion of such a large protein to the target protein will negatively impact the results. This is especially true if the target proteins are smaller proteins with comparable MW to GFP (Piston and Kremers, 2007). Therefore, extensive control experiments have to be carried out to evaluate the validity of the results using GFP-technique. Even with these control experiments, sometimes the situation inside the cells is complex and no definite conclusion can be made using fluorescence imaging. In contrast, our fluorescence labeling strategy utilizes small fluorophores (<1 kDa) and labels the protein *in vitro*, and then delivers the fluorescence labeled protein into the cells for fluorescence imaging studies of protein location, trafficking, and protein–protein interactions. We anticipate that our fluorescence imaging technique should yield much less experimental artifacts, thus, obtaining more reliable results.

G. The QQ-Reagent Delivered Protein is Properly Folded Inside the Cells

To provide evidence for the physiological and pathological relevance of the QQ-reagent based protein transduction technology, the first question we have to address is if the intracellular folding machinery can refold the misfolded exogenous proteins that are bacterially expressed. The protein that we used for this purpose is LBD-apoER2 which contains 21 intraCR disulfide bonds and seven Ca^{2+}-binding sites. The folding of this complicated protein is a challenging task. The bacterial expressed LBD-apoER2 does not fold properly, forming different oligomers (Fig. 4, Panel B). Our goal is to deliver this protein into HeLa cells to allow the intracellular folding machinery of the cell to fold this protein properly. As shown in Fig. 4, Panel B, the purified LBD-apoER2 from the HeLa cell lysate only showed a single monomer band, suggesting that the delivered LBD-apoER2 may be refolded properly by the HeLa cell folding machinery.

To prove that this monomeric LBD-apoER2 is properly refolded, we carried out functional assays. Since the main function of LBD-apoER2 is to bind to ligands, such as RAP and apoE, we suggest that the properly folded LBD-apoER2 should be functional in terms of its ligand-binding activity. We performed a far-western blot to assess its RAP-binding activity. Briefly, the HeLa cell lysate was used to run a nonreducing native gel. The gel was then transformed to a nitrocellulose membrane for 2 h. After transfer, the membrane was incubated at room temperature

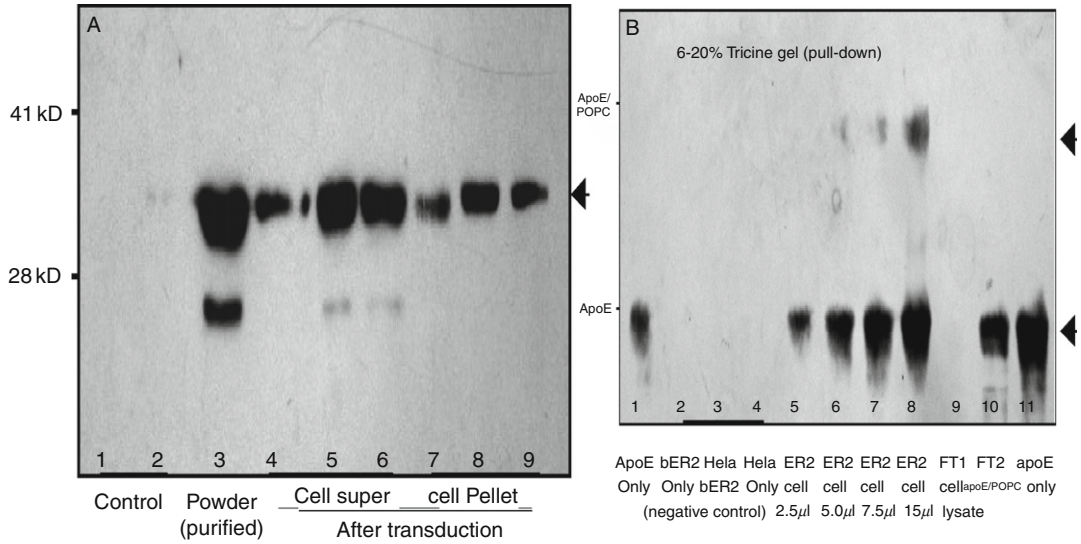

Fig. 7 Panel A: A time course of far western blot of refolded LBD-apoER2 after protein transduction, using RAP as the ligand and an antiRAP antibody. Lane 1: Bacterial expressed LBR-apoER2 as a negative control. Lane 2: HeLa cell lysate as another negative control. Lane 3: Purified LBD-apoER2 powder. HeLa cells were lysed at 44 h after protein transduction. The refolded LBD-apoER2 was purified using his-binding column and freeze-dried into powder. Lanes 4–6—Soluble fractions of HeLa cell lysate at different time points after LBD-apoER2 transduction: 5 h (Lane 4), 20 h (Lane 5), and 44 h (Lane 6). Lanes 7–9—Insoluble fractions of HeLa cell lysate at different time points after LBD-apoER2 transduction: 5 h (Lane 7), 20 h (Lane 8), and 40 h (Lane 9). Panel B: Pull down experiment results. The HeLa cell lysate, after 20 h protein transduction, was first loaded on a his-tag resin column. The flow-through of this loading was collected (Lane 9). The column was washed extensively and incubated with apoE/POPC complex, that was prepared before experiments, for 2 h and a second flow through of apoE/POPC was also collected (Lane 10). The column was then washed with PBS buffer extensively and eluted with 300 mM imidazole. The elution was then loaded on a 6–20% Tricine gel with different volumes of 2.5 μl (Lane 5), 5.0 μl (Lane 6), 7.5 μl (Lane 7), and 15 μl (Lane 8). In addition, several controls were also loaded on the gel, including apoE as the positive control (Lanes 1 and 11), bacterial expressed LBD-apoER2 (Lane 2), HeLa cell lysate mixed with bacterial expressed LBD-apoER2 (Lane 3) and HeLa cell lysate only (Lane 4). Lanes 2–4 serves as the negative controls.

with RAP for 2 h. The membrane was washed three times with 20 ml PBS/wash for 5 min each time, to remove unbound ligand (RAP). The membrane was incubated with antiRAP antibody for 1 h in 2% dry milk PBS, followed by incubation with HPR-conjugated secondary antibody for 1 h. Finally, the band is detected using ECL (Pierce). Using this assay, a band is observed at the MW of LBD-apoER2 (34 kDa) for the complex of RAP/LBD-apoER2. Fig. 7, Panel A shows the result. Lane 1 is the bacterial expressed LBD-apoER2, showing no band, indicating that bacterial expressed LBD-apoER2 does not bind RAP. Lane 2 is the HeLa cell lysate without protein transduction of LBD-apoER2, again showing no band, since HeLa cells do not contain LBD-apoER2. Lanes 4–6 and 7–9 are the

supernatant and pellet respectively of the HeLa cell lysates 5 h (Lanes 4 and 7), 20 h (Lanes 5 and 8), and 40 h (Lanes 6 and 9) after protein transduction. A strong band at 34 kDa is clearly seen in these lanes, indicating RAP-binding activity. This result suggests that the folding machinery of HeLa cells is indeed able to refold bacterial expressed LBD-apoER2 and the refolded LBD-apoER2 is functional. However, the band intensity of Lanes 4 and 7 are much weaker than Lanes 5–6 and 8–9, suggesting incomplete refolding 5 h after protein transduction, but complete refolding after 20 h. A longer time does not increase the band intensity. Lane 3 is the purified powder of LBD-apoER2 from the HeLa cell lysate, also showing a strong band, suggesting that the purified protein powder is biologically active. We noticed that a minor band is observed at ~25 kDa in Lanes 3, 5, and 6, but not in Lanes 7–9. We suggest that this band is the degradation product, since it only exists in the cell supernatant. Our data showed that the addition of protease inhibitors removed this minor band, confirming our suggestion.

For apoE-binding, we performed a pull-down assay (Fig. 7, Panel B). Briefly, the HeLa cell lysate was first loaded on a his-tag resin column. The flow-through of this loading was collected (Lane 9). After extensive washing, the column was incubated with apoE/POPC complex (prepared before experiment), for 2 h and a second flow through of apoE/POPC was collected (Lane 10). The column was washed with PBS buffer extensively and eluted with 300 mM imidazole. The elution was then loaded on an SDS-PAGE at different volumes of 2.5 μl (Lane 5), 5.0 μl (Lane 6), 7.5 μl (Lane 7), and 15 μl (Lane 8). In addition, several controls were also loaded on the gel, including apoE as the positive control (Lanes 1 and 11), bacterial expressed LBD-apoER2 (Lane 2), HeLa cell lysate mixed with bacterial expressed LBD-apoER2 (Lane 3) and HeLa cell lysate only (Lane 4), as the negative controls. It is clear that a strong band is observed for both the positive controls (Lanes 1 and 11) and the elution samples (Lanes 5–8), as well as the second flow through (Lane 10). However, this band is not observed in the negative controls (Lanes 2–4) and the first flow through (Lane 9), suggesting that the refolded LBD-apoER2 is functional in apoE-binding.

This is a very interesting result for the following two reasons: (1) HeLa cells have the ability to refold a large amount of misfolded, exogenous LBD-apoER2. This indicates that HeLa cells can be used as a refolding factory for the manufacture of a large amount of properly folded protein. We believe that this method can be used to refold any misfolded proteins. Thus, our method provides a novel technology for production of a large amount of biologically active proteins with complicated folding that cannot be achieved using bacterial expression. (2) Since our data suggested that LBD-apoER2 took >5 h to completely refold inside HeLa cells, this gives us time to perform experiments to study the folding pathway of this protein in living cells. We are currently working on these experiments.

Figure 8, Left Panel summarizes this new technology. This technology produces ~30% yield of functional protein from bacterial expressed proteins that is unfolded or misfolded. For example, we delivered 1.5 mg LBD-apoER2 into the HeLa cells and obtained 0.5 mg refolded pure LBD-apoER2 that is functional for

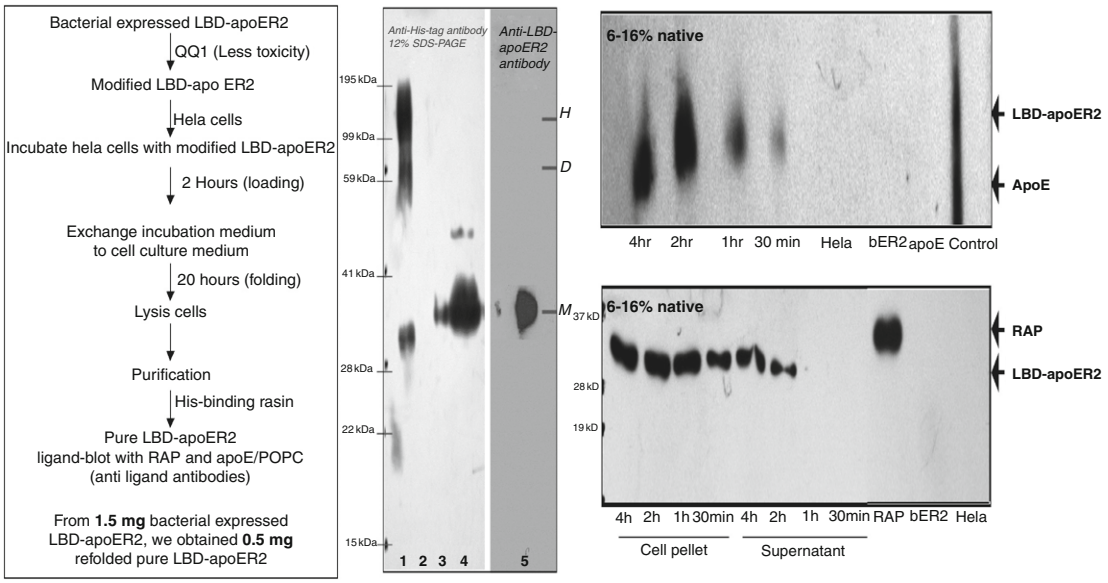

Fig. 8 Left: A schematic diagram highlights the experimental procedure of production of large quantity of properly folded, functional LBD-apoER2 using mammalian cell folding machinery. From 1.5 mg bacterial expressed LBD-apoER2, we recovered ~0.5 mg properly folded, functional LBD-apoER2. Middle: Western blots of bacterial labeled LBD-apoER2 (Lane 1), showing several bands of different oligomers, due to intermolecular disulfide bond formation. Lane 2 is an empty lane. Lane 3: Cell lysate of BHK cells, after 20 h protein transductions. Lane 4: HeLa cell lysate after 20 h protein transduction. Lanes 1–4: Used an anti-His-tag antibody. Lane 5: HeLa cell lysate after 20 h protein transduction using an anti-LBD-apoER2 antibody. Right: Far western blots of the powders of purified refolded LBD-apoER2 at different time points using RAP as the ligand with an antiRAP antibody (Lower) and apoE/POPC as a ligand with an antiapoE antibody (Upper). Both far western blots were based on 6–16% native gel of the purified LBD-apoER2. In both far western blots, RAP (lower) and apoE (Upper) were used as the positive control. In addition, bacterial expressed LBD-apoER2 (bER2) and HeLa cell lysate without LBD-apoER2 transduction (HeLa) were loaded as the negative controls.

ligand-binding activity. Figure 8, Middle Panel shows western blots of the loading of LBD-apoER2 using HeLa cells (Lanes 4 and 5) and BHK cells (Lane 3). As compared with bacterial expressed LBD-apoER2 that forms oligomers (Lane 1), LBD-apoER2 in both HeLa cells and BHK cells only forms a monomer as detected by both anti-His-tag (Lanes 3 and 4) and anti-LBD-apoER2 antibodies (Lane 5). Figure 8, Right Panel shows far western blots of the purified powder of refolded LBD-apoER2 using both apoE (Upper) and RAP (Lower) as the ligands, suggesting that the purified LBD-apoER2 powder is functional for binding to both RAP and apoE. In summary, our data indicates that the intracellular folding machinery is able to properly fold the QQ-reagent delivered protein (Huang *et al.*, 2008).

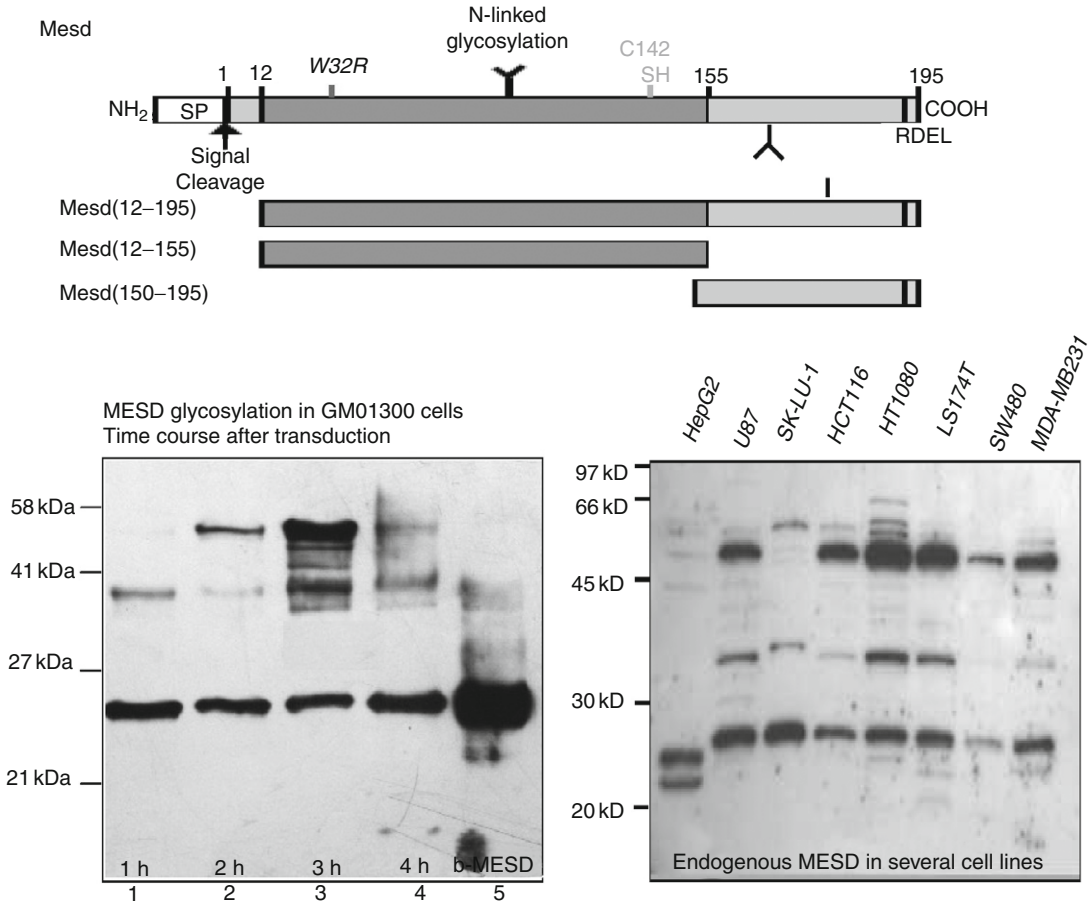

Fig. 9 Top Panel: A schematic diagram of the MESD protein, showing the DNA constructs that we used in this study. We mainly focused on full-length MESD and MESD(12–155) which is the most conserved region of MESD. Lower Panel: Left: A western blot of the cell lysate with the QQ-reagent delivered bacterial expressed MESD protein at different time points in GM01300 cells using an anti-MESD antibody. Right: A western blot of the cell lysates of eight different cell lines, showing endogenous MESD protein, using the same antiMESD antibody. A three band pattern was observed in both panels.

H. The QQ-Reagent Delivered Protein is Properly Post-Translationally Modified

MESD contains one potential N-linked glycosylation site at position: T165. This protein may also contain O-linked glycosylation sites. In addition, MESD contains an RDEL ER retention signal (Fig. 9, Upper Panel), which retains MESD in the ER and Golgi. In general, as a specialized chaperone of the LDLR family, MESD specifically promotes the proper folding of the YWTD/EGF modules of the LRP5/6 in the ER and also potentially serves as an escort protein to safe-guard the properly

folded LRP5/6 in its trafficking from the ER to Golgi for posttranslational modifications (Hsieh *et al.*, 2003; Culi and Mann, 2003; Culi *et al*, 2004). In this case, MESD will dissociate from the mature LRP5/6 and return to the ER to chaperone the newly synthesized LRP5/6. In both the ER and Golgi, MESD may be glycosylated and we do not know if the glycosylation of MESD has any functional role at this moment.

When we delivered bacterial expressed MESD into the HeLa cells, we always observed three bands at 25 kDa, ~35 kDa, and ~45 kDa in the western blot of the cell lysate (Lanes 1–4, Lower Left, Fig. 9), whereas the bacterial expressed MESD only showed one band at 25 kDa. The same result was consistently observed using a different cell line, GM01300 (Lane 5). To ensure that this was not an experimental artifact, we carried out western blots of endogenous MESD using eight different mammalian cell lines (Lower Right, Fig. 9). To our surprise, an identical band pattern was observed for endogenous MESD for all these cell lines except the HepG2 cells. The endogenous MESD displayed three bands with similar MW in the western blot using the same MESD antibody, although the intensities of the different bands in different cell lines were slightly different. The fact that both endogenous and exogenous MESD display an identical pattern of western blot bands is very interesting, suggesting that *the* exogenous MESD may undergo the same secretion pathway as that of endogenous MESD inside the mammalian cell. Based on the MESD amino acid sequence, we suggested that the MESD was posttranslationally modified, perhaps by glycosylation. We carried out experiments on the cell lysate using two deglycosylation enzymes: PNGase and NAase (Fig. 10). Dose-dependent results of PNGase and NAase clearly indicate that the higher MW bands are glycosylation products of MESD. After adding either PNGase (Middle) or NAase (Left), the higher MW bands were converted into the lower MW band that was identical to the bacterial expressed MESD (25 kDa). Taking all these together, we concluded that the QQ-reagent delivered MESD is properly posttranslationally modified (Li *et al.*, 2008b).

I. The QQ-Reagent Delivered Protein Follows the Same Secretion Pathway of Endogenous Protein

The fact that the proper folding of exogenous LBD-apoER2 and glycosylation of exogenous MESD occur inside cells indicates that these two proteins may travel through the ER and Golgi. Previous published results indicate that the newly synthesized apoER2 has to undergo a proper folding inside the ER with the help of ER folding enzymes and chaperone proteins, including two specialized chaperones: RAP and MESD (Herz and Marschang, 2003). The properly folded apoER2 will travel to the Golgi for posttranslational modification and eventually to the plasma membrane. In our case, the LBD-apoER2 will be secreted into the cell culture medium, since the transmembrane domain of apoER2 was removed. In contrast, MESD is an ER/Golgi resident protein, containing an ER retention signal (RDEL), which directs endogenous MESD to stay between the ER and

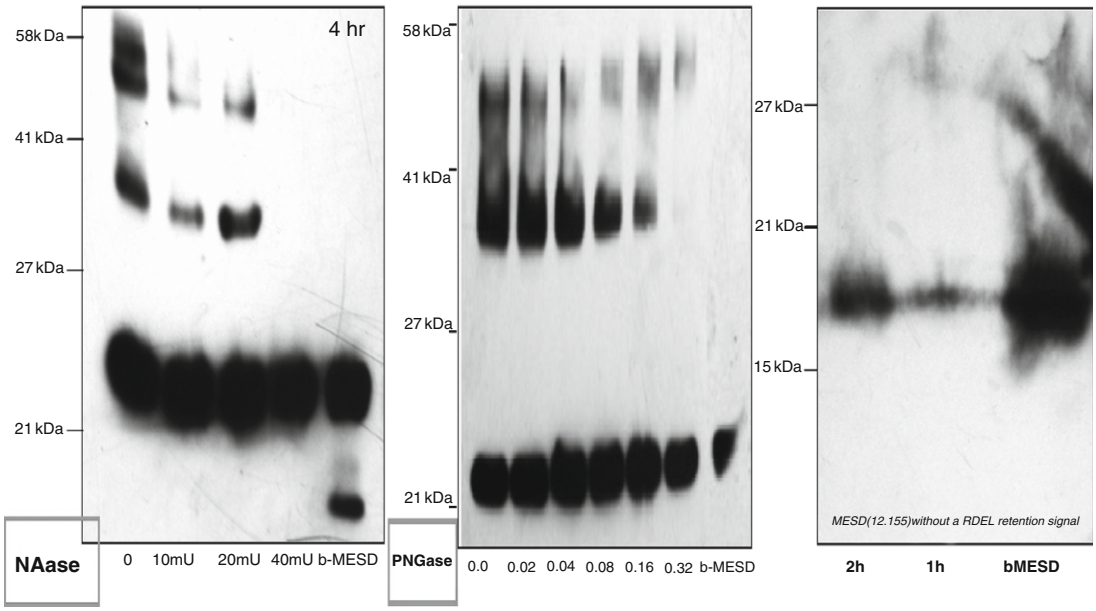

Fig. 10 Left: A western blot of the HeLa cell lysate without and with different dosages of a deglycosylation enzyme: NAase. The enzymatic reaction was carried out for 4 h at room temperature. Middle: A western blot of the HeLa cell lysate without and with different dosages of a deglycosylation enzyme: PNGase. The enzymatic reaction was carried out for overnight at room temperature. In both panels, the upper bands were converted into the MESD band, indicating the upper bands are glycosylated MESD. Right: A western blot of the HeLa cell lysate with the QQ-reagent delivered bacterial expressed MESD(12–155) at different time points in HeLa cells. Only one band was observed for MESD (12–155) which is identical to the bacterial expressed MESD(12–155) (bMESD). No glycosylated MESD(12–155) was observed under our experimental condition.

Golgi. Figure 6, Right Panel indicated that the ER retention signal of MESD might direct the exogenous MESD to the ER *and* Golgi. We further performed colocalization experiments to demonstrate that the QQ-reagent delivered MESD is indeed located in the ER and Golgi. Figure 11 shows the fluorescence imaging results of MESD colocalization with the ER. The experiment protocol is highlighted on the Top Panel of this figure. In this case, we first transfected BSC-1 cells with a GFP–ER marker DNA (Lippincott-Schwartz and Patterson, 2003; Zhang *et al.*, 2006) and then delivered ArrayIt 640 labeled MESD, which is red fluorescence labeled, into BSC-1 cells 24 h after transfection. The BSC-1 cells were loaded with fluorescence labeled MESD for 20 min and spun down gently and washed with PBS three times. The washed BSC-1 cells were cultured in a cell culture medium for another 3 h. Fluorescence imaging experiments were performed and both red (Rhodamine) and green (FITC) channels were recorded using living cells. Clearly, the transfected GFP-ER marker DNA expressed the ER marker protein and bright green fluorescence signals were observed (Middle Panel). In the

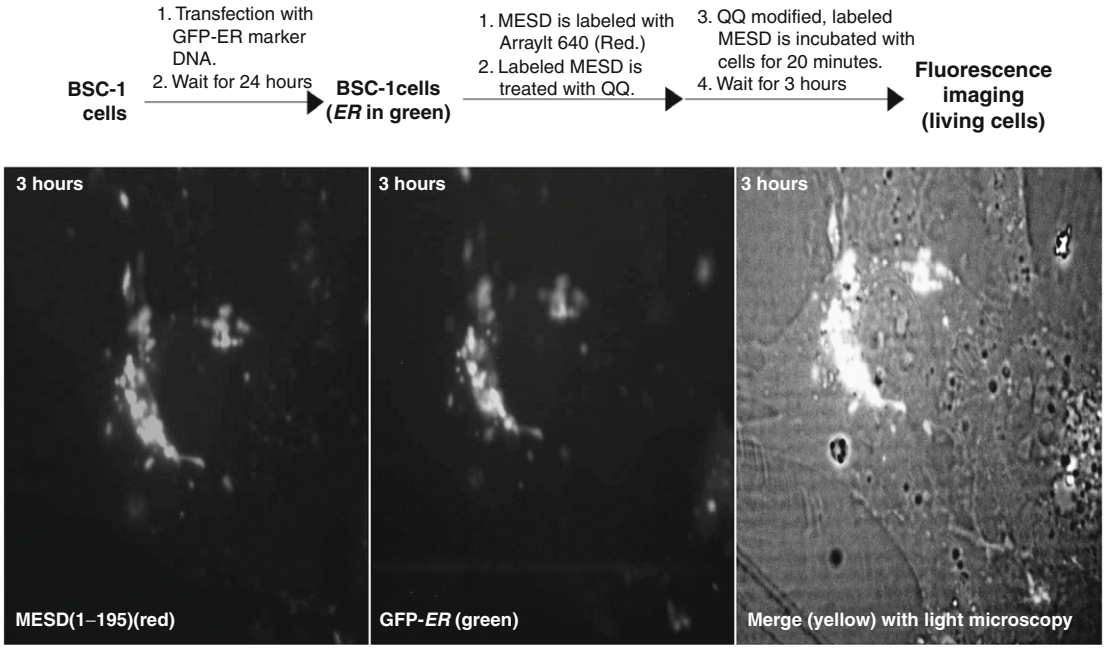

Fig. 11 Top Panel: A schematic diagram of the experimental procedure for the experiment that generates this figure. Bottom Panel: Left: Fluorescence image of live BSC-1 cells in red channel (Rhodamine), showing locations of the ArrayIt 640 labeled MESD (red). Middle: Fluorescence image of live BSC-1 cells in green channel (FITC), showing location of the ER, which is labeled by GFP-ER marker (green). Right: A merge of green and red fluorescence images, which is superimposed with light microscopy image, showing colocation of MESD in the ER.

meantime, we also observed bright red fluorescence signals (Left Panel), suggesting that the red fluorescence labeled MESD was efficiently delivered into the cells. Interestingly, both green and red fluorescence signals were in the same intracellular locations so that a merging of these two images yielded a bright yellow image inside BSC-1 cells, demonstrating that the QQ-reagent delivered MESD is indeed localized in the ER (Left Panel). Figure 12 shows the fluorescence imaging results of MESD colocalization with the Golgi. In this case, we first transfected BSC-1 cells with a CFP–Golgi marker DNA (Nichols *et al.*, 2001) and then delivered DyLight 488 labeled MESD, which is green fluorescence labeled, into BSC-1 cells 72 h after transfection. The BSC-1 cells were loaded with fluorescence labeled MESD for 30 min and spun down gently and washed with PBS five times. The washed BSC-1 cells were cultured in a cell culture medium for another 2–3 h. The BSC-1 cells were fixed and mounted on a glass plate. Fluorescence imaging experiments were performed and we recorded red (Rhodamine), green (FITC), and blue (CFP) channels on these fixed cells (Top, Fig. 12). The Panel A shows green fluorescence signals of DyLight 488 labeled MESD and Panel C shows blue fluorescence signals

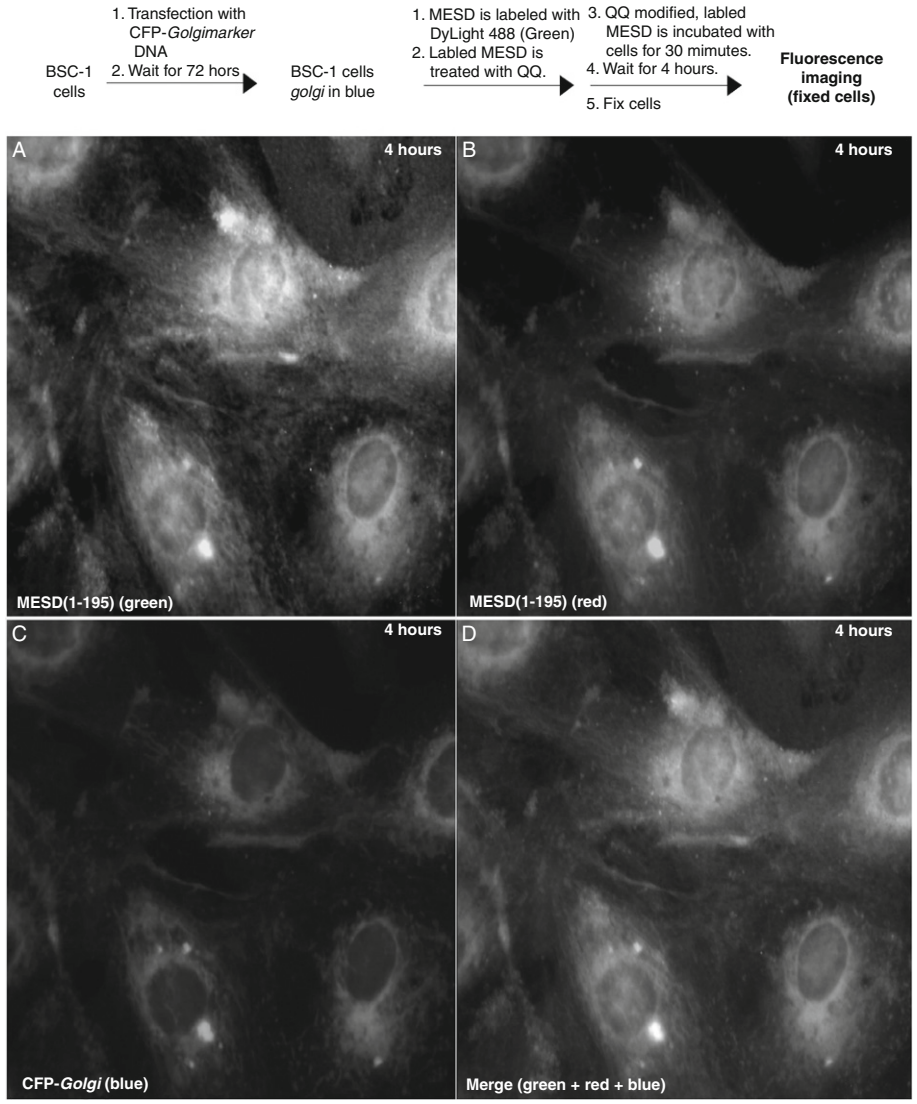

Fig. 12 Top Panel: A schematic diagram of the experimental procedure for the experiment that generates this figure. Bottom Panel: (A) Fluorescence image of fixed BSC-1 cells in green channel (FITC), showing the location of the DyLight 488 labeled MESD (green). (B) Fluorescence image of fixed BSC-1 cells in red channel (Rhodamine), also showing the location of the DyLight 488 labeled MESD with a fluorescence color change (red shift). (C) Fluorescence image of fixed BSC-1 cells in blue channel (CFP), showing the location of the Golgi, since the BSC-1 cells were transfected with CFP-Golgi marker DNA for 72 h before protein transduction. (D) A merge of three fluorescence colors (Blue + Green + Red), showing that the red fluorescence image is colocalized with blue fluorescence image, indicating that the red-shifted DyLight 488 labeled MESD is localized in the Golgi.

of CFP-Golgi, indicating the intracellular locations of Golgi compartments. Interestingly, we also observed significant amount of red fluorescence signals (Panel B) that seemed to colocalize with the blue fluorescence signals. We suggest that the red fluorescence signals represent the Golgi-location of MESD, whereas the green fluorescence signals represent the ER-location of MESD. We suggest that the red shift in fluorescence signals of Golgi-located MESD is presumably due to the complex glycosylation of MESD in the Golgi. A merge of all three fluorescence images shows both the ER-located MESD (Green) and the Golgi-located MESD (Light Gray) (Panel D). Nevertheless, based on these results, we conclude that the QQ-reagent delivered MESD is only located in the ER and Golgi, which are the identical intracellular locations of endogenous MESD. These results suggest that the exogenous MESD follows the identical secretion pathway as the endogenous MESD (Li *et al.*, 2008b).

In addition, Fig. 9 demonstrated that the exogenous MESD underwent glycosylation that was identical to the endogenous MESD, further confirming that the QQ-reagent delivered MESD indeed traveled to the ER and Golgi. These results provide additional important experimental evidence that the QQ-reagent delivered MESD may follow the same secretion pathway as that of the endogenous MESD. We further prepared a truncation mutant, MESD(12–155) with the REDL signal removed. The HeLa cell lysate of the QQ-reagent delivered MESD(12–155) only showed a single band that was identical to the bacterial expressed MESD(12–155), 2 h after protein transduction, as revealed by a western blot (Right Panel, Fig. 10), indicating that no glycosylation was observed for MESD(12–155). This result indicates that it is the REDL ER retention signal that directs exogenous MESD protein to the ER and Golgi. Therefore, the QQ reagent delivered exogenous MESD follows the same secretion pathway as the endogenous MESD (Li *et al.*, 2008b).

This is a very important conclusion, since this conclusion indicates that the exogenous proteins follow the Blobel's "Signal Theory," suggesting that the signal sequences of proteins direct the fate of all proteins, regardless of their endogenous or exogenous origins, once they are inside the cell. Thus, our data extended Blobel's "Signal Theory" from endogenous proteins to exogenous proteins using the QQ reagents as protein transduction reagents. This conclusion further demonstrates the physiological and pathological relevance of the applications of QQ-reagent based protein transduction technology (Li *et al.*, 2008b).

J. Application to Fluorescence Imaging in Cell Biology Studies

Once the physiological and pathological relevance of the QQ-reagent based protein transduction technology had been established, we applied this novel technology to fluorescence imaging to study real time protein folding, location, trafficking, and protein–protein interactions in living cells (Li and Wang, 2008b). We used two proteins for these studies: LBD-apoER2 and MESD. Traditionally, GFP technology is used to fuse the GFP protein to either the N- or C-terminus of

the target protein and to monitor the GFP-fused protein trafficking inside cells by fluorescence imaging. However, GFP technology will not be useful for LBD-apoER2 and MESD, since GFP is a 238-residue protein (27 kDa), whereas LBD-apoER2 is a 294-residue protein (34 kDa), and MESD is a 195-residue protein (23 kDa). The GFP-fusion of these two proteins may cause significant artifacts to appear in the results. In addition, GFP is an independently folded, rigid protein and its green color is stable and usually insensitive to the chemical environmental changes, such as conformational changes or posttranslational modification, of the target protein. Furthermore, although the GFP/RFP fusion pair is used to study protein–protein interactions or domain–domain interactions within a protein by FRET experiments, accurate distance measurements between GFP and RFP are impossible due to the large size of these two proteins. Therefore, significant structural and functional information of the target protein is lost using the GFP-technology. In contrast, our new fluorescence labeling strategy solves these problems. First, we used a small fluorophore to label the protein, causing minimal perturbation in structure and trafficking of the target protein. Second, our strategy attaches the small fluorophores to surface-located amino acids, which will be very sensitive to the chemical environment of the target proteins. A chemical environmental change of the target protein, such as a conformational change or a posttranslational modification, may cause a chemical environmental change of the fluorophores, resulting in a fluorescence color change, either a blue shift or a red shift. Therefore, our strategy adds another dimension to fluorescence imaging. Finally, using our strategy, we can accurately measure the distance between fluorescence donor and acceptor within the target protein. Such FRET-based distance measurement is routinely used *in vitro* and yields important high-resolution structural data of proteins, DNAs, and RNAs (dos Remedios and Moens, 1995). Using our strategy, we can apply these *in vitro* FRET-based distance measurements to the living cells, which may potentially push cell biology to a much higher resolution (Li and Wang, 2008b).

Figure 13 shows two examples. Panels A and B show fluorescence images of DyLight 488 labeled LBD-apoER2 in the BSC-1 cells either 1 h (Panel A) or 7 h (Panel B) after protein transduction. In this case, we labeled LBD-apoER2 with a small molecule green fluorophore, DyLight 488 (MW: 1011 Da). The labeled LBD-apoER2 was purified using a spin column to remove the free fluorescence dye and then incubated with QQ1 reagent overnight. The QQ-reagent modified, DyLight 488 labeled LBD-apoER2 was further purified using the spin column to remove free QQ reagents. The purified LBD-apoER2 was incubated with BSC-1 cells for 30 min and the cells were washed three times using PBS buffer. The washed cells were cultured in the cell culture medium for either 1 h or 7 h and fluorescence imaging was performed on these two samples. We recorded fluorescence images of both the green channel (FITC) and red channel (Rhodamine) and Panels A and B show the superposition of the fluorescence images of both green and red fluorescence signals.

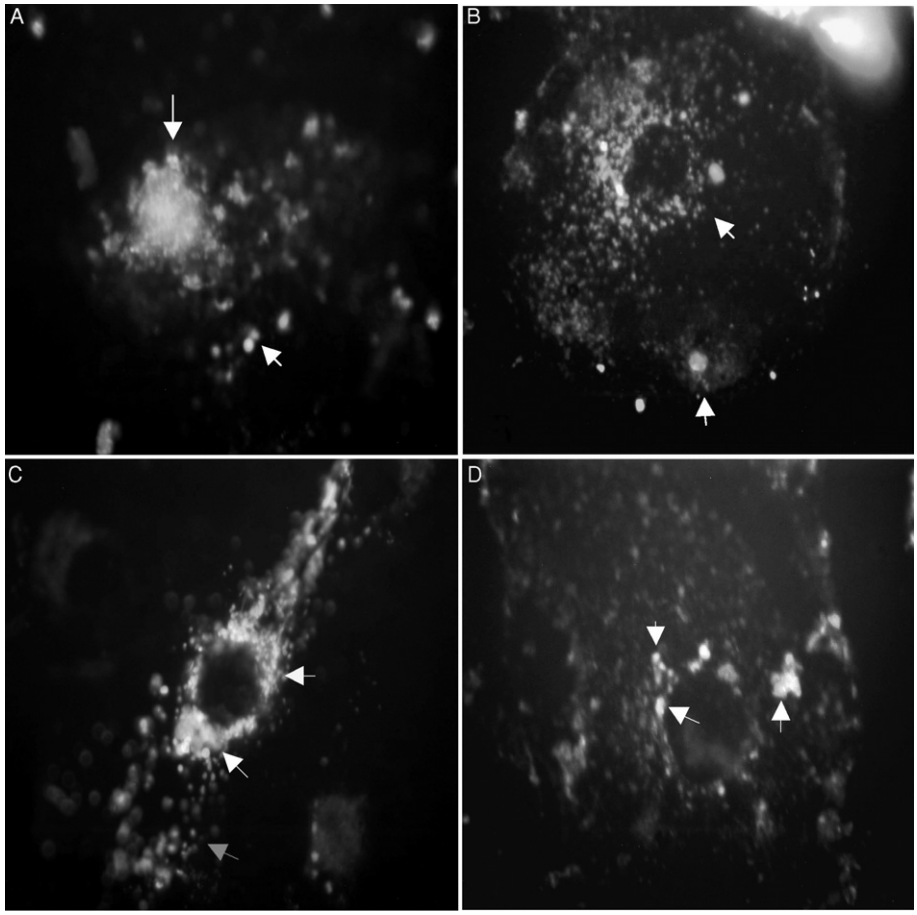

Fig. 13 Panels A and B shows merges of red and green fluorescence images of DyLight 488 labeled LBD-apoER2 (green) in the BSC-1 cells either 1 h (Panel A) or 7 h (Panel B) after protein transduction. Both green and red fluorescence images show in both panels, however, they are located in different intracellular locations as highlighted by white arrows, suggesting that the green fluorescence labeled LBD-apoER2 has a red shift due to environmental changes. Panel C shows a merged fluorescence image of both red and green fluorescence images of ArrayIt 640 labeled MESD (red) in the BSC-1 cells with transfection of GFP-ER marker (green). Panel D shows a merged fluorescence image of three color images of DyLight 488 labeled MESD (green) in the BSC-1 cells with transfection of CFP-Golgi marker (blue).

Clearly, in addition to green fluorescence signals, we also observed orange signals. Interestingly, green and orange fluorescence signals were located in different intracellular locations, as highlighted by the white arrows. In addition, a clear trend of fluorescence color conversion from green to orange is observed as a function of incubation time. For example, shortly after protein transduction, the

majority of fluorescence signals are green with a minor population of orange fluorescence signals (Panel A). In contrast, 7 h after protein transduction, the majority of the fluorescence signals are orange with a minor population of green signals (Panel B). Indeed, at 7 h, green fluorescence signals nearly disappear and orange fluorescence signals are much stronger and spread throughout the cell. As we discussed in last paragraph, we expect to observe fluorescence color changes using our strategy, since the small fluorophore, DyLight 488, is sensitive to the chemical environmental changes of LBD-apoER2. Our results shown in Panels A and B confirm this suggestion. In addition, we noticed that this fluorescence color change is consistent with the oligomer dissociation and proper folding of LBD-apoER2 as revealed in Figs. 4B and 7. Based on these results, we suggest that the green fluorescence represents the unfolded, oligomeric LBD-apoER2 and red fluorescence represents the properly folded, monomeric LBD-apoER2. Although currently we are conducting more experiments to verify this suggestion, our results clearly demonstrate that the lost information of GFP-technology is retrieved using our fluorescence strategy. Importantly, this retrieved information may link the fluorescence color changes with the folding, conformational change, trafficking, posttranslational modification, and protein–protein interaction of the target protein, allowing fluorescence imaging to be developed into a functional imaging of living cells at the molecular level. Finally, our suggestion, if proved, will allow us to investigate protein folding in real time using living cells, which will be a breakthrough discovery in the protein folding field.

The second example is MESD. Panel C shows a merged fluorescence image of both red and green fluorescence images of ArrayIt 640 labeled MESD (red) in the BSC-1 cells with transfection of GFP-ER marker (green). Panel D shows a merged fluorescence image of three color images of DyLight 488 labeled MESD (green) in the BSC-1 cells with transfection of CFP-Golgi marker (blue). In this case, we first transfect BSC-1 cells with either GFP-ER or CFP-Golgi marker DNA, and MESD protein is labeled with either ArrayIt 640 (red fluorophore, MW: 799 Da) or DyLight 488 (Green fluorophore, MW: 1011 Da). The fluorescence labeled MESD was purified to remove free dye and then incubated with the QQ1 reagent overnight. The QQ-reagent modified, fluorescence labeled MESD was incubated with BSC-1 cells, 72 h after transfection, for 30 min. The BSC-1 cells were washed five times with PBS buffer and then cultured for 1.5 h (Panel D) and 4 h (Panel C). In Panel C, BSC-1 cells express ER-located GFP and MESD is red fluorescence labeled. Thus, a superposition of the green and red fluorescence images gives a yellow fluorescence image, which can be seen in the perinuclear area (Yellow Arrow), indicating MESD protein is located in the ER. In addition, 4 h after protein transduction, many reddish dots are scattered inside the cell, which are the ER/Golgi intermediate compartment (ER*GIC*, Appenzeller-Herzog and Hauri, 2006), as highlighted by red arrows. Green fluorescence was also observed in Panel C (White Arrow), indicating that MESD traveled out the ER. This is a very interesting result, since Panel C allows us to distinguish two different kinds of ER compartments inside of cell: the ER compartment that contains MESD

(Yellow) and the ER compartment that does not contain MESD (Green). The MESD-empty ER compartment is near the ER*GIC* location. One hypothesis is that MESD comes out from the ER in this area, resulting in temporarily MESD-empty ER. We further noticed, in Panel C, that the color of the ER*GIC* is slightly red shifted, compared with the yellow color in the ER, indicating that the chemical environment of the MESD between the ER and ER*GIC* may not be the same. In Panel D, BSC-1 cells express Golgi-located CFP and MESD is green fluorescence labeled. In addition, we also collected fluorescence images of the red channel, in case there is a red shift in fluorescence signals of MESD. Since we have three different colors, the superposition of the different colors will produce different color patterns. An analysis of these different merged color patterns will allow us to gain important information on MESD location, trafficking, and chemical environment. For example, a merge of blue and red generates purple, whereas a merge of blue and green produces teal. In Panel D, a large area of green fluorescence is observed, which is expected, since MESD is green fluorophore labeled and primarily located in the ER shortly after protein transduction (1.5 h) as evidenced in Panel C. Thus, we suggest that the green fluorescence represents the ER-located MESD. In Panel D, no yellow is observed, indicating there is no colocation of red and green fluorescence signals. However, light purple color is clearly seen as highlighted by arrows, demonstrating a merge of red and blue fluorescence. This data suggests that there is an independent MESD population inside BSC-1 cell which is Golgi-located and has a different chemical environment that causes a red shift of DyLight 488 labeled MESD. Our data also indicated that the bacterial expressed MESD is properly folded, which allowed us to determine the NMR structure of this protein (Chen *et al.*, 2008b). Therefore, the folding of MESD inside cells is unlikely to be the reason that caused this red shift. In contrast, the glycosylation of MESD adds ~10 kDa to this protein, an increase in mass that implies a complicated glycosylation (Fig. 9). Such a complicated glycosylation is unlikely to occur in the ER but rather in the Golgi, since glycosylation in the ER is usually simple glycosylation, whereas glycosylation in the Golgi is complicated (Spiro, 2002). We suggest that the Golgi-located MESD is the glycosylated MESD and glycosylation of MESD may cause a change in the chemical environment that results in a red shift of the fluorescence probe, whereas the ER-located MESD is not glycosylated and maintains the green color. Although more experiments are required to confirm our hypotheses, it is evident that the fluorescence color changes of the small fluorophores that are attached to the target proteins indeed provide important information regarding the folding, location, trafficking, posttranslational modification, and protein–protein information of the target proteins. (Li and Wang, 2008b; Li *et al.*, 2008b).

To study protein–protein interactions, we applied our fluorescence labeling strategy to LBD-apoER2 and RAP. We colored LBD-apoER2 and RAP with different fluorophores and carried out a FRET experiment to study their interactions. In this case, we labeled LBD-apoER2 with ArrayIt 540 (Green) and RAP with ArrayIt 640 (Red) and delivered the labeled proteins into the HeLa cells

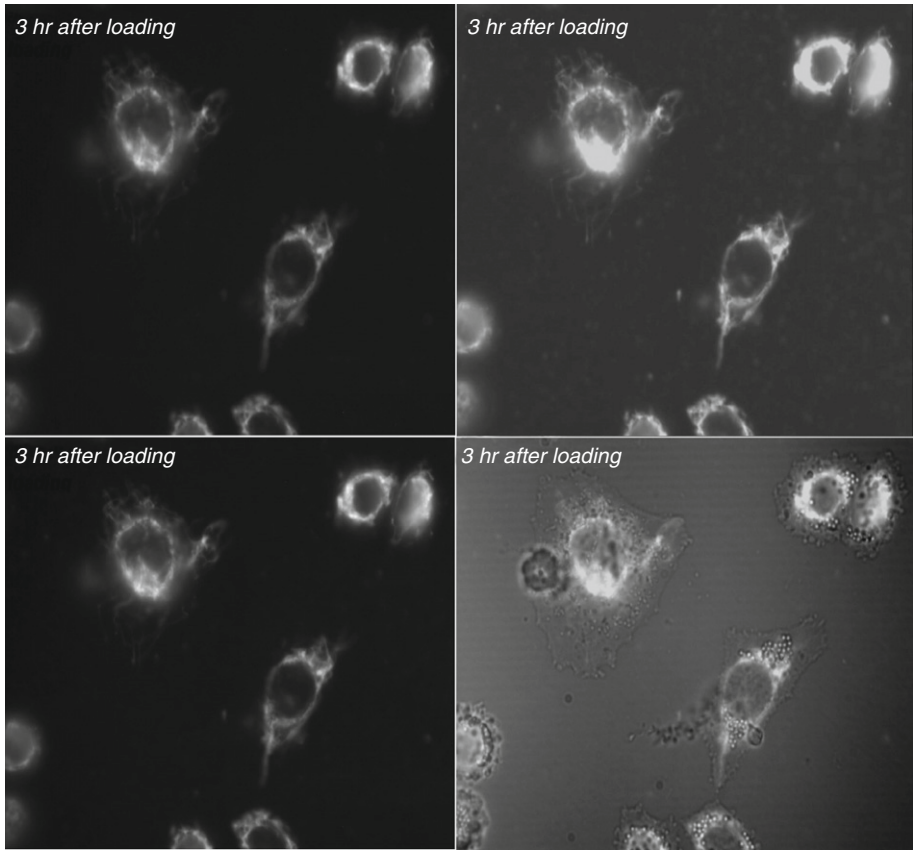

Fig. 14 Upper Left: Fluorescence image of ArrayIt 540 (Green) labeled LBD-apoER2 (FITC channel). Upper Right: Fluorescence image of ArrayIt 640 (red) labeled RAP (Rhodamine channel). Both fluorescence images were collected 3 h after protein transduction. Both LBD-apoER2 and RAP were codelivered into HeLa cells at a molar ratio of 1:1. Lower Left: A merge of red and green fluorescence merge, showing resulting yellow color, suggesting that LBD-apoER2 and RAP are colocalized inside cells. Lower Right. Panel C with light microscopy.

simultaneously. After incubation of HeLa cells with a cell culture medium that contains 1:1 molar ratio of LBD-apoER2:RAP for 30 min, the cells were washed with PBS three times and incubated for another 3 h. Fluorescence imaging was performed and both green and red channels were recorded. Figure 14 clearly shows that the green and red fluorescence signals are colocalized in the identical intracellular area, suggesting that both LBD-apoER2 (Green, Upper Left) and RAP (Red, Upper Right) are colocalized. The Lower, Right Panel shows the green and red fluorescence merges and light microscopy, indicating that the yellow fluorescence is located in the perinuclear areas that are the ER and Golgi. This result demonstrates that our fluorescence labeling strategy can be used for FRET study of

protein–protein interactions, similar to the GFP technology. However, since we only introduce small molecule fluorophore into the target proteins, we will be able to measure accurate distance between fluorescence donor and acceptor, which the GFP-based fluorescence technique is incapable of. We are currently pursuing these studies.

IV. Summary

We provide a review of a novel protein transduction technology recently developed in our laboratory and its applications. This protein transduction method is based on the QQ reagents with their unique and novel features that are distinctly different from the current available protein transduction reagents. These novel features include: (1) A high protein transduction efficiency (near nM). (2) A capability of specific delivery of exogenous protein into their target intracellular compartments. (3) Protection of target protein from intracellular protease degradation. (4) Either covalent or noncovalent association with the target protein. (5) Simple one step incubation with the cells for protein delivery. We performed experiments to demonstrate that the QQ-reagent delivered proteins are properly folded and posttranslationally modified by the mammalian cell machinery. These results allow us to develop a novel technology to produce a large quantity of properly folded and posttranslationally modified proteins with a complicated fold that results in misfolded protein using bacterial expression. We further demonstrated that the QQ-reagent delivered exogenous protein follows the identical secretion pathway as the endogenous protein, demonstrating the physiological and pathological relevance of the QQ-reagent based protein transduction technology. We applied this protein transduction technology to fluorescence imaging for cell biology studies. Our strategy is to *in vitro* label proteins with small fluorescence probes and then deliver the fluorescence labeled protein into the cells using the QQ reagents for fluorescence imaging. In contrast to GPF-based technology which is insensitive to the chemical environmental change of the target proteins, our fluorescence imaging technology introduces fluorescence probes into target protein that is very sensitive to the structural and functional changes of the target proteins, resulting in fluorescence color changes, either a red or a blue shift. We demonstrated that with the proper control experiments, these fluorescence color changes report the folding, structure, modification, trafficking, and functional information of the target proteins, and thus may add an additional dimension to fluorescence imaging. We believe that this new fluorescence imaging technique will provide a powerful tool for us to carry out real time investigation of protein folding, structure, posttranslational modification, trafficking, location, and protein–protein interaction in living cells.

Acknowledgments

This work was supported by a US NIH grant (HL76435 to J.W). The authors are also thankful for the generous support by the Microscopy & Imaging Resources Laboratory of Karmanos Cancer Institute for fluorescence imaging facility. Jianglei Chen is a recipient of an AHA predoctoral fellowship (AHA 0515582Z to J. C).

References

Alberts, B., Johnson, A., Lewis, J., Raff, M., Roberts, K., and Walter, P. (2002). *In* "Molecular Biology of the Cell." 4th edn. pp. 1463. Garland Science, New York, NY.

Appenzeller-Herzog, C., and Hauri, H. P. (2006). The ER-Golgi intermediate compartment (ERGIC): In search of its identity and function. *J. Cell. Sci.* **119,** 2173–2183.

Blobel, G., and Sabatini, D. D. (1971). Ribosome-membrane interaction in eukaryotic cells. *In* "Biomembranes" (L. A. Manson, ed.), pp. 193–195. Plenum, New York.

Breyer, B., Jiang, W., Cheng, H., Zhou, L., Paul, R., Feng, T., and He, T. C. (2001). Adenoviral vector-mediated gene transfer for human gene therapy. *Curr. Gene Ther.* **1,** 149–162.

Bu, G., and Schwartz, A. L. (1998). RAP, a novel type of ER chaperone. *Trends Cell Biol.* **8,** 272–276.

Burz, D. S., Dutta, K., Cowburn, D., and Shekhtman, A. (2006). Mapping structural interactions using in-cell NMR spectroscopy (STINT-NMR). *Nat. Methods* **3,** 91–93.

Chen, J., Cheng, J., Li, Q., Bu, G., and Wang, J. (2008a). NMR structure and dynamics of the most conserved domain of MESD, a specialized chaperone for the LDL receptor super-family. *Biochemistry* Submitted for Publication.

Chen, J., Cheng, J., Li, Q., Bu, G., and Wang, J. (2008b). MESD uses different domains to regulate its chaperone function and escort activity. *Mol. Cell* Submitted for Publication.

Culi, J., and Mann, R. S. (2003). Boca, an endoplasmic reticulum protein required for wingless signaling and trafficking of LDL receptor family members in Drosophila. *Cell* **112**(3), 343–354.

Culi, J., Springer, T. A., and Mann, R. S. (2004). Boca-dependent maturation of beta-propeller/EGF modules in low-density lipoprotein receptor proteins. *EMBO J.* **23**(6), 1372–1380.

D'Arcangelo, G. (2005). Apoer2: A reelin receptor to remember. *Neuron* **47,** 471–473.

Deshayes, S., Morris, M. C., Divita, G., and Heitz, F. (2005). Cell-penetrating peptides: Tools for intracellular delivery of therapeutics. *Cell Mol. Life Sci.* **62,** 1839–1849.

dos Remedios, C. G., and Moens, P. D. (1995). Fluorescence resonance energy transfer spectroscopy is a reliable "ruler" for measuring structural changes in proteins. Dispelling the problem of the unknown orientation factor. *J. Struct. Biol.* **115,** 175–185.

Ellis, R. J., and Minton, A. P. (2006). Protein aggregation in crowded environments. *Biol. Chem.* **387**(5), 485–497.

Foged, C., and Nielsen, H. M. (2008). Cell-penetrating peptides for drug delivery across membrane barriers. *Expert Opin. Drug Deliv.* **5,** 105–117.

Frank, J. (2006). "Three-Dimensional Electron Microscopy of Macromolecular Assemblies." Oxford University Press, New York.

Futami, J., Kitazoe, M., Maeda, T., Nukui, E., Sakaguchi, M., Kosaka, J., Miyazaki, M., Kosaka, M., Tada, H., Seno, M., Sasaki, J., Huh, N. H., *et al.* (2005). Intracellular delivery of proteins into mammalian living cells by polyethylenimine-cationization. *J. Biosci. Bioeng.* **99,** 95–103.

Giepmans, B. N., Adams, S. R., Ellisman, M. H., and Tsien, R. Y. (2006). The fluorescent toolbox for assessing protein location and function. *Science* **312,** 217–224.

Hatters, D. M., Peters-Libeu, C. A., and Weisgraber, K. H. (2006). Apolipoprotein E structure: Insights into function. *Trends Biochem. Sci.* **31,** 445–454.

He, X., Semenov, M., Tamai, K., and Zeng, X. (2004). LDL receptor-related proteins 5 and 6 in Wnt/beta-catenin signaling: Arrows point the way. *Development* **131,** 1663–1677.

Heikkila, J. J., Kaldis, A., and Abdulle, R. (2006). Analysis of molecular chaperones using a *Xenopus* oocyte protein refolding assay. *Methods Mol. Biol.* **322,** 213–222.

Herz, J., and Marschang, P. (2003). Coaxing the LDL receptor family into the fold. *Cell* **112,** 289–292.

Hsieh, J. C., Lee, L., Zhang, L., Wefer, S., Brown, K., DeRossi, C., Wines, M. E., Rosenquist, T., and Holdener, B. C. (2003). Mesd encodes an LRP5/6 chaperone essential for specification of mouse embryonic polarity. *Cell* **112**(3), 355–367.

Hu, Y. C. (2008). Baculoviral vectors for gene delivery: A review. *Curr. Gene Ther.* **8,** 54–65.

Huang, Y. C., Riddle, K., Rice, K. G., and Mooney, D. J. (2005). Long-term *in vivo* gene expression *via* delivery of PEI-DNA condensates from porous polymer scaffolds. *Hum. Gene Ther.* **16,** 609–617.

Huang, Y. F., Wang, J., and Li, Q. (2008). Using intracellular folding machinery to produce large quantity of properly folded, functional proteins. *Nat. Biotechnol.* Submitted for Publication.

Jeon, H., Meng, W., Takagi, J., Eck, M. J., Springer, T. A., and Blacklow, S. C. (2001). Implications for familial hypercholesterolemia from the structure of the LDL receptor YWTD-EGF domain pair. *Nat. Struct. Biol.* **8,** 499–504.

Kelly, A. E., Ou, H. D., Withers, R., and Dötsch, V. (2002). Low-conductivity buffers for high-sensitivity NMR measurements. *J. Amer. Chem. Soc.* **124,** 12013–12019.

Korthout, H. A., Berecki, G., Bruin, W., van Duijn, B., and Wang, M. (2000). The presence and subcellular localization of caspase 3-like proteinases in plant cells. *FEBS Lett.* **475**(2), 139–144.

Lakowicz, J. R. (2006). *In* "Principles of Fluorescence Spectroscopy." 3rd edn. XXVI, pp. 954. Springer.

Li, Y., Cam, J., and Bu, G. (2001). Low-density lipoprotein receptor family: Endocytosis and signal transduction. *Mol. Neurobiol.* **23,** 53–67.

Li, Q., Huang, Y. F., and Wang, J. (2008a). A novel protein transduction method with target capability to specific intracellular compartment. *Nat. Method* Submitted for Publication.

Li, Q., and Wang, J. (2008a). The QQ-reagent based protein transduction technology and its applications. US patent (Pending).

Li, Q., and Wang, J. (2008b). A novel fluorescence imaging technique with potential third dimension. *Nat. Methods* Submitted for Publication.

Li, Q., Zhang, K., Bu, G., and Wang, J. (2008b). Exogenous proteins follow Blobal's "signal theory" for the intracellular trafficking and secretion upon transduction inside cells. *Nature, Cell Biology* Submitted for Publication.

Liljas, A., Piskur, J., Liljas, L., Lindblom, G., Nissen, P., and Kjeldgaard, M. (2008). "Textbook of Structural Biology." 1st edn. World Scientific, (ISBN 978-981-277-207-7).

Lippincott-Schwartz, J., and Patterson, G. (2003). Development and use of fluorescent protein markers in living cells. *Science* **300,** 87–91.

Marcel, Y. L., and Kiss, R. S. (2003). Structure-function relationships of apolipoprotein A-I: A flexible protein with dynamic lipid associations. *Curr. Opin. Lipidol.* **14,** 151–157.

Marshall, E. (2000). Gene therapy on trial. *Science* **288,** 951–957.

May, P., Herz, J., and Bock, H. H. (2005). Molecular mechanism of lipoprotein receptor signaling. *Cell Mol. Life Sci.* **62,** 2325–2338.

McIntosh, L. P., and Dahlquist, F. W. (1990). Biosynthetic incorporation of ^{15}N and ^{13}C for assignment and interpretation of nuclear magnetic resonance spectra of proteins. *Q Rev. Biophys.* **23,** 1–38.

Melikov, K., and Chernomordik, L. V. (2005). Arginine-rich cell penetrating peptides: From endosomal uptake to nuclear delivery. *Cell Mol. Life Sci.* **62,** 2739–2749.

Nichols, B. J., Kenworthy, A. K., Polishchuk, R. S., Lodge, R., Roberts, T. H., Hirschberg, K., Phair, R. D., and Lippincott-Schwartz, J. (2001). Rapid cycling of lipid raft markers between the cell surface and Golgi complex. *J. Cell Biol.* **153,** 529–541.

Nykjaer, A., and Willnow, T. E. (2002). The low-density lipoprotein receptor gene family: A cellular Swiss army knife? *Trends Cell Biol.* **12,** 273–280.

Okuyama, M., Laman, H., Kingsbury, S. R., Visintin, C., Leo, E., Eward, K. L., Stoeber, K., Boshoff, C., Williams, G. H., and Selwood, D. L. (2007). Small-molecule mimics of an alpha-helix for efficient transport of proteins into cells. *Nat. Methods* **4,** 153–159.

Park, K., Kim, W. J., Cho, Y. H., Lee, Y. I., Lee, H., Jeong, S., Cho, E. S., Chang, S. I., Moon, S. K., Kang, B. S., Kim, Y. J., and Cho, S. H. (2008). Cancer gene therapy using adeno-associated virus vectors. *Front Biosci.* **13,** 2653–2659.

Piston, D. W., and Kremers, G. J. (2007). Fluorescent protein FRET: The good, the bad and the ugly. *Trends Biochem. Sci.* **32,** 407–414.

Royer, C. A. (2006). Probing protein folding and conformational transitions with fluorescence. *Chem. Rev.* **106,** 1769–1784.

Schwarze, S. R., Ho, A., Vocero-Akbani, A., and Dowdy, S. F. (1999). *In vivo* protein transduction: Delivery of a biologically active protein into the mouse. *Science* **285,** 1569–1572.

Schwendener, R. A. (2007). Liposomes in biology and medicine. *Adv. Exp. Med. Biol.* **620,** 117–128.

Selenko, P., Frueh, D. P., Elsaesser, S. J., Haas, W., Gygi, S. P., and Wagner, G. (2008). *In situ* observation of protein phosphorylation by high-resolution NMR spectroscopy. *Nat. Struct. Mol. Biol.* **15,** 321–329.

Selenko, P., Serber, Z., Gadea, B., Ruderman, J., and Wagner, G. (2006). Quantitative NMR analysis of the protein G B1 domain in *Xenopus laevis* egg extracts and intact oocytes. *Proc. Natl. Acad. Sci. USA* **103,** 11904–11909.

Selenko, P., and Wagner, G. (2007). Looking into live cells with in-cell NMR spectroscopy. *J. Struct. Biol.* **158,** 244–253.

Serber, Z., Selenko, P., Hänsel, R., Reckel, S., Löhr, F., Ferrell, J. E., Jr., Wagner, G., and Dötsch, V. (2006). Investigating micromolecules inside cultured and injected cells by in-cell NMR spectroscopy. *Nat. Protoc.* **1,** 2701–2709.

Shaikh, S. A., Jain, T., Sandhu, G., Latha, N., and Jayaram, B. (2007). From drug target to leads--sketching a physicochemical pathway for lead molecule design in silico. *Curr. Pharm. Des.* **13,** 3454–3470.

Shaner, N. C., Patterson, G. H., and Davidson, M. W. (2007). Advances in fluorescent protein technology. *J. Cell Sci.* **120**(Pt 24), 4247–4260.

Sivashanmugam, A., Victoria, Meiners., Chunxian, Cui., Yunhuang, Yang., Jianjun, Wang., and Qianqian, L. i. (2008). Practical protocols for production of very high-yield of recombinant proteins in *Eschericia coli*. *Protein Sci.* Submitted for Publication.

Spiro, R. G. (2002). Protein glycosylation: Nature, distribution, enzymatic formation, and disease implications of glycopeptide bonds. *Glycobiology* **12,** 43R–56R.

Strickland, D. K., Gonias, S. L., and Argraves, W. S. (2002). Diverse roles for the LDL receptor family. *Trends Endocrinol. Metab.* **13,** 66–74.

Tréhin, R., and Merkle, H. P. (2004). Chances and pitfalls of cell penetrating peptides for cellular drug delivery. *Eur. J. Pharm. Biopharm.* **58,** 209–223.

Tugarinov, V., Kanelis, V., and Kay, L. E. (2006). Isotope labeling strategies for the study of high-molecular-weight proteins by solution NMR spectroscopy. *Nat. Protoc.* **1,** 749–754.

Usón, I., and Sheldrick, G. M. (1999). Advances in direct methods for protein crystallography. *Curr. Opin. Struct. Biol* **9**(5), 643–648.

Wadia, J. S., and Dowdy, S. F. (2002). Protein transduction technology. *Curr. Opin. Biotechnol.* **13,** 52–56.

Wadia, J. S., and Dowdy, S. F. (2005). Transmembrane delivery of protein and peptide drugs by TAT-mediated transduction in the treatment of cancer. *Adv. Drug. Deliv. Rev.* **57,** 579–596.

Wu, G. Y., and Wu, C. H. (1991). Delivery systems for gene therapy. *Biotherapy* **3,** 87–95.

Zhang, Z., Shen, X., Wu, J., Sakaki, K., Saunders, T., Rutkowski, D., Back, S., and Kaufman, R. (2006). Endoplasmic reticulum stress activates cleavage of CREBH to induce a systemic inflammatory response. *Cell* **124,** 587–599.

CHAPTER 15

Structural Basis of Human High-density Lipoprotein Formation and Assembly at Sub nanometer Resolution

Arun Sivashanmugam, Yunhuang Yang, Victoria Murray, Christopher McCullough, Bin Chen, Xuefeng Ren, Qianqian Li, and Jianjun Wang

Department of Biochemistry and Molecular Biology
Wayne State University
School of Medicine
Detroit, Michigan 48021

METHODS IN CELL BIOLOGY, VOL. 90

0091-679X/08 $35.00
DOI: 10.1016/S0091-679X(08)00815-7

Abstract

Human high-density lipoproteins (HDL) are protein/lipid particles of nanometer sizes. These nano particles are critical for transportation of the ''bad cholesterol'' from peripheral tissues back to the liver for clearance. An inverse correlation has been observed between the plasma HDL concentration and atherosclerosis. Furthermore, the HDL particle has also been utilized as a vehicle for drug delivery and for intracellular cell biology studies of membrane proteins. The structural basis of HDL formation and assembly, however, is poorly understood. Using high-resolution structural approaches, the formation and assembly of the HDL particle is being examined at atomic resolution, which is reviewed in this chapter. We will mainly focus on our own NMR studies of different apoAI conformations with a brief summary of previously published work by other laboratories.

I. Introduction

A. Human HDL and apoAI

HDL is a key player in the reverse cholesterol transport (RCT) pathway that transports the ''bad cholesterol'' from peripheral tissues back to the liver for clearance (Lund-Katz *et al.*, 2003; Rader 2006). Blocking this pathway may cause accumulation of cholesterol in the peripheral tissues, potentially leading to deposition of cholesterol plaques in arterial blood vessels, the major pathological event of atherosclerosis. In contrast, plasma concentrations of HDL cholesterol are inversely associated with atherosclerotic disease (Miller and Miller, 1975). HDLs have long been considered to be an important endogenous factor that protect against atherosclerosis and are thus an attractive therapeutic target (Rader, 2006). On December 2, 2006, Pfizer made a major announcement about their decision to suspend the Phase III clinical trials for Torcetrapib, which was a new drug that Pfizer invested nearly $1 billion in a hope to enhance HDL levels for treatment of heart disease. Unfortunately, it was discovered that patients whose HDL cholesterol levels increased with Torcetrapib actually experienced an increased risk for heart disease (Barter *et al.*, 2007). This result raises an important question regarding how much we actually understand about HDL cholesterol and how it works?

Human apolipoprotein AI (apoAI) is a 243-residue exchangeable apolipoprotein, which constitutes ~70% of HDL protein and is present on virtually all HDL particles (Marcel and Kiss, 2003; Segrest *et al*., 2000). Gene deletion of *APOAI/APOAI* causes very low levels of HDL cholesterol in mice (Williamson *et al*., 1992) and in humans (Schaefer *et al*., 1982). Atherosclerosis prone mice lacking apoAI develop significantly enhanced atherosclerosis (Moore *et al*., 2005). In particular, the conformational flexibility seems to be critical to HDL formation and assembly (Marcel and Kiss, 2003). During HDL assembly, apoAI goes through a cycle starting from lipid-free apoAI, progressing to different lipid/HDL-bound states, and finally back to lipid-free/lipid poor apoAI. Each of the apoAI states, depending on the extent of lipidation, adopts a distinct conformation, mediating apoAI's different biological functions that direct HDL formation, maturation, transport, and metabolism.

B. apoAI Cycle and HDL Pathway

Figure 1 shows a brief schematic diagram of the apoAI cycle or the RCT pathway, with the main focus on the four distinct conformations of apoAI during HDL formation, assembly, and transport. apoAI is synthesized in both the liver and the intestine. Newly synthesized apoAI has to acquire lipids in order to generate HDL particles. While up to 5–10% of circulating apoAI is lipid-free, the lipid-free apoAI conformation seems to be specifically linked to the uptake of cellular phospholipids (Brouillette *et al*., 2001). In addition, lipid-free apoAI also activates ABC–AI for efficient cholesterol efflux (Rothblat *et al*., 1999). Upon binding to a small amount of phospholipid, apoAI forms preβHDLs. Experimental evidence, both *in vitro* and *in vivo*, has demonstrated that preβHDL is the most active acceptor for free cholesterol (Rothblat *et al*., 1992; Sparks *et al*., 1999). It is interesting that apoAI seems to undergo a conformational change from lipid-free apoAI to preβHDL that exposes the binding sites for free cholesterol. The addition of cholesterol and phospholipid to preβHDL generates larger and lipid-rich particles, triggering the assembly of HDL particles. During the initial stages of HDL assembly, discoidal HDL is formed. apoAI on discoidal HDL adopts another conformation, the "Discoidal HDL apoAI conformation", which activates the enzyme, LCAT, converting cholesterol into cholesterol ester (CE) (Duriez and Fruchart, 1999; Neary *et al*., 1991). This results in accumulation of CE in the center of discoidal HDL and eventually the formation of a small mature spherical HDL particle known as HDL_3. Further maturation of spherical HDL_3 depends on the activity of LCAT, which promotes continued transfer of cholesterol and phospholipid into HDL particles, forming large spherical HDL particles (HDL_2). apoAI on spherical HDL particles adopts a fourth conformation, the "Spherical HDL apoAI conformation", which is able to bind to the HDL-receptor, SR-BI (Connelly and Williams, 2004). HDL_2 is transported back to the liver through the HDL-receptor mediated selective lipid uptake, with HDL-associated apoAI serving as the ligand (Trigatti, 2005). This process regenerates lipid-free and

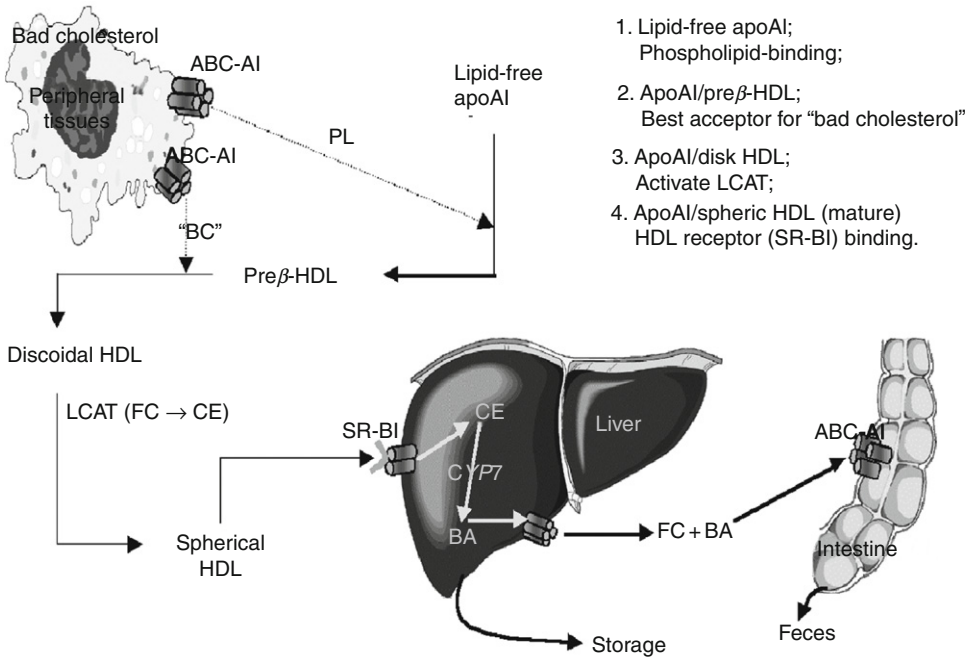

Fig. 1 A brief schematic diagram of the apoAI cycle/reverse cholesterol transport (RCT) pathway, mainly focusing on four conformations of apoAI during HDL formation, assembly, and transport. BC: bad cholesterol. PL: phospholipids. FC: free cholesterol. BA: bile acid. CE: cholesterol ester. LCAT: lecithin:cholesterol acyltransferase. ABC–AI: ATP binding cassette transporter-AI. CYP7A: cholesterol 7α-hydroxylase. SR-BI: scavenger receptor class B type I or the HDL receptor.

lipid-poor apoAI, thus completing the apoAI cycle. The regenerated lipid-free and lipid-poor apoAI start a new apoAI cycle to again scavenge peripheral cellular cholesterol and phospholipid before returning to the liver. apoAI on HDL particles also activates two lipid transfer proteins: cholesterol ester transfer protein (CETP) and phospholipid transfer protein (PLTP), which regulate dynamic inter-conversions between HDL and LDL (de Grooth *et al.*, 2004; Huuskonen *et al.*, 2001).

C. apoAI Conformational Plasticity and HDL Formation, Maturation, and Assembly

During the apoAI cycle, four different apoAI conformations dictate HDL formation, maturation, and assembly. The conformational plasticity of apoAI clearly plays a critical role in the inter-conversion among these four conformations. To understand the structural basis of HDL formation, maturation, and assembly, we have to elucidate this conformational plasticity of apoAI protein, which requires high-resolution structural information of each apoAI conformation. A large body of research has been compiled over the past two decades in the

efforts to determine the structures of apoAI at different states (Davidson and Silva, 2005; Gursky, 2005; Klon *et al*., 2002; Lund-Katz *et al*., 2003). However, most of these studies are performed at low resolution by using DSC, fluorescence spectroscopy, analytical ultracentrifugation, limited proteolysis, and monoclonal antibody mapping. A general consensus from these studies is that lipid-free apoAI may contain a helix-bundle structure in the N-terminal domain whereas the C-terminal part of the protein is flexible (Saito *et al*., 2004). The plasticity of the C-terminal domain facilitates the lipid-binding activity of apoAI in initiating HDL formation. In addition, the conformational plasticity of apoAI is also critical for HDL assembly from preβHDL to discoidal HDL. The conformational plasticity of the "hinge domain" in apoAI is essential for the activation of LCAT that acts to convert discoidal HDL into mature spherical HDL. Another suggestion is that apoAI exhibits a "molten globule" structure with well-defined secondary structure elements that display no or minimum tertiary contacts (Gursky and Atkinson, 1996).

In 1997, a 4.0 Å resolution X-ray crystal structure of a N-terminal deletion mutant of human apoAI, apoAI(44–243), in the absence of lipids was reported. The authors suggested that this structure was a putative "*lipid-bound like*" structure (Borhani *et al*., 1997). It adopted an unusual, extended, amphipathic α-helical open conformation, which was a tetrameric, continuously curved, horseshoe-shaped structure. A new crystal form of apoAI(44–243) has been reported; although the structure of this new crystal form has not been solved, the author seemed to indicate that it might adopt a helix-bundle structure (Borhani *et al*., 1999). In 2006, an X-ray crystal structure of lipid-free, full-length apoAI was published (Ajees *et al*., 2006). Unlike the crystal structure of apoAI(44–243), this new crystal structure of full-length apoAI forms a trimer and each monomer adopts a four helix-bundle in the N-terminal domain and two helix-bundle in the C-terminal domain. The authors indicate that the N-terminal helix-bundle plays a prominent role in maintaining the lipid-free apoAI conformation and a deletion in the N-terminal domain forms inadequate models for explaining functional properties of apoAI. This new crystal structure is attractive and may represent a major progress in the high-resolution structural studies of apoAI. However, several lines of evidence indicate that a crystal artifact may exist in this crystal structure. For example, the overall helical content of the crystal structure is about 83%, which is much higher than previously published data obtained using CD spectroscopy (~50–55%) (Davidson and Silva, 2005). Furthermore, the C-terminal domain of the lipid-free apoAI is very flexible as suggested by several different techniques (Brouillette *et al*., 2001), whereas the C-terminal domain of this crystal structure adopts a rigid two helix-bundle. Finally, limited proteolysis studies of lipid-free apoAI demonstrated that a central region of apoAI between residues 115 to 150 was flexible and potentially unstructured since it was sensitive to proteolysis (Roberts *et al*., 1997). This region displayed a great conformational flexibility even in the HDL associated states, thus it may potentially serve as a "hinge" domain (Córsico *et al*., 2001; Dalton and Swaney; 1993; Davidson and Silva, 2005).

However, this region in the X-ray crystal structure is mostly in a well-defined α-helix within the helix-bundle, displaying limited flexibility. Overall, this new crystal structure of lipid-free apoAI seems to be so well structured that it lacks the seemingly necessary conformational plasticity for dictating HDL formation and assembly.

No high-resolution structural studies have been reported on apoAI conformations in any HDL-associated states. This is mainly due to the difficulty of obtaining ultra pure HDL samples for either X-ray crystal structure or NMR studies. HDL particles are also extremely dynamic which prevents them from forming crystals. In addition, lipid-free apoAI, like other exchangeable apolipoproteins, aggregates in a concentration-dependent manner, forming a mixture of different oligomers. This aggregation property of lipid-free apoAI inhibits NMR and X-ray crystallographic studies of this important protein in its physiological conformation. The reported X-ray crystal structures of lipid-free apoAI are derived from either the tetramer (Borhani *et al.*, 1997) or the trimer of apoAI (Ajees *et al.*, 2006), which might not be the physiological relevant structures of lipid-free apoAI. Therefore, these two crystal structures do not provide the sufficient conformational flexibility that is required for apoAI to convert its conformation among different states of HDL formation and assembly. We have been working on NMR structural studies of apoAI in both lipid-free and HDL-associated states for several years (Ren *et al.*, 2006). The main goals of our NMR studies are: (1) Preparation of a monomeric, biologically active apoAI for NMR studies of lipid-free apoAI and (2) Preparation of ultra pure samples of different HDL states for NMR studies of apoAI conformations. In this article, we will focus on reviewing our NMR studies of the possibly four distinct apoAI conformations.

II. Rationale

A. General Strategy

Our general rationale is straightforward: to obtain high-quality, high-resolution structural data on apoAI, so that we can determine the four conformations of apoAI in its lipid-free and HDL-associated states using NMR techniques. Once we determine the four different conformations, we will be able to elucidate the conformational flexibility of apoAI that is necessary for HDL formation and assembly at atomic resolution. In addition, these apoAI conformations will also allow us to study how each conformation interacts with different lipids to assemble HDL.

B. Strategy for Lipid-Free apoAI

For lipid-free apoAI, our first goal was to solve apoAI aggregation problem. We developed a novel strategy for quick identification of the critical residues that are responsible for protein aggregation (Ren *et al.*, 2005). This strategy also includes a high throughput method for quickly characterizing the oligomeric states of

proteins at high concentrations. Once we identified the residues that were critical for apoAI aggregation, we mutated them to prepare a monomeric apoAI. We also carried out experiments to characterize the structure and function of the apoAI monomeric mutant to ensure that the mutations did not alter apoAI structure and function. Using this strategy, we quickly identified a monomeric mouse apoAI that was functional and maintained the same secondary and tertiary structure as wild-type apoAI. Most importantly, this monomeric apoAI produced high quality NMR data that allowed us to completely assign the NMR spectra of lipid-free apoAI.

C. Strategy for apoAI on HDL-Associated States

For apoAI on different HDL-associated states, our approach was to prepare ultra pure HDL samples with isotope-labeled apoAI, so that we can carry out NMR experiments. This is a very difficult project since the smallest HDL particle, apoAI/preβHDL, is ~38 kDa lipid/protein complex, containing one apoAI molecule. A larger apoAI/preβHDL may contain two molecules of apoAI and ~20 phospholipids which gives a molecular weight of ~70 kDa. The sizes of discoidal HDL particles range between 140 and 230 kDa, whereas spherical HDL is even larger with molecular weights between 200 to 300 kDa. The large size of HDL particles makes high-resolution NMR structural studies difficult. In addition, HDL particles contain both protein and different lipids, including phospholipids, cholesterol, triacylglycerol, and CE. The lipid composition makes the HDL particle very dynamic. NMR techniques provide us with a powerful, high-resolution tool to study conformational dynamics of biomolecules. Thus, we pursue NMR structural determination of apoAI conformations in lipid-free and HDL-associated states, for the purpose of elucidation of conformational plasticity of apoAI at atomic resolution and how this conformational plasticity responds to lipid-binding of different lipids during HDL formation and assembly.

III. Methods and Materials

We will mainly focus on our own high-resolution NMR structural studies of different apoAI conformations with a very brief summary of previously published work by other laboratories, which are related to high-resolution structural studies of apoAI in different states.

A. Lipid-Free apoAI

Experimental data documented that the plasma concentration of apoAI in humans is ~1 mg/ml, which includes both 5–10% lipid-free/lipid-poor apoAI and ~90–95% HDL-associated apoAI (Naito, 1986; Rye and Barter, 2004). Lipid-free

apoAI under this plasma concentration (<0.1 mg/ml) is monomeric, thus, the monomeric form of lipid-free apoAI may serve as the biologically active form of this protein. We focused our initial efforts on preparation of a monomeric apoAI mutant that is biologically active. We chose mouse apoAI since this protein aggregates much less than its human counterpart (Reschly *et al*., 2002). Since the C-terminal domain of apoAI causes aggregation (Laccotripe *et al*., 1997), we prepared several C-terminal truncation mutants of mouse apoAI, including apoAI(1–206), apoAI(1–216), and apoAI(1–229). Using our novel strategy reported by Ren *et al*., we quickly identified two regions of mouse apoAI that potentially caused its aggregation (Fig. 2), including residues 186–203 (helix 7) and residues 118–121 (loop 3). Helical wheel diagram of helix 7 and sequence comparison of loop 3 allowed us to identify that the residues T191/T195/T199 in helix 7 and V118/A119/L121 in loop 3 were the potential residues that might cause apoAI aggregation. Thus, we prepared a mutation of apoAI (V118A/A119S/L121Q/T191S/T195S/T199S) and quickly identified that this mutant was predominantly a monomer (Ren *et al*., 2005). Figure 3, Left Panel shows the crosslinking result, suggesting that this mutant is largely monomeric even at 8 mg/ml. We demonstrated that this monomeric apoAI protein maintained the same secondary and tertiary structure and stability of wild-type apoAI using CD, DSC, and GdnHCl denaturation techniques (Fig. 3, Middle and Right Panels). We further showed that the monomeric apoAI displays a nearly identical lipid-binding activity as that of the wild-type apoAI (data not shown). Based on these results, we conclude that this monomeric apoAI(1–216) mutant is a biologically active apoAI that can be used for NMR structural determination (Ren *et al*., 2005).

Indeed, this monomeric apoAI protein produced high-quality NMR spectra as shown in Fig. 4, Left Panel. The spectral pattern of the monomeric apoAI(1–216) at a high concentration (30 mg/ml) is nearly identical to that of the wild-type apoAI(1–240) at a lower concentration (5 mg/ml) (Fig. 4, Right panel), suggesting that the monomeric apoAI shares an identical structure as that of the wild-type, full-length apoAI. The broader NMR signals in the right panel are due to oligomerization of full-length apoAI, which causes a slow tumbling and decreased signal-to-noise ratio, resulting in missing of NMR signals. Previous published data also suggests that the C-terminal 22-residue fragment is unstructured (Brouillette *et al*., 2001). Using this monomeric apoAI, we collected 3D/4D-NMR experiments, including 3D HNCA, HN(CO)CA, HN(CA)CB, HN(COCA)CB and ^{15}N-edited NOESY, and 4D ^{15}N/^{13}C-edited NOESY and 4D ^{15}N/^{15}N-edited NOESY for backbone atom assignment and 3D HCC-TOCSY-NNH, CCC-TOCSY-NNH, HCCH-TOCSY and 4D ^{13}C/^{15}N-edited NOESY and ^{13}C/^{13}C-edited NOESY for side chain atom assignment. With these experiments, we completely assigned NMR spectra of apoAI(1–216) (Yang *et al*., 2007). Based on the chemical shift and NOE data, we identified four rigid helical segments in the N-terminal domain that formed an up-and-down helix bundle (Helix 1: 8–46, Helix 2: 60–95, Helix 3: 103–117, Helix 3′: 123–128, Helix 4: 145–180). In addition, two short helices are also observed between residues 196 to 200 and 209 to 213 (Fig. 5).

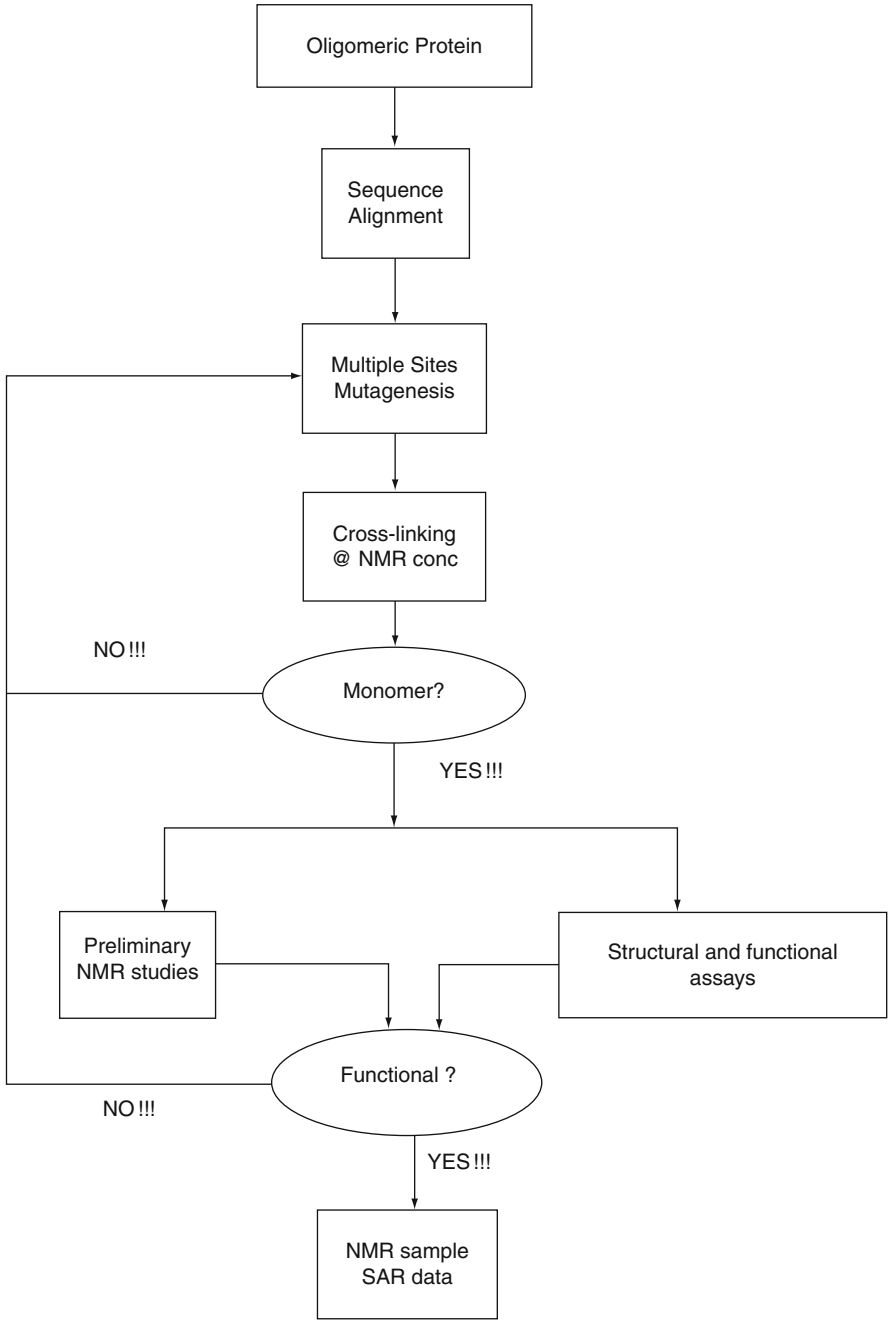

Fig. 2 A flowchart of the strategy to generate a monomeric, biologically active protein from an oligomeric protein for structural studies.

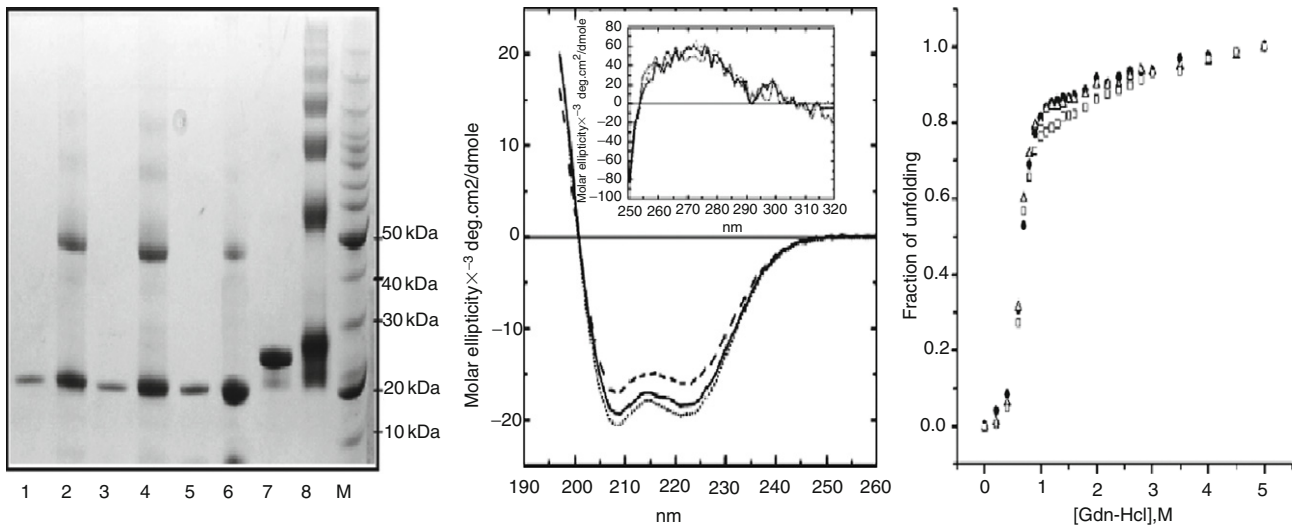

Fig. 3 Left Panel: Tricine gel (6–12%) of apoAI proteins in 50 mM sodium phosphate saline, pH 7.2. Lanes: 1, apoAI(1–216)-P4, no cross-linking; 2, apoAI (1–216)-P4, cross-linking (7 mg/ml); 3, apoAI(1–216)-WT, no cross-linking; 4, apoAI(1–216)-WT, crosslinking (5 mg/ml); 5, apoAI(1–216)-P4/ L3, no cross-linking; 6, apoAI(1–216)-P4/L3, cross-linking (8 mg/ml); 7, human apoAI-(1–243), no cross-linking; 8, human apoAI(1–243), cross-linking (1 mg/ml). Middle Panel: Far-UV CD spectra of apoAI(1–216)-WT, apoAI(1–216)-P4/L3 mutant, and apoAI(1–240) at 0.2 mg/ml in 50 mM sodium phosphate saline, pH 7.2. Dotted line, apoAI(1–216)-WT; solid line, apoAI(1–216)-P4/L3 mutant; dashed line, apoAI(1–240). Inset: near-UV CD spectra of these proteins. Two apoAI-(1–216) proteins, including apoAI(1–216)-WT and apoAI(1–216)-P4/L3, display nearly identical near-UV CD spectra, whereas apoAI(1–240) shows a slightly different near-UV CD spectrum. Right Panel: Guanidine hydrochloride denaturation of mouse apoAI-(1–216)-WT (solid circle), apoAI(1–216)-P4/L3 (open triangle), and apoAI(1–240) (open square) in 50 mM sodiumphosphate saline, pH 7.2 (0.2 mg/ml). The fraction of unfolding was plotted as a function of guanidine hydrochloride concentration.

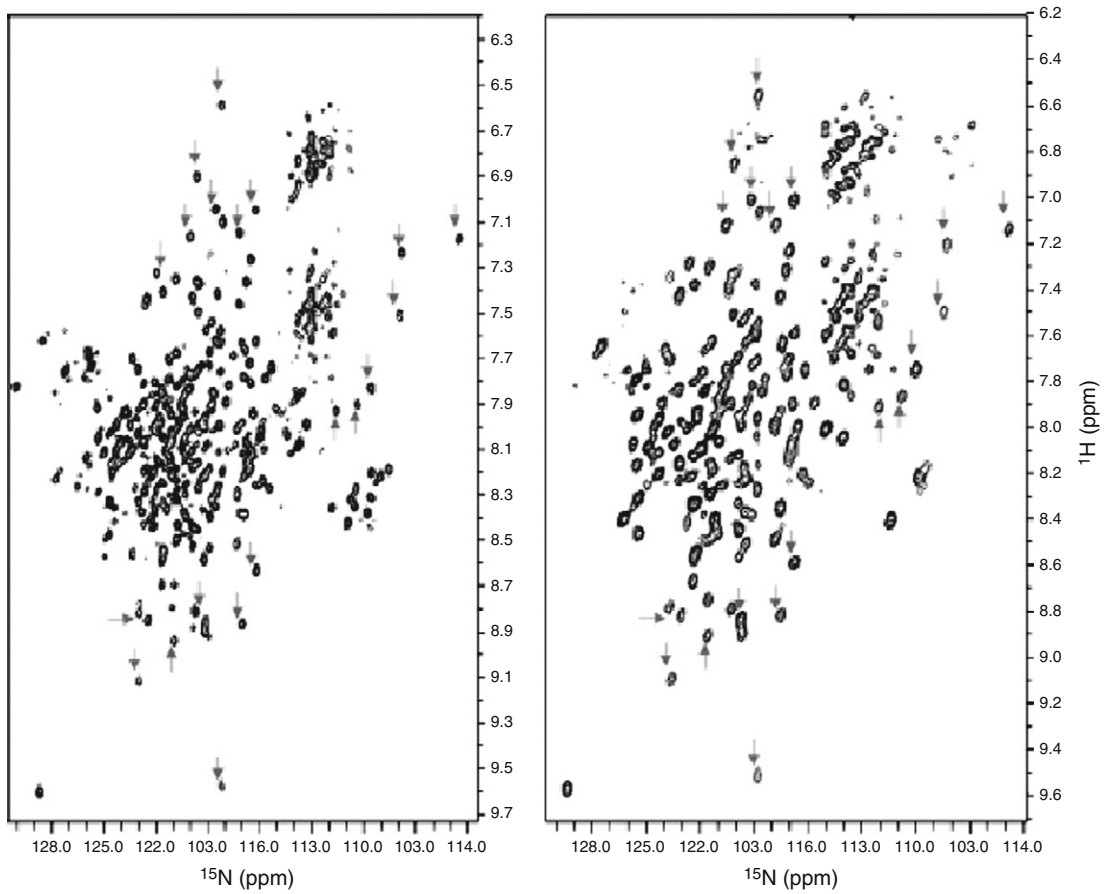

Fig. 4 The two-dimensional TROSY 1H-15N HSQC spectra of $^{2}H/^{15}N/^{13}C$-labeled mouse apoAI (1–240) (5 mg/ml, right panel, 180 transients) and apoAI(1–216)-P4/L3 mutant (30 mg/ml, left panel, 8 transients) in 25 mM phosphate buffer containing 25 mM NaCl, 5 mM EDTA, and 0.1 mM NaN_3, pH 7.2. Both spectra were processed using identical parameters.

The helical content observed in the NMR structure is about 60.0%, which is similar to the helical content determined by CD spectroscopy (55.5%, Ren *et al.*, 2005). When compared with the X-ray crystal structure of human apoAI, a clear difference in secondary structural locations is observed. Helix 3 is much shorter and a large flexible loop containing 18-residues is between helices 3 and 4. This so-called "hinge domain", residues 110–146, is flexible, although a short helix is observed between residues 122 to 130, providing the conformational plasticity necessary for activating LCAT. Although two helices are observed in the C-terminal domain of mouse apoAI, these helices are much shorter (5 residues only) and much more flexible, which is also essential for apoAI to provide conformational plasticity for

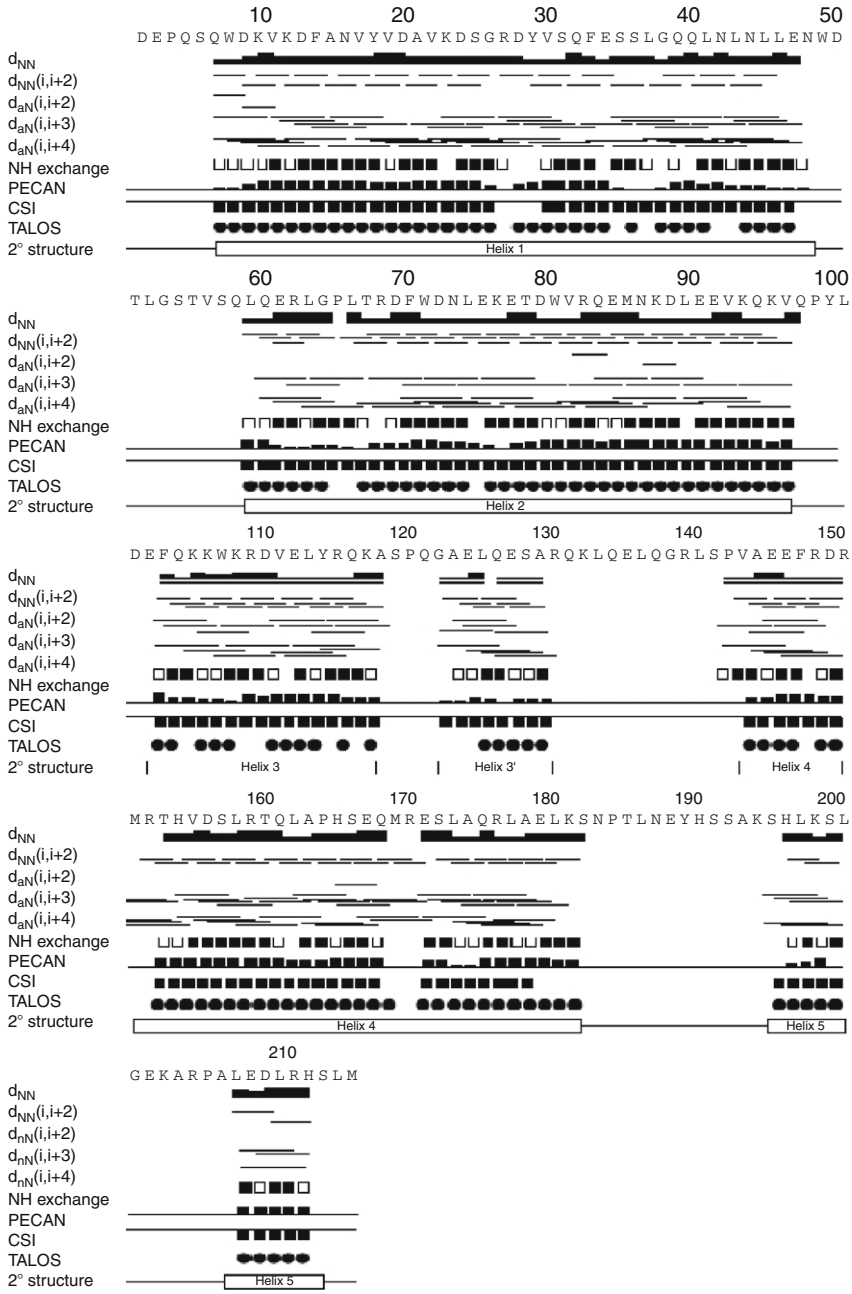

Fig. 5 Summary of HN–HN NOE connectivities, amide exchange rates of lipid-free mouse apoAI(1–216). Below the one-letter code for amino acids, relative strengths of d_{NN} NOE cross-peak intensities are indicated by the bar thickness. $d_{NN}(i, i + 2)$ NOE connectivities observed between specific proton pairs are indicated by a solid line between two residues. Amide proton exchange rate is designated as follows: filled box, slow exchange rate; open box, medium exchange rate; no box, fast exchange rate. Residues that the backbone amide proton and nitrogen atoms haven't been assigned are labeled in grey.

binding to different lipids. We believe that our NMR structure of mouse apoAI (1–216) is a physiologically relevant structure that can be used to explain the published biological data of lipid-free apoAI (Yang and Wang, 2008).

B. apoAI on PreβHDLs

We designate preβHDL as lipid-poor apoAI (Rye and Barter, 2004) and consider discoidal HDL as a different HDL category even though it displays preβ electrophoretic mobility. Discoidal HDLs are larger HDL particles with molecular weights of 140–200 kDa. In contrast, preβHDLs are small HDL precursors with molecular weights ranging between 40 to 75 kDa. They are lipid-poor HDL particles that may serve as an early acceptor of cell-derived phospholipids and unesterified cholesterol in the process mediated by ABC–AI transporter (Rye and Barter, 2004). There is compelling evidence that apoAI in plasma is subject to continual cycling between lipid-free/lipid-poor apoAI and HDL forms. Lipid-poor apoAI may have a substantial impact on HDL assembly and transport (Rye and Barter, 2004). In addition, it is confirmed, both *in vivo* and *in vitro*, that preβHDLs are the best cholesterol acceptors, which avidly bind to cholesterol and phospholipids to initiate HDL formation (Zhao *et al*., 1996). Thus, preβHDLs may serve as a drug target to enhance HDL formation.

To date, no study has been reported for apoAI structure on preβHDL at high-resolution. Sparks' laboratory developed a method for preparation of well-defined preβHDL particles that either contained one (Lp1AI) or two apoAI (Lp2AI) (Zhao *et al*., 1996). Their results indicated that poorly lipidated Lp1AI was a much better acceptor for cholesterol from fibroblasts than lipid-free apoAI and that further progressive lipidation of Lp1AI and Lp2AI enhances this process. In addition, Lp1AI is also a good substrate for LCAT and can promote greater rates of cholesterol esterification than some Lp2AI particles. CD spectroscopy and GdnHCl denaturation of Lp1AI and Lp2AI particles indicated that the α-helical content of Lp1AI was slightly increased whereas the stability of Lp1AI was significantly decreased when compared to lipid-free apoAI. This finding suggests that Lp1AI or preβHDL is uniquely reactive during RCT pathway as a result of a low metastability of Lp1AI particles (Sparks *et al*., 1999).

In collaboration with Sparks' laboratory, we prepared Lp1AI particles (POPC: apoAI = 5:1) using triple-labeled apoAI and carried out NMR experiments on these lipid-poor particles (Ren *et al*., 2007). We first characterized Lp1AI particles (Yang *et al*., 2008). A native gel shows that Lp1AI has a molecular weight of ~40 kDa which is slightly larger than lipid-free apoAI. Crosslinking results show that Lp1AI indeed contained only one apoAI molecule even at 5 mg/ml, which contrasts with lipid-free apoAI that aggregates into a mixture of monomer, dimer, trimer, and higher oligomers at 1 mg/ml. Phospholipid-binding experiments using a DMPC clearance assay indicates that Lp1AI shares an identical phospholipid-binding activity as that of lipid-free apoAI, which is much higher than discoidal HDL particles. We then carried out preliminary NMR experiments using

triple-labeled Lp1AI. Our NMR data shows that the ^{1}H-^{15}N HSQC-TROSY spectrum of freshly prepared Lp1AI displays a well-dispersed crosspeak pattern.

We collected a series of 3D/4D-NMR experiments, including the TROSY version of 3D HNCA, HN(CO)CA, HN(CA)CB, HN(COCA)CB, and ^{15}N-edited NOESY, as well as 4D HNCACO, HNCOCA, and $HNCOCA_{sim}$. We carried out NMR spectral assignment and have assigned the backbone atoms (H, HN, $C_{\alpha,}$ and C_{β}) (Ren *et al*., 2007). We also collected NMR spectra for side chain assignment, including 3D CCC-TOCSY-NNH, HCC-TOCSY-NNH and 4D $^{13}C/^{15}N$-edited NOESY, $^{13}C/^{13}C$-edited NOESY using a 30% deuterated $^{13}C/^{15}N$-labeled Lp1AI sample. In addition, we also collected 3D HCCH-TOCSY and MQ-(H)CCH-TOCSY (Xu *et al*., 2005). The spectrum of an uniformly labeled Lp1AI is complicated since each amino acid produces one crosspeak. In contrast, a specific ^{15}N amino acid labeled apoAI only labels one type of amino acid whereas the other 19 amino acids remain unlabeled. This way, the NMR spectrum is significantly simplified. Figure 6 gives three examples of specific ^{15}N amino acid labeled Lp1AI. For example, apoAI contains seven tyrosines, thus seven crosspeaks are observed in the middle panel (Yang *et al*., 2008). The NMR crosspeak provides a fingerprint of this amino acid. Therefore, the ^{1}H-^{15}N HSQC spectra of the specific ^{15}N amino acid labeled Lp1AI samples serve as a simple map for NMR titration experiments using either phospholipids or cholesterol or potential binding proteins, such as LCAT and ABC–AI. By chemical shift mapping, we will obtain three important pieces of information: (1) the binding residues in Lp1AI to either the lipids or proteins, (2) the binding stoichiometry between Lp1AI and lipids or proteins, and (3) the structural changes of Lp1AI upon binding to lipids or proteins. We are currently carrying out these NMR titration experiments.

Figure 7 Left Panel summarizes the NMR parameters based on the backbone atom assignment, suggesting that apoAI on Lp1AI contains four helices in the N-terminal (first 2/3 of sequence) whereas the C-terminal domain (last 1/3 of sequence) seems to be much less well-defined with great flexibility. Figure 7, right panel shows a schematic diagram of the NMR structure of apoAI on Lp1AI. Overall, the NMR structure shown in Fig. 7 adopts a similar global fold of a four helix-bundle in the N-terminal domain of apoAI as shown in the X-ray crystal structure (Ajees *et al*., 2006). However, two major regions show significant differences between the NMR and the X-ray crystal structures: (1) residues 120–145 and (2) the C-terminal domain, residues 185–243. The NMR parameters show that residues 120–145 are in the flexible loop region whereas the crystal structure shows that these residues adopt a well-defined α-helical structure, except the loop residues 139–144 between helices 3 and 4. The NMR derived structure provides a basis of the conformational plasticity of the ''hinge domain'' (Davidson and Silva, 2005, Meng *et al*., 1993). Similarly, the NMR derived structure also displayed a significant conformational plasticity in the C-terminal domain that facilitates lipid-binding. Finally, the NMR structure only contains ~60% α-helical content which agrees with the previously published CD data.

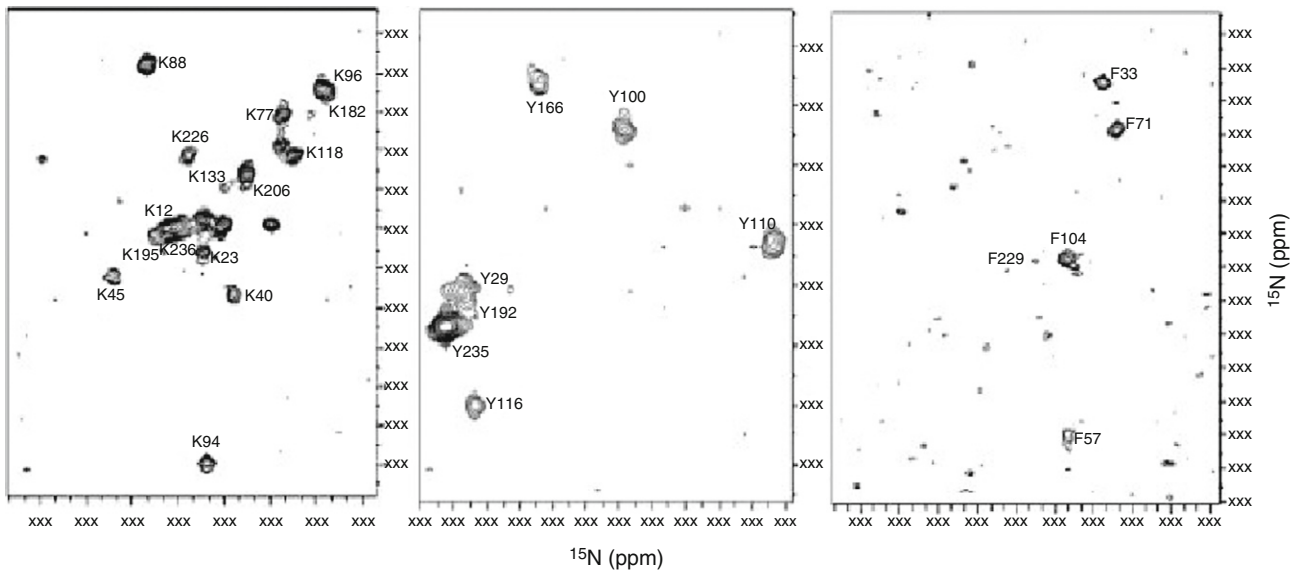

Fig. 6 ^{1}H-^{15}N HSQC spectra of ^{15}N- specific amino acid labeled Lp1AI obtained at 30 °C. The labeled amino acid and residue number are assigned as red. Left Panel: ^{15}N-lys labeled Lp1AI, Middle Panel: ^{15}N-Tyr labeled Lp1AI, Right Panel: ^{15}N-Phe Lp1AI.

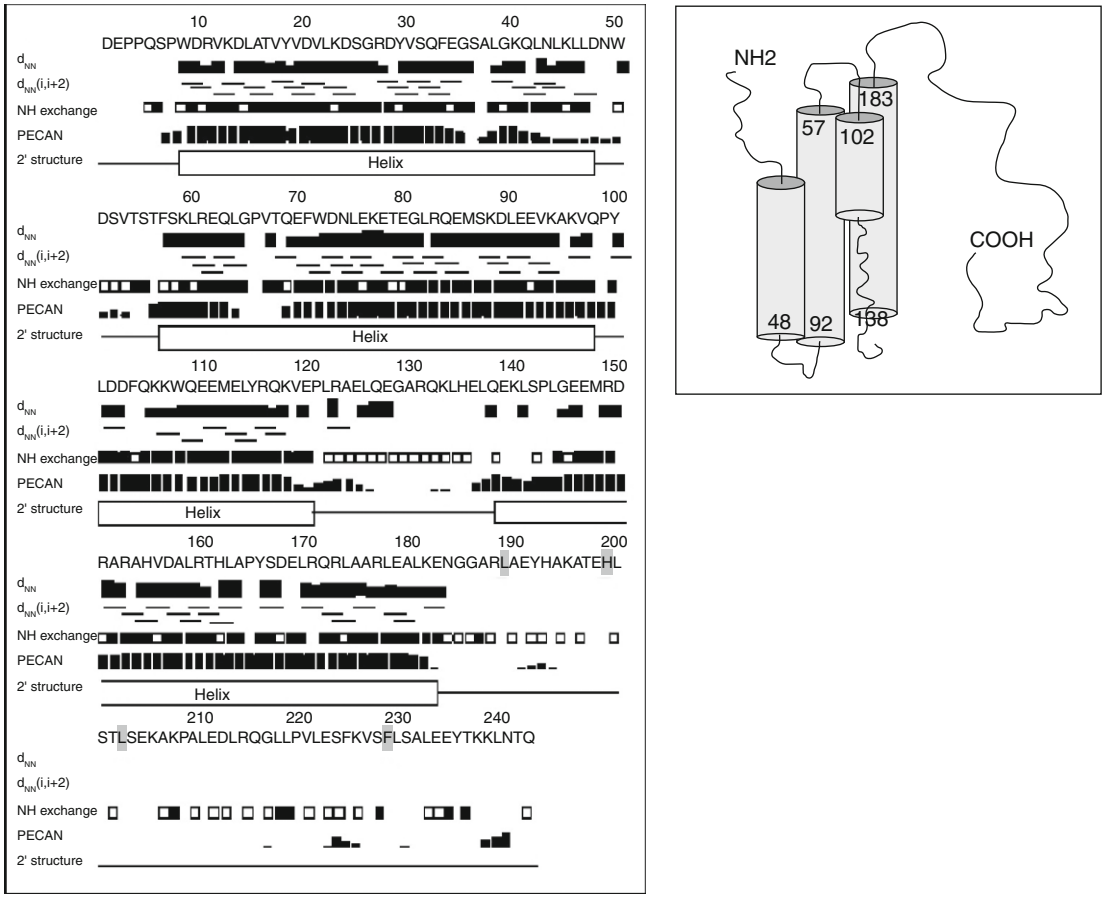

Fig. 7 Left Panel: Summary of HN–HN NOE connectivities, amide exchange rates for triple-labeled apoAI on Lp1AI. Below the one-letter code for amino acids, relative strengths of d_{NN} NOE cross-peak intensities are indicated by the bar thickness. $d_{NN}(i, i + 2)$ NOE connectivities observed between specific proton pairs are indicated by a solid line between two residues. Amide proton exchange rate is designated as follows: filled box, slow exchange rate; open box, medium exchange rate; no box, fast exchange rate. Resides that the backbone amide proton and nitrogen atoms haven't been assigned are labeled in blue. Right Panel: A schematic diagram of the NMR structure of apoAI on Lp1AI particles. The data shown in this figure is based on backbone atom spectral assignment only.

Using triple-labeled mouse apoAI, we have also prepared preβHDL that contains two apoAI molecules (Lp2AI). Figure 8, Left Panel shows a native gel of this preparation, indicating that the prepared preβHDL is a 70-kDa particle. We collected 3D/4D NMR experiments and carried out spectral assignment. Figure 8, Right Panel, shows a TROSY version of ^{1}H-^{15}N HSQC spectrum with partial spectral assignment. We noticed that some crosspeaks were missing in this

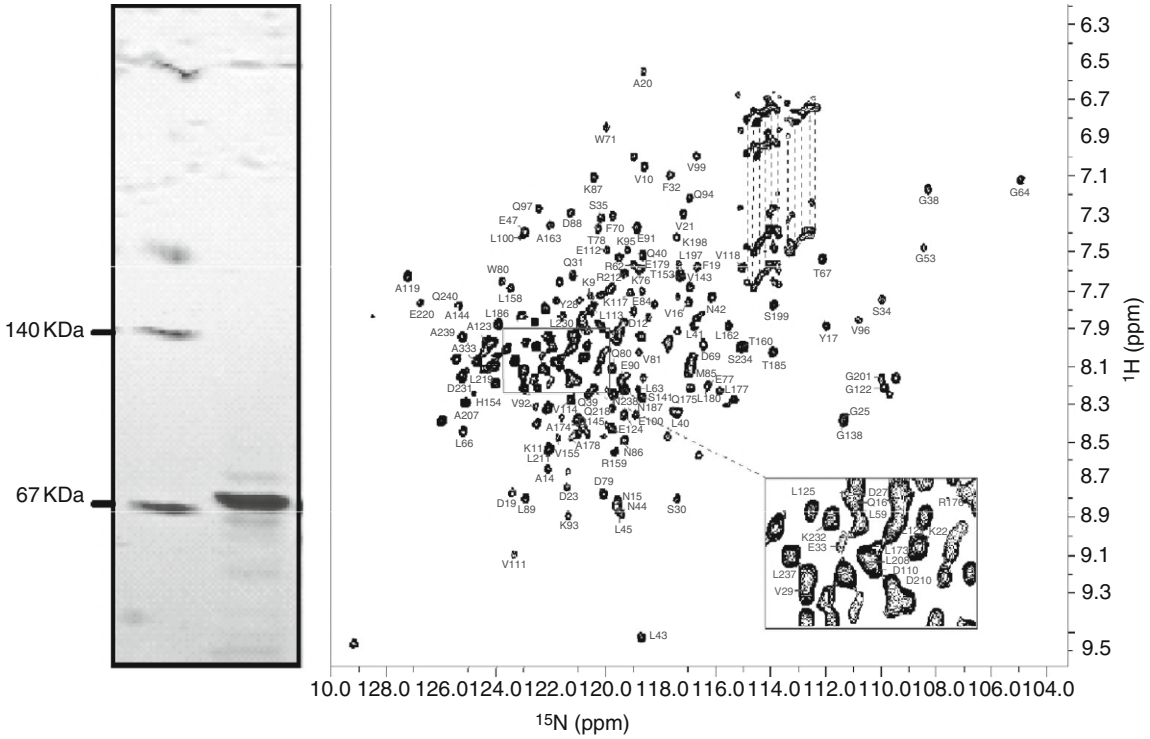

Fig. 8 Left Panel: An 8–25% native gel of preβHDL (Lp2AI) preparation using mouse apoAI, indicating that this preβHDL preparation is pure and has a molecular weight of ~70 kDa. Right Panel: ^{1}H-^{15}N HSQC-TROSY NMR spectrum of preβHDL (Lp2AI), in the presence of 50 mM sodium phosphate, pH 7.2, 50 mM NaCl, 0.1 mM NaN3, 5 mM EDTA. The NMR data was collected at a 500 MHz NMR instrument at 30 °C. A partial spectral assignment is shown in this figure.

spectrum, potentially due to the large particle size of this preβHDL (70 kDa). The missing peaks prohibit us from complete NMR spectral assignment. We are currently working on careful characterization of Lp2AI particle and optimizing its NMR spectra for a complete NMR spectral assignment.

C. apoAI on Discoidal HDLs

It is very difficult to isolate discoidal HDL from human blood. In addition, plasma HDL can't be used for high-resolution structural studies since it is very heterogeneous, containing a variety of HDL subspecies of different sizes, shapes, and protein/lipid compositions. It is nearly impossible to purify HDL at this moment. Therefore, the cholate dialysis method, a reconstitution technique developed by the Jonas laboratory in the 1980s, is critical to structural studies of discoidal HDL since it permits us to prepare relatively homogenous discoidal

HDL particles (Jonas and Matz, 1982, Matz and Jonas, 1982). Earlier theoretical consideration of discoidal HDL particles by Segrest led him to propose a ''belt'' model, suggesting that the α-helices of apoAI wrap around perpendicularly to the acyl chains of the phospholipid bilayer of discoidal HDL (Segrest, 1977). A separate model, the ''picket fence'' model, argued that the 22 amino acid helical repeats of apoAI, punctuated by turns, could traverse the bilayer edge parallel to the acyl chains of phospholipids (Wald *et al.*, 1990). The debate over the ''belt'' and ''picket fence'' model sparked many experimentalists and computer modelers to design experiments and simulations to test these two models (Segrest *et al.*, 1994). Based on the crystal structure of apoAI(44–243), Segrest and coworkers carried out computer simulations and derived a detailed molecular ''double belt'' model for apoAI in discoidal HDL particles (Segrest *et al.*, 1999). This double belt model suggested that each of the two ring-shaped apoAI proteins wraps around a leaflet in an anti-parallel orientation to maintain a registry between the monomers with similar intermolecular salt bridge connections in the crystal structure.

A number of experiments have been carried out to define the conformation of apoAI on discoidal HDL using the fluorescence resonance energy transfer (FRET) technique. These experiments, which were mainly from the Jonas, Sorci-Thomas, and Davidson laboratories, tried to measure the distance information of apoAI on discoidal HDL particles that distinguished the ''double belt'' model from others. However, the results from different laboratories did not agree with each other. For example, an early report from Jonas' laboratory suggested that their data did not support either the ''picket fence'' or the ''double belt'' models. Instead, they suggested that apoAI on discoidal HDL particle could adopt a mixture of head-to-head and head-to-tail hairpins (Tricerri *et al.*, 2001). Data from both Sorci-Thomas and Davidson's laboratories seemed to support the ''double belt'' model (Li *et al.*, 2000; Panagotopulos *et al.*, 2001). However, their results could not distinguish between the ''double belt'' and hairpin models (Li *et al.*, 2002). Recently, a technique that combined crosslinking and mass spectroscopy was used by the Davidson, Sorci-Thomas, and Thomas laboratories to study apoAI structure on discoidal HDL particles. While the data from these laboratories supported the ''double belt'' model, differences in the detailed belt orientations of apoAI protein did exist. The result from Davidson's laboratory suggested that the predominant conformation for the two apoAI molecules on a discoidal HDL particle closely resembles the predicted LL5/5 double-belt model. In addition, their data also argued that a second stable form of the double-belt might exist in a LL5/2 conformer. Finally, they indicated that their data could not eliminate a possibility of the hairpin model of apoAI on the discoidal HDL particles that contained odd numbers of apoAI proteins per particle (Davidson and Hilliard, 2003; Silva *et al.*, 2005). In contrast, data from Sorci-Thomas and Thomas laboratories suggested a double-belt model in which the N-terminal globular domain of one monomer apoAI interacted with the C-terminal domain of the other apoAI monomer (Bhat *et al.*, 2005, 2007). They further suggested that these intermolecular interactions stabilize the apoAI conformation on the discoidal HDL particles.

Although these studies significantly enhanced our understanding of the apoAI structure on discoidal HDL particles, no consensus conclusion has been reached to date about the exact conformation of apoAI on discoidal HDL particles. In addition, these studies used low-resolution techniques and could not provide data on apoAI structure on discoidal HDL particles at atomic resolution.

An NMR structural study of apoAI structure on discoidal HDL particles is certainly a challenging project. First, discoidal HDL particles are protein/lipid complexes of 140–200 kDa which certainly push the limits of NMR structural determination. In addition, apoAI protein on discoidal HDLs display tremendous conformational flexibility, preventing them from crystallizing and complicating NMR structural analysis. Furthermore, the purity of discoidal HDL particles is critical for high-resolution structural studies and the cholate dialysis method may not be able to prepare such ultra pure samples. Finally, a discoidal HDL particle contains both protein and lipids. To determine its structure, both the apoAI and lipid structures have to be defined. However, no well-defined lipid structure has been reported to date due to its flexibility (Cushley and Okon, 2002). Thus, a new technique may have to be developed to achieve this goal.

For NMR study, we have to solve several technical problems. The first problem is the high cost of the study. Our first NMR sample of discoidal HDL cost ~$6,000, since apoAI protein had to be triple-labeled with $^{2}H/^{13}C/^{15}N$. apoAI protein production from bacterial expression in 99.9% D_2O was low and it took several difficult steps to obtain pure discoidal HDL. To solve this problem, we worked on the optimization of apoAI expression to achieve a very high yield of triple-labeled proteins. We utilized an auto-induction bacterial expression method developed by Studier (2005), along with several practical protocols we developed for a fully optimized auto-induction system in D_2O. This optimized auto-induction protocol allows us to routinely produce ~14 mg triple-labeled apoAI from a 50 ml cell culture (Sivashanmugam *et al.*, 2008a). We further developed a new method that takes advantage of both auto-induction and IPTG-induction bacterial expressions. This method uses ^{13}C-labeled glucose, instead of ^{13}C-glycerol (which is much more expensive) (Sivashanmugam *et al.*, 2008a). Now, we can prepare a discoidal HDL NMR sample at a few hundred dollars.

With the triple-labeled apoAI/rHDL sample prepared using the cholate dialysis method, we carried out NMR studies. Figure 9, Panel C shows a TROSY version ^{1}H-^{15}N HSQC spectrum of discoidal HDL particles, indicating a well-dispersed spectrum. A comparison between this spectrum (Panel C) with that of the Lp1AI (Panel B) indicates that both spectra display a similar spectral pattern (Chen *et al.*, 2008). In particular, regions highlighted in red dotted line and red arrows in both panels show identical crosspeaks, suggesting that the spectrum of panel C may contain crosspeaks of lipid-poor apoAI. However, significant differences between panels B and C are also observed in the regions that are highlighted in blue dotted lines and blue arrows. This suggests that the NMR sample in Panel C is not pure which may potentially contain both lipid-poor and discoidal HDL particles. This suggestion is supported by the differences in line widths of the crosspeaks shown in

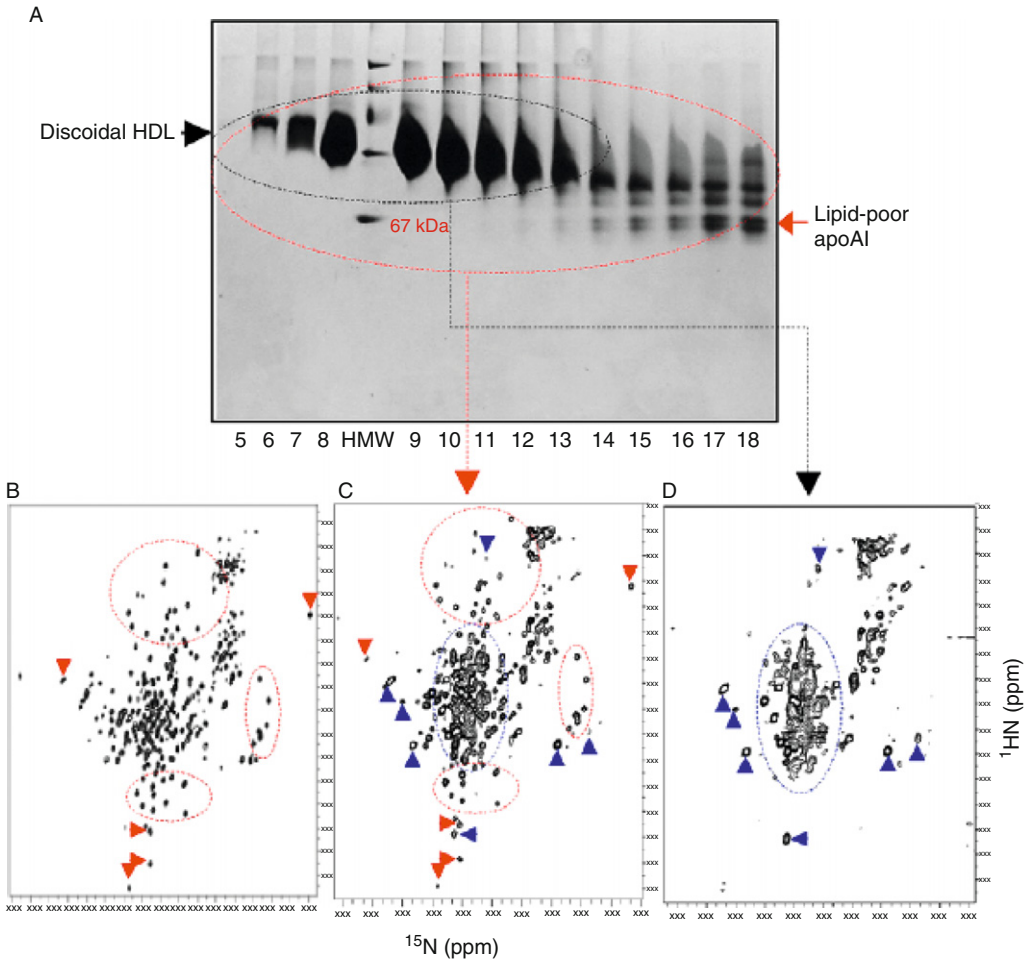

Fig. 9 Panel A: An 8–20% native gel of the fractions of ultracentrifugation. Fractions 1–4 and 19–20 show no protein. HMW: high molecular marker. Panel B: ^{1}H-^{15}N HSQC-TROSY NMR spectra of Lp1AI particle (1 mM of apoAI) in the presence of 50 mM sodium phosphate, pH 7.2, 50 mM NaCl. Panel C: ^{1}H-^{15}N HSQC-TROSY NMR spectra of a discoidal HDL preparation before ultracentrifugation. The sample is in 50 mM phosphate buffer, pH 7.2, 50 mM NaCl, 0.01 mM NaN3, 5% D_2O with ~0.1 mM apoAI on reconstituted discoidal HDL particle. Panel D: ^{1}H-^{15}N HSQC–TROSY NMR spectra of a discoidal HDL preparation after ultracentrifugation. The sample contains fractions 6–13 and is in 50 mM phosphate buffer, pH 7.2, 50 mM NaCl, 0.01 mM NaN3, 5% D_2O with ~0.1 mM apoAI on reconstituted discoidal HDL particle.

regions that are highlighted either in red or in blue. Visual inspections of these two regions clearly indicate that crosspeaks in blue region are much broader than those crosspeaks in red region. We suggest that the crosspeaks in blue regions are from discoidal HDL particles which are much larger particles than lipid-poor apoAI.

A large discoidal HDL particle gives rise to a slow tumbling that produces a broader line width. To confirm this, we carried out experiments to purify the discoidal HDL particles. Purification of a millimolar amount of discoidal HDL using FPLC will be difficult and time consuming. We then developed a quick method to separate lipid-poor apoAI from discoidal HDL using ultracentrifugation (Chen *et al*., 2008). A certain amount of KBr was added to the discoidal HDL sample and the volume was adjusted to 2 ml (density 1.27 g/ml). The samples were transferred to 5 ml Beckman open centrifuge tubes, overlaid with 2 ml of 0.9% NaCl (density 1.063), and centrifuged at 49,000 rpm for 16 h at 4 °C using a SW 50.1 swinging bucket rotor with a Beckman optima LE-80K ultracentrifuge. After ultracentrifugation, the sample was fractionated into 20 fractions from the top layer to the bottom layer with each fraction of 200 μl. Aliquots of each fraction were subjected to native gradient gel to check the particle size of each fraction. Figure 9, Panel A shows the native gel of the fractions 5–18, suggesting that discoidal HDL preparation indeed contains lipid-poor apoAI (fractions 14–18, red arrow). We have repeated the discoidal HDL preparation using the cholate dialysis method many times and always observed the presence of 5–10% lipid-poor apoAI among the discoidal HDL particles. Fractions 5–13 seemed to show a single broad band of discoidal HDL particles of molecular weight >140 kDa, and thus were pooled together, dialyzed against buffer exhaustively and then concentrated using a centricon for NMR sample preparation. Panel D shows the TROSY version ^{1}H-^{15}N HSQC spectrum of fractions 5–13. It is obvious that this spectrum is totally different from Panel B, confirming our hypothesis that the crosspeaks in the blue region of Panel C are from discoidal HDL particles.

Interestingly, NMR signals from a very low concentration of lipid-poor apoAI ($\sim$50 μM) showed a similar intensity to those of the crosspeaks from a much higher concentration of discoidal HDL (500 μM). This is due to the particle size difference between lipid-poor apoAI (40–70 kDa) and discoidal HDL (140–200 kDa). A smaller particle produces sharper NMR signals, resulting in better signal-to-noise. In contrast, larger discoidal HDL particles produces much broader NMR signals due to a slower molecular tumbling, resulting in a much worse signal-to-noise, even when using TROSY NMR experiments with a triple-labeled NMR sample. In this case, a 5–10% lipid-poor apoAI impurity may cause serious errors in the spectral analysis of larger discoidal reconstituted HDL (rHDL). This may not be a problem when the contamination comes from a protein of similar size to the protein under investigation, because a 5–10% contamination (0.025–0.05 mM) does not produce NMR signals that are strong enough to interfere with NMR spectral analysis of the protein (0.5 mM) under investigation. Thus, our data clearly demonstrates that one has to be extremely careful in terms of NMR sample purity when working with large proteins. A minor population of smaller protein contamination (5–10%) may cause serious errors in the NMR spectral analysis of this large protein (Chen *et al*., 2008).

We noticed that the purified discoidal HDL particles shown in Fig. 9, Panel A displayed a very broad band, ranging between 140 to 232 kDa according to the

molecular weight marker. To further separate discoidal HDLs, we carried out a second ultracentrifugation step using a four-layer density gradient (1.15 g/ml, 1.10 g/ml, 1.08 g/ml, and 1.07 g/ml). This second ultracentrifugation can efficiently separate large discoidal HDL from small discoidal HDL. However, we have to repeat this four-layer density gradient ultracentrifugation several times, in order to obtain a sufficient amount of purified small and large particles. Figure 10, Panel A shows the result of this ultracentrifugation, demonstrating that two different sizes of discoidal HDL particles are separated. Figure 10, Panel B shows the purified large (Lane 1) and small (Lane 2) discoidal HDL particles, confirming the purity. Clearly, large discoidal HDL particles have a molecular weight ~200 kDa and small discoidal HDL particles have a molecular weight of ~140 kDa (Chen *et al.*, 2008).

Electron microscopy shows that both purified discoidal HDL particles are disk-shaped, with a particle size of 7.6 ± 1.6 nm for small particles and 9.8 ± 1.7 nm for large particles. In contrast to the large range of size distribution of the discoidal HDL particles before the second ultracentrifugation (8.8 ± 3.7 nm), the size distribution of both purified small (7.6 ± 1.6 nm) and large (9.8 ± 1.7 nm) discoidal HDL particles are significantly narrower. To characterize apoAI protein structure and stability on these two discoidal HDL particles, we carried out CD and GdnHCl denaturation experiments. Figure 11, Panel A compares far-UV CD spectra of purified small and large discoidal HDL, indicating no difference in terms of secondary structure of apoAI. CD data further suggests that apoAI on

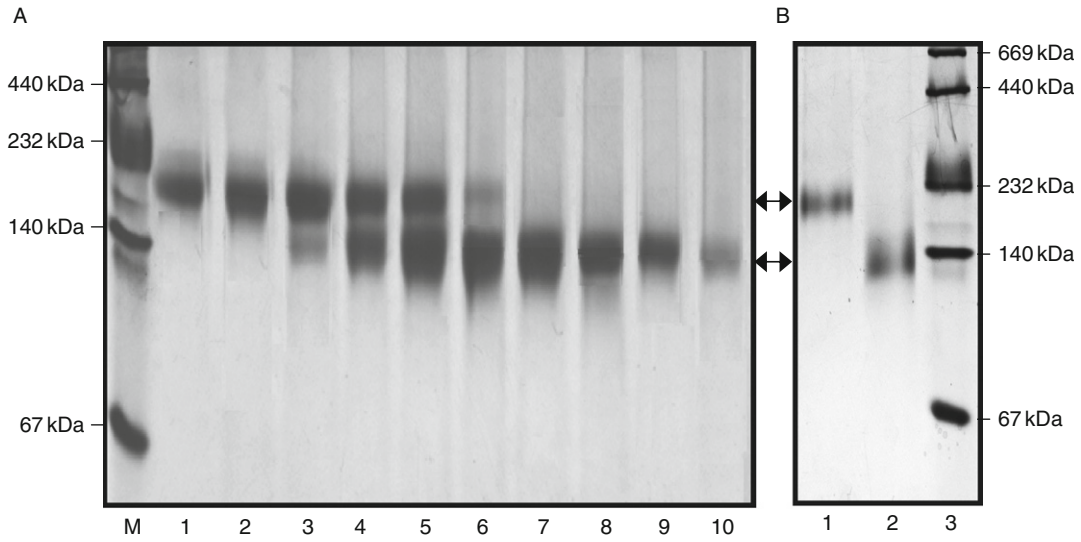

Fig. 10 Panel A: A 4–20% native gel of the fractions of the second ultracentrifugation, showing the purification of small and large discoidal rHDL particles can be achieved using this second ultracentrifugation method. Panel B: A 4–20% native gel of the purified large (Lane 1) and small (Lane 2) discoidal rHDL. M: High molecular weight marker.

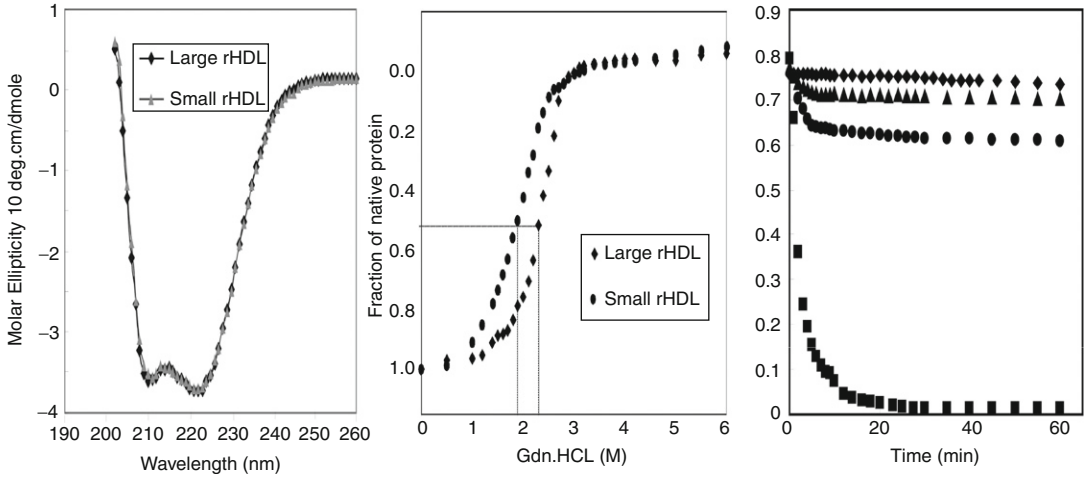

Fig. 11 Panel A: Far-UV CD spectra of small (black diamonds) and large discoidal rHDL (gray triangles) at 0.2 mg/ml in 50 mM sodium phosphate, 150 mM NaCl, pH 7.2. Panel B: GdnHCl denaturation of small (circle) and large discoidal rHDL (diamond) under the same condition. The fraction of unfolding was plotted as a function of GndHCl concentration. Panel C: Phospholipid vesicle clearance. DMPC vesicles were incubated at 23.9 °C in the absence (diamond) and presence of lipid-free apoAI (square), small rHDL (circle), and large rHDL (triangle) in 20 mM Tris-HCl, pH 7.2, 250 mM NaCl, and 1 mM EDTA. Vesicle clearance as a function of time was followed by OD at 490 nm. DMPC to apoAI (w/w) is 1:1.

both discoidal HDL particles displays ~68% helical content, whereas lipid-free apoAI only displays ~53.4% helical content. Figure 11, Panel B shows the GdnHCl denaturation data. To our surprise, a stability difference of apoAI for purified small and large discoidal HDL is observed. The small HDL has a $[GdnHCl]_{1/2}$ at 1.90 M whereas the large HDL has a $[GdnHCl]_{1/2}$ at 2.32 M. This difference indicates that apoAI protein on small HDL is less stable than it is on large HDL. This is confirmed by the calculated ΔG_d^{H2O}, indicating apoAI on small HDL has a ΔG_d^{H2O} of 5.3 ± 0.2 kcal/mol and apoAI on large HDL has a ΔG_d^{H2O} of 7.9 ± 0.7 kcal/mol. Before the second ultracentrifugation, the stability of apoAI on the mixed size of HDL is between those of small and large discoidal HDL ($\Delta G_d^{H2O} = 6.2 \pm 0.9$ kcal/mol and $[GdnHCl]_{1/2} = 2.14$ M). To assess lipid-binding activity, we carried out a DMPC clearance assay of both small and large discoidal HDL. Figure 11, Panel C shows the results of DMPC clearance assay. As a control, we also carried out DMPC clearance assays using lipid-free apoAI. Panel C demonstrates the difference between small and large discoidal HDL in terms of phospholipid-binding activity, suggesting that small HDL has a stronger phospholipid-binding activity than that of large HDL (Chen *et al.*, 2008).

Our data showed that apoAI protein displayed an identical secondary structure, but different stability and phospholipid-binding activity on small and large discoidal HDLs. This raises an interesting question: How does the apoAI structure

affects its stability and lipid-binding activity? To address this question, we carried out high-resolution NMR and negative stain EM, to investigate apoAI tertiary structure and morphology. Figure 12 shows two ^{1}H-^{15}N TROSY-HSQC NMR spectra overlaid on top of each other, with the black spectrum from small and blue spectrum from large discoidal HDL, indicating that apoAI protein on small and large discoidal HDL particles displays a different HSQC spectral pattern. This spectral difference is further highlighted by the inset of Fig. 12 showing four crosspeaks of the $^{15}N\varepsilon$ and $^{15}NH\varepsilon$ of the Trp side chain. Indeed, blue crosspeaks (large discoidal HDL) display a different pattern from those of the black crosspeaks (small discoidal HDL), suggesting that the Trp side chain of apoAI may adopt a different conformation between large and small discoidal HDL. We also negatively stained more dilute solutions of rHDL particles with uranyl formate for detailed ultrastructural observation. Figure 13 shows the results, with 30 selected high-quality representative particles for either the small (Panel A) or large (Panel B) discoidal HDL, displayed in window size of 15 nm. In both Panels, the top two rows show possible side views, middle two rows show possible top views,

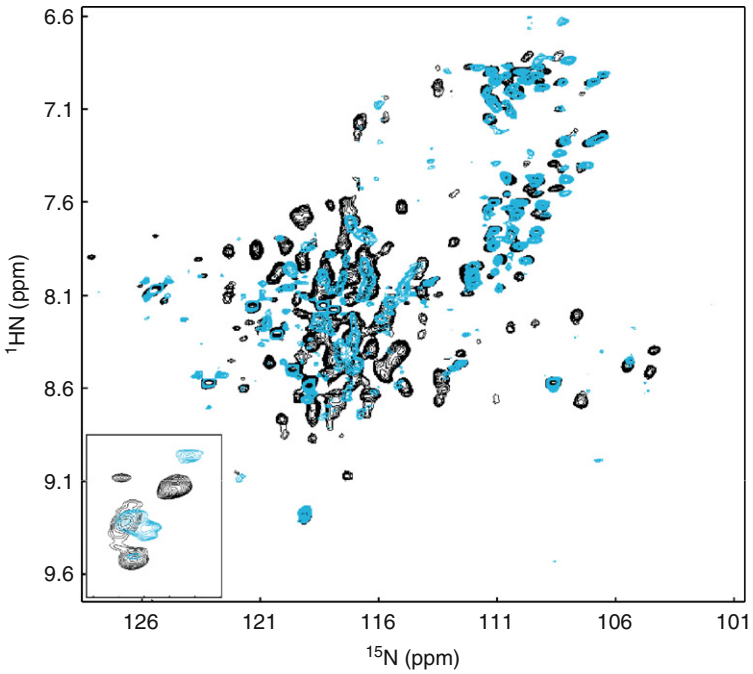

Fig. 12 A comparison of [^{15}N, ^{1}H] TROSY–HSQC spectra of small rHDL (black) and large rHDL (blue) collected on a 600 MHz NMR instrument with a cold probe at 30 °C. NMR samples contain 0.2–0.5 mM triple-labeled rHDL in 50 mM phosphate buffer containing 50 mM NaCl, 0.01 mM NaN_3, 1 mM EDTA, 5–7% D_2O at pH 7.2. Inset: the crosspeaks of the Trp side chain $H^{\varepsilon 1}/N^{\varepsilon 1}$ atoms of the apoAI on small (black) and large (blue) discoidal rHDL particles.

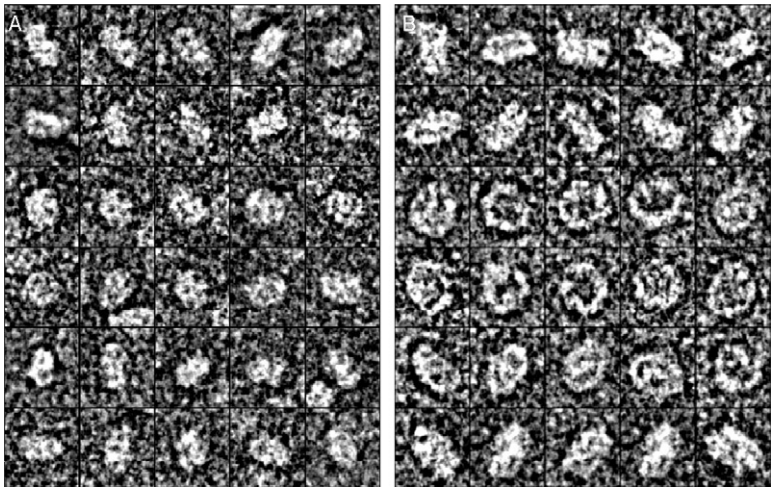

Fig. 13 Uranyl formate negatively stained electron microscopy of purified small and large discoidal rHDLs. Wide field micrographs of small HDL (Panel A) and large HDL (Panel B) demonstrates the homogeneity of particle size and shape (each box corresponds to 15 nm).

and bottom two rows show possible tilted top views of the purified small and large discoidal HDL. A careful examination of the morphology shows significant differences in the shape and size between small and large discoidal HDLs. While the top two rows in Panel B show that large rHDL displays a typical discoidal shape with particle's width about twice as the particle height, the same rows in Panel A indicate a much smaller ratio of particle diameter over particle height, suggesting a more ''globular shape'' for small discoidal HDL. In addition, the bottom four rows in Panel B show that large discoidal HDLs display a black background in the middle of the particles, whereas the same rows in Panel A indicate that the center of small discoidal HDL is filled with white material. We suggest that the black background is the phospholipid moiety, whereas the white material is the image of apoAI protein. Thus, the difference in particle morphology between small and large discoidal HDLs observed by negative stain EM imaging may suggest a potential conformational difference of apoAI on these different particles, which is consistent with our NMR data. Overall, apoAI on small discoidal HDL seems to adopt a more ''globular structure'', which is packed more tightly and more compact, while apoAI on large discoidal HDL seems to display a more extended α-helical structure. This apoAI conformational difference between small and large discoidal HDL further indicates apoAI conformational plasticity. Clearly, this apoAI conformational plasticity is critical to the assembly of different HDL particles with different lipids. Our results further demonstrate that for any structural studies of discoidal HDL particles, it is absolutely necessary to obtain pure discoidal HDL particles with unique morphology, biophysical properties, biological activity, and apoAI conformation. Discoidal HDL obtained using the

cholate dialysis method without further purification may result in controversial results that may cause confusion (Chen *et al.*, 2008).

In summary, our data indicates that discoidal HDL prepared using the cholate dialysis method contains 5–10% lipid-poor apoAI and two major discoidal HDL species. An ultracentrifugation method can be used to purify discoidal HDL from lipid-poor apoAI and to isolate large quantities of two different HDL species. Characterizations of purified discoidal HDLs indicate that the two species of isolated discoidal HDL particles have different stabilities and phospholipid-binding activities, although the apoAI protein shares the same secondary structure content. Further experiments using high-resolution techniques, including NMR and negative stain EM, indicate different morphology and tertiary structure of apoAI protein on different discoidal HDL particles. These results allow us to suggest that the tertiary structure, rather than secondary structure, determines the different morphology, stability, and phospholipid-binding activity between small and large discoidal HDL particles. With well-characterized discoidal HDLs, we are now well positioned to carry out high-resolution NMR structural studies of different discoidal HDL particles and are currently actively pursuing these studies.

D. apoAI on Spherical HDLs

It is generally accepted that a mature spherical HDL particle contains a neutral lipid core of CE and triacylglycerol (Lund-Katz *et al.*, 2003). This neutral lipid core is surrounded by a surface monolayer of phospholipids to stabilize the entire HDL particle. Currently, we have few clues on how the apoAI protein is associated with spherical HDL particles. Based on the crystal structure of apoAI(44–243), Borhani *et al.* hypothesized that the belt shape helices of apoAI wrap around the neutral lipid core, potentially floating among the phospholipid monolayer. They have built a computer model of spherical HDL particles based on this hypothesis (Borhani *et al.*, 1997), however, no details have been given in this computer model on how apoAI binds to lipids. A snorkel model has also been proposed, suggesting that the apoAI helices might bind to the phospholipid monolayer in such a way that the hydrophobic faces of the apoAI helices penetrate into the monolayer to interact with the acyl chains, whereas the hydrophilic faces of the helices interact with the phosphate head groups via charge–charge interactions (Mishra *et al.*, 1994). However, experimental evidence has yet to be provided to either prove or disprove these models. By studying the motion of the head groups of phospholipids in insect lipophorin using ^{31}P and ^{13}C-NMR, we proposed a model similar to the snorkel model to explain how apolipophorin-III, an insect exchangeable apolipoprotein, interacts with phospholipids and cholesterol on the surface of insect high-density lipoproteins, HDLp (Wang *et al.*, 1992, 1995). Several reports have studied the apoAI conformational difference between discoidal and spherical HDL particles and generally concluded that apoAI displayed a different conformation on the spherical HDL from that of apoAI on discoidal HDL, however, no details of this

conformational difference has been elucidated (Curtiss *et al.*, 2000; Sparks *et al.*, 1992). In particular, a study by Sorci-Thomas's laboratory measured several distances between the fluorescence donors and acceptors using the FRET technique and indicated that these distances are different between spherical HDL and discoidal HDL particles (Li *et al.*, 2002). To date, there is no high-resolution structural study reported for spherical HDL particles probably due to the complexity of the mature, spherical HDL particle, in terms of heterogeneity of the particle size and lipid and protein content.

We have carried out structural/functional characterizations of the major lipid-binding domain of apoAI, the C-terminal domain, apoAI(173–243) (Sivashanmugam *et al.*, 2008b). Our data shows that apoAI(173–243) is unstructured in the lipid-free state, but becomes α-helical in the presence of DPC micelles, a phospholipid-mimetic. When examining the lipid-binding activity using a DMPC clearance assay, both apoAI and apoAI(173–243) show an identical clearance curve, suggesting that the C-terminal domain of apoAI may serve as the major lipid-binding domain. Indeed, previously published data indicated that this domain might initiate apoAI-phospholipid interactions (Brouillette *et al.*, 2001). However, the cholate dialysis method using either apoAI or apoAI(173–243) generated different rHDL particles. Figure 14 shows the EM pictures of the rHDL particles prepared using either full-length apoAI (Upper Panel) or the apoAI C-terminal domain, apoAI(173–243) (Lower Panel). The upper panel clearly shows that the prepared rHDL particles using full-length apoAI are in the

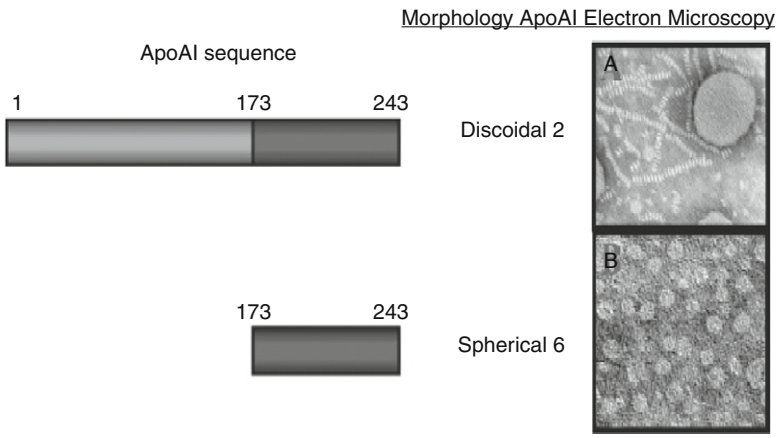

Fig. 14 The left bar graph shows apoAI sequence with the major lipid-binding domain of apoAI highlighted in grey. Panel A: Electron microscopic picture of the discoidal HDL particles prepared using the full-length apoAI, apoAI(1–243). Panel B: Electron microscopic picture of the spherical HDL particles prepared using the major lipid-binding domain of apoAI, apoAI(173–243). Crosslinking results indicate that there are two apoAI molecules per discoidal HDL particle prepared using apoAI (1–243), whereas there are six apoAI molecules per spherical HDL prepared using apoAI(173–243).

typical disk shape. However, the lower panel displays a completely different morphology, a spherical shape. This result demonstrates that the major lipid-binding domain of apoAI, apoAI(173–243), can only form spherical HDL particles. Figure 14 further suggests that the prepared spherical HDLs using apoAI(173–243) display homogenous morphology and particle size, which are about 10 nm in diameter. Crosslinking experiments indicated that there are six apoAI(173–243) molecules per spherical HDL particle. This is a very interesting result since there are two molecules of full-length apoAI on the discoidal HDL particles and apoAI(173–243) is about one third of the length of full-length apoAI. This result seems to suggest that during HDL assembly, the apoAI protein utilizes a defined stoichiometry to assemble nonneutral lipid core containing HDL particles with the same size but different shapes, including both discoidal HDL and spherical HDL. This result raises an important question: how does apoAI's primary sequence recruit lipids for assembly of the HDL particles with different shapes (Sivashanmugam *et al.*, 2008b). To investigate the potential effect of cholesterol on HDL assembly, we prepared rHDL particles using apoAI(173–243) with POPC and cholesterol (80:5:1 = POPC:cholesterol: apoAI(173–243)). Our results indicated that even with cholesterol, apoAI(173–243) assembles into the spherical HDL particles as shown in Fig. 14. In contrast, full-length apoAI only assembles discoidal HDL particles with POPC and cholesterol. This data allows us to confirm that it is the apoAI protein sequence that dictates the shapes of HDL particle assembly (Sivashanmugam *et al.*, 2008b).

The HDL particles prepared using apoAI(173–243) are homogenous, small spherical HDL particles with a ~10–12 nm diameter, and a molecular weight of ~230 kDa. These small spherical HDL particles contain apoAI protein, POPC and cholesterol, which may serve as a good model for high-resolution structural studies of mature, spherical HDL. It is a challenging project, since this ~230 kDa protein/lipid particle pushes the limit of NMR structural determination. However, this project will allow us to develop new techniques to study such large protein/lipid complexes, to define the protein–protein interactions on HDL particles, and to identify protein–phospholipid and protein–cholesterol interactions. This is critical information that will allow us to understand the structure and dynamics of HDL's functions. In addition, this project will also allow us to accumulate working experience in studying mature, spherical HDL particles, HDL_2, and HDL_3.

IV. Discussion

A. Two Structural Domains of Lipid-Free and Lipid-Poor of apoAI

The NMR structures of lipid-free mouse apoAI and human apoAI/preβHDL indicate a similar overall molecular architecture of apoAI that contains a four helix-bundle in the first two-thirds of the protein (residues 1–186) and a flexible

region in the last one third (residues 187–243). Structural comparisons between lipid-free mouse apoAI and human apoAI/preβHDL indicate a major difference in the C-terminal flexible region. Mouse lipid-free apoAI contains two short helices (five residues each), whereas human apoAI/preβHDL does not have these two short helices in this flexible C-terminal region. Both apoAI structures are monomeric and contain helical content that are consistent with the CD measurements of lipid-free apoAI and apoAI/preβHDL. In contrast to lipid-free apoAI, apoAI/preβHDL is a lipid-poor particle which binds to only a few phospholipids. Although minor changes in biophysical properties (such as stability) and biological functions (such as lipid-binding specificity) are observed for apoAI upon binding a few phospholipids, interestingly, both lipid-free and lipid-poor apoAI/preβHDL share a nearly identical structure. In this sense, both lipid-free and lipid-poor apoAI are in a similar conformational state, although minor differences are indeed observed. We suggest that apoAI contains two structural domains: an N-terminal helix-bundle domain and a C-terminal flexible domain. We believe that these two apoAI domains mediate different biological functions. For example, the C-terminal flexible domain is considered to be the major lipid-binding domain of apoAI that initiates lipid-binding and HDL formation. In addition, the N-terminal four helix-bundle domain contains the LCAT activation region which is located between residues 110 to 145. These residues include the short helix 3 and the loops between helices 2 and 3 and helices 3 and 4. This part of the helix-bundle displays tremendous conformational plasticity that may be necessary for activating LCAT. We further suggest that the N-terminal helix-bundle may also serve other functions in assembling the different shapes of HDL particles.

B. ApoAI Conformational Plasticity versus HDL Assembly

Clearly, the conformational plasticity plays a critical role in the conformational inter-conversions of apoAI among different apoAI states, including lipid-free, lipid-poor, discoidal HDL, and spherical HDL. As we discussed earlier, the conformational flexibility in the C-terminal domain may be critical for binding to different lipids that initiates HDL formation and assembly. Indeed, when lipid-free apoAI binds to a few phospholipids in the flexible C-terminal domain, the two flexible, short helices in the C-terminal domain (Fig. 5) are interrupted and the entire C-terminal domain of apoAI/preβHDL becomes more dynamic (Fig. 6), causing the observed reduction in stability (Sparks *et al.*, 1999). A reduced stability of preβHDL indicates that this apoAI state is an HDL precursor during HDL assembly that is an important intermediate state, but metabolically unstable. Interestingly, our data also showed that such an enhancement in conformational plasticity in the C-terminal domain significantly reduced the aggregation property of apoAI. apoAI/preβHDL becomes monomeric even at 5 mg/ml, whereas lipid-free apoAI forms a mixture of monomer, dimer, trimer, and higher oligomers at 1 mg/ml. Since the C-terminal domain is the region that causes aggregation, we suggest that an increase in flexibility in the C-terminal domain, upon phospholipid-binding,

significantly reduces the potential for oligomerization. Phospholipid, an amphipathic molecule, is the perfect lipid candidate to interact with apoAI oligomers, in which the surface residues are hydrophilic and the center of the oligomer is hydrophobic. We suggest that phospholipids utilize their hydrophilic head groups to initiate interaction with the apoAI oligomer, resulting in dissociation of the oligomer. The fatty acid chain of phospholipids will then bind to the hydrophobic surface of the apoAI monomer, that otherwise would be exposed in solution. This will stabilize the apoAI/preβHDL monomer, resulting in formation of this HDL precursor. In addition, phospholipid-binding also interrupts the two short helices in the phospholipid-binding C-terminal domain of lipid-free apoAI, causing apoAI/preβHDL to be more dynamic and less stable. Indeed, a dynamic HDL precursor, apoAI/preβHDL, facilitates HDL assembly later in the apoAI cycle.

The major driving force for protein oligomerization is the hydrophobic interaction by hydrophobic residues within proteins. This driving force allows hydrophobic residues of different protein molecules to cluster together to form oligomers. This way, the hydrophobic residues of each protein monomer will be shielded from aqueous solution, thus making the oligomers more stable. In addition, the nature of a protein–cholesterol interaction is also purely hydrophobic and the protein utilizes hydrophobic residues to interact with cholesterol. Oligomerization in the C-terminal domain may block the binding sites for cholesterol, thus, lipid-free apoAI primarily binds to amphipathic phospholipids. Once lipid-free apoAI binds the phospholipids, we suggested that there is a dissociation of the oligomer and an enhancement of conformational plasticity in the C-terminal domain. Both of these processes may expose the cholesterol-binding sites in apoAI, thus allowing apoAI/pre$\beta-$HDL to avidly interact with cholesterol to initiate assembly of discoidal HDL particles. In contrast to lipid-free apoAI, both *in vivo* and *in vitro* data indeed suggest that apoAI on preβHDL primarily binds to cholesterol avidly, in addition to phospholipid-binding (Rye and Barter, 2004, Sparks *et al*., 1999), supporting this suggestion.

We further suggest that cholesterol-binding induces a major conformational change in apoAI, which may cause the N-terminal helix-bundle to open and adopt an open ring conformation on discoidal HDL. We cannot accurately elucidate how this apoAI helix-bundle opens during discoidal HDL assembly at this moment, since this requires a high-resolution NMR structure of apoAI/preβHDL (Fan *et al*., 2003, Wang *et al*., 2002). Currently, we are actively working on determining the NMR structure of apoAI/preβHDL. However, we believe that apoAI conformational plasticity plays a key role in directing this helix-bundle opening upon cholesterol-binding during assembly of discoidal HDL. Once the discoidal HDL is formed, apoAI still maintains conformational plasticity in certain regions, although overall conformational stability is significantly enhanced. For example, previously published data suggested a hinge domain in the middle of apoAI that is flexible and does not tightly associate with lipids (Martin *et al*., 2006; Wu *et al*., 2007). Data from Oda's laboratory indicated that this hinge loop was located between residues 134 to 145, whereas Wu *et al.* suggested that residues

159–180 formed a protruding solvent-exposed loop. While the location of the hinge domain is debatable, data from both laboratories indicated an anti-parallel double belt model of apoAI on discoidal HDL. In addition, this hinge loop region is located in the domain for LCAT activation. It is suggested that this flexible hinge loop conferred on apoAI an intrinsic conformational plasticity to adapt its structure to accommodate changing particle lipid content for LCAT activation (Martin *et al.*, 2006). The activity of LCAT helps discoidal HDL mature into spherical HDL, thus completing HDL assembly.

C. The N-Terminal Helix-Bundle Domain of apoAI Regulates Normal apoAI Cycle

It is amazing to see how the apoAI protein adjusts its conformational plasticity to regulate its aggregation properties and lipid-binding specificity. This raises an important question about the role of apoAI N-terminal helix-bundle domain. If only conformational flexibility is required for lipid-binding and HDL assembly, why does lipid-free apoAI contains an N-terminal helix-bundle? We believe that this N-terminal domain is an important structural domain in apoAI for the regulation of assembly of different HDL particles (Fig. 15). During the apoAI cycle, discoidal HDL is a critical HDL intermediate that activates LCAT, loading CEs into HDL for formation of the mature, spherical HDL. Although some

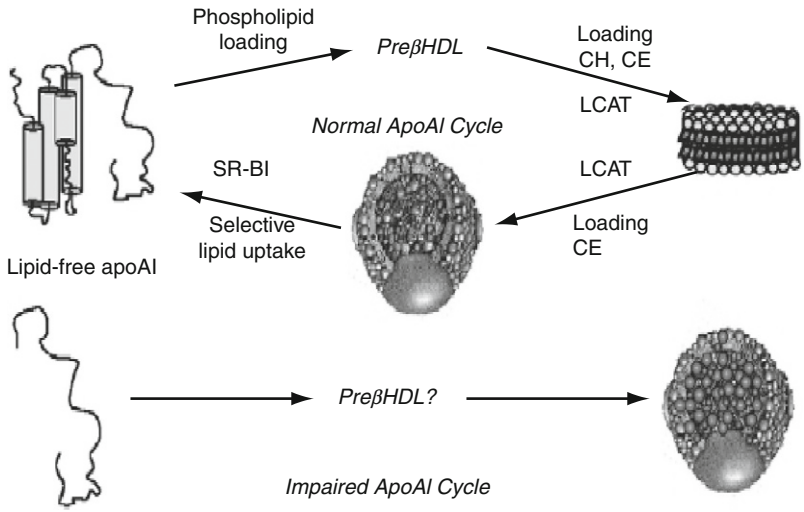

Fig. 15 A schematic representation of the hypothesis based on our results of high-resolution NMR studies of apoAI conformations in lipid-free and HDL-associated states. Upper Panel: A normal apoAI cycle which goes through four apoAI conformational states. The lipid-free apoAI contains two structural domains: An N-terminal helix-bundle domain and a C-terminal flexible domain. Lower Panel: A potential impaired apoAI cycle by the apoAI C-terminal flexible domain, which may skip the formation of discoidal HDL step.

previous reports suggested that lipid-poor apoAI also has the ability to activate LCAT (Rye and Barter, 2004; Sparks *et al.*, 1999), it is the consensus that the discoidal HDL is the main HDL species that activates LCAT *in vivo*. Knocking out the discoidal HDL species may prevent HDL from maturing. Therefore, the efficiency of transporting the ''bad lipids'' back to the liver will be significantly reduced.

Our data indicates that the major lipid-binding domain of apoAI, apoAI(173–243), has an ability to assemble a small spherical HDL particle, but fails to form a discoidal HDL *in vitro*. This small spherical HDL particle may not contain a neutral lipid core, thus it would not be able to efficiently transport the ''bad lipids'' back to the liver for clearance. It seems that apoAI(173–243), may not undergo the full apoAI cycle, by skipping the discoidal HDL step, although this apoAI domain displays an equal phospholipid-binding activity as that of the full-length apoAI (Fig. 15, Lower Panel). In contrast, full-length apoAI is able to make discoidal HDL particles and undergoes the normal apoAI cycle. This result demonstrates that the apoAI protein sequence may play a critical role in regulating HDL assembly *via* the normal apoAI cycle with its optimized efficiency for the removal of the ''bad lipids'' in the RCT pathway.

An important question is raised based on the above result: Is it the apoAI primary sequence that dictates apoAI to assemble into the different shapes of the HDL particles or is it the apoAI three dimensional structure that regulates the normal apoAI cycle to go through all four apoAI conformations during HDL assembly? A careful inspection of the structure of lipid-free/lipid-poor apoAI indicates that the major lipid-binding domain is found in the C-terminal flexible domain. The intact apoAI protein contains both the N-terminal helix-bundle domain and the C-terminal flexible domain, to ensure a normal apoAI cycle that initiates HDL formation and regulates HDL maturation and assembly. In contrast, the major lipid-binding domain of apoAI lacks the N-terminal domain helix-bundle and fails to form discoidal HDL particles, and thus can only undergo an impaired apoAI cycle which generates spherical HDL particles without a neutral lipid core. Therefore, it seems that the N-terminal helix-bundle structure of apoAI plays a critical role in regulating HDL assembly by forcing discoidal HDL formation to complete a normal apoAI cycle for an optimal RCT pathway.

Segrest proposed in 1970s that an amphipathic α-helix represents an essential secondary structural motif for the lipid-binding activity of exchangeable apolipoproteins (Segrest *et al.*, 1974). Later, these amphipathic α-helices were further classified into several different classes. The Class A amphipathic α-helix was suggested to be the major helix that displays lipid-binding activity of exchangeable apolipoproteins (Segrest *et al.*, 1990). Experimental evidence supported Segrest's hypothesis and indicated that small amphipathic α-helical peptides indeed bind to lipid surfaces (Navab *et al.*, 2005). However, no evidence indicates that these small amphipathic helical peptides can assemble different HDL particles. This raises an important question about the essential structural requirement of an exchangeable apolipoprotein that is critical for lipoprotein assembly. In addition to lipoprotein

assembly, exchangeable apolipoproteins also play major roles in lipoprotein and lipid transport and metabolism via protein–protein interactions with receptors, enzymes, and lipid transport proteins. A simple amphipathic α-helical peptide may not be able to serve this role in mediating protein–protein interactions. Indeed, the available structures of exchangeable apolipoproteins, except the apoCs, indicate that the helix-bundle structures seem to be the common structural domain of this protein family. These helix-bundle structures of exchangeable apolipoproteins include the X-ray crystal structure of the apoE N-terminal domain (Wilson *et al.*, 1991), two apolipophorin-IIIs from insects (Fan *et al.*, 2003, Wang *et al.*, 1997,2002) and apoAI (Ajees *et al.*, 2006). This common structural feature of exchangeable apolipoproteins suggests that a more complex structural domain than a simple Class A amphipathic helix motif is required to regulate the functions of exchangeable apolipoproteins, in terms of lipoprotein assembly, transport, and metabolism. This structural domain should contain tertiary interactions of the secondary structures including Class A amphipathic helices. The observed helix-bundle structures of exchangeable apolipoproteins perfectly represent such a structural domain.

Based on our results, we hypothesize that the helix-bundle structure in the N-terminal domain of apoAI regulates HDL assembly via a normal apoAI cycle that includes four different apoAI conformational states. In particular, we suggest that the helix-bundle domain of apoAI regulates the assembly of discoidal HDL particles, whereas the C-terminal flexible domain may initiate the interaction between apoAI and phospholipids. Removal of this N-terminal helix-bundle may cause an impaired apoAI cycle in which apoAI fails to form a discoidal HDL particle, thus primarily knocking out the LCAT activity in the plasma, resulting in an inefficient RCT pathway. Although more experimental evidence is required, especially *in vivo* evidence, to verify this hypothesis, we feel that this hypothesis, for the first time, correlates the structural domains of apoAI protein with assembly of different HDL particles, addressing the structural basis of HDL assembly at an atomic resolution.

V. Summary

Human HDL plays a key role in the RCT pathway that transports the "bad cholesterol" back to the liver for clearance. HDL particles contain different components, including proteins such as apoAI and apoA-II as well as lipids such as phospholipids, cholesterol, CE, and triacylglycerol. During the RCT pathway, apoAI protein adopts different conformations that assemble different HDL species: lipid-free apoAI, preβHDL, discoidal HDL, and spherical HDL particles. Each of the apoAI conformations carries out one specific function that either initiates HDL formation, activates enzyme, and regulates HDL assembly. The conformational plasticity of apoAI seems to play a major role during HDL assembly. In this paper, we primarily focus on our own high-resolution NMR

structural studies of apoAI protein in lipid-free and HDL-associated states, with a brief summary of the previously published work by other laboratories that is related to high-resolution structural studies of apoAI proteins. Based on our NMR structures of lipid-free and lipid-poor apoAI, we proposed that apoAI protein contains two structural and functional domains: a N-terminal four helix-bundle domain and a C-terminal flexible domain. Our data further indicates that different apoAI domains play different roles during HDL formation and assembly. The C-terminal flexible domain of lipid-free apoAI binds to phospholipids to enhance apoA conformational plasticity in this domain, breaking up the potential oligomer formation and triggering the monomeric HDL precursor, apoAI/preβHDL, formation. The formation of monomeric apoAI/preβHDL may expose cholesterol-binding sites in the flexible C-terminal domain, thus allowing for tight binding to cholesterol to form discoidal HDL. In contrast, the conformational plasticity in the hinge loop of the N-terminal four helix-bundle domain is critical for apoAI's adjustment of its bundle conformation, thus activating LCAT for the formation of mature, spherical HDL. In addition, it seems that this four helix-bundle domain also directs apoAI to follow the normal apoAI cycle, by forcing the assembly of discoidal HDL. This will allow apoAI to adopt an optimal conformation for LCAT activation, core lipid accumulation, and the maturation of HDL, therefore, creating the most efficient reverse cholesterol transport pathway.

Acknowledgments

This work was supported by an International HDL Research Award to J.W. and by the US NIH grants (HL76620 and HL76435 to J.W). The authors are also thankful for the generous support from Isotec Inc. for providing ^{13}C-labeled glycerol for this work. X.R. and A.S. are recipients of an AHA predoctoral fellowship (AHA 0415063Z to XR and AHA 0415059Z to A.S). Part of the NMR experiments described in this manuscript were performed at the W. R. Wiley Environmental Molecular Sciences Laboratory, a national scientific user facility sponsored by the U.S. Department of Energy's Office of Biological and Environmental Research and located at Pacific Northwest National Laboratory (PNNL). PNNL is operated for the Department of Energy by Battelle. This work was supported by an International HDL research Award and a RO1 grant from NIH (HL076620 to JW).

References

Ajees, A. A., Anantharamaiah, G. M., Mishra, V. K., Hussain, M. M., and Murthy, H. M. (2006). Crystal structure of human apolipoprotein A-I: Insights into its protective effect against cardiovascular diseases. *Proc. Natl. Acad. Sci. USA* **103,** 2126–2131.

Barter, P. J., *et al*. (2007). Effects of torcetrapib in patients at high risk for coronary events. *N. Engl. J. Med.* **357,** 2109–2122.

Bhat, S., Sorci-Thomas, M. G., Alexander, E. T., Samuel, M. P., and Thomas, M. J. (2005). Intermolecular contact between globular N-terminal fold and C-terminal domain of ApoA-I stabilizes its lipid-bound conformation: Studies employing chemical crosslinking and mass spectrometry. *J. Biol. Chem.* **280,** 33015–33025.

Bhat, S., Sorci-Thomas, M. G., Tuladhar, R., Samuel, M. P., and Thomas, M. J. (2007). Conformational adaptation of apolipoprotein A-I to discretely sized phospholipid complexes. *Biochemistry* **46,** 7811–7821.

Brouillette, C. G., Anantharamaiah, G. M., Engler, J. A., and Borhani, D. W. (2001). Structural models of human apolipoprotein A-I: A critical analysis and review. *Biochim. Biophys. Acta* **1531,** 4–46.

Borhani, D. W., Rogers, D. P., Engler, J. A., and Brouillette, C. G. (1997). Crystal structure of truncated human apolipoprotein A-I suggests a lipid-bound conformation. *Proc. Natl. Acad. Sci. USA* **94,** 12291–12296.

Borhani, D. W., Engler, J. A., and Brouillette, C. G. (1999). Crystallization of truncated human apolipoprotein A-I in a novel conformation. *Acta Crystallogr. D Biol. Crystallogr.* **55,** 1578–1583.

Chen, B., Ren, X., Neville, T., Jerome, W., Sparks, G. D., and Wang, J. (2008). Apolipoprotein AI tertiary structures determine stability and functions of discoidal high-density lipoprotein particles of different sizes. *Protein Sci.* Submitted for Publication.

Connelly, M. A., and Williams, D. L. (2004). SR-BI and HDL cholesteryl ester metabolism. *Endocr. Res.* **30,** 697–703.

Córsico, B., Toledo, J. D., and Garda, H. A. (2001). Evidence for a central apolipoprotein A-I domain loosely bound to lipids in discoidal lipoproteins that is capable of penetrating the bilayer of phospholipid vesicles. *J. Biol. Chem.* **276,** 16978–16985.

Curtiss, L. K., Bonnet, D. J., and Rye, K. A. (2000). The conformation of apolipoprotein A-I in high-density lipoproteins is influenced by core lipid composition and particle size: A surface plasmon resonance study. *Biochemistry* **39,** 5712–5721.

Cushley, R. J., and Okon, M. (2002). NMR studies of lipoprotein structure. *Annu. Rev. Biophys. Biomol. Struct.* **31,** 177–206.

Dalton, M. B., and Swaney, J. B. (1993). Structural and functional domains of apolipoprotein A-I within high density lipoproteins. *J. Biol. Chem.* **268,** 19274–19283.

Davidson, W. S., and Hilliard, G. M. (2003). The spatial organization of apolipoprotein A-I on the edge of discoidal high density lipoprotein particles: A mass spectrometry study. *J. Biol. Chem.* **278,** 27199–27207.

Davidson, W. S., and Silva, R. A. (2005). Apolipoprotein structural organization in high density lipoproteins: Belts, bundles, hinges and hairpins. *Curr. Opin. Lipidol.* **16,** 295–300.

de Grooth, G. J., Klerkx, A. H., Stroes, E. S., Stalenhoef, A. F., Kastelein, J. J., and Kuivenhoven, J. A. (2004). A review of CETP and its relation to atherosclerosis. *J. Lipid Res.* **45,** 1967–1974.

Duriez, P., and Fruchart, J. C. (1999). High-density lipoprotein subclasses and apolipoprotein A-I. *Clin. Chim. Acta* **286,** 97–114.

Fan, D., Zheng, Y., Yang, D., and Wang, J. (2003). NMR solution structure and dynamics of an exchangeable apolipoprotein, Locusta migratoria apolipophorin III. *J. Biol. Chem.* **278,** 21212–21220.

Gursky, O. (2005). Apolipoprotein structure and dynamics. *Curr. Opin. Lipidol.* **16,** 287–294.

Gursky, O., and Atkinson, D. (1996). Thermal unfolding of human high-density apolipoprotein A-1: Implications for a lipid-free molten globular state. *Proc. Natl. Acad. Sci. USA* **93,** 2991–2995.

Huuskonen, J., Olkkonen, V. M., Jauhiainen, M., and Ehnholm, C. (2001). The impact of phospholipid transfer protein (PLTP) on HDL metabolism. *Atherosclerosis* **155,** 269–281.

Jonas, A., and Matz, C. E. (1982). Reaction of human lecithin: Cholesterol acyltransferase with micellar substrates is independent of the phase state of the lipid. *Biochemistry* **21,** 6867–6872.

Klon, A. E., Segrest, J. P., and Harvey, S. C. (2002). Comparative models for human apolipoprotein A-I bound to lipid in discoidal high-density lipoprotein particles. *Biochemistry* **41,** 10895–10905.

Laccotripe, M., Makrides, S. C., Jonas, A., and Zannis, V. I. (1997). The carboxyl-terminal hydrophobic residues of apolipoprotein A-I affect its rate of phospholipid binding and its association with high density lipoprotein. *J. Biol. Chem.* **272,** 17511–17522.

Li, H., Lyles, D. S., Thomas, M. J., Pan, W., and Sorci-Thomas, M. G. (2000). Structural determination of lipid-bound ApoA-I using fluorescence resonance energy transfer. *J. Biol. Chem.* **275,** 37048–37054.

Li, H. H., Lyles, D. S., Pan, W., Alexander, E., Thomas, M. J., and Sorci-Thomas, M. G. (2002). ApoA-I structure on discs and spheres. Variable helix registry and conformational states. *J. Biol. Chem.* **277,** 39093–39101.

Lund-Katz, S., Liu, L., Thuahnai, S. T., and Phillips, M. C. (2003). High density lipoprotein structure. *Front. Biosci.* **8,** d1044–d1054.

Marcel, Y. L., and Kiss, R. S. (2003). Structure-function relationships of apolipoprotein A-I: A flexible protein with dynamic lipid associations. *Curr. Opin. Lipidol.* **14,** 151–157.

Martin, D. D., Budamagunta, M. S., Ryan, R. O., Voss, J. C., and Oda, M. N. (2006). Apolipoprotein A-I assumes a ''looped belt'' conformation on reconstituted high density lipoprotein. *J. Biol. Chem.* **281,** 20418–20426.

Matz, C. E., and Jonas, A. (1982). Micellar complexes of human apolipoprotein A-I with phosphatidylcholines and cholesterol prepared from cholate-lipid dispersions. *J. Biol. Chem.* **257,** 4535–4540.

Meng, Q. H., Calabresi, L., Fruchart, J. C., and Marcel, Y. L. (1993). Apolipoprotein A-I domains involved in the activation of lecithin:Cholesterol acyltransferase. Importance of the central domain. *J. Biol. Chem.* **268,** 16966–16973.

Miller, G. J., and Miller, N. E. (1975). Plasma-high-density- ipoprotein concentration and development of ischaemic heart-disease. *Lancet* **1,** 16–19.

Mishra, V. K., Palgunachari, M. N., Segrest, J. P., and Anantharamaiah, G. M. (1994). Interactions of synthetic peptide analogs of the class A amphipathic helix with lipids. Evidence for the snorkel hypothesis. *J. Biol. Chem.* **269,** 7185–7191.

Moore, R. E.,, *et al*. (2005). Increased atherosclerosis in mice lacking apolipoprotein A-I attributable to both impaired reverse cholesterol transport and increased inflammation. *Circ. Res.* **97,** 763–771.

Navab, M., Anantharamaiah, G. M., Reddy, S. T., Hama, S., Hough, G., Grijalva, V. R., Yu, N., Ansell, B. J., Datta, G., Garber, D. W., and Fogelman, A. M. (2005). Apolipoprotein A-I mimetic peptides. *Arterioscler. Thromb. Vasc. Biol.* **25,** 1325–1331.

Neary, R., Bhatnagar, D., Durrington, P., Ishola, M., Arrol, S., and Mackness, M. (1991). An investigation of the role of lecithin: Cholesterol acyltransferase and triglyceride-rich lipoproteins in the metabolism of pre-beta high density lipoproteins. *Atherosclerosis* **89,** 35–48.

Naito, H. K. (1986). The clinical significance of apolipoprotein measurements. *J. Clin. Immunol.* **9,** 11–20.

Panagotopulos, S. E., Horace, E. M., Maiorano, J. N., and Davidson, W. S. (2001). Apolipoprotein A-I adopts a belt-like orientation in reconstituted high density lipoproteins. *J. Biol. Chem.* **276,** 42965–42970.

Rader, D. J. (2006). Molecular regulation of HDL metabolism and function: Implications for novel therapies. *J. Clin. Invest.* **116,** 3090–3100.

Ren, X., Zhao, L., Sivashanmugam, A., Miao, Y., Korando, L., Yang, Z., Reardon, C. A., Getz, G. S., Brouillette, C. G., Jerome, W. G., and Wang, J. (2005). Engineering mouse apolipoprotein A-I into a monomeric, active protein useful for structural determination. *Biochemistry* **44,** 14907–14919.

Ren, X., Sivashanmugam, A., Chen, B., Li, C., Yang, Y., Neville, T., Jerome, W. G., Sparks, D., Li, Q. and Wang, J. (2006). NMR structural studies of human apolipoprotein A-I at the lipid-free and HDL-associated States–A progress report. An invited review by *Research Signpost* for a review book on ''Functional and structural biology on the lipo-netwrok.'' pp. 65–93.

Ren, X., Yang, Y., Neville, T., Hoyt, D., Sparks, D., and Wang, J. (2007). A complete backbone spectral assignment of human apolipoprotein AI on a 38 kDa pre*b*HDL (Lp1-AI) particle. *Biomol. NMR Assign.* **1,** 69–71.

Reschly, E. J., Sorci-Thomas, M. G., Davidson, W. S., Meredith, S. C., Reardon, C. A., and Getz, G. S. (2002). Apolipoprotein A-I alpha -helices 7 and 8 modulate high density lipoprotein subclass distribution. *J. Biol. Chem.* **277,** 9645–9654.

Roberts, L. M., Ray, M. J., Shih, T. W., Hayden, E., Reader, M. M., and Brouillette, C. G. (1997). Structural analysis of apolipoprotein A-I: Limited proteolysis of methionine-reduced and -oxidized lipid-free and lipid-bound human apo A-I. *Biochemistry* **36,** 7615–7624.

Rothblat, G. H., Mahlberg, F. H., Johnson, W. J., and Phillips, M. C. (1992). Apolipoproteins, membrane cholesterol domains, and the regulation of cholesterol efflux. *J. Lipid Res.* **33,** 1091–1097.

Rothblat, G. H., de la Llera-Moya, M., Atger, V., Kellner-Weibel, G., Williams, D. L., and Phillips, M. C. (1999). Cell cholesterol efflux: Integration of old and new observations provides new insights. *J. Lipid Res.* **40,** 781–796.

Rye, K. A., and Barter, P. J. (2004). Formation and metabolism of prebeta-migrating, lipidpoor apolipoprotein A-I. *Arterioscler. Thromb. Vasc. Biol.* **24,** 421–428.

Saito, H., Lund-Katz, S., and Phillips, M. C. (2004). Contributions of domain structure and lipid interaction to the functionality of exchangeable human apolipoproteins. *Prog. Lipid Res.* **43,** 350–380.

Schaefer, E. J., Heaton, W. H., Wetzel, M. G., and Brewer, H. B., Jr. (1982). Plasma apolipoprotein A-1 absence associated with a marked reduction of high density lipoproteins and premature coronary artery disease. *Arteriosclerosis* **2,** 16–26.

Segrest, J. P. (1977). Amphipathic helixes and plasma lipoproteins: Thermodynamic and geometric considerations. *Chem. Phys. Lipids* **18,** 7–22.

Segrest, J. P., De Loof, H., Dohlman, J. G., Brouillette, C. G., and Anantharamaiah, G. M. (1990). Amphipathic helix motif: Classes and properties. *Proteins* **8,** 103–117.

Segrest, J. P., Garber, D. W., Brouillette, C. G., Harvey, S. C., and Anantharamaiah, G. M. (1994). The amphipathic alpha helix: A multifunctional structural motif in plasma apolipoproteins. *Adv. Protein Chem.* **45,** 303–369.

Segrest, J. P., Jackson, R. L., Morrisett, J. D., and Gotto, A. M., Jr. (1974). A molecular theory of lipid-protein interactions in the plasma lipoproteins. *FEBS Lett.* **38,** 247–258.

Segrest, J. P., Jones, M. K., Klon, A. E., Sheldahl, C. J., Hellinger, M., De Loof, H., and Harvey, S. C. (1999). A detailed molecular belt model for apolipoprotein A-I in discoidal high density lipoprotein. *J. Biol. Chem.* **274,** 31755–31758.

Segrest, J. P., Li, L., Anantharamaiah, G. M., Harvey, S. C., Liadaki, K. N., and Zannis, V. (2000). Structure and function of apolipoprotein A-I and high-density lipoprotein. *Curr. Opin. Lipidol.* **11,** 105–115.

Silva, R. A., Hilliard, G. M., Li, L., Segrest, J. P., and Davidson, W. S. (2005). A mass spectrometric determination of the conformation of dimeric apolipoprotein A-I in discoidal high density lipoproteins. *Biochemistry* **44,** 8600–8607.

Sivashanmugam, A., Victoria, M., Chunxian, C., Yunhuang, Y., Jianjun, Wang, and Qianqian, (2008a). Practical protocols for production of very high-yield of recombinant proteins in *Eschericia coli*. *Protein Sci.* Submitted for Publication.

Sivashanmugam, A., Ren, X., Li, Q., Jerome, W. G., and Wang, J. (2008b). The four helix-bundle structure in the N-terminal domain of apolipoprotein A-I regulates the formation of discoidal HDL particles. Manuscript in preparation.

Sparks, D. L., Phillips, M. C., and Lund-Katz, S. (1992). The conformation of apolipoprotein A-I in discoidal and spherical recombinant high density lipoprotein particles. 13C NMR studies of lysine ionization behavior. *J. Biol. Chem.* **267,** 25830–25838.

Sparks, D. L., Frank, P. G., Braschi, S., Neville, T. A., and Marcel, Y. L. (1999). Effect of apolipoprotein A-I lipidation on the formation and function of pre-beta and alphamigrating LpA-I particles. *Biochemistry* **38,** 1727–1735.

Studier, F. W. (2005). Protein production by auto-induction in high density shaking cultures. *Protein Expr. Purif.* **41,** 207–234.

Tricerri, M. A., Behling Agree, A. K., Sanchez, S. A., Bronski, J., and Jonas, A. (2001). Arrangement of apolipoprotein A-I in reconstituted high-density lipoprotein disks: An alternative model based on fluorescence resonance energy transfer experiments. *Biochemistry* **40,** 5065–5074.

Trigatti, B. L. (2005). Hepatic high-density lipoprotein receptors: Roles in lipoprotein metabolism and potential for therapeutic modulation. *Curr. Atheroscler. Rep.* **7,** 344–350.

Wald, J. H., Coormaghtigh, E., De Meutter, J., Ruysschaert, J. M., and Jonas, A. (1990). Investigation of the lipid domains and apolipoprotein orientation in reconstituted high density lipoproteins by fluorescence and IR methods. *J. Biol. Chem.* **265,** 20044–20050.

Wang, J., Liu, H., Sykes, B. D., and Ryan, R. O. (1992). ^{31}P-NMR study of the phospholipid moiety of lipophorin subspecies. *Biochemistry* **31,** 8706–8712.

Wang, J., Liu, H., Sykes, B. D., and Ryan, R. O. (1995). Identification and localization of two distinct microenvironments for the diacylglycerol component of lipophorin particles by ^{13}C NMR. *Biochemistry* **34,** 6755–6761.

Wang, J., Gagne, S. M., Sykes, B. D., and Ryan, R. O. (1997). Insight into lipid surface recognition and reversible conformational adaptations of an exchangeable apolipoprotein by multidimensional heteronuclear NMR techniques. *J. Biol. Chem.* **272,** 17912–17920.

Wang, J., Sykes, B. D., and Ryan, R. O. (2002). Structural basis for the conformational adaptability of apolipophorin III, a helix-bundle exchangeable apolipoprotein. *Proc. Natl. Acad. Sci. USA* **99,** 1188–1193.

Williamson, R., Lee, D., Hagaman, J., and Maeda, N. (1992). Marked reduction of high density lipoprotein cholesterol in mice genetically modified to lack apolipoprotein A-I. *Proc. Natl. Acad. Sci. USA* **89,** 7134–7138.

Wilson, C., Wardell, M. R., Weisgraber, K. H., Mahley, R. W., and Agard, D. A. (1991). Threedimensional structure of the LDL receptor-binding domain of human apolipoprotein E. *Science* **252,** 1817–1822.

Wu, Z., Wagner, M. A., Zheng, L., Parks, J. S., Shy, J. M., 3rd, Smith, J. D., Gogonea, V., and Hazen, S. L. (2007). The refined structure of nascent HDL reveals a key functional domain for particle maturation and dysfunction. *Nat. Struct. Mol. Biol.* **14,** 861–868.

Xu, Y., Lin, Z., Ho, C., and Yang, D. (2005). A general strategy for the assignment of aliphatic sidechain resonances of uniformly ^{13}C,^{15}N-labeled large proteins. *J. Am. Chem. Soc.* **127,** 11920–11921.

Yang, Y., Hoyt, D., and Wang, J. (2007). A complete NMR spectral assignment of the lipid-free mouse apolipoprotein A-I (apoAI) C-terminal truncation mutant, apoAI(1–216). *Biomol. NMR Assign.* **1,** 109–111.

Yang, Y., Ren, X., Li, Q., Neville, T., Sparks, D., and Wang, J. (2008). NMR structural studies of a preβHDL (Lp1A-I) particle. Manuscript in Preparation.

Yang, Y., and Wang, J. (2008). NMR structure and dynamics of a physiologically relevant lipid-free mouse apolipoprotein AI. Nature Structural and Molecular Biology, Submitted for publication.

Zhao, Y., Sparks, D. L., and Marcel, Y. L. (1996). Specific phospholipid association with apolipoprotein A-I stimulates cholesterol efflux from human fibroblasts. Studies with reconstituted sonicated lipoproteins. *J. Biol. Chem.* **271,** 25145–25151.

CHAPTER 16

Nano-scale Characterization of the Dynamics of the Chloroplast Toc Translocon

L. Evan Reddick,[*] Prakitchai Chotewutmontri,[†] Will Crenshaw,[*] Ashita Dave,[*] Michael Vaughn,[*,1] and Barry D. Bruce[*,†,‡]

[*]Department of Biochemistry
Cellular and Molecular Biology
University of Tennessee at Knoxville
Knoxville, Tennessee 37996

[†]Graduate School of Genome Science and Technology
University of Tennessee at Knoxville
Knoxville, Tennessee 37996

[‡]Department of Microbiology
University of Tennessee at Knoxville
Knoxville, Tennessee 37996

[1] Current Address: Department of Chemistry and Biochemistry, Arizona State University, Arizona

METHODS IN CELL BIOLOGY, VOL. 90

0091-679X/08 $35.00
DOI: 10.1016/S0091-679X(08)00816-9

Abstract

Translocons are macromolecular nano-scale machines that facilitate the selective translocation of proteins across membranes. Although common in function, different translocons have evolved diverse molecular mechanisms for protein translocation. Subcellular organelles of endosymbiotic origin such as the chloroplast and mitochondria had to evolve/acquire translocons capable of importing proteins whose genes were transferred to the host genome. These gene products are expressed on cytosolic ribosomes as precursor proteins and targeted back to the organelle by an N-terminal extension called the transit peptide or presequence. In chloroplasts the transit peptide is specifically recognized by the Translocon of the Outer Chloroplast membrane (Toc) which is composed of receptor GTPases that potentially function as gate-like switches, where GTP binding and hydrolysis somehow facilitate preprotein binding and translocation. Compared to other translocons, the dynamics of the Toc translocon are probably more complex and certainly less understood. We have developed biochemical/biophysical, imaging, and computational techniques to probe the dynamics of the Toc translocon at the nanoscale. In this chapter we provide detailed protocols for kinetic and binding analysis of precursor interactions in organeller, measurement of the activity and nucleotide binding of the Toc GTPases, native electrophoretic analysis of the assembly/organization of the Toc complex, visualization of the distribution and mobility of Toc apparatus on the surface of chloroplasts, and conclude with the identification and molecular modeling Toc75 POTRA domains. With these new methodologies we discuss future directions of the field.

I. Introduction

A. Chloroplast Origin and Role of Protein Translocation

A hallmark of eukaryotic cells is its remarkable compartmentalization. This compartmentalization is accomplished largely through the formation of membrane-delineated sub-compartments, known as organelles. The lipid bilayers, surrounding the organelle, present an obstacle for protein transport from the site of synthesis in the cytoplasm. Localized within these membranes are specialized-protein conducting molecular machines known as translocons. The architecture of these translocons have been characterized from many membranes, including the archebacterial plasma membrane (Van den Berg *et al.*, 2004), the yeast endoplasmic reticulum (Beckmann *et al.*, 2001), the outer membrane of mitochondria (Model *et al.*, 2008), and the outer membrane of the chloroplast envelope (Schleiff *et al.*, 2003). These translocons facilitate the selective and active transport of proteins across the lipid bilayer. Through a combination of cryoEM and X-ray crystallography, it is clear that these molecular machines are nanometer-sized complexes that can occur with a range of conformations, including individual monomers in the archebacterial plasma membrane (diameter of 4.0 nm), a dimeric, and/or trimeric triangular complex in yeast mitochondrial outer membrane (edge length of 14.5 nm), to a tetramer in the chloroplast outer membrane (diameter of ~14 nm).

In plant cells, the compartmentalization is even more complex since these cells have two semi-autonomous organelles, the mitochondria and the plastid. The plastid gains its name from its tremendous plasticity in form and function. One of these plastid subtypes is the chlorophyll containing chloroplast, which is the site of photosynthesis. The chloroplast is widely accepted to have evolved from an endosymbiotic event involving phagocytosis of a primitive cyanobacterium by an autonomous eukaryotic cell, ~1.6 billion years ago (Basu *et al.*, 2008). Following internalization, the ancestral cyanobacteria began a slow transfer of its genome to the nucleus, such that modern chloroplasts typically encode only ~100 genes. This is much less than the many thousand of genes encoded by existing cyanobacteria (Cavalier-Smith, 2003). Although evolution resulted in a minimal plastid genome, the plastid proteome has remained remarkably large and complex, with over 2000 gene products identified (Kleffmann *et al.*, 2006). The large plastid proteome is maintained via the process of posttranslational translocation of nuclear-encoded preproteins (Keegstra and Cline, 1999), which contain an N-terminal extension known as the transit peptide (tp) (Bruce, 2000). Two complexes, known as the translocons of the outer/inner chloroplast membrane, or *Toc* and *Tic* complexes, mediate chloroplast protein import (Fig. 1). Components of the Toc translocon, Toc34 and Toc159, both GTPase preprotein receptors, facilitate the unidirectional and highly specific protein import by recognizing and binding to the transit peptide.

While phylogenetic evidence may argue that many components of the Tic complex were derived from preexisting cyanobacterial proteins (Jarvis and Soll, 2001), the origins of the Toc GTPases are most likely eukaryotic; the other member

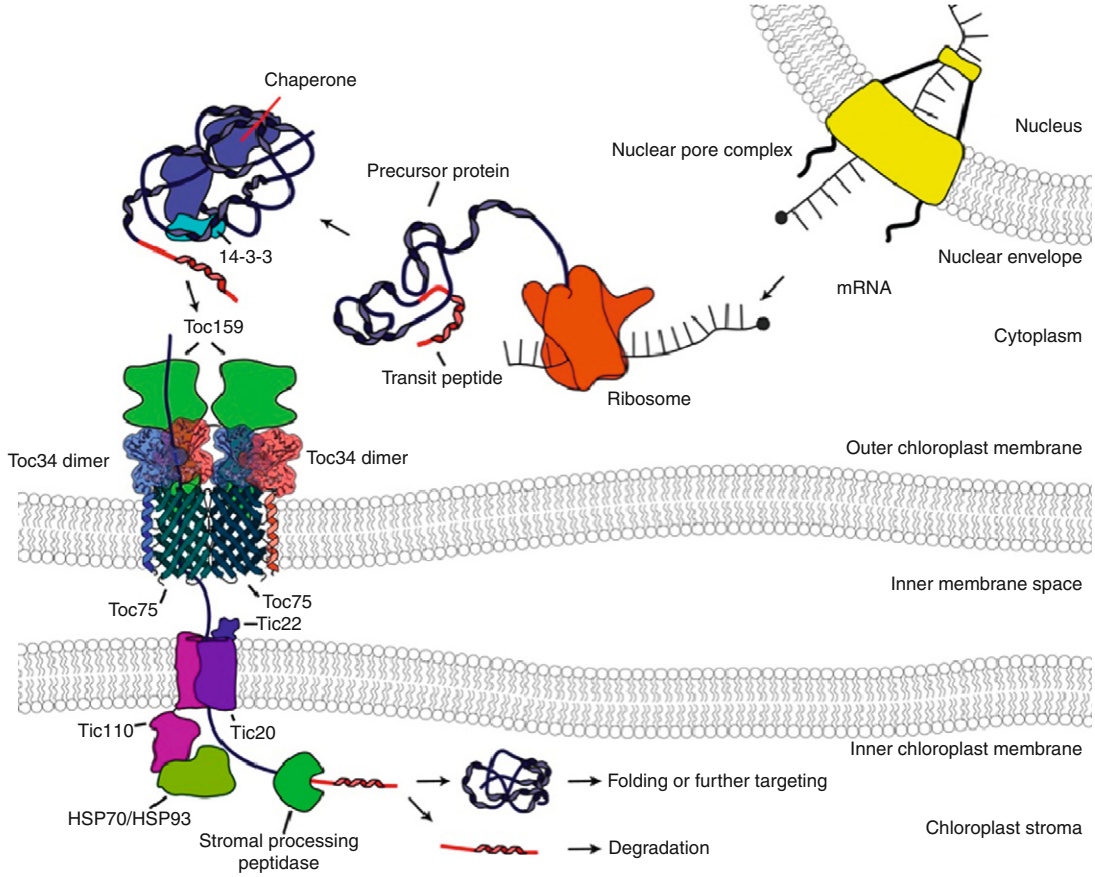

Fig. 1 Chloroplast protein import schematic. Genes encoding proteins destined for the chloroplast are transcribed in the nucleus where they must exit through the nuclear pore. This mRNA is translated on ribosomes into precursor proteins that have an N-terminal extension known as the transit peptide. The solubility and protease resistance of the precursor protein is maintained through the interaction of 14–3–3 proteins and chaperones where it is ultimately targeted to the chloroplast Toc translocon. Through the interaction of the receptor GTPases Toc159 and Toc34, the transit peptide drives the precursor protein entry through the beta-barrel protein Toc75 where it interacts with the Tic complex. The actions of cytosolic, IMS and stromal chaperones and Hsp proteins drive the import of the precursor protein using ATP. Stromal processing peptidase cleaves the transit peptide and the precursor protein folds to its ultimate active form, or proceeds to a suborganeller location for further import/processing. The tp is degraded via the presequence processing peptidase.

of the Toc complex, the β-barrel Toc75, is of prokaryotic origin (Reumann *et al.*, 1999). This prompted a recent postulation that the transit peptide has origins as a virulence factor, possibly excreted through the *Synechocystis* (PCC6803) β-barrel protein *Syn*Toc75 (Bolter *et al.*, 1998; Reddick *et al.*, 2007). Despite advances in identification of many of the components found in Toc and Tic, as well as the

availability of a low-resolution structure of the Toc apparatus (Schleiff *et al.*, 2003), the molecular mechanism of how preproteins are selected and translocated across both of these membranes is still very poorly understood.

Here, we introduce and discuss methods to quantitatively analyze the activity of this protein translocation process *in vitro*. This process can be distinguished into a binding step and a translocation step (Olsen *et al.*, 1989; Theg *et al.*, 1989), which differ in their energy requirements. *In organeller* experiments such as competitive chloroplast import and binding assays are powerful tools available for the quantitative measurement of chloroplast protein import. Here, we describe in detail the protocols for the import and binding competition assays based on *in vivo* labeled precursor of the small subunit of ribulose-1,5-bisphosphate carboxylase/oxygenase (prSSU) and reveal a new scintillation based method of quantitation that abrogates the need for chloroplast binding gel quantitation. These assays can be utilized to determine comparative affects of test subjects to prSSU import/binding. Through the use of fluorescently labeled antibodies, we can visualize a bound transit peptide to isolated chloroplasts. Additionally, following the identification of the receptor GTPases, Toc34 and Toc159, we have been able to express the soluble, cytosolic domains of these proteins in *Escherichia coli.* Using these recombinant proteins, we have now been able to develop very sensitive GTPase activity assays that allow the dynamics of these GTPase to be explored in detail using *in vitro* methods. We provide detailed methods for measuring both GTP binding, hydrolysis, and nucleotide exchange. Further aspects of the translocon organization and dynamics are revealed using a rapid native gel analysis that provides insight into the size and composition of the Toc apparatus. By utilizing a new technique, total internal reflectance fluorescence (TIRF), we can visualize intact chloroplasts and locate Toc complexes using fluorescent antibody techniques to determine the velocity and acceleration of the complexes on the chloroplast membrane. Finally, we have begun to use molecular modeling to provide structural insights of the Toc components based on crystallographic data from functionally related proteins. Using these models, we can now start to dissect the contributions of individual domains of Toc75.

B. Outline of Chapter

This chapter first addresses the production of chloroplast import substrates followed by rapid and reproducible chloroplast isolation techniques along with import and binding assays; included is a section on the quantitative analysis of data generated in said experiments. We also discuss novel methods of imaging the distribution of the ''active'' translocon by using Laser Scanning Confocal Microscopy (LCSM) and with appropriately fluorescent reporters, we can also observe the topology of a bound transit peptide within the translocon. Using BN-PAGE, 2-D PAGE, and western blotting, we demonstrate that the translocon itself is a dynamic apparatus, existing as an oligomer with multiple observed stoichiometries. Using total internal reflectance fluorescence microscopy (TIRFM), we can

visualize the mobility of individual Toc complexes in real time, and use particle tracking to observe the behavior of individual complexes. Finally, detailed kinetic analysis of the Toc associated GTPases is presented to dissect the properties of this molecular switch including nucleotide binding, hydrolysis, and exchange assays. Finally, with the availability of new membrane protein structures, we use molecular modeling to investigate the structure and function of β-barrel preprotein translocation channel, Toc75, and its associated soluble POTRA domains. A final concluding paragraph is offered to indicate future possible directions to investigate the structure and function of these nanoscale protein-conducting channels.

II. *In organeller* Chloroplast Import and Binding Assays

One of the powerful means of studying chloroplast protein import comes from the ability of perform *in organellar* assays using isolated and intact chloroplasts. These assays allow the design of very specific experiments where we can manipulate both the identity, the quantity of the precursor as either an *in vitro* translated product or as a chemically pure recombinant protein. In addition, we can further control the experiment by regulating the energy source by providing purified NTPs and by preventing photophosphorylation. We describe below the procedures for conducting both import experiments and binding experiments. By using ^{35}S-precursors and cold competitors, we can measure the affinity of the competitors for both binding and translocation.

A. Chloroplast Isolation

1. Prepare 2 Percoll step gradients in a 15 ml tube by carefully combining 2 ml of 80% Percoll in Import Buffer (IB; 50 mM HEPES–KOH pH 8.0, 330 mM Sorbitol) and 4 ml of 40% Percoll in IB, and keep on ice. Care in handling will prevent mixing and result in a sharper step gradient, and thus a better recovery of intact chloroplasts.
2. Harvest ~30 g of 12–14-day-old pea plants. Using scissors, coarsely chop the plants and further homogenize with a food processor in 3 short pulses (1–2 s each). Transfer to an ice-cold mortar; add 30 ml of ice-cold Grinding Buffer (GB; 50 mM HEPES–KOH pH 7.3, 330 mM Sorbitol, 1 mM $MgCl_2$, 1 mM $MnCl_2$, 2 mM EDTA, 0.1% BSA) containing about 0.3 g of sodium ascorbate and reduced glutathione.
3. Grind for 1–2 min, minimizing foam and filter through 1 layer of Miracloth on top of 1 layer of cheesecloth into a 50 ml tube. Centrifuge the filtrate at 900*g* for 5 min; decant the supernatant.

4. Resuspend the chloroplasts in 4–5 ml ice-cold IB with a natural bristle paintbrush. Gently paint the chloroplasts up the side of the tube until an even consistency is obtained.
5. Gently transfer the crude chloroplast suspension using a 14-gauge stainless steel cannula with a 10 ml plastic syringe onto the ice-cold Percoll step gradient (Fig. 2A) generated in step 1.
6. Centrifuge in a swinging bucket rotor at 3400*g* for 15 min with acceleration and deceleration set to medium. Two bands will form: an upper band of broken chloroplasts and thylakoids on top of the 40% Percoll and a lower band of intact chloroplasts at the interface of 40% and 80% (Fig. 2B). Carefully collect the intact chloroplasts with a syringe. Care should be taken to minimize the shear forces common with syringe manipulations.
7. With the same syringe, pull up about 3–5 ml ice-cold IB and gently resuspend the intact chloroplasts by inverting the syringe 3 times. Repeat steps 5–6.
8. Transfer the intact chloroplasts into a new 15-ml tube and pellet at 900*g* for 5 min.
9. Decant the supernatant and resuspend the intact chloroplasts in a minimal volume of ice-cold IB. Determine the chlorophyll concentration using Eq. (1) and by methods described previously (Arnon, 1949). We generally made about 0.4 mg of chlorophyll from 30 g of pea plants.

$$\text{mg/ml Chlorophyll} = \left[\frac{(8.02 \times A_{663}) + (20.2 \times A_{645})}{0.01\,ml \times 1000\,\mu g/mg}\right]$$

Eq. 1 Chlorophyll concentration calculation.

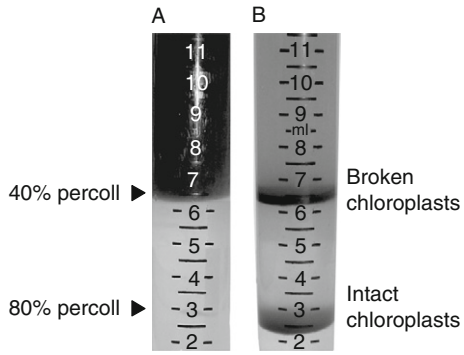

Fig. 2 Rapid isolation of intact chloroplasts. After tissue homogenization, filtration, and sedimentation, intact chloroplasts are isolated by centrifugation through a Percoll step gradient. The broken chloroplasts accumulate at the interface of the 40% Percoll whereas the intact chloroplasts collect on the 80% Percoll cushion.

Note: Care should be taken in the preparation of chloroplasts to minimize the overall time and keep all reagents on ice; proteases present in the cytosol will degrade the Toc proteins and result in semi-import competent chloroplasts. Further, the brushing and syringe, while requisite, will introduce shear forces and significantly contribute to the population of lysed chloroplasts if care is not taken to be gentle. Do not water the plants immediately prior to the harvest, as this water, albeit a small fraction will cause the buffers to become hypotonic and lead to chloroplast lysis. Finally, fresh preparation of GB and IB is not necessary, but due to the high sugar content in these buffers, they should be stored frozen, and thus will require thorough mixing prior to use due to the differential freezing rates of sugars and bulk water.

B. *In vivo* Radiolabeling of prSSU

1. *E. coli* BL21 (DE3) harboring the prSSU sequence in pET-11 vector is used (Klein and Salvucci, 1992) to inoculate 5 ml of Terrific Broth (TB) media containing 150 μg/ml ampicillin. Grow at 37 °C, 250 rpm, until OD_{600} 0.6 is reached.
2. Inoculate 3 ml of the culture into 30 ml of Dulbecco's Modification of Eagle's Medium (DMEM) deficient in methionine, cysteine, and glutamine containing 150 μg/ml ampicillin in a 50 ml tube.
3. When OD_{600} 0.6–0.8 is reached, induce with 1 mM IPTG; after 5 min of induction, 7 mCi of Trans ^{35}S-Label metabolic labeling reagent is added. Grow for 4–6 h.
4. Harvest the cells by centrifugation and wash twice with 15 ml of Buffer I (50 mM Tris–HCl, 2 mM EDTA, pH 8.0), resuspend in 15 ml of Buffer II (50 mM Tris–HCl, 2 mM EDTA, 0.5% TritionX-100, 1 mM DTT, pH 8.0). Lyse the cells by sonication, adding Benzonase to remove nucleic acids and lower the viscosity.
5. Collect inclusion bodies by centrifugation at 40,000*g* for 20 min. The inclusion bodies are then subjected to an extensive washing using a Dounce homogenizer. First, wash with 15 ml of Buffer II containing salt (300 mM NaCl), 4 times, and then wash with 15 ml of Buffer II, twice, followed by final wash with 15 ml of H_2O to remove salt and detergent.
6. Resuspend the inclusion body pellet in 300 μl of 8 M urea containing 50 mM DTT and 20 mM Tris–HCl, pH 8.0 and incubate with shaking overnight at 37 °C, 200 rpm. Most of the impurities are solubilized in this step. Centrifuge at 40,000*g* for 30 min to recover inclusion bodies.
7. Resuspend the inclusion body pellet again in 300 μl of 8 M Urea containing 50 mM DTT, 20 mM Tris–HCl, pH 8.0 with shaking at 37 °C, 200 rpm. The supernatant now contains the purified ^{35}S-prSSU. Insoluble impurities are removed by another centrifugation at 40,000*g* for 30 min. The supernatant can be stored at −80 °C.

C. Expression and Purification of prSSU and mSSU from Inclusion Bodies

The expression and purification of prSSU and mSSU proteins (Fig. 3, lanes 1 and 2) is accomplished by following the protocol listed in Section II.B., with the following variations Step 2, TB medium is used instead of deficient DMEM medium. The culture volume is scaled up to 50 ml in a 250 ml flask. Step 3, no labeling reagent is added. The volumes of buffers in step 4–5 are increased to 25 ml and the volumes of 8 M urea solutions in step 6–7 are increased to 500 μl. By employing the French Pressure Cell, we routinely achieve higher purity proteins; this is most likely due to sonic disruption of the inclusion body by sonication.

D. Expression and Purification of Transit Peptides

The standard IMPACT system (New England BioLabs) is used for expression and purification of all transit peptides (Fig. 3, lane 3). The transit peptide sequences are encoded on the pTYB2 plasmid, transformed into competent

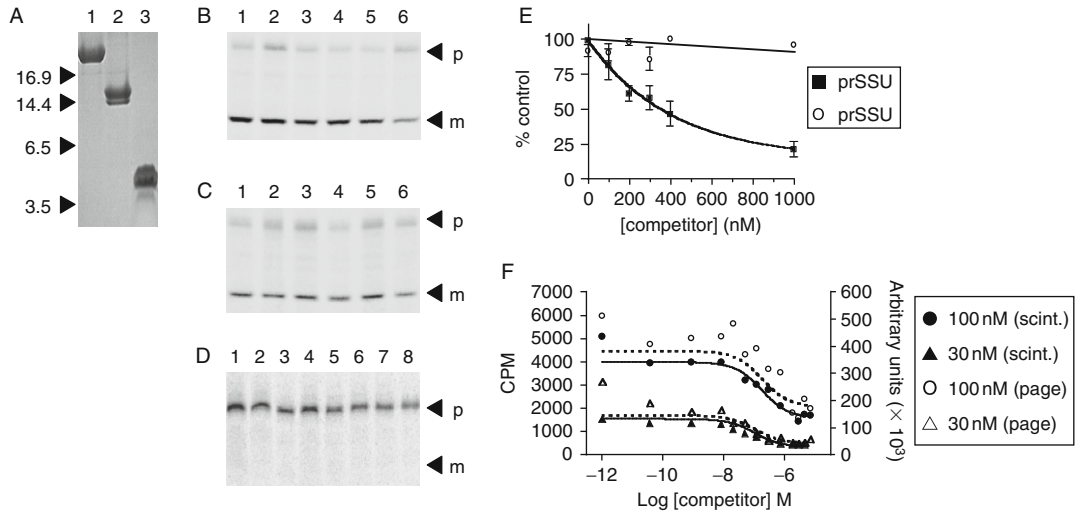

Fig. 3 Purified recombinant proteins and chloroplast Import and binding competitions. Panel A, Purified proteins used in chloroplast binding and import. Lane 1, purified prSSU, the precursor to the small subunit of rubisco. Lane2, mSSU, the mature form of prSSU is characterized by a smaller size due to the lack of the transit peptide. Lane 3, SStpNt, the small subunit transit peptide from *Nicotiana tobacum*. Panel B, SDS-PAGE digital autoradiograph of import competitions between 100 nM ^{35}S-prSSU and prSSU. Panel C is competition with mSSU; the competitors in lane 1–6 of both B and C are 0, 0.1, 0.2, 0.3, 0.4, and 1.0 μM cold competitor. Panel D, binding competitions between ^{35}S-prSSU and prSSU. The competitors in lane 1–7 are 0, 0.25, 0.5, 0.75, 1.0, 2.0, and 3.0 μM. Lane 8 is ^{35}S-prSSU loading control. Panel E, graphical analysis of import competition data generated from autoradiographs. Panel F, graphical analysis of binding competition data generated from autoradiograph (dashed line) and scintillation counting (solid line). Two concentrations of ^{35}S-prSSU were used, 30 and 100 nM. The K_d from autoradiograph and scintillation count are 31 nM and 91 nM, respectively.

ER2566 *E. coli* cells and induced via IPTG induction as fusion proteins with intein and chitin binding domains at the C-terminus of the expressed construct. Recombinant constructs are affinity purified on a chitin column and transit peptides are released by reductant mediated specific self-cleavage of the intein domain. By minimizing the preparation time and including protease inhibitor cocktails (PICs), one can prevent the loss of transit peptides to enzymatic degradation. The purified transit peptides are purified and stored as lyophilized powder at −80 °C. A recent publication details this procedure (Reddick *et al.*, 2007).

E. Chloroplast Import Competition Assay

1. The assay is performed in total volume of 300 μl. The reaction mixtures contain 100 nM ^{35}S-prSSU, 1 mM β-ME, 2 mM Mg–ATP, 0.5% BSA, 250 mM urea, and 0.125 mg chlorophyll/ml chloroplasts in the presence of IB with various concentrations of cold competitor. Stock solutions include freshly prepared 8 M urea solution (containing 20 mM β-ME, 20 mM Tris–HCl, pH 8.0), 1×IB, 2×IB, 100 mM β-ME, fresh 100 mM Mg–ATP, and 10% BSA. Prepare a set of 1.6 ml microfuge tubes containing 700 μl of 40% Percoll in IB for reisolation of the chloroplasts; keep everything on ice.
2. Resuspend the purified intact chloroplasts in IB containing 2% BSA, and adjust the concentration of chloroplasts to 1 mg chlorophyll/ml. Keep on ice.
3. Dilute ^{35}S-prSSU at least 2-fold with freshly prepared 8 M urea solution. Resuspend lyophilized transit peptide competitor in 8 M urea solution.
4. Pipette various concentrations of transit peptide competitor into fresh 1.6 ml reaction tubes. Add requisite volumes of 8 M urea solution into each tube to reach final concentration of 250 mM (take into account the urea in ^{35}S-prSSU and competitor solutions). When finished, every tube should contain an equal volume.

Note: It is important to not let the total urea concentration go above 350 mM. Urea levels above this lead to loss of import activity through some disruption of the chloroplast.

5. Prepare a ''master mix'' of IB, β-ME, Mg–ATP, BSA, and ^{35}S-prSSU for all reactions.
6. Pipette equal volume of the master mix into each tube, mix by vortex, and equilibrate the temperature by incubation at room temperature for 10 min.
7. To start the assay, add 37.5 μl of chloroplasts (Step 2) to each tube. Gently mix by inverting the tube 5 times. Incubate at room temperature for 15 min (mix occasionally by inverting 1 time).
8. Stop the reactions by adding 700 μl of ice-cold IB, mix, and keep on ice in the dark.
9. Reisolate the intact chloroplasts by overlaying the reaction solution on top of the 40% Percoll. Centrifuge in a swinging bucket rotor at 3400*g* for 5 min with acceleration and deceleration set to medium. Intact chloroplasts will

pellet at the bottom of the tube, broken chloroplasts and free ^{35}S-prSSU will remain at or above the interface.

10. Remove the broken chloroplasts and the Percoll. Gently resuspend the pellet in 1 ml of ice-cold IB using a Pasteur pipette and remove a 50 μl aliquot for quantification of the total protein using the BCA protein assay. Pellet the remaining 950 μl by centrifugation at 12,000*g* for 1 min.
11. Aspirate the supernatant and resuspend the pellet in 60 μl of ice-cold H_2O. Add 40 μl of 4× SDS sample buffer mix and boil for 4 min. From the result of BCA protein assay, equalize the protein concentration of all tubes using 2× SDS sample buffer.
12. For analysis, run 50 μl of the samples on a 10–20% SDS-PAGE gradient gel at constant 8 mA overnight. Dry the gels and place on phosphor screen for 3–24 h. The digital autoradiograph is acquired by scanning the screen with Storm Phosphorimager; ImageQuant software is used for quantification of the bands (Fig. 3B and C).

The same cautions and concerns (presented at the end of Section II.E., Chloroplast Import Assay) apply to the import competition assay. Intact chloroplasts should be prepared in parallel to minimize proteolysis. Freshly prepare urea to ensure the full solubilization of prSSU.

F. Chloroplast Binding Competition Assay

1. The assay is performed in total volume of 300 μl. The reaction mixtures contain 100 nM ^{35}S-prSSU, 10 mM DTT, 100 μM Na–ATP, 2 mM $MgCl_2$, 1% BSA, 300 mM urea, and 0.25 mg chlorophyll/ml chloroplasts in the presence of 1× IB with various concentrations of cold competitor. Stock solutions include freshly prepared 8 M urea solution (containing 50 mM DTT, 20 mM Tris–HCl pH 8.0), 1×IB, 2×IB, 100 mM DTT, fresh 10 mM Na–ATP, 100 mM $MgCl_2$, and 10% BSA. Prepare a set of 1.6 ml tubes containing 700 μl 40% Percoll in IB for reisolation of the chloroplasts; keep on ice.
2. To minimize the internal ATP in the chloroplast, the pea plants are harvested at the end of the dark cycle and chloroplast isolation is performed under dim light. The purified intact chloroplasts are resuspended in IB containing 2% BSA at the concentration of 1 mg chlorophyll/ml. Keep in the dark and on ice.
3. Dilute ^{35}S-prSSU at least 2-fold with freshly prepared 8 M urea solution to final concentration of 6 mM (6 μl will be used in each reaction). Resuspend lyophilized transit peptide competitor in 8 M urea solution. Generate serial dilutions of the competitor in 8 M urea solution (5 μl will be used in each reaction).

Note: It is important not to let the total urea concentration go above 350 mM. Urea levels above this will lead to loss of binding activity through some disruption of the chloroplast. By adding the urea denatured precursors last, we prevent them from precipitation upon dilution.

4. Prepare a master mix of required IB, DTT, Na–ATP, $MgCl_2$ BSA, and urea for all reactions (in total volume of 214 μl for each reaction)
5. Pipette 214 μl of the master mix into a set of new 1.6 ml reaction tubes, equilibrate the temperature by incubation at room temperature for 10 min.

Note: The following steps are performed under dim light to minimize ATP synthesis. Add 75 μl of chloroplasts to each tube. Gently mix by inverting the tube 5 times.

6. To start the assay, 6 μl of ^{35}S-prSSU and 5 μl of competitor are added in rapid succession. Gently mix by inverting the tube 5 times. Incubate at room temperature for 25 min (mix occasionally by inverting 1 time).
7. Follow steps 8–12 of the chloroplast import competition assay.
8. For analysis by liquid scintillation, 30 μl of the samples are bleached by adding 90 μl of 30% H_2O_2 and incubated at 80 °C for 30 min. Transfer bleached samples to a scintillation vial containing 2–4 ml Scintillation fluid and count.

G. Analysis Precursor Binding and Import

The process of precursor import can be broken down into a binding process and an import process. Using radiolabeled preproteins, it is possible to quantitate these steps into the number of molecules/chloroplast/min bound or imported as described above. The import data is acquired by quantifying the imported ^{35}S-prSSU by first running and subsequently drying an SDS-PAGE gel and subjecting it to a Phosphorimager. SDS-PAGE is required to separate the bound ^{35}S-prSSU from the imported ^{35}S-prSSU (processed to mSSU) labeled as p and m in Fig. 3B and C. As the name implies, import is prevented in the binding assay (II.F) and no bands of imported ^{35}S-prSSU are detected on the gel (Fig. 3D). This allows direct quantification using liquid scintillation counting without running SDS-PAGE to separate the species.

The import experiment generates data that can be fit with linear regression (competitors that do not compete, i.e., mSSU) while a one phase exponential decay fits data with competitors that do compete (prSSU). With the exponential decay fit, we can determine the IC_{50} for the competition import data (Fig. 3E). Varying the concentration of the radioactive prSSU with other variables held constant generates two sets of competitive binding data that can be globally fit using the GraphPad Prism program. The binding data are fit to a homologous binding event to determine the dissociation constant (K_d) and maximum number of binding sites (B_{max}, Fig. 3F). Analysis of competitive binding data of ^{35}S-prSSU with other proteins will determine the equilibrium dissociation constant (K_i) of the competitor. By comparing data in Fig. 3F fit to solid lines (closed circles and triangles, left y-axis, data from scintillation counting) and data fit to dashed lines (open circles and triangles, right y-axis, data from Phosphorimager analysis) scintillation analysis provides excellent data with a higher signal-to-noise ratio over

Phosphorimager data; a Pearson correlation test reveals a correlation of 0.978. This argues against the need to run gels and subject them to Phosphorimager analysis.

H. LSCM Imaging of the Bound Transit Peptide

The orientation and interaction of the transit peptide at the surface of the chloroplast is of importance, especially in light of the binding and import data. We have previously described a dual-tagged transit peptide His-S-SStp, which interacts with the Toc apparatus with the same affinity as the WT peptide yet accumulates in the Toc translocon (Subramanian *et al.*, 2001). This construct allows us to detect the short S-tag using a high affinity, monovalent S-protein detection system that can be FITC coupled for microscopy (Kim and Raines, 1993). Using this system, we created several C-terminal deletion constructs of the transit peptide (Fig. 4A). Additionally, using antibodies against the full length transit peptide, we confirmed the position of the cross-reacting epitope that was predicted to be located at the C-terminal portion of the transit peptide (Fig. 4B). Using these truncations, we observe that Δ25 and Δ36 but not Δ5 of SS-tp lose cross-reactivity (Fig. 4C) identifying the reactive epitope shown in yellow. Coomassie stained lanes 1–4 and anti-SStpNt lanes 5–8 refer to the truncations in A and their slight mobility difference is reflective of their deletions. Using S-protein FITC, we observe a punctate distribution of the transit peptide associated with the Toc apparatus. An identical labeling pattern was observed when we used the FITC coupled anti-SS-tp antibodies indicating that both the N-terminus and the C-terminus of the bound transit peptide are concurrently accessible to the cytosolic face of the chloroplast. Dual labeling using two different fluorescent detections indicates that these two detections colocalize to the same particle within the resolution of technique (data not shown). These results suggest that at least for this transit peptide construct, the conformation of the bound transit peptide is such that both the N- and C-terminus remain exposed to the cytoplasm (Fig. 4D).

III. Toc Translocon Dynamics

A. Solubilization of Intact Translocons and Dissociation of the Toc Complex

Our laboratory has revealed many features of the heterologously expressed, recombinant, purified Toc components through both standard and advanced experimentation (Reddick *et al.*, 2007). However recently, we have developed and refined existing methods including Blue Native PAGE (BN-PAGE) and 2D-PAGE (Fig. 5A-C). BN-PAGE is a charge shift technique developed by Schagger and von Jagow to separate native membrane multiprotein complexes (Schagger and von Jagow, 1991). These membrane protein complexes are solubilized by a minimal amount of a neutral detergent such as Triton X-100, *n*-decyl-maltoside, or digitonin (Eubel *et al.*, 2005), and a negative charge is induced by the binding of Coomassie blue

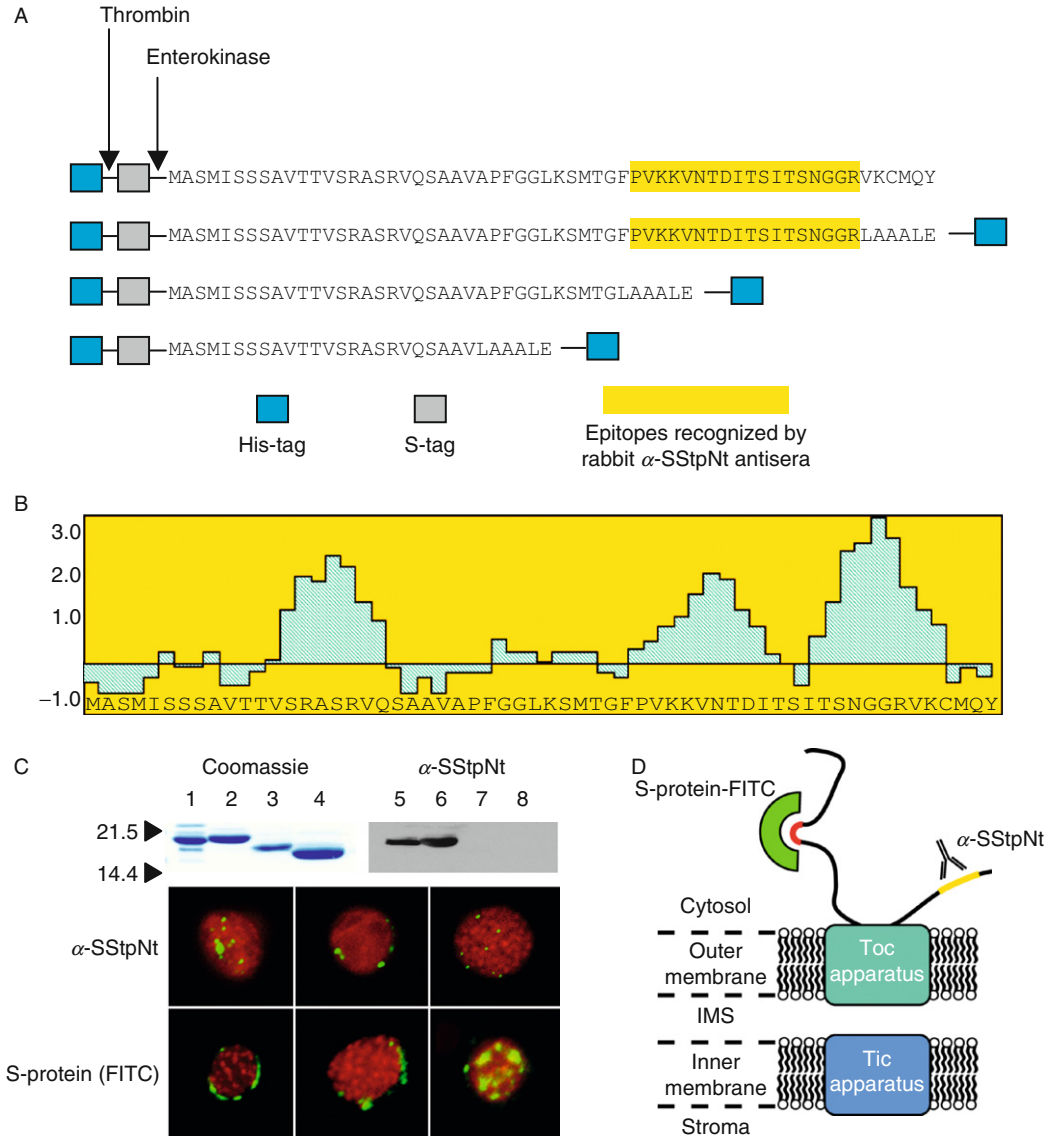

Fig. 4 Mapping the topology of a bound transit peptide in the Toc translocon. Panel A, Sequences of full length and C-terminal deletion mutants of His-S-SStp (Subramanian *et al.*, 2001) and placement of the dual-epitope tags (His-tag and S-tag). Panel B, Plot of predicted antigenicity of the SS-tp using the Hopp and Wood algorithm in DNAstar Protean software. Panel C, Top indicates the CBB stained SDS-PAGE gel and Western Blots of the His-S-SStp deletions, mapping the location of the dominant epitope recognized by our rabbit anti-SStpNT antibody to the C-terminus. Lower images show three representative chloroplasts with a bound His-S-SStp fluorescently labeled with either (1) a FITC-conjugated GAR secondary antibody (top three) or (2) a FITC-conjugated S-protein that reacts with the N-terminally placed S-tag. Panel D. Model indicating the topology of the bound transit peptide with both the C and the N-termini of the bound His-S-SStp are exposed to the cytosol.

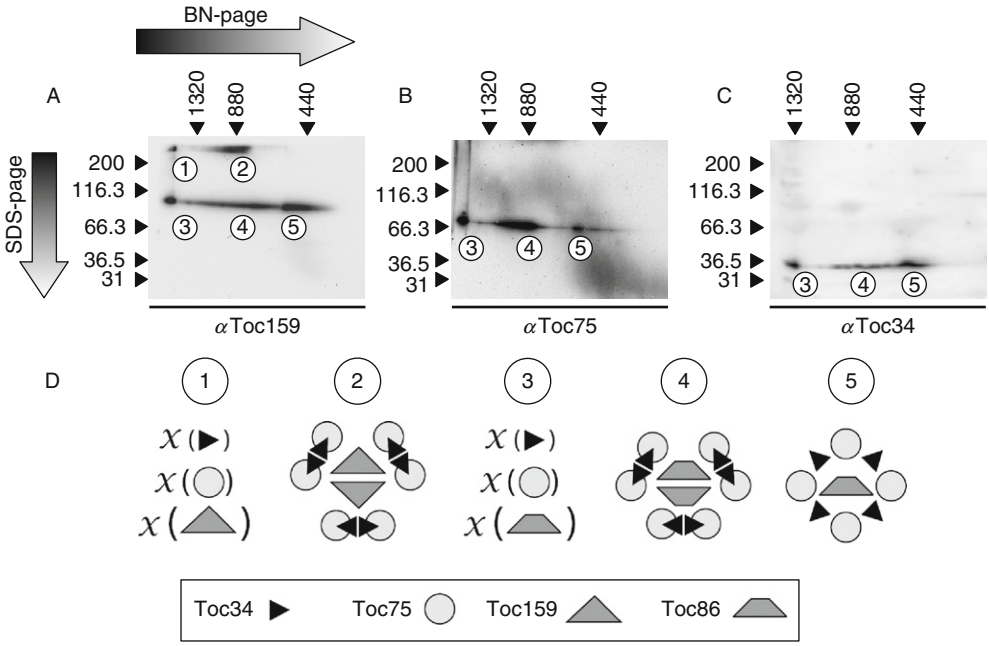

Fig. 5 2D-PAGE analysis of Toc translocon dynamics. The horizontal arrow above the gel represents the direction of electrophoresis in the Blue Native PAGE (1st dimension) and the vertical arrow represents the direction of electrophoresis in the SDS-PAGE (2nd dimension) in A–C. Molecular weight markers are presented above and to the left of each blot. Panel A–C represent the western analysis of intact chloroplast 2-D PAGE using antibodies against Toc159 (A), Toc75 (B), and Toc34 (C). Presumably, a Tic–Toc supercomplex has difficulty migrating into the BN-gel and therefore the stoichiometry of Toc34, Toc75, and Toc159 is questionable in number 1. A complex of 6:6:2 Toc34:Toc75:Toc159 is seen in 2. Degradation is a common aspect of chloroplast preparations, and the majority of Toc159 is present as Toc86 in 3–5. The possible stoichiometries are unknown (3), 6:6:2 (4) and 4:4:1 (5). In panel D, complexes 1 and 3 are represented as unknown stoichiometries of Toc34, Toc75, and Toc159 (1) whereas the degradation product Toc86 is present in 3. Numbers 2, 4, and 5, presented from the perspective of looking down upon the chloroplast outer membrane, represent the following stoichiometries: 6:6:2 (Toc34:Toc75:Toc159); 4, 6:6:2 (Toc34:Toc75:Toc86); 5, 4:4:1 (Toc34:Toc75:Toc86). From the intensities present, we conclude that the 6:6:2 stoichiometry is favored over 4:4:1.

G-250 to the hydrophobic domains on the surface of proteins; the use of Coomassie to both abrogate hydrophobic collapse and concomitantly stain the protein(s) is of beneficial significance. Initial runs should be performed on steep gradient gels (~4–20%), as uniform gels will not be satisfactory (Schagger *et al.*, 1994).

Previously, researchers purified the Toc core complex from outer envelope membrane vesicles by *n*-decyl-*β*-maltoside solubilization followed by sucrose density gradient centrifugation. The core complex was analyzed by size exclusion chromatography, was determined to contain the 86-kDa fragment of Toc159, Toc75, and Toc34, and eluted at around 500 kDa. The stoichiometry of the core complex was

determined to be 1:4:4–5 between Toc159, Toc75, and Toc34 giving a calculated molecular mass of ~522 kDa (Schleiff *et al.*, 2003); however, this reported stoichiometry might be the result of the experimental conditions. BN-PAGE has been utilized to characterize the mitochondrial import machineries (Dekker *et al.*, 1996, 1998; Meisinger *et al.*, 2001) as well as the Tic complex (Caliebe *et al.*, 1997; Kuchler *et al.*, 2002). Kikuchi *et al.* recently reported that the intact Toc complex, solubilized from intact chloroplasts, has an observed molecular mass of 800–1000 kDa, and contains at least Toc159, Toc75, and Toc34 (Kikuchi *et al.*, 2006). Further, Chen and Li have reported that during active import, precursors interact with two complexes: an 880-kDa Toc complex and a 1320-kDa complex containing the Toc components as well as Ticl 10, Hsp93, and an Hsp70 homolog, before associating with the Tic/Toc supercomplex, which is too large to be analyzed by BN-PAGE (Chen and Li, 2007). Analysis of western blot hybridization of BN-PAGE and 2D-PAGE of the core Toc complex will allow for the observation of organizational and dynamic changes induced by the incubation of nucleotides, preproteins, and exogenously added Toc components to purified chloroplasts.

B. Blue Native PAGE of Intact Chloroplast for Analysis of Toc Assembly

1. Follow the chloroplast isolation protocol above in II A, steps 1–8 with the following modifications: To all buffers add 5 μl/ml PIC for plant cell and tissue extracts, Sigma P-9599 except GB and solubilization buffer (SB, 1% digitonin in 50 mM BisTris–methane pH 7.0, 500 mM aminocaproic acid, 10% glycerol) to which add 10 μl/ml PIC.
2. Resuspend the pellet in 1 ml IB, divide into three 1.6 ml microfuge tubes.
3. Make 700 μl of a 2× solution in IB of the nucleotide or protein to be tested for complex dissociation. Keep chloroplasts in the dark, and mix 330 μl of the experimental solution with one tube of chloroplasts to start the longest time point incubation. After 15 min, repeat for the second time point, and mix 330 μl of IB with the control chloroplasts.
4. After 15 min, repurify intact chloroplasts over 500 μl of 40% Percoll. Aspirate the Percoll, supernatant, and broken chloroplasts, leaving a pellet of intact chloroplasts.
5. Resuspend intact chloroplasts in 175 μl of SB and solubilize for 10 min on ice in the dark. Remove insoluble material by ultracentrifugation at 100,000*g* for 10 min.
6. Decant supernatant and mix with Coomassie G-250 solution (5% Brilliant Blue G-250, 50 mM BisTris, 500 mM aminocaproic acid) to achieve an 8:1 detergent to Coomassie ratio.
7. Load and run a 0.75 mm thick 4–10% polyacrylamide gradient gel containing 50 mM BisTris and 500 mM aminocaproic acid for 5 h at 200 V at 4 °C. BSA (66 and 132 kDa) and Ferritin (440, 880, and 1320 kDa) are used as molecular weight markers.

8. Cut-off lane containing markers and stain (general Coomassie staining protocol). Separate individual lanes and heat at 65 °C in buffer containing 3.3% SDS, 4% βME, and 65 mM Tris–HCl pH 6.8 for 20 min.

C. 2D SDS-PAGE and Western Blot Analysis

1. Pour a 1.5 mm 8–16% SDS-PAGE gradient gel and allow polymerization. Overlay ~1 ml of 4.8% stacking gel on the gradient gel, top with 50% isopropanol, and allow polymerization.
2. Remove a strip of a BN-PAGE gel as per section B, step 8 above and gently place it horizontally above the stacking gel. Pour 4.8% stacking gel around the BN-PAGE lane and a small, one well comb (for molecular weight markers) to seal the gel slice in place. Allow polymerization.
3. Run the gel at 30 mA for ~1 h until the dye front has run off.
4. Transfer proteins from gel to Immobilon PVDF using a Genie electrophoretic transfer apparatus (Idea Scientific) for 4 h at 4 °C. The choice of transfer buffer will depend on your choice of analysis parameters: For western blotting against Toc75 and Toc159, transfer in high molecular weight transfer buffer (48 mM Tris, 390 mM Glycine, 0.1% SDS, 20% methanol). For western blotting against Toc34, use high pH transfer buffer (100 mM Tris, 192 mM Glycine, 20% methanol).
5. Block the Immobilon with TBST (25 mM Tris–HCl pH 8.0, 137 mM NaCl, 3 mM KCl, 0.1% Tween 20) containing 3% nonfat milk and 0.5% BSA for 1 h. All incubations can be carried out at room temperature with rocking.
6. Incubate the 1° antibody with the blots for 2 h at 1:25,000.
7. Wash blots for 10 min, 3 times with TBST.
8. Incubate the 2° antibody with the blots for 1 h at 1:25,000, repeat step 7.
9. Incubate blots with chemiluminescent substrate (HRP) and photon count on a Chemidoc system (BioRad).
10. Analyze blots with Quantity One software (BioRad) and quantitate the complexes formed at different sizes.

Figure 5 details the western results obtained by the previous protocol. BN-PAGE separates the complexes while SDS-PAGE separates the individual proteins for easy identification and correlation with the native size of the complex with which a given protein is associated. In panel A, antibodies against Toc159 indicate that this protein exists as both Toc159, numbers 1 and 2, and Toc86, numbers 3–5. Numbers 1 and 3 refer to complexes in which the stoichiometry is unknown, indicated by an X before the representative cartoon in D. The stoichiometry is unknown due to the large size of the complex in the first dimension (greater than 1320 kDa). Number 2 represents the migration of a 6:6:2 (Toc34:Toc75:Toc159) complex whereas number 4 represents a similar 6:6:2 with Toc86, the more

proteolytically resistant form of Toc159. Number 5 in panel D represents a stoichiometry of 4:4:1, again with Toc86. Panels B and C underscore this distribution by using antibodies against Toc75 and Toc34, respectively.

D. TIRF Imaging of Toc Dynamics

TIRFM allows for the excitation of fluorophores only within the cell surface, leading to very low background fluorescence and yielding a high signal-to-noise ratio. An evanescent field is produced by the total internal reflection of the excitation beam. Proximal fluorophores will be excited within this evanescent field without exciting more distant fluorophores (Axelrod, 2001). TIRFM allows for the observation of single fluorescent molecules and the study of their dynamics and kinetics while cellular photodamage and photobleaching are minimized (Toomre and Manstein, 2001). In contrast, TIRFM allows for the illumination of <100 nm from the surface, whereas confocal systems typically show an optical section of $\sim$500–800 nm. Toc159 on the surface of intact chloroplasts is labeled with fluorescent antibodies allowing the real time visualization of the dynamic environment of this translocon component while minimizing the effects of chlorophyll autofluorescence. The following general protocol details the preparation of chloroplasts for TIRFM analysis.

1. Block purified intact chloroplasts with 1% BSA in IB with rocking for 30 min.
2. Incubate the 1° antibodies with the chloroplasts for 1 h with rocking at a titer of 1:500.
3. Wash by carefully injecting 40% Percoll under the chloroplasts, centrifuge for 10 min at 3400*g*, and resuspend in IB containing 1% BSA. Perform this wash for a second time.
4. Incubate the 2° fluorescent antibodies with the chloroplasts for 1 h with rocking at a titer of 1:500.
5. Repeat step 3.
6. Labeled chloroplasts are then visualized on a Nikon TIRFM.

In the future, this technique shows promise for the labeling of multiple Toc components with different fluorophores and analyzing the kinetic and dynamic properties of the Toc complex through the utility of various excitation and emission wavelengths. Presently, we have used this technique to visualize intact chloroplasts that have been immunodecorated with fluorescent antibodies against atToc159 which can be viewed in bright field and subsequently deconvoluted, Fig. 6A and B, respectively. Using Nikon particle tracking software, we can follow individual labeled translocons on the chloroplast surface and calculate their mobility. Panels C–E represent different chloroplasts on which a fluorescent spot has been selected and its velocity and acceleration as a function of time has been determined and graphed. Interestingly, like most single molecule detections, we observe a discontinuity in mobility, with relatively long periods of stasis

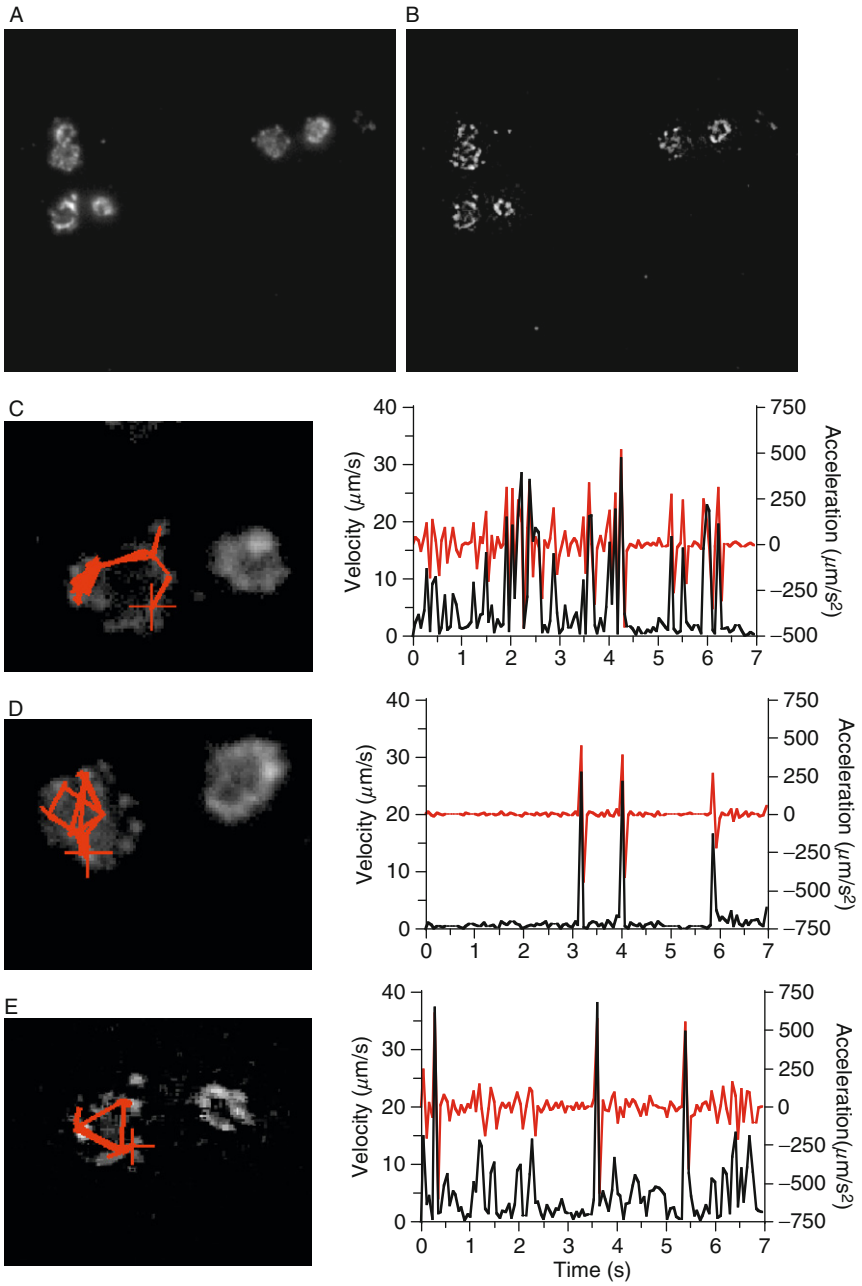

Fig. 6 TIRF microscopic analysis of Toc159 dynamics. Panel A and B is a wide field image of isolated chloroplasts immunodecorated with anti-Toc159 antibodies. Deconvolution using the bundled Nikon software yields the image in panel B in which dynamic background subtraction has been performed. Panels C–E represent isolated chloroplasts in which an isolated fluorescent spot has been selected and both velocity and acceleration have been determined as a function of time (associated graph to the right).

punctuated by short bursts of mobility. In the future, this technique allows us to monitor the association/dissociation dynamics of individual translocon subunits by utilizing multi-color immunolabeling with anti-Toc34, anti-Toc75, and anti-Toc159 antibodies. Additionally, by varying the nucleotide and preprotein/transit peptide status, we can determine whether the energetics and translocation activity alter its mobility and subunit composition.

IV. Activity and Enzymology of Toc GTPases

GTPase proteins have historically low basal hydrolytic rates, existing in either a GDP (off) or a GTP (on) state in order to function as molecular switches rather than molecular motors (Bourne *et al.*, 1990, 1991). This basal hydrolytic rate can be stimulated through the interaction of regulatory proteins, such as GTPase Activating Proteins (GAP) and Guanine nucleotide Exchange Factors (GEF) (Bos *et al.*, 2007). GAPs are generally specific for their target GTPase acting to accelerate the rate of hydrolysis, effectively turning the switch "off." Recently, we showed that the transit peptide is the GAP for psToc34 (Reddick *et al.*, 2007). A GEF catalyzes the dissociation of bound GDP from the GTPase effectively turning it "on." A GEF acts through interaction either directly with the GTPase switch domains, or allosterically at an auxiliary location to lower the affinity for nucleotide, such that GTP, largely through mass action, replaces GDP; the cellular concentration of GTP is several times greater than that of GDP (Vetter and Wittinghofer, 2001). Here, we describe in detail the methods used to quantitatively measure the hydrolytic rates of isolated Toc proteins *in vitro*, determine the K_d and K_i through competitive nucleotide binding experiments and carefully measure the rate of GDP/GTP exchange.

A. Purification of Toc Proteins

The growth and purification of Toc proteins from *E. coli* follows standard bacterial culture techniques. Briefly, the cDNA encoding the truncated, soluble domains of the Toc proteins were inserted into pET hexahistidine tag vectors and transformed into competent BL21(DE3)-RIL *E. coli* cells by standard procedures. The cells are grown at 37 °C with shaking to an $O.D._{600}$ of 0.5 at which time they are induced with 1 mM IPTG, after which the cells are harvested via centrifugation. Cells are lysed via French Pressure Cell; supernatant and pellet are separated via centrifugation and psToc34 protein is purified using the PrepEase system (USB Corp., Cleveland, Ohio). Protein is eluted and quantitated. (For further information, please refer to Reddick *et al.*, 2007.)

B. GTP Hydrolysis Assay

In order to determine the rate of hydrolysis of these GTPases, a highly quantitative hydrolysis assay was developed. This was done due to the fact that an assay of this kind was not available. This assay relies on the enzymatic release

of a radiolabeled γ-$^{32}P_i$ from [γ-^{32}P]GTP and its subsequent isolation and quantitation to determine the enzymatic activity of the Toc protein. A 96-well plate will be used for this assay such that column 1, rows A–H will be the reaction wells and columns 2–6, rows A–H will be the quenching wells for column 1 at five aliquot removal time points. An additional assay with varying parameters or a duplicate of the current assay can be carried out in column 7 with quenching wells in columns 8–12. Column 1, rows A–H will have a final total volume of 100 μl and will be composed of three parts: (1) cold GTP solution, (2) radioactive GTP solution, and (3) Toc protein solution. The addition of Toc protein solution to the well will start the reaction, and thus the timing of aliquot removals. Aliquots of 15 μl will be removed at precise times from each well in column 1 and added to specific wells (rows 2–6, A–H), which will contain 200 μl of quenching suspension (10% (w/v) activated charcoal suspension in 100 mM HCl and 5 mM H_3PO_4). The acids are present to stop the reaction and reduce spontaneous hydrolysis while the activated charcoal can remove from solution the carbon containing compounds, leaving inorganic phosphate, buffer components, acids, and water. The assay wells are put together as per the following protocol; wells are denoted by their grid number and corresponding letter (e.g., 1E refers to the well in column 1 at row E):

Part 1: Cold GTP Solution

1. Add 3.3 μl 10× GBS (200 mM Tricine–KOH, pH 7.65, 10 mM $MgCl_2$, 500 mM NaCl, 10 mM βMe) to each well (1A–H) along with 30 μl ddH_2O to 1A.
2. Add 0.3 μl of 33.3 mM GTP and 27.7 μl ddH_2O to 1B.
3. Add 1.5 μl 33.3 mM GTP and 28.5 μl ddH_2O to 1C. 1D–1H will have 3, 7.5, 15, 22.5, and 30 μl 33.3 mM GTP solution with the requisite volume of ddH_2O to bring the total volume of part 1 to 33 μl.

This ensures that during the assay, rows A–H will have 0, 1, 5, 10, 25, 50, 75, and 100 μM cold GTP creating the substrate titration curve necessary for Michaelis–Menten kinetic measurements.

Part 2: Hot GTP Solution

1. Add 1.76 μl 10 nM [γ-^{32}P]GTP (800 Ci/mmol) and 0.01 mCi/μl) to 14.66 μl 10× GBS and 130.24 μl ddH_2O to create a final volume of 146.66 μl of radioactive GTP solution in a 1.6 ml microfuge tube.
2. Add 16.66 μl of this solution to wells 1A–H.

Part 3: Toc Protein Solution

1. Add 22.76 μl of 5 mg/ml Toc protein to 44 μl 10× GBS and 373.24 μl ddH_2O.

This solution is the "start" solution, as its addition to wells in column 1 of the 96-well plate will start the reaction.

Part 4: GTP Hydrolysis Assay

1. At time equals 0:00 (min:s), add 50 μl ddH_2O to 1A.
2. At 0:15, add 50 μl Part 3 to 1B.
3. At 0:30, 50 μl Part 3 to 1C; 0:45, 1D; 1:00, 1E; 1:15, 1F; 1:30, 1G; 1:45, 1H.
4. At 5:00, remove 15 μl from 1A and place it into 2A.
5. At 5:15, remove 15 μl from 1B and place it into 2B; 5:30, 15 μl from 1C to 2C, etc.
6. At 10:00, remove 15 μl from 1A and place into 3A; 10:15, 15 μl from 1B to 3B, etc.

Columns 2–6 represent the 5, 10, 15, 20, and 25-min time points for each of the reaction wells. Once the last aliquot is removed and added to the activated charcoal, use a multichannel pipettor to vigorously mix the contents of all wells, being careful to avoid well-to-well contamination.

7. Transfer the contents of wells 2–6, rows A–H to a 96-well 0.2 μm filter plate. Place in a 96-well vacuum manifold, and apply vacuum.

This will transfer the liquid content to the receiving plate below, while retaining the charcoal. This step effectively separates unhydrolyzed [γ-^{32}P]GTP from $^{32}P_i$.

8. Place 100 μl MicroScint 40 scintillation fluid into wells 2–6, A–H of a TopCount MicroScintillation Plate (Perkin Elmer). Transfer 20 μl of the radioactive filtrate from each well to the corresponding well in the scintillation plate, pipetting vigorously to ensure even distribution of aqueous material in the scintillant.
9. A TopSeal sealing film is applied to the top of the scintillation plate which is placed into a TopCount NXT Microplate Scintillation Counter, Perkin Elmer Life Sciences. Scintillation counting should be performed for (at minimum) 5 min/well and cross talk filters applied.

There are several factors that one must determine in order to calculate the activity of the enzyme; according to Michaelis–Menten kinetics, this rate is reported as mole substrate consumed or hydrolyzed per unit time per mole enzyme. Equation (2) shows the general formula needed to transform scintillation counts into enzyme activity, and in our case, has been incorporated into a Microsoft Excel spreadsheet. First, counts per minute are graphed as a function of time generating a CPM versus Time plot for each substrate concentration along with a spontaneous hydrolysis rate that should be subtracted from the rate of hydrolysis prior to analysis. The slope of this line will represent ΔCPM/min, or C_m. The isotope per time point, I_m, must be determined; it is simply the isotope concentration in the reaction multiplied by the volume of each time point aliquot. Determine the ratio of your stock cold GTP to the volume of cold GTP in each reaction. The hot ratio is also determined in the same manner by taking the ratio of the [γ-^{32}P]GTP stock (MP Biomedicals) to the actual volume of hot GTP in each reaction. The cold:hot ratio (R_{GTP}) is simply the ratio of these two ratios. Next, S_f is the scintillation fraction factor, or the reciprocal of the scintillation sample volume divided by the sum of the HCl–charcoal volume and the time point volume. Since CPM is not

directly related to a scintillation event, only DPM, or disintegrations per minute, one must convert CPM to DPM. This is accomplished by multiplying the Ci per time point (which is determined by multiplying the Ci concentration in the reaction by the time point volume) by 1 Ci (expressed as 2.22×10^{12} dpm) to give D_m. The number of Toc molecules, M_{Toc}, is determined by dividing the product of the volume of enzyme in each reaction and the stock mg/ml of enzyme by the molecular weight of the enzyme. The HCl–charcoal dilution factor, or C_{dil}, is determined by dividing the time point volume by the sum of the time point and the HCl/charcoal volume. The counting efficiency, C_{eff}, and isotope purity factor, P_f, are determined empirically and by contacting the manufacturer of the radionucleotide, respectively.

Once all of these parameters have been determined and placed into a spreadsheet, the assay is very simple and highly reproducible, save pipetting errors by the experimenter. With each concentration of substrate, this spreadsheet will generate a single data point, expressed as mol GTP hydrolyzed per unit time per mol enzyme. In this case, we have chosen to express it as nmol GTP hydrolyzed per minute per μmol Toc protein. Since each substrate concentration has an associated rate, one can create a graph such that substrate concentration is on the x-axis and rate is on the y-axis; this is also known as a Michaelis–Menten plot. By applying the Michaelis–Menten equation, a nonlinear fit can be made and V_{max} and K_M can be determined.

Since it has been shown in the past that transit peptide was recognized and bound by Toc34 (Reddick *et al.*, 2007; Schleiff *et al.*, 2002), we incorporated it into our GTPase hydrolysis assay. Simply by performing several GTP titration experiments (as described above) and incorporating different concentrations of transit peptide in each GTP titration experiment, one can see that the CPM versus time graph indicates a greater release of radioactivity as a function of time for the different treatments (Fig. 7A), indicating that a greater amount of hydrolysis is occurring per unit time. After determining these linear rates (in ΔCPM/min) and applying the calculation in Eq. (2), one can determine the V_{max} and K_M of psToc34 in the presence of transit peptide, prSSU and mSSU and compare this to the previous enzymatic parameters in its absence (Fig. 7B). This allowed us in 2007 to determine how the transit peptide increases the overall hydrolytic rate of psToc34 while concomitantly decreasing the K_M (increasing the affinity for substrate). This represents the first time that a GAP, or GTPase Activating Protein, was identified for the Toc GTPases (Reddick *et al.*, 2007).

C. GTP Binding Assay

The 96-well nucleotide competition binding experiment relies on the capture of His-tagged Toc proteins bound to magnetic Ni–NTA agarose beads (Qiagen Inc. Valencia, California) via a hybrid plate magnet developed by the Joint Genome Institute at Lawrence Berkeley National Laboratory (Humphries *et al.*, 2004). This

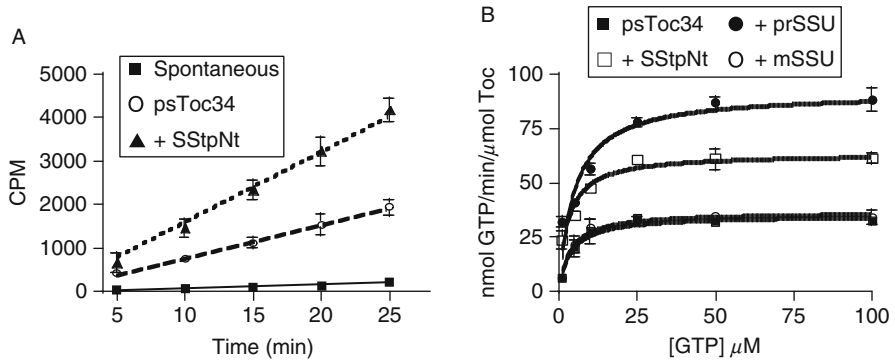

Fig. 7 Panel A shows the evolution of $^{32}P_i$ per unit time data generated by the hydrolysis assay. For simplicity, three traces are shown, each at 25 μM GTP; if an entire experiment were shown, low [GTP] has a large slope whereas high [GTP] has a lower slope due to the ratio of [Hot] to [Cold] in each well. The slope of the spontaneous is very small, whereas the slope of the psToc34 + SStpNt indicates a higher rate of hydrolysis as compared to psToc34 alone. Panel B shows the data after the activity calculation (Eq. 1). psToc34 has a basal rate of ~35 nmol GTP/min/μmol Toc, and is unchanged by the addition of mSSU. However, the addition of SStpNt increases the V_{max} to ~65 nmol/min/μmol and prSSU further increases that rate to ~90 nmol/min/μmol indicating that portions of prSSU may also stimulate the hydrolytic rate.

$$\text{Activity} = \frac{C_m I_m R_{GTP} S_f}{D_m M_{Toc} C_{dil} C_{eff} P_f}$$

Eq. 2 GTPase Activity Calculation. Specific activity of Toc protein, measured in nmol GTP hydrolyzed per minute per mol Toc. C_m, Δcpm/min; I_m, isotope/time point; R_{GTP}, Ratio (cold:hot) GTP; S_f, scintillation fraction factor; D_m, dpm/time point; M_{Toc}, Toc molecules; C_{dil}, HCl/charcoal dilution factor; C_{eff}, counting efficiency; P_f, isotope purity factor

assay was developed in order to accurately and quantitatively determine the K_d and K_i for the Toc GTPases and was first published in 2007 (Reddick *et al.*, 2007).

1. A 25 μl serial dilution of unlabeled competitor is performed across the 96-well plate such that each row of wells is either a different competitor, or each competitor is represented twice on the plate for duplicate analysis.

2. A constant volume of 25 μl (of various concentrations per experiment[2]) of 3000 Ci/mmol [α-^{32}P]GTP is added to all wells.

3. Ni–NTA magnetic agarose beads are incubated with the His-tagged Toc protein of choice on ice to allow sufficient affinity binding. A 50 μl suspension of magnetic beads and enzyme is added to each well of the 96-well plate to start the reaction.

4. Allow the reaction to proceed for 30 min on ice. Place the 96-well reaction plate on a 96-well plate magnet. This will draw down the magnetic beads and allow efficient washing of the plate. Wash with a volume of 300 μl 1× GBS buffer with

[2] The author recommends performing, at minimum, 3 plate experiments with varying [α-^{32}P]GTP to determine an appropriate amount for global fit analysis.

either a continual microplate washer or repeated pipetting of buffer manually for 2–3 min. This will remove all nonspecific background counts.

5. While still on the magnetic plate, aspirate to near dryness without disturbing the Ni–NTA beads.

6. Add 100 μl 500 mM imidazole in GBS buffer, remove plate from magnet, and allow to incubate for 10 min on ice with gentle agitation.

7. Place the 96-well plate back onto the magnet for 5 min to ensure complete draw down of the magnetic beads and remove 20 μl of the reaction mixture to a TopCount MicroScintillation Plate containing 100 μl MicroScint 40 scintillation fluid.

8. Repeat step 9 from the GTP Hydrolysis Assay.

This highly quantitative assay was employed to determine the K_d (GTP) and the K_i (various nucleotides and analogues) for four Toc proteins: atToc33, atToc34, psToc34, and atToc159G (Reddick *et al.*, 2007). Presented here are the binding curves of GTP and GDP to psToc34 (Fig. 8A). In order to avoid ambiguous results common with homologous competition experiments, the assay was repeated twice with different initial [α-^{32}P]GTP concentrations and all data was fit using the GlobalFit parameters in GraphPad Prism 4.0c. Using this experimental procedure, we generate 12 data sets per global fit analysis: two replicates, each counted in triplicate at two different [α-^{32}P]GTP concentrations. These data are fit to Eq. (3) (K_d) with the log K_d value shared for global fitting and the amount of hot and cold nucleotide constrained according to the above protocol. For heterologous binding competitions to determine K_i, the experiments are set up in the same manner with

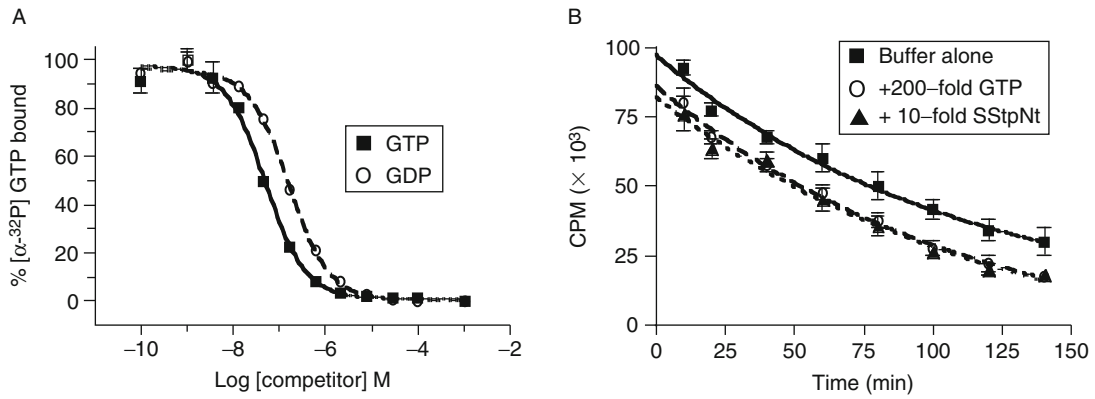

Fig. 8 Quantitative GTP binding and GTP/GDP exchange assays. Panel A shows data obtained from a binding experiment and reports the K_d of GTP (~50 nM) and the K_i of GDP (~151 nM). Panel B indicates the loss of bound [α-^{32}P]GTP over time (squares, solid line) and the addition of 200-fold [GTP] (circles, dashed line) only modestly increases this rate. Finally, the addition of 200-fold [GTP] with 10-fold [transit peptide] (triangles, dotted line) does not increase this rate of exchange.

$$\text{Total Binding} = \frac{B_{\max}[Hot]}{[Hot] + [Cold] + K_d} + NS$$

Eq. 3 K_d Calculation. Total Binding is defined as the non specific counts (NS) plus the ratio of the product of the maximal binding of GTP (B_{max}) and the concentration of the radioactive nucleotide ([Hot]) in the assay divided by the sum of the radioactive nucleotide concentration, cold competitor ([Cold]) and the dissociation constant (Kd)

the analysis fit to Eq. (4). In the case of measuring K_i, one must first determine K_d and use that value in order to determine K_i. The value for K_i was shared in the global fit and the amount of labeled and unlabeled GTP remained constant. For data analysis, 95% confidence is recommended.

D. *In vitro* Toc GTPase Nucleotide Exchange Assay

As a general rule, GTP-binding proteins have a very low basal hydrolytic rate and for efficient hydrolysis they require interaction with a GAP in order to accelerate the GTP cleavage step. The transit peptide acts as a GAP for psToc34, but a GEF protein has not yet been identified. Our nucleotide binding assay, described above, was modified such that a GEF experiment could be performed.

1. Toc protein is incubated with an excess of [α-^{32}P]GTP over night at 10 °C.
2. The protein is desalted on a PD-10 column (BD Biosciences) equilibrated with 1× GBS buffer in order to remove unbound GTP.
3. Similar to the GTP binding experiment earlier, the Toc protein is incubated with Ni–NTA magnetic agarose beads for ~1 h to allow affinity binding. The affinity bound protein and magnetic bead slurry is adjusted to 200 nM Toc protein and 50 μl is aliquoted into each well of a 96-well plate.
4. The time course of dissociation of bound radiolabeled nucleotide is started with the 50 μ1 addition of either GBS, GBS + 100-fold BSA, GBS + 100-fold cold GTP, GBS + various concentrations of transit peptide (or any other suspected GEF). Each column of the 96-well plate represents a time point, while each row of the plate represents an experimental condition.
5. At time = 10 min the plate is placed on the 96-well plate magnet and column 1 is washed three times with 200 μ1 GBS buffer. Then 200 μ1 500 mM imidazole in GBS buffer is added and incubated for 10 min off the magnet with gentle agitation.

$$\text{Total Binding} = \frac{B_{\max}[Hot]}{[Hot] + K_d\left(1 + \frac{[Cold]}{K_i}\right)}$$

Eq. 4 K_i Calculation. Total Binding is defined as the ratio of the product of the maximal binding of GTP (B_{max}) and the concentration of the radioactive nucleotide in the assay ([Hot]) divided by the sum of the radioactive nucleotide concentration and the product of the dissociation constant (K_d) and 1+ the cold nucleotide competitor concentration ([Cold]) over the inhibition constant (K_i)

6. The plate is placed back on the magnet, and 20 μ1 from 1A–H in the reaction plate is removed to 1A–H of a TopCount MicroScintillation Plate containing 100 μ1 MicroScint 40 scintillation fluid.
7. This procedure is repeated every 10 min for each following column such that column 2 = 20 min; 3 = 30 min; 4 = 40 min, etc.
8. Once the assay is complete, repeat step 9 from the GTP Hydrolysis Assay.

The GTPase assay indicated that transit peptides stimulate the V_{max} and lowered the K_M while the GEF assay indicated that transit peptide does not stimulate the exchange reaction, Fig. 8B. This allowed us to conclude that the transit peptide is indeed the GAP for psToc34, however to date, no GEF has been identified. It is possible that other Toc components or even 14–3–3 proteins and chaperones could be the GEF for psToc34. This GTP/GDP exchange assay will afford us the opportunity to determine the answer to that question in a very quantitative manner.

V. Molecular Modeling of Toc Proteins

A. Introduction to Toc75 and POTRA Domains

Toc75 falls into a broad category known as the outer-membrane protein family (OMPs) that are folded and inserted into membranes by a process conserved between prokaryotes and eukaryotes (Paschen *et al.*, 2003; Reumann *et al.*, 1999). The central transmembrane component is a highly conserved β-barrel protein; members of this family of proteins are involved in protein translocation into and across the outer membrane of gram negative bacteria (Omp85/YaeT), chloroplast (Toc75), and mitochondria (Sam50/Tob55) (Gentle *et al.*, 2005).

Folded soluble domains at the termini of β-barrel proteins have been involved in recognizing peptides or other unstructured proteins as substrates for translocation (Gentle *et al.*, 2005). These polypeptide transport associated (POTRA) domains are present in three copies in the Toc75 protein (Sanchez-Pulido *et al.*, 2003). Using HMMer to perform Hidden Markov Profile searches and the HMM profiles of POTRA2 and the related Bacterial Surface Antigen (both downloaded from the pFam database, Sanger Institute), the POTRA domains of psToc75 were identified as POTRA1, residues 161–237, POTRA2, residues 266–355, and POTRA3 residues 366–439 (all residue numbers correspond to the preprotein, that is, 131 residues in transit peptide (Ertel *et al.*, 2005)). Although the C-terminal, β-barrel portion of psToc75 is >75% similar to FhaC, an Omp-related protein of known structure (Fig. 9A), the N-terminal portion has little similarity. However, with the POTRA domains already identified, there is adequate information to give a reasonable homology model including POTRA 2 and 3 as well as the β-barrel, Fig. 9B. Modeller 9v2 (Eswar *et al.*, 2008) was used along with alignments generated by align2d (also in the Modeller package) and hand edited to properly align the POTRA domains as identified by HMMer, Fig. 9C and D. Since the results of the modeling were reasonable, the POTRA domains were subsequently cloned and purified via IMPACT system (Fig. 10A), as discussed previously in IIB. After obtaining purified

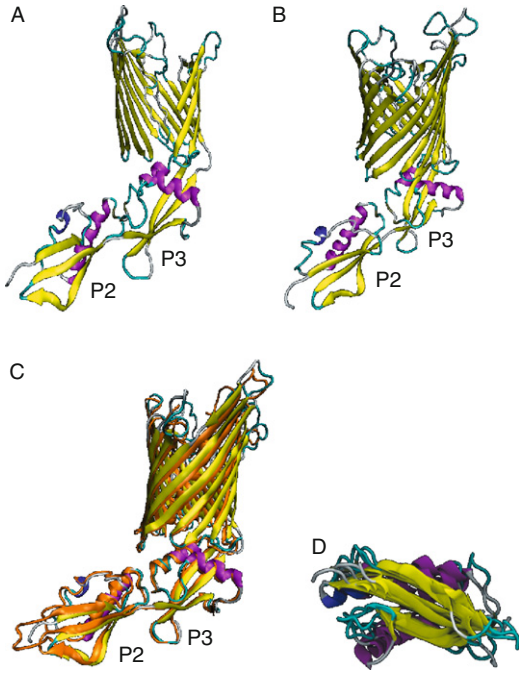

Fig. 9 Structural modeling of Toc75 and POTRA domains. Panel A shows the structure of FhaC (Clantin *et al.*, 2007). Panel B is the structural estimation of Toc75 based on the structure of FhaC; only POTRA 2 and 3 are modeled since FhaC only has 2 POTRA domains on which to model. Panel C shows the superimposition of the FhaC and Toc75 models; in panels A–C P2 and P3 refer to PORTA 2 and 3, respectively. Panel D, two POTRA domains of FhaC and the four POTRA domains of YaeT from *Bordetella pertussis* and *E. coli,* respectively, are easily super-imposable indicating a high degree of structural similarity. The fold in each domain revealed the presence of three-stranded β-sheets and two helices. The β-strands are labeled in yellow and the helices are labeled in purple; the loops are shown in light blue.

POTRA, we analyzed the overall fold of the POTRA domain using circular dichroism spectroscopy and determined that it was folded as predicted as compared to observed secondary structure of the six known POTRA structures, seen in Fig. 10B and summarized in Fig. 10C. Here we show purified psToc75-POTRA1 and CD spectra confirming reasonable amounts of each secondary structural element. This and the other purified POTRA domains will make critical tools for further quantitative inquiries into the function of the TOC apparatus.

VI. Conclusions and Perspectives

The chloroplast import apparatus is a remarkable nanoscale molecular gate and molecular motor. The Toc translocon is responsible for distinguishing between thousands of soluble cytosolic proteins and selecting only those containing an

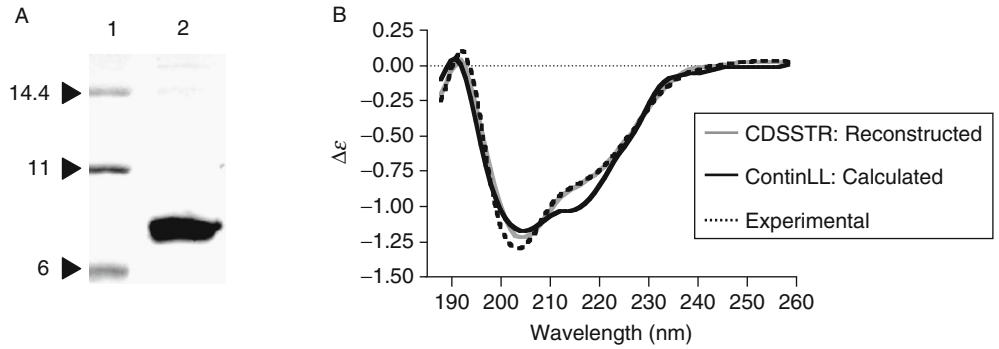

C

Comparison of psTOC75-POTRA1 with known POTRA secondary structures

	YaeT				FhaC			psToc75
Structural elements	Potra 1	Potra 2	Potra 3	Potra 4	Potra1	Potra 2	Average	Potra 1
Helix	0.29	0.33	0.30	0.32	0.28	0.20	0.27 ± 0.05	0.06
Strand	0.37	0.33	0.35	0.31	0.35	0.29	0.33 ± 0.03	0.33
Turn	0.16	0.23	0.22	0.23	0.23	0.39	0.26 ± 0.09	0.24
Unordered	0.19	0.12	0.14	0.14	0.14	0.12	0.14 ± 0.02	0.37

Fig. 10 POTRA production, and secondary structural analysis. Panel A shows purified POTRA 1 from subcloning; lane 1 is markers, listed at the left in kDa and 2 is the purified POTRA protein. Panel B is the experimental CD spectra of POTRA graphed with the theoretical CD spectra of two different secondary structure estimation tools (CDSSTR and ContinLL). Panel C represents the deconvolution of CD spectra and provided an estimation of the secondary structure of observed data which compares with the residues of the calculated composition of the average of the four *E. coli YaeT* and the two *B. pertussis* POTRA domains.

N-terminal transit peptide for import. This activity is sufficiently robust to enable the rapid development of chloroplasts in only a few days during the greening process of adolescent plants (Pilon *et al.*, 1992). *In vitro* analysis has demonstrated that the Toc apparatus can import proteins on the order 40,000 molecules per chloroplast per minute (Cline *et al.*, 1993), however despite this remarkable activity, neither the mechanism of preprotein selection nor the process of preprotein translocation is well understood. This chapter describes some of the current methods used in our laboratory to explore the activity and dynamics of the Toc apparatus *in vitro* and *in organeller*.

We describe the isolation and purification of chloroplasts in order to perform highly quantitative binding and import assays which have helped us to accurately determine the K_d and K_i of prSSU and nonprSSU competitors for binding (i.e., mutants of prSSU) as well as the IC_{50} of prSSU for import. Additionally, the solubilization of the Toc translocon from intact chloroplasts was described, after

which BN-PAGE separates the complexes according to native size and 2-D PAGE separates the individual components according to nominal molecular mass. This technique lends itself very well to Western analysis where we can decipher translocon components and estimate stoichiometry. By employing this technique, our laboratory has been afforded the opportunity to perform translocon solubilization under a host of conditions (the addition of prSSU, mSSU, transit peptide, as well as various nucleotide loading states) to understand how the dynamics of this complex are related to substrates and nucleotides. Utilizing a novel $^{32}P_i$ activated charcoal filter assay, we have accurately determined the V_{max} and K_M of Toc proteins under a host of conditions. Next, with the use of a magnetic affinity capture technique, we can determine the K_d and K_i of GTP and other various nucleotides as well as perform GTP/GDP exchange experiments. Finally, through the use of molecular modeling and circular dichroism spectroscopy, we have estimated and confirmed the secondary structure of POTRA domains of the β-barrel protein Toc75. These domains have therefore been implicated as important portions of the protein and are most likely involved in the overall process of protein translocation into the chloroplast. Fig. 11 artistically indicates that through these quantitative techniques, we can visualize the transit peptide bound to the chloroplast surface and show that the inner and outer chloroplast membranes come together to facilitate Toc–Tic interaction and import, which on the most nanoscale represents the transit peptide's interactions with the Toc subunits which ultimately facilitate import.

Future Directions and Opportunities: Future work in chloroplast protein import will benefit from not only the quantitative methods that we describe above but also from other areas of biology that are rapidly developing. For example, as a result of high throughput crystallography efforts, the availability of new and potentially related structures is growing. This resource as well as new computational tools permit homology modeling of Toc subunits with higher confidence, which in turn, allows for the current design of powerful experiments prior to the successful determination of the structure of the Toc translocon. Our ability to estimate the structure of the POTRA domains of psToc75 through *in silico* methodology is one example of such modeling progress.

Another opportunity is linked to the wealth of new genomic resources and genomic tools. Recent progress has been made in predictive algorithms that can predict chloroplast localized proteins based on analysis of their N-terminal sequence. Recently, a new tool, the transit peptide prediction program MultiP (http://sbi.postech.ac.kr/MultiP/), has been developed (Lee *et al.*, 2008) that reports an accuracy of ~94% which is considerably better than ChloroP (77%) which has been the most popular tool used to date (Emanuelsson *et al.*, 1999). In addition, the number of new plant and algal genomes is rapidly expanding. There are five currently available plastid containing genomes as either completed or in draft form with another eight in progress (Rubin, 2008). As these genomes become available, the identification and analysis of the plastid predicted proteome will provide new information on the metabolic role of the chloroplast as well as provide new insight into the structure and diversity of transit peptides.

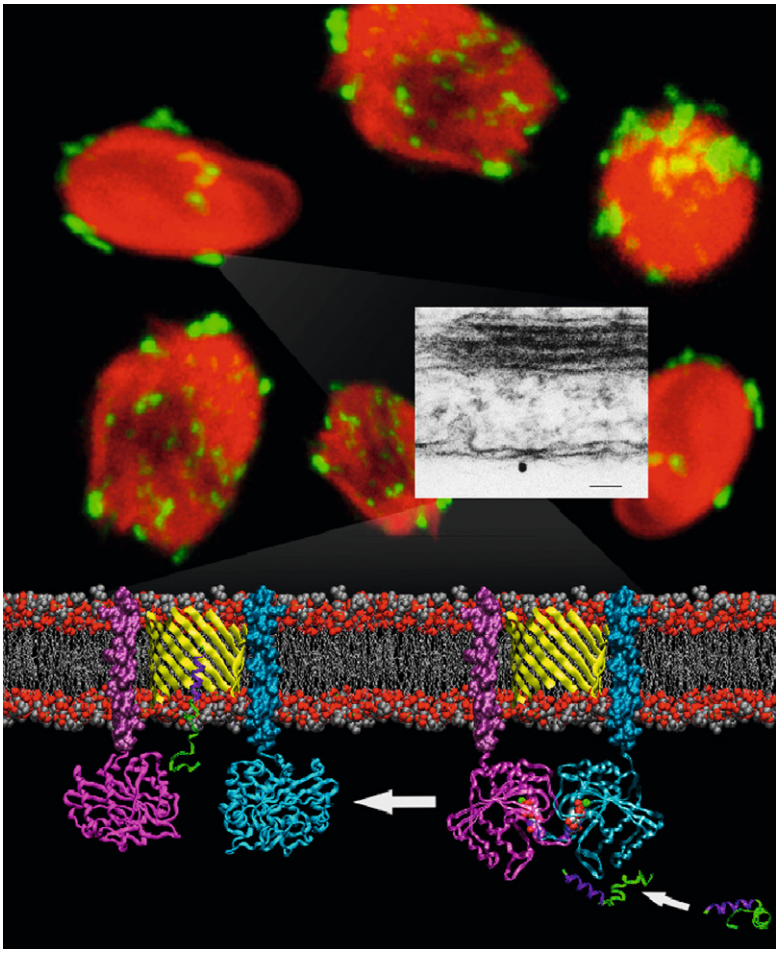

Fig. 11 The big picture. Chloroplasts appearing red in color due to the inflorescence of chlorophyll are immunodecorated with FITC-conjugated antibodies against bound transit peptide. When visualized using electron microscopy (insert), the bound transit peptide is identified using an antibody conjugated to a nano-gold particle (for detection with EM) and implies that translocation across the outer and inner membranes of the chloroplast occur simultaneously. Finally, using molecular modeling, we hypothesize on the molecular dynamics involved with transit peptide recognition by members of the Toc translocon, which lead to protein import.

Acknowledgments

We would like to thank Ian M. Campbell for his assistance with Fig. 1. We are appreciative of the technical expertise of Dr. John Biggerstaff and his undergraduate student Bill McCartt in the analysis of the TIRF data. We also thank Dr. Chitra Subramanian and Mr. Anton V. Mitsky for their assistance with analysis of His-S-SStpNt. Jeffrey D. Whyte at MP Biomedical has continued to provide excellent service and support. We received support from the NSF program in Cell Biology; award numbers MCB0628670 and MCB0344601.

References

Arnon, D. I. (1949). Copper enzymes in isolated chloroplasts. Polyphenoloxidase in beta vulgaris. *Plant Physiol.* **24,** 1–15.

Axelrod, D. (2001). Selective imaging of surface fluorescence with very high aperture microscope objectives. *J. Biomed. Opt.* **6,** 6–13.

Basu, M. K., Rogozin, I. B., Deusch, O., Dagan, T., Martin, W., and Koonin, E. V. (2008). Evolutionary dynamics of introns in plastid-derived genes in plants: Saturation nearly reached but slow intron gain continues. *Mol. Biol. Evol.* **25,** 111–119.

Beckmann, R., Spahn, C. M., Eswar, N., Helmers, J., Penczek, P. A., Sali, A., Frank, J., and Blobel, G. (2001). Architecture of the protein-conducting channel associated with the translating 80S ribosome. *Cell* **107,** 361–372.

Bolter, B., Soll, J., Schulz, A., Hinnah, S., and Wagner, R. (1998). Origin of a chloroplast protein importer. *Proc. Natl. Acad. Sci. USA.* **95,** 15831–15836.

Bos, J. L., Rehmann, H., and Wittinghofer, A. (2007). GEFs and GAPs: Critical elements in the control of small G proteins. *Cell* **129,** 865–877.

Bourne, H. R., Sanders, D. A., and McCormick, F. (1990). The GTPase superfamily: A conserved switch for diverse cell functions. *Nature.* **348,** 125–132.

Bourne, H. R., Sanders, D. A., and McCormick, F. (1991). The GTPase superfamily: Conserved structure and molecular mechanism. *Nature.* **349,** 117–127.

Bruce, B. D. (2000). Chloroplast transit peptides: Structure, function and evolution. *Trends Cell Biol.* **10,** 440–447.

Caliebe, A., Grimm, R., Kaiser, G., Lubeck, J., Soll, J., and Heins, L. (1997). The chloroplastic protein import machinery contains a Rieske-type iron-sulfur cluster and a mononuclear iron-binding protein. *EMBO J.* **16,** 7342–7350.

Cavalier-Smith, T. (2003). Genomic reduction and evolution of novel genetic membranes and protein-targeting machinery in eukaryote-eukaryote chimaeras (meta-algae). *Philos. Trans. R. Soc. Lond. B, Biol. Sci.* **358,** 109–133.

Chen, K. Y., and Li, H. M. (2007). Precursor binding to an 880-kDa Toc complex as an early step during active import of protein into chloroplasts. *Plant J.* **49,** 149–158.

Clantin, B., Delattre, A. S., Rucktooa, P., Saint, N., Méli, A. C., Locht, C., Jacob-Dubuisson, F., and Villeret, V. (2007 Aug 17). Structure of the membrane protein FhaC: a member of the Omp85-TpsB transporter superfamily. *Science* **317,** 957–961.

Cline, K., Henry, R., Li, C., and Yuan, J. (1993). Multiple pathways for protein transport into or across the thylakoid membrane.. *EMBO J.* **12,** 4105–4114.

Dekker, P. J., Muller, H., Rassow, J., and Pfanner, N. (1996). Characterization of the preprotein translocase of the outer mitochondrial membrane by blue native electrophoresis. *Biol. Chem.* **377,** 535–538.

Dekker, P. J., Ryan, M. T., Brix, J., Muller, H., Honlinger, A., and Pfanner, N. (1998). Preprotein translocase of the outer mitochondrial membrane: Molecular dissection and assembly of the general import pore complex. *Mol. Cell Biol.* **18,** 6515–6524.

Emanuelsson, O., Nielsen, H., and von Heijne, G. (1999). ChloroP, a neural network-based method for predicting chloroplast transit peptides and their cleavage sites. *Protein Sci.* **8,** 978–984.

Ertel, F., Mirus, O., Bredemeier, R., Moslavac, S., Becker, T., and Schleiff, E. (2005). The evolutionarily related beta-barrel polypeptide transporters from *Pisum sativum* and Nostoc PCC7120 contain two distinct functional domains. *J. Biol. Chem.* **280,** 28281–28289.

Eswar, N., Eramian, D., Webb, B., Shen, M. Y., and Sali, A. (2008). Protein structure modeling with MODELLER. *Methods Mol. Biol.* **426,** 145–159.

Eubel, H., Braun, H. P., and Millar, A. H. (2005). Blue-native PAGE in plants: A tool in analysis of protein–protein interactions. *Plant Methods.* **1,** 11.

Gentle, I. E., Burri, L., and Lithgow, T. (2005). Molecular architecture and function of the Omp85 family of proteins. *Mol. Microbiol.* **58,** 1216–1225.

Humphries, D., Pollard, M., Elkin, C., Petermann, K., Reiter, C., and Cepeda, M. (2004). New high performance magnet structures for bead based molecular separation. *Lawrence Berkeley Natl. Lab. Rep.* **58894,** 1–12.

Jarvis, P., and Soll, J. (2001). Toc, Tic, and chloroplast protein import. *Biochim. Biophys. Acta.* **1541,** 64–79.

Keegstra, K., and Cline, K. (1999). Protein import and routing systems of chloroplasts. *Plant Cell.* **11,** 557–570.

Kikuchi, S., Hirohashi, T., and Nakai, M. (2006). Characterization of the preprotein translocon at the outer envelope membrane of chloroplasts by blue native PAGE. *Plant Cell Physiol.* **47,** 363–371.

Kim, J. S., and Raines, R. T. (1993). Ribonuclease S-Peptide as a carrier in fusion proteins. *Protein Sci.* **2,** 348–356.

Kleffmann, T., Hirsch-Hoffmann, M., Gruissem, W., and Baginsky, S. (2006). plprot: A comprehensive proteome database for different plastid types. *Plant Cell Physiol.* **47,** 432–436.

Klein, R. R., and Salvucci, M. E. (1992). Photoaffinity labeling of mature and precursor forms of the small subunit of RIBULOSE-1,5-Bisphosphate carboxylase/oxygenase after expression in *Escherichia coli*. *Plant Physiol.* **98,** 546–553.

Kuchler, M., Decker, S., Hormann, F., Soll, J., and Heins, L. (2002). Protein import into chloroplasts involves redox-regulated proteins. *EMBO J.* **21,** 6136–6145.

Lee, D. W., Kim, J. K., Lee, S., Choi, S., Kim, S., and Hwang, I. (2008). Arabidopsis nuclear-encoded plastid transit peptides contain multiple sequence subgroups with distinctive chloroplast-targeting sequence motifs. *Plant Cell.* **20,** 1603–1622.

Meisinger, C., Ryan, M. T., Hill, K., Model, K., Lim, J. H., Sickmann, A., Muller, H., Meyer, H. E., Wagner, R., and Pfanner, N. (2001). Protein import channel of the outer mitochondrial membrane: A highly stable Tom40-Tom22 core structure differentially interacts with preproteins, small tom proteins, and import receptors. *Mol. Cell Biol.* **21,** 2337–2348.

Model, K., Meisinger, C., and Kuhlbrandt, W. (2008). Cryo-Electron microscopy structure of a yeast mitochondrial preprotein translocase. *J. Mol. Biol.* **383,** 1049–1057.

Olsen, L. J., Theg, S. M., Selman, B. R., and Keegstra, K. (1989). ATP is required for the binding of precursor proteins to chloroplasts. *J. Biol. Chem.* **264,** 6724–6729.

Paschen, S. A., Waizenegger, T., Stan, T., Preuss, M., Cyrklaff, M., Hell, K., Rapaport, D., and Neupert, W. (2003). Evolutionary conservation of biogenesis of beta-barrel membrane proteins. *Nature* **426,** 862–866.

Pilon, M., Weisbeek, P. J., and de Kruijff, B. (1992). Kinetic analysis of translocation into isolated chloroplasts of the purified ferredoxin precursor. *FEBS Lett.* **302,** 65–68.

Reddick, L. E., Vaughn, M. D., Wright, S. J., Campbell, I. M., and Bruce, B. D. (2007). *In vitro* comparative kinetic analysis of the chloroplast Toc GTPases. *J. Biol. Chem.* **282,** 11410–11426.

Reumann, S., Davila-Aponte, J., and Keegstra, K. (1999). The evolutionary origin of the protein-translocating channel of chloroplastic envelope membranes: Identification of a cyanobacterial homolog. *Proc. Natl. Acad. Sci. USA* **96,** 784–789.

Rubin, E. M. (2008). Genomics of cellulosic biofuels. *Nature* **454,** 841–845.

Sanchez-Pulido, L., Devos, D., Genevrois, S., Vicente, M., and Valencia, A. (2003). POTRA: A conserved domain in the FtsQ family and a class of beta-barrel outer membrane proteins. *Trends Biochem. Sci.* **28,** 523–526.

Schagger, H., and von Jagow, G. (1991). Blue native electrophoresis for isolation of membrane protein complexes in enzymatically active form. *Anal. Biochem.* **199,** 223–231.

Schagger, H., Cramer, W. A., and von Jagow, G. (1994). Analysis of molecular masses and oligomeric states of protein complexes by blue native electrophoresis and isolation of membrane protein complexes by two-dimensional native electrophoresis. *Anal. Biochem.* **217,** 220–230.

Schleiff, E., Soll, J., Sveshnikova, N., Tien, R., Wright, S., Dabney-Smith, C., Subramanian, C., and Bruce, B. D. (2002). Structural and guanosine triphosphate/diphosphate requirements for transit peptide recognition by the cytosolic domain of the chloroplast outer envelope receptor, Toc34. *Biochemistry* **41,** 1934–1946.

Schleiff, E., Soll, J., Kuchler, M., Kuhlbrandt, W., and Harrer, R. (2003). Characterization of the translocon of the outer envelope of chloroplasts. *J. Cell Biol.* **160,** 541–551.

Subramanian, C., Ivey, R., and Bruce, B. D. (2001). Cytometric analysis of an epitope-tagged transit peptide bound to the chloroplast translocation apparatus. *Plant J.* **25,** 349–363.

Theg, S. M., Bauerle, C., Olsen, L. J., Selman, B. R., and Keegstra, K. (1989). Internal ATP is the only energy requirement for the translocation of precursor proteins across chloroplastic membranes. *J. Biol. Chem.* **264,** 6730–6736.

Toomre, D., and Manstein, D. J. (2001). Lighting up the cell surface with evanescent wave microscopy. *Trends Cell Biol.* **11,** 298–303.

Van den Berg, B., Clemons, W. M., Jr., Collinson, I., Modis, Y., Hartmann, E., Harrison, S. C., and Rapoport, T. A. (2004). X-ray structure of a protein-conducting channel. *Nature* **427,** 36–44.

Vetter, I. R., and Wittinghofer, A. (2001). The guanine nucleotide-binding switch in three dimensions. *Science* **294,** 1299–1304.

CHAPTER 17

A System Biology Approach to Understand Functional Activity of Cell Communication Systems

Julio Vera and Olaf Wolkenhauer

Systems Biology and Bioinformatics Group
Department of Computer Science
University of Rostock
18051 Rostock, Germany

Abstract

Systems Biology is the quantitative analysis of dynamic interactions among several components of a biochemical system, aiming at an understanding of the behavior of the system as a whole. From an experimental perspective, systems biology is a suitable tool to support the biologist in the process of hypotheses generation and the efficient design of experiments. In this chapter, we discuss the elements of a systems biology methodology based on the interaction between experimental biologists and theoreticians. We, furthermore, show the use of such a methodology in a case study, analyzing receptor and transcription factor modulation affecting the responsiveness of the JAK2/STAT5 pathway.

METHODS IN CELL BIOLOGY, VOL. 90

0091-679X/08 $35.00
DOI: 10.1016/S0091-679X(08)00817-0

I. Introduction

In cellular signal transduction, the core of cellular mechanisms involved in cell communication are networks of interacting proteins that detect, modulate, and transfer cellular signals which control gene expression and ultimately, cell function. In recent times, the increase in the complexity of the signaling pathways investigated has made approaches like bioinformatics and proteomics a useful tool, complementary to conventional molecular biology, elucidating the structure and function of pathways. In addition, the development of experimental techniques enabling the generation of time-resolved quantitative data (Albeck *et al.*, 2006) has revealed that in most of the cases, the dynamics of protein interactions play an essential role to understand the function of the signaling systems. In this context, systems biology emerges as a new way of thinking in cell biology in which the dynamics and structure of the biochemical pathways are investigated through quantitative experimental techniques and mathematical modeling.

In a recent report for the Royal Academy of Medical Sciences, Dollery *et al.* (2007) define systems biology as the quantitative analysis of dynamic interactions between components of a biological system, with the aim to understand the behavior of the system as a whole. Another essential feature of this new approach for Dollery *et al.* (2007) is the use of concepts from systems theory to study biological systems through iteration between computational mathematical modeling and experimentation.

From an experimental perspective, systems biology is a suitable tool to support biologists in the generation of hypotheses and the design of experiments (Kitano, 2007; Wolkenhauer, 2007). Firstly, the combination of quantitative experiments and mathematical modeling may decrease the experimental effort necessary to characterize a biological system, saving expensive and time-consuming experiments. In addition, the use of suitable mathematical models allows the investigation of the effect of pathway modifications that are not accessible with current experimental techniques (Ferrell, 2002; Jordan *et al.*, 2000; Kitano, 2004). Finally, there are specific properties of the signaling pathways (e.g., ultrasensitivity, multistability, self-sustained oscillations, etc.) that can be understood only in terms of systems biology (Ferrell, 2002; Kholodenko, 2006; Tyson *et al.*, 2003; Wolkenhauer *et al.*, 2005). In the description given by Tyson *et al.* (2003), it is shown how signaling pathways containing positive and negative feedback loops can generate complex dynamical behavior, including toggle, amplifier, switches, and oscillators. Interestingly, in recent times the notion of a systemic understanding of signaling pathways shifted from a theoretical use to investigate the features of basic, nonrealistic, dynamical motifs (Tyson *et al.*, 2003) to its application in real case studies. The combination of mathematical modeling with state-of-the-art quantitative experimental techniques allowed the discovery of "exotic" nonlinear behavior in signaling pathways, which can exhibit sustained oscillations (NFkB signaling, Nelson *et al.*, 2004), bistability (EGFR activation, Reynolds *et al.*, 2003),

or sigmoidal-like signal amplification (JAK2-STAT5 signaling, Vera *et al.*, 2008) (see Fig. 1 for further discussion on these examples).

From a biomedical point of view, differences at the dynamical level between healthy and pathologic configurations of biological pathways can be investigated through mathematical modeling and the consequences of such differences on the cell development can be assessed (Kitano, 2004). In this way, a systems biology approach can enhance the drug discovery process by helping in the detection of fragilities in cancer-related signaling pathways (Kitano, 2003) or the critical modulators in metabolic and degenerative diseases (Kitano, 2004; Vera *et al.*, 2007b).

In this work, we first discuss how to implement a system biology approach in order to investigate basic features in signaling pathways. We apply this approach to the analysis of signal modulation in the JAK2-STAT5 signaling pathway.

II. Methods

The methodology that we discuss here is to investigate signaling pathways with a limited number of biological inputs and outputs, but involving regulatory structures (e.g., positive and negative feedback loops). These regulatory motifs provoke dynamical complex properties, such as robustness, bistability, and/or oscillations. In our systems biology approach, hypotheses about the signaling pathway are encoded as mathematical equations. Biological data are used to characterize, refine, and assess the quality of the mathematical model in a way the model mimics the basic features of the modeled pathway. Furthermore, the pathway is investigated through computational simulation, but the outcome of such simulations is new biological knowledge than can be validated through experiments. The methodology requires a complete integration between the work performed by mathematical modelers and experimental biologists. Experimentalists must be involved not only in the data generation but also in the modeling process, the validation and the analysis of the model predictions.

The general structure of the approach is illustrated in Fig. 2. Modelers, together with experimentalists, define the list of interesting proteins and basic interactions to be considered in the model as well as the structure of the mathematical model. For this purpose, biological and clinical information provided by specialists, biomedical literature, and suitable databases are used. This information is complemented with quantitative data generated by the experimentalists groups in experiments specially defined to set up and calibrate the mathematical model (Balsa-Canto *et al.*, 2006). Biological databases describing protein–protein interactions (BIND, Bader and Hogue, 2000; HPRD, Peri and Navarro, 2003; GO, Ashburner *et al.*, 2000) but also the text mining of the literature (Hoffmann and Valencia, 2005) can be used to define the set of critical interactions integrating the investigated pathway. Quantitative experimental techniques that can be used in the calibration of the mathematical model for a signaling pathway include quantitative Western blots of time series (Schilling *et al.*, 2005), live cell imaging (Lippincott-

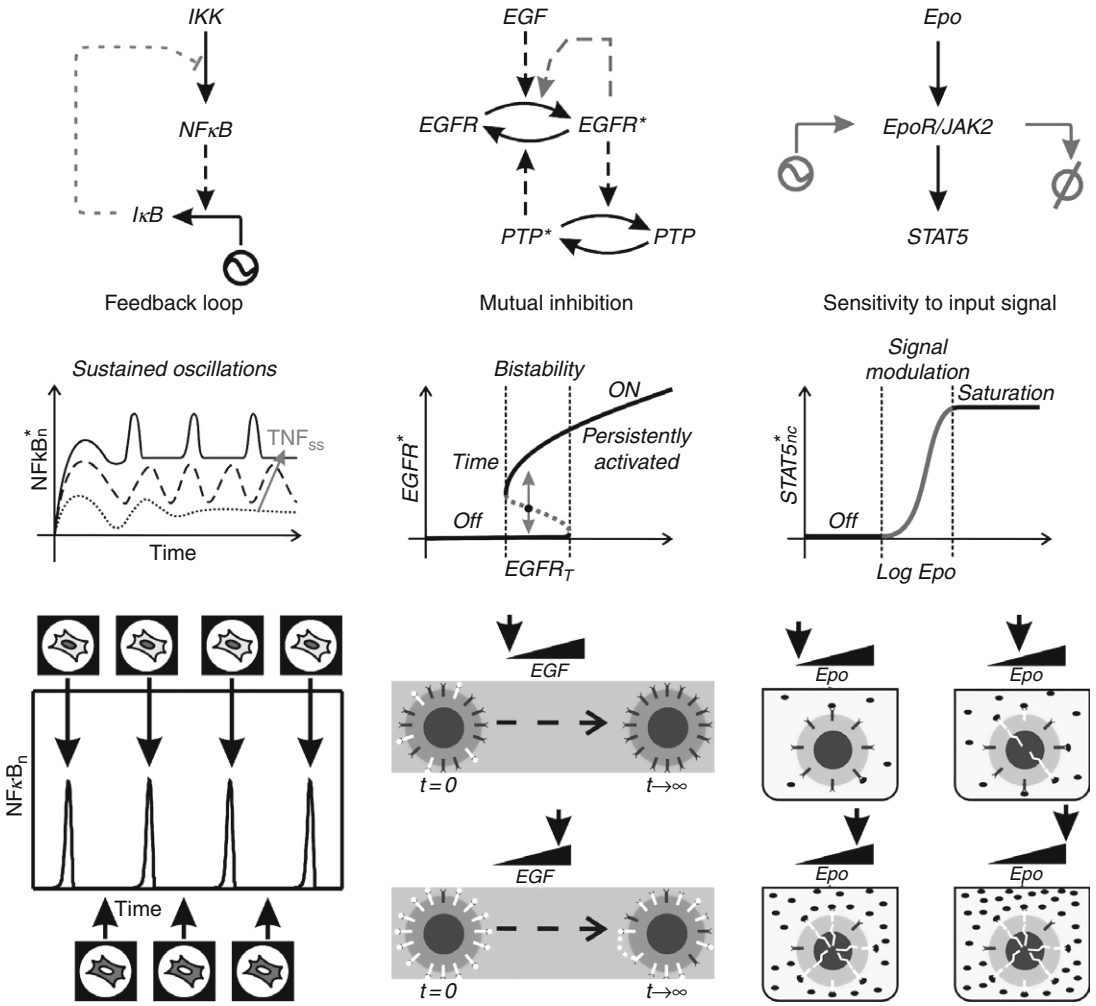

Fig. 1 Signaling pathways exhibiting nonlinear dynamical motifs. (A) The NFκB signaling pathway has been investigated through mathematical modeling in recent times by several groups. There, the feedback loop provoked by the transcriptional induction of IκBα can produce a fast inhibition of NFκB activation when a stimulus (e.g., TNF stimulation) is applied as a short pulse (Hoffmann *et al.*, 2002), but also the appearance of sustained oscillations in the NFκB nucleo-cytoplasmic shuttling, $NF\kappa B_n$, which has been detected using live imaging by Nelson *et al.* (2004). (B) Reynolds *et al.* (2003) used live imaging together with mathematical modeling to investigate the implications of lateral signaling propagation via receptor–receptor interaction in the coupling between the dynamics of the epidermal growth factor receptor, EGFR, and the protein tyrosine phosphatase, PTP. Their results suggest that bistability can emerge from lateral signaling propagation for an interval of values in the total concentration of EGFR, $EGFR_T$. This dynamical feature could explain how significant amounts of phosphorylated receptors can be maintained in regions of the plasma membrane not exposed to ligand, but also the existence of experimental conditions (e.g., intense EGF stimulation) for which persistent receptor activation after stimulation happens and is induced by lateral signal propagation. (C) In Vera *et al.* (2008) quantitative Western blots and mathematical modeling were used to investigate the

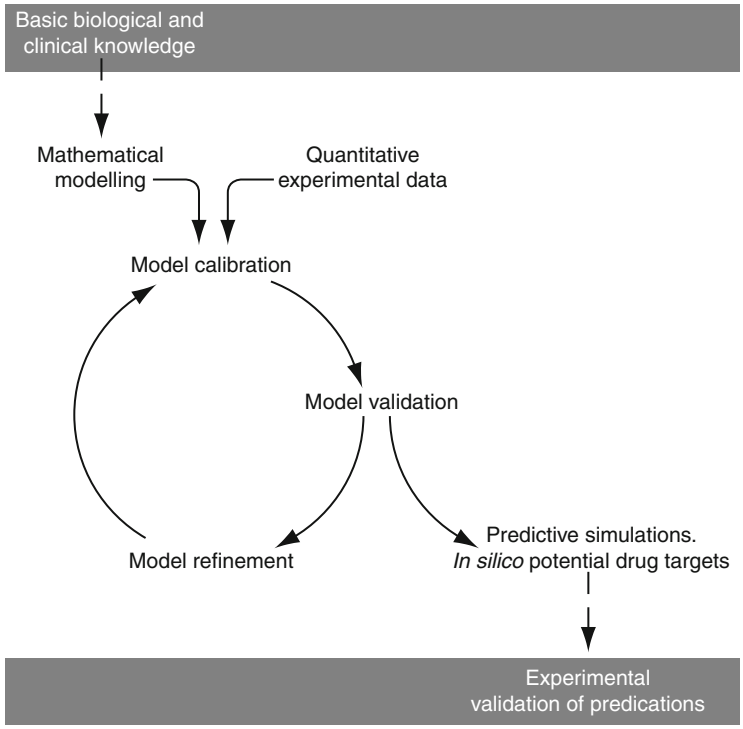

Fig. 2 The systems biology iterative approach. General structure of the iterative procedure proposed to build up a mathematical model and use it for the prediction of basic dynamical features of the studied pathway. The procedure includes: (i) set up of the mathematical model, using existing information; (ii) model calibration, using quantitative experimental data; (iii) model assessment and model refinement; (iv) model validation through experiments; and (v) use of the model to make predictions, which will then be tested with new experiments.

Schwartz *et al.*, 2001), ELISA kits (Heyman, 2006) for proteins and phosphoproteins, and quantitative RT-PCR (Schefe *et al.*, 2006) and northern blots (Roth, 2002) for microRNAs involved in the pathway.

After calibration, the quality of the obtained model is tested using qualitative analysis with simulations and other computational tools (e.g., sensitivity analysis; Saltelli *et al.*, 2004) as well as additional experimental validation. A failure of the model to reproduce the behavior of the systems leads to a refinement of the mathematical representation of the pathway, whereas a sufficiently validated

responsiveness of the JAK2-STAT5 pathway. The features of the activation of the EpoR/JAK2 complex by Epo were analyzed, but also the receptor recruitment and deactivation. The model predicts that the system acts as an amplifier, which is sensitive to the features of the input signal, *Epo*. The system reaches maximum performance for input signals whose intensity match physiological values for Epo concentration, switches off for weaker Epo stimulation signal and gets saturation for very intense stimulation.

model can be used to make predictions based on computer simulations. In this case, predictive simulations and other methodologies are used to detect the key biochemical processes and dynamical features of the signaling pathway. The information generated (critical protein–protein interactions, nonlinear dynamical motifs, etc.) is analyzed together with experimentalists and additional experiments are designed and performed to validate these results. The experimental techniques that can be used to this validation include knockout experiments, downregulation and overexpression experiments and other experimental techniques.

III. Materials

A. Background and Aims for a Model-Based Investigation

The Janus Kinase-Signal Transducer and Activator of Transcription (JAK-STAT) pathways are a complete family of signaling pathways that have been intensively investigated in recent years (Aaronson and Horvath, 2002). Among them, the JAK2-STAT5 pathway can be activated through various receptors, including the erythropoietin receptor (EpoR). Cytokine-activated phosphorylation of EpoR is mediated by the cytosolic kinase JAK2, which is constitutively associated with the cytoplasmic domain of the receptor. When the hormone erythropoietin (Epo) binds the receptor, JAK2 is activated and phosphorylates several tyrosine residues in the receptor (Klingmüller, 1997). Subsequently, the transcription factor STAT5 is recruited to the activated EpoR, becomes phosphorylated, dimerizes, and gets activated. Once activated, STAT5 translocates to the nucleus, where it initiates the transcription of several target genes, some of them involved in erythropoiesis (Jelkmann, 2004). Furthermore, JAK2-STAT5 signaling is crucial for the proper differentiation of red blood cells and the pathway appears often deregulated in several kinds of leukemia and cancer (Kisseleva *et al.*, 2002). Previous work, based on mathematical modeling of this pathway, studied the relevance of the nucleo-cytoplasmic shuttling of STAT5 (Swameye *et al.*, 2003) and the signal responsiveness and amplification (Vera *et al.*, 2008). Here, we use predictive simulations to investigate the effects of receptor and transcription factor downregulation and overexpression on the responsiveness of the pathway.

B. Mathematical Modeling

Several mathematical frameworks are available for the modeling of biochemical processes. When spatial effects of protein distributions and their effectors are negligible and proteins exist in sufficient quantities to discard the role of stochasticity, a well-established mathematical modeling framework to investigate intracellular processes is based on ordinary differential equations (Heinrich *et al.*, 2002). These models describe spatiotemporal changes of protein concentrations and other

biological small proteins (gene products, RNA, metabolites, etc.) with simple kinetic equations. In our investigation, we used a special kind of mathematical models in ordinary differential equations that allow for noninteger kinetic orders (Vera *et al.*, 2007a) with the following structure:

$$\frac{\mathrm{d}}{\mathrm{d}t} X_i = \sum_j c_{ij} \cdot \gamma_j \cdot \prod_{k=1}^{p} X_k^{g_{jk}} i = 1, \ldots, n_d \tag{1}$$

Where X_i represents any of the n_d dependent variables of the model (e.g., proteins or phosphoprotein concentrations, RNA, level of gene expression, etc.). Every biochemical process j is described as a product of a rate constant (γ_j) and the p variables of the system involved in the process to characteristic kinetic orders (g_{jk}). c_{ij} are the so-called stoichiometric coefficients of the system that describe mass conservation in the processes. There are biophysical (Kopelman, 1988; Savageau, 1998) and practical reasons (Vera *et al.*, 2007a) to use power-law representations for modeling signaling pathways. The main difference between power-law and conventional ODEs models used in systems biology is that in the former kinetic orders are parameters, estimated from experimental data. Negative values for the kinetic order represent inhibition, while a zero indicates that the variable does not affect the described process. When positive values are considered several alternatives are possible (g between zero and one represents saturation-like behavior; g higher than one means cooperative process; g equal to one represent a conventional kinetic-like process).

In the present work, we use the mathematical model describing the JAK2-STAT5 pathway derived, calibrated, and tested in Vera *et al.* (2008). In that model, a simplified description of the dynamics of EpoR at the plasma membrane (including receptor recruitment, degradation, and deactivation) and the dynamics of STAT5 (activation, translocation, and deactivation) are described (see Fig. 3 for a graphical representation of the model). An additional simplification of the model is that EpoR and JAK2 were assumed to form a stable complex, EpoR/JAK2, for all biochemical processes included and the variables refer to populations of the receptor at the plasma membrane. The model considers two possible states for the EpoR/JAK2 complex: EpoR/JAK2 not bound to Epo and therefore nonactivated, *EJ*, and activated Epo-bound EpoR/JAK2 complex, *pEpJ*; the biochemical processes included in the model for the receptor complex are receptor activation by Epo, receptor deactivation, recruitment of new EpoR/JAK2 complexes to the plasma membrane, and the degradation of nonactivated EpoR/JAK2. In case of STAT5, the model considered three possible states: nonactivated cytosolic STAT5, *S*; activated cytosolic STAT5, *DpS*; and activated nuclear STAT5, DpS_{nc}; the processes considered in the model for the STAT5 dynamics are the activation (phosphorylation + dimerisation) of STAT5 by the activated receptor complex EpoR/JAK2, the translocation of cytosolic activated STAT5 to the nucleus, and the deactivation and subsequent translocation of nuclear STAT5 back to the cytoplasm. Finally, the concentration of Epo in the extracellular medium, *Epo*, is

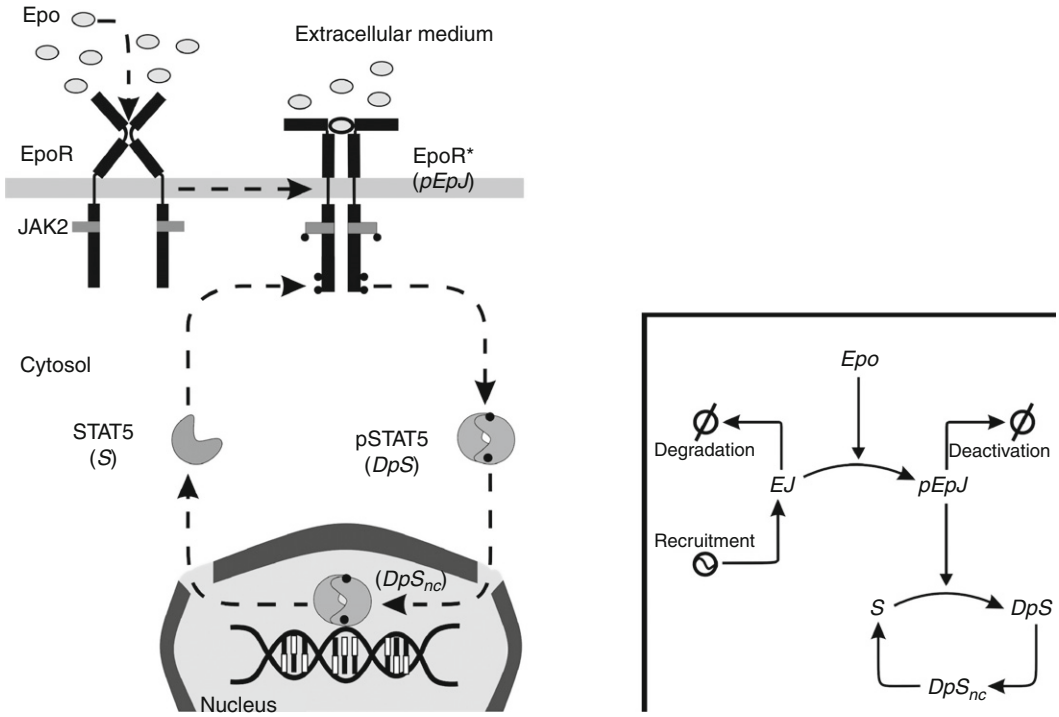

Fig. 3 Structure of the JAK2-STAT5 pathway model. The model is a simplified representation of the pathway where we consider the essential biochemical processes defining the system as well as the processes that are essential for our investigation on the dynamical effects of receptor and transcription factor downregulation and overexpression. In the figure, the left-hand side represents the initial conceptual scheme used in our investigation, which highlights the biochemical processes considered, and the right-hand side is the translation of this into a compact graphical representation of our mathematical model. Legend: *Epo*, concentration of Epo in the extracellular medium; *EJ*, fraction of nonactivated EpoR/JAK2 complex; *pEpJ*, fraction of activated EpoR/JAK2 complex; *S*, fraction of nonactivated and nondimerised STAT5 in the cytosol; *DpS*, fraction of activated and dimerised STAT5 in the cytosol; $DpS_{nc,}$ fraction of activated and dimerized STAT5 inside the nucleus (Vera *et al.* 2008).

considered the input signal of the system. A complete description of the mathematical model, the assumption used in its derivation and calibration, and the mathematical equations can be found in Vera *et al.* (2008).

We notice that the simplification made in the model relates to the technological impossibility to characterize every biochemical process in the pathway, in detail. On the basis of this practical limitation, we set up a mathematical model fulfilling the following criteria: (i) it is a meaningful model and includes the basic processes that characterize the pathway; (ii) it is an aim-oriented model and contains the

description of protein states and protein–protein interactions relevant for our particular investigation, the effects of receptor and transcription factor down-regulation and overexpression; and (iii) the simplifications and additional hypothesis applied are based on the current published knowledge in the pathway and the practical experience of the experimental group who collaborated with us deriving the mathematical model.

C. Quantitative Data Generation and Model Calibration

Once the model is constructed based on prior biological knowledge, it consists on mathematical equations which are characterized by a set of parameters. In some works recently published, the mathematical structure of the model itself, no matter the precise value of the parameters, contains enough information to investigate some properties of the pathway (Barkai and Leibler, 1997). But in general, the numerical values of these parameters are essential to make the model match with the dynamical behavior of the system and specific biological experiments are required to find suitable values for these parameters. This requires the design and performance of a new kind of biological experiments able to catch and measure the basic dynamical features of the investigated system. In cell signaling, these experiments imply the generation of quantitative time-series measuring the amounts of at least some of the proteins and phosphoproteins involved in the pathway (Albeck *et al.*, 2006). The model calibration procedure consist on the finding of the appropriate numerical values for the model parameters that make the mathematical model able to reproduce with numerical simulations the behavior of the system ''registered'' during the quantitative experiments (Balsa-Canto *et al.*, 2006). This process is actually iterative and can involve the refinement of the model structure and model equations to improve the fit between the quantitative experimental data and the numerical predictions of the model.

In our case, specific experiments were designed and performed by our experimental colleagues from the group of Dr. Ursula Klingmüller in the German Cancer Research Institute, in Heidelberg, to characterize the mathematical model for the JAK2-STAT5 pathway (Vera *et al.*, 2008). The essentials of the experimental procedure are depicted in Fig. 4. The cells were starved for hours and then stimulated with Epo (5 units/ml). Afterwards, at every timepoint considered for the measurement, 10^7 cells were extracted from culture and lysed under the assumption that this extract represents the dynamical features of the system (concentrations of proteins and phosphoproteins involved in the pathway) at the considered time. The quantification of the proteins at each timepoint is for mathematical modeling mandatory, and can be performed using different quantitative experimental techniques. In our case, the experimental partners measured the cytoplasmic concentration of activated STAT5, [$pSTAT5_{cyt}$], and the concentration of activated EpoR/JAK2 complex, [pEpoR], using quantitative Western blots, which accuracy was enhanced using normalization, protein calibrators, and other experiment design techniques (Schilling *et al.*, 2005). Additional equations stating

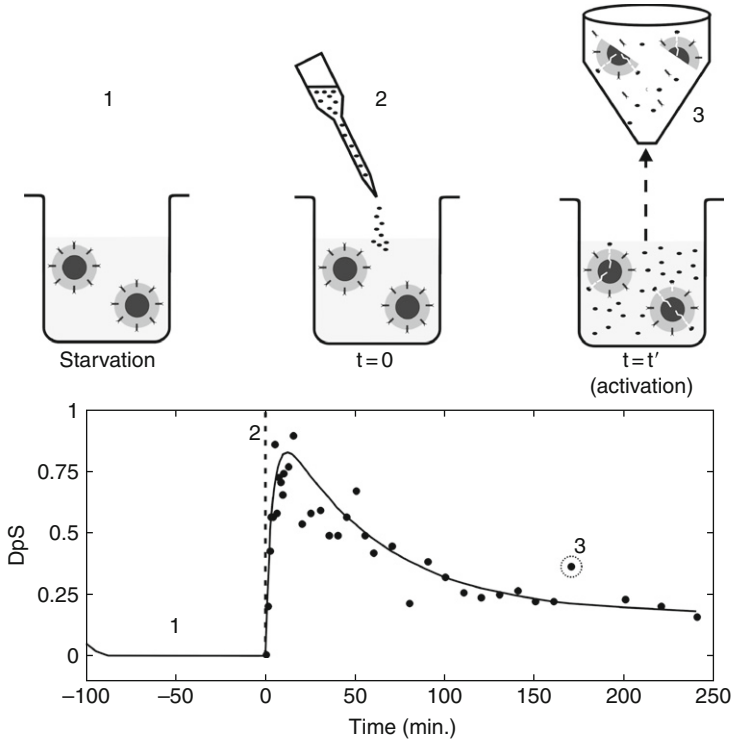

Fig. 4 Sketch of the experimental procedure performed to calibrate the mathematical model for the JAK2-STAT5 pathway. In the procedure, the cells were starved for 5 h (1) and then stimulated with 5 units/ml Epo (2). Afterwards, at every timepoint considered for the measurements (3), a fraction of the culture was extracted and used for measuring. In our case, the cytoplasmic concentration of activated STAT5, the concentration of activated EpoR/JAK2 complex and extracellular Epo were quantified. For measuring the extracellular Epo, an independent experiment was performed with BaF3 cells stably expressing murine EpoR. [^{125}I]-Epo (Amersham Biosciences) was used, cells were centrifuged to separate free [^{125}I]-Epo from cell-associated [^{125}I]-Epo and supernatants were measured in a gamma counter (Packard). For measuring activated Epo receptor and STAT5, the extracted cells were lysed with NP-40 lysis buffer. For immunoprecipitation, lysates were incubated with anti-EpoR antibodies (Santa Cruz) and anti-STAT5 antibodies (Santa Cruz). Immunoblots were incubated with ECL substrate (Amersham Biosciences), exposed on a Lumilmager (Roche Diagnostics) and quantified using LumiAnalyst software (Roche Diagnostics). The accuracy of the quantification was enhanced using normalization, protein calibrators, and other experiment design techniques (Schilling *et al.*, 2005). For a complete description of the experimental procedure, see Vera *et al.* (2008).

the relation between the measured quantities and the variables in the model were defined ([pEpoR] = $pEpJ$; [pSTAT5$_{cyt}$] = 2 × DpS). In an independent but identical experiment, they also measured the time-course of the extracellular Epo, which was used in the model calibration as input signal of the system (Vera *et al.*, 2008).

The experimental data produced were processed, normalized, and finally used for model calibration. This process was performed in an iterative way and several models with an increasing level of structural complexity (i.e., more equations and variables describing the states and processes of the proteins) were tested until the obtaining of a suitable mathematical model, structurally simple but able to fit the quantitative experimental data. Finally, additional tests were applied to the model in order to ensure its quality and validate its predictive abilities.

D. Predictive Simulations and Model Analysis

The systems biology approach is based on the ability of mathematical models, characterized using quantitative experimental data, to predict and analyze the behavior of the pathway under other experimental conditions. Thus, the model can be used to perform numerical simulations of the system that reproduce the behavior (variation on time of the protein and phosphoproteins concentration) that can be expected when the pathway is stimulated with a different input signal, characterized by signal intensity, duration and profile within a certain interval of confidence for the model (Fig. 5). In this way, numerical simulations with a calibrated (good enough) model can be used as "virtual" experiments that mimic the dynamics of the system saving experimental effort. In addition, several analytical methods can be used to infer dynamical features of the system based on the

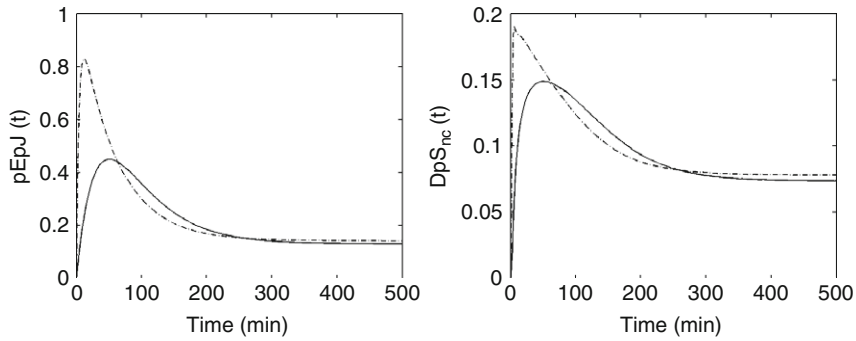

Fig. 5 Predictive simulations of the dynamics of the JAK2-STAT5 pathway using the mathematical model discussed. The behavior of the system was numerically simulated with the mathematical model for two experimental conditions: 5 units/ml sustained Epo stimulation (dashed black line) and 0.5 units/ml sustained Epo stimulation (solid black line). We represent here the variation on time of the fraction of activated EpoR/JAK2 at the plasma membrane (*pEpJ*, left-hand side) and the activated dimeric nuclear STAT5 (DpS_{nc}, right-hand side). Both variables are normalized: for *pEpJ*, a value equal to one represents the initial amount of receptor complex available before stimulation; in case of DpS_{nc}, it a dimeric activated form of STAT5 and therefore, 0.5 represents the total amount available of STAT5. The computer simulation for the variation on time of the other states represented in the model is also possible but was not displayed in this example.

analysis of an accurate well-calibrated mathematical model (Giliberto *et al.*, 2005; Kitano, 2007; Nikolov *et al.*, 2008; Saltelli *et al.*, 2004).

Moreover, mathematical modeling can be used to simulate experimental conditions and pathway modifications that are either not feasible at the state-of-the-art of the experimental techniques or very complex and time-consuming to be implemented. This is the case of the predictive simulations that we performed for our investigation. In the description given by Vera *et al.* (2008), we analyzed the responsiveness and the ability of the system to amplify signals. Towards this end, predictive simulations of the discussed model were used to infer the dynamical properties of the signaling pathway under three different experimental conditions: sustained stimulation, transient stimulation, and oscillatory stimulation with Epo. As a result of the analysis, we stated that the system is not significantly activated when small stimulus is applied, while for intense stimuli the system reaches saturation and becomes virtually insensitive to any increase in the stimulus. Sensitivity to the intensity of Epo stimulation comes only for interval of values on (sustained, transient, or oscillatory) Epo stimulation around the physiological concentration found in natural serum (7.9×10^{-3} units/ml, Noe *et al.*, 1999). In addition, the pathway acts as a strong amplifier within a physiological interval of values for Epo in the three kinds of processes simulated. The model predicted as well that the system is more efficient when weak stimuli are applied. We now want to expand this analysis investigating how the responsiveness of the system is modified when the amount of the available receptor complex EpoR/JAK2 or the transcription factor STAT5 is overexpressed or downregulated. We defined the responsiveness of the systems as the steady-state value for the fraction of activated STAT5 at the nucleus (DpS_{nc}) induced by the sustained stimulation of the system with extracellular Epo. Predictive simulations were run in which the performance of the system was simulated for different values of sustained Epo stimulation when the amounts of EpoR/JAK2 or STAT5 were modulated.

We first investigated the modulation of the EpoR/JAK2 complex (Fig. 6). We simulated the behavior of the system for an interval of EpoR/JAK2 values ranging from intense downregulation (10% of the original amount of receptor complex at the plasma membrane) to an extreme overexpression (25 times the original amount). The interval of sustained stimulation with Epo analyzed was [10^{-7}, 10] in a scale where one represents the stimulation used in the experiments for model calibration (5 units/ml, Vera *et al.*, 2008). For all the levels of EpoR simulated, the pathway shows the characteristic sigmoidal curve discussed in Vera *et al.* (2008), with the system switched off for low Epo stimulation, saturation for intense stimulation and signal modulation in the interval around the physiological value of Epo discussed. This is clearly started in Fig. 6 (centre top) where we show the results for the original level of expression for EpoR. The effect of an increase in the available amount of EpoR at the plasma membrane is to increase the level of sustained stimulation from a reduced signal response for low levels of EpoR expression to a saturated-like signal response for strong overexpression (Fig. 6, centre bottom). Thus, the single overexpression of EpoR can increase significantly

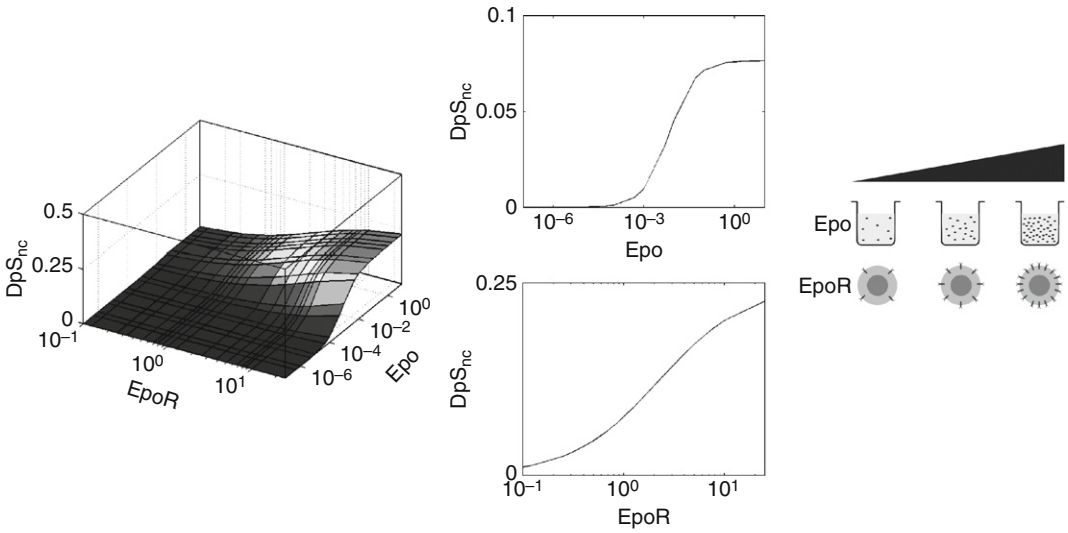

Fig. 6 Numerical simulation of the responsiveness of the JAK2-STAT5 pathway when modulation is applied to the amount of receptor complex EpoR/JAK2. The left-hand side figure represents the responsiveness of the system when we simulated changes in the receptor complex expression and the Epo sustained stimulation at the same. In the centre, we represent the behavior of the system when only the stimulus is modified (top) or when only the receptor complex concentration is modified (bottom). The right-hand side figure is a diagrammatic representation of what modulation of Epo concentration and EpoR/JAK2 expression means in our numerical simulations.

the responsiveness of the system, but after a certain level of EpoR overexpression no further increase in the signal response is obtained.

In addition, we also investigated the modulation of the STAT5 expression (Fig. 7). We simulated the behavior of the system for an interval of total STAT5 values ranging from intense downregulation (10% of the original amount) to an extreme overexpression (25 times the original amount). The interval of sustained stimulation with Epo analyzed was the same used in Fig. 6 [10^{-7}, 10]. In accordance with the previous figure, for all the levels of total STAT5 simulated the pathway shows the same characteristic sigmoidal curve for the modulation of the Epo stimulation that we found in Vera *et al.* (2008) (Fig. 7, centre top). In contrast, the effect of an increase in the available amount of STAT5 is to monotonously increase the signal response for sustained Epo stimulation, showing no activation for STAT5 downregulation and intense signal response for STAT5 overexpression (Fig. 7, centre bottom). In addition, the system seems to show the ability to multiply its signal response for intense STAT5 overexpression. From our predictive simulations, the modulation of STAT5 rather than the receptor complex modulation seems to be a much more efficient mechanism to regulate the responsiveness of the system.

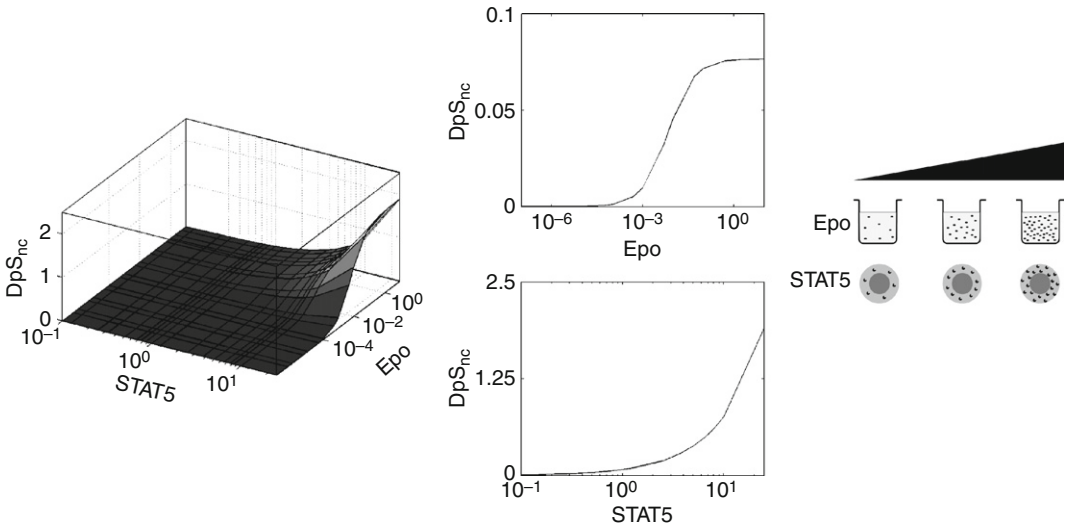

Fig. 7 Numerical simulation of the responsiveness of the JAK2-STAT5 pathway when modulation is applied to the amount of total STAT5. The left-hand side figure represents the responsiveness of the system when we simulated changes in STAT5 expression and the Epo sustained stimulation at the same. In the centre, we represent the behavior of the system when only the stimulus is modified (top) or when only the transcription factor concentration is modified (bottom). The right-hand side figure is a diagrammatic representation of what modulation of Epo concentration and STAT5 expression means in our numerical simulations.

IV. Discussion

In this chapter, we have presented and discussed the features of a systems biology approach, based on the use of quantitative experimental data and mathematical models, to analyze and investigate the dynamical features of cell signaling pathways. We applied this methodology to the investigation of receptor complex and transcription factor modulation in the JAK2/STAT5 pathway. The results of our analysis provide guidance to design and perform new more effective experiments, but also allowed the construction of hypothesis with biomedical relevance about the dynamics of the pathways in cancer-subverted cell lines.

Our numerical predictions indicate that the production of cell lines with modulated STAT5 expression is a much more efficient mechanism to induce intense changes in the system response. In addition, medium levels of EpoR/JAK2 complex (similar to the ones used in Vera *et al.*, 2008) must be maintained in order to get measurable signal. Finally, experiments will require in any case strong stimulation, in the range of Epo concentrations used in the experiments performed for Vera *et al.* (2008) to get intense enough signal response. From a biomedical perspective, our simulations could suggest that the STAT5 overexpression rather than receptor overexpression could be a more effective mechanism to subvert the normal functioning of the pathway in cancerous cells and leukemia.

The systems biology approach requires a close interaction between experimentalists and theoreticians/modelers. This interaction ensures that the mathematical models encode properly the biology of the pathways investigated, but from a more practical perspective helps saving experimental effort (time and money) by focusing the investigation in the relevant features of the system. In addition, systems biology can be a road map to guide experimental efforts full of nonlinear, nonintuitive, nonexpected behavior. On the other hand, an important weakness of the systems biology approach is that it requires an effort from the side of both theoreticians and experimentalists to understand each other. A new common language must be created to guide this interdisciplinary interaction, and this is a long-time task for the groups interested in the field. In future, new educational programs will emphasize this interdisciplinary perspective of the molecular biology, creating experimental biologists willing to participate in the construction and analysis of mathematical models and theoreticians able to discuss the design of biological experiments.

Acknowledgments

This work was supported by the European Commission 6th Framework program as part of the COSBICS project under contract LSHG-CT-2004-512060 (*www.sbi.uni-rostock.de/cosbics*). The contribution of Julio Vera was also supported by the German Federal Ministry of Education and Research (BMBF) as part of the project CALSYS-FORSYS under contract 0315264 (www.sbi.uni-rostock.de/calsys).

References

Aaronson, D. S., and Horvath, C. M. (2002). A road map for those who don't know JAK-STAT. *Science* **296**(5573), 1653–1655.

Albeck, J. G., MacBeath, G., White, F. M., Sorger, P. K., Lauffenburger, D. A., and Gaudet, S. (2006). Collecting and organizing systematic sets of protein data. *Nat. Rev. Mol. Cell Biol.* **7**(11), 803–812.

Ashburner, M., Ball, C., Blake, J., Botstein, D., Butler, H., Cherry, J., Davis, A., Dolinski, K., Dwight, S., Eppig, J., Harris, M., Hill, D., *et al.* (2000). Gene ontology: Tool for the unification of biology. The gene ontology consortium. *Nat. Genet.* **25,** 25–29.

Bader, G., and Hogue, C. (2000). BIND—A data specification for storing and describing biomolecular interactions, molecular complexes and pathways. *Bioinformatics* **16,** 465–477.

Balsa-Canto, E., Rodríguez-Fernández, M., Alonso, A. A., and Banga, J. R. (2006). Computational design of optimal dynamic experiments in systems biology: A case study in cell signalling. *In* ''Understanding and Exploiting Systems Biology in Bioprocesses and Biomedicine'' (M. Cánovas, J. L. Iborra, and A. Manjón, eds.). Fundación Cajamurcia, Murcia, Spain.

Barkai, N., and Leibler, S. (1997). Robustness in simple biochemical networks. *Nature* **387**(6636), 913–917.

Dollery, C., Kitney, R., Challis, R., Delpy, D., Edwards, D., Henney, A., Kirkwood, T., Noble, D., Rowland, M., Tarassenko, L., Williams, D., Smith, L., *et al.* (2007). Systems biology: A vision for engineering and medicine. *In* ''Report of the Royal Academy of Engineering and Academy of Medical Sciences'' London (ISBN No. 1-904401-13-5).

Ferrell, J. E., Jr. (2002). Self-perpetuating states in signal transduction: Positive feedback, double-negative feedback and bistability. *Curr. Opin. Cell. Biol.* **14,** 140–148.

Giliberto, A., Novak, B., and Tyson, J. (2005). Steady states and oscillations in the p53/Mdm2 network. *Cell Cycle* **4,** 488–493.

Heinrich, R., Neel, B. G., and Rapoport, T. A. (2002). Mathematical models of protein kinase signal transduction. *Mol. Cell* **9**(5), 957–970.

Heyman, J. (2006). Nature Methods Application Notes. DOI: 10.1038/an1562.

Hoffmann, A., Levchenko, A., Scott, M., and Baltimore, D. (2002). The I*k*B-NF-*k*B signalling module: Temporal control and selective gene activation. *Science* **298,** 1241–1245.

Hoffmann, R., and Valencia, A. (2005). Implementing the iHOP concept for navigation of biomedical literature. *Bioinformatics* **21**(Suppl. 2), ii252–ii258.

Jelkmann, W. (2004). Molecular biology of erythropoietin. *Intern. Med.* **43**(8), 649–659.

Jordan, J. D., Landau, E. M., and Iyengar, R. (2000). Signaling networks: The origins of cellular multitasking. *Cell* **103**(2), 193–200.

Kholodenko, B. N. (2006). Cell-signalling dynamics in time and space. *Nat. Rev. Mol. Cell. Biol.* **7**(3), 165–176.

Kisseleva, T., Bhattacharya, S., Braunstein, J., and Schindler, C. W. (2002). Signaling through the JAK/STAT pathway, recent advances and future challenges. *Gene* **285,** 1–24.

Kitano, H. (2003). Cancer robustness: Tumour tactics. *Nature* **426,** 125.

Kitano, H. (2004). Biological robustness. *Nat. Rev. Genet.* **5,** 826–837.

Kitano, H. (2007). Towards a theory of biological robustness. *Mol. Syst. Biol.* **3,** 137.

Klingmüller, U. (1997). The role of tyrosine phosphorylation in proliferation and maturation of erythroid progenitor cells—signals emanating from the erythropoietin receptor. *Eur. J. Biochem.* **249**(3), 637–647.

Kopelman, R. (1988). Fractal reaction kinetics. *Science* **241,** 1620–1626.

Lippincott-Schwartz, J., Snapp, E., and Kenworthy, A. (2001). Studying protein dynamics in living cells. *Nat. Rev. Mol. Cell Biol.* **2,** 444–456.

Nelson, D., Ihekwaba, A., Elliott, M., Johnson, J., Gibney, C., *et al.* (2004). Oscillations in NF-*k*B signalling control the dynamics of gene expression. *Science* **306,** 704–708.

Nikolov, S., Vera, J., Kotev, V., Wolkenhauer, O., and Petrov, V. (2008). Dynamic properties of a delayed protein cross talk model. *Biosystems* **91,** 51–68.

Noe, G., Riedel, W., Kubanek, B., and Rich, I. N. (1999). An ELISA specific for murine erythropoietin. *Brit. J. Haematol.* **104,** 838–840.

Peri, S., Navarro, J. D., *et al.* (2003). Development of human protein reference database as an initial platform for approaching systems biology in humans. *Genome Res.* **13,** 2363–2371.

Reynolds, A. R., Tischer, C., Verveer, P. J., Rocks, O., and Bastiaens, P. I. (2003). EGFR activation coupled to inhibition of tyrosine phosphatases causes lateral signal propagation. *Cell Biol.* **5,** 447–453.

Roth, C. M. (2002). Quantifying gene expression. *Curr. Issues Mol. Biol.* **4**(3), 93–100.

Saltelli, A., Tarantola, S., Campolongo, F., and Ratto, M. (2004). ''Sensitivity Analysis in Practice: A Guide to Assessing Scientific Models.'' Wiley, New York.

Savageau, M. A. (1998). Development of fractal kinetic theory for enzyme-catalysed reactions and implications for the design of biochemical pathways. *Biosystems* **47**(1–2), 9–36.

Schefe, J. H., Lehmann, K. E., Buschmann, I. R., Unger, T., and Funke-Kaiser, H. (2006). Quantitative real-time RT-PCR data analysis: Current concepts and the novel ''gene expression's CT difference'' formula. *J. Mol. Med.* **84**(11), 901–910.

Schilling, M., Maiwald, T., Bohl, S., Kollmann, M., Kreutz, C., Timmer, J., and Klingmüller, U. (2005). Computational processing and error reduction strategies for standardized quantitative data in biological networks. *FEBS J.* **272,** 6400–6411.

Swameye, I., Mueller, T. G., Timmer, J., Sandra, O., and Klingmüller, U. (2003). Identification of nucleocytoplasmic cycling as a remote sensor in cellular signaling by data-based modeling. *Proc. Natl. Acad. Sci.* **100,** 1028–1033.

Tyson, J. J., Chen, K. C., and Novak, B. (2003). Sniffers, buzzers, toggles and blinkers: Dynamics of regulatory and signaling pathways in the cell. *Curr. Opin. Cell Biol.* **15,** 221–231.

Vera, J., Bachmann, J., Pfeifer, A. C., Becker, V., Hormiga, J., Torres Darias, N. V., Timmer, J., Klingmuller, U., and Wolkenhauer, O. (2008). A systems biology approach to analyse amplification in the JAK2-STAT5 signalling pathway. *BMC Syst. Biol.* **2,** 38.

Vera, J., Balsa-Canto, E., Wellstead, P., Banga, J. R., and Wolkenhauer, O. (2007a). Power-law models of signal transduction pathways. *Cell. Signal.* **19,** 1531–1541.

Vera, J., Curto, R., Cascante, M., and Torres, N. V. (2007b). Detection of potential enzyme targets by metabolic modelling and optimization. Application to a simple enzymopathy. *Bioinformatics* **23**(17), 2281–2289.

Wolkenhauer, O. (2007). Defining systems biology: An engineering perspective. *IET Syst. Biol.* **1**(4), 1–4.

Wolkenhauer, O., Ullah, M., Wellstead, P., and Cho, K. (2005). The dynamic systems approach to control and regulation of intracellular networks. *FEBS Lett.* **579,** 1846–1853.

CHAPTER 18

THz Investigations of Condensed Phase Biomolecular Systems

Hailiang Zhang,[⋆] Karen Siegrist,[†] Kevin O. Douglas,[‡] Susan K. Gregurick,[⋆] and David F. Plusquellic[‡]

[⋆]Department of Chemistry and Biochemistry
University of Maryland
Baltimore County
Baltimore, Maryland 21250.

[†]Electro-optical and Infrared Systems and Technologies Group
Johns Hopkins Applied Physics Laboratory
Laurel, Maryland 20723

[‡]Biophysics Group
Physics Lab, National Institute of Standards and Technology
Gaithersburg, Maryland 20899-8443

Abstract

Terahertz (THz) spectroscopic investigations of crystalline dipeptide nanotubes are discussed in the frequency region from 0.6 (2 cm^{-1}) to 3 THz (100 cm^{-1}). The THz region provides access to collective modes of biomolecular systems and is therefore sensitive to the large scale motions important for understanding the impact of environmental stimuli in biomolecular systems. The focus of this chapter is on THz spectral changes observed in this region when crystals of alanyl isoleucine (AI) and isoleucyl alanine (IA) nanotubes are exposed to water. Of biological

METHODS IN CELL BIOLOGY, VOL. 90

0091-679X/08 $35.00
DOI: 10.1016/S0091-679X(08)00818-2

significance is the water permeability through hydrophobic pore regions as exemplified in the disparate behavior of these two dipeptide nanotubes. AI is known from X-ray studies and confirmed here to act reversibly to the exchange of water while IA does not accept water into its pore region. Both quantum chemical and classical calculations are performed to better understand the subtle balance that determines guest molecule absorption and conduction through these hydrophobic channels. Examination of the vibrational character of the THz modes with and without water suggests water mode coupling/decoupling with collective modes of the nanotube may play an important role in the permeability dynamics.

I. Introduction

Water is ubiquitous in biological systems. Biomolecular interactions with water are vital to facilitating conformational changes, and to cellular transport through membrane pores, processes which rely on the concerted motions, and interactions of many atoms or molecules. Water transport through membranes has itself been a topic of much interest, since the first structural determination of a membrane channel, the water-selective aquaporin AQP1 (Preston *et al.*, 1992). Further investigation of membrane transport processes has proceeded at a rapid rate. Such processes are highly sensitive to the delicate balance in chemical potentials between hydrophilic (hydrogen bonding) and hydrophobic interactions with water. Terahertz (THz) vibrational modes, involving the same types of nonlocal and collective motions relevant to such processes, are similarly sensitive to hydrogen bonding and hydrophobic interactions with water. Here, we demonstrate the THz spectral sensitivity of small biomolecules to the presence or absence of water, and in particular, to the interactions of water with pore-forming crystalline dipeptides having vastly different water permeability.

THz spectroscopy is a natural tool for probing the mechanisms important to biological function. The characteristic modes found in this low energy spectral region correspond to collective motions of many atoms or molecules that extend over the nanometer length scale. In contrast to the localized motions of two or three atoms probed in the higher frequency infrared region (typically carbonyl and amide stretching or bending modes), THz modes are exemplified by the tail-wagging and backbone-bending motions intrinsic to the conformational changes and the collective motions of many biological processes. Recent work in this rapidly growing field has proven its potential for unraveling picosecond dynamics of biomolecular interactions (Ebbinghaus *et al.*, 2007, 2008; Heugen *et al.*, 2006; Heyden *et al.*, 2008), identifying conformations (Whitmire *et al*, 2003) and imaging biological processes (Masson *et al.*, 2006). In much of this recent work, the high sensitivity of the THz response to the interactions of biological molecules with water has been demonstrated. For example, probing the picosecond dynamics occurring at THz frequencies has revealed a dynamical hydration shell that extends out to 5 Å from the surface of lactose (Heugen *et al.*, 2006), even further for trehalose (Heyden *et al.*, 2008), and as far as 10 Å from protein surfaces

(Ebbinghaus *et al.*, 2007). These dynamics are unveiled by variations in the THz dielectric response to additional solvation layers, thus demonstrating the qualitative difference in bulk water versus biological water at THz frequencies, as well as the surprisingly long range effects of biomolecules on surrounding water. This verification of the differential dielectric response of hydration shells versus bulk water supports previous predictions from molecular dynamics (MD) simulations of water confined in pores (Sansom *et al.*, 1997). These investigations give credibility to the usefulness of THz spectroscopy for investigating interactions of biomolecules with water.

In much of the recent work directed at developing a theoretical understanding of THz vibrational modes of biomolecules, crystalline solids have been investigated. The highly degenerate vibrational modes of small crystalline systems can often give rise to sparse and well-resolved spectral features providing benchmark data ideally suited for development and validation of theoretical models. To this end, much progress has been demonstrated in reproducing the experimentally observed THz vibrational spectra for biomolecular crystalline systems (Allis *et al.*, 2007; Jepsen and Clark, 2007; Siegrist *et al.*, 2006).

In initial work, the alanine tripeptide gives striking evidence of the impact of hydrogen-bonded water on the THz spectra of the crystalline solids (Siegrist *et al.*, 2006). In the present work, our focus is on the effect of hydration on the THz spectra of two hydrophobic dipeptide nanotubes, L-alanyl-L-isoleucine (AI) and L-isoleucyl-L-alanine (IA). These two pore-forming peptides belong to a seven-member family of dipeptide nanotubes which share the same hexagonally symmetric crystal structure, but have different pore diameters and different solvation characteristics. Of this pair, AI is known to absorb water molecules, whereas IA does not take up water (Gorbitz, 2003). Structural modeling at the quantum chemical (density functional theory) and empirical force field levels are used to gain understanding of the mechanisms impacting the permeability of the dipeptide pores to water.

For pores of small diameter, MD simulations have shown that water molecules can permeate small hydrophobic pores by forming highly correlated single chains threading down the nanotube (Allen *et al.*, 1999). MD simulations have indicated that permeability of membrane pores to water (or other ions) depends upon a critical pore radius, but a number of factors other than geometry can influence the critical radius for permeability, so that a pore may not be physically occluded yet nonetheless impermeable to certain solvents (Beckstein and Sansom, 2004). In particular, perturbations in pore wall polarity can induce large changes in critical pore radius and thus impact transport (Beckstein and Sansom, 2004; Hummer *et al.*, 2001). In MD simulations of the aquaporin channel AQP1, De Groot and Grubmuller (2001) attribute high rates of water transmission through the hydrophobic pore to collective motions of the intrapore water. Similarly, Hummer and coworkers (2001) report pulse-like transmission of water through hydrophobic carbon nanotubes, while the work of Pomes and Roux (1998) implies that collective motions are needed to sustain proton conduction along intrapore water chains. We suggest that THz vibrational mode couplings of the pore wall to the intrapore

water can drive the collective motions that may be necessary for water (or proton) transmission through nanoscale pores. The results of structural modeling of these simple dipeptide nanotubes further suggest that the character of the low frequency THz modes can bear on the ability of pores to admit or exclude solvent molecules, via the picosecond timescale dipole coupling which can impact the critical radius for permeability, as well as affect the physical diameter of the pore.

The simplified pore model described by Lynden-Bell and Rasaiah (1996) can provide an intuitive basis for relating the collective nature of THz modes to the process of water transport. This extremely simple model treats the pore as an infinite cylinder with a very steep wall potential. Within the radially symmetric charge distribution we imagine giving rise to this potential, no electrostatic radial field can exist, although variations along the pore axis can give rise to electrostatic axial fields. Perturbations of such a system, however, clearly can give rise to periodic fields which can be visualized as similar to the allowed modes of a cylindrical waveguide. Such fields involve periodic axial and radial constriction forces, as well as torsional forces which can periodically twist or kink the tube, and can be expected to couple to the current provided by a central water chain, possibly driving transmission. Our structural modeling in fact shows the existence of pore "breathing" modes, for these model nanotubes (Zhang *et al.*, 2008). In these THz frequency "breathing" modes, the pore alternately constricts and relaxes, its inner diameter visibly changing throughout the vibration. This result is suggestive that the character of low frequency nonlocal THz modes of nanopores can impact pore permeability. We will discuss the impact of water–biomolecule interactions on THz spectra of small peptides, using structural modeling to understand the nature and functional impact of THz modes.

II. Instrumentation

The continuous wave THz spectrometer used in these studies has been described in detail elsewhere (Korter and Plusquellic, 2004; Pine *et al.*, 1996; Plusquellic *et al.*, 2003). Briefly, the system shown in Fig. 1 consists of a GaAs photomixer (McIntosh *et al.*, 1995; Verghese *et al.*, 2001) as the source of THz radiation, a liquid He-cooled (LHe) sample assembly and a LHe bolometer detector. The photomixer is driven at the difference frequency of two infrared lasers. Output from a fixed frequency laser at 840 nm is combined with that from a grating-tuned standing wave cavity Ti:Sapphire laser having a resolution of $\approx$0.04 cm^{-1} (1.2 GHz). The two collinear beams are focused onto the photomixer to produce the THz radiation at the difference frequency. Tuning of the Ti:Sapphire laser is achieved over the range (0–3) THz (0–100 cm^{-1}) by stepper-controlled grating. A maximum power estimated at 5 μW is obtained near 0.6 THz (20 cm^{-1}). The THz source, sample, and detector are enclosed in a vacuum chamber to permit LHe sample temperatures ($\approx$4 K) to be reached and to avoid absorption by atmospheric water–vapor. The THz beam is collimated by a silicon lens and then

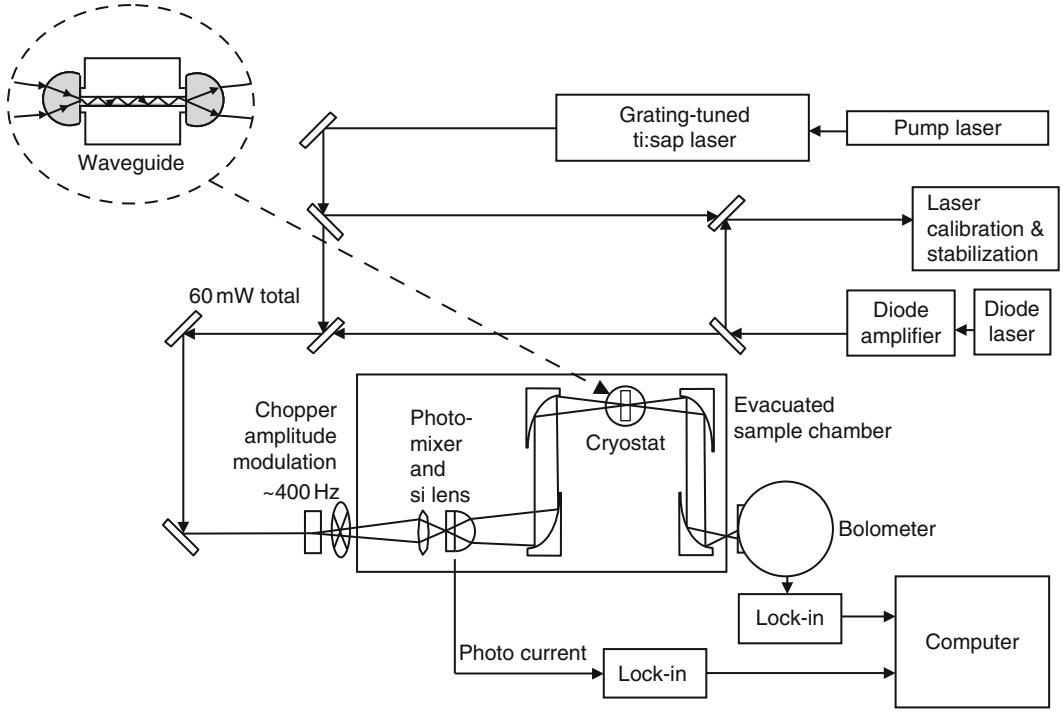

Fig. 1 Schematic of the continuous wave THz spectrometer. The sample is placed in a holder on the cold finger of the cryostat. For thin film samples, the parallel plate waveguide assembly shown in the inset replaces the standard sample holder.

focused by off-axis parabolic mirrors onto the sample fixed to the cold finger of a cryostat and then onto a LHe silicon composite bolometer having a power detection sensitivity of <1 nW up to 3 THz in a 400 Hz bandpass (Noise Equivalent Power of the bolometer is 1 pW/Hz$^{1/2}$). The photocurrent of the photomixer is simultaneously recorded with absorption to correct changes in laser powers at the photomixer.

For scans performed on bulk sample pellets, the crystalline peptides obtained directly from Bachem (see disclaimer) at >99% purity were diluted with fine grain polyethylene (PE) powder (average particle diameter 4 μm), and 100 mg of a 10%–15% concentration mixture were pressed at 2×10^7 Pa (3000 psi) to form a disk ~750 μm thick and 13 mm in diameter. This disk was placed in a brass holder attached to the cryostat coldfinger. A pure PE pellet sample was also prepared to obtain the power transmission spectra for rationing purposes.

THz experiments using a plane-parallel waveguide (Melinger *et al.*, 2006, 2007; Mendis and Grischkowsky, 2001) required a modification of the sample system. The inset of Fig. 1 shows the plane-parallel waveguide assembly, fabricated of copper for high thermal conductivity and coated with gold to minimize surface reactivity. The waveguide path length of 2.5 cm was chosen to enable the assembly

to be mounted inside of the cryostat heat shield. Hyper-hemicylindrical silicon lenses couple the THz radiation into and out of the waveguide. The lenses have a diameter of 12 mm and a shoulder offset to place the focal point at the flat silicon surface. A small ($\approx$50 μm) gap exists between the lens and the waveguide. A thin film of the crystalline dipeptide was prepared on the upper removable plate of the waveguide. Acetone was added to a nearly saturated aqueous solution of dipeptide to aid the wetting of the gold surface (which is prone to induce hydrophobic beading of the solution). A few hundred microliters of solution were drop cast on the gold surface and evaporated at 75–80 °C. A uniform crystalline film, composed of a patchwork of oriented crystallites, provided visual confirmation of the successful deposition of sample. The quantity of sample was determined to give optimal signals between 10% and 90% fractional absorption. Based on this quantity, the dipeptide films are estimated to be 1–2 μm thick.

The waveguide assembly was fixed to the cold finger of the cryostat and inserted into the beam path at nearly the same position occupied by the sample holder in prior experiments. For our incompletely optimized system, only minor adjustments were made to the THz beam collimation to improve coupling into the waveguide. A waveguide plate separation of 250 μm was maintained using Teflon spacers at the edges of the 3.75 cm (1.5 in.) wide assembly and this rather large gap gave sufficient sensitivity for the $\sim$1 mg of dipeptide film. Fine adjustment of these short focal length lenses is necessary to achieve good parallel alignment with the gap at the correct vertical position. The assembly allows adjustment via set screws. A place-holding bracket was then locked in place to fix the correct lens position, which allowed disassembly and reassembly of the waveguide without losing lens alignment. An additional positioning system was used to improve the stability and repeatability of the cryostat position in the beam path.

During acquisition of spectra, the helium-cooled sample assembly was held at 4.2 K in vacuum for the PE-diluted disk-shaped samples in the smaller brass assembly. The larger gold-coated copper waveguide assembly was held at 4.6 K, the minimum temperature which could be achieved due to the necessary removal of one radiation shield. It is possible that the temperature of the sample is higher than the readout indicates, since the thermistor is placed at the base of the cold finger, and not at the sample location. However, since the temperature is not observed to rise immediately after cessation of helium flow, it is assumed to be within 1 K of the nominal 4.6 K indicated on the control box.

III. Theory

An overview of the computational methods used to model some of the THz spectra presented here has been given elsewhere (Plusquellic *et al.*, 2007). Quantum chemical calculations were performed using density functional theory (DFT) as implemented in the software suite, DMol^3 (Delley, 1990, 2000). Periodic boundary conditions were enforced for all crystalline systems. The PW91 exchange

correlation functional based on the generalized gradient approximation (GGA) in the parameterization of Perdew and Wang (1992) was chosen for these studies. A double numerical plus polarization atomic orbital basis set (equivalent to double-ζ) was used and all electrons were included in the calculations. The minimum-energy geometry was optimized with a convergence criteria of 1×10^{-6} hartrees (Ha) for energy, 2×10^{-4} Ha/Å for the maximum gradient, and 5×10^{-4} Å for maximum displacement, and with the atomic orbital cutoff for integration set at the default value, $R_c = 3.7$ Å. All the DMol^3 calculations were performed on unit cell dimensions determined from X-ray crystallographic data and for the dipeptide nanotubes, hexagonal space group symmetry was preserved throughout. Harmonic frequencies and normal-mode displacements were obtained at the Γ-point by a two-point numerical differentiation of the forces, following diagonalization of the mass-weighted Hessian matrix (Wilson *et al.*, 1955) of the unit cell. These conditions were similar to those previously for predicting the THz spectra of trialanine (Siegrist *et al.*, 2006).

In addition to the DFT calculations, empirical force-field calculations were done using periodic boundary conditions in CHARMM22 (MacKerell *et al.*, 1998a,b, 2000). Periodic structures were created using the CRYSTAL facility in the CHARMM-c32b2 package (Brooks *et al.*, 1983) to include a set of image cells surrounding a core block of one unit cell. The core atom cut off radius for including pairwise nonbonded interactions, which determines the number of image cells generated, was set at 20 Å; changes in energy were negligible for larger cut off radii. Inclusion of three-atom hydrogen bonding terms to model interactions between core and image cells are not currently possible. Therefore, all intermolecular hydrogen bonds are treated with two-atom terms. The Ewald approximation (Ewald, 1921) was used to ensure convergence in the electrostatic energy sums, and a Gaussian width of 0.34 cm^{-1} was used in transitioning from real to k-space sums. The number of grid points in k-space was set to approximately twice the unit-cell dimensions. Normal mode frequencies were found from the eigenvalues of the mass-weighted Hessian matrix using a two-point finite difference method. Simulated Gaussian lineshape functions of 1 cm^{-1} in width were convoluted with all predicted spectral lines used for comparison of experimental and computational spectra.

IV. Dipeptides Nanotubes

The crystalline structures of a series of dipeptides have recently been reported by Görbitz (2002, 2003) and Gorbitz and Gundersen (1996). The dipeptide pairs of this structural class, the VA group, have hexagonal space group structures ($P6_1$ Hermann Mauguin space group) and have crystalline structures similar to that shown in Fig. 2A for AI. Other members of this group include alanyl valine (AV), AI, and valyl isoleucine (VI) and their retroanalogs, valyl alanine (VA), IA, and isoleucyl valine (IV). A key property of this class is the hydrophobic surface that

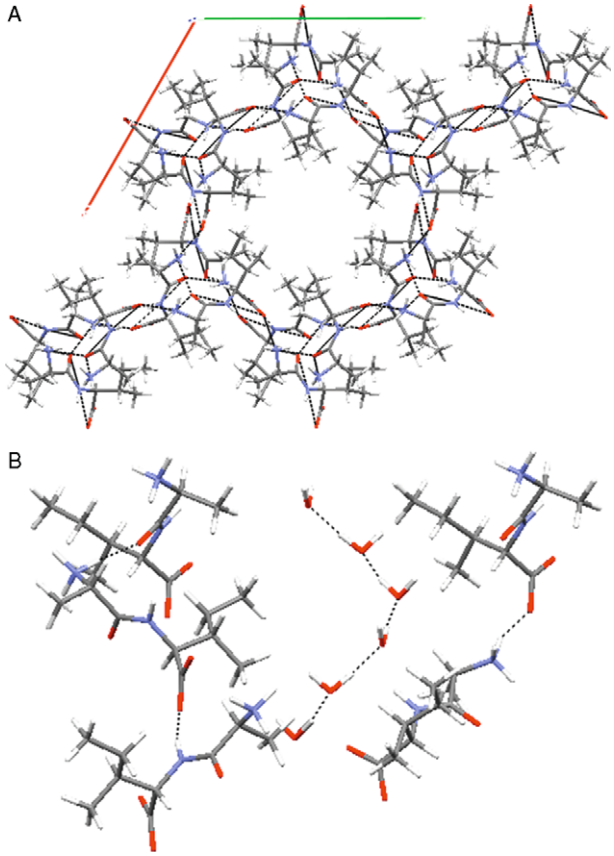

Fig. 2 Crystalline structure of the dipeptide AI (Görbitz and Gundersen, 1996). Top panel illustrates the structure as viewed down the 6_1 axis. The structure of AI–H_2O (1:1 ratio) is shown in the lower panel along an axis perpendicular to the 6_1 axis. Hydrogen bonds are shown with dashed lines. The hydrogen atom positions of water were determined from Density Functional Theory (DFT) predictions (see text for details).

forms the inner lining of the nanotube channels where the side chains are seen to cluster around the hexagonal axis, $\mathbf{6_1}$. The framework of each channel constitutes a double helix that is linked by consecutive $-NH_3^{+}\cdots{}^{-}OOC-$ head-to-tail hydrogen bonds.

The van der Waals pore diameters of the nanotubes have been found to range from 0.33 to 0.6 nm over this series. For several of these nanotube structures, Görbitz and Gundersen (1996) and Görbitz (2002, 2003) were also able to obtain X-ray data of systems where the pore regions contained hydrophilic solvents such as H_2O, isopropanol, acetone, acetonitrile, and so on. Of particular interest here is the retro-analog pair, AI and IA, where in the former case, the guest solvent, water, was found to be easily drawn into the pores while in the latter case, permeation of water was prohibited. A cross-sectional view of the $\mathbf{6_1}$ structure of AI containing

water in a 1:1 ratio within the pore is shown in Fig. 2B. Like the helical structure of the nano-tubes, the water network takes the form of a spiral with each water molecule binding to its neighbors with two hydrogen bonds (H-bonds). Because of the hydrophobic nature of the tube, the water network is expected to be essentially noninteracting with the network of peptide backbone H-bonds that defines the shape of the nano-tubes. The corresponding pore size changes from 6×4.5 Å in AI to 5×2.5 Å in IA.

The THz absorption spectra obtained at 4 K for bulk (pellet) samples of AI and IA are shown as the middle traces in the upper and lower panels of Fig. 3, respectively. Simulated spectra are superimposed on top of the experimental data traces. The simulations were obtained by fitting the data to a minimum number of Gaussian features to give a quantitative measure of the phonon mode count across this region. Notice the differences in these spectra upon simple reversal of the sequence. The spectrum of AI has more than twice the number of lines as IA. The corresponding spectra of hydrated samples are shown as the upper traces in each panel of Fig. 3. These spectra were obtained shortly after these samples were recrystallized from H_2O according to the prescription given by Gorbitz (Görbitz and Gundersen, 1996) while the lower traces were obtained for samples dried in vacuum for several days following recrystallization. It is clear in the lower panel that little change occurs between the spectra of IA and IA–H_2O. However, while the overall patterns of the two spectra of AI and AI–H_2O are quite similar, features of the hydrated sample are shifted to lower frequency by up to 2.5 cm^{-1} and all features display some added width. The changes are reproducible and easily verified at the resolution of our spectrometer. These studies further confirm the vastly different water permeability dynamics of the two nanotube structures. We further note that this property of AI is in sharp contrast to the absorption of H_2O in alanine tripeptide where significant changes in the THz absorption spectrum were observed for the antiparallel sheet (Seigrist *et al.*, 2006).

The corresponding THz spectra of thin film samples of AI and IA deposited on one surface of a waveguide are shown as the lowest trace in each panel in Fig. 3. The thin films are estimated to be (1–2) μm thick. Furthermore, the thin films were placed under vacuum prior to cooling and data collection and therefore have no water in the nanotubes. Similar to the advantages realized for polymers (Melinger *et al.*, 2006, 2007), the waveguide spectra were obtained with ≈10-fold less sample compared to the bulk pellet spectra and the spectral lines are significantly reduced in width and nearly completely resolved. Furthermore, the vibrational lines are well-aligned with corresponding features in the bulk samples. However, for some lines, the spectral intensities are very different from their bulk sample counterparts. This is a result of selective absorption between the well-aligned polarization supported in the waveguide and orientated crystal growth pattern on the waveguide interface, a property that will be exploited in future studies to elucidate the types of nuclear motions associated with the THz features (Melinger *et al.*, 2007). Like the bulk sample spectra, all features are well-fit to Gaussian lineshape functions indicating that contributions to the spectral widths are due to crystal defects

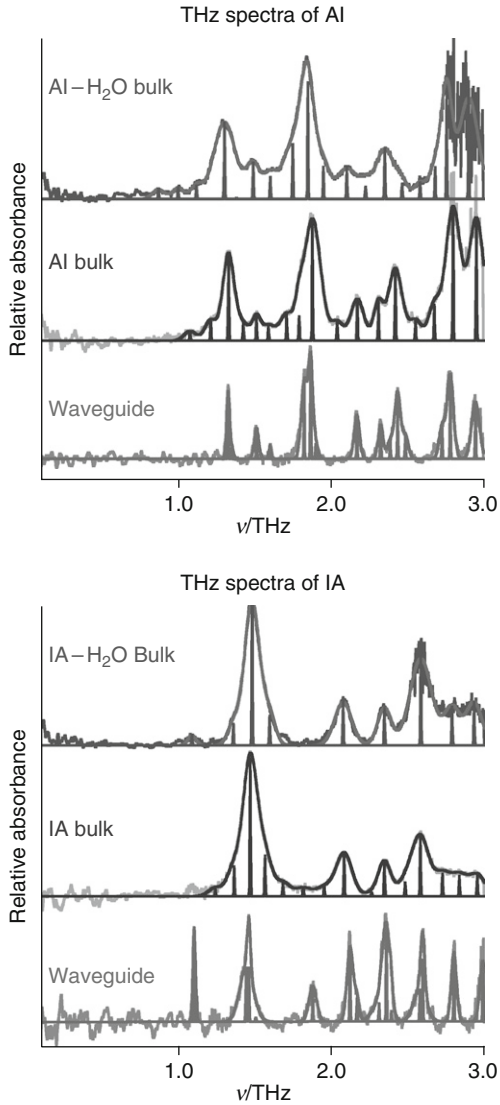

Fig. 3 THz spectra of crystalline samples of AI (top) and IA (bottom). The middle trace in each panel was obtained for samples dried under vacuum for several days while the upper traces were obtained for samples cooled to 4 K immediately following recrystallization from the solvent, water. While the two spectra of IA are nearly identical, the features of AI–H_2O are shifted to the red by $\approx$2.5 cm^{-1} relative to AI. The bottom traces in each trace are from dry samples deposited in a waveguide. Spectra are shifted along the absorbance axis for clarity.

and/or surface anomalies. Such broadening properties keep open the possibility of still further improvements in spectral fidelity.

To gain some understanding of why water behaves so differently in these two dipeptide nanotubes, a series of classical (CHARMM) and quantum chemical calculations (DFT/PW91) were performed on periodic structures with and without water. For these calculations, the unit cell dimensions were held fixed at those determined in the X-ray studies and full geometry optimizations were performed on the *P 61* unit cells with and without water. For AI, the initial positions of the oxygen atoms were taken from the X-ray data while for IA, the initial water network was taken from the optimized geometry of AI. The full optimized structures of the water helices after removal of the dipeptide nanotubes were also performed for each of the *P 61* structures. In these cases, the water networks retained their same three dimensional helical structures.

The THz spectral predictions from CHARMM for AI and IA are shown as the top two traces in the upper and lower panels of Fig. 4, respectively. For both AI and IA without water, the predicted spectra have the correct number of features although the overall patterns of both are rather severely red-shifted relative to experiment. We demonstrate in recent work (Zhang *et al.*, 2008) that predictions from CHARMM improved significantly for seven different nanotube structures (including AI and IA) when anharmonic effects are taken into account using vibrational self-consistent theory (VSCF) (Gregurick *et al.*, 1997, 1999, 2002). In line with the observed features, the VSCF vibrational frequencies blue-shift relative to the harmonic frequencies shown in Fig. 4. These shifts are attributed to the overall positive coupling strengths from a stiffening of the effective potential particularly for the sidechain squeezing modes. Shown as the top traces in each panel of Fig. 4 are the calculated spectra for the hydrated nanotubes. Particularly for AI, the overall pattern of lines is very different from that of the dry nanotubes. Furthermore, the main features seem to show a slight tendency to blue-shift. Both of these properties are inconsistent with observed spectra where the overall pattern of AI–H_2O is very similar except for a small red-shift relative to AI (see Fig. 3).

The THz spectral predictions from quantum chemical theory (DFT) for AI and IA are shown as the top two traces in the upper and lower panels of Fig. 5, respectively. The experimental data of the dehydrated pellet and waveguide samples are shown as the lower two traces for comparison. The optimized theoretical structures are shown in Fig. 6. Except for a small red-shift, the theoretical spectrum of AI is in good agreement with experiment, reproducing nearly all experimental features up through 3 THz. The agreement with the predicted spectrum of IA is also good except for a small blue-shift from theory. Furthermore, in the top panel, the calculated spectrum of the hydrated form, AI–H_2O, is similar to that of AI except for a small uniform red-shift. This property seems to reproduce the experimental observations in Fig. 3. In contrast, the corresponding simulated spectrum of IA–H_2O appears much more complex relative to IA with additional features predicted throughout this region. Examination of the ''extra'' normal modes associated with IA–H_2O indicates a higher propensity for the water motion relative

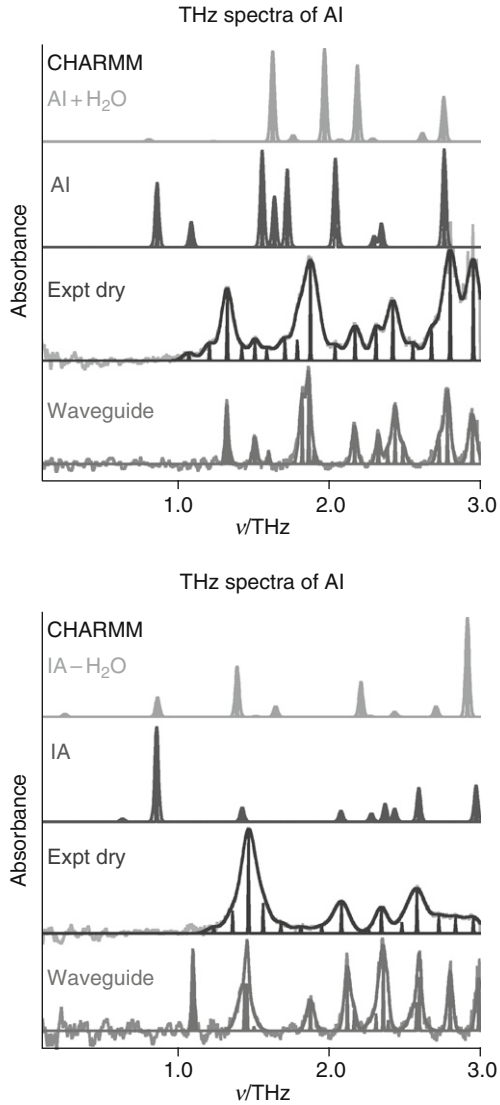

Fig. 4 Spectral predictions of AI (top) and IA (bottom) from CHARMM and the TIP3P Water model. The predicted spectrum shown as the top trace in each panel is for the nanotube structure that includes the helical network of water in the pores. The experimental data of the bulk and waveguide samples are shown below for comparison. Spectra are shifted along the absorbance axis for clarity.

to other modes in this region. In contrast, the relative displacements of water for AI–H_2O appear to be more uniform over all of the THz modes. Hence, the water fluctuations in IA–H_2O appear to be decoupled from those of the nanotube frame. From the thermodynamics perspective, such a decoupling may lead to an increase

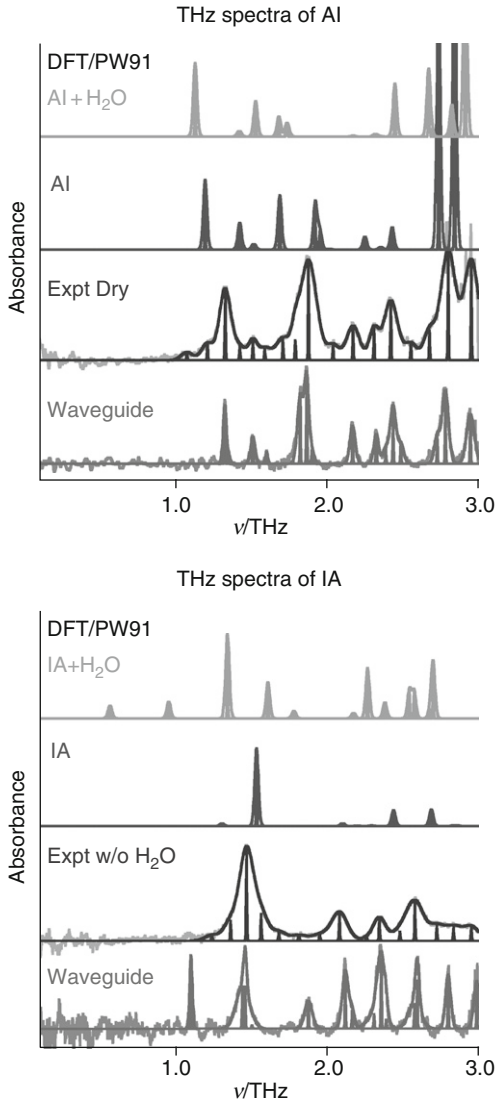

Fig. 5 Spectral predictions of AI (top) and IA (bottom) from DFT and the PW91 functional. The predicted spectrum shown as the top trace in each panel is for the nanotube structure that includes the helical network of water in the pores. The experimental data of the bulk and waveguide samples are shown below for comparison. Spectra are shifted along the absorbance axis for clarity.

in the excess chemical potential and may partially explain why water does not permeate this tube. It is clear from the structural similarities of the hydrogen bonding water network shown in Fig. 6 that such effects may be important.

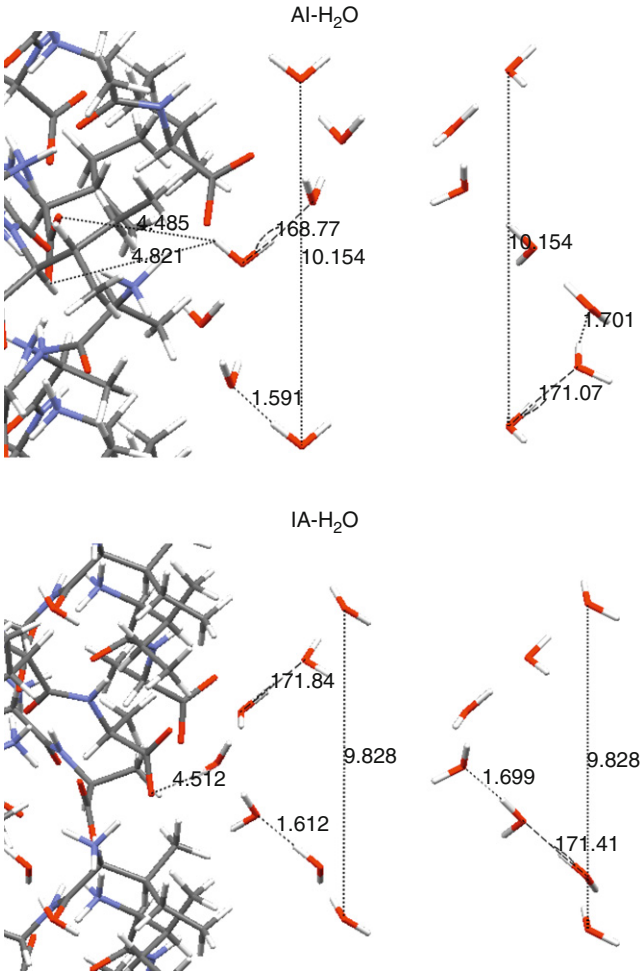

Fig. 6 Theoretical minimum energy structures of AI–H_2O (top) and IA–H_2O (bottom) from DFT. The minimum energy structure of the water helix alone is shown to the right of each.

From both the classical and quantum chemical results, examination of the nuclear motions associated with the THz vibrational normal modes revealed significant participation of the hydrogen bonding network of the nanotube backbone, explaining the high flexibility of the nanotube region for guest molecule permeability. As discussed in more detail elsewhere (Zhang *et al.*, 2008), we find from three-dimensional animations that for many of these modes the side chain motions lead to channel wall deformation (e.g., side chain wagging or channel squeezing motions) but with little change in nanotube volume. However, there were always one or more normal modes associated with a channel-breathing motion

Table I
Results of CHARMM and DFT calculations for the periodic systems of AI and IA with and without H_2O.

	Energy (kJ mol^{-1})				
CHARMM	With H_2O	No H_2O	ΔE^a	H_2O Only	ΔE^b
AI[c]	−3078.2	−2833.2	−245.0	−190.4	−54.64
IA[d]	−3145.0	−2860.2	−289.7	−208.4	−81.38
ΔE	+71.7	+27.0	**+44.7**	**+18.0**	**+26.7**
DFT/PW91					
AI[c]	−4755.6	−4353.7	−401.9	−375.51	−26.40
IA[d]	−4748.5	−4354.2	−394.3	−376.18	−18.11
ΔE	−7.15	+0.46	**−7.61**	**+0.67**	**−8.29**

[a]Differences are specified relative to the dipeptide with water.
[b]Differences are specified relative to the value given in footnote *a*.
[c]X-ray lattice parameters: a=14.2570 Å, c=10.1530 Å for AI.
[d]X-ray lattice parameters: a=14.3720 Å, c=9.8282 Å for IA.

that enlarges the channel capacity significantly (VA was the only exception). For AI, the enhanced coupling of such modes with those of the water helix may further facilitate pathways for guest molecule absorption, substitution and removal.

From the rigorous thermodynamic perspective, the acceptance of water by AI but not IA is directly related to the excess chemical potential compared to bulk water. For a similar system of water in carbon nanotubes (8.1 Å in diameter), estimates of this energy have been reported at the classical level using MD simulations (Hummer *et al.*, 2001). While such classical studies are currently being explored for AI and IA, it is instructive to examine the relative energies of stabilization predicted at the classical and quantum chemical levels. The enthalpies per unit cell are given in Table I. (These energies exclude contributions from the vibrational zero-point energies which are within ±0.8 kJ mol^{-1} (±0.2 kcal mol^{-1}) for these two systems.) Surprisingly, at the CHARMM level, the stabilization of IA with and without the six water molecules +44.8 kJ mol^{-1} (+10.7 kcal mol^{-1}) greater than the corresponding energy difference predicted for AI (i.e., the dry cell energy differences account for +27 kJ mol^{-1} of the total +71.5 kJ mol^{-1}). Comparison with the relative energies of the water helices by themselves gives some measure of the water-water vs water-nanotube contributions; here +26.8 kJ mol^{-1} of the +44.8 kJ mol^{-1} (6.4 kcal mol^{-1} of the 10.7 kcal mol^{-1}) may be attributed to increased water-tube stabilization and the remaining to increases in the water network itself. Therefore, IA is predicted by CHARMM and the TIP3P water model to be significantly more stable with hydration than AI which is opposite to what is observed.

A similar comparison is given in Table I from the results of quantum chemical calculations. Here, hydration of AI verses IA is slight more favorable by +7.6 kJ mol^{-1} (+1.8 kcal mol^{-1}) with nearly all of increased stability arising from water-tube interactions. This difference per water molecule is small (+1.3 kJ mol^{-1} or

+0.30 kcal mol^{-1}) but comparable to the difference in excess chemical potentials (−3.4 kJ mol^{-1} or −0.82 kcal mol^{-1}) that enables water permeability in carbon nanotubes (Hummer *et al.*, 2001). However, unlike the water/carbon nanotube system, the difference of >4 kJ mol^{-1} per water from CHARMM is unlikely to be overcome by gains in stability from decreased assess to high energy states that dominate the free energy.

A full analysis of the normal modes responsible for the observed THz features including VSCF corrections to the CHARMM frequencies for the hydrated nanotubes will be given elsewhere. We also plan to perform MD simulations to better understand the vastly different permeability dynamics across these different hydrophobic nanotube systems. An attempt to refine these MD simulations will be made based on improving the force field predictions based on the observed THz features.

References

Allen, T. W., Kuyucak, S., and Chung, S. H. (1999). The effect of hydrophobic and hydrophilic channel walls on the structure and diffusion of water and ions. *J. Chem. Phys.* **111,** 7985–7999.

Allis, D. G., Fedor, A. M., Korter, T. M., Bjarnason, J. E., and Brown, E. R. (2007). Assignment of the lowest-lying THz absorption signatures in biotin and lactose monohydrate by sold-state density functional theory. *Chem. Phys. Lett.* **440,** 203–209.

Beckstein, O., and Sansom, M. S. P. (2004). The influence of geometry, surface character, and flexibility on the permeation of ions and water through biological pores. *Phys. Biol.* **1,** 42–52.

Brooks, B. R., Bruccoleri, R. E., Olafson, B. D., States, D. J., Swaminathan, S., and Karplus, M. (1983). CHARMM: A program for macromolecular energy, minimization, and dynamics calculations. *J. Comp. Chem.* **4,** 187–217.

De Groot, B. L., and Grubmuller, H. (2001). Water permeation across biological membranes: Mechanism and dynamics of aquaporin-1 and GlpF. *Science* **294,** 2353–2357.

Delley, B. (1990). An all-electron numerical method for solving the local density functional for polyatomic molecules. *J. Chem. Phys.* **92,** 508.

Delley, B. (2000). From molecules to solids with the $DMol^3$ approach. *J. Chem. Phys.* **113,** 7756.

Ebbinghaus, S., Kim, S. J., Heyden, M., Yu, X., Greubele, M., Leitner, D. M., and Havenith, M. (2008). Protein sequence- and pH-dependent hydration probed by terahertz spectroscopy. *J. Am. Chem. Soc.* **130,** 2374–2375.

Ebbinghaus, S., Kim, S. J., Heyden, M., Yu, X., Heugen, U., Greubele, M., Leitner, D. M., and Havenith, M. (2007). An extended dynamical hydration shell around proteins. *Proc. Natl. Acad. Sci.* **104,** 20749–20752.

Ewald, P. (1921). Die Berechnung opticher und elektrostatischer Gotterpotentiale (Evaluation of optical and electrostatic lattice potentials). *Ann. Phys.* **64,** 253–287.

Görbitz, C. H. (2002). An exceptionally stable peptide nanotube system with flexible pores. *Acta Crystallogr.* **B58,** 849–854.

Gorbitz, C. H. (2003). Nanotubes from hydrophobic dipeptides: Pore size regulation through side chain substitution. *New J. Chem.* **27,** 1789–1793.

Görbitz, C. H., and Gundersen, E. (1996). Valyl Alanine. *Acta Crystallogr. C* **52,** 1764–1767.

Gregurick, S. K., Chaban, G. M., and Gerber, R. B. (2002). Ab initio and improved empirical potentials for the calculation of the anharmonic vibrational states and intramolecular mode coupling of n-methylacetamide. *J. Phys. Chem. A* **106,** 8696–8707.

Gregurick, S. K., Fredj, E., Elber, R., and Gerber, R. B. (1997). Vibrational spectroscopy of peptides and peptide-water cmplexes: Anharmonic coupled-mode calculations. *J. Phys. Chem. B* **101,** 8595–8606.

Gregurick, S. K., Liu, J. H.-Y., Brant, D. A., and Gerber, R. B. (1999). Anharmonic vibrational self-consistent field calculations as an approach to improving force fields for monosaccharides. *J. Phys. Chem. B* **103,** 3476–3488.

Heugen, U., Schwaab, G., Brundermann, E., Heyden, M., Yu, X., Leitner, D. M., and Havenith, M. (2006). Solute-induced retardation of water dynamics probed directly by terahertz spectroscopy. *Proc. Nat. Acad. Sci.* **103,** 12301–12306.

Heyden, M., Brundermann, E., Heugen, U., Niehues, G., Leitner, D. M., and Havenith, M. (2008). Long-range influence of carbohydrates on the salvation dynamics of water—Answers from terahertz absorption measurements and molecular modeling simulations. *J. Am. Chem. Soc.* **130,** 5773–5779.

Hummer, G., Rasaiah, J. C., and Noworyta, J. P. (2001). Water conduction through the hydrophobic channel of a carbon nanotube. *Nature* **414,** 188–190.

Jepsen, P. U., and Clark, S. J. (2007). Precise ab-initio prediction of Terahertz vibrational modes in crystalline systems. *Chem. Phys. Lett.* **442,** 275–280.

Korter, T. M., and Plusquellic, D. F. (2004). Continuous-wave terahertz spectroscopy of biotin: Vibrational anharmonicity in the far-infrared. *Chem. Phys. Lett.* **385,** 45.

Lynden-Bell, R. M., and Rasaiah, J. C. (1996). Mobility and salvation of ions in channels. *J. Chem. Phys.* **105,** 9266–9280.

MacKerell, A. D., Banavali, N., and Foloppe, N. (2000). Development and current status of the CHARMM force field for nucleic acids. *Biopolymers* **56,** 257.

MacKerell, A. D., Jr., Bashford, D., Bellott, M., Dunbrack, R. L., Jr., Evanseck, J. D., Field, M. J., Fischer, S., Gao, J., Guo, H., Ha, S., Joseph-McCarthy, D., Kuchnir, L., *et al.* (1998). All-atom empirical potential for molecular modeling and dynamics studies of proteins. *J. Phys. Chem. B* **102,** 3586–3616.

MacKerell, A. D., Jr., Brooks, B., Brooks, C. L., III, Nilsson, L., Roux, B., Won, Y., and Karplus, M. (1998b). "The Encyclopedia of Computational Chemistry 1." Wiley, Chichester, UK.

Masson, J. B., Sauviat, M. P., Martin, J. L., and Gallot, G. (2006). Ionic contrast terahertz near-field imaging of axonal water fluxes. *Proc. Natl. Acad. Sci.* **103,** 4808–4812.

McIntosh, K. A., Brown, E. R., Nichols, K. B., McMahon, O. B., DiNatale, W. F., and Lyszczarz, T. M. (1995). Terahertz photomixing with diode lasers in low-temperature-grown GaAs. *Appl. Phys. Lett.* **67,** 3844.

Melinger, J. S., Laman, N., Sree Harsha, S., Cheng, S., and Grischkowsky, D. (2007). High-resolution waveguide terahertz spectroscopy of partially oriented organic polycrystalline films. *J. Phys. Chem. A* **111,** 10977–10987.

Melinger, J. S., Laman, N., Sree Harsha, S., and Grischkowsky, D. (2006). Line narrowing of terahertz vibrational modes for organic thin polycrystalline films within a parallel plate waveguide. *Appl. Phys. Lett.* **89,** 251110.

Mendis, R., and Grischkowsky, D. (2001). Undistorted guided-wave propagation of sub-picosecond terahertz pulses. *Opt. Lett.* **26,** 846–848.

Perdew, J. P., and Wang, Y. (1986). Accurate and simple density functional for the electronic exchange energy: Generalized gradient approximation. *Phys. Rev. B* **33,** 8800–8802.

Pine, A. S., Suenram, R. D., Brown, E. R., and McIntosh, K. A. (1996). A terahertz photomixing spectrometer: Application to SO_2 broadening. *J. Mol. Spectro.* **175,** 37.

Plusquellic, D. F., Korter, T. M., Fraser, G. T., Lavrich, R. J., Benck, E. C., Bucher, C. R., Domench, J., and Hight Walker, A. R. (2003). *In* "Terahertz Sensing Technology. Volume 2: Emerging Scientific Applications and Novel Device Concepts" (D. L. Wollard, W. R. Loerop, and M. S. Shur, eds.), Vol. 13(4), pp. 385. World Scientific.

Plusquellic, D. F., Siegrist, K., Heilweil, E., and Esenturk, O. (2007). Applications of THz spectroscopy in biosystems. *Chem. Phys. Chem.* **8**(17), 2412.

Pomes, R., and Roux, B. (1998). Free energy profiles for H+ conduction along hydrogen-bonded chains of water molecules. *Biophys. J.* **75,** 33–40.

Preston, G. M., Carroll, T. P., Guggino, W. B., and Agre, P. (1992). Appearance of water channels in Xenopus oocytes expressing red cell CHIP28 protein. *Science* **256,** 385–387.

Sansom, M. S. P., Smith, G. R., Adcock, C., and Biggin, P. C. (1997). The dielectric properties of water within model transbilayer pores. *Biophys. J.* **73,** 2404–2415.

Siegrist, K., Bucher, C. R., Mandelbaum, I., Hight-Walker, A., Balu, A. R. R., Gregurick, R. S. K., and Plusquellic, D. F. (2006). High resolution Terahertz spectroscopy of crystalline trialanine: Extreme sensitivity to β-sheet structure and cocrystallized water. *J. Am. Chem. Soc.* **128,** 5764–5775.

Verghese, S, McIntosh, K. A., Jackson, A., Gossard, A. C., and Matsuura, S. (2001). Accurate modeling of dual dipole and slot elements used with photomixers for coherent terahertz output power. *IEEE Trans. Microwave Theory Tech.* **49,** 1032.

Whitmire, S. E., Wolpert, D., Markelz, A. G., Hillebrecht, J. R., Galan, J., and Birge, R. R. (2003). Protein flexibility and conformational state: A comparison of collective vibrational modes of wild-type and D96N bacteriorhodopsin. *Biophys. J.* **85,** 1269–1277.

Wilson, E. B., Jr., Decius, J. C., and Cross, P. C. (1955). "Molecular vibrations: The theory of Infrared and raman vibrational spectra." McGraw-Hill, New York.

Zhang, H., Siegrist, K., Plusquellic, D. F., and Gregurick, S. K. (2008). Terahertz spectra and normal mode analysis of the crystalline VA class dipeptide nanotubes. *J. Am. Chem. Soc. In press*.

Disclaimer

Certain commercial equipment, instruments, or materials are identified in this paper to adequately specify the experimental procedure. In no case does identification imply recommendation or endorsement by NIST, nor does it imply that the materials or equipment identified are necessarily the best available for the purpose.

CHAPTER 19

Combined Single-Molecule Electrical Recording and Single-Molecule Spectroscopy Studies of Ion Channel Conformational Dynamics

H. Peter Lu

Department of Chemistry
Bowling Green State University
Center for Photochemical Sciences
Bowling Green, Ohio 43403

METHODS IN CELL BIOLOGY, VOL. 90

0091-679X/08 $35.00
DOI: 10.1016/S0091-679X(08)00819-4

Abstract

Stochastic and inhomogeneous conformational changes regulate the function and dynamics of ion channels. Such complexity makes it difficult, if not impossible, to characterize ion channel dynamics using conventional electrical recording alone since that the measurement does not specifically interrogate the associated conformational changes but rather the consequences of the conformational changes. Recently, new technology developments on single-molecule spectroscopy, and especially, the combined approaches of using single ion channel patch-clamp electrical recording and single-molecule fluorescence imaging have provided us the capability of probing ion channel conformational changes simultaneously with the electrical single channel recording. The function-regulating and site-specific conformational changes of ion channels are now measurable under physiological conditions in real-time, one molecule at a time. In this chapter, we will focus our discussion on the new development of real-time imaging of the dynamics of individual ion channels using a novel combination of single-molecule fluorescence spectroscopy and single-channel current recordings. We will then discuss a specific example of single-molecule gramicidin ion channel dynamics studied by the new approach and the future prospects.

I. Introduction

Ion channels control ion flux across the cell membranes. Subtle conformational changes of ion-channel proteins are often critical in the conductivity and functioning of the ion channels. However, the conformational dynamics for most ion-channel proteins are still largely unknown due to lack of direct measurements in real time. Subtle structural changes of ion channels play an important role in regulating their function (Hille, 2001; Sakmann and Neher, 1995). Real-time channel conductance analysis and kinetic modeling, together with site-directed mutagenesis, protein modifications, and static NMR and X-ray crystallography protein structural analyses provide significant insights into the conformational changes that control channel activity (Hille, 2001; Sakmann and Neher, 1995). However, such methods do not directly measure the associated protein conformational dynamics and how these motions determine the mechanisms of channel function. Many critical conformational changes, involving in ion channel activation, function, deactivation, and desensitization, are not measurable by ion channel electrical current measurements as there are often no current on and off activity directly associated with these important functions. The time-course of events before and following activation of a particular channel may be modulated by the local membrane structure resulting in a static inhomogeneity in rates, which may change the time scale of ion-current dynamics, resulting in a dynamic disorder in rates. Currently, the dynamic structural changes that control channel activity have mostly been inferred from complex kinetic models that are fitted to the data from

electrophysiological measurements. X-ray crystallography and, to some extent, NMR spectroscopy provide information on static sample averaged structures (Armstrong and Gouaux, 2000; Armstrong *et al.*, 1998; Chen *et al.*, 1999; Hille, 2001; Jiang *et al.*, 2003; Sakmann and Neher, 1995) but not on channel kinetics and structural change dynamics. By combining fluorescence imaging (fluorescence self-quenching and fluorescence resonant energy transfer (FRET)) with single-channel patch-clamp electrical current recording, it is now a reality that correlate single-channel kinetics with structural changes can be measured simultaneously in real-time.

II. Development of Simultaneous Single-Molecule Fluorescence Spectroscopy and Patch-Clamp Electrical Recordings

A. Simultaneous Single-Molecule Fluorescence Imaging and Patch-Clamp Electrical Current Measurements of Ion Channel Conformational Dynamics and Open–Close Activity

The patch-clamp recording technique (Hille, 2001; Sakmann and Neher, 1995), which records ion currents of cations or anions such as chloride ions, sodium ions, potasium ions, and protons flowing across biological membranes through ion channel proteins, has had a major impact on the understanding of ion-channel processes. However, the conformational dynamics of the ion channel proteins has been primarily extrapolated by model analyses of the electrical current trajectories that are not particularly sensitive to subtle conformational intermediate states, including electrically undetectable "silent" conformational states. When an ion channel involves no open–close activity, there are no electrical current signals, and the ion channel is "silent." However, it has been known for many years, that the ion channel can involve many significant channel activities, such as ligand binding, conformational motions, and relaxations, that are crucial for an ion channel to be functional. The conventional patch-clamp electrical current measurements are not effective in analyzing the channel dynamics during silent time. Using the combined single-molecule FRET imaging and patch-clamp electrical current measurement can definitely provide new information on the silent molecular interaction and conformational activities of an ion channel.

Single-molecule measurements permit determination of the distribution of molecular properties in complex systems (Lu, 2005; Moerner and Orrit, 1999; Nie and Zare, 1997; Weiss, 1999; Xie and Lu, 1999; Xie and Trautman, 1998). The distributions, which can be either static (Craig *et al.*, 1996; Dickson *et al.*, 1996; Edman *et al.*, 1999; Lu *et al.*, 1998; Xie and Lu, 1999; Xu and Yeung, 1997) or dynamic (Edman *et al.*, 1999; Lu *et al.*, 1998; Lu and Xie 1997, Xie and Lu, 1999), cannot usually be determined by ensemble-averaged measurements. Ensemble-averaged fluorescence spectra do not reflect fluctuations in the local environment. In contrast, single-molecule fluorescence spectroscopy reveals intrinsic molecular conformational dynamics and environmental change dynamics.

Since 1999, there have been significant efforts and advancements in combining single-molecule fluorescence spectroscopy with conventional single ion channel electrical current measurements (Borisenko *et al*., 2003; Davis *et al*., 2004; Demuro and Parker, 2004; Harms *et al*., 2001, 2003, 2004; Ide and Yanagida, 1999, 2002; Lu, 2005; Orr *et al*., 2001, 2002; Sonnleitner *et al*., 2002; Zheng and Zegotta, 2000). For example, Yanagida and co-workers (Ide and Yanagida, 1999) reported single-channel fluorescence images acquired before or after a single-channel current measurement on the same sample lipid bilayer, utilizing a micro-pinhole patch technique. Lu and co-workers (Harms *et al*., 2003, 2004; Lu, 2005; Orr *et al*., 2002, 2001) demonstrated simultaneous patch-clamp electrical current measurement correlated with single-molecule FRET imaging and single-molecule ultrafast spectroscopy to probe gramicidin ion channel dynamics in a lipid bilayer. Woolley and Schutz (Borisenko *et al*., 2003) demonstrated a simultaneous optical and electrical recording of single gramicidin channels in a lipid bilayer on a micro-pinhole. Since 2001, there are also a number of significant efforts to use optical imaging to study single receptor proteins or ion channel dynamics in living cells, some of the work even made the advance of correlated whole-cell ion channel electrical current measurement.(Davis *et al*., 2004; Demuro and Parker, 2004; Zheng and Zegotta, 2000) For example, a related experimental effort, led by Zagotta Glauner *et al*., 1999, has studied multiple ion channels (~500–1000 channels), by correlating fluorescence imaging and patch-clamp current recording (Zagotta, 2000; Zheng and Zagotta, 2000). These research efforts have begun to provide a new paradigm for studying ion-channel conformational dynamics and mechanisms, and for obtaining information not obtainable by the conventional patch current recording measurements, a primary experimental approach for decades.

B. Revealing Complex Conformational Dynamics of a Model Ion Channel System: A Gramicidine Dimer in a Lipid Bilayer

To illustrate how the combined single-molecule approach probe the ion channel conformational dynamics simultaneously recording the single ion channel open–close activity time trajectories, we use a work done in Lu's laboratory on studying single molecule gramicidin ion channel dynamics using their new approach that correlates single-channel current trajectories with images of single molecules taken by a CCD camera or avalanche photodiode (APD) detectors with a single-photon detection efficiency. This correlation allowed the identification of the conformational events that are responsible for the channel kinetic behavior.

The gramicidin channel (Cha *et al*., 1999; Koeppe and Anderson, 1996; Koeppe *et al*., 2000; Nielsen and Anderson, 2000; O'Connell *et al*., 1990; Sigworth *et al*., 1987; Busath and Szabo, 1980; Nielsen and Anderson, 2000; Woolf and Roux, 1994; Veatch *et al*., 1975) was chosen as a model system for demonstrating the technique, and for investigating the dimerization states that govern channel activity. Gramicidin C, one of the gramicidin analogs, is a 15-amino acid β-helix that forms a channel by dimerizing head-to-head at the N-terminal in the interior of a lipid

bilayer. Each monomer was tagged at its C-terminal tail with either tetramethylrhodamine (TMR) or Cy5 (Hermanson, 1996; Lougheed *et al.*, 2001). Using gramicidin-TMR alone, homodimers were formed in the bilayer, creating a self-quenching pair. When gramicidin-TMR was applied together with gramicidin-Cy5, heterodimers were formed, creating a FRET pair within single dimers. Changes in fluorescence intensity could then detect changes in the distance between the two tails of the monomers, reporting changes in the dimerization state of the channel. Because changes in fluorescence intensity were acquired simultaneously with single-channel current, it was possible to identify the changes in dimerization states that correlated with each kinetic state.

C. Technical Approaches of the Combined Patch-Clamp Electrical Recording and Single-Molecule Spectroscopy and Imaging

1. Recording Single-Channel Currents

Single-channel current is recorded using the patch-clamp electrical recording experimental methods. Briefly, recording is achieved by using EPC-9 amplifier (HEKA Electronics, Lambrecht/Pfalz, Germany), and data is acquired using ITC-16 interface (InstruTech, Port Washington, New York) and Pulse/PulseFit acquisition software (v 8.11, HEKA Electronics). Records are filtered at 3 kHz and sampled at 10 kHz. Off line analysis is done using TAC (Bruxton Corporation, Seattle, WA) and in house software (Lu *et al.*, 1998, 2001).

2. Single-Molecule FRET Imaging Microscopy

Figures 1 and 2A describe the combined experimental setup. Single channel currents were recorded from gramicidin channels in the bilayer that was formed at the tip of a patch pipette. Single-molecule imaging was done using Nikon Diaphot 300, equipped with a 60× objective (NA = 1.4) and 4× relay lens. The illumination intensity was set to 5 kW/cm^2 for TMR at 514 or 532 nm, and 1.5 kW/cm^2 for Cy5 at 632 nm in the gramicidin ion channel experiments. Control of the polarization of the excitation light was achieved by introducing a $\lambda/4$ wave-plate (Meadowlark Optics). Filter combinations for TMR consisted of DCLP555, HQ625/100 (Chroma), and OG550 (Schott), and for Cy-5 of DCLP645, HQ690/90, and RG645 (Schott). The spFRET measurements were done using a custom-built dual-dichroic beam-splitter and band-pass filter in addition to either OG550 or RG645, permitting the detection of single fluorophores by a nitrogen-cooled CCD-camera (Spec-10 1340×400B or 700B, Roper Scientific) with a detection efficiency of 12% for TMR and 8% for Cy5. This device ensured the toggling of the excitation wavelength between 532 and 632 nm, and the detection of the emission at 8 ± 1% efficiency for TMR and 5 ± 1% efficiency for Cy5 with the FRET filters. The tip was exposed to the wide-field laser illumination for 5 ms at 1–10 Hz, and the exposure onsets were marked on a second channel of the amplifier, simultaneously

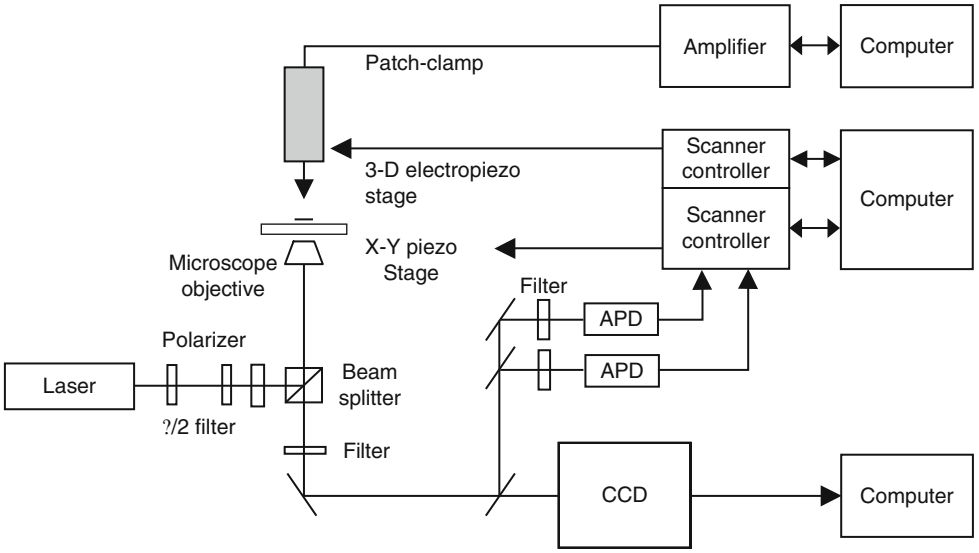

Fig. 1 Schematic diagram of the combined patch-clamp electric recording and single-molecule fluorescence imaging experimental setup. Different cw or pulse lasers and multicolor excitation are selected to improve the signal-to-noise ratio and the time resolution. A 3-D piezoelectro scanning micromanipulator (Newport) is used to scan the patch-clamp tip, and align the laser focal spot with the fluorescent molecule. The development of automation and multichannel optical detection, as well as the synchronization of the patch-clamp recording with the optical imaging/time trajectories hold the key development of this new approach.

with the single-channel current (Fig. 2B). The correlation of the images with channel current was done by matching the time-stamps with the snapshot consecutive numbers (Fig. 2C).

3. Fluorescence Imaging Data Analyses

Fluorescence imaging data analyses was done by first subtracting the fluorescence background (the average pixel value of the photon counts) from each pixel value, or by fitting the background to a wide 2-D Gaussian. The individual fluorescent "hotspots" were identified by the maxima of a 2-D Gaussian-correlation filter (Harms *et al.*, 2003, 2004; Orr *et al.*, 2001, 2002). The region around these maxima was fitted to a 2-D Gaussian by a Leavenberg–Marquardt algorithm reporting the intensity, width and position, and errors of the best fit by optimizing the χ^2 (Harms *et al.*, 1999; Schmidt *et al.*, 1996).

4. Single-Molecule Fluorescence Self-Quenching

Using gramicidin-TMR alone, a histogram of the intensities of more than 200 spots was fitted by a probability distribution function (pdf) that peaked at 43 $\pm$ 15 counts/ms. To determine whether the diffraction-limited spots at the patch were

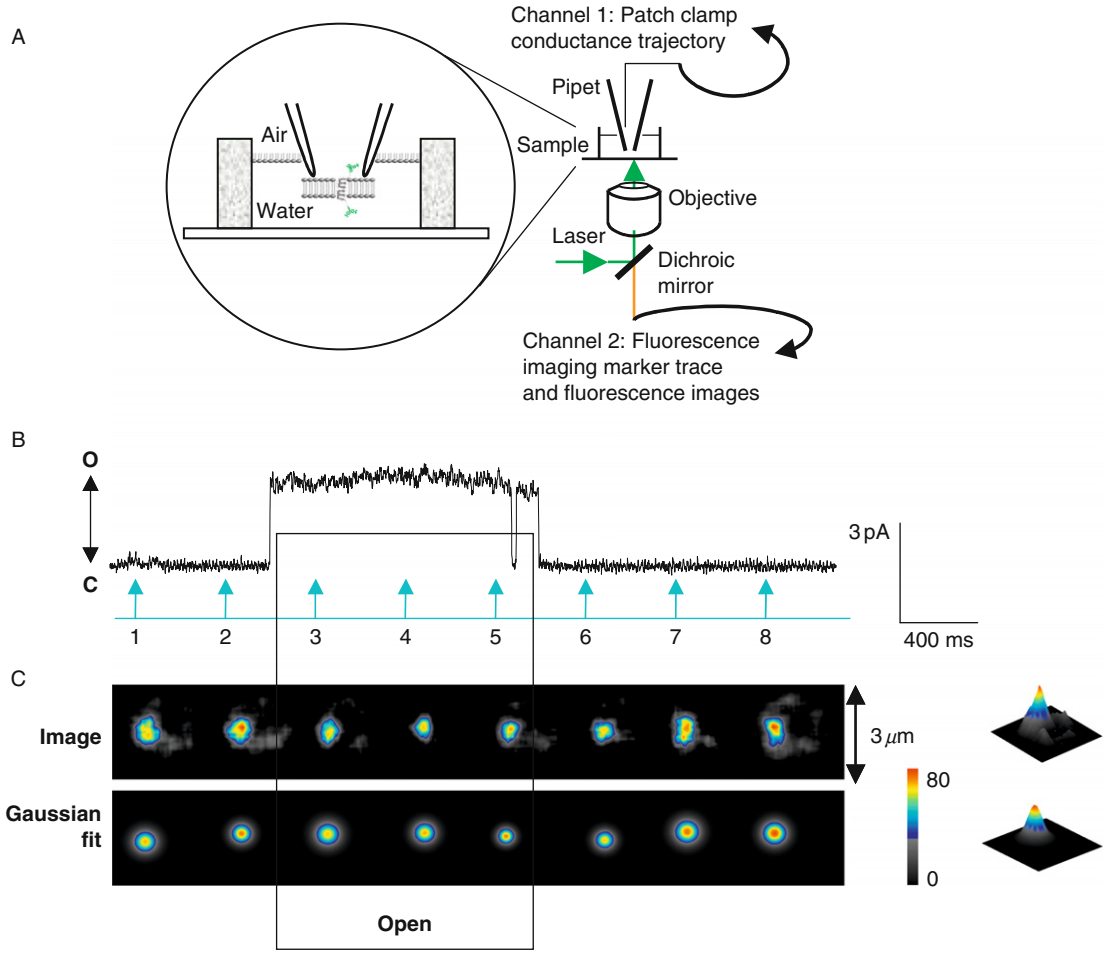

Fig. 2 (A) Experimental apparatus and sample preparation. Bilayers were formed at the tip of patch pipettes by apposition of two lipid monolayers. Dye-labeled gramicidin monomers are introduced from both sides of the bilayer and single-channel currents are recorded by patch-clamp instrumentation. (B) Upper trace: single-channel current recorded at 50 mV from a TMR-labeled single gramicidin channel incorporated in a lipid bilayer. Lower trace: time flags indicating the 5 ms of laser excitation. C and O, denote the current corresponding to closed and open states, respectively. (C) (top) Consecutive 3×3 μm fluorescence images of the pipette-tip taken simultaneously with the single-channel current shown in (B). (bottom) 2-D Gaussian fitting for the above image. (right) 3-D plot of the first image (top) and 3-D plot of the 2-D Gaussian fitting (bottom) with subtracted background intensity added to the base shown in gray.

single molecules, a control experiment was done with the same optical parameters. Low concentrations of labeled gramicidin molecules at the nM range were mixed with the lipids that were then used to form an artificial bilayer on a glass slide.

The peak value of the pdf, fitted to the hotspots on the glass, was similar to the peak value at the patch. This observation indicates that the hotspots at the patch were the lowest fluorescence entities of TMR-gramicidin dimers undergoing fluorescence self-quenching. The intensities tended to be larger when the channels were closed and smaller when the channels were open, consistent with the expectation that the channel is conductive when the dimer is fully associated, leading to maximal fluorescence self-quenching. The quenching occurs between the two dye molecules when the two monomers become closer and form a conductive pore. The broader distribution of hotspot intensities during the closed state, suggests that the two monomers form nonconductive channels of different conformations.

5. Fluorescence Colocalization and FRET

It is important to identify that the FRET signal changes are due to real protein conformational changes, or photophysical blinking, or reversible photobleaching, in order to obtain correct analysis of the ion channel conformational change dynamics. A confirmation of the observed relationship between fluorescence self-quenching and the conformational changes of the channel was demonstrated by FRET within a single ion channel protein. Adding gramicidin-TMR and gramicidin-Cy5 to the bilayer, led to the formation of channels containing FRET pairs. Figure 3A demonstrates the colocalization of monomers labeled with TMR and Cy5 within the spatial resolution of the diffraction-limited imaging. Figure 2B shows an example, where FRET occurs during channel opening but not when the channel is closed. By counting many images that correlated with the activity of single channels, it was found that ~70% of channel-opening events were correlated with spFRET. FRET efficiency was evaluated by the activity of the channels at the time that the images were taken (Fig. 3C). Measured when the channels were open, the Gaussian-like distribution of the efficiency showed a mean value of 0.59 with a FWHM of 0.21. Typical control experiment of polarization-dependent imaging indicates that the rotational diffusion of the TMR and Cy5 dye molecules has a much faster rate than the imaging rate, and the orientation effect of the dye dipoles on the FRET efficiency can be averaged out during the 5-ms imaging collection time. The mean spFRET efficiency corresponds to a mean donor–acceptor distance of ~56 Å (~52 Å $\leq$ d $\leq$ ~ 63 Å). Measured when the channels were closed, the distribution of FRET efficiency extended to a maximum efficiency of 0.57. This observation suggests that the channels could be in nonconductive states even when the two gramicidin monomers are fully dimerized. The minimum donor–acceptor distance of ~52 Å that was found when the channels were open represents the energy-minimized structure of the TMR/Cy5 gramicidin heterodimer FRET pair, which is consistent with the ~50 Å donor–acceptor distance derived from our molecular dynamics simulation (Harms *et al.*, 2002, 2003, 2004). The mean value of 56 Å can be explained by differences in the relative dihedral angle between the two monomers at different conformations of the conducting dimer. The maximum value of ~63 Å of donor–acceptor distance is likely associated with the effects of

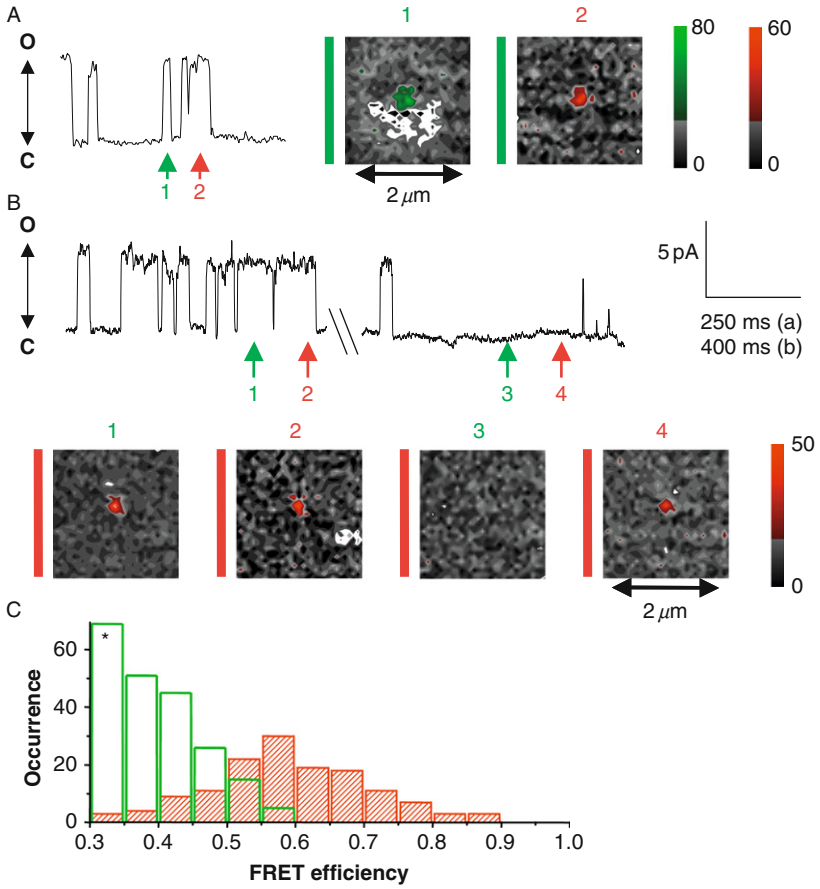

Fig. 3 (A) Colocalization of two gramicidin monomers labeled with two different dyes. Single-channel current trajectory recorded at 100 mV with arrows indicating the point of exposure of two consecutively recorded frames. The first frame was taken at $\lambda_{exc} = 514$ nm (with the OG550 long-pass filter), indicating single-molecule fluorescence of TMR. The second frame was taken at $\lambda_{exc} = 632$ nm, indicating single-molecule fluorescence of Cy5. From 2-D Gaussian fitting, the molecules were found to be within 30 nm of each other (the minimal positional accuracy allowed by the measurement system). c and o denote the current corresponding to closed and open states, respectively. (B) spFRET between two gramicidin monomers labeled with two different dyes. Single-channel current trajectory (upper panel) with four arrows indicating the exposure of four consecutively acquired frames (lower panel). Frames 1 and 3 are scaled in green and were taken at $\lambda_{exc} = 514$ nm and with a red emission long-pass filter (RG645). Frames 2 and 4 are scaled in red and were taken at $\lambda_{exc} = 632$ nm and with a red emission long-pass filter (RG645). Frame 1 indicates that FRET occurred between the TMR/Cy5 FRET pair when the channel was open. Frame 2 verified that a single Cy5 molecule was present. Frame 3 indicates that no FRET occurred when the channel was closed. Frame 4 verified that the Cy5 was still present. Subsequent images taken without the red long-pass filter (RG645) did show colocalization as shown in (A). (C) FRET efficiency distribution of "channel on" TMR/Cy5 heterodimers (shaded bars) with mean of 0.59 and width of 0.21 and "channel off" (open bars) with a maximum value of 0.57. An asterisk is inserted to indicate the 70% of channels showing no appreciable FRET (below 0.3) in the channel-closed state (or 30% of channels in the channel-open state). Conductive heterodimers, tagged with two different dyes, correlate with maximum spFRET. The broad distributions of FRET efficiency at open and closed states indicate the existence of multiple conformational states corresponding to different degrees of FRET.

shot noise and photophysical dark states. Nevertheless, spFRET imaging results (Fig. 3C) provide unambiguous evidence that the gramicidin channel dynamics involve multiple open and closed states.

There are two key elements of the new approach that are demonstrated: (1) using single-pixel photon counting detector to locate an ion channel protein at the patch, and (2) obtain fluorescence detection at a high-time resolution. Fast conformational motions control the kinetic activity of ion-channels. To capture these motions, the combined single-molecule approach has also utilized ultrafast pulse laser excitation and a point APD detector to acquire the fluorescence emission photons at nanosecond to second time scale (Hu *et al.*, 2002; Hu and Lu, 2003). The micropipette, mounted on the preamplifier, was attached to a micromanipulator that was driven by computer-controlled 3-D piezo-translators. Once the tip was located using wide-field illumination, this configuration allowed the use of a stationary focused laser to identify the position of the fluorescent molecule and excite it while using APD to acquire the emission at nanosecond time resolution (Figs. 4 and 5).

D. The Conformational Change Dynamics of the Gramicidin Dimer Ion Channels

Figure 6A shows a single-channel electrical current trajectory simultaneously recorded with a synchronized fluorescence-quenching time trajectory. The fluorescence intensity and the electrical current trajectories show a distinctive anticorrelated pattern when the channel is in an open state due to the close proximity of the pair of fluorophores across the lipid bilayer. A further analysis (Fig. 6A–C) shows that there are statistically-significant time mismatches between the two trajectories among the channel-opening and -closing events. The time mismatches were attributed to conformation-associated activity induction times or the silent times, Δ_1 and Δ_2, between the channel conformational changes and the channel opening and closing events, respectively (Fig. 6A). The distributions of the stochastic Δ_1 and Δ_2 are essentially Poisson and can be fitted with single-exponential decays (Fig. 6B and C). The mean time of conformational change among the intermediate states and open–closed states was determined to be 200 ± 50 ms for D_1 and 400 ± 50 ms for D_2. The multiple intermediate states are involved in gramicidin channel dynamics, in addition to the channel open and closed states, and their interconversion time is at a subsecond time-scale. Based on the experimental results, a new model of multistate gramicidin channel dynamics was proposed (Fig. 6D). The open (upper left), closed (upper right), and intermediate (middle) states can presumably be the outcomes of intramolecular and intermolecular conformational changes. It was postulated that the intermediate conformers result predominantly from the six intermolecular H-bond fluctuations that disrupt the pore structure of the gramicidin dimer. Lately, this mechanism has been supported by MD simulations. Subtle conformational changes at the N-terminal linkage of the dimer may significantly disrupt the channel cavity structure and the electrostatic field within the channel, thereby perturbing the channel conductance.

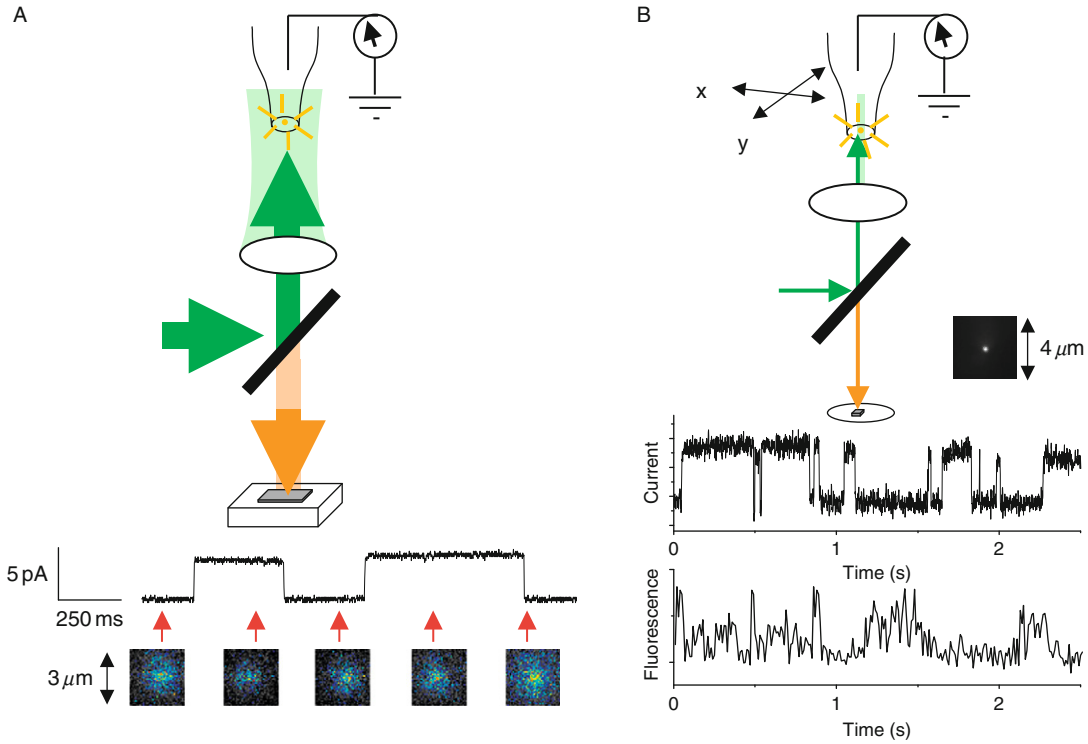

Fig. 4 (A) Diagram showing wide-field configuration (top) and simultaneously acquired current recordings and wide-field images (bottom) of TMR labeled gramicidin. Arrows indicate when a 5-ms image was acquired respective to the ion channel current record. The advantage of wide-field images is that one can obtain a large image very quickly. (B) Diagram (top) and image (right) of raster scanning a pipette tip through confocal excitation of a single TMR-labeled gramicidin channel. The upper sweep shows single-channel current record acquired by the patch-clamp amplifier, and the lower sweep shows the correlated single-molecule fluorescence emission acquired by the APD (15 MHz maximal counting rate). In this case, the photon detection is limited only by the emission photon flux, and the time resolution can reach microseconds (Harms, 2003, 2004; Lu, 2005).

There are many choices for the single-molecule spectroscopy to combine with the patch-clamp electrical recording measurements. In this section, we specifically discussed the experiment using simultaneous ultrafast fluorescence spectroscopy and single-channel electrical current recording (Figs. 4–6). This approach allows probing ion channel conformational changes from nanosecond to second time scales. Fast time resolution is particularly desirable as ion channel dynamics can involve in a wide time scale from nanosceonds to seconds. For example, as part of the gramicidin ion channel dynamics, hidden conformational changes were observed that strongly suggest the dynamics associated with multiple intermediate conformation states are complex.

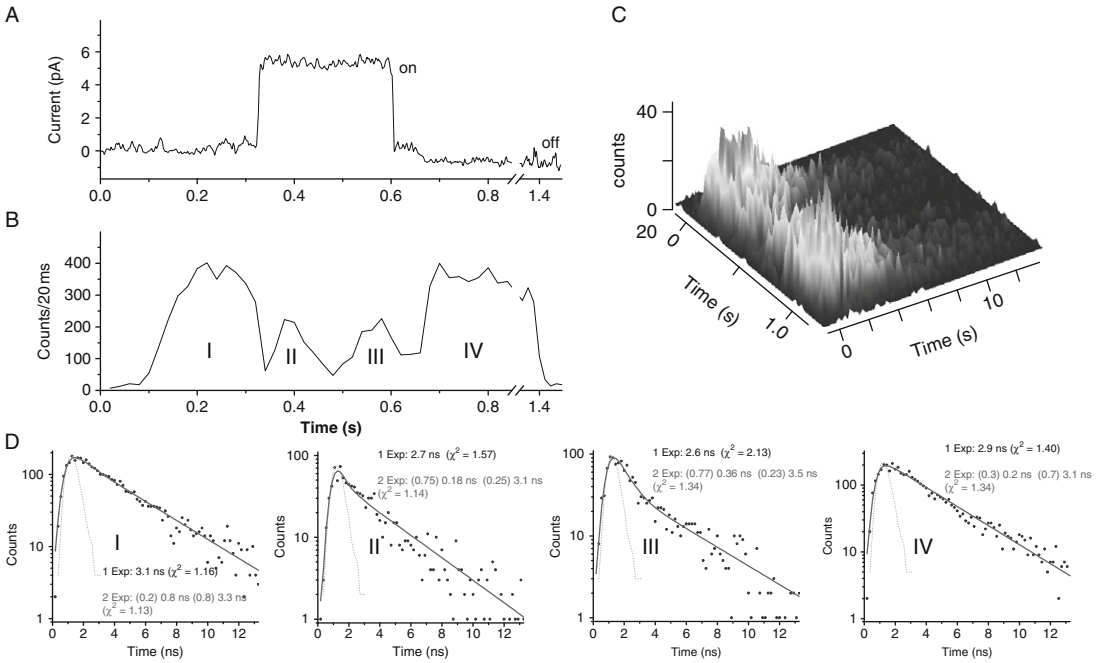

Fig. 5 (A) Single channel current event of a TMR-labeled, gramicidin channel simultaneously acquired with (B) the fluorescence time-stamping trace that shows a fluorescence quenching during the channel open state. The 2D histogram in (C) depicts the time-course (Time (s) axis) of the fluorescence decay (Time (ns) axis) of the data acquired in (B). The charts in (D) (labeled from I– IV) are the binned fluorescence decays over the time-periods shown in (B). The periods that correspond to channel opening (II and III) show a statistically significant biexponential decay, typical of dynamic fluorescence quenching (In this case, between the TMR-labeled monomers of the gramicidin dimer). The nanosecond time resolution of the kinetics shown (D) does not directly reflect the rate of the protein conformational changes, but rather reflects the chromophor excited-state lifetime, reporting the local environment changes and the involved photophysical processes. These results could be informative in reporting conformational change dynamics as will bediscussed later in the chapter (Harms, 2003, 2004; Lu, 2005).

III. Summary and Prospects

The combined single-molecule patch-clamp electrical recording and single-molecule spectroscopy is capable of probing critical conformational changes that regulate the ion channel dynamics. As an example discussed, this powerful approach has resolved a hitherto undetectable correlation of multiple conformational states with multiple conductance levels of the gramicidin channel consistent with transitions between closed, intermediate, and open states. The multiple conformational states of a single gramicidin channel that control the changes in single-channel conductance are revealed. This finding provides an advanced molecular-level understanding of the complex conformational mechanism of this

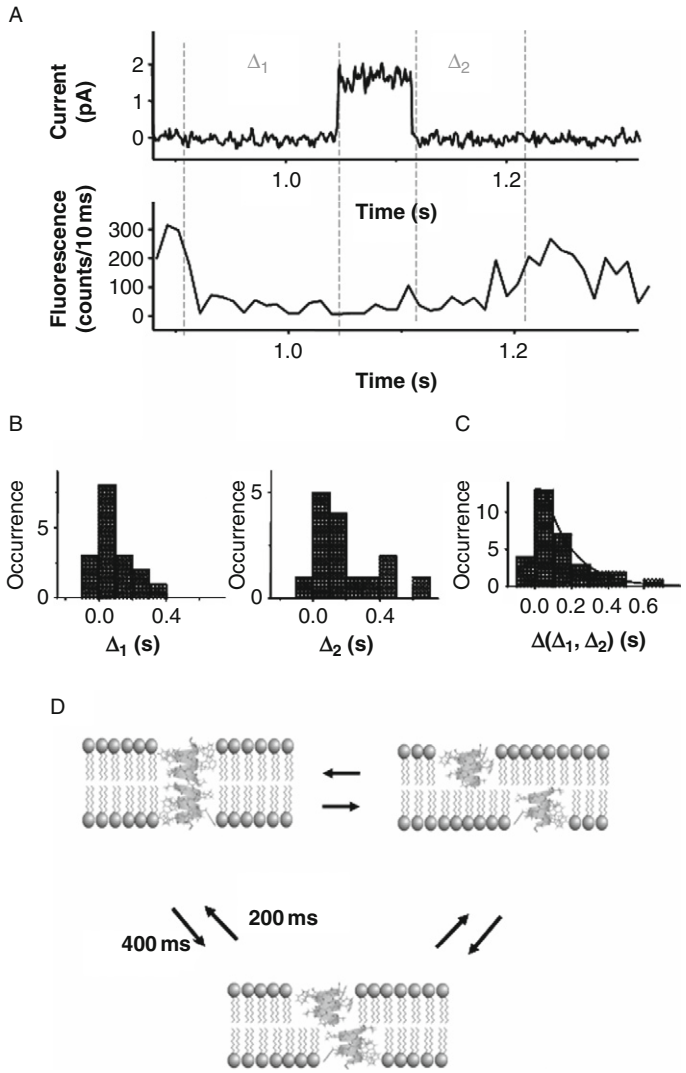

Fig. 6 Identification and distribution of the conformation-associated silent time. The fluorescence self-quenching of a TMR-dye pair on a gramicidin dimer causes an intensity decrease. (A) Identification of the silent times, the time lags between the channel electrical current changes and fluorescence intensity changes. (B) The distribution of the silent times. (C) The collective distribution of the silent times. (D) A proposed multistate model of gramicidin dynamics indicating a third "multistate" or a set of intermediate conformation states of nonconducting or partially conducting channels with larger separation between the fluorophore probes (middle).

"model" ion channel, and represents a significant departure from the current two-state model of gramicidin channel dynamics (Busath and Szabo, 1981; O'Connell *et al*., 1990; Sigworth *et al*., 1987; Veatch *et al*., 1975).

A large body of research has identified the kinetic behavior of the channel and has elucidated the structural determinants that govern desensitization, inactivation, and to some extent activation and deactivation. The limited knowledge about the conformational changes that govern specific kinetic states of the channel has been only inferred, and a dynamic picture of inhomogeneous motions is still missing. The single-molecule fluorescence detection techniques will allow the identification of inhomogeneous dynamic conformational motions at time scales ranging from nanoseconds to seconds. Acquired simultaneously with single channel current records, changes in FRET efficiency between two fluorescence-tagged subunits of the receptor as well as changes in donor fluorescence lifetime, will identify subtle dynamic changes in the distance between the protein functional domains of the two subunits. Acquired at nanosecond to second time scales, the fluorescence information will be translated to conformational motions of the receptor during the open and closed states.

The methodology, we discussed in this chapter, provides a novel paradigm for studying ion-channel conformational dynamics and mechanisms with site-specific reporters by combining two state-of-the-art real-time single-molecule approaches. Such unprecedented capabilities open a new stage for the study of ion-channel conformational dynamics at the single-molecule level under physiologically relevant conditions and in living cells (Borisenko *et al*., 2003; Davis *et al*., 2004; Demuro and Parker, 2004; Harms *et al*., 2001, 2003, 2004; Ide and Yanagida, 1999, 2002; Lu, 2005; Orr *et al*., 2001, 2002; Sonnleitner *et al*., 2002; Zheng and Zegotta, 2000). It is anticipated that more and more application of the combined single-molecule measurements will shed light on complex ion channel dynamics and receptor protein dynamics. Many critical properties and behaviors of the ion channel proteins can be studied using this new approach to obtain new information that is not obtainable from conventional patch-clamp electrical current measurement alone or static structural analyses alone or ensemble-averaged dynamic studies. For example, the allosteric effect in ion channel dynamics induced by agonist or antagonist binding, cell-signaling molecular interactions, and phosphorylation; voltage-regulated ion channel conformational changes, and channel dynamics; and inhomogeneous conformational motions of the receptor control the activation, inactivation, desensitization, and deactivation of a channel receptor protein in cell membrane.

Acknowledgments

The author thanks Greg Harms and Galya Orr for their experimental work; Maurice Montal for a productive collaboration; Alan Finckelston for a collaboration; Steve Colson and Bran Thrall for helpful discussions. We also thank for the financial support from the Laboratory Directed Research and Development grant from the Pacific Northwest National Laboratory, operated for the U.S. Department of Energy by Battelle Memorial Institute.

References

Armstrong, N., and Gouaux, E. (2000). Mechanisms for activation and antagonism of an AMPA-sensitive glutamate receptor: Crystal structures of the GluR2 ligand binding core. *Neuron* **28**(1), 165–181.

Armstrong, N., Sun, Y., Chen, G. Q., and Gouaux, E. (1998). Structure of a glutamate-receptor ligand-binding core in complex with kainite. *Nature* **395**(6705), 913–917.

Bartko, P., Xu, K., and Dickson, R. M. (2002). Three-dimensional single molecule rotational diffusion in glassy state polymer films–Art. no. 026101. *Phys. Rev. Lett.* **8902,** 6101.

Borisenko, V., Lougheed, T., Hesse, J., Fureder-Kitzmuller, E., Fertig, N., Behrends, J. C., Woolley, G. A., and Schutz, G. J. (2003). Simultaneous optical and electrical recording of single gramicidin channels. *Biophys. J.* **84,** 612–622.

Busath, D., and Szabo, G. (1981). Gramicidin forms multi-state rectifying channels. *Nature* **294,** 371–373.

Catterall, W. A. (1998). Structure and function of voltage-sensitive ion channels. *Science* **242**(4875), 50–61. [Review].

Cha, G. E., Snyder, P. R., Selvin, P., and Bezanilla, P. (1999). Atomic scale movement of the voltage-sensing region in a potassium channel measured *via* spectroscopy. *Nature* **402,** 809–817.

Chen, G. Q., Cui, C., Mayer, M. L., and Gouaux, E. (1999). Functional characterization of a potassium-selective prokaryotic glutamate receptor. *Nature* **402**(6763), 817–821.

Craig, D. G., Arriaga, E. A., Wong, J. C. Y., Lu, H. P., and Dovichi, N. J. (1996). Studies on single alkaline phosphatase molecules: Reaction rate and activation energy of a reaction catalyzed by a single molecule and the effect of thermal denaturation—the denaturation of an enzyme. *J. Am. Chem. Soc.* **118,** 5245.

Davis, R. W., *et al.* (2004). Thermodynamic properties of single ion channel formation: Gramicidin. *J. Phys. Chem. B.* **108,** 15364–15369.

Demuro, A., and Parker, I. (2004). Imaging the activity and localization of single voltage-gated Ca2+ channels by total internal reflection fluorescence microscopy. *Biophys. J.* **86,** 3250–3259.

Dickson, R. M., Norris, D. J., Tzeng, Y. L., and Moerner, W. E. (1996). Three-dimensional imaging of single molecules solvated in pores of poly(acrylamide) gels. *Science* **274,** 966.

Edman, L., Foldes-Papp, Z., Wennmalm, S., and Rigler, R. (1999). The fluctuating enzyme: A single molecule approach. *Chem. Phys.* **247,** 11.

Glauner, K. S., Mannuzzu, L. M., Gandhi, C. S., and Isacoff, E. Y. (1999). Spectroscopic mapping of voltage sensor movement in the Shaker potassium channel. *Nature* **402,** 813–817.

Harms, G., Orr, G., and Lu, H. P. (2004). Probing ion channel conformational dynamics using simultaneous single-molecule ultrafast spectroscopy and patch-clamp electrical recording. *Appl. Phys. Lett.* **84,** 1792–1794.

Harms, G. S., Cognet, L., Lommerse, P. H. M., Blab, G. A., Kahr, H., Gamsjager, R., Spaink, H. P., Soldator, N. M., Romanin, C., and Schmidt, Th. (2001). Single-molecule imaging of L-type $Ca2^{+}$ channels in live cells. *Biophys. J.* **81,** 2639–2646.

Harms, G. S., Orr, G., Montal, M., Thrall, B. D., Colson, S. D., and Lu, H. P. (2002). Combined patch-clamp recording and single-molecule imaging microscopy study of single-molecule ion channel dynamics. *Biophys. J.* **82**(1), 193a.

Harms, G. S., Orr, G., Montal, M., Thrall, B. D., Colson, S. D., and Lu, H. P. (2003). Conformational dynamics of an ion channel by simultaneous single-molecule fluorescence imaging and patch-clamp recording. *Biophys. J.* **85,** 1826–1838.

Harms, G. S., Sonnleitner, M., Schutz, G. J., Gruber, H. J., and Schmidt, T. (1999). Single-molecule anisotropy imaging. *Biophys. J.* **77,** 2864.

Hermanson, G. T. (1996). "Bioconjugate Techniques." Academic Press, New York.

Hille, B. (2001). "Ion Channels of Excitable Membranes." 3rd edn. Sinauer, Massachusetts.

Hu, D., Chen, Y., Vorpagel, E. R., and Lu, H. P. (2002). Single-molecule conformational mode-specific dynamics under enzymatic reaction. *Biophys. J.* **82**(1), 139a.

Hu, D., and Lu, H. P. (2003). Single-molecule nanosecond anisotropy dynamics of tethered protein motions. *J. Phys. Chem. B* **107,** 618–626.

Ide, T., Takeuchi, Y., and Yanagida, T. (2002). Development of an experimental apparatus for simulataneous observation of optical and electricalal signals from single ion channels. *Single Mol.* **3,** 33–42.

Ide, T., and Yanagida, T. (1999). An artifical bilayer formed on an agarose-coated glass for simultaneoous electrical and optical measurement of single ion channels. *Biochem. Biophys. Res. Comm.* **265,** 595–599.

Jia, Y., Talaga, D. S., Lau, W. L., Lu, H. S. M., Degrado, W. F., and Hochstrasser, R. M. (1999). Folding dynamics of single GCN4 peptides by fluorescence resonant energy transfer confocal microscopy. *Chem. Phys.* **247,** 69.

Jiang, Y. X., Lee, A., Chen, J. Y., Ruta, V., Cadene, M., Chait, B. T., and MacKinnon, R. (2003). X-ray structure of a voltage-dependent K+ channel. *Nature* **423**(6935), 33–41.

Koeppe, R. E., and Andersen, O. S. (1996). Engineering the gramicidin channel. *Annu. Rev. Biophys. Biomol. Struct.* **25,** 231–258.

Koeppe, R. E., Hatchett, J., Jude, A. R., Providence, L. L., Andersen, O. S., and Greathouse, D. V. (2000). Neighboring aliphatic/aromatic side chain interactions between residues 9 and 10 in gramicidin channels. *Biochemistry* **39,** 2235–2242.

Lougheed, T., Borisenko, V., Hand, C. E., and Woolley, G. A. (2001). Fluorescent gramicidin derivatives for single-molecule fluorescence and ion channel measurements. *Bioconjug. Chem.* **12,** 594–602.

Lu, H. P. (2005). Probing single-molecule protein conformational dynamics. *Acc. Chem. Res.* **38,** 557–565.

Lu, H. P., Iakoucheva, L. M., and Ackerman, E. J. (2001). Single-molecule conformational dynamics of fluctuating noncovalent protein–DNA interactions in DNA damage recogntion. *J. Am. Chem. Soc.* **123,** 9184.

Lu, H. P., and Xie, X. S. (1997). Single-molecule spectral fluctuations at room temperature. *Nature* **385,** 143.

Lu, H. P., Xun, L., and Xie, X. S. (1998). Single-molecule enzymatic dynamics. *Science* **282,** 1877.

MacKinnon, R., *et al*. (2003). *Nature* **423** 33–48.

Moerner, W. E., and Orrit, M. (1999). Illuminating molecules in condensed matter. *Science* **283,** 1670.

Nie, S., and Zare, R. N. (1997). Optical detection of single molecules. *Ann. Rev. Biophys. Biomol. Struct.* **26,** 567.

Nielsen, C., and Andersen, O. S. (2000). Inclusion-induced bilayer deformations: Effects of monolayer equilibrium curvature. *Biophys. J.* **79,** 2583–2604.

O'Connell, A. M., Koeppe, R. E., and Andersen, O. S. (1990). Kinetics of gramicidin channel formation in lipid bilayers: Transmembrane monomer association. *Science* **250,** 1256–1259.

Orr, G., Montal, M., Thrall, B. D., Colson, S., and Lu, H. P. (2001). Single-channel patch-clamp recording coupled with linear and non-linear confocal scanning fluorescence spectroscopy: Towards the simultaneous probing of single-ion channel conformational changes and channel kinetics. *Biophys. J.* **80,** 151a.

Orr, G., Harms, G. S., Thrall, B. D., Montal, M., Colson, S. D., and Lu, H. P. (2002). Probing single-molecule ligand-channel interaction dynamics in a living cell. *Biophys. J.* **82**(1), 255a.

Sakmann, B., and Neher, E. (1995). "Single-channel recording." 2nd edn. Plenum Press, New York.

Schmidt, T., Schutz, G. J., Baumgartner, W., Gruber, H. J., and Schindler, H. (1996). Imaging of single molecule diffusion. *Proc. Natl. Acad. Sci. USA* **93,** 2926.

Sigworth, F. J., Urry, D. W., and Prasad, K. U. (1987). Open channel noise. III. High-resolution recordings show rapid current fluctuations in gramicidin A and four chemical analogues. *Biophys. J.* **52,** 1055–1064.

Sonnleitner, A., Mannuzzu, L. M., Terakawa, S., and Isacoff, E. Y. (1990). Structural rearrangements in single ion channels detected optically in living cells. *Proc. Natla. Acad. Sci. USA* **99,** 12759–12764.

Szabo, G., and Urry, D. W. (1978). *N*-acetyl gramicidin: Single-channel properties and implications for channel structure. *Science* **203,** 55–57.

Unwin, N. (1995). Acetylcholine receptor channel imaged in the open state. *Nature* **373**(6509), 37–43.

Veatch, W. R., Mathies, R., Eisenberg, M., and Stryer, L. (1975). Simultaneous fluorescence and conductance studies of planar bilayer membranes containing a highly active fluorescent analog of gramicidin A. *J. Mol. Biol.* **99,** 75–92.

Villarroel, A., Regalado, M. P., and Lerma, J. (1998). Glycine-independent NMDA receptor desensitization: Localization of structural determinants. *Neuron* **20**(2), 329–339.

Weiss, S. (1999). Fluorescence spectroscopy of single biomolecules. *Science* **283,** 1676.

Wennmalm, S., Edman, L., and Rigler, R. (1997). Conformational fluctuations in single DNA molecules. *Proc. Natl. Acad. Sci. USA* **94,** 10641.

Wilson, G., and Karlin, A. (2001). Acetylcholine receptor channel structure in the resting, open, and desensitized states probed with the substituted-cysteine-accessibility method. *Proc. Natl. Acad. Sci. USA* **98**(3), 1241–1248.

Woolf, T. B., and Roux, B. (1994). Molecular dynamics simulation of the gramicidin channel in a phopholipid bilayer. *PNAS USA* **91,** 11631–11635.

Xie, X. S., and Lu, H. P. (1999). Single-molecule enzymology. *J. Biol. Chem.* **274,** 15967.

Xie, X. S., and Trautman, J. K. (1998). Optical studies of single molecules at room temperature. *Ann. Rev. Phys. Chem.* **49,** 441.

Xu, X. H., and Yeung, E. S. (1997). Direct measurement of single-molecule diffusion and photodecomposition in free solution. *Science* **275,** 1106–1109.

Yamakura, T., and Shimoji, K. (1999). Subunit- and site-specific pharmacology of the NMDA receptor channel. *Prog. Neurobiol.* **59**(3), 279–98. [Review].

Zheng, J., and Zagotta, W. N. (2000). Gating rearrangements in cyclic nucleotide-gated channels revealed by patch-clamp fluorometry. *Neuron* **28,** 369–374.

Zhuang, X., Ha, T., Kim, H. D., Centner, T., Labeit, S., and Chu, S. (2000). Flurescence quenching: A tool for single molecule protein-folding study. *Proc. Natl. Acad. Sci. USA* **97,** 14241–14244.

INDEX

J

L

VOLUMES IN SERIES

Founding Series Editor
DAVID M. PRESCOTT

Volume 1 (1964)
Methods in Cell Physiology
Edited by David M. Prescott

Volume 2 (1966)
Methods in Cell Physiology
Edited by David M. Prescott

Volume 3 (1968)
Methods in Cell Physiology
Edited by David M. Prescott

Volume 4 (1970)
Methods in Cell Physiology
Edited by David M. Prescott

Volume 5 (1972)
Methods in Cell Physiology
Edited by David M. Prescott

Volume 6 (1973)
Methods in Cell Physiology
Edited by David M. Prescott

Volume 7 (1973)
Methods in Cell Biology
Edited by David M. Prescott

Volume 8 (1974)
Methods in Cell Biology
Edited by David M. Prescott

Volume 9 (1975)
Methods in Cell Biology
Edited by David M. Prescott

Volume 10 (1975)
Methods in Cell Biology
Edited by David M. Prescott

Volume 11 (1975)
Yeast Cells
Edited by David M. Prescott

Volume 12 (1975)
Yeast Cells
Edited by David M. Prescott

Volume 13 (1976)
Methods in Cell Biology
Edited by David M. Prescott

Volume 14 (1976)
Methods in Cell Biology
Edited by David M. Prescott

Volume 15 (1977)
Methods in Cell Biology
Edited by David M. Prescott

Volume 16 (1977)
Chromatin and Chromosomal Protein Research I
Edited by Gary Stein, Janet Stein, and Lewis J. Kleinsmith

Volume 17 (1978)
Chromatin and Chromosomal Protein Research II
Edited by Gary Stein, Janet Stein, and Lewis J. Kleinsmith

Volume 18 (1978)
Chromatin and Chromosomal Protein Research III
Edited by Gary Stein, Janet Stein, and Lewis J. Kleinsmith

Volume 19 (1978)
Chromatin and Chromosomal Protein Research IV
Edited by Gary Stein, Janet Stein, and Lewis J. Kleinsmith

Volume 20 (1978)
Methods in Cell Biology
Edited by David M. Prescott

Advisory Board Chairman
KEITH R. PORTER

Volume 21A (1980)
Normal Human Tissue and Cell Culture, Part A: Respiratory, Cardiovascular, and Integumentary Systems
Edited by Curtis C. Harris, Benjamin F. Trump, and Gary D. Stoner

Volume 21B (1980)
Normal Human Tissue and Cell Culture, Part B: Endocrine, Urogenital, and Gastrointestinal Systems
Edited by Curtis C. Harris, Benjamin F. Trump, and Gray D. Stoner

Volume 22 (1981)
Three-Dimensional Ultrastructure in Biology
Edited by James N. Turner

Volume 23 (1981)
Basic Mechanisms of Cellular Secretion
Edited by Arthur R. Hand and Constance Oliver

Volume 24 (1982)
The Cytoskeleton, Part A: Cytoskeletal Proteins, Isolation and Characterization
Edited by Leslie Wilson

Volume 25 (1982)
The Cytoskeleton, Part B: Biological Systems and *In Vitro* Models
Edited by Leslie Wilson

Volume 26 (1982)
Prenatal Diagnosis: Cell Biological Approaches
Edited by Samuel A. Latt and Gretchen J. Darlington

Series Editor
LESLIE WILSON

Volume 27 (1986)
Echinoderm Gametes and Embryos
Edited by Thomas E. Schroeder

Volume 28 (1987)
***Dictyostelium discoideum:* Molecular Approaches to Cell Biology**
Edited by James A. Spudich

Volume 29 (1989)
Fluorescence Microscopy of Living Cells in Culture, Part A: Fluorescent Analogs, Labeling Cells, and Basic Microscopy
Edited by Yu-Li Wang and D. Lansing Taylor

Volume 30 (1989)
Fluorescence Microscopy of Living Cells in Culture, Part B: Quantitative Fluorescence Microscopy—Imaging and Spectroscopy
Edited by D. Lansing Taylor and Yu-Li Wang

Volume 31 (1989)
Vesicular Transport, Part A
Edited by Alan M. Tartakoff

Volume 32 (1989)
Vesicular Transport, Part B
Edited by Alan M. Tartakoff

Volume 33 (1990)
Flow Cytometry
Edited by Zbigniew Darzynkiewicz and Harry A. Crissman

Volume 34 (1991)
Vectorial Transport of Proteins into and across Membranes
Edited by Alan M. Tartakoff

Selected from Volumes 31, 32, and 34 (1991)
Laboratory Methods for Vesicular and Vectorial Transport
Edited by Alan M. Tartakoff

Volume 35 (1991)
Functional Organization of the Nucleus: A Laboratory Guide
Edited by Barbara A. Hamkalo and Sarah C. R. Elgin

Volume 36 (1991)
***Xenopus laevis:* Practical Uses in Cell and Molecular Biology**
Edited by Brian K. Kay and H. Benjamin Peng

Series Editors
LESLIE WILSON AND PAUL MATSUDAIRA

Volume 37 (1993)
Antibodies in Cell Biology
Edited by David J. Asai

Volume 38 (1993)
Cell Biological Applications of Confocal Microscopy
Edited by Brian Matsumoto

Volume 39 (1993)
Motility Assays for Motor Proteins
Edited by Jonathan M. Scholey

Volume 40 (1994)
A Practical Guide to the Study of Calcium in Living Cells
Edited by Richard Nuccitelli

Volume 41 (1994)
Flow Cytometry, Second Edition, Part A
Edited by Zbigniew Darzynkiewicz, J. Paul Robinson, and Harry A. Crissman

Volume 42 (1994)
Flow Cytometry, Second Edition, Part B
Edited by Zbigniew Darzynkiewicz, J. Paul Robinson, and Harry A. Crissman

Volume 43 (1994)
Protein Expression in Animal Cells
Edited by Michael G. Roth

Volume 44 (1994)
***Drosophila melanogaster:* Practical Uses in Cell and Molecular Biology**
Edited by Lawrence S. B. Goldstein and Eric A. Fyrberg

Volume 45 (1994)
Microbes as Tools for Cell Biology
Edited by David G. Russell

Volume 46 (1995)
Cell Death
Edited by Lawrence M. Schwartz and Barbara A. Osborne

Volume 47 (1995)
Cilia and Flagella
Edited by William Dentler and George Witman

Volume 48 (1995)
***Caenorhabditis elegans:* Modern Biological Analysis of an Organism**
Edited by Henry F. Epstein and Diane C. Shakes

Volume 49 (1995)
Methods in Plant Cell Biology, Part A
Edited by David W. Galbraith, Hans J. Bohnert, and Don P. Bourque

Volume 50 (1995)
Methods in Plant Cell Biology, Part B
Edited by David W. Galbraith, Don P. Bourque, and Hans J. Bohnert

Volume 51 (1996)
Methods in Avian Embryology
Edited by Marianne Bronner-Fraser

Volume 52 (1997)
Methods in Muscle Biology
Edited by Charles P. Emerson, Jr. and H. Lee Sweeney

Volume 53 (1997)
Nuclear Structure and Function
Edited by Miguel Berrios

Volume 54 (1997)
Cumulative Index

Volume 55 (1997)
Laser Tweezers in Cell Biology
Edited by Michael P. Sheetz

Volume 56 (1998)
Video Microscopy
Edited by Greenfield Sluder and David E. Wolf

Volume 57 (1998)
Animal Cell Culture Methods
Edited by Jennie P. Mather and David Barnes

Volume 58 (1998)
Green Fluorescent Protein
Edited by Kevin F. Sullivan and Steve A. Kay

Volume 59 (1998)
The Zebrafish: Biology
Edited by H. William Detrich III, Monte Westerfield, and Leonard I. Zon

Volume 60 (1998)
The Zebrafish: Genetics and Genomics
Edited by H. William Detrich III, Monte Westerfield, and Leonard I. Zon

Volume 61 (1998)
Mitosis and Meiosis
Edited by Conly L. Rieder

Volume 62 (1999)
Tetrahymena thermophila
Edited by David J. Asai and James D. Forney

Volume 63 (2000)
Cytometry, Third Edition, Part A
Edited by Zbigniew Darzynkiewicz, J. Paul Robinson, and Harry Crissman

Volume 64 (2000)
Cytometry, Third Edition, Part B
Edited by Zbigniew Darzynkiewicz, J. Paul Robinson, and Harry Crissman

Volume 65 (2001)
Mitochondria
Edited by Liza A. Pon and Eric A. Schon

Volume 66 (2001)
Apoptosis
Edited by Lawrence M. Schwartz and Jonathan D. Ashwell

Volume 67 (2001)
Centrosomes and Spindle Pole Bodies
Edited by Robert E. Palazzo and Trisha N. Davis

Volume 68 (2002)
Atomic Force Microscopy in Cell Biology
Edited by Bhanu P. Jena and J. K. Heinrich Hörber

Volume 69 (2002)
Methods in Cell–Matrix Adhesion
Edited by Josephine C. Adams

Volume 70 (2002)
Cell Biological Applications of Confocal Microscopy
Edited by Brian Matsumoto

Volume 71 (2003)
Neurons: Methods and Applications for Cell Biologist
Edited by Peter J. Hollenbeck and James R. Bamburg

Volume 72 (2003)
Digital Microscopy: A Second Edition of Video Microscopy
Edited by Greenfield Sluder and David E. Wolf

Volume 73 (2003)
Cumulative Index

Volume 74 (2004)
Development of Sea Urchins, Ascidians, and Other Invertebrate Deuterostomes: Experimental Approaches
Edited by Charles A. Ettensohn, Gary M. Wessel, and Gregory A. Wray

Volume 75 (2004)
Cytometry, 4th Edition: New Developments
Edited by Zbigniew Darzynkiewicz, Mario Roederer, and Hans Tanke

Volume 76 (2004)
The Zebrafish: Cellular and Developmental Biology
Edited by H. William Detrich, III, Monte Westerfield, and Leonard I. Zon

Volume 77 (2004)
The Zebrafish: Genetics, Genomics, and Informatics
Edited by William H. Detrich, III, Monte Westerfield, and Leonard I. Zon

Volume 78 (2004)
Intermediate Filament Cytoskeleton
Edited by M. Bishr Omary and Pierre A. Coulombe

Volume 79 (2007)
Cellular Electron Microscopy
Edited by J. Richard McIntosh

Volume 80 (2007)
Mitochondria, 2nd Edition
Edited by Liza A. Pon and Eric A. Schon

Volume 81 (2007)
Digital Microscopy, 3rd Edition
Edited by Greenfield Sluder and David E. Wolf

Volume 82 (2007)
Laser Manipulation of Cells and Tissues
Edited by Michael W. Berns and Karl Otto Greulich

Volume 83 (2007)
Cell Mechanics
Edited by Yu-Li Wang and Dennis E. Discher

Volume 84 (2007)
Biophysical Tools for Biologists, Volume One: *In Vitro* Techniques
Edited by John J. Correia and H. William Detrich, III

Volume 85 (2008)
Fluorescent Proteins
Edited by Kevin F. Sullivan

Volume 86 (2008)
Stem Cell Culture
Edited by Dr. Jennie P. Mather

Volume 87 (2008)
Avian Embryology, 2nd Edition
Edited by Dr. Marianne Bronner-Fraser

Volume 88 (2008)
Introduction to Electron Microscopy for Biologists
Edited by Prof. Terence D. Allen

Volume 89 (2008)
Biophysical Tools for Biologists, Volume Two: *In Vivo* Techniques
Edited by Dr. John J. Correia and Dr. H. William Detrich, III